Nuclear shapes and collectivity investigated using lifetime measurements and γ-ray spectroscopy

Joa Ljungvall

Nuclear shapes and collectivity investigated using lifetime measurements and γ-ray spectroscopy

Joa Ljungvall

February 28, 2020

Contents

Part I

A Short Introduction

A "Habilitation à Diriger des Recherches (HDR)" is, in my mind, the recognition that the scientist in question has reached a level so that the scientist can in a meaningful way supervise the work of a student. I profit from the occasion to write my HDR to convince myself, and hopefully a few others, that this is indeed my case. Most of this knowledge consist of well established facts, on which the present day front-line research is based. I have tried to assure myself that I have some understanding of both the established facts as well as the present frontiers by summarizing theoretical methods, experimental achievements, and developments in this HDR. This means that the about 60 pages of text I have written for this HDR do not only treat what I have done. I expect the selected and included publications to cover most of that. The text written for the HDR is more general, and written with the goal to expand my horizon a bit. This also explains why the text treating the techniques surrounding Recoil Distance Doppler Shift methods and all technical issues around AGATA are rather short. My publications on the subjects are sufficiently detailed, and included.

The HDR beginning with the foundations of "Nuclear shapes and..." discussed in chapter 1. In chapters 2 and 3 the developments in the field since the end of my PhD thesis (May 2005) are treated. Here chapter 2 is a short snapshot of the status in 2005 and chapter 3 an interleaved description of how the field advanced and more in-depth looks, found in boxes, on topics which I have worked on. A final chapter 4 tries to position me in the future of nuclear structure research. As I have been involved in the study of nuclei of all mass ranges, both neutron rich and proton deficient nuclei, and studying both collective as well single particle aspects of nuclear excitations I feel a very short summary of this here is in its place. I think it makes reading the rest of the HDR easier. So in figure 1 I've summarized what I have done the years 2005-2019 by marking the regions in the Segré chart of nuclei where the studied nuclei are located. Topics typical this period are present, with focus on shell evolution in exotic nuclei and shape coexistence. Worth noting is also the long excursion into the terrain of heavy and super heavy nuclei. Although divided into four color-coded groups, to give the main theme for the experiment and the following publication, there is a common theme; The interplay between the terms of the Hamiltonian keeping nuclei spherical and states "single particle" like and parts driving different correlations in nuclei.

As I have worked with the development of AGATA, and the exploitation of AGATA, for the last 15 years chapter 5 is devoted to a short description of high resolution γ-ray spectroscopy and γ-ray tracking. Also here the idea to keep a coherent text about the generalities and boxes filled with contributions from me. There are also publications that relate to the "AGATA topic" in the included publications. Together with the chapter 6 covering the use of so-called "Plunger devices" for measuring picosecond lifetimes and g-factors of excited states, these two chapter also provides an outlook to the means that I think will be used to achieve the objectives as described in chapter 4. Again, to give an overview aiding in reading the rest of the HDR, my involvement in the development of instrumentation for nuclear-structure physics studies, not including the work done during my thesis, is summarized in figure 2. The top row illustrates what is my large involvement in the development of the Advanced GAmma Tracking Array, AGATA. I've been working with detector characterisation, modelling of detectors, pulse-shape analysis, and simulations and characterisation of the complete AGATA. In parallel with this work I've developed and coordinated the use of the Orsay Universal Plunger System in different version for use at the ALTO facility, and in two slightly different versions for use at GANIL together with the VAMOS spectrometer or the DIAMANT/NEDA setup.

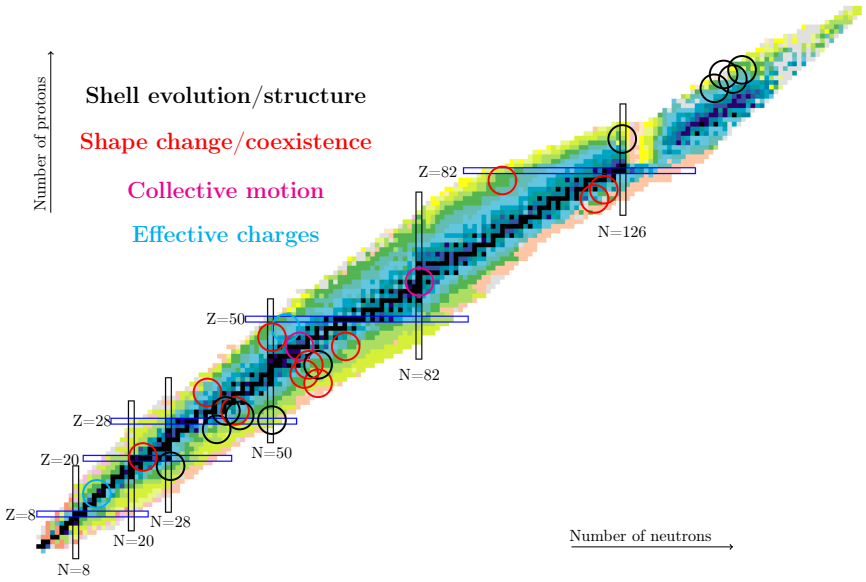

Figure 1: Nuclear chart showing an overview of my activities with nuclear structure physics

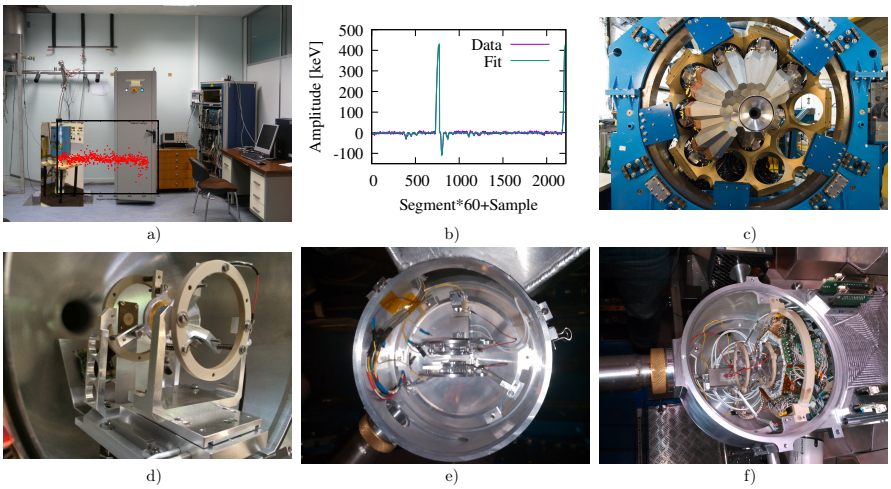

Figure 2: Instrumentation related activities, a) represents AGATA detector characterisation, b) pulse-shape analysis, c) characterisation and simulation of AGATA, d) is the Orsay Universal Plunger System (OUPS) Mk I, e) OUPS Mk II, f) OUPS MKIII

In most scientists career there are also the experiments that did not quite give a result, but might still have something in them to learn from... I have decided to profit and include some of this material in this manuscript, to leave a written trace of the work done and the possibility to not do the same mistakes in the future. Two such experiments are described in the chapters 9 and 10. These two chapters are in my mind more documentation than a part of this HDR.

Part II

Nuclear shapes and collectivity investigated using lifetime measurements and γ-ray spectroscopy

Chapter 1

Nuclear shapes, shape coexistence, collectivity, and their observables

Nuclei that are at closed shells develop non-spherical matter distributions. As the underlaying Hamiltonian is invariant under rotation this is an example of spontaneous symmetry breaking. The splitting of degenerate orbitals by the deformation, lowering some in energy whereas others increase in energy, allows to lower the total energy if the orbitals that were degenerate at spherical shape were not fully filled. This is in analogy with the Jahn-Teller effect as stated for atomic systems. Quadrupole deformed examples of nuclear shapes are shown in figure 1.1.

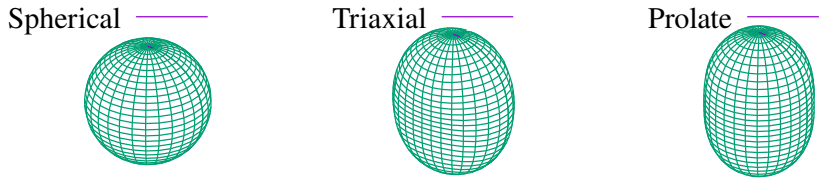

Figure 1.1: Examples of nuclear shapes. To the left a spherical shape. In the middle a triaxial shape where all three axes of the spheroidal shape are different, and finally to the right a prolate shape.

It is the breaking of the rotational symmetry that allows for excitations by rotating the nucleus. As mentioned this can be considered as an example of spontaneous symmetry breaking and the rotational excitation corresponds to the Goldstone modes. This is however not really enough if one wants to phrase nuclear rotations in this language as Goldstone modes for broken global symmetries are ”mass less”, i.e. they require zero energy to be excited. This is not observed as it would corresponds to degenerate rotational bands in nuclei. It is possible to make an analogy between nuclear rotations and the Higgs mechanism [1], providing a formalism that tackles this problem. By writing the nuclear Lagrangian as a one dimensional (the only independent coordinate is time) field theory where the nuclear quadrupole vibrations ϕ (a vector of five elements $\phi_{-2}, \phi_{-1}, \phi_0, \phi_1, \phi_2$) are interpreted as fields. As spherical symmetric

potential up to order four in the fields ϕ is combined with a kinetic energy term that is half of the square of the time derivative of ϕ. By adding a second order term to the potential the possibility of spontaneous axial symmetry breaking is created, as is the case for the scalar field associated to the Higgs field. By imposing a local gauge symmetry on this system, i.e. demanding it to be invariant under rotations with a time-dependent angle $\theta(t)$ a gauge field is needed to maintain the symmetry, which can be identified with the angular velocity ω of the rotating nucleus. This gives a Lagrangian of the form:

$$\frac{1}{2}|D_t\phi(t)|^2 - \frac{\mu^2}{2}|\phi|^2 - B(\phi \times \phi \times \phi) - C|\phi|^4 \tag{1.1}$$

where D_t is the covariant derivative $\partial_t - i\omega(t)L$, L the angular momentum operator. By setting μ^2 negative, as is done for the Higgs field, the vacuum gets a non-zero expectation value, axially symmetric deformation in our case. By developing the field ϕ_0 around this expectation value and inserting in into the Lagrangian 1.1 it can be shown how the fields ϕ couples to the "gauge field" ω, and generates its mass, in this case inertia. For the electro-weak case this corresponds to the Z and W bosons acquiring masses via the Higgs field, where "our" ϕ is the Higgs field and ω corresponds to the mass-less gauge fields that becomes Z and W bosons.

Staying within the view of the nucleus as a deformed object the most used model is the Bohr-Mottelson model of collective excitation in nuclei [2]. In this model it is assumed to be possible to write the wave function of the nucleus as a product of a function depending on only the orientation of the nucleus in space (Euler angles) and a function describing the shape of the nucleus: A spheroid object that can rotate as well as vibrate. This is a very successful model that provides us with the language used to describe collective excitation in nuclei, and its success is the rationalisation for discussing the shape of nuclei in an "internal reference system", i.e. body-fixed. It has however no direct connection to the nuclear many-body problem when this is thought of as a solution in terms of mixed single particle states to a many-body Hamiltonian (although it can be derived using the Coordinate Generator Method and use parameters calculated from, e.g., mean-field calculations and hence connecting the results to more microscopic models [3]).

Microscopic approaches to calculate properties of nuclei applicable all over the nuclear chart are the Energy Density Functionals. In the nuclear case they have emerged from Hartree-Fock like calculations. Because of the need for density dependent terms in the interactions to produce good results they are better called "Nuclear Density Functional Theories". A, at the limit of being excessive, simplification of these methods is that they as a first approximation aim to describe the true solution of the quantum system as a product of non-interacting single particles wave functions by minimizing the energy calculated from these single particles states (to be precise, the particle densities given by these single particle states) in a self consistent way. The "self consistence" means that the density given by the single-particle wave functions generates a potential that reproduces the single-particle wave functions. This way a large fraction of two (and more) body interactions can be absorbed into a one-body potential which allows a good description of the physics while remaining in single particle basis. As this is not done in an infinite basis that would allow an exact description, these correlations give wave functions that no longer preserve the symmetries of the Hamiltonian, i.e. the symmetries are broken. Examples are that of translation symmetry (wave function located in space), rotation symmetry (wave function has a preferred axis in space), and particle number conservation (wave function does not

have a sharp particle number). To compare observables such as transition rates with experimental data these symmetries should be restored. This is done via "projection" methods. Staying in the scope of extreme simplification "projecting" is constructing a wave function which is the superposition of the symmetry breaking wave function transformed in all possible ways in accordance with the symmetry that should be restored. This generates by construction a wave function that has the wanted symmetry. It can also be shown that it is possible to find a weighting function that allows both this symmetry and minimizes the energy [3]. This weighting function is given by expanding it in functions that are eigenfunctions of the symmetry in question and then minimizing the total energy based on the variation principle. This is a specialisation of the Coordinator Generator Method also used to include beyond mean-field correlations [3, 4, 5].

The interacting shell model also gives useful descriptions of deformed and/or collective nuclei. The possibility to calculate deformed nuclei in a spherical basis, with as only symmetry breaking that of translation symmetry, was in the early days of nuclear structure not given and the connection between geometrical models and shell model calculations not clear. Such a connection was given explicitly by Elliot [6, 7]. Having notices that the Harmonic Oscillator plus a specific quadrupole-quadrupole form of the nucleon nucleon interaction follows a SU(3) symmetry he explicitly showed how to find the irreducible representations of this SU(3) within the SU(N) group. The SU(3) is here as an intermediary step to find the irreducible representations of the R(3) on the reduction of SU(3), i.e. the angular momenta included in each SU(3) irreducible representations. Here it was shown that the L values found had the correct $L(L+1)$ energy dependence on. He further showed that the SU(3) wave functions corresponded to $> 90\%$ of the wave functions of full diagonalisation. This of course suggests that the in-medium nuclear interaction is quite well described by a mean field and quadrupole interaction. In a second paper it was demonstrated how, from an intrinsic state labeled by its SU(3) quantum numbers and with given quadrupole moment, but not good angular momentum, rotational bands can be constructed using projection on good angular momentum. This provides the connection between an intrinsic state with a shape (for each SU(3) irreducible representation) and the rotational band. The SU(3) symmetry is not valid for heavier nuclei as the spin-orbit interaction breaks the degeneracy of the harmonic oscillator shells and hence the states needed to span the representation no longer have the same energy. For heavier nuclei the so-called pseudo spin symmetry generates levels that are close to degenerate allowing the use of pseudo-SU(3) to single out important configurations. It has also been realised that a large fraction of the "true" wave function can be given by only including only $\Delta j = 2$ sequences in harmonic oscillator shells (referred to as quasi-SU(3) [8]). This can also be traced back to the dominance of monopole and quadrupole components of the effective nuclear interaction. The combination of pseudo- and quasi-SU(3) has found applications both as guide to truncate model spaces and as a tool to explain the results of large-scale nuclear shell model calculations.

All collective states found in nuclei are not "rotational", and excitations in the form of vibrations are also found. Different types of collective excitations are differentiated by model independent quantities such as the ratio of excitation energies and transition probabilities as well as the coherence in, from models, extracted values of quadrupole moments. When moving from structures described as single particle states towards more collective structures the typical behaviour in an isotopic or isotonic chain is that of passing over an region of "vibrational behaviour" before entering a regime of static deformation and an yrast band in the form of a rotational sequence of states. This

change in structure, i.e. single particle towards collective, does not only come with changing number of nucleons but also with excitation energy, i.e., how the nucleons distributed over different orbitals in a nucleus. This gives rise to "shape coexistence" in nuclei [9, 10]. It can be defined as states at similar energy but very different structures. The canonical region for shape coexistence is around lead with shape staggering in Mercury isotopes and several known excited 0^+ states in neutron deficient lead isotopes. A modern view is that shape coexistence manifests itself not only close to the classic "magic numbers" but at all places where rapid changes in collectivity is seen in the Segré chart. Shape coexistence is a phenomena that offers stringent tests of nuclear models as small changes in the relative energy between the coexisting structures have large effect on some nuclear observables. Here the observables are not so much the excitation energies but rather lifetimes of excited states and Coulomb-excitation cross sections. If the basic spectroscopic information for a nucleus is well enough known lifetimes and Coulomb-excitation cross sections give model-independent values for electromagnetic transition elements, e.g. $\langle I_f||M(E/ML)||I_i\rangle$ where $I_f \neq I_i$ in the case of life times whereas Coulomb-excitation gives the possibility to extract also the sign and magnitude of diagonal matrix elements (i.e. transitions between different m states). The transition strengths are readily compared to calculations from different models and offer a larger sensitivity than just comparing the energy of the levels with calculations. Another interesting concept, presented by Kumar [11], is that of quadrupole sum rules. If one knows at least the few lowest transitional and diagonal matrix elements this gives an invariant definition of quantities that can be put into correspondence with absolute deformation, triaxiality, γ-softness etc. This way a extraction of nuclear deformation without reference to a specific nuclear model can be made.

Chapter 2

Nuclear Structure Physics at the end of my PhD

The material for this section is mainly drawn from the NuPECC Long Range Plan of 2004 [12], an admittedly biased sampling of publications between 2000-2005 in the Nuclear Sciences References [13], and with my contribution a posterior as a very strong weighting factor. The paragraph on the state on nuclear structure theory is my ten-line vision of what is written by Bender at al. [4], Caurier et al. [14], and Dean et al. [15].

In the beginning of this millennium the open questions in the nuclear structure fields where summarized by the European community as:

1. The limits of bound nuclei in terms of Z,N, and A.
2. The Z/N dependence of the nuclear force.
3. How does collectivity emerge.
4. How are nuclei built from the particles of the standard model?

With these larger questions in mind, or with the language of physics: assuring a non-zero projection on the hyperspace spanned by these large questions smaller tangible questions can be asked for which single experiments can add a part of the answer. Some of the ”hot” subjects at the turn of the century, fueled by fundamental questions as well as new experimental opportunities, were:

- The evolution of ”the magic numbers” when moving away from stable nuclei. First seen in the island of inversion in neutron-rich nuclei with masses around 20-30 amu, experimental techniques allowed the investigation of this phenomena both for heavier nuclei as well with higher precision for lighter nuclei and closer to the drip lines. The weakening of N=8, 20, 28, 40 and 50 was seen and the development of or suggestion of new ”magic numbers” such as N=16 or N=32 found. Examples are the mapping of the first ”island of inversion” [16, 17], investigation of the N=40 [18] sub-shell closure. There was intensive work trying to approach the N=50 shell closure [19, 20]. Many of the observation are understood as rooted in monopole part of the tensor interaction [21, 22].

- Closely connected to shell-evolution but to some extent viewed as subject of itself is that of shape, shape-evolution and shape coexistence. Regions of interest related to shape coexistence were neutron deficient lead nuclei, nuclei around the N=Z Se and Kr isotopes [23, 24]. But also close to the N=60 Zr and Sr isotopes [25, 26]. Super deformation as well as exotic shapes transitions ("Jacobi" shapes) were also often present in discussions.

- The combination of high-performance separators, high-beam intensities and large γ-ray spectrometer arrays allowed for an important push forward in the spectroscopy of very heavy nuclei. Spectroscopy in these lighter nuclei was viewed as giving access to orbitals that are crucial for the island of stability. Prompt and decay spectroscopy nuclei such as ^{253,254}No [27, 28], ^{250}Fm [29] are performed.

- The question of three-body forces, and to what extent they are needed and how to include them in nuclear structure calculations is discussed [30, 31, 32].

- Efforts to see and characterise ^{100}Sn using different experimental techniques [33, 34].

- Is there a strong T=0 n,p pairing? This question was investigated using spectroscopy of high-spin states in N~Z nuclei [35, 36] as well as using mass measurements [37].

- Isospin non-conserving interaction terms, probing the charge symmetry and charge independence of the nucleon-nucleon interaction. The rather large push forward in this topic came as a direct consequence of the technical development on the γ ray spectrometer side and on shell-model calculations. This is described in detail by Bentley et al. [38].

On the theoretical side, as of the middle of the first decade of this century, the combined development of computer power and algorithms to solve the numerical problems, had allowed both energy density functional based theories and the interacting shell model to better understand and separate the "many-body" aspect of the problem and the "interaction" aspect of the problem. For neutron-rich nuclei the role on the monopole part of the effective interaction of the tensor component is pointed out. For the shell model exact solution for light nuclei clearly showed the need for, at least, a 3-body force in order to reproduce both excited states and the total binding energies. Further more, efficient truncation schemes based on the quadrupole dominance in nuclear structure allowed meaningful calculations of even super deformation in a interacting spherical shell model.

The different versions of energy density functional methods (Relativistic, Skyrme, and Gogny and all versions of them) had started to extensively use what is often referred to as "beyond the mean field", i.e. the restoration of symmetries or phrased a bit differently: provide wave functions with sharp quantum numbers where a symmetry suggests the quantum numbers should be sharp. As such they provide good spectroscopic description over all of the Segrè chart. However, although not obviously the right thing to compare, single particle energies from mean-field calculations were not always those deduced from experiments and the rapid (as interpreted) shell-quenching seen in exotic light nuclei was not reproduced.

Chapter 3

What has happened in the field since my PhD?

Where have we made progress in our understanding of the nucleus since 2005? These almost 15 years of time correspond to about 10 % of the lifetime of the nuclear physics subject. A small but non negligible fraction. A simple way is to compare the content of the NUPECC Long range plan from 2004 [12] with that one of 2017 [39]. Although phrased differently it stands clear that the "large" questions that were open when I finished my thesis in large remains unanswered, or to be more precise, only a bit more answered then they were in 2004. This does however not mean, as contradictory as it might sound, that no progress has been made. What it means is that nuclear physics is an old, and rather successful field forcing us to work hard for every increase in our understanding of the nuclei.

Before exploring the experimental advances and my contributions to these, I give my version of the development in the theory we use to interpret data and claim understanding with. During the this period substantial progress has been made in theoretical nuclear structure physics. Ab initio methods have been added to the nuclear shell model and energy density functional based nuclear structure theory methods. These models today give the solution to the "many-body" problem leaving us with the problem of finding the correct form of the nuclear interaction [40]. The ab initio label is typically given to nuclear models that use an interaction fitted on nucleon-nucleon and nucleon-nucleon-nucleon data and that uses controlled and systematically improvable approximations [41]. Today the interaction are often derived from Chiral effective field theory [42] where only a few constants taking care of unresolved high-energy physics are fitted to few-nucleon data. These interaction can then be used "as is" or after having been made "softer" using similarity transformations (that in itself induced multi-body interactions). Examples of ab-initio methods are the No Core Shell Model (NCSM) that solves the full A body system with a truncation at high energies [43]. This is viable to somewhere around oxygen isotopes. Other often used method for semi-magic nuclei are the Coupled Cluster methods [44], the in-medium similarity normalisation group [45], Quantum Monte Carlo methods [46], and nuclear lattice effective field theories [47, 48]. Examples of recent application (I will not differentiate between them) of ab-initio is in the calculation of ^{11}Be [49]. The problems in resolving the ordering of the lowest states in ^{11}Be is linked to the interactions used. The distribution the neutron matter in light N isotopes was addressed by Bagchi et

al. [50]. Here ab-initio calculations do a overall good job but fail to reproduce the evolution of the neutron skin as a function of neutron number. Ab-initio, and the coupled cluster method in particular, have been extensively used to interpret data on Calcium isotopes [51, 52]. Results concerning the quenching of the coupling between the weak force and the nucleon [53] have been presented as well as wealth of more shell structure oriented work [52, 54, 55]. Common for the ab-initio methods are that they are not yet as good as more phenomenological methods in terms of reproducing observables (absolute errors in energies are in the order of some to a few percent) and the conclusion that, as stated earlier, the low-energy limit of the strong interaction still is not fully understood.

The scientific basis for and the technical aspects of the interacting shell-model has not changed a lot the last 15 years and papers such as [8, 14, 32, 56, 57] and [58] still gives a good description of the field. However, the increased computer capacity together with refinements of algorithms used so solve the diagonalisation has allowed the user of larger and larger spaces, in some cases including more than 10^{10} states. With these increased valances spaces new shell model interactions have been developed such as LNPS [59], PFSDG-U [60], SDPFMU-DB [61], and A3DA [58].

For the energy density functionals (this is based on the review of Grasso [5]) the connection to Density Functional Theories used in atomic and molecular physics has been closely investigated (e.g. Messud al. [62]) showing that "our" use of energy functionals can be considered as sound (the unknown nuclear interaction stops us from calling what we do DFT, this in difference with atomic and molecular physics). With the importance of the tensor force having been shown for shell evolution investigations on its influence on mean-field calculations have been done (see [63] and references therein). A tensor terms seems needed but its actual impact is difficult to find as the fitting procedure used when constructing the energy functionals includes important aspects of the tensor interaction even without an explicit tensor term. Based on (failed) efforts to improve the classical energy density functionals [64] the community has tried to find new functional forms more closely connected to the nucleon-nucleon interaction, e.g. [65], or by including higher order derivatives of the density without direct connection to the bare nucleon nucleon force. The redefinition of the functional forms used in EDF calculations also comes from their use in beyond-mean field calculations. This is from both the possibility for double counting correlations as well as pathologies found when restoring broken symmetries using the coordinator generator method [66, 67, 68]. Beyond-mean field methods are now able to tackle even odd systems such as ^{25}Mg [69] with descent success but also here there are deficiency pointing to the need for other energy functionals.

Experimentally the question of shell evolution, i.e. the appearance of new shells closures and the disappearance of others has been thoroughly investigated. Staring at low masses the investigations of the "first" spin-orbit shell gap N,Z=6 where a combination of experimental methods and ab-initio calculations using modern 2N and 3N nuclear forces based on chiral effective field theory [70], showed that there indeed is such a gap. The last stable oxygen isotope ^{24}O is also suggested to be double magic with Z=8 and N=16 as new magic number [71]. This shell closure is driven by the same 3N forces that is used to explain "the oxygen anomaly", i.e. the low number of stable neutron-rich oxygen isotopes [72]. Moving towards heavier nuclei there are suggestions of "tensor force driven" new shell closures in neutron-rich calcium isotopes [73]. It has been shown that ^{78}Ni is a doubly magic nucleus. Based on experimental data and calculations performed with several state-of-the-art nuclear theory models it is concluded that there is a low laying deformed structure in ^{78}Ni, i.e. shape coexistence,

although higher in energy than the first excited 2_1^+ state [74]. This results excludes ^{78}Ni from the island of inversion in the region. The last known doubly magic nucleus without known excited states is ^{100}Sn. However, β-decay studies suggest that it is indeed a good doubly magic nucleus [75]. A longstanding question regarding the tin isotopes, the asymmetric collectivity around the neutron mid-shell with a surprisingly large B(E2)'s approaching ^{100}Sn has been given an explanation [76] using the Monte Carlo Shell Model. For neutron-deficient tin isotopes the quadrupole correlation energy for protons in the $1\pi g_{7/2}$ can compete with the pairing, something that is not true from N=66 and the expected typical seniority like nuclei reappear. The magicity of ^{132}Sn was confirmed in a transfer reaction study performed at Holifield radioactive beam facility, this by comparing deduced spectroscopic factors with that of ^{208}Pb [77].

Island of inversion at N=40 and beyond

Neutron-rich nuclei with Z close to the last harmonic-oscillator magic number (28) attracted interest as there are sub-shell closures at N=34,36 [78, 79] and a weakening of the N=40 harmonic oscillator shell moving away from the Z=28 Ni isotopes. From the second half of the first decade of this century there is a consensus that the increased collectivity when removing protons from nickel is the result of an increase in the numbers of neutrons in the $1\nu g_{9/2}$ orbital as the result of the decreased gap between it and the $1\nu f_{5/2}$ orbital. This rapprochement of orbitals is a result of the tensor force [21, 22] between protons in the $1f_{7/2}$ and neutrons in the $1f_{5/2}$ and $1g_{9/2}$ orbitals. The monopole part of the tensor force is attractive between protons and neutrons having anti-parallel spins (i.e. $1\pi f_{7/2}$ and $2\nu p_{1/2}$,$1\nu f_{5/2}$) and repulsive when the spins are parallel (i.e. $1\pi f_{7/2}$ and $1\nu g_{9/2}$). This way removing protons in the $1\pi f_{7/2}$ orbital decreases the gap between the $1\nu g_{9/2}$ and the $2\nu p_{1/2}$,$1\nu f_{5/2}$. This removes the (weak) N=40 gap. With the no N=40 gap quadrupole correlations energy can be gained by as both protons ($1\pi f_{7/2}$-$2\pi p_{3/2}$) and neutrons ($1\nu g_{9/2}$-$2\nu d_{5/2}$) have active quadrupole partners.

The iron isotopes $^{60-64}$Fe spans N=32-36 and are therefore of interest to address questions concerning the onset of collectivity close to N=40 and the question of N=32,34 sub-shell closures. An experiment was performed at GANIL using the EXOGAM γ-ray spectrometer for γ-ray detection coupled to the VAMOS spectrometer for event-by-event identification of the reaction product. The Cologne compact Plunger device [80] was used in inverse kinematics with a ^{238}U beam impinging on a ^{68}Ni target. A magnesium foil was used as a degrader in the plunger. This was a pioneering experiment that was carefully prepared by extensive simulations. The experiment, performed during autumn 2008, was successful and measured the lifetime of the first 2_1^+ states in $^{62-64}$Fe, and confirmed the lifetime of the 2_1^+ state in ^{60}Fe. The results showed clearly that not only the $1\nu g_{9/2}$ is populated as protons are removed from Ni, but also the $2\nu d_{5/2}$ orbital, being a part of the quasi-SU(3) scheme. The paper [81], cited 86 times as of February 28, 2020, is included as an appendix 7.2. Results, including ^{66}Fe, from MSU collaborated the conclusions [82].

The same experiment gave rise to exploitable data for the Cobalt isotopes ^{63,65}Co. Lifetimes for yrast $9/2_1^-$ states where measured as well as for the

$3/2^-_1$ state in ^{63}Co. Using these Dijon et al. [83] investigated if the $9/2^-_1$ states can be seen as a state with the structure $|(1\pi f_{7/2})^{-1} \otimes 2^+_1(\text{Ni})|9/2>$ and the $3/2^-_1$ states as $|1\pi f_{7/2} \otimes 2^+_1(\text{Fe})|3/2>$ as suggested by energy systematic. The conclusion is that this is not the case, and that such a simple model does not correctly capture the physics. An experiment with the same setup aiming at measuring lifetimes in ^{70,72}Ni was also performed in 2010. Unfortunately the 2^+_1 and 4^+_1 in ^{72}Ni were out of reach and the 2^+_1 in ^{70}Ni was known. Lifetimes in odd ^{69,71}Zn isotopes could however be measured [84]. The conclusion was that low-laying states in these nuclei can not be considered as a single neutron coupled to the even-even core and that to correctly describe them calculations need a valence space larger than $2p_1 1f_{5/2} 1g_{9/2}$.
The first experiment performed with AGATA@GANIL, for which I was one out of two spokespersons, was a continuation of the work performed on moderately neutron-rich iron nuclei. The aims of the experiment were very ambitious: Remeasuring the lifetimes of the 2^+_1 states in ^{62,64}Fe using $\gamma\gamma$ coincidences, measuring yrast lifetimes up 6^+ in the ^{62,64,66}Fe isotopes and finally to measure the g-factor of the 2^+_1 states in ^{66}Ni and the iron isotopes. This was believed to be possible thanks to the increase in efficiency of AGATA as compared to EXOGAM and improvements in the detection system of VAMOS. The physics goal of the experiment was to investigate to what extent the collectivity in the iron isotopes was developed by looking at the variation of B(E2) in the yrast band, and address questions regarding shape coexistence in the neutron-rich irons [85]. Compared to the ambitions the outcome of the experiment is not impressive. The reasons for this is however understood and identified:

- Instead of the 33 AGATA detectors that should have been installed an average of only 19 detectors could be used.
- The beam intensity that was possible on the target was one third of what had been achieved in 2008, at least in part because the shorter distances needed because of the shorter lifetimes of the higher laying states in the yrast band.
- Time was lost debugging both AGATA and VAMOS as this was the first real experiment. An example is the increased load on the entrance detector in VAMOS because of the elastic scattering on the Mg degrader foil.

The data was analysed in collaboration between me and a student at the University of Oslo, Malin Klintefjord. Lifetimes for the 4^+_1 states in ^{62,64}Fe were extracted, together with $11/2^-_1$ states in $61, 63$Co and ^{59}Mn. The resulting transition strengths were compared to large scale shell model calculations as well as beyond mean-field calculations. These results strengthen our understanding of the region, in particular the limit of the onset of the "island of inversion" close to N=40. The shell model calculations are in good agreement with experimental data whereas the beyond mean field calculations does not suggest a structural change close to N=40. The beyond mean field calculations suggest more of a vibrational structure for the neutron-rich irons. Details are found in Klintefjord et al. [86], also included as appendix 7.7.

Considerable experimental effort has also been invested in neutron-rich nuclei close to N=40, and even more moving towards N=50 during the second decade of the century [85, 87, 88, 89, 90, 91, 92, 93, 94, 95]. At the same time large theoretical efforts have been made, using shell models calculations [59, 96, 97, 60], interacting boson models [96], and different beyond mean field calculations [98, 99]. This body of work consolidates the idea of a N=40 island of inversion build on the same mechanism as the N=20 island of inversion, i.e. the lowering of intruder configurations by the strong quadrupole interaction in the residual proton-neutron interaction. In figure 3.1 this is illustrated for ^{64}Cr with the differences in occupation numbers for spherical orbits when performing a full Symmetry Conserving Configuration Mixing beyond-mean-field calculations and spherical mean-field calculations. The increased population of the $1\nu g_{9/2}$ and $2\nu d_{5/2}$ is a clear illustration of the quadrupole coupling and the usefulness of the quasi-SU(3) scheme for truncating shell model calculations. The strong connection between shape coexistence and "islands on inversion" has also been emphasized.

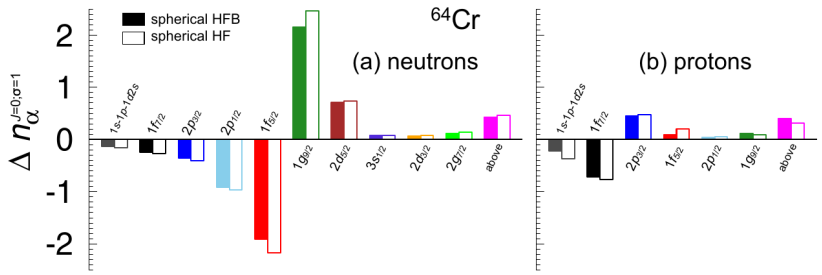

Figure 3.1: Illustration of the structure of the ground state of ^{64}Cr, located in the center of the N=40 island of inversion. The difference between the occupation numbers for spherical orbits calculated with the SCCSM method and the occupation numbers for the same orbits when using spherical HFB or HF (normal filling) approximations. Figure taken from Rodríguez et al. [99].

THE island of island of inversions is the one centered around ^{32}Mg. This region of the nuclear chart is rather well explored but high-precision g-factor measurements of the 2_1^+ states in the magnesium chain is missing. At CSNSM we have, together with A. Stuchbery of Australian National University, put in place a program to move towards the measurement of g-factors in the first island of inversion. A proof of principle experiment was performed using the OUPS at the ALTO facility, also giving exciting physics results [100]. The technique, Time Dependent Recoil-In-Vacuum modified for radioactive beams [101], is based on the hyperfine interaction between a 1s electron and the nuclear spin. As the magnetic field at the nuclear site for a 1s electron can be calculated from first principles the g-factor can be measured with, in principle, only statistical errors. A second experiment in this line of investigations was performed at ISOLDE in the end of 2017. The goal was to measure the g-factor of the 2_1^+ state in ^{28}Mg by the TDRIV technique and Coulomb excitation of the state in interest. The analysis was started as a part of the PhD of Amar Boukhari, for which I was co-supervisor. A part from being a stepping stone

towards the island of inversion it is quite possibly a sensible amount of "intruder" configuration to be found already in ^{28}Mg, something that a g-factor measurement is very sensible to.

The last 15 years there has been considerable progress made in our knowledge about how the nuclear shape evolves as Z,N, and/or excitation energy. It has been shown that shape coexistence is a rather generally occurring phenomenon. This has been possible, to a large extent, thanks to radioactive beam facilities such as REX ISOLDE, MSU/NSCL, GANIL, and RIKEN. For evolution of collectivity, shapes, and shape coexistence electromagnetic transition strengths and moments are key observables and it is therefore not surprising that the larger body of the experimental data is from Coulomb excitation measurements and lifetime measurements using plungers or fast timing.

Already in quite light nuclei examples of how shape and shape evolution is closely related to shell closures and shell evolution are found. In ^{30,32}Mg excited 0^+_1 states have been studied proving shape coexistence, the lighter isotope have a spherical ground state [102] whereas the heavier of the two has a deformed ground state and a what seems to be rather complicated excited 0^+ state [103]. This shape coexistence is created by the same mechanism that gives rise to the island of inversion. Shape coexistence is also found close to the N=28 shell closure, e.g., neutron-rich Sulfur isotopes where the deformed structure gains quadrupole correlation energy. A combination of a smaller N=28 shell closure and the change of relative positions for the $2\pi s_{1/2}$ and $1\pi d_{3/2}$ allowing $\Delta l = 2$ excitation for both protons ($1\pi d_{5/2}$-$1\pi s_{1/2}$) and neutrons ($1\nu f_{7/2}$-$2\nu p_{3/2}$). This is driven by the monopole part of the tensor force [104, 105, 106].

A classical region for the study for nuclear shape, is that of revisited region of germanium isotopes. The stable ^{72}Ge was Coulomb excited, using the γ-ray tracking array GRETINA to detect the γ rays. The result of this experiment, showing the interest in improving precision on old measurements using knew tools, show that ^{72}Ge can be understood on the simple picture of two mixed triaxial bands [107].

The often studied region around the nucleus ^{68}Ni has also given examples of shape coexistence in the nuclei $^{66-70}$Ni. This is well described by shell model calculations [108, 109]. With these examples shape coexistence has been found for all proton shell closures. For the neutron-rich Ni nuclei, which is unusual, shape coexistence has been suggested close the doubly magic ^{78}Ni (but also in ^{68}Ni) [74]. In ^{79}Zn a deformed isomer was investigated using laser spectroscopy and based on the magnetic moment it is speculated that one should include not only the $2\nu d_{5/2}$ orbital but also the $3\nu s_{1/2}$ orbitals beyond the N=50 shell closure [110] in order to correctly describe this in shell model calculations. In ^{84}Ge a large B(E2;$2^+_1 \rightarrow 0^+_1$) is found. This is explained as a consequence of the impact on the pseudo-spin partners (in this case the $1\pi f_{5/2}$ and $2\pi p_{3/2}$) from the change of the binding potential. This leaves the $1\pi f_{7/2}$ unaffected in agreement with observations [111], and an alternative explanation to that of the monopole part of tensor part of the nucleon nucleon interaction.

Shape coexistence at the N=Z line

Nuclei with N~Z~36 are located in a region where the shape of nuclei show rapid changes with both the number of protons, number of neutrons, and

with the excitation energy. Noticeable examples are oblate ground states in ^{68}Se [35] and shape-evolution and shape coexistence in light Kryptons [23, 112, 113]. This is understood in terms of the competing deformed shell gaps in the region, and have been addressed using different theoretical approaches such as the excited VAMPIR [114], axial beyond mean-field using the Skyrme interaction [115], and triaxial beyond mean-field using the Gogny force [116]. In figure 3.2 examples for axial and triaxial beyond-mean field calculations in the region are shown. The axial calculations by Bender et al. use particle number and angular momentum projected HFB states as generator functions for the generator coordinator method (CGM [3]), with the weights for each projected configuration found with by solving the Hill-Wheeler-Griffin equation. This corresponds to first solving the mean-field equations (dashed line in left top of figure 3.2) followed by projection on good angular momentum (solid lines) and finally allowing mixing of different intrinsic β_2 generating the physical states. This is illustrated by the labeled states in the upper left panel and by the curves in the lower left panel of figure 3.2.

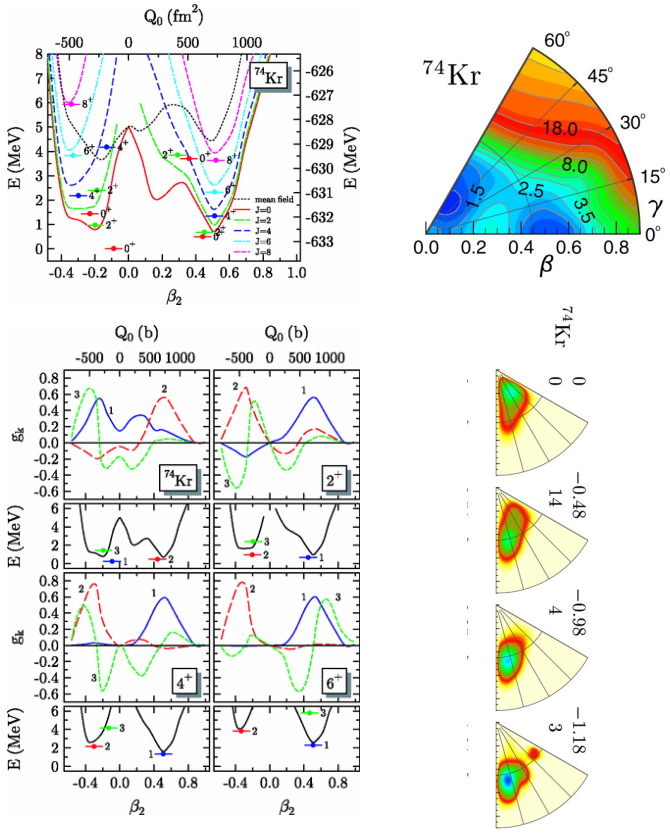

Figure 3.2: Axial and triaxial calculations for ^{74}Kr. Figure from Bender et al. (left) [115] and Girod et al. (right) [116]. The top row shows, with dashed line in the case of axial calculations, the energy for the mean field for ^{74}Kr. Below are shown the collective wave functions for the physical states.

In the approach of Girod et al. the CGM is combined with the Gaussian overlap approximation (GOA), generating an eigenvalue problem looking like an Hamiltonian where the masses and potential (”masses” include both the moment of inertia for rotation as well as collective masses for vibrations) are calculated from the solutions of constrained HFB calculations. This eigenvalue problem is then solved using a set of basis functions that have the correct symmetries imposed giving, i.e., restoring angular momentum as a symmetry to allow calculations of transition strengths and other spectroscopic quantities.

Experimental and theoretical work agreed rather well on the oblate ground state in ^{68}Se. Giving the similarity in moment of inertia found for the ground-state band in ^{70}Se and ^{68}Se it was a surprise when Coulomb excitation measurements [117] performed at REX-Isolde suggested that the ground state of ^{70}Se is prolate. A prolate ground state deformation for ^{70}Se was also deduced from Coulomb Energy Differences by Nara-Singh et al. [118]. Based on the experience gained by the nuclear structure group at Saclay with neutron deficient Krypton isotopes we proposed an experiment to remeasure lifetimes in the yrast band of ^{70,72}Se as these lifetimes are crucial for the interpretation given by Hurst et al. [117]. The experiment was performed at INFN Legnaro with the GASP [119] γ-ray spectrometer and the Cologne plunger device [120] using the reaction ^{40}Ca(^{36}Ar,α2p)^{70}Se to populate the states of interest. The experiment showed that the lifetimes of the 2_1^+ state in ^{70}Se from Heese et al. [121] were wrong. As these lifetimes were used by Hurst et al. to conclude on the shape this finding changes the interpretations, and the ground state of ^{70}Se is found to be oblate rather than prolate. The need of considering triaxial degrees of freedom was highlighted. This is described in detail in the publication "Shape Coexistence in Light Se Isotopes: Evidence for Oblate Shapes" [122], see section 7.1.
After 2008 the activity in this region of the nuclear chart has continued to be high. A multitude of experiments have been performed, mainly at fragmentation facilities [123, 124, 125, 126, 127, 128, 129, 130]. Calculations using microscopic-macroscopic models [131], shell model calculations [132, 133, 134], different version of Beyond Mean Field calculations [116, 135, 136, 137] as well as calculations based on the IBM models with its parameters extracted from Constrained HFB [138] have been performed. What has clearly come out of this work is that close to N=Z line triaxial deformation should be taken into account. For ^{70}Se and ^{70}Kr there is also a need for more data to see if the rather complex situation could be given a "simpler" shape coexistence explanation. Apart from the increased sophistication in the Beyond Mean Field calculations I like the concept of "shape entanglement" [132].

Nuclei around Z=40, N=60, i.e. ^{100}Zr, have been of interest for a long time. This because of the spectacular decrease in the energy of the 2_1^+ state when passing from N=58 to N=60 for the strontium and zirconium isotopes. As the Z=40 can not be considered a shell closure the mechanism for such a rapid change was for long not well understood. Recent data give example of shape coexistence deduced from Coulomb excitation measurements [139], lifetime measurements [140, 141], and in-elastic electron scattering [142]. The increase in collectivity has been explained using Monte Carlo Shell Model calculations [143], and is due to what has been dubbed "type-II shell evolution" where the promotion of protons impacts the effective single particle energies of the neutrons via the tensor force allowing the build up of quadrupole collectivity. The region of a sudden increase in collectivity at N=60 is limited by Z>36 [144]. Dudouet et al. also presents an interesting parallel between the Z~24 N=40 and Z=40 N~60 regions giving an explanations that corresponds to what is seen for chromium and iron isotopes close to N=40. In short one needs more than 36 protons to activate the quasi-SU(3) space ($g_{9/2}, d_{5/2}, s_{1/2}$). More recent work looking at the spectroscopy of ^{98,100}Kr moderates the conclusion that the deformed structures found in Sr and Zr are not present in Kr. These structures are present at higher energies, i.e.

shape coexistence [145].

The classic region of shape coexistence and shape evolution is neutron deficient lead and mercury isotopes. Continuous experimental and experimental efforts are made, with as an example the study of shape coexistence in mercury isotopes [146, 147]. Marsh et al. extend the measurements of averaged squared charge radii and explains the staggering seen for $^{180-186}$Hg as the result of competition between quadrupole correlation energy and pairing, where the "correlation energy" wins for odd neutron mid-shell nuclei due to blocking by the unpaired neutron.

Shape and collectivity in neutron deficient Os isotopes

The region of neutron deficient nuclei in proximity of the shell closure Z=82 shows a large number of examples of shape coexistence [9], making it an interesting region for nuclear structure research. A good example is that of ^{186}Pb with three 0^+ states close in energy [148]. Other nuclei in the region where shape coexistence have been shown are neutron deficient Polonium, Mercury and Platinum isotopes. The shape coexistence in this region is viewed as the result of proton excitation across the Z=82 shell gap [9], giving rise to highly deformed structures which are brought down in energy via the increased number of n-p interactions available in such configurations. This also explains why the intruder states are lowest in energy for a half full N=82−126 neutron shell. Lifetime measurements in Pb [149, 150, 151], Po [152], Hg [153, 154], and Pt [155] isotopes have corroborated this understanding of the shape coexistence phenomena. The model-independent measurements of the B(E2) values in the yrast bands have given firm experimental evidence for several low-energy configurations that are highly mixed at low spins. Beyond mean-field calculations support this picture [156], although the idea of "simple band mixing" is an oversimplification.

The question of shape coexistence in light osmium isotopes has been addressed several times over the last few decades [157, 158, 159]. Spectroscopy in $^{170-173}$Os and lifetime measurements in the yrast band of ^{172}Os are discussed in terms shape coexistence described by three-band mixing or particle alignment. More recent work concerning neutron deficient Os isotopes such as ^{162}Os [160, 161], including a lifetime measurement of the $17/2^+$ state in ^{167}Os [162], give evidence for a shape transition from prolate deformed via γ soft nuclei to spherical shapes close to the N=82 shell gap. For ^{168}Os shape coexistence is a possible explanation for observations [160].

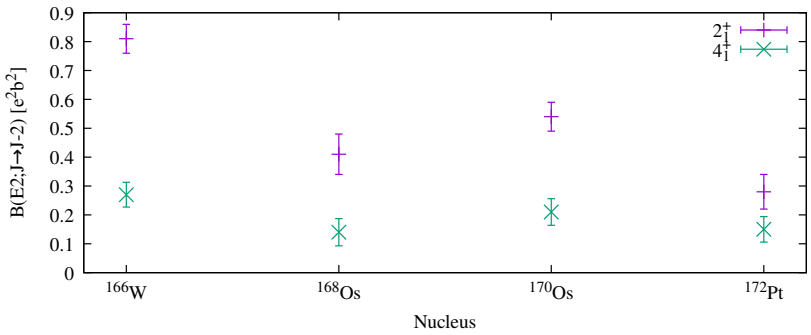

Figure 3.3: Transition strengths for the $4_1^+ \rightarrow 2_1^+$ and $2_1^+ \rightarrow 0_1^+$ for ^{166}W [163], ^{168}Os [164], ^{170}Os, and ^{172}Pt [165].

To try to clarify the question of shape coexistence in ^{170}Os an experiment was performed during 2012 to measure lifetimes in the yrast band of ^{170}Os using the ORGAM array and the OUPS [166] (see "OUPS box") at the ALTO facility [a]. Excited states in ^{170}Os were populated using the reaction ^{142}Nd(^{32}S,4n)^{170}Os. The target, evaporated onto a 2 mg/cm^2 thick Ta foil facing the beam, was made of isotopically enriched ^{142}Nd and had a thickness of 1 mg/cm^2. A 5 mg/cm^{2}Au thick foil was used as a stopper for the fusion-evaporation fragments. The experiment, a part of the post-doc project of Alain Goasduff, was successful and the data analysis was performed within the two years of the post-doc. However, as a paper was started do be drafted in 2014 it stood clear that the results that we had found were difficult to explain as the collectivity decreased from the 2_1^+ state to the 4_1^+ state, which was not supported by the beyond-mean-field calculations performed for the publication. This problem combined with the end of the post-doc of Alain Goasduff and my increased involvement in preparing and executing the first campaign of AGATA@GANIL led to that the osmium paper was put a side, without being forgotten. As a set of surprising results, shown in figure 3.3, from the same region showing the same anomaly as ^{170}Os in the yrast band were published [163, 164, 165] a renewed effort was made to finish the publication for ^{170}Os [167], see appendix 7.9. Looking at the energy systematics of the lowest yrast and yrare levels of the osmium isotopes, see figure 3.4, there is the increase in excitation energy moving away from the middle of the N=83-126 shell. Also seen is an indication that the 0_2^+ state will be above the 2_2^+ state in ^{170}Os. Calculations give in general a too stretched energy spectrum, and in particular too high laying 0_2^+ states. There is however nothing that could explain the decrease of the B(E2; $4_1^+ \rightarrow 2_1^+$) transition strength seen moving from ^{172}Os to ^{170}Os. Cederwall et al. [165] suggests that the explanation is to be found in a transition into a seniority like phase at N=92. The high collectivity of the 2_1^+ states and their conformity to systematics in the region are not properly given a satisfactory explanation in a seniority like scheme.

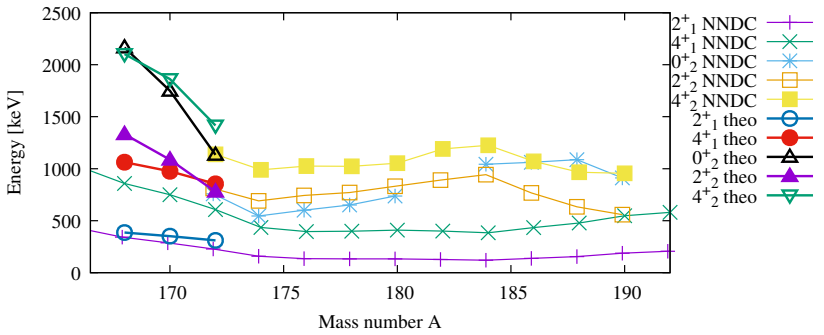

Figure 3.4: Energy systematics for the lower states in osmium isotopes. Beyond-mean-field calculations performed using the Symmetry Conserving Configuration Mixing method are also shown. The calculations were performed by T. R. Rodríguez.

[a] A comment in the proposal that in the future it could be possible to perform Coulomb excitation of Os isotopes at Spiral2 using the S3 spectrometer could deserve a comment but I will not...

Looking at the nuclei in the region showing the unusually low B(E2; $4_1^+ \rightarrow 2_1^+$) one can observe, see figure 3.3, that while the B(E2; $2_1^+ \rightarrow 0_1^+$) are different and in agreement with the distance to shell closures (N=82 and Z=82) the B(E2; $4_1^+ \rightarrow 2_1^+$) values are rather constant. An explanation to the low B(E2; $4_1^+ \rightarrow 2_1^+$) value found in ^{170}Os could have been that the 4_1^+ is not a part of the same band as the 2_1^+ state. However, the SCCM calculations do not support such a scenario. For ^{44}S [168], such a scenario was found i.e. that the 4_1^+ state is of single particle character and is produced by the alignment of a pair of nucleons. In figure 3.5 calculations expanded by performing PN-VAP including cranking and by extending the range of triaxial quadrupole deformations to $-60^\circ < \gamma < 120^\circ$ as done in Ref. [168] are shown. Such a single-particle state would manifest itself in these calculations by a minimum present for the PES calculated with $J_c = 4$ (third row in figure 3.5) not present for $J_c = 0, 2$. As no such minima are found the calculations are not capable of explaining the low B(E2; $4_1^+ \rightarrow 2_1^+$) value.

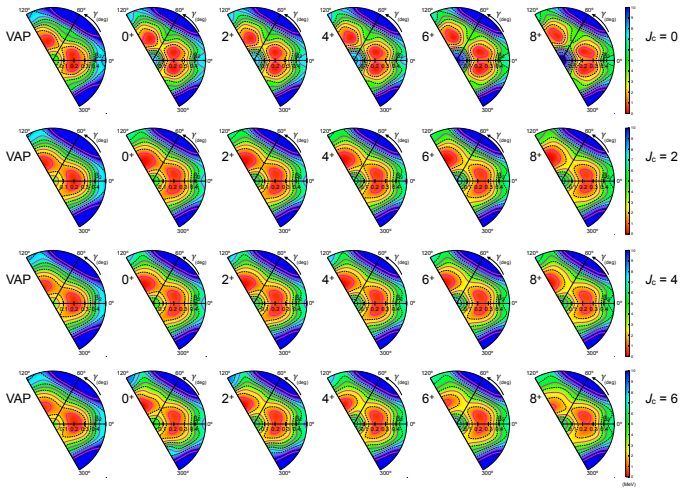

Figure 3.5: Potential energy surfaces for ^{170}Os generated by Variation After Particle number projection followed by projection on good angular momentum. This for four different rotational frequencies used for the cranking. Calculations by T. R. Rodríguez.

The unusually low B(E2; $4_1^+ \rightarrow 2_1^+$)'s found in the region around ^{168}Os raise questions. Are we looking at a common cause failure in the lifetime measurements? Is there yet to be understood new physics? Effort will surly be devoted to answering these questions despite the experimental difficulties given that these nuclei are for the moment only accessible via fusion-evaporation reactions making if difficult to try to measure the transition strengths using Coulomb excitation [b] or to populate non-yrast low-laying states in the reactions.

[b] Coulomb excitation at S3 would not have been without interest...

A nuclear physics highlight related to shapes in the last decade was the discovery of permanent octupole in ^{224}Ra [169]. Similar work on Radon isotopes has also been performed showing that although they perform octupole vibrations no static octupole deformation is seen [170]. Apart from the intrinsic interest in "exotic" nuclear deformations static octupole is of interest because their application in the search for static permanent electric-dipole moments. This is an indicator of physics beyond the standard model and nuclear structure physics enters via the Schiff moment (e.g. [171]).

The era of measuring the shape of very heavy nuclei has also arrived. With the help of a Penning trap connected to the SHIP separator at GSI the mean squared radius (or the difference with respect...) of the nobelium isotopes ^{253,253,254}No [172] were measured together with the magnetic dipole moment for ^{253}No [173]. The authors compare their results with energy-density functional calculations that are giving good

agreement between calculated and measured deformation.

Prompt spectroscopy of very-heavy and superheavy nuclei

Starting with the prediction from the 1960's [174] of an island of stability for superheavy nuclei around Z=114 and N=184, intensive experimental work to synthesis and/or find so-called super heavy nuclei has been performed. This work has mainly been divided between the synthesises of superheavy nuclei to explore the limits of the table of isotopes and the spectroscopy of lighter heavy nuclei. The often stated goal of spectroscopy of very-heavy and superheavy nuclei is to benchmark theoretical models as close as possible to the predicted island of stability. It is hoped that this way reliable predictions for the next magic proton and neutron numbers can be made. This is illustrated by an example taken from Dobaczewski et al. [175] shown in figure 3.6 where the single-particle levels, as given by relativistic mean-field calculations, for different deformations are shown. By comparing experimental determination of the ordering of the nuclear levels with such calculations at experimentally determined deformation the quality of the theoretical description can be scrutinized. The experimental determination of particle configuration in these very-heavy and superheavy nuclei can in some cases be done by prompt γ-ray spectroscopy using recoil- and/or recoil-decay tagging (for description of these methods see [176] and references therein). In such studies so-called K isomers [177] provide very pure configuration and hence excellent data for theory bench marking. Such an isomer and the rotational band built on top of it in ^{252}No was studied in an experiment at the Accelerator Laboratory of the University of Jyväskylä. Here the configuration of the 8^- isomer was determined to be spin singlet two-quasi neutron state with the configuration $7/2^+[624]_\nu \otimes 9/2^-[734]_\nu$ [178]. In close relation to this I also worked with the MUSETT segmented Si array for Recoil-Decay-Tagging studies at VAMOS [179].

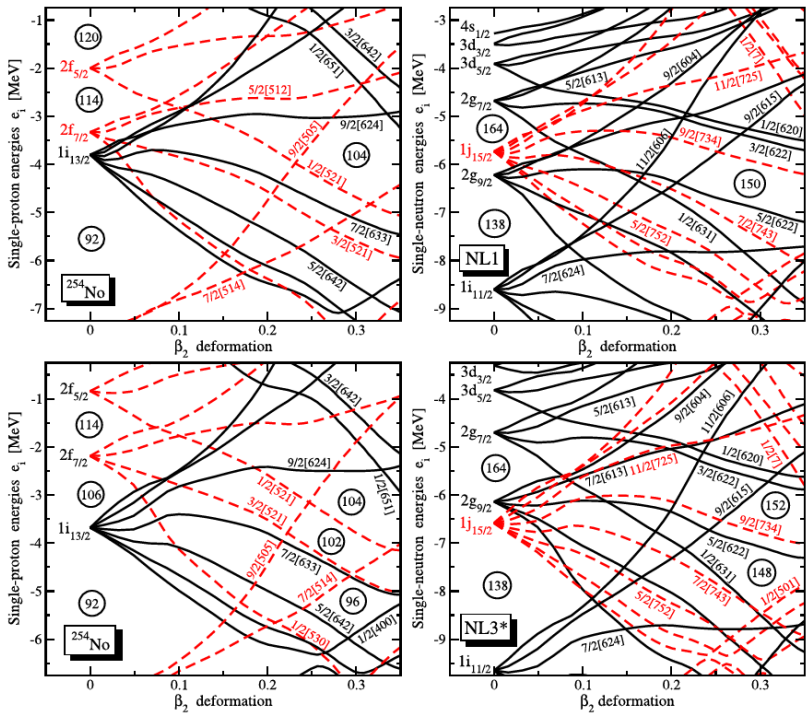

Figure 3.6: Illustration of the development of deformed shell gaps for ^{254}No as calculated using the NL1 and NL3* covariant EDFs. Figure taken from Dobaczewski et al. [175].

The experimentally determined deformed shell gaps of Z=100 and N=152 [176] for deformation of about $\beta_2 = .3$ are not yet correctly reproduced [175].

Starting at around the turn of the century, there has been an impressive collection of experimental data on heavy- and superheavy nuclei as well as progress in the production of superheavy nuclei. Today the element Z=118 is the heaviest nuclei that has been synthesized and its and the decay chains of Z=117 have been extensively studied proving not only existence of the isotopes but also allowing insights to shell structure from Q values and showing the need of using x-rays to identify the Z [180, 181, 182, 183, 184, 185].

A large extension of the spectroscopy of lighter nuclei has also been achieved. Here K isomers have been used to determine the orbital ordering in heavy nuclei. The limited number of possible ways to create the K-isomers allows for good comparisons between theory [186, 187] and experiments. It has also been suggested that K isomerism might offer longer lived states for superheavy nuclei than the ground states of the same nuclei [188]. K isomers are useful for assigning spin and parity to states is the prompt spectroscopy of odd nuclei [189, 190], but to move forward it seems as a new generation of γ-ray spectrometers, such as AGATA, is needed. For this reason most prompt spectroscopy has been performed on even-even heavy and superheavy nuclei. These studies have helped to confirm the existence of deformed shell closures at Z=100 and N=152. An example is that of ^{256}Rf [191]. A recent review

of in-beam γ-ray spectroscopy is given by Theisen et al. [192]. Spectroscopy after α decay is much used to determine the nuclear structure and also useful for assigning spin and parities to states allowing careful comparison with theory. It is found that theory often fail to reproduce the correct level ordering [193]. The question of where the next spherical shell closures are located remains open as the microscopic nuclear models still fail to reproduce spectroscopic data for lighter nuclei Z~100-108 and N~150-160 and the extrapolation to heavier system therefore remains shaky.

Chapter 4

Nuclear structure between now and the end of my life...

The general questions and open subjects are described in length in the NUPECC 2017 long range plan [39]. I will not repeat those here but instead explain how I see my involvement, using γ-ray spectroscopy and the measurement of collectivity, in the work of answering these questions. The focus will be on using Doppler Shift methods (in combination with Coulomb excitation). With this I do not make a statement about the merits of different techniques or the importance of observables, I just stay close "to home". I will also take me the freedom to be generous in the sense that no strict feasibility filter will be applied. And, there is of course the assumption of the existence of a high-performance γ-ray spectrometer such as a $3-4\pi$ AGATA.

The open question in nuclear structure physics can be phrased as [39] (over stricken means I think that what I do have no direct relevance):

- ~~How does the nuclear chart emerge from fundamental interactions?~~
- Where are the limits of stability and what is the heaviest element?
- How does nuclear structure evolve across the nuclear landscape and what shapes can nuclei adopt?
- ~~How does the structure change with temperature and angular momentum?~~
- ~~How to unify nuclear structure and reaction approaches?~~
- How complex are nuclear excitations?
- ~~How do correlations appear in dilute neutron matter, both in structure and reactions?~~
- ~~What is the density and isospin dependence of the nuclear equation of state?~~

The question about structure- and shape-evolution across the nuclear chart can be addressed with a few observables; the mass, the energy of the first excited state in even-even nuclei, and the reduced transition probability of the transition depopulating the first excited state. There is as well the spectroscopy of even-odd close to closed shell nuclei. The nuclei of great interest for which these observables are not

already measured (February 28, 2020), i.e. ^{60}Ca, ^{100}Sn, and nuclei close to the hard-to-get-to-region around ^{208}Pb will be addressed by experiments performed in large-scale collaboration at facilities such as RIKEN, HFRIB, or FAIR using state-of-the art detectors such as AGATA and GRETA. While this is clearly some of the most important work there is to be done I do not see myself as a driving force in it. This because what attracted me to nuclear structure physics in the first place was the "medium sized science" of it.

What I have in mind of trying to do instead is to look for "exotic" states in less exotic nuclei in experiment that can be performed at medium sized or even small facilities (but assuming state of the art detection systems). The number of experimentally known lifetimes for non-yrast states is illustrated in figure 4.1 where nuclei with known lifetimes for the first and second 2^+ and 4^+ are shown, respectively. It can be seen that the known non-yrast states are closely clustered around stable nuclei. This reflects that the best way of exciting the non-yrast states are with low-energy Coulomb excitation and hence requires stable targets or post-accelerated radioactive beams. These levels give important information about the wave functions and hence are excellent for probing our understanding of the nuclear system. Non-yrast states will be accessible via low-energy Coulomb excitation at facilities like Spiral1, HEISOLDE, and SPES, using HPGe detectors such as AGATA or MINIBALL to detect γ rays. The radioactive beams will also be combined with Plunger devices using non-conventional targets to allow transfer reactions in combination with the RDDS technique. This are also reactions that can be performed with high-intensity stable beams where powerful ancillary detector systems such as magnetic spectrometers and/or particle detectors adds large selectivity to select the reaction product. Near future possibilities includes studies of non-yrast states around N=40,50 and also the region of shape change around ^{100}Zr. This is a region of interest because it is accessible for calculations using the interacting shell model, mean-field methods and, although with less precision for the moment, in ab-initio calculations. To exemplify some physics cases from a letter of intent, for which I am the spokesperson, for the second AGATA at Legnaro campaign are given here:

Yrast and non-yrast states close to ^{68}Ni is accessible using multi-nucleon transfer reactions with either heavy beams (targets) for yrast states in more neutron-rich nuclei or lighter beams (targets) for less neutron-rich species non-yrast states. Here the general goal would be to complete existing information on transition strengths.

- Transition strength of non-yrast and "high spin" states close to ^{68}Ni.

Different versions of fission (fusion-fission, Coulomb induced fission etc) and multi-nucleon transfer reactions allow the population of nuclei around N=54 and N=86. These are regions with signs of substantial γ softness or deformation. As spectroscopic information now is rather abundant the next step to better characterize these nuclei and challenge the theoretical description of them (accessible both with large scale shell model calculations and symmetry restored energy density functional theory calculations) is to measure transition strengths of at least a few of the yrast states.

- Transition strengths in the region of γ softness N=54 and N=86.

Another observable is the g-factor, which is a sensitive probe of the occupation of orbitals. Recent work has shown how g factors probe the structure of 2^+_1 states in the semi-magic tin isotopes [194]. Nickel shares with tin that it has a closed proton shell, and has a large number of bound isotopes, which allows the study of how nuclear

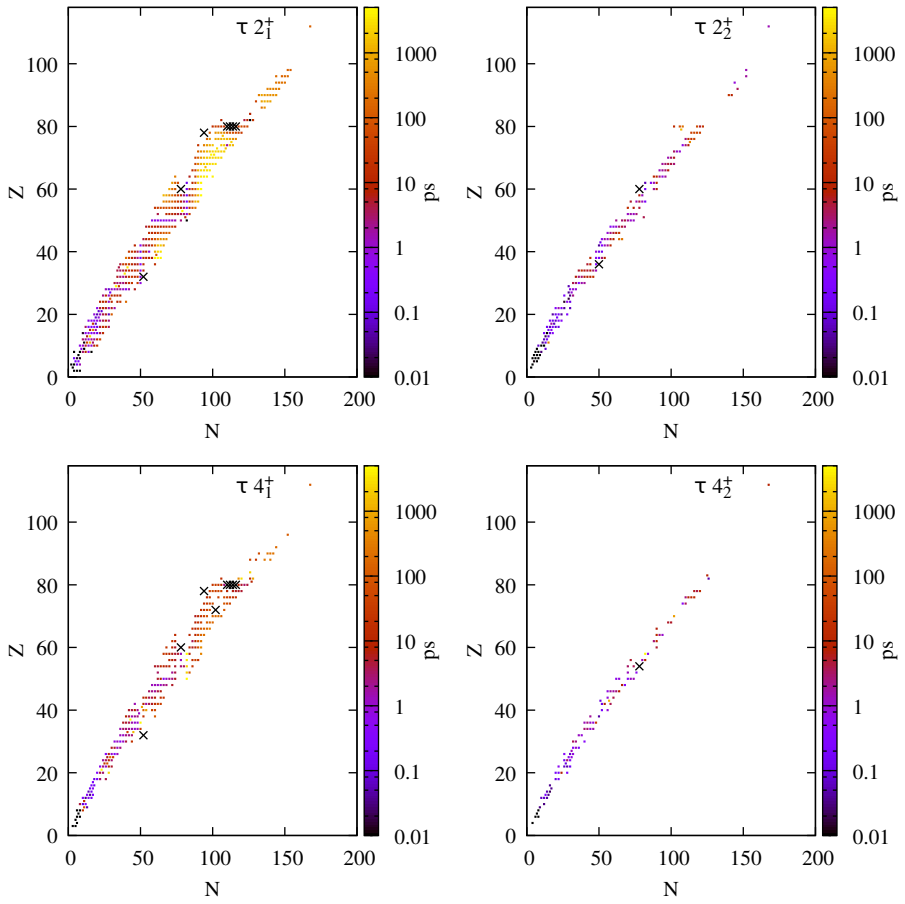

Figure 4.1: Illustration of how the number of datum decreases for non-yrast states and how they cluster around the valley of stability. The black crosses are new data from 2018-2019 from a quick search using NSR.

structure develops as neutron orbitals are filled. As recent shell-model calculations have proven capable of reproducing both excitation energies and transition strengths in nickel and iron isotopes close to ^{68}Ni, a natural next step would be to test them against g factor measurements. The picosecond scale lifetimes of the 2_1^+ states in ^{66}Ni and in $^{62-64}$Fe make it feasible to measure the g factors using recoil-in-vacuum methods. It should be recognized that the g factor measurements also depend critically on the lifetime of the state, and the alignment given in the reaction, which are not well known in advance. Vacuum deorientation effects must be evaluated in plunger-type lifetime measurements, making the determination of alignment and deorientation important also for estimating systematical errors in lifetime measurements. It is therefore important to explore the possibility to also extract the g factors from the lifetime data, along the lines of recent recoil in vacuum measurements on the neutron-rich Sn isotopes [194]. Multi-nucleon transfer reaction has proven capable of populating these moderately neutron-rich nuclei and the yrast states of interest. Here an AGATA covering a fairly large solid angle coupled to the PRISMA together with a Plunger device is an attractive setup for an attempts at measuring g factors in the region close to ^{68}Ni.

- Measure g-factors close to ^{68}Ni.

As amply discussed in this HDR intriguing results for the B(E2) strengths in the yrast bands for neutron deficient nuclei close to N=94 have been found the last few years [163, 164, 165, 167]. In this nuclei a lower B(E2;$4_1^+ \rightarrow 2_1^+$) than the have been measured. B(E2;$2_1^+ \rightarrow 0_1^+$). This observation has not yet a satisfactory theoretical explanation. As ^{170}Os can be produced with a high cross-section in fusion evaporation reactions, dedicated studies of both pure spectroscopy and transition strengths of higher laying yrast and non-yrast offers a good laboratory for investigating this surprising loss in collectivity with spin. As the fusion cross section is dominated by fission in this region, the coupling of AGATA with the recoil filter detector would be beneficial to clean the γ-ray spectra. Also, the use of a Plunger with a degrader foil together with the RFD can be envisioned.

- In-depth investigation of ^{170}Os.

I will finish my perspectives with a very ambitious and more worked out example. One of the experiments that I've proposed as a letter of intent with AGATA at several occasions is the measurement of lifetimes in the yrast band of ^{254}No with the RDDS technique. Such an experiment would be a tour de force using a Plunger, a γ-ray spectrometer such as AGATA, and a separator for recoil-tagging of the ^{254}No events. The motivation behind this experiment is that there are no measured absolute transition strengths for very heavy nuclei. There are theoretical predictions for B(E2) values in the yrast band of ^{254}No[195] based on the relativistic density functional DD-PC1, which are presented in figure 4.2. The goal is then to measure another type of anchor point for nuclear theory trying to predict the stability of superheavy nuclei and states in superheavy nuclei. This to make the extrapolation more reliable (is such a thing as reliable extrapolation exists).

What I humbly suggest is to measure the lifetimes of excited states in ground-state rotational band in ^{254}Nousing the RDDS technique with Oups plunger device coupled with a spectrometer such as VAMOS Gas Filled mode, the AGATA germanium array and the focal plane detector such as MUSETT [179].

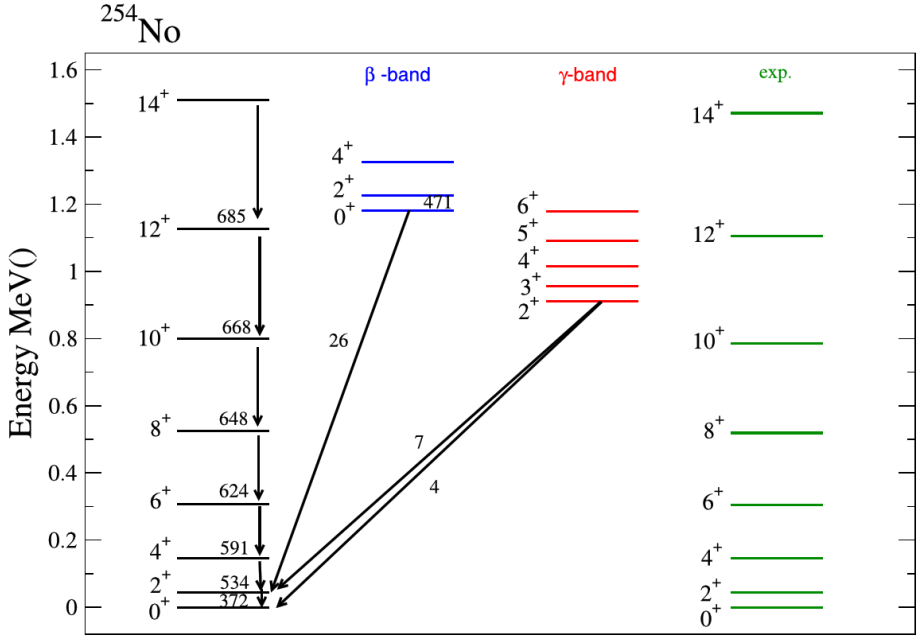

Figure 4.2: The low-energy collective spectra of ^{254}No calculated with the collective Bohr Hamiltonian based on the relativistic density functional DD-PC1 and a separable pairing force of finite range, compared to the experimental yrast sequences. The calculated B(E2) values, in Weisskopf units, refer to transitions depicted by arrows. Figure taken from Heenen et al. [195].

Considering the population mechanisms and the very large conversion coefficients for such heavy and deformed nuclei one would expect that states above the 8_1^+ or 10_1^+ are our best candidates when using the RDDS technique. This is advantageous as the lifetime of the lower spin members in the yrast band possibly can be measured using other techniques ("charged plunger", "in-trap decay"), and we would have the possibility to investigate if the yrast states are pure rotational states or if there are variation in the intrinsic quadrupole moment in the yrast band.

The proposed experiment uses the fusion evaporation reaction ^{48}Ca(^{208}Pb,2n)^{254}No in inverse kinematics which will populate ^{254}No with a cross section of about 2 μb. In order to use the RDDS technique, and have sufficient recoil velocity to pass a gas-filled separator inverse kinematics is the only option. After the separation by the gas filled separator the evaporation residues will pass through a focal plane detection system to measure the energy loss and give a timing signal. The residues will finally be implanted in a focal plane detector, providing the energy, the position and implantation time information of both the recoiling nuclei as well as their subsequent decay. Using Recoil Decay Tagging and recoil gates, clean γ spectra of the interested nuclei will be reconstructed. The long half life of the ^{254}No nuclei (55 s) and its relatively high production cross section could make it beneficial to the Recoil Decay Tagging method in order to gain statistics.

Table 4.1: Experimental Parameters

Reaction	
Target fronting	2mg/cm^2 ^{nat}Au
Target	0.5mg/cm^2 ^{48}Ca
Target Backing	0.5mg/cm^2 ^{nat}Au
Beam	16pnA ^{208}Pb
Degrader	5 mg/cm^2 ^{nat}Au or 2 mg/cm^2 ^{nat}Mg
Rate and beam time estimates	
Beam time request	Two effective weeks on target
Cross section to gsb	0.8μb
Transmission of ^{254}No	80%
Efficiency MUSETT	50%
Efficiency AGATA	10%
Magnetic rigidity [Bρ] in gas, Ghiroso [196]	
Residues (^{254}No)	1.78
Beam (^{208}Pb)	1.64
Scattered degrader (^{nat}Au)	1.59
Scattered Target ^{48}Ca	1.54
Scattered degrader (^{nat}Mg)	0.900

I would suggest an experiment with a 0.5 mg/cm^2 ^{48}Ca target, made as a sandwich between 2 mg/cm^2 gold upstream the target and 0.5 mg/cm^2 gold downstream the target. Taking into account the energy loss in the front of the target, a beam energy of 1039 MeV would be needed, giving a center-of-target energy of 950 MeV. A degrader foil of 5 mg/cm^2 gold or 2 mg/cm^2 magnesium would be used at a short distance downstream from the target in order to slow down the reaction products recoiling from the target. The fusion-evaporation residues, i.e. ^{254}No, will leave the target

with a velocity of about 8% of the speed of light. After the degrader the speed will be about 6% of the speed of light. This is a sufficiently large change to allow for peak separation when analyzing the RDDS data.

The first major challenges with such an experiment is the separation of the beam in the separator. This aspect has been investigated to some extent by C. Theisen while preparing the LOI that this paragraph is based on. In table 4.1 the expected magnetic rigidity of the different ion species are shown. The conclusion is that in a gas-filled separator such as the projected gas-filled VAMOS it would be possible to separate the wanted fusion-evaporation residues from other unwanted ions (beam, elastically scattered target and degraders etc.). The second important challenge for such an experiment would be that of the target itself. In order to protect the ^{48}Ca from oxidation and to be able to stretch it would have to be sandwiched in gold. This is a technique that works well with light beams (e.g. it was use for lifetime measurements in ^{70}Se [122] and ^{74}Kr [112]). How such a target would withstand the heavy ^{208}Pb is not clear.

If I convince myself all the problems can be solved and I try to make the most realistic simulation of the experiment the results are very promising. Using parameters for the reaction and efficiencies of the separator and focal-plane detection as given in table 4.1 for the basic kinematics. Further taking into account energy losses in target and degrader and straggling to refine the modeling of the peak shapes. Finally adding Coulomb excitation on the rather large amounts of gold, and a random γ-ray background (shape and amount calibrated on ^{254}No spectra from Jyväskylä) to make give more realistic spectra. For 1π AGATA (max useful solid angle for RDDS in this case) and 48 hours of beam time these simulations suggest that we would have spectra like those shown in figure 4.3.

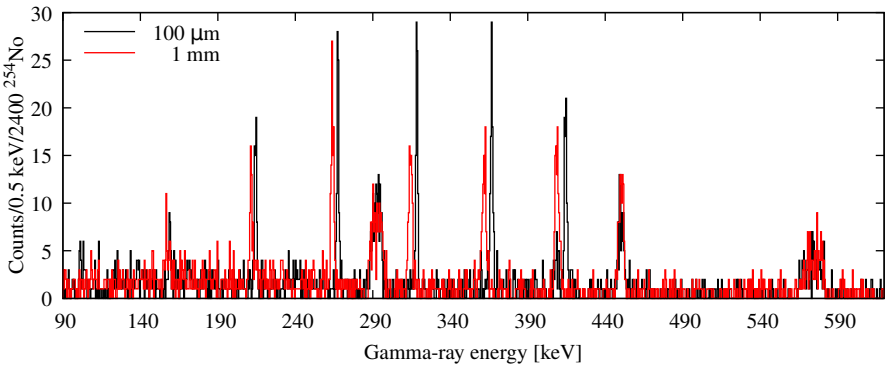

Figure 4.3: Simulations of the expected statistics for 48 hours of beam on target per distance. The simulation includes a background not coming from the gsb of ^{254}No. For details, see text.

Chapter 5

High resolution γ-ray spectroscopy

The energy scale for the atomic nucleus is MeV. So when nuclei deexcite the excess energy is mostly emitted as γ rays. For particle-bound excitations in the nucleus the width of the energy level is small as compared to its energy and compared to the average level densities with identical quantum numbers (e.g. spin and parity). As a consequence high resolution γ-ray spectroscopy is a valuable tool for investing the structure at low excitation energy in atomic nuclei. Furthermore, as the angular momentum and linear polarisation of the emitted γ rays can be measured the spin and parity of the state emitting the γ ray can often be deduced. Using more advanced spectroscopic techniques transition strengths, magnetic moments, and quadrupole moments can also be measured.

The ultimate in high resolution is given by Bragg diffraction spectrometers such as the GAMS [197] used with the high-flux reactor at Institut Laue-Langevin (ILL), Grenoble, France. Here a resolution of a few ppm can be achieved, but with a very low efficiency. This technique is used for performing complete spectroscopy, and lifetime measurements using the GRID technique. The low efficiency prohibits its use when $\gamma\gamma$ correlations are needed or in-beam experiments when heavy ions are used to populate excited states in the nuclei of interest. Here detector systems with higher efficiency are needed. If the demands on resolution is moderate, i.e. low γ-ray multiplicity experiments and simple excitation schemes, highly efficient scintillator detectors such as $LaBr_3$ or NaI are used with great success (e.g. DALI [198] and DALI2 [199] at RIKEN). As the average γ-ray multiplicity in an experiment increases or nuclei with more complex deexcitation schemes higher energy resolution is needed. This need is addressed using semi-conductor detectors, and in particular High Purity Germanium detectors. For more details on γ-ray spectroscopy see classic text books [200, 201].

5.1 The High-Purity Germanium detector

With an energy resolution of about 1-2 ‰, individual crystals up to 150% relative efficiency [1], and a peak-to-total of 25% High-Purity Germanium detectors is the detector technology that gives the best compromise between energy resolution, peak-

[1] Measured at a γ ray energy of 1332 keV and compared to a 2×2 inch NaI detector at 25 cm

to-total, and efficiency for γ-ray spectroscopy. If combined with different techniques to increase the peak-to-total (anti-Compton shields, γ-ray tracking...) HPGe detectors make excellent building blocks for large detector arrays for detailed γ-ray spectroscopy. For a recent and comprehensive review of the technology advances and use of HPGe detectors see [202].

5.2 AGATA

The Advanced GAmma-ray Tracking Array [203] is a European project born at the end of the 1990s. It capitalizes on the advancements made with the Euroball [204], EXOGAM [205], and MINIBALL [206] HPGe detector arrays. With arrays such as Euroball the sensitivity limit for high-spin experiments with the optimization of high Peak-to-Total (Compton shields) and low multi-hit probability (large number of detector elements) had been reached. The main limitation comes from the loss of effective solid angle due too the BGO Compton Shields. In parallel HPGe detector arrays were optimized for reaction using radioactive beams, such as Coulomb excitation and single particle transfer reaction, where the emphasis was on high efficiency and Doppler Correction. Without Compton Shields the HPGe crystals are positioned very close to the target giving a high detection efficiency for reaction with low γ-ray multiplicity (« number of detector elements). However, as the recoil velocity in general is rather high a good Doppler Correction capability was needed forcing the development of segmented detectors and pulse-shape analysis [207].

Once segmented encapsulated HPGe detectors were a proven reality the step towards γ-ray tracking was not long. By tiling a 4π sphere in irregular hexagons it is possible to close pack coaxial tapered HPGe crystals covering more than 80% of the solid angle. To keep an acceptable peak-to-total an alternative Compton suppression have to be used, which is the γ-ray tracking. This is made possible by the position sensitivity of the highly segmented HPGe detectors. In the case of AGATA, and the sister project GRETA in the USA, 36 folded segmentation is used. The outer contact of the crystal is segmented six times longitudinally and six times along its depth axis. This is shown in figure 5.1 together with the not yet segmented crystal, a sketch of the AGATA triple cryostat and finally an encapsulated crystal. All 37 seven signals are continuously digitized and sent to FPGAs where energy and time information is extracted if the central contact energy, corresponding to the total energy deposited in the crystal, is above a threshold (typically 10-20 keV). In that case the energy, time, and about 1 µs of signal is sent forward to perform pulse-shape analysis where the γ-ray interaction positions are calculated. After this step the γ-ray hits are sent to event building and the actual γ-ray tracking. This is illustrated in figure 5.2.

5.2.1 The AGATA detectors

The individual AGATA detectors are made out of HPGe crystals that are 90 mm long and have a diameter of 80 mm. In AGATA, as can be seen in figure 5.2 there are three slightly different shapes for the crystals. There are referred to Red, Green, and Blur or as A, B, and C. To extract the best possible energy resolution from such complex detectors care has to be taken to correct for crosstalk between the channels inside one crystal (this is enough for AGATA, however if less care is taken when designing the front-end electronics there might also be crosstalk between crystals). A novel feature is the use of pulse shape analysis to correct for neutron-damage induced trapping to

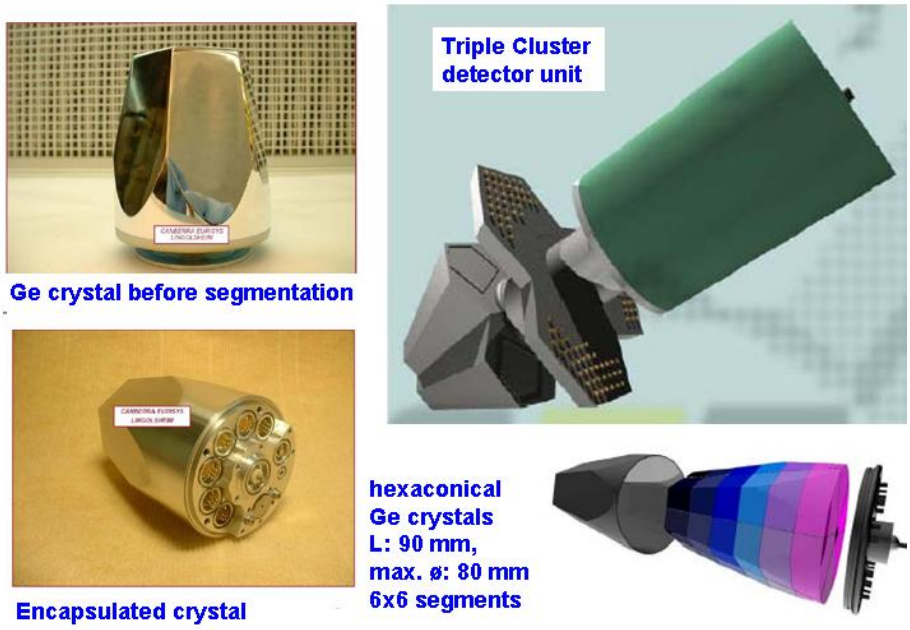

Figure 5.1: AGATA HPGe crystal and cryostat. The shaped Germanium crystal before segmentation is shown in the upper left corner of the figure. In the lower left corner the encapsulated crystal is shown. On the upper right side the AGATA triple cryostat is shown. Finally, the lower right corner is showing the segmentation of the AGATA crystals.

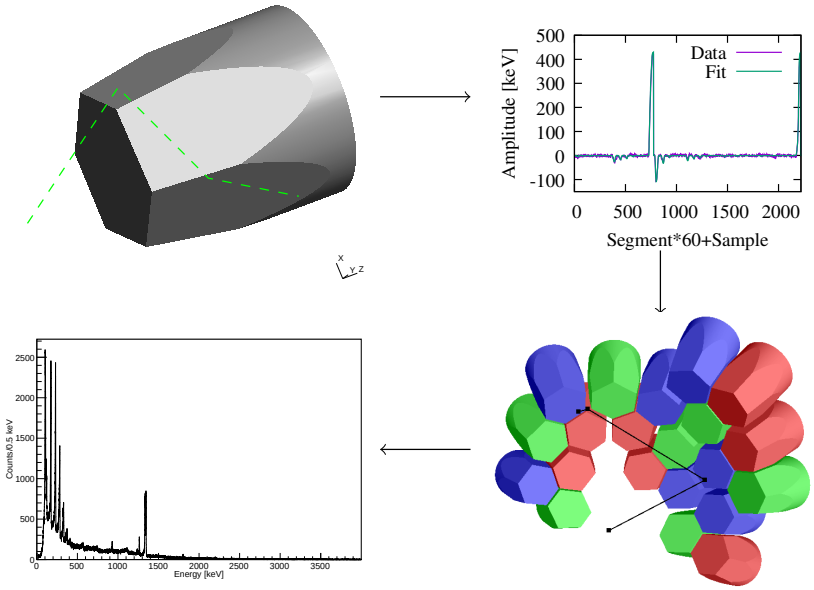

Figure 5.2: Schematic view over the γ-ray tracking detector array AGATA. In the top left corner an AGATA crystal is hit by a γ ray. Pulse shapes are shown in top right corner. The result of the PSA goes into the global frame for tracking, illustrated by the many AGATA crystals in the bottom right corner. Finally, the result of the tracking is a γ-ray spectrum, shown in the bottom left corner.

recuperate the energy resolution. Many excellent publication exists describing these detectors, cryostats [208], and calibration procedures used [209, 210, 211].

My contribution to Costumer Acceptance Testing and cross-talk measurements

During my post-doc at CEA Saclay I was involved in setting up the AGATA customer acceptance laboratory, shown in figure 5.3. I did participate in mounting several crystals in single-crystal cryostats. In order to accept the crystals a set of tests have to be performed. They included validation of the energy resolution of all 37 channels and characterisation of the crosstalk in the detector. The crosstalk is dominated by the capacitive coupling between the segments and central contact. There is also a small coupling between segments. These couplings are removed by the calibration procedure in the case of only one segment having a net charge, but generate a shift of the full energy peak in the case of multi-segment events, see figure 5.4. This has been modeled with high accuracy by B. Bruyneel et al. [209]. The electronics of the laboratory consisted of one analog channel used for reference measurements and a 40 channel digital DAQ system based upon 10 TNT2 card [212], each card measuring 4 channels. As a results of this timestamped events where written into 10 different files that were sorted and time correlated offline.

Figure 5.3: Photo of the AGATA test laboratory at CEA Saclay

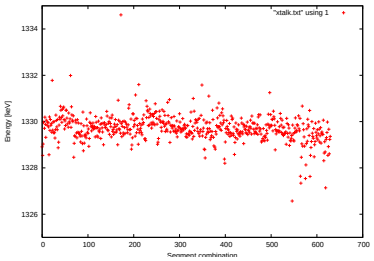

Figure 5.4: Example of crosstalk measurement of a AGATA crystal.

In addition to participating in setting up the laboratory I also wrote the software used for energy measurements and crosstalk characterisation. The software time correlates the data from the different TNT2 cards, performs energy calibration and creates ROOT trees [213] containing the calibrated and event-build data. Histograms for characterisation of the detector in either so-called singles or coincidence mode can also be created with the program. This software is still used at CEA and IPHC (as in 2019).

5.2.2 Detector modeling, characterization and PSA basis generation

It was understood early on within the AGATA and GRETA projects that a key for performing PSA is the fidelity with which the pulse shapes from the highly segmented HPGe detectors can be modeled (or experimentally determined). If this condition is fulfilled one can expect a PSA that gives accurate position information, has some capability to estimate the number of interaction inside a single segment with net-charge, and delivers a good estimate on the error of the deduced position. In the AGATA collaboration this work was taken on with a two-legged approach. The first leg being simulations of the detectors and the second leg being detailed measurements of the detector response as function of interaction position, referred to as scanning. Examples of packages for pulse-shape calculations are MGS [214], JAZZ [215, 216], and ADL [217, 218]. Scanning of detectors have been performed and is performed at several location within the AGATA collaboration (amply treated in [219, 220, 221, 222, 223]). Careful characterisation of the electronics response and innovative techniques to measure the space-charge profiles based on capacitance measurements have given valuable information about the detectors [208, 209, 224, 225, 226, 227]. Within the AGATA community the work of adapting simulations to this body of experimental data has been performed using the ADL by B. Bruyneel et al. [217, 218] in the IKP Cologne group. The result of this work is used in the form of the pulse-shape data bases used for the PSA in the AGATA.

AGATAGeFEM - A Finite Element Method based signal modeling program.

In the beginning of 2006 I started an effort to develop a pulse-shape calculation code. The difference as compared to what existed and was used within the AGATA community was that the description of the geometry was to be exact within machine precision for the transport of charge carriers and when solving the Poisson and Laplace equations. Therefore an adaptive finite element methods was to be used so that any geometry can be adequately described. The program, named AGATAGeFEM, is written in C++ and leverage quite heavily both object orientation and the template features of C++ (but very little C++11). For the charge-carrier transport the ordinary differential equation solvers of the Gnu Scientific Library [228] were chosen. Typically a 4th order Runge-Kutta solver with adapted time step is used for the calculations. For describing the geometry two different version exist, one written in its totality by me and one that use the geometry packages of geant4. Earlier versions of the program used mainly a library called dealii [229, 230]. Dealii is a very flexible code that allows an iterative refinement of the FEM mesh in a very simple way. However, the mesh cell geometry is limited to quadrilaterals and hexahedra. This is for solving the partial differential equations very good choices. I did, however, not want to project down the solutions to a regular grid when using them in charge-carrier transport processes and calculations of the induced signals via the Shockley-Ramo theorem, the quadrilaterals and hexahedra are however challenging. Behind this is the idea that the refinement procedure tells where high granularity is needed and all projections to regular grids deteriorates this information. The problem is then that to find the correct cell in an irregular mesh one has to ask cells if a point belongs to

them or not. Hexahedra cells have boundaries that are curved making these calculations quite flop intensive. As a result the first version of AGATAGeFEM was capable of calculating about 2-3 pulse-shapes per second. While this is enough to calculate a basis for use with PSA it is far from enough for using the code in fitting of parameters used in the pulse-shape calculations or to use it in a complete Monte Carlo simulation chain. I therefore moved the FEM part of the program into using the libmesh library [231]. It uses tetrahedra with each side defined by three points making the calculation whether a point is inside a cell or not much faster. I further more restrained to the use of only linear basis function in the solution. This way the code reproduced the results from before but is almost a factor of 100 faster.
Other features of the AGATAGeFEM is that it is fully parallelized using both threads and the MPI interface. Field calculations are parallelized by using one MPI process per field that is calculated. If the libmesh library was built with thread support further threads are used for each field. Pulse-shape calculations and χ^2 fitting of the parameters that enter into pulse-shape calculations are also parallelized with a combination of threads and MPI. The χ^2 fitting is based on the Minuit and Minuit2 [232] that comes with ROOT [213]. ROOT has further been used to create an interface allowing calculating of both fields and pulses. The fields and pulses can also be displayed inside the chosen detector geometry from the ROOT interpreter interface (the cint and cling interpreter). AGATAGeFEM has further a very simple server client mechanism allowing other programs to ask the server to calculate pulse shapes.
All the needed miscellaneous codes for applying pre-amplifier response (defined in time domain), cross talk, to re-sample pulse shapes, compare pulse shapes, calculate pulse shapes from the output of the AGATA geant4 MC [233] etc. are also included in the AGATAGeFEM.
Details can be found in a planned publication 7.11. As written in the OASIS application (see section 7.13) the AGATAGeFEM code will be used in an effort to improve our understanding of the detectors and where to concentrate our efforts to improve the final result.

A method to scan the response as a function of position using an uncollimated source was developed and tested using simulated pulse shapes (using MGS [214] and AGATAGeFEM) and pulse shapes from the Liverpool scanning table [234, 235]. The use of an "in-situ" method can help to solve many issues of the PSA as the pulse-shape bases created includes effects such as crosstalk, time alignment between different segments etc.

In-situ determination of a pulse-shape basis for PSA

I initiated a project together with GANIL to test the ideas of Desesquelles et al. [234, 235] on source data taken at the GANIL site. The work was performed in close collaboration with two post-docs at GANIL, Hongjie Li and Caterina Michelagnoli.
The method proposed by Desesquelles et al. is based on finding experimental estimators of the interaction position of a γ ray that can be calculated from the pulse shapes. The estimators should have monotonous relations to the coordinates of the interaction position. Having found such estimators re-

alistic simulations are performed giving the "true" distributions of interaction positions from the γ rays. The distribution of the experimental estimator can then be matched with the simulated distribution of interaction positions. This is done starting from one side of the simulated distribution and the distribution of the experimental estimator and demanding the fraction of total area in the two distributions that coincide. This is illustrated in figure 5.5.

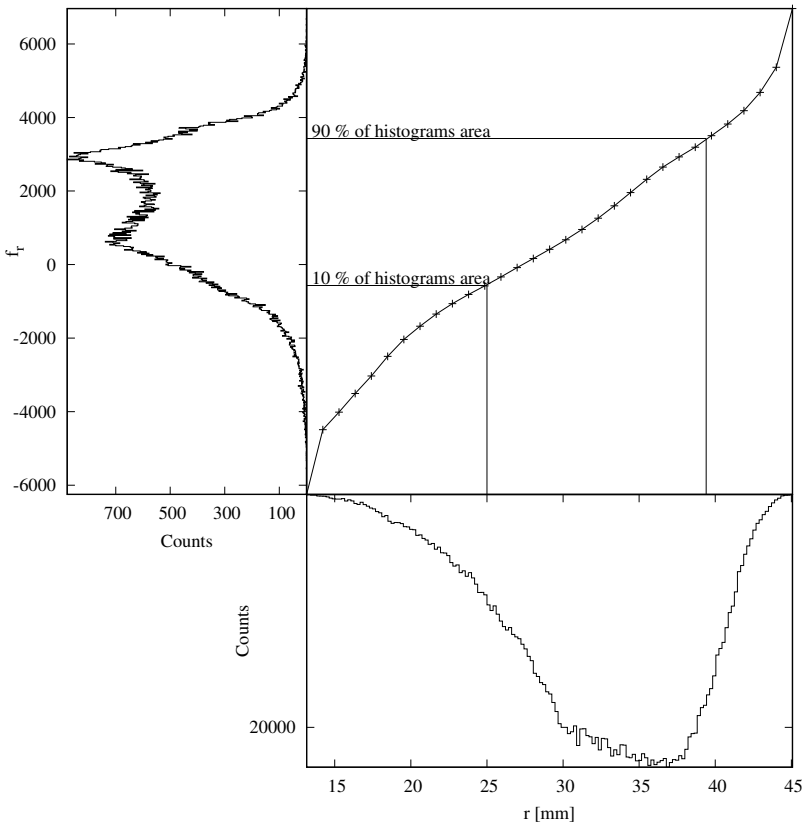

Figure 5.5: Example of matching the relative area for the simulated distribution and the distribution of the experimental estimator. The y axis (f_r) is the experimental estimator for the radial coordinate. On the x axis the simulated distribution of the radial coordinate of interaction points is given (r).

This work is published, see Li et al. [236], and I refer to this paper for further details.

5.2.3 Pulse-shape analysis

For γ-ray tracking to work a prerequisite is the correct determination of the positions of the γ-ray interactions. Because of the finite distance needed for the energetic electron created to lose all of its energy a lower limit of a position resolution of about 1 mm is expected. This is to be (favorable) compared with the 5 mm FWHM resolution needed for γ-ray tracking.

Many different methods for pulse-shape analysis (PSA) have been tried within the AGATA and GRETA community. In the AGATA community grid search (GS) [237], extensive GS [237], particle swarm minimization [215], matrix method [238], genetic algorithm [239], recursive subtraction [240], and neural networks (mainly for timing) [241] have been tried. The GRETINA (and GRETA) collaboration uses similar approaches, "With a realistic set of basis signals, signal decomposition is reduced to the task of fitting the waveform data, event-by-event, with the best possible linear combination of basis signals." [242]. In real life experiments, as of 2019, there is one big difference between how PSA is performed in the AGATA and GRETA collaborations: In the AGATA collaboration PSA allows for only one interaction point per segment, whereas the PSA done in the GRETA collaboration allows for more than one interaction in a segment. Comparing to Monte Carlo simulations the consequences of this are that within the AGATA community the number of interactions made by a γ-ray is underestimated whereas the GRETA collaboration overestimates this number [243]. This is one of the problems the OASIS ANR project tries to address. The OASIS ANR application is included as an appendix to this work, section 7.13.

The different approaches used all have in common that they compare a set of pulse-shapes for known positions in the detectors with the experimental pulse shapes. A metric of the type $\sum_i \left|y_i^{exp} - y_i^{bases}\right|^a$ is used. For $a = 2$ this is just the square sum. The grid search codes of AGATA [237] has been shown to give the best result with $a = 0.3$. This is indicative of the possibility to improve the bases used in the PSA. As, in the beginning of 2019, no error estimates are made there is no need to include an estimate of the noise on the experimental signals. Adding error estimates is considered as an important step forward. Considerable efforts have been put into estimating the performance of the PSA within both the AGATA [244, 245, 246] and GRETA/GRETINA collaborations [247, 248]. The conclusions from these efforts are that the resolution needed for γ-ray tracking is achieved. This is however a conclusion that is somewhat contradicted by γ-ray tracking optimisations, discussed in detail in section 2, taken from the ANR application for the project OASIS.

My efforts related to PSA in the AGATA project

In 2005 the first in-beam experiment with the AGATA symmetric triple cluster was performed. The goal of the experiment was to measure the position resolution for γ-ray interactions in the AGATA prototypes. The symmetric triple cluster consists of three 36 segmented symmetric HPGe crystals, and served as the prototype to the asymmetric triple clusters [208] used in AGATA today. Doppler Correction capabilities was chosen as the method to measure the position resolution. The experiment used a ^{48}Ti beam with an energy of 100 MeV impinging on a 220 μg/cm^2 deuterated titanium target, with the reaction ^{48}Ti(d,p)^{49}Ti populating excited states in ^{49}Ti. Outgoing protons where detected in a double sided silicon strip detector, allowing for suppression of background from Coulomb excitation and the reconstruction of the direction of the outgoing ^{49}Ti nucleus. A picture of the setup is shown in figure 5.6.

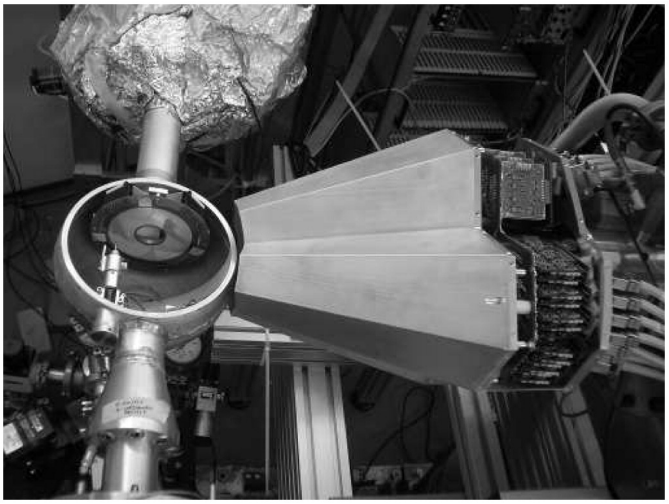

Figure 5.6: Photo of the experimental setup used to measure the position resolution of the AGATA triple cluster prototype. To the left inside the target chamber the double sided silicon strip detector is visible with the AGATA triple cluster in the center of the picture. Picture taken from Recchia et al. [244].

The process of extracting the position resolution from such an experiment passes via Monte Carlo simulations of the experiment taking into account all other effects than the position resolution of the PSA. By varying the assumed position resolution for the γ-ray interactions the FWHM of the γ-ray peak of interest as a function of position resolution is created and compared to the experimental FWHM of the γ-ray peak of interest. This is described in detail in [244].
At the time of the experiment (Aug-Sep 2005) the signal bases used for the PSA were calculated using the MGS code [214] developed at Strasbourg. The work of analysing the data was shared between different groups in the AGATA collaboration. I took the responsibility to analyse the data using two different PSA approaches, the so called MINIBALL approach [206] and the matrix-inversion method [238].
In figure 5.7 the result for the grid-search algorithm presently used (with some modifications) is compared to the result from the MINIBALL and Matrix PSA algorithms. The MINIBALL algorithm can only be used for events with one net-charge segment, and it was used as a baseline reference. The Matrix algorithm developed by Desesquelles et al. [238] is based on the fact that an experimental signal can approximately be built up as a superposition of signals originating from fixed positions by giving a non-negative weight to each position. This problem is formulated as a matrix inversion problem solved using the non-negative least squares algorithm of Hanson and Lawson [249]. To further improve the signal-to-noise ratio a singular value decomposition is used. As can be seen in figure 5.7 the results are disappointing as compared to what was expected on the basis of the results on

simulated but realistic signals. The explanation is thought to be lack of fidelity for the basis of signals used. Given this and the improvements in the signal bases, improved treatment of crosstalk, and determination of the t_0 that have been made [209, 217, 218, 224, 225, 226] a renewed effort concerning the Matrix PSA is well worth considering. This is particularly true as it provides event-by-event error estimates on the given interaction positions.

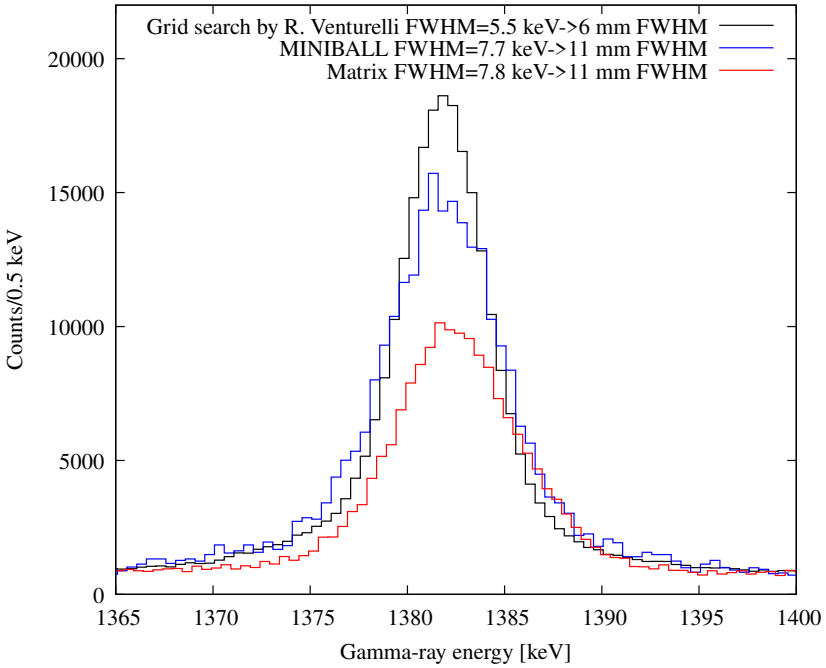

Figure 5.7: Comparison between different PSA methods used to analyse the data from the AGATA symmetric triple cluster test experiment performed at IKP Cologne in Aug-Sep 2005.

As data from the Liverpool scanning table (see Dimmock et al. [250, 251] and references therein) became available I also tried the Matrix PSA using a pulse-shape data basis calculated using MGS on the data from the scanning table. This work, combined with efforts to try to coordinate work with PSA and detector characterisation was presented within the AGATA collaboration. It was decided that the DAQ of AGATA was to be based on the NARVAL [252]. As NARVAL is written in the programming language ADA an interface to allow the implementation of different algorithms in C (and hence C++) was defined by X. Grave (IPN Orsay) and J. Cresswell (University of Liverpool). Using this interface I created an architecture of a PSA base class on which any PSA algorithm class can inherit and be used together with the AGATA DAQ. The first, (and of 2019 still only fully) algorithm to be fully included in the AGATA DAQ was the grid search algorithm [237], with the first version implemented by me.
Using the code AGATAGeFEM (see publication in progress 7.11) I've also investigated the resolution for Grid-search methods and the Singular Value De-

composition methods as a function of noise and inclusion of differential and linear crosstalk. Assuming that the detector physics of a segmented germanium detector is well known, the problem of determining the coordinates of a γ-ray interaction in a large volumes HPGe detector dependence closely on the knowledge of the response of the electronics and on the signal-to-noise ratio. These two aspects have been studied by performing PSA on a data set calculated using the same code used to calculate the reference data set of pulse shapes. On this reference set of shapes different amounts of noise were then added. Each position where then analysed 20 times, each time with different noise added. Also added were linear and differential cross talk. This has been done both for the grid-search method and for the matrix method [238]. The conclusion is that, if it is correctly added to the basis, cross-talk does not have an influence on the result of PSA, and that for very noisy signals the SVD matrix inversion method performs better than grid search. A paper is being prepared on the subject, see section 7.11.

5.2.4 Gamma-ray tracking

Gamma rays with energies in the interval of tens of keV to a few MeV, as those emitted when nuclei deexcite, are absorbed in a HPGe detector by a photoelectric event, preceded by one or several Compton scatterings. At the upper edge of the energy range pair production starts to become important whereas at the lower edge direct photoelectric absorption dominates. In figure 5.8 the cross sections for photoelectric, Rayleigh scattering, Compton scattering, and pair production are shown. Although Rayleigh scattering does not produce an energy deposition in the detector, the direction of the photon changes.

The concept of γ-ray tracking array is based on energy-angle relation of Compton scattering,

$$\Delta E_\gamma^i = E_\gamma \frac{(E_\gamma/m_e c^2)(1-\cos\theta^i)}{1+(E_\gamma/m_e c^2)(1-\cos\theta^i)}, \tag{5.1}$$

and the extraction of the position of each interaction of the γ ray providing an alternative way of deducing the scattering angle θ^i, namely

$$\cos\theta^i = \frac{\overrightarrow{r_{i-1}r_i}\cdot\overrightarrow{r_i r_{i+1}}}{|\overrightarrow{r_{i-1}r_i}||\overrightarrow{r_i r_{i+1}}|}. \tag{5.2}$$

Looking at equation 5.1 one sees that the energy of the photon (E_γ) before the scattering is needed. From equation 5.2 one deduces that at least three positions are needed. There are two main families of solutions to these problems, γ-ray Forward Tracking (FT) and γ-ray Backtracking (BT). In the case of BT, tracking is performed by first identifying an interaction point with an energy of more than 100 keV (and if possible less than 250 keV), as this most often corresponds to the final photoelectric absorption. The closest point to this start point is then chosen and the total energy before scattering can be calculated as then sum of the two interaction points. This in turn allows for the calculation of the scattering angle. If this angle coincides (to some specified precision) with the assumed emission point of the γ ray the track is considered as complete. If the angle does not point towards the target a search for

another interaction point in the track is performed. This is repeated until no more γ-ray tracks can be constituted. For details see [253, 254].

The Forward Tracking algorithms work by first clustering interaction points together. Looking from the emission point of the γ rays all points within a solid angle are assumed to belong to one γ ray. Cluster with different opening angles are created. An interaction point can be part of more than one cluster. By assuming that the total energy of the γ ray is the sum of the interaction points in a cluster equations 5.1 and 5.2 can be used to calculate a figure of merit for each possible permutation of the order of interaction points, starting from the emission point. The clusters are then ordered according to the best figure of merit. All cluster that have a too bad figure of merit are rejected. For details of different implementation see [255, 256, 257].

Early in the AGATA project the two tracking philosophies were evaluated [257] and it was concluded that FT is most suitable for an array such as AGATA. The tracking code developed for this work, the Orsay Forward Tracking (OFT) code is also one out of two tracking codes used within the AGATA collaboration.

It is useful to point out that the devil is to be found in the details. How is the figure of merit calculated for the different implementations of forward γ-ray tracking? One can compare angles as given by interaction positions and interaction energies, one can compare the cosine of the angles, or one can compare energies calculated from angles (as is presently done in OFT). Without the smearing coming from the momentum distribution of the electrons and the experimental uncertainties the results would of course be the same, but as the real data even occasionally gives results that are nonphysical (e.g. $|\cos\theta| > 1$) and the high non linearity of trigonometric function the choice seems to matter. Exactly how much is under investigation (as of February 28, 2020).

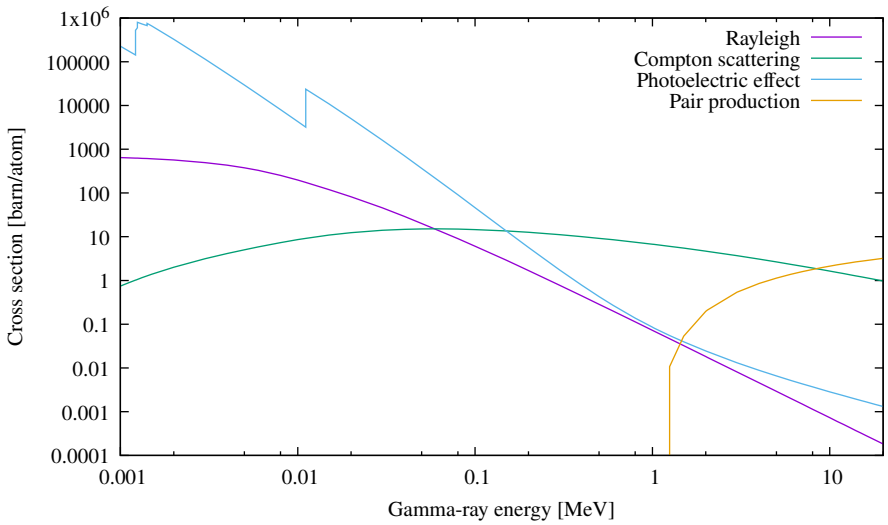

Figure 5.8: Cross sections of different processes for γ-ray interactions in Germanium.

5.2.5 Monte Carlo simulations

Early in the AGATA project a Geant4 [258] based Monte Carlo simulation was developed by Enrico Farnea et al. [233]. This code has then been developed and added to by

a large number of persons. It is extensively used in the planning of experiments and in the writing of proposals. To a lesser extent the code is also used when analyzing data to, e.g., determine peak shapes or find normalisation for the extraction of angular correlations. It has been benched marked against experimental data with good results [259, 260]. As AGATA moved from Legnaro to GSI, and then to GANIL site specific functions were added to the code, especially in developing both built in and external event generators. The code is presently hosted at a svn server at the STFC Daresbury Laboratory.

Work done by me with and for the AGATA MC simulation package

When AGATA was to move from GSI to GANIL I got involved in the simulations of the expected performance. This included simulations of the expected efficiency and simulations of Recoil Distance Doppler shift experiments. The first step in this process was to benchmark the physics of the simulations and of the event generators I added. To do this I added a "test" geometry consisting of a sphere. All particles are stopped and the energy deposited locally when they intersect the sphere. This feature is implemented via the inheritance of a geant4 G4VProcess class that kills all particles when they enter the volume named "TestSpherePhys". This allows for simple investigation of quantities such as attenuation coefficients for γ rays, energy loss for heavy ions in materials etc. These test allowed the validation of the physics used in the AGATA simulations and the discovery of a few problems and bugs in the geant4 code [261, 262].
Having validated the basic physics of the simulations I added an event generator to include the kinematics of fusion-fission reactions and Coulomb excitations. During this time I also introduced features to include radioactive sources with a specific source strength and model the experiments with given beam intensities and beam structures. This work was done to a large extent for reasons not related to AGATA, but to model an experiment performed at GANIL in 2012 (see section 9). This work is to be detailed in a future publication (see section 7.12).

5.2.6 Performance of AGATA as of today (February 28, 2020)

The estimation of the AGATA performance on which the project is based came from early simulations. As such they represented an "ideal" detection system characteristics included. The actual performance of AGATA has as a consequence deviated a bit from the simulations. Quantifying and understanding from where the loss of performance comes is important to improve AGATA. It is not only this "bench marking" aspect of performance that is important. In many experiments one needs to know the efficiency of the detection as function of γ-ray energy, count rate, emission angle etc. The first large work to quantify the performance of AGATA was made during the first GSI campaign [259]. The efficiency of GSI AGATA was thoroughly measured using sources of known strengths and using the so-called coincidence method. The driving force behind was the need to exactly know the efficiency of AGATA in order to elucidate on the isomeric ratio in lead isotopes as a function of how they were produced [263]. During this work it was found that simulations overestimate the efficiency with respect to the real AGATA detector, this by about 10%.

Leader of the AGATA performance working group

There is a dedicated working group within the AGATA community to evaluate the performance of AGATA. As one of two leaders of this group I have been leading this work. By combining source data (^{152}Eu,^{60}Co) with in-beam data a thorough characterization of AGATA for the early to mid-GANIL campaign has been done. This work is presented in full in the included the paper presented in section 7.10 but some further details will be given here.
As the size of AGATA has increased, and with it the angular coverage, more effort has been put into using AGATA for angular correlations and distributions. This has proven a bit of a challenge and is of today (February 28, 2020) not fully resolved. An example of the issues presently found can be seen in figure 5.9. Here the angular distribution for the γ rays depopulating the $2_1^+ \rightarrow 0_1^+$ and $3_1^- \rightarrow 4_1^+$ in ^{46}Ti are shown together with fits of previous measurements [264] for the same reaction ^{16}O(^{36}Ar,α2p)^{46}Ti.

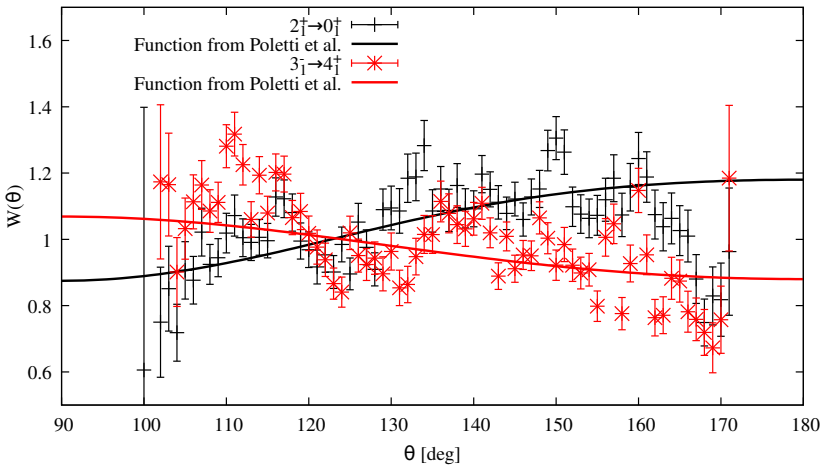

Figure 5.9: Angular distributions measured using AGATA at GANIL. The non-physical high-frequency structures seen are not understood.

It has proven difficult to produce angular distributions that are satisfying and give fits with low χ^2. This in contrast to $\gamma\gamma$ angular correlations that are rather straight forward (see 7.10). The reason for this is not yet understood but clustering effects such as those shown in figure 5.10 might be a reason, although it is not clear why even when normalizing with in-beam data these clustering effects are still present. In figure 5.11 the difficulty to normalize in-beam data is shown. The number of counts in each detector for the γ-ray of interest has been normalized using the γ ray closest in energy from the decay of ^{152}Eu. As can be seen the relative efficiency of each detector is not the same for in-beam and source measurements. This makes the use of source data for normalization of the solid angular coverage and efficiencies difficult.

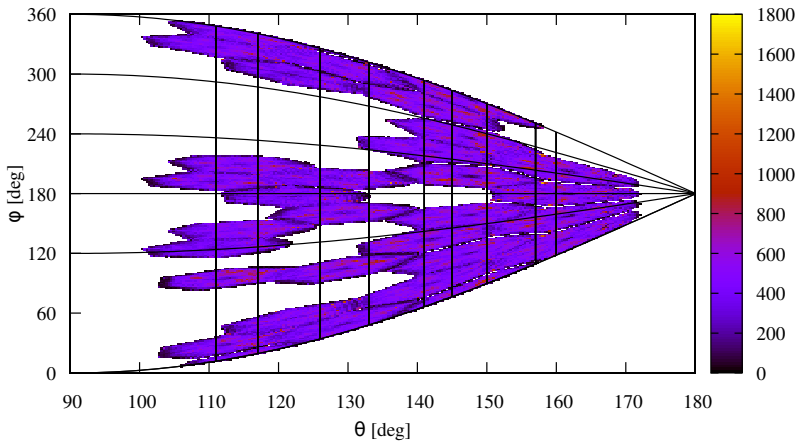

Figure 5.10: Density plot of interaction positions in AGATA. Note that for some θ angles there are an excess of counts.

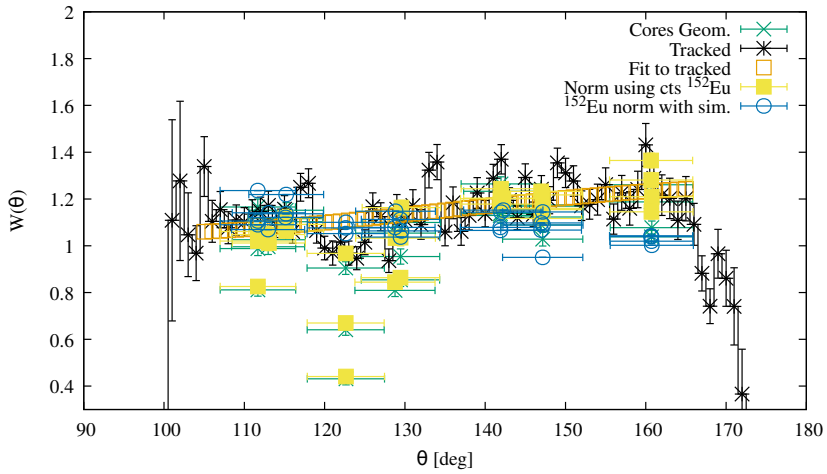

Figure 5.11: The difference in angular distribution using tracked data or counts in detectors. Note how the source data, which is isotropic, is correctly normalized using a simulation of isotropic γ rays.

5.2.7 What should we do to improve AGATA?

If we compare the expected performance of AGATA (or GRETINA) from simulations with experimental results, do we find room for improvement? In general the experimental efficiency is some 10 % lower than simulations suggest (without doing γ-ray tracking). This might partly be from the active volume of the detectors that differs from the theoretical volume and from charge-carrier cloud effects close to the borders of the Germanium diodes. It is therefore not obvious that any improvements can

be made. It is also found that the measured peak-to-total is lower than is expected from simulations. Experimentally a peak-to-total of 36 % is measured whereas "first order simulations" give 49 %. If one adds material in the simulations (walls, dipole magnets from VAMOS, dead layers in the HPGe crystal) the simulated peak-to-total comes down to 41 %. Tentatively the difference can be attributed to a γ-ray tracking efficiency that is lower in experiments than for simulations. An increase of the tracking efficiency with 10 % would give an experimental peak-to-total of 41 %. This is a significant improvement and means of achieving it should be investigated. An effort to do this is the OASIS ANR. The short story is that I believe that if it is possible to improve on the performance of γ-ray tracking this is done by improving PSA by better understanding of the detectors (if possible, we know well what is going on) and finding a way of correctly count the number of interactions in a segment. Also, not only for γ-ray tracking but also for, e.g., understanding the peak shape in γ-ray spectra after Doppler Correction, correct event-by-event error estimations would be of great value.

As list of ideas that I would like to investigate is:

1. To couple the determination of the interaction positions of the γ rays with the γ-ray tracking to create an overall best fit. If the problem of computer power is neglected (one can imagine powerful trigger algorithms...) the first question I ask myself if how to balance the fit of the pulse-shapes to the fit of the γ-ray interaction sequence. Non-absorbed γ rays? Gamma-rays absorbed in one interaction?

2. To propose multiple PSA solutions to γ-ray tracking and let tracking figure out the best. My gut feeling is that this would need good error estimates from PSA (worked on within the OASIS project).

3. Let the γ-ray tracking algorithm move the interaction points in order to optimize the figure of merit of a track. The distance the points can be moved should be determined by the estimated error on the positions. The final interaction position given would be the optimized one (this is not a unique way of thinking [265, 266]).

4. Full scale machine learning, give traces of crystals and energies, ask for γ rays and positions. Or maybe something a bit less dramatic. Ask for number of interaction in segments, number of γ rays etc...

The first three points are rather straight forward to try, but the amount of work needed is rather large. I point out that many features implemented in the AGATAGeFEM code have been implemented with these kind of developments in mind (it is easily connected to output from the AGATA simulations, can produce output files in the format used by AGATA tools, can work in server-client mode to be used as a "producer" in the AGATA DAQ chain etc.). I estimate each of the three first points to something like up to a year work for me, full time. Each points can be considered a PhD project. The fourth point concerns a subject that has not been investigated within the AGATA community in a long time (work was done by the Munich group and M. Schlarb [241] but mainly on timing). What can be expected is therefore not at all clear for me, nor do I have a clear idea of where to start. However, within the AGATA different projects concerning the use of artificial intelligence have started.

Chapter 6

Measuring picosecond lifetimes of excited states in nuclei

The absolute transition strengths between excited states in nuclei is one of a few accessible observables. If the spin, branching ratios, and mixing ratios of the involved states are known the reduced transition strength can be extracted in a model-independent way. These reduced transition strengths B(EL/ML) are therefore the preferred quantities to compare to theoretical calculations as all phase-space factors are removed. The theory of electromagnetic decays in nuclei is presented in several classic textbooks such as "Alpha, Beta, and Gamma-ray spectroscopy" [267] and "The electromagnetic interaction in nuclear spectroscopy" [268] and a repetition here is of no value.

For lifetimes in the picosecond range, say a bit less than 1 ps to some hundred picoseconds, methods based on the Doppler shift of γ rays emitted in-flight by the ions were developed as soon as acceleration of heavy ions was available, see e.g. chapter VII.H by Fossan and Warburton in "Nuclear spectroscopy and reactions Part C" [269]. Traditionally two different methods have been used, the Doppler Shift Attenuation Method (DSAM) where the peak shape coming from the slowing down inside foil is analysed and the Recoil Distance Doppler Shift (RDDS). My work has focused on the RDDS by the use of a Plunger. In figure 6.1 a sketch of an experiment using a Plunger is shown. High-Purity Germanium detectors, placed at angles where the Doppler Shift is considerable, surround the target. Downstream the target a stopper or degrader foil is placed. This foil changes the velocity of the recoiling ion and hence the Doppler shift of the detected γ rays. The emission of γ rays at different velocities give rise to two components from the same γ-ray transition. By using the plunger device to carefully control the distance between the target and the stopper/degrader foil the relative intensity between these two components is changed. As the recoil velocity is known (can always be deduced from the Doppler Shift) this corresponds to tracing out the fraction of decays before the stopper/degrader as a function of time. Recent developments and considerations are given in Dewald et al. [80].

Example of spectra from a few experiments using different version of the Orsay Universal Plunger System (see separate box for details) are shown in figure 6.2. The spectra are taken from three different experiments performed with the OUPS. The leftmost column shows data from the commissioning experiment of the OUPS, where

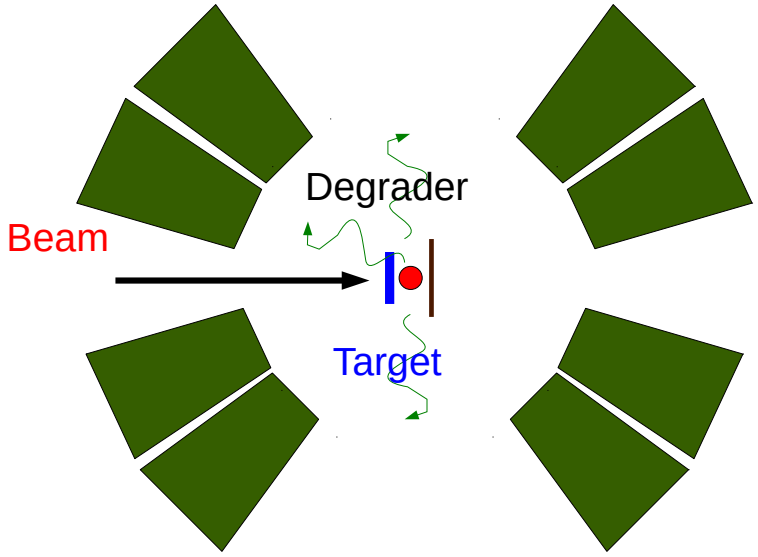

Figure 6.1: A sketch over a Plunger setup. The beam of heavy ions impinge on the target from the left and the excited reaction product recoils out of the target to the right. Gamma rays are emitted from the excited state either before or after the second foil. The second foil can be either a stopper or degrader foil.

excited states in ^{74}Kr where produced in the reaction ^{45}Sc(^{35}Cl,2p2n)^{76}Kr with a beam energy of 126 MeV. This was an experiment where there was sufficient statistics to gate on the in-flight component of the feeding $6_1^+ \rightarrow 4_1^+$ transition. The lifetime of about 4 ps for the 4_1^+ state is long compared to the stopping time of the ^{76}Kr ion in the gold stopper foil used in the experiment. Peak intensities are relatively easily extracted from these spectra by fitting Gaussian functions to the peaks. Further more, the gating from above on the in-flight component of the feeding transition removes systematical errors from unknown feeding. This is an example of where the use of Differential Decay Curve Method [270] can provide lifetimes that are both accurate and free from systematical uncertainty. Also errors from the deorientation effect seen in nuclei recoiling in vacuum are canceled [271] (note that this is only valid for a "stopper foil" in which the recoiling ions are stopped and the hyperfine interaction is "frozen").

In the middle column of figure 6.2 data from an experiment, performed with the γ-ray spectrometer AGATA at GANIL, is shown. A ^{238}U beam impinged on a 1.86 mg/cm^2 thick ^{9}Be foil, creating fission fragments. These fission fragments were identified in the VAMOS spectrometer. VAMOS also provides the velocity vector for an event-by-event Doppler Correction. A 4.5 mg/cm^2 thick ^{nat}Mg foil was used as a degrader foil. The γ-ray spectra shown are γ-ray singles. As compared to the $\gamma\gamma$ coincidence measurement shown in the left-most column this data poses more challenges. First of all there is the problem of dealing with long-lived unobserved feeding that introduces systematic errors towards longer lifetimes. The best remedy against such bias is to have a rather large number of distances to work with, allowing the identification of a distance dependence on the resulting lifetime, a clear indication of problem with feeding transitions (see discussion in Dewald et al. [270]). Secondly, the influence of the deorientation from recoil-in-vacuum can not be assumed of no importance. A third complication arises from the non-Gaussian components in the peak shapes, arising from the distributions in velocity due to the large acceptance of VAMOS, and the relatively long transit time in the degrader as compared to the shorter lifetimes that are measured (down to some picosecond). For this type of experiments the velocity distribution is also large, and care has to be taken when extracting the lifetimes [272]. As lifetimes measurements, using first the AGATA demonstrator at Legnaro and later on different sub-arrays of AGATA at GANIL have been corner stones in the explored physics, the question concerning systematical biases are not without interest.

The third and final column of figure 6.2 shows the 2_1^+ transition from ^{112}Xe, produced in the fusion-evaporation experiment performed with AGATA for γ-ray detection, NEDA [273] for neutrons and DIAMANT [274] for charged particles. The OUPS Mk III was used as the plunger. The spectra are background subtracted and gated on 2 protons, 2 neutrons, and the in-flight component of the $4_1^+ \rightarrow 2_1^+$ transition. The reaction used was ^{58}Ni(^{58}Ni,2p2n)^{112}Xe. The main challenge here is the statistics. In this experiment a degrader was used, although no detection of the recoiling ions was done. This to allow the measurement of lifetimes short compared the stopping time of the ^{112}Xe ion recoil in a stopper foil and to optimize the peak width for γ rays, emitted both before and after the degrader foil. As a degrader was used, there is a theoretical risk for influence from reorientation effects. Once a preliminary lifetime, with corresponding statistical errors, has been determined possible biases from vacuum reorientation should be investigated.

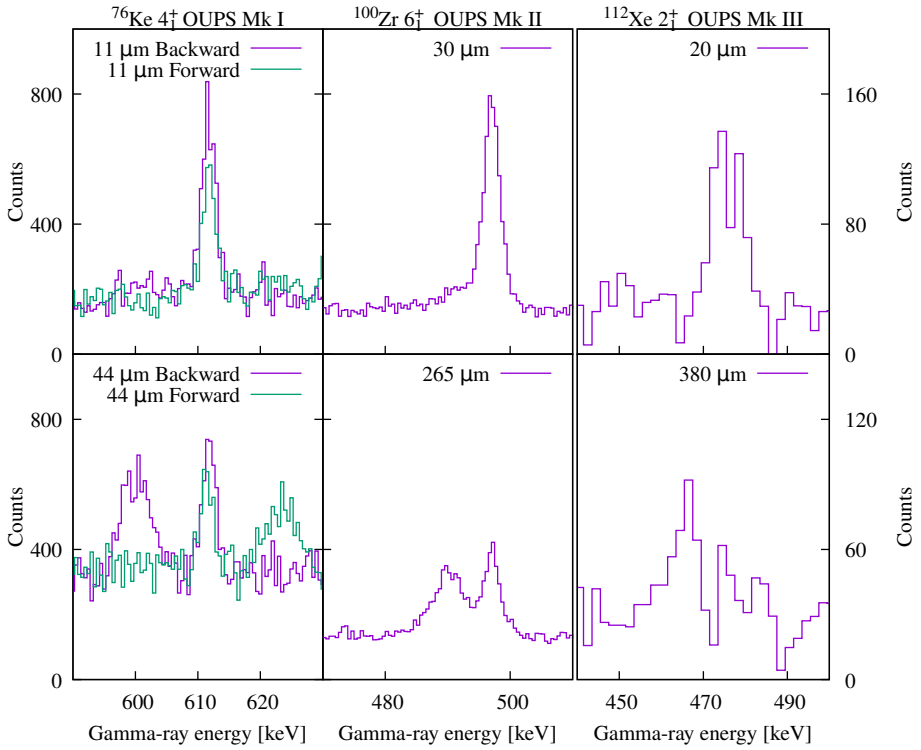

Figure 6.2: Spectra from experiments using Oups Mk I,Mk II, or Mk III. Each column have spectra from two different distances showing the variation in intensity for the peak emitted before or after the change in velocity induced by the stopper/degrader foil. For details see text.

the Orsay Universal Plunger System (OUPS)

The development of the Orsay Universal Plunger System started in 2009-2010 with the explicit goal of creating a Plunger that easily could be adapted to different installations, mainly in France. At the time Spiral2 with the possibility of post-accelerated beams was still a perspective.
A Plunger device to be used for RDDS measurements, and for g-factor measurements using the recoil-in-vacuum method, should fulfill a set of requirements:

- the possibility to vary the distances between target and stopper foil from some micrometers to some tens of millimeters with a sub-micrometer precision,
- small absorption of γ rays emitted from the deexciting nuclei,
- a mechanism to stretch target and stopper foils,
- and an active feedback to compensate for changes in target-stopper foil distance induced by the target-beam interaction.

For the OUPS a choice was made to try to meet these requirements using commercially available piezo step-motors. These motors have linear movement with a range of up to 20 mm and a smallest step-size in the order of 20 nm. Mark I of OUPS was build upon the Physics Instruments PI N-661 linear motor. Its core is shown in figure 6.3. By the means of pre-threaded holes a stopper-foil support is mounted on the moving upper half of the piezo motor. The PI N-661 itself is mounted on an aluminum support plate, to which the target-holder support is also attached. This structure is supposed to remain the same independently of the type of experiment performed. Due to the relative thickness of the PI linear motor assembly the amount of material in the downward direction is quite large, but this is of lesser importance since the Doppler shift of emitted γ rays usually is too small for RDDS measurement at angles close to 90 degrees.

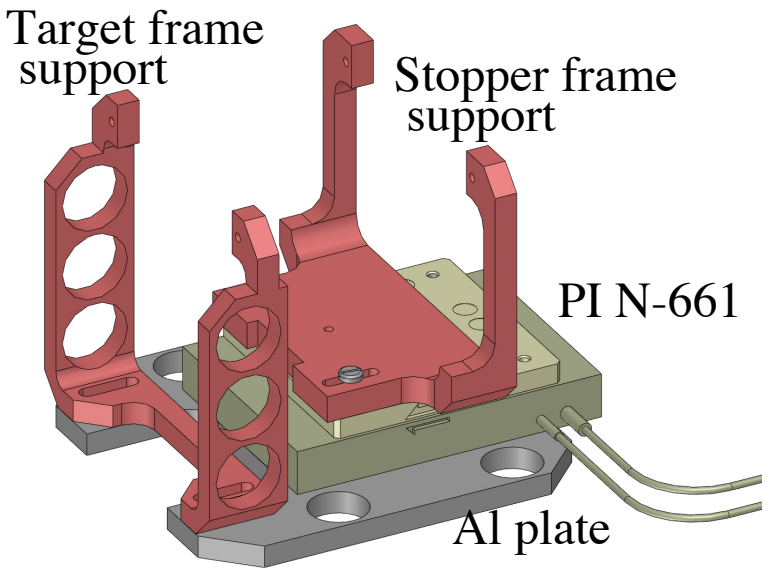

Figure 6.3: (color online) Main components of the Orsay plunger.

A photo of OUPS Mk I is shown in figure 6.4.

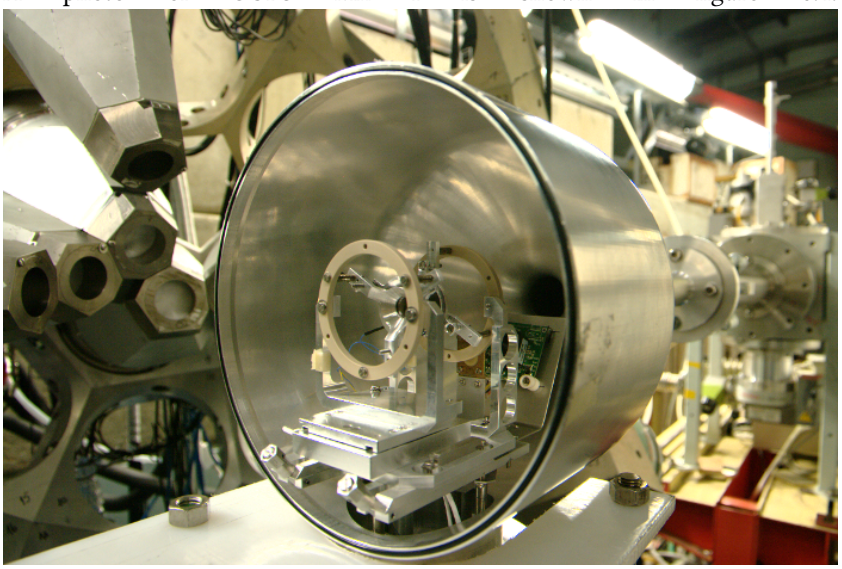

Figure 6.4: Photo showing the Mark I OUPS.

Electronics used for Mk I was a classic setup with a high-precision pulse generator, a spectroscopic amplifier and acquisition and a motor control using a National Instrument Data Acquisition Card. It is described in detail in Ljungvall et al. [166] (included as a publication, see 7.3). The Mk I has been used at the ALTO facility for several campaigns [100, 275].
When OUPS was adapted for use at GANIL together with AGATA and

the VAMOS spectrometer, the used linear motor N-661 was no longer in production with Physik Instrumente. It was replaced with the LPS-24 stage from Physik Instrumente. Furthermore, the target and degrader holders were modified to be compatible with the design of the Compact Cologne Plunger (see section 5.5 in Dewald et al. [80]). In figure 6.5 a drawing of OUPS Mark II is shown inside the VAMOS reaction chamber.

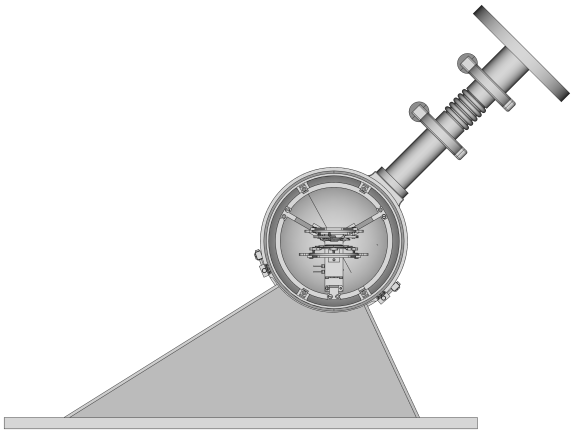

Figure 6.5: Bird eyes view of the Oups Mk II inside the VAMOS reaction chamber. The beam comes from up right, and VAMOS is positioned at the bottom of the picture.

The main difference in design between Oups Mk I and Mk II is that for Mk II emphasis has been put on the possibility to have a beam that impinged on the target with an angle. This because, when used with VAMOS, the excited ions are typically produced using fusion-fission of multi nucleon transfer reactions which requires VAMOS to be positioned with an angle relative to the beam axis, typically between 20° and 45°. Furthermore, VAMOS has a large acceptance angle ($\approx \pm 7°$). As the time of flight between the target and the degrader foil has to be known with high precision for RDDS measurements it is necessary to keep the foils orthogonal to the VAMOS axis rather, than to the beam axis. This requirement largely determines the design of a plunger device to be used in this setup. In figure 6.6 AGATA, VAMOS, and the target chamber containing the Oups Mk II is shown.

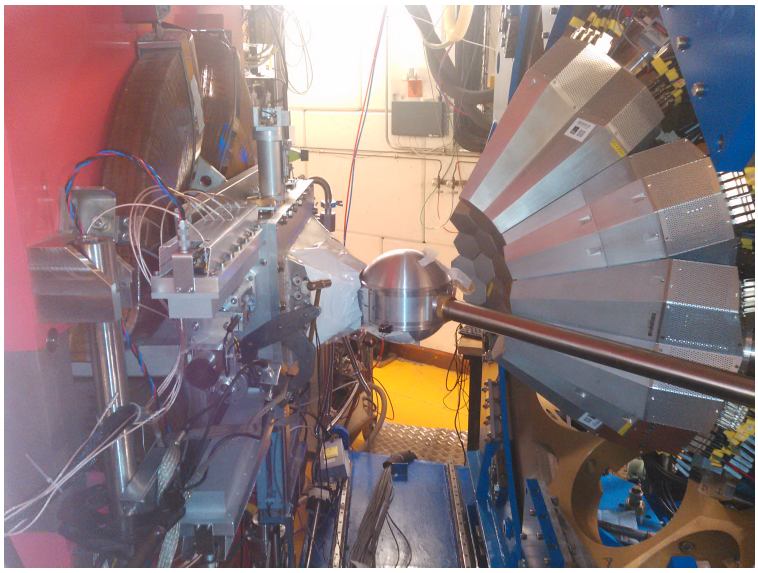

Figure 6.6: Photo of AGATA, VAMOS, and the target chamber

For the campaign using Oups Mk II. at GANIL the electronics used was also simplified, relying on the National Instruments PCIE-6361 X Series DAQ - a PCI express card mounted in the control PC, both to generate the periodic test signal and to measure the output from the plunger. When needed the output was amplified and filtered using a spectroscopic amplifier. In some experiments the amplifier was replaced with a simple low-pass filter, made out of high-precision components for thermal stability.
A third version of the Oups, Mk III, was developed to be used together with AGATA for γ detection, NEDA [273] for neutrons and DIAMANT [274] for charged particles. For Mk III the target holders and frames used for Mk II were reused. However, as the DIAMANT detector requires space in the target chamber, the holding structure of the motor and target and stopper assemblies had to be modified. This while trying to minimize the shadowing of both AGATA and DIAMANT. The final design is shown in figure 6.7, where the plunger rests on the ring used to adjust its position inside the chamber (mostly not visible). Also shown are the DIAMANT charged particle detector and some of the box-like ending of the target chamber, collecting different vacuum feedthroughs needed to bring the signals for the Oups Mk III and the DIAMANT detector out from the target chamber.

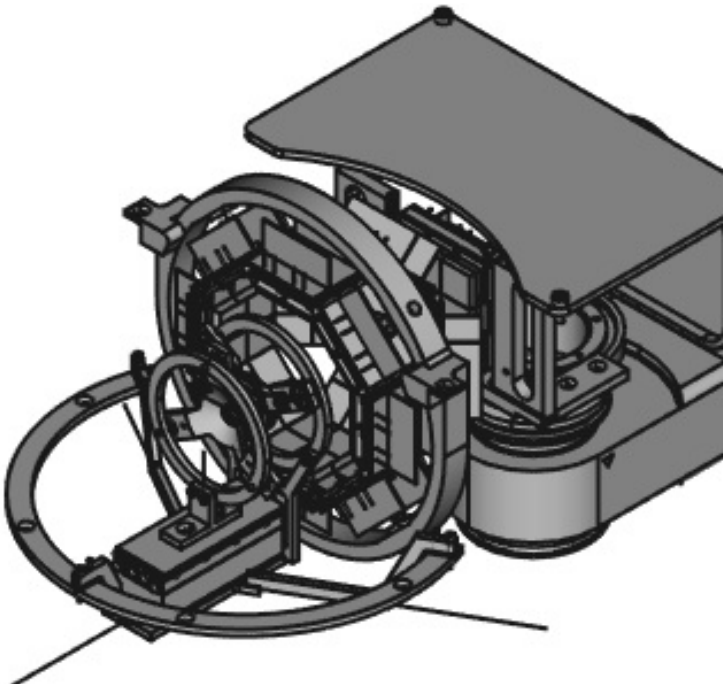

Figure 6.7: CAD drawing of Oups Mk III inside the AGATA target chamber used during the AGATA+NEDA+DIAMANT campaign.

Experiments performed with an Orsay Universal Plunger

This is a complete list of experiments performed with the Oups family. "No publication" means that no publication is expected, "No publication as of February 28, 2020" means that at least one publication is expected.

1. Commissioning
    - Spokesperson J. Ljungvall
    - At the ALTO using ORGAM 2011
    - ^{45}Sc(^{35}Cl,2p2n)^{76}Kr
    - 1.1mg/cm2 ^{45}Sc target, 5mg/cm^2 Au stopper
    - Published [166]
2. Probing the boundary of shape coexistence south of Z=82: Lifetime measurements of excited states in ^{170}Os using the RDDS method
    - Spokesperson J. Ljungvall
    - At the ALTO using ORGAM 2012
    - ^{142}Nd(^{32}S,4n)^{170}Os
    - Ta backing, Au stopper

- Published [167]

3. Search for X(5) symmetry in the ^{168}W nucleus
    - Spokesperson K. Gladnishki
    - At the ALTO using ORGAM 2012
    - ^{141}Pr(^{31}P,4nγ)^{168}W
    - ^{141}Pr on 2mg/cm^2 Ta foil, Au stopper
    - No publication
4. Development of the Time Dependent Recoil In Vacuum technique for "radioactive-beam geometry"
    - Spokespersons G. Georgiev and A. Stuchberry
    - At the ALTO using ORGAM 2012
    - ^{24}Mg(^{93}Nb,γ)^{24}Mg
    - ^{93}Nb 2.4 mg/cm^2, Au "reset foil", Coulex
    - Published [100]
5. Lifetime measurements using RDDS method after incomplete fusion
    - Spokesperson A. Goasduff, J. Ljungvall
    - At the ALTO using ORGAM 2013
    - ^{70}Zn(^{7}Li,αxpyn)
    - $LiSO_4$ 1mg/cm^2 on 1μm Ni
    - No publications, see 10.
6. Octupole collectivity in ^{156}Gd: lifetime measurements of the first 4$^-$ and 6$^-$ states in ^{156}Gd
    - Spokesperson Loïc Sengelé
    - At the ALTO using ORGAM 2013
    - ^{12}C(^{150}Nd,α2n)^{156}Gd
    - Discussed in thesis by L. Sengelé [276].
7. Lifetime measurement of ^{100}Ru: A possible candidate for the E(5) Critical Point symmetry
    - Spokesperson T. Konstantinopoulos
    - At the ALTO using MINORCA 2014
    - ^{14}C(^{88}Sr,2n)^{100}Ru
    - SrF_2 0.6 mg/cm^2 on 1mg/cm^2 Au, Au stopper
    - Published [275]
8. Lifetime measurements in ^{113}Te: Determining Optimal effective charges approaching the N=Z=50 doubly-magic shell closure.

- Spokesperson D. Cullen
- At the ALTO using MINORCA 2014
- ^{63}Cu(^{54}Fe,3pn)^{113}Te
- ^{54}Fe 1mg/cm^2 12mg/cm^2 Au stopper
- No publication as of February 28, 2020

9. Time dependent recoil in vacuum for Na-like ^{56}Fe ions
    - Spokesperson Andrew Stuchbery
    - At the ALTO using MINORCA 2014
    - ^{56}Fe(,γ)^{56}Fe (coulex)
    - ^{12}C 230 µg/cm^2 on natNi backing (0.5 µm), reset foils thin Ni
    - No publication as of February 28, 2020
10. Lifetime and g-factor measurements in the vincinity of ^{68}Ni using the AGATA, Oups and VAMOS
    - Spokespersons J. Ljungvall and Andreas Görgen
    - At GANIL using AGATA and VAMOS 2015
    - ^{238}U(^{64}Ni,)^{62}Fe
    - ^{64}Ni 1.25mg/cm^2, 3.3 mg/cm^2 natMg degrader
    - Published [86]
11. Neutron monopole drifts near the N=50 closed shell towards ^{78}Ni
    - Spokesperson David Verney
    - At GANIL using AGATA and VAMOS 2015
    - ^{238}U(^{9}Be,)Fission
    - 10 um ^{9}Be, 5 mg/cm^2 Mg
    - Published [111]
12. Shape evolution in neutron-rich fission fragments in the mass A~100 region
    - Spokespersons Wolfram Korten and Andreas Görgen
    - At GANIL using AGATA and VAMOS 2017
    - ^{238}U(^{9}Be,)Fission
    - 1.85 mg/cm^2 ^{9}Be target, 4.5 mg/cm^2 Mg degrader
    - No publication as of February 28, 2020
13. Shell evolution of neutron-deficient Xe isotopes: Octupole and Quadrupole Correlations above ^{100}Sn
    - Spokespersons Emanuel Clément, J.J Valiente-Dobón, A. Gadea
    - At GANIL using AGATA+NEDA+DIAMANT 2018
    - ^{58}Ni(^{58}Ni,2p2n)^{112}Xe
    - 1 mg/cm^2 ^{58}Ni target, 5 mg/cm^2 Au degrader
    - No publication as of February 28, 2020

6.1 Lifetime measurements using Recoil Distance Doppler Shift with AGATA at Legnaro and GANIL

Once the decision of starting the AGATA demonstrator phase at INFN Legnaro with AGATA coupled to the PRISMA spectrometer [277] had been taken it stood clear that the AGATA+PRISMA would be a very interesting setup for RDDS measurements of moderately neutron-rich nuclei. The concentration of solid angle, and hence efficiency, at angles close to 180° as compared to the entrance axis of PRISMA assured this. For this campaign the Cologne group developed a Compact Plunger [80] that was, and is, used extensively. There was also an emphasis on lifetime measurements the first part of the AGATA at GANIL campaign, this time with Oups Mk II and the Cologne Compact Plunger sharing the burden. Several publications have come out of these campaigns (e.g. [86, 90, 278, 279, 280, 281, 282, 283]). These experiments have been characterized by the rather low production rates and total efficiencies of the detection system (AGATA+spectrometer) limiting the total number of distances that has been measured in each experiment. Another consequence of the limited statistics is that all data have been analyzed in γ singles. This opens up for potential issues with unobserved feeding giving apparent longer lifetimes of the excited nuclear state of interest. The canonical way of checking that unobserved feeding is negligible or correctly modeled is to assure that the deduced lifetime is independant of the target-degrader distance (e.g. see discussion in Dewald et al. [270]). This has not been possible for these experiments as the number of distances within the sensitive region have been small. To compensate, by using the spectrometers, the excitation energy in the system has been limited to control the feeding. For the most exotic nuclei this is not possible as the loss in statistics then prohibits a measurement. Ways of dealing with the low statistics have been developed, aiming at a complete solution of the Bateman equations allowing summing the distances used during a measurement [279, 281]. This type of analysing techniques requires a good knowledge of the absolute distances, which is more difficult that just knowing the relative distances (which is what is calibrated using the plungers). Another complication is that the compact geometry given of AGATA gives difficulties when recoil-in-vacuum effects are to be estimated. Only angles close to 180° are covered by AGATA making measurements of angular distributions (or rather correlations as the outgoing ion is detected) of the γ rays all but impossible. It is therefore not a surprise that some of the lifetimes measured during these campaigns are in contradiction with earlier B(E2) measurements performed with low-energy Coulomb excitation (e.g. B(E2;$4_1^+ \rightarrow 2_1^+$) in ^{74}Zn, compare Van de Walle et al. [284] and Louchart et al. [90]). I here take the stand that the Coulomb excitation, despite the underlying assumption of a zero quadrupole moment of the 4_1^+ state, is a more reliable measurement. A indepth discussion of the challenges, faced when doing plunger measurements, can be found in the review by Dewald et al. [80].

The lack of statistics and limited number of distances measured removes, in my opinion, some of the intrinsic benefits of the Plunger technique. This is also true for the use at high energy facilities such as RIKEN and NSCL/FRIB. Other techniques, than the RDDS, to measure lifetimes or transition strengths offer under these condition good alternatives. Centroid shifts, resulting from the varying emission point for a nuclear state with a finite lifetime, as well as Coulomb excitation (limited to low spin states in case of relativistic Coulomb excitation) offer interesting alternatives at radioactive beam facilities. For recent examples of the use of "alternative" techniques

to measure lifetimes see the following references [285, 286, 287, 288].

The question of choice of method to measure a lifetime (or if there is the alternative, directly measure the B(E/ML) of a state) is therefore raised. My answer would be that the Plunger technique has added value when the statistics allows for a time-dependent measurement as this allows for easier detection of and correction for unobserved feeding. This translates into the need to measure at least lifetimes within the "sensitive" region that are independent. This translates into four distances in the sensitive region, which is very difficult when studying exotic nuclei.

6.2 Future developments for Recoil Distance Lifetime measurements and the Oups family in particular

I observe a trend of performing ever more demanding experiments, always at the limit of feasibility, with an increasing reliance on simulation and modelling of the experiment to extract the lifetimes. The time-dependant aspect of RDDS is also less pronounced as the number of measured distances are reduced to achieve a significant statistics for the γ-ray peaks in the spectra. It is suggested that at facilities such as FRIB or RIKEN the use plungers with two degrader foils can help with the statistics problem [289] but the need to model and simulate the experiments remain. I feel this removes an important aspect of the RDDS technique as compared to when used together with the Differential Decay Curve Method [270] method as the "time-dependence" is crucial to discover unobserved feeding and other systematical errors. Despite these reservation one is left with little choice for exotic nuclei. The development of these tools is therefore natural, and some of these methods, such as the simulation of the γ-ray peak shapes was developed and used during the analysis of the first AGATA+VAMOS experiment, published by Klintefjord et al. [86], see figure 6.8. The adaptation of already existing frameworks for this or some more original work is foreseen for the Oups family.

It is my opinion that it would be nice to construct a system that allows for reproducible foil tensions and foil alignments for a plunger. This is not so much related to performance in terms of what is the closest distance between the two foils that can be used during an experiment, or max beam current. This is mainly limited by the target and degrader foil quality and material. The main motivations are instead the predictability of the performance, and hence the experiment and the possibility to have the system in an inert atmosphere allowing the use of targets which are sensitive to oxidation. To measuring foil tensions, and in the prolongation of that have automated systems that stretches the foil to a preset tension, is a non-trivial task on foils with a thickness of mg/cm^2. What I have in mind is the development of an opto-acoustic system where piezo-elements are exciting the proper modes of the foils and optical elements are detecting and imaging these modes. Standing wave patterns, combined with mathematical modeling of the target, frames, etc allows for the determination of the ratio tension/mass per area of a target. A second measurement is needed to determine the thickness of the target. An idea would be to apply a small pressure difference and measure the deflection of the target foil. It would be presumptuous of me to think that the thin foils we use for our experiments have reproducible mechanical characteristics. Therefore one of the goals of such a setup would be to make statistics on when and how target foils would fail from stretching. This would allow reasonable predictions for experiments. In an ideal world this system would be mounted on the

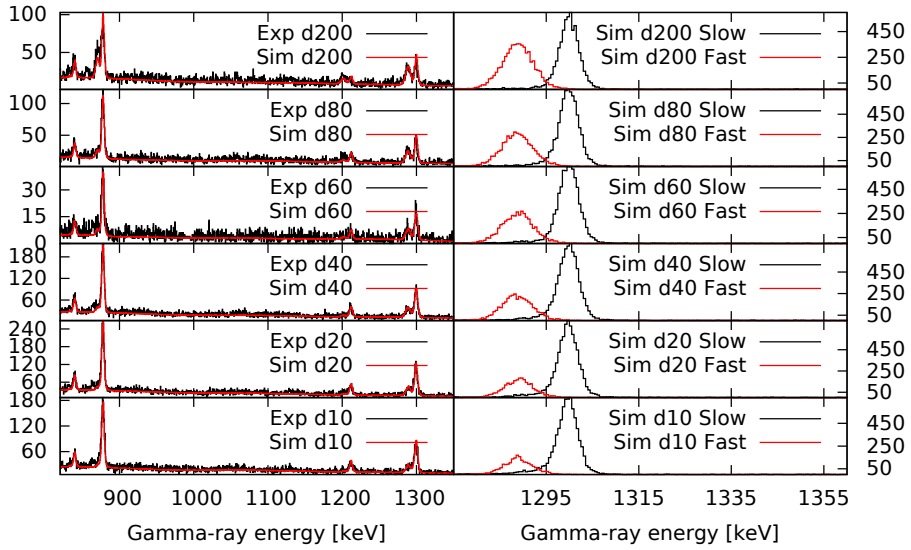

Figure 6.8: Realistic simulation of the first AGATA@GANIL experiment. In these simulations the populations and lifetime of levels have been adapted to reproduce experimental spectra as a function of distance between the target and the degrader foil. The purpose of the simulations was to determine the peak shape of the "slow" component.

plunger itself, also providing protective atmosphere to the foils. While dreaming it is also transparent to γ rays and can be remotely controlled in order to open valves for the beam to enter and exit the plunger.

Of great importance for plunger experiments is the target production. With the arrival of reasonably high-intensity radioactive beams, targets that will allow inverse kinematics transfer reactions are very desirable. More precisely targets containing ions such as deuterium, lithium, or oxygen. This is a part of the development that I have yet to involve myself in but I do believe it is important for the pertinence of the Plunger technology for the feature.

Finally, for the Oups family, there remains some control software developments to be made. There are some minor details that should be added such as the possibility to use a joystick for controlling the distance between the two foils which would make the setup phase of the plunger easier.

Bibliography

[1] K. Fujikawa, H. Ui, Nuclear Rotation, Nambu-Goldstone Mode and Higgs Mechanism, Progress of Theoretical Physics 75 (1986) 997–1013. doi:10.1143/PTP.75.997.

[2] A. Bohr, B. Mottelson, Nuclear Structure, no. vol. 2 in Nuclear Structure, World Scientific, 1998.

[3] P. Ring, P. Schuck, The nuclear many-body problem, Springer-Verlag, 1980.
URL https://books.google.fr/books?id=v79PAQAAIAAJ

[4] M. Bender, P.-H. Heenen, P.-G. Reinhard, Self-consistent mean-field models for nuclear structure, Rev. Mod. Phys. 75 (2003) 121–180. doi:10.1103/RevModPhys.75.121.
URL https://link.aps.org/doi/10.1103/RevModPhys.75.121

[5] M. Grasso, Effective density functionals beyond mean field, Progress in Particle and Nuclear Physics 106 (2019) 256 – 311. doi:https://doi.org/10.1016/j.ppnp.2019.02.002.
URL http://www.sciencedirect.com/science/article/pii/S0146641019300043

[6] J. P. Elliott, Collective motion in the nuclear shell model. ii. the introduction of intrinsic wave-functions, Proceedings of the Royal Society of London. Series A, Mathematical and Physical Sciences 245 (1243) (1958) 562–581.
URL http://www.jstor.org/stable/100297

[7] J. P. Elliott, Collective motion in the nuclear shell model. i. classification schemes for states of mixed configurations, Proceedings of the Royal Society of London. Series A, Mathematical and Physical Sciences 245 (1240) (1958) 128–145.
URL http://www.jstor.org/stable/100416

[8] A. P. Zuker, J. Retamosa, A. Poves, E. Caurier, Spherical shell model description of rotational motion, Phys. Rev. C 52.

[9] K. Heyde, J. L. Wood, Shape coexistence in atomic nuclei, Rev. Mod. Phys. 83 (2011) 1467–1521. doi:10.1103/RevModPhys.83.1467.
URL https://link.aps.org/doi/10.1103/RevModPhys.83.1467

[10] J. Wood, K. Heyde, W. Nazarewicz, M. Huyse, P. van Duppen, Coexistence in even-mass nuclei, Physics Reports 215 (3) (1992) 101 – 201. doi:https://doi.org/10.1016/0370-1573(92)90095-H.
URL http://www.sciencedirect.com/science/article/pii/037015739290095H

[11] K. Kumar, Intrinsic quadrupole moments and shapes of nuclear ground states and excited states, Phys. Rev. Lett. 28 (1972) 249–253. doi:10.1103/PhysRevLett.28.249.
URL https://link.aps.org/doi/10.1103/PhysRevLett.28.249

[12] M. Harakeh, D. Guerreau, W. Henning, M. Huyse, H. Leeb, K. Riisager, G. van der Steenhoven, G.-E. Körner, Nupecc long range plan 2004, Tech. rep., NuPECC (2004).

[13] B. Pritychenko, E. Běták, M. Kellett, B. Singh, J. Totans, The nuclear science references (nsr) database and web retrieval system, Nuclear Instruments and Methods in Physics Research Section A: Accelerators, Spectrometers, Detectors and Associated Equipment 640 (1) (2011) 213 – 218. doi:https://doi.org/10.1016/j.nima.2011.03.018.
URL http://www.sciencedirect.com/science/article/pii/S0168900211005584

[14] E. Caurier, G. Martínez-Pinedo, F. Nowacki, A. Poves, A. P. Zuker, The shell model as a unified view of nuclear structure, Rev. Mod. Phys. 77 (2005) 427–488. doi:10.1103/RevModPhys.77.427.
URL http://link.aps.org/doi/10.1103/RevModPhys.77.427

[15] D. Dean, T. Engeland, M. Hjorth-Jensen, M. Kartamyshev, E. Osnes, Effective interactions and the nuclear shell-model, Progress in Particle and Nuclear Physics 53 (2) (2004) 419 – 500. doi:https://doi.org/10.1016/j.ppnp.2004.05.001.
URL http://www.sciencedirect.com/science/article/pii/S0146641004000912

[16] V. Tripathi, S. L. Tabor, P. F. Mantica, C. R. Hoffman, M. Wiedeking, A. D. Davies, S. N. Liddick, W. F. Mueller, T. Otsuka, A. Stolz, B. E. Tomlin, Y. Utsuno, A. Volya, ^{29}Na: Defining the edge of the island of inversion for $z = 11$, Phys. Rev. Lett. 94 (2005) 162501. doi:10.1103/PhysRevLett.94.162501.
URL https://link.aps.org/doi/10.1103/PhysRevLett.94.162501

[17] O. Niedermaier, H. Scheit, V. Bildstein, H. Boie, J. Fitting, R. von Hahn, F. Köck, M. Lauer, U. K. Pal, H. Podlech, R. Repnow, D. Schwalm, C. Alvarez, F. Ames, G. Bollen, S. Emhofer, D. Habs, O. Kester, R. Lutter, K. Rudolph, M. Pasini, P. G. Thirolf, B. H. Wolf, J. Eberth, G. Gersch, H. Hess, P. Reiter, O. Thelen, N. Warr, D. Weisshaar, F. Aksouh, P. Van den Bergh, P. Van Duppen, M. Huyse, O. Ivanov, P. Mayet, J. Van de Walle, J. Äystö, P. A. Butler, J. Cederkäll, P. Delahaye, H. O. U. Fynbo, L. M. Fraile, O. Forstner, S. Franchoo, U. Köster, T. Nilsson, M. Oinonen, T. Sieber, F. Wenander, M. Pantea,

A. Richter, G. Schrieder, H. Simon, T. Behrens, R. Gernhäuser, T. Kröll, R. Krücken, M. Münch, T. Davinson, J. Gerl, G. Huber, A. Hurst, J. Iwanicki, B. Jonson, P. Lieb, L. Liljeby, A. Schempp, A. Scherillo, P. Schmidt, G. Walter, "safe" coulomb excitation of ^{30}Mg, Phys. Rev. Lett. 94 (2005) 172501. doi:10.1103/PhysRevLett.94.172501.
URL https://link.aps.org/doi/10.1103/PhysRevLett.94.172501

[18] O. Sorlin, S. Leenhardt, C. Donzaud, J. Duprat, F. Azaiez, F. Nowacki, H. Grawe, Z. Dombrádi, F. Amorini, A. Astier, D. Baiborodin, M. Belleguic, C. Borcea, C. Bourgeois, D. M. Cullen, Z. Dlouhy, E. Dragulescu, M. Górska, S. Grévy, D. Guillemaud-Mueller, G. Hagemann, B. Herskind, J. Kiener, R. Lemmon, M. Lewitowicz, S. M. Lukyanov, P. Mayet, F. de Oliveira Santos, D. Pantalica, Y.-E. Penionzhkevich, F. Pougheon, A. Poves, N. Redon, M. G. Saint-Laurent, J. A. Scarpaci, G. Sletten, M. Stanoiu, O. Tarasov, C. Theisen, $^{68}_{28}$ni$_{40}$: Magicity versus superfluidity, Phys. Rev. Lett. 88 (2002) 092501. doi:10.1103/PhysRevLett.88.092501.
URL http://link.aps.org/doi/10.1103/PhysRevLett.110.242701

[19] S. Franchoo, M. Huyse, K. Kruglov, Y. Kudryavtsev, W. F. Mueller, R. Raabe, I. Reusen, P. Van Duppen, J. Van Roosbroeck, L. Vermeeren, A. Wöhr, H. Grawe, K.-L. Kratz, B. Pfeiffer, W. B. Walters, Monopole migration in ^{69,71,73}Cu observed from β decay of laser-ionized $^{68--74}$Ni, Phys. Rev. C 64 (2001) 054308. doi:10.1103/PhysRevC.64.054308.
URL https://link.aps.org/doi/10.1103/PhysRevC.64.054308

[20] M. Sawicka, R. Grzywacz, I. Matea, H. Grawe, M. Pfützner, J. M. Daugas, M. Lewitowicz, D. L. Balabanski, F. Becker, G. Bélier, C. Bingham, C. Borcea, E. Bouchez, A. Buta, M. La Commara, E. Dragulescu, G. de France, G. Georgiev, J. Giovinazzo, M. Górska, F. Hammache, M. Hass, M. Hellström, F. Ibrahim, Z. Janas, H. Mach, P. Mayet, V. Méot, F. Negoita, G. Neyens, F. de Oliveira Santos, R. D. Page, O. Perru, Z. Podolyák, O. Roig, K. P. Rykaczewski, M. G. Saint-Laurent, J. E. Sauvestre, O. Sorlin, M. Stanoiu, I. Stefan, C. Stodel, C. Theisen, D. Verney, J. Żylicz, Low energy levels in ^{72}Ni, Phys. Rev. C 68 (2003) 044304. doi:10.1103/PhysRevC.68.044304.
URL https://link.aps.org/doi/10.1103/PhysRevC.68.044304

[21] T. Otsuka, T. Suzuki, R. Fujimoto, H. Grawe, Y. Akaishi, Evolution of nuclear shells due to the tensor force, Phys. Rev. Lett. 95 (2005) 232502. doi:10.1103/PhysRevLett.95.232502.
URL http://link.aps.org/doi/10.1103/PhysRevLett.95.232502

[22] T. Otsuka, R. Fujimoto, Y. Utsuno, B. A. Brown, M. Honma, T. Mizusaki, Magic numbers in exotic nuclei and spin-isospin properties of the NN interaction, Phys. Rev. Lett. 87 (2001) 082502. doi:10.1103/PhysRevLett.87.082502.
URL http://link.aps.org/doi/10.1103/PhysRevLett.87.082502

[23] E. Bouchez, I. Matea, W. Korten, F. Becker, B. Blank, C. Borcea, A. Buta, A. Emsallem, G. de France, J. Genevey, F. Hannachi, K. Hauschild, A. Hürstel, Y. Le Coz, M. Lewitowicz, R. Lucas, F. Negoita, F. d. O. Santos, D. Pantelica, J. Pinston, P. Rahkila, M. Rejmund, M. Stanoiu, C. Theisen, New shape isomer in the self-conjugate nucleus ^{72}Kr, Phys. Rev. Lett. 90 (2003) 082502. doi:10.1103/PhysRevLett.90.082502.
URL https://link.aps.org/doi/10.1103/PhysRevLett.90.082502

[24] A. Gade, D. Bazin, A. Becerril, C. M. Campbell, J. M. Cook, D. J. Dean, D.-C. Dinca, T. Glasmacher, G. W. Hitt, M. E. Howard, W. F. Mueller, H. Olliver, J. R. Terry, K. Yoneda, Quadrupole deformation of the self-conjugate nucleus ^{72}Kr, Phys. Rev. Lett. 95 (2005) 022502. doi:10.1103/PhysRevLett.95.022502.
URL https://link.aps.org/doi/10.1103/PhysRevLett.95.022502

[25] C. Y. Wu, H. Hua, D. Cline, Shape coexistence and their configuration mixing in ^{98}Sr and ^{100}Zr, Phys. Rev. C 68 (2003) 034322. doi:10.1103/PhysRevC.68.034322.
URL https://link.aps.org/doi/10.1103/PhysRevC.68.034322

[26] P. von Brentano, V. Werner, R. F. Casten, C. Scholl, E. A. McCutchan, R. Krücken, J. Jolie, Alternative interpretation of sharply rising $e0$ strengths in transitional regions, Phys. Rev. Lett. 93 (2004) 152502. doi:10.1103/PhysRevLett.93.152502.
URL https://link.aps.org/doi/10.1103/PhysRevLett.93.152502

[27] P. Reiter, T. L. Khoo, I. Ahmad, A. V. Afanasjev, A. Heinz, T. Lauritsen, C. J. Lister, D. Seweryniak, P. Bhattacharyya, P. A. Butler, M. P. Carpenter, A. J. Chewter, J. A. Cizewski, C. N. Davids, J. P. Greene, P. T. Greenlees, K. Helariutta, R.-D. Herzberg, R. V. F. Janssens, G. D. Jones, R. Julin, H. Kankaanpää, H. Kettunen, F. G. Kondev, P. Kuusiniemi, M. Leino, S. Siem, A. A. Sonzogni, J. Uusitalo, I. Wiedenhöver, Structure of the odd-a, shell-stabilized nucleus $^{253}_{102}$No, Phys. Rev. Lett. 95 (2005) 032501. doi:10.1103/PhysRevLett.95.032501.
URL https://link.aps.org/doi/10.1103/PhysRevLett.95.032501

[28] R. D. Humphreys, P. A. Butler, J. E. Bastin, P. T. Greenlees, N. J. Hammond, R.-D. Herzberg, D. G. Jenkins, G. D. Jones, H. Kankaanpää, A. Keenan, H. Kettunen, T. Page, P. Rahkila, C. Scholey, J. Uusitalo, N. Amzal, P. M. Brew, K. Eskola, J. Gerl, K. Hauschild, K. Helariutta, F.-P. Heßberger, A. Hürstel, P. M. Jones, R. Julin, S. Juutinen, T.-L. Khoo, W. Korten, P. Kuusiniemi, Y. Le Coz, M. Leino, A.-P. Leppänen, M. Muikku, P. Nieminen, S. W. Ødegård, J. Pakarinen, P. Reiter, G. Sletten, C. Theisen, H.-J. Wollersheim, In-beam electron spectroscopy of ^{226}U and ^{254}No, Phys. Rev. C 69 (2004) 064324. doi:10.1103/PhysRevC.69.064324.
URL https://link.aps.org/doi/10.1103/PhysRevC.69.064324

[29] J. E. Bastin, R.-D. Herzberg, P. A. Butler, G. D. Jones, R. D. Page, D. G. Jenkins, N. Amzal, P. M. T. Brew, N. J. Hammond, R. D. Humphreys, P. J. C. Ikin, T. Page, P. T. Greenlees, P. M. Jones, R. Julin, S. Juutinen, H. Kankaanpää, A. Keenan, H. Kettunen, P. Kuusiniemi, M. Leino, A. P. Leppänen, M. Muikku, P. Nieminen, P. Rahkila, C. Scholey, J. Uusitalo, E. Bouchez, A. Chatillon, A. Hürstel, W. Korten, Y. L. Coz, C. Theisen, D. Ackermann, J. Gerl, K. Helariutta, F. P. Hessberger, C. Schlegel, H. J. Wollerscheim, M. Lach, A. Maj, W. Meczynski, J. Styczen, T. L. Khoo, C. J. Lister, A. V. Afanasjev, H. J. Maier, P. Reiter, P. Bednarczyc, K. Eskola, K. Hauschild, In-beam gamma ray and conversion electron study of $^{250}\mathrm{Fm}$, Phys. Rev. C 73 (2006) 024308. doi:10.1103/PhysRevC.73.024308.
URL https://link.aps.org/doi/10.1103/PhysRevC.73.024308

[30] P. Mermod, J. Blomgren, A. Hildebrand, C. Johansson, J. Klug, M. Österlund, S. Pomp, U. Tippawan, B. Bergenwall, L. Nilsson, N. Olsson, O. Jonsson, A. Prokofiev, P.-U. Renberg, P. Nadel-Turonski, Y. Maeda, H. Sakai, A. Tamii, Evidence of three-body force effects in neutron-deuteron scattering at 95 mev, Phys. Rev. C 72 (2005) 061002. doi:10.1103/PhysRevC.72.061002.
URL https://link.aps.org/doi/10.1103/PhysRevC.72.061002

[31] P. Navrátil, W. E. Ormand, C. Forssén, E. Caurier, Ab initio no-core shell model calculations using realistic two- and three-body interactions, The European Physical Journal A - Hadrons and Nuclei 25 (1) (2005) 481–484. doi:10.1140/epjad/i2005-06-145-6.
URL https://doi.org/10.1140/epjad/i2005-06-145-6

[32] A. P. Zuker, Three-body monopole corrections to realistic interactions, Phys. Rev. Lett. 90 (2003) 042502. doi:10.1103/PhysRevLett.90.042502.
URL http://link.aps.org/doi/10.1103/PhysRevLett.90.042502

[33] A. Blazhev, M. Górska, H. Grawe, J. Nyberg, M. Palacz, E. Caurier, O. Dorvaux, A. Gadea, F. Nowacki, C. Andreoiu, G. de Angelis, D. Balabanski, C. Beck, B. Cederwall, D. Curien, J. Döring, J. Ekman, C. Fahlander, K. Lagergren, J. Ljungvall, M. Moszyński, L.-O. Norlin, C. Plettner, D. Rudolph, D. Sohler, K. M. Spohr, O. Thelen, M. Weiszflog, M. Wisell, M. Wolińska, W. Wolski, Observation of a core-excited $e4$ isomer in $^{98}\mathrm{Cd}$, Phys. Rev. C 69 (2004) 064304. doi:10.1103/PhysRevC.69.064304.
URL https://link.aps.org/doi/10.1103/PhysRevC.69.064304

[34] A. Banu, J. Gerl, C. Fahlander, M. Górska, H. Grawe, T. R. Saito, H.-J. Wollersheim, E. Caurier, T. Engeland, A. Gniady, M. Hjorth-Jensen, F. Nowacki, T. Beck, F. Becker, P. Bednarczyk, M. A. Bentley, A. Bürger, F. Cristancho, G. d. Angelis, Z. Dombrádi, P. Doornenbal, H. Geissel, J. Grebosz, G. Hammond, M. Hellström, J. Jolie, I. Kojouharov, N. Kurz, R. Lozeva, S. Mandal, N. Mărginean, S. Muralithar, J. Nyberg, J. Pochodzalla, W. Prokopowicz, P. Reiter, D. Rudolph, C. Rusu, N. Saito, H. Schaffner, D. Sohler, H. Weick, C. Wheldon, M. Winkler, $^{108}\mathrm{Sn}$ studied with intermediate-energy coulomb excitation,

Phys. Rev. C 72 (2005) 061305. doi:10.1103/PhysRevC.72.061305.
URL https://link.aps.org/doi/10.1103/PhysRevC.72.061305

[35] S. M. Fischer, C. J. Lister, D. P. Balamuth, Unravelling the band crossings in ^{68}Se and ^{72}Kr : the quest for $t = 0$ pairing, Phys. Rev. C 67 (2003) 064318. doi:10.1103/PhysRevC.67.064318.
URL https://link.aps.org/doi/10.1103/PhysRevC.67.064318

[36] N. Mărginean, C. Rossi Alvarez, D. Bucurescu, C. A. Ur, A. Gadea, S. Lunardi, D. Bazzacco, G. de Angelis, M. Axiotis, M. De Poli, E. Farnea, M. Ionescu-Bujor, A. Iordăchescu, S. M. Lenzi, T. Kröll, T. Martinez, R. Menegazzo, D. R. Napoli, G. Nardelli, P. Pavan, B. Quintana, P. Spolaore, Observation of the $n = z = 44^{88}$Ru nucleus, Phys. Rev. C 63 (2001) 031303. doi:10.1103/PhysRevC.63.031303.
URL https://link.aps.org/doi/10.1103/PhysRevC.63.031303

[37] J. Jänecke, T. O'Donnell, Isospin inversion and n-p pairing in self-conjugate nuclei a=58-98, Physics Letters B 605 (1) (2005) 87 – 94. doi:https://doi.org/10.1016/j.physletb.2004.11.037.
URL http://www.sciencedirect.com/science/article/pii/S0370269304016065

[38] M. Bentley, S. Lenzi, Coulomb energy differences between high-spin states in isobaric multiplets, Progress in Particle and Nuclear Physics 59 (2) (2007) 497 – 561. doi:https://doi.org/10.1016/j.ppnp.2006.10.001.
URL http://www.sciencedirect.com/science/article/pii/S0146641006000743

[39] Nupecc long range plan 2017 perspectives in nuclear physics, Tech. rep., NuPECC (2017).

[40] T. Duguet, Public communication during nuspin2019.

[41] W. Leidemann, G. Orlandini, Modern ab initio approaches and applications in few-nucleon physics with a≥4, Progress in Particle and Nuclear Physics 68 (2013) 158 – 214. doi:https://doi.org/10.1016/j.ppnp.2012.09.001.
URL http://www.sciencedirect.com/science/article/pii/S014664101200110X

[42] E. Epelbaum, H.-W. Hammer, U.-G. Meissner, H.-I. fuer Strahlen-und Kernphysik, H.-I. fuer Strahlen-und Kernphysik, Modern theory of nuclear forces, Reviews of Modern Physics 81 (4). doi:10.1103/REVMODPHYS.81.1773.

[43] B. R. Barrett, P. Navrátil, J. P. Vary, Ab initio no core shell model, Progress in Particle and Nuclear Physics 69 (2013) 131 – 181. doi:https://doi.org/10.1016/j.ppnp.2012.10.003.
URL http://www.sciencedirect.com/science/article/pii/S0146641012001184

[44] G. Hagen, T. Papenbrock, M. Hjorth-Jensen, D. J. Dean, Coupled-cluster computations of atomic nuclei, Reports on Progress in Physics 77 (9) (2014) 096302. doi:10.1088/0034-4885/77/9/096302.
URL https://doi.org/10.1088%2F0034-4885%2F77%2F9%2F096302

[45] H. Hergert, S. Bogner, T. Morris, A. Schwenk, K. Tsukiyama, The in-medium similarity renormalization group: A novel ab initio method for nuclei, Physics Reports 621 (2016) 165 – 222, memorial Volume in Honor of Gerald E. Brown. doi:https://doi.org/10.1016/j.physrep.2015.12.007.
URL http://www.sciencedirect.com/science/article/pii/S0370157315005414

[46] J. Carlson, S. Gandolfi, F. Pederiva, S. C. Pieper, R. Schiavilla, K. E. Schmidt, R. B. Wiringa, Quantum monte carlo methods for nuclear physics, Rev. Mod. Phys. 87 (2015) 1067–1118. doi:10.1103/RevModPhys.87.1067.
URL https://link.aps.org/doi/10.1103/RevModPhys.87.1067

[47] D. Lee, Lattice simulations for few- and many-body systems, Progress in Particle and Nuclear Physics 63 (1) (2009) 117 – 154. doi:https://doi.org/10.1016/j.ppnp.2008.12.001.
URL http://www.sciencedirect.com/science/article/pii/S014664100800094X

[48] T. A. Lähde, E. Epelbaum, H. Krebs, D. Lee, U.-G. Meißner, G. Rupak, Lattice effective field theory for medium-mass nuclei, Physics Letters B 732 (2014) 110 – 115. doi:https://doi.org/10.1016/j.physletb.2014.03.023.
URL http://www.sciencedirect.com/science/article/pii/S0370269314001798

[49] A. Calci, P. Navrátil, R. Roth, J. Dohet-Eraly, S. Quaglioni, G. Hupin, Can ab initio theory explain the phenomenon of parity inversion in ^{11}Be?, Phys. Rev. Lett. 117 (2016) 242501. doi:10.1103/PhysRevLett.117.242501.
URL https://link.aps.org/doi/10.1103/PhysRevLett.117.242501

[50] S. Bagchi, R. Kanungo, W. Horiuchi, G. Hagen, T. Morris, S. Stroberg, T. Suzuki, F. Ameil, J. Atkinson, Y. Ayyad, D. Cortina-Gil, I. Dillmann, A. Estradé, A. Evdokimov, F. Farinon, H. Geissel, G. Guastalla, R. Janik, S. Kaur, R. Knöbel, J. Kurcewicz, Y. Litvinov, M. Marta, M. Mostazo, I. Mukha, C. Nociforo, H. Ong, S. Pietri, A. Prochazka, C. Scheidenberger, B. Sitar, P. Strmen, M. Takechi, J. Tanaka, Y. Tanaka, I. Tanihata, S. Terashima, J. Vargas, H. Weick, J. Winfield, Neutron skin and signature of the n = 14 shell gap found from measured proton radii of 17–22n, Physics Letters B 790 (2019) 251 – 256. doi:https://doi.org/10.1016/j.physletb.2019.01.024.
URL http://www.sciencedirect.com/science/article/pii/S0370269319300401

[51] G. Hagen, A. Ekström, C. Forssén, G. R. Jansen, W. Nazarewicz, T. Papenbrock, K. A. Wendt, S. Bacca, N. Barnea, B. Carlsson, C. Drischler, K. Hebeler,

M. Hjorth-Jensen, M. Miorelli, G. Orlandini, A. Schwenk, J. Simonis, Neutron and weak-charge distributions of the 48ca nucleus, Nature Physics 12 (2015) 186, article. doi:10.1038/nphys3529.
URL https://doi.org/10.1038/nphys3529

[52] R. F. Garcia Ruiz, M. L. Bissell, K. Blaum, A. Ekström, N. Frömmgen, G. Hagen, M. Hammen, K. Hebeler, J. D. Holt, G. R. Jansen, M. Kowalska, K. Kreim, W. Nazarewicz, R. Neugart, G. Neyens, W. Nörtershäuser, T. Papenbrock, J. Papuga, A. Schwenk, J. Simonis, K. . A. Wendt, D. T. Yordanov, Unexpectedly large charge radii of neutron-rich calcium isotopes, Nature Physics 12 (2016) 594, article. doi:10.1038/nphys3645.
URL https://doi.org/10.1038/nphys3645

[53] P. Gysbers, G. Hagen, J. D. Holt, G. R. Jansen, T. D. Morris, P. Navrátil, T. Papenbrock, S. Quaglioni, A. Schwenk, S. R. Stroberg, K. A. Wendt, Discrepancy between experimental and theoretical β-decay rates resolved from first principles, Nature Physics 15 (5) (2019) 428–431. doi:10.1038/s41567-019-0450-7.
URL https://doi.org/10.1038/s41567-019-0450-7

[54] T. D. Morris, J. Simonis, S. R. Stroberg, C. Stumpf, G. Hagen, J. D. Holt, G. R. Jansen, T. Papenbrock, R. Roth, A. Schwenk, Structure of the lightest tin isotopes, Phys. Rev. Lett. 120 (2018) 152503. doi:10.1103/PhysRevLett.120.152503.
URL https://link.aps.org/doi/10.1103/PhysRevLett.120.152503

[55] H. N. Liu, A. Obertelli, P. Doornenbal, C. A. Bertulani, G. Hagen, J. D. Holt, G. R. Jansen, T. D. Morris, A. Schwenk, R. Stroberg, N. Achouri, H. Baba, F. Browne, D. Calvet, F. Château, S. Chen, N. Chiga, A. Corsi, M. L. Cortés, A. Delbart, J.-M. Gheller, A. Giganon, A. Gillibert, C. Hilaire, T. Isobe, T. Kobayashi, Y. Kubota, V. Lapoux, T. Motobayashi, I. Murray, H. Otsu, V. Panin, N. Paul, W. Rodriguez, H. Sakurai, M. Sasano, D. Steppenbeck, L. Stuhl, Y. L. Sun, Y. Togano, T. Uesaka, K. Wimmer, K. Yoneda, O. Aktas, T. Aumann, L. X. Chung, F. Flavigny, S. Franchoo, I. Gašparić, R.-B. Gerst, J. Gibelin, K. I. Hahn, D. Kim, T. Koiwai, Y. Kondo, P. Koseoglou, J. Lee, C. Lehr, B. D. Linh, T. Lokotko, M. MacCormick, K. Moschner, T. Nakamura, S. Y. Park, D. Rossi, E. Sahin, D. Sohler, P.-A. Söderström, S. Takeuchi, H. Törnqvist, V. Vaquero, V. Wagner, S. Wang, V. Werner, X. Xu, H. Yamada, D. Yan, Z. Yang, M. Yasuda, L. Zanetti, How robust is the $n = 34$ subshell closure? first spectroscopy of ^{52}Ar, Phys. Rev. Lett. 122 (2019) 072502. doi:10.1103/PhysRevLett.122.072502.
URL https://link.aps.org/doi/10.1103/PhysRevLett.122.072502

[56] M. Hjorth-Jensen, T. T. Kuo, E. Osnes, Realistic effective interactions for nuclear systems, Physics Reports 261 (3) (1995) 125 – 270. doi:https://doi.org/10.1016/0370-1573(95)00012-6.
URL http://www.sciencedirect.com/science/article/pii/0370157395000126

[57] M. Dufour, A. P. Zuker, Realistic collective nuclear hamiltonian, Phys. Rev. C 54 (1996) 1641–1660. doi:10.1103/PhysRevC.54.1641.

URL http://link.aps.org/doi/10.1103/PhysRevC.54.1641

[58] T. Otsuka, M. Honma, T. Mizusaki, N. Shimizu, Y. Utsuno, Monte carlo shell model for atomic nuclei, Progress in Particle and Nuclear Physics 47 (1) (2001) 319 – 400. doi:https://doi.org/10.1016/S0146-6410(01)00157-0.
URL http://www.sciencedirect.com/science/article/pii/S0146641001001570

[59] S. M. Lenzi, F. Nowacki, A. Poves, K. Sieja, Island of inversion around ^{64}Cr, Phys. Rev. C 82 (2010) 054301. doi:10.1103/PhysRevC.82.054301.
URL http://link.aps.org/doi/10.1103/PhysRevC.82.054301

[60] F. Nowacki, A. Poves, E. Caurier, B. Bounthong, Shape coexistence in ^{78}Ni as the portal to the fifth island of inversion, Phys. Rev. Lett. 117 (2016) 272501. doi:10.1103/PhysRevLett.117.272501.
URL https://link.aps.org/doi/10.1103/PhysRevLett.117.272501

[61] Y. Iwata, N. Shimizu, T. Otsuka, Y. Utsuno, J. Menéndez, M. Honma, T. Abe, Large-scale shell-model analysis of the neutrinoless $\beta\beta$ decay of ^{48}Ca, Phys. Rev. Lett. 116 (2016) 112502. doi:10.1103/PhysRevLett.116.112502.
URL https://link.aps.org/doi/10.1103/PhysRevLett.116.112502

[62] J. Messud, M. Bender, E. Suraud, Density functional theory and kohn-sham scheme for self-bound systems, Phys. Rev. C 80 (2009) 054314. doi:10.1103/PhysRevC.80.054314.
URL https://link.aps.org/doi/10.1103/PhysRevC.80.054314

[63] H. Sagawa, G. Colò, Tensor interaction in mean-field and density functional theory approaches to nuclear structure, Progress in Particle and Nuclear Physics 76 (2014) 76 – 115. doi:https://doi.org/10.1016/j.ppnp.2014.01.006.
URL http://www.sciencedirect.com/science/article/pii/S0146641014000076

[64] M. Kortelainen, J. McDonnell, W. Nazarewicz, E. Olsen, P.-G. Reinhard, J. Sarich, N. Schunck, S. M. Wild, D. Davesne, J. Erler, A. Pastore, Nuclear energy density optimization: Shell structure, Phys. Rev. C 89 (2014) 054314. doi:10.1103/PhysRevC.89.054314.
URL https://link.aps.org/doi/10.1103/PhysRevC.89.054314

[65] M. Stoitsov, M. Kortelainen, S. K. Bogner, T. Duguet, R. J. Furnstahl, B. Gebremariam, N. Schunck, Microscopically based energy density functionals for nuclei using the density matrix expansion: Implementation and pre-optimization, Phys. Rev. C 82 (2010) 054307. doi:10.1103/PhysRevC.82.054307.

URL https://link.aps.org/doi/10.1103/PhysRevC.82.054307

[66] M. Bender, T. Duguet, D. Lacroix, Particle-number restoration within the energy density functional formalism, Phys. Rev. C 79 (2009) 044319. doi:10.1103/PhysRevC.79.044319.
URL https://link.aps.org/doi/10.1103/PhysRevC.79.044319

[67] T. Duguet, M. Bender, K. Bennaceur, D. Lacroix, T. Lesinski, Particle-number restoration within the energy density functional formalism: Nonviability of terms depending on noninteger powers of the density matrices, Phys. Rev. C 79 (2009) 044320. doi:10.1103/PhysRevC.79.044320.
URL https://link.aps.org/doi/10.1103/PhysRevC.79.044320

[68] D. Lacroix, T. Duguet, M. Bender, Configuration mixing within the energy density functional formalism: Removing spurious contributions from nondiagonal energy kernels, Phys. Rev. C 79 (2009) 044318. doi:10.1103/PhysRevC.79.044318.
URL https://link.aps.org/doi/10.1103/PhysRevC.79.044318

[69] B. Bally, B. Avez, M. Bender, P.-H. Heenen, Beyond mean-field calculations for odd-mass nuclei, Phys. Rev. Lett. 113 (2014) 162501. doi:10.1103/PhysRevLett.113.162501.
URL https://link.aps.org/doi/10.1103/PhysRevLett.113.162501

[70] D. T. Tran, H. J. Ong, G. Hagen, T. D. Morris, N. Aoi, T. Suzuki, Y. Kanada-En'yo, L. S. Geng, S. Terashima, I. Tanihata, T. T. Nguyen, Y. Ayyad, P. Y. Chan, M. Fukuda, H. Geissel, M. N. Harakeh, T. Hashimoto, T. H. Hoang, E. Ideguchi, A. Inoue, G. R. Jansen, R. Kanungo, T. Kawabata, L. H. Khiem, W. P. Lin, K. Matsuta, M. Mihara, S. Momota, D. Nagae, N. D. Nguyen, D. Nishimura, T. Otsuka, A. Ozawa, P. P. Ren, H. Sakaguchi, C. Scheidenberger, J. Tanaka, M. Takechi, R. Wada, T. Yamamoto, Evidence for prevalent z = 6 magic number in neutron-rich carbon isotopes, Nature Communications 9 (1) (2018) 1594. doi:10.1038/s41467-018-04024-y.
URL https://doi.org/10.1038/s41467-018-04024-y

[71] K. Tshoo, Y. Satou, H. Bhang, S. Choi, T. Nakamura, Y. Kondo, S. Deguchi, Y. Kawada, N. Kobayashi, Y. Nakayama, K. N. Tanaka, N. Tanaka, N. Aoi, M. Ishihara, T. Motobayashi, H. Otsu, H. Sakurai, S. Takeuchi, Y. Togano, K. Yoneda, Z. H. Li, F. Delaunay, J. Gibelin, F. M. Marqués, N. A. Orr, T. Honda, M. Matsushita, T. Kobayashi, Y. Miyashita, T. Sumikama, K. Yoshinaga, S. Shimoura, D. Sohler, T. Zheng, Z. X. Cao, $n = 16$ spherical shell closure in $^{24}\mathbf{O}$, Phys. Rev. Lett. 109 (2012) 022501. doi:10.1103/PhysRevLett.109.022501.
URL https://link.aps.org/doi/10.1103/PhysRevLett.109.022501

[72] T. Otsuka, T. Suzuki, J. D. Holt, A. Schwenk, Y. Akaishi, Three-body forces and the limit of oxygen isotopes, Phys. Rev. Lett. 105 (2010) 032501.

doi:10.1103/PhysRevLett.105.032501.
URL https://link.aps.org/doi/10.1103/PhysRevLett.105.032501

[73] D. Steppenbeck, S. Takeuchi, N. Aoi, P. Doornenbal, M. Matsushita, H. Wang, H. Baba, N. Fukuda, S. Go, M. Honma, J. Lee, K. Matsui, S. Michimasa, T. Motobayashi, D. Nishimura, T. Otsuka, H. Sakurai, Y. Shiga, P.-A. Söderström, T. Sumikama, H. Suzuki, R. Taniuchi, Y. Utsuno, J. J. Valiente-Dobón, K. Yoneda, Evidence for a new nuclear magic number from the level structure of 54ca, Nature 502 (2013) 207. doi:10.1038/nature12522.
URL https://doi.org/10.1038/nature12522

[74] R. Taniuchi, C. Santamaria, P. Doornenbal, A. Obertelli, K. Yoneda, G. Authelet, H. Baba, D. Calvet, F. Château, A. Corsi, A. Delbart, J.-M. Gheller, A. Gillibert, J. D. Holt, T. Isobe, V. Lapoux, M. Matsushita, J. Menéndez, S. Momiyama, T. Motobayashi, M. Niikura, F. Nowacki, K. Ogata, H. Otsu, T. Otsuka, C. Péron, S. Péru, A. Peyaud, E. C. Pollacco, A. Poves, J.-Y. Roussé, H. Sakurai, A. Schwenk, Y. Shiga, J. Simonis, S. R. Stroberg, S. Takeuchi, Y. Tsunoda, T. Uesaka, H. Wang, F. Browne, L. X. Chung, Z. Dombradi, S. Franchoo, F. Giacoppo, A. Gottardo, K. Hadyńska-Klęk, Z. Korkulu, S. Koyama, Y. Kubota, J. Lee, M. Lettmann, C. Louchart, R. Lozeva, K. Matsui, T. Miyazaki, S. Nishimura, L. Olivier, S. Ota, Z. Patel, E. Şahin, C. Shand, P.-A. Söderström, I. Stefan, D. Steppenbeck, T. Sumikama, D. Suzuki, Z. Vajta, V. Werner, J. Wu, Z. Y. Xu, 78ni revealed as a doubly magic stronghold against nuclear deformation, Nature 569 (7754) (2019) 53–58. doi:10.1038/s41586-019-1155-x.
URL https://doi.org/10.1038/s41586-019-1155-x

[75] C. B. Hinke, M. Böhmer, P. Boutachkov, T. Faestermann, H. Geissel, J. Gerl, R. Gernhäuser, M. Górska, A. Gottardo, H. Grawe, J. L. Grębosz, R. Krücken, N. Kurz, Z. Liu, L. Maier, F. Nowacki, S. Pietri, Z. Podolyák, K. Sieja, K. Steiger, K. Straub, H. Weick, H.-J. Wollersheim, P. J. Woods, N. Al-Dahan, N. Alkhomashi, A. Ataç, A. Blazhev, N. F. Braun, I. T. Čeliković, T. Davinson, I. Dillmann, C. Domingo-Pardo, P. C. Doornenbal, G. de France, G. F. Farrelly, F. Farinon, N. Goel, T. C. Habermann, R. Hoischen, R. Janik, M. Karny, A. Kaşkaş, I. M. Kojouharov, T. Kröll, Y. Litvinov, S. Myalski, F. Nebel, S. Nishimura, C. Nociforo, J. Nyberg, A. R. Parikh, A. Procházka, P. H. Regan, C. Rigollet, H. Schaffner, C. Scheidenberger, S. Schwertel, P.-A. Söderström, S. J. Steer, A. Stolz, P. Strmeň, Superallowed gamow–teller decay of the doubly magic nucleus 100sn, Nature 486 (2012) 341, article. doi:10.1038/nature11116.
URL https://doi.org/10.1038/nature11116

[76] T. Togashi, Y. Tsunoda, T. Otsuka, N. Shimizu, M. Honma, Novel shape evolution in sn isotopes from magic numbers 50 to 82, Phys. Rev. Lett. 121 (2018) 062501. doi:10.1103/PhysRevLett.121.062501.
URL https://link.aps.org/doi/10.1103/PhysRevLett.121.062501

[77] K. L. Jones, A. S. Adekola, D. W. Bardayan, J. C. Blackmon, K. Y. Chae, K. A. Chipps, J. A. Cizewski, L. Erikson, C. Harlin, R. Hatarik, R. Kapler, R. L. Kozub, J. F. Liang, R. Livesay, Z. Ma, B. H. Moazen, C. D. Nesaraja, F. M. Nunes, S. D. Pain, N. P. Patterson, D. Shapira, J. F. Shriner Jr, M. S. Smith, T. P. Swan, J. S.

Thomas, The magic nature of 132sn explored through the single-particle states of 133sn, Nature 465 (2010) 454. doi:10.1038/nature09048.
URL https://doi.org/10.1038/nature09048

[78] A. Bürger, T. Saito, H. Grawe, H. Hübel, P. Reiter, J. Gerl, M. Górska, H. Wollersheim, A. Al-Khatib, A. Banu, T. Beck, F. Becker, P. Bednarczyk, G. Benzoni, A. Bracco, S. Brambilla, P. Bringel, F. Camera, E. Clément, P. Doornenbal, H. Geissel, A. Görgen, J. Grębosz, G. Hammond, M. Hellström, M. Honma, M. Kavatsyuk, O. Kavatsyuk, M. Kmiecik, I. Kojouharov, W. Korten, N. Kurz, R. Lozeva, A. Maj, S. Mandal, B. Million, S. Muralithar, A. Neußer, F. Nowacki, T. Otsuka, Z. Podolyák, N. Saito, A. Singh, H. Weick, C. Wheldon, O. Wieland, M. Winkler, Relativistic coulomb excitation of neutron-rich 54,56,58cr: On the pathway of magicity from n=40 to n=32, Physics Letters B 622 (1) (2005) 29 – 34. doi:https://doi.org/10.1016/j.physletb.2005.07.004.
URL http://www.sciencedirect.com/science/article/pii/S0370269305009524

[79] R. Janssens, B. Fornal, P. Mantica, B. Brown, R. Broda, P. Bhattacharyya, M. Carpenter, M. Cinausero, P. Daly, A. Davies, T. Glasmacher, Z. Grabowski, D. Groh, M. Honma, F. Kondev, W. Królas, T. Lauritsen, S. Liddick, S. Lunardi, N. Marginean, T. Mizusaki, D. Morrissey, A. Morton, W. Mueller, T. Otsuka, T. Pawlat, D. Seweryniak, H. Schatz, A. Stolz, S. Tabor, C. Ur, G. Viesti, I. Wiedenhöver, J. Wrzesiński, Structure of 52,54ti and shell closures in neutron-rich nuclei above 48ca, Physics Letters B 546 (1) (2002) 55 – 62. doi:https://doi.org/10.1016/S0370-2693(02)02682-5.
URL http://www.sciencedirect.com/science/article/pii/S0370269302026825

[80] A. Dewald, O. Möller, P. Petkov, Developing the recoil distance doppler-shift technique towards a versatile tool for lifetime measurements of excited nuclear states, Progress in Particle and Nuclear Physics 67 (3) (2012) 786 – 839. doi:http://dx.doi.org/10.1016/j.ppnp.2012.03.003.
URL http://www.sciencedirect.com/science/article/pii/S0146641012000713

[81] J. Ljungvall, A. Görgen, A. Obertelli, W. Korten, E. Clément, G. de France, A. Bürger, J.-P. Delaroche, A. Dewald, A. Gadea, L. Gaudefroy, M. Girod, M. Hackstein, J. Libert, D. Mengoni, F. Nowacki, T. Pissulla, A. Poves, F. Recchia, M. Rejmund, W. Rother, E. Sahin, C. Schmitt, A. Shrivastava, K. Sieja, J. J. Valiente-Dobón, K. O. Zell, M. Zielińska, Onset of collectivity in neutron-rich fe isotopes: Toward a new island of inversion?, Phys. Rev. C 81 (2010) 061301. doi:10.1103/PhysRevC.81.061301.
URL http://link.aps.org/doi/10.1103/PhysRevC.81.061301

[82] W. Rother, A. Dewald, H. Iwasaki, S. M. Lenzi, K. Starosta, D. Bazin, T. Baugher, B. A. Brown, H. L. Crawford, C. Fransen, A. Gade, T. N. Ginter, T. Glasmacher, G. F. Grinyer, M. Hackstein, G. Ilie, J. Jolie, S. McDaniel, D. Miller, P. Petkov, T. Pissulla, A. Ratkiewicz, C. A. Ur, P. Voss, K. A. Walsh, D. Weisshaar, K.-O. Zell, Enhanced quadrupole collectivity at $n = 40$: The case of neutron-rich fe isotopes, Phys. Rev. Lett. 106 (2011) 022502.

doi:10.1103/PhysRevLett.106.022502.
URL http://link.aps.org/doi/10.1103/PhysRevLett.106.022502

[83] A. Dijon, E. Clément, G. de France, P. Van Isacker, J. Ljungvall, A. Görgen, A. Obertelli, W. Korten, A. Dewald, A. Gadea, et al., Lifetime measurements in ^{63}Co and ^{65}Co, Phys. Rev. C 83 (2011) 064321. doi:10.1103/PhysRevC.83.064321.
URL http://link.aps.org/doi/10.1103/PhysRevC.83.064321

[84] I. Čeliković, A. Dijon, E. Clément, G. de France, P. Van Isacker, J. Ljungvall, A. Dewald, C. Fransen, G. Georgiev, A. Görgen, A. Gottardo, M. Hackstein, T. W. Hagen, C. Louchart, P. Napiorkowski, A. Obertelli, F. Recchia, W. Rother, S. Siem, B. Sulignano, P. Ujić, J. J. Valiente-Dobón, M. Zielińska, Probing collectivity in zn isotopes with one particle or hole outside the $n = 40$ subshell closure, Phys. Rev. C 91 (2015) 044311. doi:10.1103/PhysRevC.91.044311.
URL http://link.aps.org/doi/10.1103/PhysRevC.91.044311

[85] M. P. Carpenter, R. V. F. Janssens, S. Zhu, Shape coexistence in neutron-rich nuclei near $n = 40$, Phys. Rev. C 87 (2013) 041305. doi:10.1103/PhysRevC.87.041305.
URL http://link.aps.org/doi/10.1103/PhysRevC.87.041305

[86] M. Klintefjord, J. Ljungvall, A. Görgen, S. M. Lenzi, F. L. Bello Garrote, A. Blazhev, E. Clément, G. de France, J.-P. Delaroche, P. Désesquelles, A. Dewald, D. T. Doherty, C. Fransen, A. Gengelbach, G. Georgiev, M. Girod, A. Goasduff, A. Gottardo, K. Hadyńska-Klęk, B. Jacquot, T. Konstantinopoulos, A. Korichi, A. Lemasson, J. Libert, A. Lopez-Martens, C. Michelagnoli, A. Navin, J. Nyberg, R. M. Pérez-Vidal, S. Roccia, E. Sahin, I. Stefan, A. E. Stuchbery, M. Zielińska, D. Barrientos, B. Birkenbach, A. Boston, L. Charles, M. Ciemala, J. Dudouet, J. Eberth, A. Gadea, V. González, L. Harkness-Brennan, H. Hess, A. Jungclaus, W. Korten, R. Menegazzo, D. Mengoni, B. Million, A. Pullia, D. Ralet, F. Recchia, P. Reiter, M. D. Salsac, E. Sanchis, O. Stezowski, C. Theisen, J. J. Valiente Dobon, Measurement of lifetimes in ^{62,64}Fe,^{61,63} Co, and ^{59}Mn, Phys. Rev. C 95 (2017) 024312. doi:10.1103/PhysRevC.95.024312.
URL http://link.aps.org/doi/10.1103/PhysRevC.95.024312

[87] S. N. Liddick, S. Suchyta, B. Abromeit, A. Ayres, A. Bey, C. R. Bingham, M. Bolla, M. P. Carpenter, L. Cartegni, C. J. Chiara, H. L. Crawford, I. G. Darby, R. Grzywacz, G. Gürdal, S. Ilyushkin, N. Larson, M. Madurga, E. A. McCutchan, D. Miller, S. Padgett, S. V. Paulauskas, J. Pereira, M. M. Rajabali, K. Rykaczewski, S. Vinnikova, W. B. Walters, S. Zhu, Shape coexistence along $n = 40$, Phys. Rev. C 84 (2011) 061305. doi:10.1103/PhysRevC.84.061305.
URL https://link.aps.org/doi/10.1103/PhysRevC.84.061305

[88] J. M. Daugas, I. Matea, J.-P. Delaroche, M. Pfützner, M. Sawicka, F. Becker, G. Bélier, C. R. Bingham, R. Borcea, E. Bouchez, A. Buta, E. Dragulescu, G. Georgiev, J. Giovinazzo, M. Girod, H. Grawe, R. Grzywacz, F. Hammache, F. Ibrahim, M. Lewitowicz, J. Libert, P. Mayet, V. Méot, F. Negoita, F. de Oliveira Santos, O. Perru, O. Roig, K. Rykaczewski, M. G. Saint-Laurent, J. E. Sauvestre, O. Sorlin, M. Stanoiu, I. Stefan, C. Stodel, C. Theisen, D. Verney, J. Żylicz, β-decay measurements for $n\>40$ mn nuclei and inference of collectivity for neutron-rich fe isotopes, Phys. Rev. C 83 (2011) 054312. doi:10.1103/PhysRevC.83.054312.
URL http://link.aps.org/doi/10.1103/PhysRevC.83.054312

[89] S. N. Liddick, B. Abromeit, A. Ayres, A. Bey, C. R. Bingham, M. Bolla, L. Cartegni, H. L. Crawford, I. G. Darby, R. Grzywacz, S. Ilyushkin, N. Larson, M. Madurga, D. Miller, S. Padgett, S. Paulauskas, M. M. Rajabali, K. Rykaczewski, S. Suchyta, Low-energy structure of ${}^{66}_{27}\mathrm{co}_{39}$ and ${}^{68}_{27}\mathrm{co}_{41}$ populated through β decay, Phys. Rev. C 85 (2012) 014328. doi:10.1103/PhysRevC.85.014328.
URL https://link.aps.org/doi/10.1103/PhysRevC.85.014328

[90] C. Louchart, A. Obertelli, A. Görgen, W. Korten, D. Bazzacco, B. Birkenbach, B. Bruyneel, E. Clément, P. J. Coleman-Smith, L. Corradi, D. Curien, G. de Angelis, G. de France, J.-P. Delaroche, A. Dewald, F. Didierjean, M. Doncel, G. Duchêne, J. Eberth, M. N. Erduran, E. Farnea, C. Finck, E. Fioretto, C. Fransen, A. Gadea, M. Girod, A. Gottardo, J. Grebosz, T. Habermann, M. Hackstein, T. Huyuk, J. Jolie, D. Judson, A. Jungclaus, N. Karkour, S. Klupp, R. Krücken, A. Kusoglu, S. M. Lenzi, J. Libert, J. Ljungvall, S. Lunardi, G. Maron, R. Menegazzo, D. Mengoni, C. Michelagnoli, B. Million, P. Molini, O. Möller, G. Montagnoli, D. Montanari, D. R. Napoli, R. Orlandi, G. Pollarolo, A. Prieto, A. Pullia, B. Quintana, F. Recchia, P. Reiter, D. Rosso, W. Rother, E. Sahin, M.-D. Salsac, F. Scarlassara, M. Schlarb, S. Siem, P. P. Singh, P.-A. Söderström, A. M. Stefanini, O. Stézowski, B. Sulignano, S. Szilner, C. Theisen, C. A. Ur, J. J. Valiente-Dobón, M. Zielinska, Collective nature of low-lying excitations in ${}^{70,72,74}\mathrm{zn}$ from lifetime measurements using the agata spectrometer demonstrator, Phys. Rev. C 87 (2013) 054302. doi:10.1103/PhysRevC.87.054302.
URL http://link.aps.org/doi/10.1103/PhysRevC.87.054302

[91] S. N. Liddick, B. Abromeit, A. Ayres, A. Bey, C. R. Bingham, B. A. Brown, L. Cartegni, H. L. Crawford, I. G. Darby, R. Grzywacz, S. Ilyushkin, M. Hjorth-Jensen, N. Larson, M. Madurga, D. Miller, S. Padgett, S. V. Paulauskas, M. M. Rajabali, K. Rykaczewski, S. Suchyta, Low-energy level schemes of ${}^{\mathbf{66,68}}\mathrm{fe}$ and inferred proton and neutron excitations across $\mathbf{Z = 28}$ and $\mathbf{N = 40}$, Phys. Rev. C 87 (2013) 014325. doi:10.1103/PhysRevC.87.014325.
URL http://link.aps.org/doi/10.1103/PhysRevC.87.014325

[92] H. L. Crawford, R. M. Clark, P. Fallon, A. O. Macchiavelli, T. Baugher, D. , Bazin, C. W. Beausang, J. S. Berryman, D. L. Bleuel, C. M. Campbell,

M. Cromaz, G. d. Angelis, A. Gade, R. O. Hughes, I. Y. Lee, S. M. Lenzi, F. Nowacki, S. Paschalis, M. Petri, A. Poves, A. Ratkiewicz, T. J. Ross, E. Sahin, D. Weisshaar, K. Wimmer, R. Winkler, Quadrupole collectivity in neutron-rich fe and cr isotopes, Phys. Rev. Lett. 110 (2013) 242701. doi:10.1103/PhysRevLett.110.242701.
URL http://link.aps.org/doi/10.1103/PhysRevLett.110.242701

[93] C. Santamaria, C. Louchart, A. Obertelli, V. Werner, P. Doornenbal, F. Nowacki, G. Authelet, H. Baba, D. Calvet, F. Château, A. Corsi, A. Delbart, J.-M. Gheller, A. Gillibert, T. Isobe, V. Lapoux, M. Matsushita, S. Momiyama, T. Motobayashi, M. Niikura, H. Otsu, C. Péron, A. Peyaud, E. C. Pollacco, J.-Y. Roussé, H. Sakurai, M. Sasano, Y. Shiga, S. Takeuchi, R. Taniuchi, T. Uesaka, H. Wang, K. Yoneda, F. Browne, L. X. Chung, Z. Dombradi, S. Franchoo, F. Giacoppo, A. Gottardo, K. Hadynska-Klek, Z. Korkulu, S. Koyama, Y. Kubota, J. Lee, M. Lettmann, R. Lozeva, K. Matsui, T. Miyazaki, S. Nishimura, L. Olivier, S. Ota, Z. Patel, N. Pietralla, E. Sahin, C. Shand, P.-A. Söderström, I. Stefan, D. Steppenbeck, T. Sumikama, D. Suzuki, Z. Vajta, J. Wu, Z. Xu, Extension of the $n = 40$ island of inversion towards $n = 50$: Spectroscopy of ^{66}Cr, ^{70,72}Fe, Phys. Rev. Lett. 115 (2015) 192501. doi:10.1103/PhysRevLett.115.192501.
URL http://link.aps.org/doi/10.1103/PhysRevLett.115.192501

[94] K. Wimmer, F. Recchia, S. Lenzi, S. Riccetto, T. Davinson, A. Estrade, C. Griffin, S. Nishimura, F. Nowacki, V. Phong, A. Poves, P.-A. Söderström, O. Aktas, M. Al-Aqeel, T. Ando, H. Baba, S. Bae, S. Choi, P. Doornenbal, J. Ha, L. Harkness-Brennan, T. Isobe, P. John, D. Kahl, G. Kiss, I. Kojouharov, N. Kurz, M. Labiche, K. Matsui, S. Momiyama, D. Napoli, M. Niikura, C. Nita, Y. Saito, H. Sakurai, H. Schaffner, P. Schrock, C. Stahl, T. Sumikama, V. Werner, W. Witt, P. Woods, First spectroscopy of 61ti and the transition to the island of inversion at n = 40, Physics Letters B 792 (2019) 16 – 20. doi:https://doi.org/10.1016/j.physletb.2019.03.018.
URL http://www.sciencedirect.com/science/article/pii/S0370269319301728

[95] A. Gade, R. V. F. Janssens, J. A. Tostevin, D. Bazin, J. Belarge, P. C. Bender, S. Bottoni, M. P. Carpenter, B. Elman, S. J. Freeman, T. Lauritsen, S. M. Lenzi, B. Longfellow, E. Lunderberg, A. Poves, L. A. Riley, D. K. Sharp, D. Weisshaar, S. Zhu, Structure of ^{70}Fe: Single-particle and collective degrees of freedom, Phys. Rev. C 99 (2019) 011301. doi:10.1103/PhysRevC.99.011301.
URL https://link.aps.org/doi/10.1103/PhysRevC.99.011301

[96] J. Kotila, S. M. Lenzi, Collective features of cr and fe isotopes, Phys. Rev. C 89 (2014) 064304. doi:10.1103/PhysRevC.89.064304.
URL http://link.aps.org/doi/10.1103/PhysRevC.89.064304

[97] L. Coraggio, A. Covello, A. Gargano, N. Itaco, Realistic shell-model calculations for isotopic chains "north-east" of ^{48}Ca in the (n,z) plane, Phys. Rev. C 89 (2014) 024319. doi:10.1103/PhysRevC.89.024319.

URL http://link.aps.org/doi/10.1103/PhysRevC.89.024319

[98] K. Sato, N. Hinohara, K. Yoshida, T. Nakatsukasa, M. Matsuo, K. Matsuyanagi, Shape transition and fluctuations in neutron-rich cr isotopes around $n = 40$, Phys. Rev. C 86 (2012) 024316. doi:10.1103/PhysRevC.86.024316.
URL http://link.aps.org/doi/10.1103/PhysRevC.86.024316

[99] T. R. Rodríguez, A. Poves, F. Nowacki, Occupation numbers of spherical orbits in self-consistent beyond-mean-field methods, Phys. Rev. C 93 (2016) 054316. doi:10.1103/PhysRevC.93.054316.
URL https://link.aps.org/doi/10.1103/PhysRevC.93.054316

[100] A. Kusoglu, A. E. Stuchbery, G. Georgiev, B. A. Brown, A. Goasduff, L. Atanasova, D. L. Balabanski, M. Bostan, M. Danchev, P. Detistov, K. A. Gladnishki, J. Ljungvall, I. Matea, D. Radeck, C. Sotty, I. Stefan, D. Verney, D. T. Yordanov, Magnetism of an excited self-conjugate nucleus: Precise measurement of the g factor of the 2_1^+ state in ^{24}Mg, Phys. Rev. Lett. 114 (2015) 062501. doi:10.1103/PhysRevLett.114.062501.
URL http://link.aps.org/doi/10.1103/PhysRevLett.114.062501

[101] A. E. Stuchbery, P. F. Mantica, A. N. Wilson, Electron-configuration-reset time-differential recoil-in-vacuum technique for excited-state g -factor measurements on fast exotic beams, Phys. Rev. C 71 (2005) 047302. doi:10.1103/PhysRevC.71.047302.
URL http://link.aps.org/doi/10.1103/PhysRevC.71.047302

[102] W. Schwerdtfeger, P. G. Thirolf, K. Wimmer, D. Habs, H. Mach, T. R. Rodriguez, V. Bildstein, J. L. Egido, L. M. Fraile, R. Gernhäuser, R. Hertenberger, K. Heyde, P. Hoff, H. Hübel, U. Köster, T. Kröll, R. Krücken, R. Lutter, T. Morgan, P. Ring, Shape coexistence near neutron number $n = 20$: First identification of the $e0$ decay from the deformed first excited $J^\pi = 0^+$ state in ^{30}Mg, Phys. Rev. Lett. 103 (2009) 012501. doi:10.1103/PhysRevLett.103.012501.
URL https://link.aps.org/doi/10.1103/PhysRevLett.103.012501

[103] K. Wimmer, T. Kröll, R. Krücken, V. Bildstein, R. Gernhäuser, B. Bastin, N. Bree, J. Diriken, P. Van Duppen, M. Huyse, N. Patronis, P. Vermaelen, D. Voulot, J. Van de Walle, F. Wenander, L. M. Fraile, R. Chapman, B. Hadinia, R. Orlandi, J. F. Smith, R. Lutter, P. G. Thirolf, M. Labiche, A. Blazhev, M. Kalkühler, P. Reiter, M. Seidlitz, N. Warr, A. O. Macchiavelli, H. B. Jeppesen, E. Fiori, G. Georgiev, G. Schrieder, S. Das Gupta, G. Lo Bianco, S. Nardelli, J. Butterworth, J. Johansen, K. Riisager, Discovery of the shape coexisting 0^+ state in ^{32}Mg by a two neutron transfer reaction, Phys. Rev. Lett. 105 (2010) 252501. doi:10.1103/PhysRevLett.105.252501.
URL https://link.aps.org/doi/10.1103/PhysRevLett.105.252501

[104] C. Force, S. Grévy, L. Gaudefroy, O. Sorlin, L. Cáceres, F. Rotaru, J. Mrazek, N. L. Achouri, J. C. Angélique, F. Azaiez, B. Bastin, R. Borcea, A. Buta, J. M. Daugas, Z. Dlouhy, Z. Dombrádi, F. De Oliveira, F. Negoita, Y. Penionzhkevich, M. G. Saint-Laurent, D. Sohler, M. Stanoiu, I. Stefan, C. Stodel, F. Nowacki, Prolate-spherical shape coexistence at $n = 28$ in $^{44}\mathbf{S}$, Phys. Rev. Lett. 105 (2010) 102501. doi:10.1103/PhysRevLett.105.102501.
URL https://link.aps.org/doi/10.1103/PhysRevLett.105.102501

[105] L. Gaudefroy, J. M. Daugas, M. Hass, S. Grévy, C. Stodel, J. C. Thomas, L. Perrot, M. Girod, B. Rossé, J. C. Angélique, D. L. Balabanski, E. Fiori, C. Force, G. Georgiev, D. Kameda, V. Kumar, R. L. Lozeva, I. Matea, V. Méot, P. Morel, B. S. N. Singh, F. Nowacki, G. Simpson, Shell erosion and shape coexistence in $^{43}_{16}S_{27}$, Phys. Rev. Lett. 102 (2009) 092501. doi:10.1103/PhysRevLett.102.092501.
URL https://link.aps.org/doi/10.1103/PhysRevLett.102.092501

[106] A. D. Davies, A. E. Stuchbery, P. F. Mantica, P. M. Davidson, A. N. Wilson, A. Becerril, B. A. Brown, C. M. Campbell, J. M. Cook, D. C. Dinca, A. Gade, S. N. Liddick, T. J. Mertzimekis, W. F. Mueller, J. R. Terry, B. E. Tomlin, K. Yoneda, H. Zwahlen, Probing shell structure and shape changes in neutron-rich sulfur isotopes through transient-field g-factor measurements on fast radioactive beams of ^{38}S and ^{40}S., Phys. Rev. Lett. 96 (2006) 112503. doi:10.1103/PhysRevLett.96.112503.
URL https://link.aps.org/doi/10.1103/PhysRevLett.96.112503

[107] A. Ayangeakaa, R. Janssens, C. Wu, J. Allmond, J. Wood, S. Zhu, M. Albers, S. Almaraz-Calderon, B. Bucher, M. Carpenter, C. Chiara, D. Cline, H. Crawford, H. David, J. Harker, A. Hayes, C. Hoffman, B. Kay, K. Kolos, A. Korichi, T. Lauritsen, A. Macchiavelli, A. Richard, D. Seweryniak, A. Wiens, Shape coexistence and the role of axial asymmetry in 72ge, Physics Letters B 754 (2016) 254 – 259. doi:https://doi.org/10.1016/j.physletb.2016.01.036.
URL http://www.sciencedirect.com/science/article/pii/S0370269316000538

[108] S. Leoni, B. Fornal, N. Mărginean, M. Sferrazza, Y. Tsunoda, T. Otsuka, G. Bocchi, F. C. L. Crespi, A. Bracco, S. Aydin, M. Boromiza, D. Bucurescu, N. Cieplicka-Oryńczak, C. Costache, S. Călinescu, N. Florea, D. G. Ghiţă, T. Glodariu, A. Ionescu, L. Iskra, M. Krzysiek, R. Mărginean, C. Mihai, R. E. Mihai, A. Mitu, A. Negreţ, C. R. Niţă, A. Olăcel, A. Oprea, S. Pascu, P. Petkov, C. Petrone, G. Porzio, A. Şerban, C. Sotty, L. Stan, I. Ştiru, L. Stroe, R. Şuvăilă, S. Toma, A. Turturică, S. Ujeniuc, C. A. Ur, Multifaceted quadruplet of low-lying spin-zero states in ^{66}Ni: Emergence of shape isomerism in light nuclei, Phys. Rev. Lett. 118 (2017) 162502. doi:10.1103/PhysRevLett.118.162502.
URL https://link.aps.org/doi/10.1103/PhysRevLett.118.162502

[109] B. Crider, C. Prokop, S. Liddick, M. Al-Shudifat, A. Ayangeakaa, M. Carpenter, J. Carroll, J. Chen, C. Chiara, H. David, A. Dombos, S. Go, R. Grzywacz, J. Harker, R. Janssens, N. Larson, T. Lauritsen, R. Lewis, S. Quinn, F. Recchia, A. Spyrou, S. Suchyta, W. Walters, S. Zhu, Shape coexistence from lifetime and branching-ratio measurements in 68,70ni, Physics Letters B 763 (2016) 108 – 113. doi:https://doi.org/10.1016/j.physletb.2016.10.020.
URL http://www.sciencedirect.com/science/article/pii/S0370269316305913

[110] X. F. Yang, C. Wraith, L. Xie, C. Babcock, J. Billowes, M. L. Bissell, K. Blaum, B. Cheal, K. T. Flanagan, R. F. Garcia Ruiz, W. Gins, C. Gorges, L. K. Grob, H. Heylen, S. Kaufmann, M. Kowalska, J. Kraemer, S. Malbrunot-Ettenauer, R. Neugart, G. Neyens, W. Nörtershäuser, J. Papuga, R. Sánchez, D. T. Yordanov, Isomer shift and magnetic moment of the long-lived $1/2^+$ isomer in ${}^{79}_{30}\mathrm{zn}_{49}$: Signature of shape coexistence near ${}^{78}\mathrm{Ni}$, Phys. Rev. Lett. 116 (2016) 182502. doi:10.1103/PhysRevLett.116.182502.
URL https://link.aps.org/doi/10.1103/PhysRevLett.116.182502

[111] C. Delafosse, D. Verney, P. Marević, A. Gottardo, C. Michelagnoli, A. Lemasson, A. Goasduff, J. Ljungvall, E. Clément, A. Korichi, G. De Angelis, C. Andreoiu, M. Babo, A. Boso, F. Didierjean, J. Dudouet, S. Franchoo, A. Gadea, G. Georgiev, F. Ibrahim, B. Jacquot, T. Konstantinopoulos, S. M. Lenzi, G. Maquart, I. Matea, D. Mengoni, D. R. Napoli, T. Nikšić, L. Olivier, R. M. Pérez-Vidal, C. Portail, F. Recchia, N. Redon, M. Siciliano, I. Stefan, O. Stezowski, D. Vretenar, M. Zielinska, D. Barrientos, G. Benzoni, B. Birkenbach, A. J. Boston, H. C. Boston, B. Cederwall, L. Charles, M. Ciemala, J. Collado, D. M. Cullen, P. Désesquelles, G. de France, C. Domingo-Pardo, J. Eberth, V. González, L. J. Harkness-Brennan, H. Hess, D. S. Judson, A. Jungclaus, W. Korten, A. Lefevre, F. Legruel, R. Menegazzo, B. Million, J. Nyberg, B. Quintana, D. Ralet, P. Reiter, F. Saillant, E. Sanchis, C. Theisen, J. J. Valiente Dobon, Pseudospin symmetry and microscopic origin of shape coexistence in the ${}^{78}\mathrm{Ni}$ region: A hint from lifetime measurements, Phys. Rev. Lett. 121 (2018) 192502. doi:10.1103/PhysRevLett.121.192502.
URL https://link.aps.org/doi/10.1103/PhysRevLett.121.192502

[112] Görgen, A., Clément, E., Chatillon, A., Dewald, A., Korten, W., Le Coz, Y., Mąrginean, N., Melon, B., Menegazzo, R., Möller, O., Theisen, Ch., Tonev, D., Ur, C. A., Zell, K. O., Lifetime measurement in 74kr and 76kr, Eur. Phys. J. A 26 (2) (2005) 153–157. doi:10.1140/epja/i2005-10174-3.
URL http://dx.doi.org/10.1140/epja/i2005-10174-3

[113] E. Clément, A. Görgen, W. Korten, E. Bouchez, A. Chatillon, J.-P. Delaroche, M. Girod, H. Goutte, A. Hürstel, Y. L. Coz, A. Obertelli, S. Péru, C. Theisen, J. N. Wilson, M. Zielińska, C. Andreoiu, F. Becker, P. A. Butler, J. M. Casandjian, W. N. Catford, T. Czosnyka, G. d. France, J. Gerl, R.-D. Herzberg, J. Iwanicki, D. G. Jenkins, G. D. Jones, P. J. Napiorkowski, G. Sletten, C. N. Timis, Shape coexistence in neutron-deficient krypton isotopes, Phys. Rev. C 75 (2007) 054313. doi:10.1103/PhysRevC.75.054313.

URL https://link.aps.org/doi/10.1103/PhysRevC.75.054313

[114] A. Petrovici, K. Schmid, A. Faessler, Microscopic aspects of shape coexistence in 72kr and 74kr, Nuclear Physics A 665 (3) (2000) 333 – 350. doi:https://doi.org/10.1016/S0375-9474(99)00811-8.
URL http://www.sciencedirect.com/science/article/pii/S0375947499008118

[115] M. Bender, P. Bonche, P.-H. Heenen, Shape coexistence in neutron-deficient kr isotopes: Constraints on the single-particle spectrum of self-consistent mean-field models from collective excitations, Phys. Rev. C 74 (2006) 024312. doi:10.1103/PhysRevC.74.024312.
URL https://link.aps.org/doi/10.1103/PhysRevC.74.024312

[116] M. Girod, J.-P. Delaroche, A. Görgen, A. Obertelli, The role of triaxiality for the coexistence and evolution of shapes in light krypton isotopes, Physics Letters B 676 (1) (2009) 39 – 43. doi:https://doi.org/10.1016/j.physletb.2009.04.077.
URL http://www.sciencedirect.com/science/article/pii/S0370269309005218

[117] A. M. Hurst, P. A. Butler, D. G. Jenkins, P. Delahaye, F. Wenander, F. Ames, C. J. Barton, T. Behrens, A. Bürger, J. Cederkäll, E. Clément, T. Czosnyka, T. Davinson, G. de Angelis, J. Eberth, A. Ekström, S. Franchoo, G. Georgiev, A. Görgen, R.-D. Herzberg, M. Huyse, O. Ivanov, J. Iwanicki, G. D. Jones, P. Kent, U. Köster, T. Kröll, R. Krücken, A. C. Larsen, M. Nespolo, M. Pantea, E. S. Paul, M. Petri, H. Scheit, T. Sieber, S. Siem, J. F. Smith, A. Steer, I. Stefanescu, N. U. H. Syed, J. Van de Walle, P. Van Duppen, R. Wadsworth, N. Warr, D. Weisshaar, M. Zielińska, Measurement of the sign of the spectroscopic quadrupole moment for the 2_1^+ state in ^{70}Se: No evidence for oblate shape, Phys. Rev. Lett. 98 (2007) 072501. doi:10.1103/PhysRevLett.98.072501.
URL https://link.aps.org/doi/10.1103/PhysRevLett.98.072501

[118] B. S. Nara Singh, A. N. Steer, D. G. Jenkins, R. Wadsworth, M. A. Bentley, P. J. Davies, R. Glover, N. S. Pattabiraman, C. J. Lister, T. Grahn, P. T. Greenlees, P. Jones, R. Julin, S. Juutinen, M. Leino, M. Nyman, J. Pakarinen, P. Rahkila, J. Sarén, C. Scholey, J. Sorri, J. Uusitalo, P. A. Butler, M. Dimmock, D. T. Joss, J. Thomson, B. Cederwall, B. Hadinia, M. Sandzelius, Coulomb shifts and shape changes in the mass 70 region, Phys. Rev. C 75 (2007) 061301. doi:10.1103/PhysRevC.75.061301.
URL http://link.aps.org/doi/10.1103/PhysRevC.75.061301

[119] D. Bazzacco, the GASP collaboration, The gamma ray spectrometer gasp, International Conference on Nuclear Structure at High Angular Momentum, Ottowa 1992, AECL Report 10613, Vol. 2, p. 376.

[120] A. Dewald, Ancillary detectors and devices for euroball.

[121] J. Heese, K. P. Lieb, L. Lühmann, F. Raether, B. Wörmann, D. Alber, H. Grawe, J. Eberth, T. Mylaeus, Lifetime measurements in70se and72se, Zeitschrift für Physik A Atomic Nuclei 325 (1) (1986) 45–53. doi:10.1007/BF01294241.
URL https://doi.org/10.1007/BF01294241

[122] J. Ljungvall, A. Görgen, M. Girod, J.-P. Delaroche, A. Dewald, C. Dossat, E. Farnea, W. Korten, B. Melon, R. Menegazzo, A. Obertelli, R. Orlandi, P. Petkov, T. Pissulla, S. Siem, R. P. Singh, J. Srebrny, C. Theisen, C. A. Ur, J. J. Valiente-Dobón, K. O. Zell, M. Zielińska, Shape coexistence in light se isotopes: Evidence for oblate shapes, Phys. Rev. Lett. 100 (2008) 102502. doi:10.1103/PhysRevLett.100.102502.
URL http://link.aps.org/doi/10.1103/PhysRevLett.100.102502

[123] A. Obertelli, T. Baugher, D. Bazin, J. P. Delaroche, F. Flavigny, A. Gade, M. Girod, T. Glasmacher, A. Goergen, G. F. Grinyer, W. Korten, J. Ljungvall, S. McDaniel, A. Ratkiewicz, B. Sulignano, D. Weisshaar, Shape evolution in self-conjugate nuclei, and the transitional nucleus ^{68}Se, Phys. Rev. C 80 (2009) 031304. doi:10.1103/PhysRevC.80.031304.
URL https://link.aps.org/doi/10.1103/PhysRevC.80.031304

[124] A. Obertelli, T. Baugher, D. Bazin, S. Boissinot, J.-P. Delaroche, A. Dijon, F. Flavigny, A. Gade, M. Girod, T. Glasmacher, G. Grinyer, W. Korten, J. Ljungvall, S. McDaniel, A. Ratkiewicz, B. Sulignano, P. V. Isacker, D. Weisshaar, First spectroscopy of 66se and 65as: Investigating shape coexistence beyond the line, Physics Letters B 701 (4) (2011) 417 – 421. doi:http://dx.doi.org/10.1016/j.physletb.2011.06.032.
URL http://www.sciencedirect.com/science/article/pii/S0370269311006538

[125] A. Nichols, R. Wadsworth, H. Iwasaki, K. Kaneko, A. Lemasson, G. de Angelis, V. Bader, T. Baugher, D. Bazin, M. Bentley, J. Berryman, T. Braunroth, P. Davies, A. Dewald, C. Fransen, A. Gade, M. Hackstein, J. Henderson, D. Jenkins, D. Miller, C. Morse, I. Paterson, E. Simpson, S. Stroberg, D. Weisshaar, K. Whitmore, K. Wimmer, Collectivity in a 70 nuclei studied via lifetime measurements in 70br and 68,70se, Physics Letters B 733 (2014) 52 – 57. doi:http://dx.doi.org/10.1016/j.physletb.2014.04.016.
URL http://www.sciencedirect.com/science/article/pii/S0370269314002482

[126] H. Iwasaki, A. Lemasson, C. Morse, A. Dewald, T. Braunroth, V. M. Bader, T. Baugher, D. Bazin, J. S. Berryman, C. M. Campbell, A. Gade, C. Langer, I. Y. Lee, C. Loelius, E. Lunderberg, F. Recchia, D. Smalley, S. R. Stroberg, R. Wadsworth, C. Walz, D. Weisshaar, A. Westerberg, K. Whitmore, K. Wimmer, Evolution of collectivity in ^{72}Kr: Evidence for rapid shape transition, Phys. Rev. Lett. 112 (2014) 142502. doi:10.1103/PhysRevLett.112.142502.
URL https://link.aps.org/doi/10.1103/PhysRevLett.112.142502

[127] J. A. Briz, E. Nácher, M. J. G. Borge, A. Algora, B. Rubio, P. Dessagne, A. Maira, D. Cano-Ott, S. Courtin, D. Escrig, L. M. Fraile, W. Gelletly, A. Jungclaus, G. Le Scornet, F. Maréchal, C. Miehé, E. Poirier, A. Poves, P. Sarriguren, J. L. Taín, O. Tengblad, Shape study of the $n = z$ nucleus ^{72}Kr via β decay, Phys. Rev. C 92 (2015) 054326. doi:10.1103/PhysRevC.92.054326.
URL https://link.aps.org/doi/10.1103/PhysRevC.92.054326

[128] A. I. Morales, A. Algora, B. Rubio, K. Kaneko, S. Nishimura, P. Aguilera, S. E. A. Orrigo, F. Molina, G. de Angelis, F. Recchia, G. Kiss, V. H. Phong, J. Wu, D. Nishimura, H. Oikawa, T. Goigoux, J. Giovinazzo, P. Ascher, J. Agramunt, D. S. Ahn, H. Baba, B. Blank, C. Borcea, A. Boso, P. Davies, F. Diel, Z. Dombrádi, P. Doornenbal, J. Eberth, G. de France, Y. Fujita, N. Fukuda, E. Ganioglu, W. Gelletly, M. Gerbaux, S. Grévy, V. Guadilla, N. Inabe, T. Isobe, I. Kojouharov, W. Korten, T. Kubo, S. Kubono, T. Kurtukián Nieto, N. Kurz, J. Lee, S. Lenzi, J. Liu, T. Lokotko, D. Lubos, C. Magron, A. Montaner-Pizá, D. R. Napoli, H. Sakurai, H. Schaffner, Y. Shimizu, C. Sidong, P.-A. Söderström, T. Sumikama, H. Suzuki, H. Takeda, Y. Takei, M. Tanaka, S. Yagi, Simultaneous investigation of the $t = 1(J^\pi = 0^+)$ and $t = 0(J^\pi = 9^+)$ β decays in ^{70}Br, Phys. Rev. C 95 (2017) 064327. doi:10.1103/PhysRevC.95.064327.
URL https://link.aps.org/doi/10.1103/PhysRevC.95.064327

[129] K. Wimmer, W. Korten, T. Arici, P. Doornenbal, P. Aguilera, A. Algora, T. Ando, H. Baba, B. Blank, A. Boso, S. Chen, A. Corsi, P. Davies, G. de Angelis, G. de France, D. Doherty, J. Gerl, R. Gernhäuser, D. Jenkins, S. Koyama, T. Motobayashi, S. Nagamine, M. Niikura, A. Obertelli, D. Lubos, B. Rubio, E. Sahin, T. Saito, H. Sakurai, L. Sinclair, D. Steppenbeck, R. Taniuchi, R. Wadsworth, M. Zielinska, Shape coexistence and isospin symmetry in a=70 nuclei: Spectroscopy of the tz=−1 nucleus 70kr, Physics Letters B 785 (2018) 441 – 446. doi:https://doi.org/10.1016/j.physletb.2018.07.067.
URL http://www.sciencedirect.com/science/article/pii/S0370269318306427

[130] J. Henderson, C. Y. Wu, J. Ash, P. C. Bender, B. Elman, A. Gade, M. Grinder, H. Iwasaki, E. Kwan, B. Longfellow, T. Mijatović, D. Rhodes, M. Spieker, D. Weisshaar, Localizing the shape transition in neutron-deficient selenium, Phys. Rev. Lett. 121 (2018) 082502. doi:10.1103/PhysRevLett.121.082502.
URL https://link.aps.org/doi/10.1103/PhysRevLett.121.082502

[131] P. Möller, A. J. Sierk, R. Bengtsson, H. Sagawa, T. Ichikawa, Global calculation of nuclear shape isomers, Phys. Rev. Lett. 103 (2009) 212501. doi:10.1103/PhysRevLett.103.212501.
URL https://link.aps.org/doi/10.1103/PhysRevLett.103.212501

[132] A. Poves, Shape coexistence: the shell model view, Journal of Physics G: Nuclear and Particle Physics 43 (2) (2016) 024010. doi:10.1088/0954-3899/43/2/024010.

URL https://doi.org/10.1088%2F0954-3899%2F43%2F2%2F024010

[133] M. Honma, T. Otsuka, T. Mizusaki, M. Hjorth-Jensen, New effective interaction for f_5pg_9-shell nuclei, Phys. Rev. C 80 (2009) 064323. doi:10.1103/PhysRevC.80.064323.
URL https://link.aps.org/doi/10.1103/PhysRevC.80.064323

[134] K. Kaneko, Y. Sun, R. Wadsworth, Shape coexistence and shape transition in self-conjugate nucleus 72kr and the tensor force, Physica Scripta 92 (11) (2017) 114008. doi:10.1088/1402-4896/aa8fdc.
URL https://doi.org/10.1088%2F1402-4896%2Faa8fdc

[135] N. Hinohara, K. Sato, T. Nakatsukasa, M. Matsuo, K. Matsuyanagi, Microscopic description of large-amplitude shape-mixing dynamics with inertial functions derived in local quasiparticle random-phase approximation, Phys. Rev. C 82 (2010) 064313. doi:10.1103/PhysRevC.82.064313.
URL https://link.aps.org/doi/10.1103/PhysRevC.82.064313

[136] T. R. Rodríguez, Structure of krypton isotopes calculated with symmetry-conserving configuration-mixing methods, Phys. Rev. C 90 (2014) 034306. doi:10.1103/PhysRevC.90.034306.
URL https://link.aps.org/doi/10.1103/PhysRevC.90.034306

[137] A. Petrovici, Isospin-symmetry breaking and shape coexistence in $a \approx 70$ analogs, Phys. Rev. C 91 (2015) 014302. doi:10.1103/PhysRevC.91.014302.
URL http://link.aps.org/doi/10.1103/PhysRevC.91.014302

[138] K. Nomura, R. Rodríguez-Guzmán, L. M. Robledo, Structural evolution in germanium and selenium nuclei within the mapped interacting boson model based on the gogny energy density functional, Phys. Rev. C 95 (2017) 064310. doi:10.1103/PhysRevC.95.064310.
URL https://link.aps.org/doi/10.1103/PhysRevC.95.064310

[139] E. Clément, M. Zielińska, A. Görgen, W. Korten, S. Péru, J. Libert, H. Goutte, S. Hilaire, B. Bastin, C. Bauer, A. Blazhev, N. Bree, B. Bruyneel, P. A. Butler, J. Butterworth, P. Delahaye, A. Dijon, D. T. Doherty, A. Ekström, C. Fitzpatrick, C. Fransen, G. Georgiev, R. Gernhäuser, H. Hess, J. Iwanicki, D. G. Jenkins, A. C. Larsen, J. Ljungvall, R. Lutter, P. Marley, K. Moschner, P. J. Napiorkowski, J. Pakarinen, A. Petts, P. Reiter, T. Renstrøm, M. Seidlitz, B. Siebeck, S. Siem, C. Sotty, J. Srebrny, I. Stefanescu, G. M. Tveten, J. Van de Walle, M. Vermeulen, D. Voulot, N. Warr, F. Wenander, A. Wiens, H. De Witte, K. Wrzosek-Lipska, Spectroscopic quadrupole moments in ^{96,98}Sr: Evidence for shape coexistence in neutron-rich strontium isotopes at $n = 60$, Phys. Rev. Lett. 116 (2016) 022701. doi:10.1103/PhysRevLett.116.022701.
URL http://link.aps.org/doi/10.1103/PhysRevLett.116.022701

[140] A. Chakraborty, E. E. Peters, B. P. Crider, C. Andreoiu, P. C. Bender, D. S. Cross, G. A. Demand, A. B. Garnsworthy, P. E. Garrett, G. Hackman, B. Hadinia, S. Ketelhut, A. Kumar, K. G. Leach, M. T. McEllistrem, J. Pore, F. M. Prados-Estévez, E. T. Rand, B. Singh, E. R. Tardiff, Z.-M. Wang, J. L. Wood, S. W. Yates, Collective structure in ^{94}Zr and subshell effects in shape coexistence, Phys. Rev. Lett. 110 (2013) 022504. doi:10.1103/PhysRevLett.110.022504.
URL https://link.aps.org/doi/10.1103/PhysRevLett.110.022504

[141] P. Singh, W. Korten, T. W. Hagen, A. Görgen, L. Grente, M.-D. Salsac, F. Farget, E. Clément, G. de France, T. Braunroth, B. Bruyneel, I. Celikovic, O. Delaune, A. Dewald, A. Dijon, J.-P. Delaroche, M. Girod, M. Hackstein, B. Jacquot, J. Libert, J. Litzinger, J. Ljungvall, C. Louchart, A. Gottardo, C. Michelagnoli, C. Müller-Gatermann, D. R. Napoli, T. Otsuka, N. Pillet, F. Recchia, W. Rother, E. Sahin, S. Siem, B. Sulignano, T. Togashi, Y. Tsunoda, C. Theisen, J. J. Valiente-Dobon, Evidence for coexisting shapes through lifetime measurements in ^{98}Zr, Phys. Rev. Lett. 121 (2018) 192501. doi:10.1103/PhysRevLett.121.192501.
URL https://link.aps.org/doi/10.1103/PhysRevLett.121.192501

[142] C. Kremer, S. Aslanidou, S. Bassauer, M. Hilcker, A. Krugmann, P. von Neumann-Cosel, T. Otsuka, N. Pietralla, V. Y. Ponomarev, N. Shimizu, M. Singer, G. Steinhilber, T. Togashi, Y. Tsunoda, V. Werner, M. Zweidinger, First measurement of collectivity of coexisting shapes based on type ii shell evolution: The case of ^{96}Zr, Phys. Rev. Lett. 117 (2016) 172503. doi:10.1103/PhysRevLett.117.172503.
URL https://link.aps.org/doi/10.1103/PhysRevLett.117.172503

[143] T. Togashi, Y. Tsunoda, T. Otsuka, N. Shimizu, Quantum phase transition in the shape of zr isotopes, Phys. Rev. Lett. 117 (2016) 172502. doi:10.1103/PhysRevLett.117.172502.
URL https://link.aps.org/doi/10.1103/PhysRevLett.117.172502

[144] J. Dudouet, A. Lemasson, G. Duchêne, M. Rejmund, E. Clément, C. Michelagnoli, F. Didierjean, A. Korichi, G. Maquart, O. Stezowski, C. Lizarazo, R. M. Pérez-Vidal, C. Andreoiu, G. de Angelis, A. Astier, C. Delafosse, I. Deloncle, Z. Dombradi, G. de France, A. Gadea, A. Gottardo, B. Jacquot, P. Jones, T. Konstantinopoulos, I. Kuti, F. Le Blanc, S. M. Lenzi, G. Li, R. Lozeva, B. Million, D. R. Napoli, A. Navin, C. M. Petrache, N. Pietralla, D. Ralet, M. Ramdhane, N. Redon, C. Schmitt, D. Sohler, D. Verney, D. Barrientos, B. Birkenbach, I. Burrows, L. Charles, J. Collado, D. M. Cullen, P. Désesquelles, C. Domingo Pardo, V. González, L. Harkness-Brennan, H. Hess, D. S. Judson, M. Karolak, W. Korten, M. Labiche, J. Ljungvall, R. Menegazzo, D. Mengoni, A. Pullia, F. Recchia, P. Reiter, M. D. Salsac, E. Sanchis, C. Theisen, J. J. Valiente-Dobón, M. Zielińska, $^{96}_{36}\mathrm{Kr}_{60}$ - low-z boundary of the island of deformatoin at n=60, Phys. Rev. Lett. 118 (2017) 162501. doi:10.1103/PhysRevLett.118.162501.
URL https://link.aps.org/doi/10.1103/PhysRevLett.118.162501

[145] F. Flavigny, P. Doornenbal, A. Obertelli, J.-P. Delaroche, M. Girod, J. Libert, T. R. Rodriguez, G. Authelet, H. Baba, D. Calvet, F. Château, S. Chen, A. Corsi, A. Delbart, J.-M. Gheller, A. Giganon, A. Gillibert, V. Lapoux, T. Motobayashi, M. Niikura, N. Paul, J.-Y. Roussé, H. Sakurai, C. Santamaria, D. Steppenbeck, R. Taniuchi, T. Uesaka, T. Ando, T. Arici, A. Blazhev, F. Browne, A. Bruce, R. Carroll, L. X. Chung, M. L. Cortés, M. Dewald, B. Ding, S. Franchoo, M. Górska, A. Gottardo, A. Jungclaus, J. Lee, M. Lettmann, B. D. Linh, J. Liu, Z. Liu, C. Lizarazo, S. Momiyama, K. Moschner, S. Nagamine, N. Nakatsuka, C. Nita, C. R. Nobs, L. Olivier, R. Orlandi, Z. Patel, Z. Podolyák, M. Rudigier, T. Saito, C. Shand, P. A. Söderström, I. Stefan, V. Vaquero, V. Werner, K. Wimmer, Z. Xu, Shape evolution in neutron-rich krypton isotopes beyond $n = 60$: First spectroscopy of ^{98,100}Kr, Phys. Rev. Lett. 118 (2017) 242501. doi:10.1103/PhysRevLett.118.242501.
URL https://link.aps.org/doi/10.1103/PhysRevLett.118.242501

[146] N. Bree, K. Wrzosek-Lipska, A. Petts, A. Andreyev, B. Bastin, M. Bender, A. Blazhev, B. Bruyneel, P. A. Butler, J. Butterworth, M. P. Carpenter, J. Cederkäll, E. Clément, T. E. Cocolios, A. Deacon, J. Diriken, A. Ekström, C. Fitzpatrick, L. M. Fraile, C. Fransen, S. J. Freeman, L. P. Gaffney, J. E. García-Ramos, K. Geibel, R. Gernhäuser, T. Grahn, M. Guttormsen, B. Hadinia, K. Hadyńska-Klęk, M. Hass, P.-H. Heenen, R.-D. Herzberg, H. Hess, K. Heyde, M. Huyse, O. Ivanov, D. G. Jenkins, R. Julin, N. Kesteloot, T. Kröll, R. Krücken, A. C. Larsen, R. Lutter, P. Marley, P. J. Napiorkowski, R. Orlandi, R. D. Page, J. Pakarinen, N. Patronis, P. J. Peura, E. Piselli, P. Rahkila, E. Rapisarda, P. Reiter, A. P. Robinson, M. Scheck, S. Siem, K. Singh Chakkal, J. F. Smith, J. Srebrny, I. Stefanescu, G. M. Tveten, P. Van Duppen, J. Van de Walle, D. Voulot, N. Warr, F. Wenander, A. Wiens, J. L. Wood, M. Zielińska, Shape coexistence in the neutron-deficient even-even $^{182-188}$Hg isotopes studied via coulomb excitation, Phys. Rev. Lett. 112 (2014) 162701. doi:10.1103/PhysRevLett.112.162701.
URL https://link.aps.org/doi/10.1103/PhysRevLett.112.162701

[147] B. A. Marsh, T. Day Goodacre, S. Sels, Y. Tsunoda, B. Andel, A. N. Andreyev, N. A. Althubiti, D. Atanasov, A. E. Barzakh, J. Billowes, K. Blaum, T. E. Cocolios, J. G. Cubiss, J. Dobaczewski, G. J. Farooq-Smith, D. V. Fedorov, V. N. Fedosseev, K. T. Flanagan, L. P. Gaffney, L. Ghys, M. Huyse, S. Kreim, D. Lunney, K. M. Lynch, V. Manea, Y. Martinez Palenzuela, P. L. Molkanov, T. Otsuka, A. Pastore, M. Rosenbusch, R. E. Rossel, S. Rothe, L. Schweikhard, M. D. Seliverstov, P. Spagnoletti, C. Van Beveren, P. Van Duppen, M. Veinhard, E. Verstraelen, A. Welker, K. Wendt, F. Wienholtz, R. N. Wolf, A. Zadvornaya, K. Zuber, Characterization of the shape-staggering effect in mercury nuclei, Nature Physics 14 (12) (2018) 1163–1167. doi:10.1038/s41567-018-0292-8.
URL https://doi.org/10.1038/s41567-018-0292-8

[148] A. N. Andreyev, M. Huyse, P. Van Duppen, L. Weissman, D. Ackermann, J. Gerl, F. P. Hessberger, S. Hofmann, A. Kleinböhl, G. Münzenberg, S. Reshitko, C. Schlegel, H. Schaffner, P. Cagarda, M. Matos, S. Saro, A. Keenan, C. Moore, C. D. O'Leary, R. D. Page, M. Taylor, H. Kettunen, M. Leino, A. Lavrentiev, R. Wyss, K. Heyde, A triplet of differently shaped spin-zero states in the atomic

nucleus 186pb, Nature 405 (2000) 430. doi:10.1038/35013012.
URL https://doi.org/10.1038/35013012

[149] A. Dewald, R. Peusquens, B. Saha, P. von Brentano, A. Fitzler, T. Klug, I. Wiedenhöver, Carpenter, A. Heinz, R. V. F. Janssens, F. G. Kondev, C. J. Lister, D. Seweryniak, K. Abu Saleem, R. Krücken, J. R. Cooper, C. J. Barton, K. Zyromski, C. W. Beausang, Z. Wang, P. Petkov, A. M. Oros-Peusquens, U. Garg, S. Zhu, Recoil-gated plunger lifetime measurements in ^{188}Pb, Phys. Rev. C 68 (2003) 034314. doi:10.1103/PhysRevC.68.034314.
URL https://link.aps.org/doi/10.1103/PhysRevC.68.034314

[150] T. Grahn, A. Dewald, O. Möller, R. Julin, C. W. Beausang, S. Christen, I. G. Darby, S. Eeckhaudt, P. T. Greenlees, A. Görgen, K. Helariutta, J. Jolie, P. Jones, S. Juutinen, H. Kettunen, T. Kröll, R. Krücken, Y. L. Coz, M. Leino, A.-P. Leppänen, P. Maierbeck, D. A. Meyer, B. Melon, P. Nieminen, M. Nyman, R. D. Page, J. Pakarinen, P. Petkov, P. Rahkila, B. Saha, M. Sandzelius, J. Sarén, C. Scholey, J. Uusitalo, Collectivity and configuration mixing in ^{186,188}Pb and ^{194}Po, Phys. Rev. Lett. 97 (2006) 062501. doi:10.1103/PhysRevLett.97.062501.
URL https://link.aps.org/doi/10.1103/PhysRevLett.97.062501

[151] T. Grahn, A. Dewald, O. Möller, R. Julin, C. Beausang, S. Christen, I. Darby, S. Eeckhaudt, P. Greenlees, A. Görgen, K. Helariutta, J. Jolie, P. Jones, S. Juutinen, H. Kettunen, T. Kröll, R. Krücken, Y. L. Coz, M. Leino, A.-P. Leppänen, P. Maierbeck, D. Meyer, B. Melon, P. Nieminen, M. Nyman, R. Page, J. Pakarinen, P. Petkov, P. Rahkila, B. Saha, M. Sandzelius, J. Sarén, C. Scholey, J. Uusitalo, M. Bender, P.-H. Heenen, Lifetimes of intruder states in 186pb, 188pb and 194po, Nuclear Physics A 801 (3) (2008) 83 – 100. doi:https://doi.org/10.1016/j.nuclphysa.2008.01.002.
URL http://www.sciencedirect.com/science/article/pii/S0375947408000043

[152] T. Grahn, A. Dewald, P. T. Greenlees, U. Jakobsson, J. Jolie, P. Jones, R. Julin, S. Juutinen, S. Ketelhut, T. Kröll, R. Krücken, M. Leino, P. Maierbeck, B. Melon, M. Nyman, R. D. Page, P. Peura, T. Pissulla, P. Rahkila, J. Sarén, C. Scholey, J. Sorri, J. Uusitalo, M. Bender, P. H. Heenen, Collectivity of ^{196}Po at low spin, Phys. Rev. C 80 (2009) 014323. doi:10.1103/PhysRevC.80.014323.
URL https://link.aps.org/doi/10.1103/PhysRevC.80.014323

[153] T. Grahn, A. Petts, M. Scheck, P. A. Butler, A. Dewald, M. B. G. Hornillos, P. T. Greenlees, A. Görgen, K. Helariutta, J. Jolie, P. Jones, R. Julin, S. Juutinen, S. Ketelhut, R. Krücken, T. Kröll, M. Leino, J. Ljungvall, P. Maierbeck, B. Melon, M. Nyman, R. D. Page, T. Pissulla, P. Rahkila, J. Sarén, C. Scholey, A. Semchenkov, J. Sorri, J. Uusitalo, R. Wadsworth, M. Zieli'nska, Evolution of collectivity in ^{180}Hg and ^{182}Hg, Phys. Rev. C 80 (2009) 014324. doi:10.1103/PhysRevC.80.014324.
URL https://link.aps.org/doi/10.1103/PhysRevC.80.014324

[154] M. Scheck, T. Grahn, A. Petts, P. A. Butler, A. Dewald, L. P. Gaffney, M. B. G. Hornillos, A. Görgen, P. T. Greenlees, K. Helariutta, J. Jolie, P. Jones, R. Julin, S. Juutinen, S. Ketelhut, T. Kröll, R. Krücken, M. Leino, J. Ljungvall, P. Maierbeck, B. Melon, M. Nyman, R. D. Page, J. Pakarinen, E. S. Paul, T. Pissulla, P. Rahkila, J. Sarén, C. Scholey, A. Semchenkov, J. Sorri, J. Uusitalo, R. Wadsworth, M. Zielińska, Lifetimes of odd-spin yrast states in ^{182}Hg, Phys. Rev. C 81 (2010) 014310. doi:10.1103/PhysRevC.81.014310.
URL https://link.aps.org/doi/10.1103/PhysRevC.81.014310

[155] K. Gladnishki, P. Petkov, A. Dewald, C. Fransen, M. Hackstein, J. Jolie, T. Pissulla, W. Rother, K. Zell, Yrast electromagnetic transition strengths and shape coexistence in 182pt, Nuclear Physics A 877 (2012) 19 – 34. doi:https://doi.org/10.1016/j.nuclphysa.2012.01.001.
URL http://www.sciencedirect.com/science/article/pii/S0375947412000036

[156] M. Bender, P. Bonche, T. Duguet, P.-H. Heenen, Configuration mixing of angular momentum projected self-consistent mean-field states for neutron-deficient pb isotopes, Phys. Rev. C 69 (2004) 064303. doi:10.1103/PhysRevC.69.064303.
URL https://link.aps.org/doi/10.1103/PhysRevC.69.064303

[157] G. Dracoulis, R. Bark, A. Stuchbery, A. Byrne, A. Baxter, F. Riess, Band crossings in 170os, Nuclear Physics A 486 (2) (1988) 414 – 428. doi:https://doi.org/10.1016/0375-9474(88)90244-8.
URL http://www.sciencedirect.com/science/article/pii/0375947488902448

[158] R. Bark, G. Dracoulis, A. Stuchbery, Shape coexistence or particle alignment in the light osmium isotopes 171os, 172os and 173os, Nuclear Physics A 514 (3) (1990) 503 – 544. doi:https://doi.org/10.1016/0375-9474(90)90154-E.
URL http://www.sciencedirect.com/science/article/pii/037594749090154E

[159] A. Virtanen, N. Johnson, F. McGowan, I. Lee, C. Baktash, M. Riley, J. Wells, J. Dudek, Transition quadrupole moments of high-spin states in 172os, Nuclear Physics A 591 (1) (1995) 145 – 160. doi:https://doi.org/10.1016/0375-9474(95)00132-K.
URL http://www.sciencedirect.com/science/article/pii/037594749500132K

[160] D. Joss, S. King, R. Page, J. Simpson, A. Keenan, N. Amzal, T. Bäck, M. Bentley, B. Cederwall, J. Cocks, D. Cullen, P. Greenlees, K. Helariutta, P. Jones, R. Julin, S. Juutinen, H. Kankaanpää, H. Kettunen, P. Kuusiniemi, M. Leino, M. Muikku, A. Savelius, J. Uusitalo, S. Williams, Identification of excited states in 167os and 168os: shape coexistence at extreme neutron deficiency, Nuclear Physics A 689 (3) (2001) 631 – 654. doi:https://doi.org/10.1016/S0375-9474(00)00692-8.

URL http://www.sciencedirect.com/science/article/pii/S0375947400006928

[161] D. T. Joss, N. Amzal, D. E. Appelbe, T. Bäck, C. J. Barton, M. A. Bentley, B. Cederwall, J. F. C. Cocks, D. M. Cullen, S. Eeckhaudt, T. Grahn, P. T. Greenlees, B. Hadinia, K. Helariutta, P. M. Jones, R. Julin, S. Juutinen, H. Kankaanpää, A. Keenan, H. Kettunen, S. L. King, P. Kuusiniemi, K. Lagergren, M. Leino, A. P. Leppänen, M. Muikku, P. Nieminen, R. D. Page, J. Pakarinen, E. S. Paul, P. Rahkila, C. Scholey, A. Savelius, J. Simpson, M. J. Taylor, J. Uusitalo, S. J. Williams, D. D. Warner, D. R. Wiseman, R. Wyss, Probing structural changes in the very neutron-deficient os isotopes with recoil-decay tagging, Journal of Physics G: Nuclear and Particle Physics 31 (10) (2005) S1593–S1598. doi:10.1088/0954-3899/31/10/039.
URL https://doi.org/10.1088%2F0954-3899%2F31%2F10%2F039

[162] D. O'Donnell, T. Grahn, D. T. Joss, J. Simpson, C.Scholey, K. Andgren, L. Bianco, B. Cederwall, D. M. Cullen, A. Dewald, E. Ganioglu, M. B. G. Hornillos, P. T. Greenlees, B. Hadinia, H. Iwasaki, U. Jakobsson, J. Jolie, P. Jones, D. S. Judson, R. Julin, S. Juutinen, S. Ketelhut, M. Labiche, M. Leino, N. M. Lumley, P. J. R. Mason, O. Möller, P. Nieminen, M. Nyman, R. D. Page, J. Pakarinen, E. S. Paul, M. Petri, A. Petts, P. Peura, N. Pietralla, T. Pissulla, P. Rahkila, P. Ruotsalainen, M. Sandzelius, P. J. Sapple, J. Saren, J. Sorri, J. Thomson, J. Uusitalo, H. V. Watkins, Spectroscopy of the neutron-deficient nucleus $^{167}\mathrm{Os}_{91}$, Phys. Rev. C 79 (2009) 064309. doi:10.1103/PhysRevC.79.064309.
URL https://link.aps.org/doi/10.1103/PhysRevC.79.064309

[163] B. Sayğ ı, D. T. Joss, R. D. Page, T. Grahn, J. Simpson, D. O'Donnell, G. Alharshan, K. Auranen, T. Bäck, S. Boening, T. Braunroth, R. J. Carroll, B. Cederwall, D. M. Cullen, A. Dewald, M. Doncel, L. Donosa, M. C. Drummond, F. Ertuğral, S. Ertürk, C. Fransen, P. T. Greenlees, M. Hackstein, K. Hauschild, A. Herzan, U. Jakobsson, P. M. Jones, R. Julin, S. Juutinen, J. Konki, T. Kröll, M. Labiche, A. Lopez-Martens, C. G. McPeake, F. Moradi, O. Möller, M. Mustafa, P. Nieminen, J. Pakarinen, J. Partanen, P. Peura, M. Procter, P. Rahkila, W. Rother, P. Ruotsalainen, M. Sandzelius, J. Sarén, C. Scholey, J. Sorri, S. Stolze, M. J. Taylor, A. Thornthwaite, J. Uusitalo, Reduced transition probabilities along the yrast line in ^{166}W, Phys. Rev. C 96 (2017) 021301. doi:10.1103/PhysRevC.96.021301.
URL https://link.aps.org/doi/10.1103/PhysRevC.96.021301

[164] T. Grahn, S. Stolze, D. T. Joss, R. D. Page, B. Sayğ ı, D. O'Donnell, M. Akmali, K. Andgren, L. Bianco, D. M. Cullen, A. Dewald, P. T. Greenlees, K. Heyde, H. Iwasaki, U. Jakobsson, P. Jones, D. S. Judson, R. Julin, S. Juutinen, S. Ketelhut, M. Leino, N. Lumley, P. J. R. Mason, O. Möller, K. Nomura, M. Nyman, A. Petts, P. Peura, N. Pietralla, T. Pissulla, P. Rahkila, P. J. Sapple, J. Sarén, C. Scholey, J. Simpson, J. Sorri, P. D. Stevenson, J. Uusitalo, H. V. Watkins, J. L. Wood, Excited states and reduced transition probabilities in ^{168}**Os**, Phys. Rev. C 94 (2016) 044327. doi:10.1103/PhysRevC.94.044327.
URL http://link.aps.org/doi/10.1103/PhysRevC.94.044327

[165] B. Cederwall, M. Doncel, O. Aktas, A. Ertoprak, R. Liotta, C. Qi, T. Grahn, D. M. Cullen, D. Hodge, M. Giles, S. Stolze, H. Badran, T. Braunroth, T. Calverley, D. M. Cox, Y. D. Fang, P. T. Greenlees, J. Hilton, E. Ideguchi, R. Julin, S. Juutinen, M. K. Raju, H. Li, H. Liu, S. Matta, V. Modamio, J. Pakarinen, P. Papadakis, J. Partanen, C. M. Petrache, P. Rahkila, P. Ruotsalainen, M. Sandzelius, J. Sarén, C. Scholey, J. Sorri, P. Subramaniam, M. J. Taylor, J. Uusitalo, J. J. Valiente-Dobón, Lifetime measurements of excited states in ^{172}Pt and the variation of quadrupole transition strength with angular momentum, Phys. Rev. Lett. 121 (2018) 022502. doi:10.1103/PhysRevLett.121.022502.
URL https://link.aps.org/doi/10.1103/PhysRevLett.121.022502

[166] J. Ljungvall, G. Georgiev, S. Cabaret, N. Karkour, D. Linget, G. Sedes, R. Chevrier, I. Matea, M. Niikura, M.-D. Salsac, B. Sulignano, The orsay universal plunger system, Nuclear Instruments and Methods in Physics Research Section A: Accelerators, Spectrometers, Detectors and Associated Equipment 679 (2012) 61 – 66. doi:http://dx.doi.org/10.1016/j.nima.2012.03.041.
URL http://www.sciencedirect.com/science/article/pii/S0168900212003427

[167] A. Goasduff, J. Ljungvall, T. R. Rodríguez, F. L. Bello Garrote, A. Etile, G. Georgiev, F. Giacoppo, L. Grente, M. Klintefjord, A. Kuşoğlu, I. Matea, S. Roccia, M.-D. Salsac, C. Sotty, $b(e2)$ anomalies in the yrast band of ^{170}Os, Phys. Rev. C 100 (2019) 034302. doi:10.1103/PhysRevC.100.034302.
URL https://link.aps.org/doi/10.1103/PhysRevC.100.034302

[168] J. L. Egido, M. Borrajo, T. R. Rodríguez, Collective and single-particle motion in beyond mean field approaches, Phys. Rev. Lett. 116 (2016) 052502. doi:10.1103/PhysRevLett.116.052502.
URL https://link.aps.org/doi/10.1103/PhysRevLett.116.052502

[169] L. P. Gaffney, P. A. Butler, M. Scheck, A. B. Hayes, F. Wenander, M. Albers, B. Bastin, C. Bauer, A. Blazhev, S. Bönig, N. Bree, J. Cederkäll, T. Chupp, D. Cline, T. E. Cocolios, T. Davinson, H. De Witte, J. Diriken, T. Grahn, A. Herzan, M. Huyse, D. G. Jenkins, D. T. Joss, N. Kesteloot, J. Konki, M. Kowalczyk, T. Kröll, E. Kwan, R. Lutter, K. Moschner, P. Napiorkowski, J. Pakarinen, M. Pfeiffer, D. Radeck, P. Reiter, K. Reynders, S. V. Rigby, L. M. Robledo, M. Rudigier, S. Sambi, M. Seidlitz, B. Siebeck, T. Stora, P. Thoele, P. Van Duppen, M. J. Vermeulen, M. von Schmid, D. Voulot, N. Warr, K. Wimmer, K. Wrzosek-Lipska, C. Y. Wu, M. Zielinska, Studies of pear-shaped nuclei using accelerated radioactive beams, Nature 497 (2013) 199, article. doi:10.1038/nature12073.
URL https://doi.org/10.1038/nature12073

[170] P. A. Butler, L. P. Gaffney, P. Spagnoletti, J. Konki, M. Scheck, J. F. Smith, K. Abrahams, M. Bowry, J. Cederkäll, T. Chupp, G. de Angelis, H. De Witte, P. E. Garrett, A. Goldkuhle, C. Henrich, A. Illana, K. Johnston, D. T. Joss, J. M. Keatings, N. A. Kelly, M. Komorowska, T. Kröll, M. Lozano, B. S. Nara Singh, D. O'Donnell, J. Ojala, R. D. Page, L. G. Pedersen, C. Raison, P. Reiter, J. A.

Rodriguez, D. Rosiak, S. Rothe, T. M. Shneidman, B. Siebeck, M. Seidlitz, J. Sinclair, M. Stryjczyk, P. Van Duppen, S. Vinals, V. Virtanen, N. Warr, K. Wrzosek-Lipska, M. Zielinska, The observation of vibrating pear-shapes in radon nuclei, Nature Communications 10 (1) (2019) 2473. doi:10.1038/s41467-019-10494-5.
URL https://doi.org/10.1038/s41467-019-10494-5

[171] J. Dobaczewski, J. Engel, Nuclear time-reversal violation and the schiff moment of ^{225}Ra, Phys. Rev. Lett. 94 (2005) 232502. doi:10.1103/PhysRevLett.94.232502.
URL https://link.aps.org/doi/10.1103/PhysRevLett.94.232502

[172] M. Block, D. Ackermann, K. Blaum, C. Droese, M. Dworschak, S. Eliseev, T. Fleckenstein, E. Haettner, F. Herfurth, F. P. Heßberger, S. Hofmann, J. Ketelaer, J. Ketter, H.-J. Kluge, G. Marx, M. Mazzocco, Y. N. Novikov, W. R. Plaß, A. Popeko, S. Rahaman, D. Rodríguez, C. Scheidenberger, L. Schweikhard, P. G. Thirolf, G. K. Vorobyev, C. Weber, Direct mass measurements above uranium bridge the gap to the island of stability, Nature 463 (2010) 785. doi:10.1038/nature08774.
URL https://doi.org/10.1038/nature08774

[173] S. Raeder, D. Ackermann, H. Backe, R. Beerwerth, J. C. Berengut, M. Block, A. Borschevsky, B. Cheal, P. Chhetri, C. E. Düllmann, V. A. Dzuba, E. Eliav, J. Even, R. Ferrer, V. V. Flambaum, S. Fritzsche, F. Giacoppo, S. Götz, F. P. Heßberger, M. Huyse, U. Kaldor, O. Kaleja, J. Khuyagbaatar, P. Kunz, M. Laatiaoui, F. Lautenschläger, W. Lauth, A. K. Mistry, E. Minaya Ramirez, W. Nazarewicz, S. G. Porsev, M. S. Safronova, U. I. Safronova, B. Schuetrumpf, P. Van Duppen, T. Walther, C. Wraith, A. Yakushev, Probing sizes and shapes of nobelium isotopes by laser spectroscopy, Phys. Rev. Lett. 120 (2018) 232503. doi:10.1103/PhysRevLett.120.232503.
URL https://link.aps.org/doi/10.1103/PhysRevLett.120.232503

[174] H. Meldner, Predictions of new magic regions and masses for super-heavy nuclei from calculations with realistic shell model single particle hamiltonians., Ark. Fys., 36: 593-8(1967).

[175] J. Dobaczewski, A. Afanasjev, M. Bender, L. Robledo, Y. Shi, Properties of nuclei in the nobelium region studied within the covariant, skyrme, and gogny energy density functionals, Nuclear Physics A 944 (2015) 388 – 414, special Issue on Superheavy Elements. doi:https://doi.org/10.1016/j.nuclphysa.2015.07.015.
URL http://www.sciencedirect.com/science/article/pii/S0375947415001633

[176] R.-D. Herzberg, P. Greenlees, In-beam and decay spectroscopy of transfermium nuclei, Progress in Particle and Nuclear Physics 61 (2) (2008) 674 – 720. doi:https://doi.org/10.1016/j.ppnp.2008.05.003.
URL http://www.sciencedirect.com/science/article/pii/S0146641008000409

[177] P. M. Walker, G. D. Dracoulis, Exotic isomers in deformed atomic nuclei, Hyperfine Interactions 135 (1) (2001) 83–107. doi:10.1023/A:1013915200556.
URL https://doi.org/10.1023/A:1013915200556

[178] B. Sulignano, C. Theisen, J.-P. Delaroche, M. Girod, J. Ljungvall, D. Ackermann, S. Antalic, O. Dorvaux, A. Drouart, B. Gall, A. Görgen, P. T. Greenlees, K. Hauschild, R.-D. Herzberg, F. P. Heßberger, U. Jakobsson, P. Jones, R. Julin, S. Juutinen, S. Ketelhut, W. Korten, M. Leino, A. Lopez-Martens, M. Nyman, A. Obertelli, J. Pakarinen, P. Papadakis, E. Parr, P. Peura, J. Piot, P. Rahkila, D. Rostron, P. Ruotsalainen, J. Sarén, C. Scholey, J. Sorri, J. Uusitalo, M. Venhart, M. Zielińska, Investigation of high-k states in ^{252}no, Phys. Rev. C 86 (2012) 044318. doi:10.1103/PhysRevC.86.044318.
URL https://link.aps.org/doi/10.1103/PhysRevC.86.044318

[179] C. Theisen, F. Jeanneau, B. Sulignano, F. Druillole, J. Ljungvall, B. Paul, E. Virique, P. Baron, H. Bervas, E. Clément, E. Delagnes, A. Dijon, E. Dossat, A. Drouart, F. Farget, C. Flouzat, G. D. France, A. Görgen, C. Houarner, B. Jacquot, W. Korten, G. Lebertre, B. Lecornu, L. Legeard, A. Lermitage, S. Lhenoret, C. Marry, C. Maugeais, L. Menager, O. Meunier, A. Navin, F. Nizery, A. Obertelli, E. Rauly, B. Raine, M. Rejmund, J. Ropert, F. Saillant, H. Savajols, C. Schmitt, M. Tripon, E. Wanlin, G. Wittwer, Musett: A segmented si array for recoil-decay-tagging studies at vamos, Nuclear Instruments and Methods in Physics Research Section A: Accelerators, Spectrometers, Detectors and Associated Equipment 747 (Supplement C) (2014) 69 – 80. doi:https://doi.org/10.1016/j.nima.2014.02.016.
URL http://www.sciencedirect.com/science/article/pii/S0168900214001727

[180] L. Stavsetra, K. E. Gregorich, J. Dvorak, P. A. Ellison, I. Dragojević, M. A. Garcia, H. Nitsche, Independent verification of element 114 production in the ^{48}Ca $+^{242}$ Pu reaction, Phys. Rev. Lett. 103 (2009) 132502. doi:10.1103/PhysRevLett.103.132502.
URL https://link.aps.org/doi/10.1103/PhysRevLett.103.132502

[181] C. E. Düllmann, M. Schädel, A. Yakushev, A. Türler, K. Eberhardt, J. V. Kratz, D. Ackermann, L.-L. Andersson, M. Block, W. Brüchle, J. Dvorak, H. G. Essel, P. A. Ellison, J. Even, J. M. Gates, A. Gorshkov, R. Graeger, K. E. Gregorich, W. Hartmann, R.-D. Herzberg, F. P. Heßberger, D. Hild, A. Hübner, E. Jäger, J. Khuyagbaatar, B. Kindler, J. Krier, N. Kurz, S. Lahiri, D. Liebe, B. Lommel, M. Maiti, H. Nitsche, J. P. Omtvedt, E. Parr, D. Rudolph, J. Runke, B. Schausten, E. Schimpf, A. Semchenkov, J. Steiner, P. Thörle-Pospiech, J. Uusitalo, M. Wegrzecki, N. Wiehl, Production and decay of element 114: High cross sections and the new nucleus ^{277}Hs, Phys. Rev. Lett. 104 (2010) 252701. doi:10.1103/PhysRevLett.104.252701.
URL https://link.aps.org/doi/10.1103/PhysRevLett.104.252701

[182] P. A. Ellison, K. E. Gregorich, J. S. Berryman, D. L. Bleuel, R. M. Clark, I. Dragojević, J. Dvorak, P. Fallon, C. Fineman-Sotomayor, J. M. Gates,

O. R. Gothe, I. Y. Lee, W. D. Loveland, J. P. McLaughlin, S. Paschalis, M. Petri, J. Qian, L. Stavsetra, M. Wiedeking, H. Nitsche, New superheavy element isotopes: $^{242}\mathrm{Pu}(^{48}\mathrm{Ca}, 5n)^{285}114$, Phys. Rev. Lett. 105 (2010) 182701. doi:10.1103/PhysRevLett.105.182701.
URL https://link.aps.org/doi/10.1103/PhysRevLett.105.182701

[183] Y. T. Oganessian, F. S. Abdullin, C. Alexander, J. Binder, R. A. Boll, S. N. Dmitriev, J. Ezold, K. Felker, J. M. Gostic, R. K. Grzywacz, J. H. Hamilton, R. A. Henderson, M. G. Itkis, K. Miernik, D. Miller, K. J. Moody, A. N. Polyakov, A. V. Ramayya, J. B. Roberto, M. A. Ryabinin, K. P. Rykaczewski, R. N. Sagaidak, D. A. Shaughnessy, I. V. Shirokovsky, M. V. Shumeiko, M. A. Stoyer, N. J. Stoyer, V. G. Subbotin, A. M. Sukhov, Y. S. Tsyganov, V. K. Utyonkov, A. A. Voinov, G. K. Vostokin, Production and decay of the heaviest nuclei $^{293,294}117$ and $^{294}118$, Phys. Rev. Lett. 109 (2012) 162501. doi:10.1103/PhysRevLett.109.162501.
URL https://link.aps.org/doi/10.1103/PhysRevLett.109.162501

[184] D. Rudolph, U. Forsberg, P. Golubev, L. G. Sarmiento, A. Yakushev, L.-L. Andersson, A. Di Nitto, C. E. Düllmann, J. M. Gates, K. E. Gregorich, C. J. Gross, F. P. Heßberger, R.-D. Herzberg, J. Khuyagbaatar, J. V. Kratz, K. Rykaczewski, M. Schädel, S. Åberg, D. Ackermann, M. Block, H. Brand, B. G. Carlsson, D. Cox, X. Derkx, K. Eberhardt, J. Even, C. Fahlander, J. Gerl, E. Jäger, B. Kindler, J. Krier, I. Kojouharov, N. Kurz, B. Lommel, A. Mistry, C. Mokry, H. Nitsche, J. P. Omtvedt, P. Papadakis, I. Ragnarsson, J. Runke, H. Schaffner, B. Schausten, P. Thörle-Pospiech, T. Torres, T. Traut, N. Trautmann, A. Türler, A. Ward, D. E. Ward, N. Wiehl, Spectroscopy of element 115 decay chains, Phys. Rev. Lett. 111 (2013) 112502. doi:10.1103/PhysRevLett.111.112502.
URL https://link.aps.org/doi/10.1103/PhysRevLett.111.112502

[185] J. Khuyagbaatar, A. Yakushev, C. E. Düllmann, D. Ackermann, L.-L. Andersson, M. Asai, M. Block, R. A. Boll, H. Brand, D. M. Cox, M. Dasgupta, X. Derkx, A. Di Nitto, K. Eberhardt, J. Even, M. Evers, C. Fahlander, U. Forsberg, J. M. Gates, N. Gharibyan, P. Golubev, K. E. Gregorich, J. H. Hamilton, W. Hartmann, R.-D. Herzberg, F. P. Heßberger, D. J. Hinde, J. Hoffmann, R. Hollinger, A. Hübner, E. Jäger, B. Kindler, J. V. Kratz, J. Krier, N. Kurz, M. Laatiaoui, S. Lahiri, R. Lang, B. Lommel, M. Maiti, K. Miernik, S. Minami, A. Mistry, C. Mokry, H. Nitsche, J. P. Omtvedt, G. K. Pang, P. Papadakis, D. Renisch, J. Roberto, D. Rudolph, J. Runke, K. P. Rykaczewski, L. G. Sarmiento, M. Schädel, B. Schausten, A. Semchenkov, D. A. Shaughnessy, P. Steinegger, J. Steiner, E. E. Tereshatov, P. Thörle-Pospiech, K. Tinschert, T. Torres De Heidenreich, N. Trautmann, A. Türler, J. Uusitalo, D. E. Ward, M. Wegrzecki, N. Wiehl, S. M. Van Cleve, V. Yakusheva, $^{48}\mathrm{Ca} + ^{249}\mathrm{Bk}$ fusion reaction leading to element $z = 117$: Long-lived α-decaying $^{270}\mathrm{Db}$ and discovery of $^{266}\mathrm{Lr}$, Phys. Rev. Lett. 112 (2014) 172501. doi:10.1103/PhysRevLett.112.172501.
URL https://link.aps.org/doi/10.1103/PhysRevLett.112.172501

[186] S. K. Tandel, T. L. Khoo, D. Seweryniak, G. Mukherjee, I. Ahmad, B. Back, R. Blinstrup, M. P. Carpenter, J. Chapman, P. Chowdhury, C. N. Davids,

A. A. Hecht, A. Heinz, P. Ikin, R. V. F. Janssens, F. G. Kondev, T. Lauritsen, C. J. Lister, E. F. Moore, D. Peterson, P. Reiter, U. S. Tandel, X. Wang, S. Zhu, k isomers in ^{254}No: Probing single-particle energies and pairing strengths in the heaviest nuclei, Phys. Rev. Lett. 97 (2006) 082502. doi:10.1103/PhysRevLett.97.082502.
URL https://link.aps.org/doi/10.1103/PhysRevLett.97.082502

[187] R.-D. Herzberg, P. T. Greenlees, P. A. Butler, G. D. Jones, M. Venhart, I. G. Darby, S. Eeckhaudt, K. Eskola, T. Grahn, C. Gray-Jones, F. P. Hessberger, P. Jones, R. Julin, S. Juutinen, S. Ketelhut, W. Korten, M. Leino, A.-P. Leppänen, S. Moon, M. Nyman, R. D. Page, J. Pakarinen, A. Pritchard, P. Rahkila, J. Sarén, C. Scholey, A. Steer, Y. Sun, C. Theisen, J. Uusitalo, Nuclear isomers in superheavy elements as stepping stones towards the island of stability, Nature 442 (7105) (2006) 896–899. doi:10.1038/nature05069.
URL https://doi.org/10.1038/nature05069

[188] H. M. David, J. Chen, D. Seweryniak, F. G. Kondev, J. M. Gates, K. E. Gregorich, I. Ahmad, M. Albers, M. Alcorta, B. B. Back, B. Baartman, P. F. Bertone, L. A. Bernstein, C. M. Campbell, M. P. Carpenter, C. J. Chiara, R. M. Clark, M. Cromaz, D. T. Doherty, G. D. Dracoulis, N. E. Esker, P. Fallon, O. R. Gothe, J. P. Greene, P. T. Greenlees, D. J. Hartley, K. Hauschild, C. R. Hoffman, S. S. Hota, R. V. F. Janssens, T. L. Khoo, J. Konki, J. T. Kwarsick, T. Lauritsen, A. O. Macchiavelli, P. R. Mudder, C. Nair, Y. Qiu, J. Rissanen, A. M. Rogers, P. Ruotsalainen, G. Savard, S. Stolze, A. Wiens, S. Zhu, Decay and fission hindrance of two- and four-quasiparticle k isomers in ^{254}Rf, Phys. Rev. Lett. 115 (2015) 132502. doi:10.1103/PhysRevLett.115.132502.
URL https://link.aps.org/doi/10.1103/PhysRevLett.115.132502

[189] S. Ketelhut, P. T. Greenlees, D. Ackermann, S. Antalic, E. Clément, I. G. Darby, O. Dorvaux, A. Drouart, S. Eeckhaudt, B. J. P. Gall, A. Görgen, T. Grahn, C. Gray-Jones, K. Hauschild, R.-D. Herzberg, F. P. Heßberger, U. Jakobsson, G. D. Jones, P. Jones, R. Julin, S. Juutinen, T.-L. Khoo, W. Korten, M. Leino, A.-P. Leppänen, J. Ljungvall, S. Moon, M. Nyman, A. Obertelli, J. Pakarinen, E. Parr, P. Papadakis, P. Peura, J. Piot, A. Pritchard, P. Rahkila, D. Rostron, P. Ruotsalainen, M. Sandzelius, J. Sarén, C. Scholey, J. Sorri, A. Steer, B. Sulignano, C. Theisen, J. Uusitalo, M. Venhart, M. Zielinska, M. Bender, P.-H. Heenen, γ-ray spectroscopy at the limits: First observation of rotational bands in ^{255}Lr, Phys. Rev. Lett. 102 (2009) 212501. doi:10.1103/PhysRevLett.102.212501.
URL https://link.aps.org/doi/10.1103/PhysRevLett.102.212501

[190] A. Chatillon, C. Theisen, E. Bouchez, P. A. Butler, E. Clément, O. Dorvaux, S. Eeckhaudt, B. J. P. Gall, A. Görgen, T. Grahn, P. T. Greenlees, R.-D. Herzberg, F. Heßberger, A. Hürstel, G. D. Jones, P. Jones, R. Julin, S. Juutinen, H. Kettunen, F. Khalfallah, W. Korten, Y. Le Coz, M. Leino, A.-P. Leppänen, P. Nieminen, J. Pakarinen, J. Perkowski, P. Rahkila, M. Rousseau, C. Scholey, J. Uusitalo, J. N. Wilson, P. Bonche, P.-H. Heenen, Observation of a rotational band in the odd-z transfermium nucleus $^{251}_{101}$Md, Phys. Rev. Lett. 98 (2007)

132503. doi:10.1103/PhysRevLett.98.132503.
URL https://link.aps.org/doi/10.1103/PhysRevLett.98.132503

[191] P. T. Greenlees, J. Rubert, J. Piot, B. J. P. Gall, L. L. Andersson, M. Asai, Z. Asfari, D. M. Cox, F. Dechery, O. Dorvaux, T. Grahn, K. Hauschild, G. Henning, A. Herzan, R.-D. Herzberg, F. P. Heßberger, U. Jakobsson, P. Jones, R. Julin, S. Juutinen, S. Ketelhut, T.-L. Khoo, M. Leino, J. Ljungvall, A. Lopez-Martens, R. Lozeva, P. Nieminen, J. Pakarinen, P. Papadakis, E. Parr, P. Peura, P. Rahkila, S. Rinta-Antila, P. Ruotsalainen, M. Sandzelius, J. Sarén, C. Scholey, D. Seweryniak, J. Sorri, B. Sulignano, C. Theisen, J. Uusitalo, M. Venhart, Shell-structure and pairing interaction in superheavy nuclei: Rotational properties of the z=104 nucleus ^{256}Rf, Phys. Rev. Lett. 109 (2012) 012501. doi:10.1103/PhysRevLett.109.012501.
URL https://link.aps.org/doi/10.1103/PhysRevLett.109.012501

[192] C. Theisen, P. Greenlees, T.-L. Khoo, P. Chowdhury, T. Ishii, In-beam spectroscopy of heavy elements, Nuclear Physics A 944 (2015) 333 – 375, special Issue on Superheavy Elements. doi:https://doi.org/10.1016/j.nuclphysa.2015.07.014.
URL http://www.sciencedirect.com/science/article/pii/S0375947415001621

[193] M. Asai, F. Heßberger, A. Lopez-Martens, Nuclear structure of elements with 100≤z≤109 from alpha spectroscopy, Nuclear Physics A 944 (2015) 308 – 332, special Issue on Superheavy Elements. doi:https://doi.org/10.1016/j.nuclphysa.2015.06.011.
URL http://www.sciencedirect.com/science/article/pii/S0375947415001402

[194] J. M. Allmond, A. E. Stuchbery, D. C. Radford, A. Galindo-Uribarri, N. J. Stone, C. Baktash, J. C. Batchelder, C. R. Bingham, M. Danchev, C. J. Gross, P. A. Hausladen, K. Lagergren, Y. Larochelle, E. Padilla-Rodal, C.-H. Yu, Magnetic moments of 2_1^+ states in ^{124,126,128}sn, Phys. Rev. C 87 (2013) 054325. doi:10.1103/PhysRevC.87.054325.
URL https://link.aps.org/doi/10.1103/PhysRevC.87.054325

[195] P.-H. Heenen, J. Skalski, A. Staszczak, D. Vretenar, Shapes and α- and β-decays of superheavy nuclei, Nuclear Physics A 944 (2015) 415 – 441, special Issue on Superheavy Elements. doi:https://doi.org/10.1016/j.nuclphysa.2015.07.016.
URL http://www.sciencedirect.com/science/article/pii/S0375947415001748

[196] A. Ghiorso, S. Yashita, M. Leino, L. Frank, J. Kalnins, P. Armbruster, J.-P. Dufour, P. Lemmertz, Sassy, a gas-filled magnetic separator for the study of fusion reaction products, Nuclear Instruments and Methods in Physics Research Section A: Accelerators, Spectrometers, Detectors and Associated Equipment 269 (1) (1988) 192 – 201. doi:https://doi.org/10.1016/0168-9002(88)90877-7.

URL http://www.sciencedirect.com/science/article/pii/0168900288908777

[197] E. Kessler, M. Dewey, R. Deslattes, A. Henins, H. Börner, M. Jentschel, H. Lehmann, The gams4 flat crystal facility, Nuclear Instruments and Methods in Physics Research Section A: Accelerators, Spectrometers, Detectors and Associated Equipment 457 (1) (2001) 187 – 202. doi:https://doi.org/10.1016/S0168-9002(00)00753-1.
URL http://www.sciencedirect.com/science/article/pii/S0168900200007531

[198] T. Motobayashi, Y. Ikeda, K. Ieki, M. Inoue, N. Iwasa, T. Kikuchi, M. Kurokawa, S. Moriya, S. Ogawa, H. Murakami, S. Shimoura, Y. Yanagisawa, T. Nakamura, Y. Watanabe, M. Ishihara, T. Teranishi, H. Okuno, R. Casten, Large deformation of the very neutron-rich nucleus 32mg from intermediate-energy coulomb excitation, Physics Letters B 346 (1) (1995) 9 – 14. doi:https://doi.org/10.1016/0370-2693(95)00012-A.
URL http://www.sciencedirect.com/science/article/pii/037026939500012A

[199] S. Takeuchi, T. Motobayashi, Y. Togano, M. Matsushita, N. Aoi, K. Demichi, H. Hasegawa, H. Murakami, Dali2: A nai(tl) detector array for measurements of γ rays from fast nuclei, Nuclear Instruments and Methods in Physics Research Section A: Accelerators, Spectrometers, Detectors and Associated Equipment 763 (2014) 596 – 603. doi:https://doi.org/10.1016/j.nima.2014.06.087.
URL http://www.sciencedirect.com/science/article/pii/S0168900214008419

[200] G. Knoll, Radiation Detection and Measurement, Wiley, 2000.

[201] W. R. Leo, Techniques for nuclear and particle physics experiments 2 rev ed, Springer, Germany, 1992.
URL http://inis.iaea.org/search/search.aspx?orig_q=RN:24023834

[202] J. Eberth, J. Simpson, From ge(li) detectors to gamma-ray tracking arrays–50 years of gamma spectroscopy with germanium detectors, Progress in Particle and Nuclear Physics 60 (2) (2008) 283 – 337. doi:https://doi.org/10.1016/j.ppnp.2007.09.001.
URL http://www.sciencedirect.com/science/article/pii/S0146641007000828

[203] S. Akkoyun, A. Algora, B. Alikhani, F. Ameil, G. de Angelis, L. Arnold, A. Astier, A. Ataç, Y. Aubert, C. Aufranc, A. Austin, S. Aydin, F. Azaiez, S. Badoer, D. Balabanski, D. Barrientos, G. Baulieu, R. Baumann, D. Bazzacco, F. Beck, T. Beck, P. Bednarczyk, M. Bellato, M. Bentley, G. Benzoni, R. Berthier, L. Berti, R. Beunard, G. L. Bianco, B. Birkenbach, P. Bizzeti, A. Bizzeti-Sona, F. L. Blanc, J. Blasco, N. Blasi, D. Bloor, C. Boiano, M. Borsato, D. Bortolato, A. Boston, H. Boston, P. Bourgault, P. Boutachkov, A. Bouty, A. Bracco, S. Brambilla, I. Brawn, A. Brondi, S. Broussard, B. Bruyneel, D. Bucurescu, I. Burrows, A. Bürger, S. Cabaret, B. Cahan, E. Calore, F. Camera, A. Capsoni,

F. Carrió, G. Casati, M. Castoldi, B. Cederwall, J.-L. Cercus, V. Chambert, M. E. Chambit, R. Chapman, L. Charles, J. Chavas, E. Clément, P. Cocconi, S. Coelli, P. Coleman-Smith, A. Colombo, S. Colosimo, C. Commeaux, D. Conventi, R. Cooper, A. Corsi, A. Cortesi, L. Costa, F. Crespi, J. Cresswell, D. Cullen, D. Curien, A. Czermak, D. Delbourg, R. Depalo, T. Descombes, P. Désesquelles, P. Detistov, C. Diarra, F. Didierjean, M. Dimmock, Q. Doan, C. Domingo-Pardo, M. Doncel, F. Dorangeville, N. Dosme, Y. Drouen, G. Duchêne, B. Dulny, J. Eberth, P. Edelbruck, J. Egea, T. Engert, M. Erduran, S. Ertürk, C. Fanin, S. Fantinel, E. Farnea, T. Faul, M. Filliger, F. Filmer, C. Finck, G. de France, A. Gadea, W. Gast, A. Geraci, J. Gerl, R. Gernhäuser, A. Giannatiempo, A. Giaz, L. Gibelin, A. Givechev, N. Goel, V. González, A. Gottardo, X. Grave, J. Grebosz, R. Griffiths, A. Grint, P. Gros, L. Guevara, M. Gulmini, A. Görgen, H. Ha, T. Habermann, L. Harkness, H. Harroch, K. Hauschild, C. He, A. Hernández-Prieto, B. Hervieu, H. Hess, T. Hüyük, E. Ince, R. Isocrate, G. Jaworski, A. Johnson, J. Jolie, P. Jones, B. Jonson, P. Joshi, D. Judson, A. Jungclaus, M. Kaci, N. Karkour, M. Karolak, A. Kaşkaş, M. Kebbiri, R. Kempley, A. Khaplanov, S. Klupp, M. Kogimtzis, I. Kojouharov, A. Korichi, W. Korten, T. Kröll, R. Krücken, N. Kurz, B. Ky, M. Labiche, X. Lafay, L. Lavergne, I. Lazarus, S. Leboutelier, F. Lefebvre, E. Legay, L. Legeard, F. Lelli, S. Lenzi, S. Leoni, A. Lermitage, D. Lersch, J. Leske, S. Letts, S. Lhenoret, R. Lieder, D. Linget, J. Ljungvall, A. Lopez-Martens, A. Lotodé, S. Lunardi, A. Maj, J. van der Marel, Y. Mariette, N. Marginean, R. Marginean, G. Maron, A. Mather, W. Meczyński, V. Mendéz, P. Medina, B. Melon, R. Menegazzo, D. Mengoni, E. Merchan, L. Mihailescu, C. Michelagnoli, J. Mierzejewski, L. Milechina, B. Million, K. Mitev, P. Molini, D. Montanari, S. Moon, F. Morbiducci, R. Moro, P. Morrall, O. Möller, A. Nannini, D. Napoli, L. Nelson, M. Nespolo, V. Ngo, M. Nicoletto, R. Nicolini, Y. L. Noa, P. Nolan, M. Norman, J. Nyberg, A. Obertelli, A. Olariu, R. Orlandi, D. Oxley, C. Özben, M. Ozille, C. Oziol, E. Pachoud, M. Palacz, J. Palin, J. Pancin, C. Parisel, P. Pariset, G. Pascovici, R. Peghin, L. Pellegri, A. Perego, S. Perrier, M. Petcu, P. Petkov, C. Petrache, E. Pierre, N. Pietralla, S. Pietri, M. Pignanelli, I. Piqueras, Z. Podolyak, P. L. Pouhalec, J. Pouthas, D. Pugnére, V. Pucknell, A. Pullia, B. Quintana, R. Raine, G. Rainovski, L. Ramina, G. Rampazzo, G. L. Rana, M. Rebeschini, F. Recchia, N. Redon, M. Reese, P. Reiter, P. Regan, S. Riboldi, M. Richer, M. Rigato, S. Rigby, G. Ripamonti, A. Robinson, J. Robin, J. Roccaz, J.-A. Ropert, B. Rossé, C. R. Alvarez, D. Rosso, B. Rubio, D. Rudolph, F. Saillant, E. ¿'Sahin, F. Salomon, M.-D. Salsac, J. Salt, G. Salvato, J. Sampson, E. Sanchis, C. Santos, H. Schaffner, M. Schlarb, D. Scraggs, D. Seddon, M. Şenyiğit, M.-H. Sigward, G. Simpson, J. Simpson, M. Slee, J. Smith, P. Sona, B. Sowicki, P. Spolaore, C. Stahl, T. Stanios, E. Stefanova, O. Stézowski, J. Strachan, G. Suliman, P.-A. Söderström, J. Tain, S. Tanguy, S. Tashenov, C. Theisen, J. Thornhill, F. Tomasi, N. Toniolo, R. Touzery, B. Travers, A. Triossi, M. Tripon, K. Tun-Lanoë, M. Turcato, C. Unsworth, C. Ur, J. Valiente-Dobon, V. Vandone, E. Vardaci, R. Venturelli, F. Veronese, C. Veyssiere, E. Viscione, R. Wadsworth, P. Walker, N. Warr, C. Weber, D. Weisshaar, D. Wells, O. Wieland, A. Wiens, G. Wittwer, H. Wollersheim, F. Zocca, N. Zamfir, M. Ziebliński, A. Zucchiatti, Agata-advanced {GAmma} tracking array, Nuclear Instruments and Methods in Physics Research Section A: Accelerators, Spectrometers, Detectors and Associated Equipment 668 (2012) 26 – 58. doi:http://dx.doi.org/10.1016/j.nima.2011.11.081.
URL http://www.sciencedirect.com/science/article/

pii/S0168900211021516

[204] J. Simpson, The euroball spectrometer, Zeitschrift für Physik A Hadrons and Nuclei 358 (2) (1997) 139–143. doi:10.1007/s002180050290.
URL http://dx.doi.org/10.1007/s002180050290

[205] J. Simpson, F. Azaiez, G. DeFrance, J. Fouan, J. Gerl, R. Julin, W. Korten, P. Nolan, B. Nyakö, G. Sletten, P. Walker, The exogam array: A radioactive beam gamma-ray spectrometer, Acta Physica Hungarica New Series Heavy Ion Physics 11 (1-2) (2000) 159–188.

[206] J. Eberth, G. Pascovici, H. Thomas, N. Warr, D. Weisshaar, D. Habs, P. Reiter, P. Thirolf, D. Schwalm, C. Gund, H. Scheit, M. Lauer, P. V. Duppen, S. Franchoo, M. Huyse, R. Lieder, W. Gast, J. Gerl, K. Lieb, Miniball a ge detector array for radioactive ion beam facilities, Progress in Particle and Nuclear Physics 46 (1) (2001) 389 – 398. doi:https://doi.org/10.1016/S0146-6410(01)00145-4.
URL http://www.sciencedirect.com/science/article/pii/S0146641001001454

[207] D. W. Weißhaar, Miniball ein neuartiges gamma-spektrometer mit ortsauflösenden germaniumdetektoren, Ph.D. thesis, Universität zu Köln (2002).
URL https://kups.ub.uni-koeln.de/718/

[208] A. Wiens, H. Hess, B. Birkenbach, B. Bruyneel, J. Eberth, D. Lersch, G. Pascovici, P. Reiter, H.-G. Thomas, The {AGATA} triple cluster detector, Nuclear Instruments and Methods in Physics Research Section A: Accelerators, Spectrometers, Detectors and Associated Equipment 618 (1-3) (2010) 223 – 233. doi:http://dx.doi.org/10.1016/j.nima.2010.02.102.
URL http://www.sciencedirect.com/science/article/pii/S0168900210003384

[209] B. Bruyneel, P. Reiter, A. Wiens, J. Eberth, H. Hess, G. Pascovici, N. Warr, D. Weisshaar, Crosstalk properties of 36-fold segmented symmetric hexagonal {HPGe} detectors, Nuclear Instruments and Methods in Physics Research Section A: Accelerators, Spectrometers, Detectors and Associated Equipment 599 (2-3) (2009) 196 – 208. doi:http://dx.doi.org/10.1016/j.nima.2008.11.011.
URL http://www.sciencedirect.com/science/article/pii/S0168900208015921

[210] B. Bruyneel, P. Reiter, A. Wiens, J. Eberth, H. Hess, G. Pascovici, N. Warr, S. Aydin, D. Bazzacco, F. Recchia, Crosstalk corrections for improved energy resolution with highly segmented hpge-detectors, Nuclear Instruments and Methods in Physics Research Section A: Accelerators, Spectrometers, Detectors and Associated Equipment 608 (1) (2009) 99 – 106. doi:https://doi.org/10.1016/j.nima.2009.06.037.
URL http://www.sciencedirect.com/science/article/pii/S0168900209012455

[211] for the AGATA Collaboration, B. Bruyneel, B. Birkenbach, J. Eberth, H. Hess, G. Pascovici, P. Reiter, A. Wiens, D. Bazzacco, E. Farnea, C. Michelagnoli, F. Recchia, Correction for hole trapping in agata detectors using pulse shape analysis,

The European Physical Journal A 49 (5) (2013) 61. doi:10.1140/epja/i2013-13061-4.
URL https://doi.org/10.1140/epja/i2013-13061-4

[212] L. Arnold, R. Baumann, E. Chambit, M. Filliger, C. Fuchs, C. Kieber, D. Klein, P. Medina, C. Parisel, M. Richer, C. Santos, C. Weber, Tnt digital pulse processor, IEEE Transactions on Nuclear Science 53 (3) (2006) 723–728. doi:10.1109/TNS.2006.873712.

[213] I. Antcheva, M. Ballintijn, B. Bellenot, M. Biskup, R. Brun, N. Buncic, P. Canal, D. Casadei, O. Couet, V. Fine, L. Franco, G. Ganis, A. Gheata, D. G. Maline, M. Goto, J. Iwaszkiewicz, A. Kreshuk, D. M. Segura, R. Maunder, L. Moneta, A. Naumann, E. Offermann, V. Onuchin, S. Panacek, F. Rademakers, P. Russo, M. Tadel, Root — a c++ framework for petabyte data storage, statistical analysis and visualization, Computer Physics Communications 180 (12) (2009) 2499 – 2512, 40 YEARS OF CPC: A celebratory issue focused on quality software for high performance, grid and novel computing architectures. doi:https://doi.org/10.1016/j.cpc.2009.08.005.
URL http://www.sciencedirect.com/science/article/pii/S0010465509002550

[214] P. Medina, C. Santos, D. Villaume, A simple method for the characterization of hpge detectors, in: Proceedings of the 21st IEEE Instrumentation and Measurement Technology Conference (IEEE Cat. No.04CH37510), Vol. 3, 2004, pp. 1828–1832 Vol.3. doi:10.1109/IMTC.2004.1351438.

[215] M. Schlarb, R. Gernhäuser, S. Klupp, R. Krücken, Pulse shape analysis for γ-ray tracking (part ii): Fully informed particle swarm algorithm applied to agata, The European Physical Journal A 47 (10) (2011) 1–9. doi:10.1140/epja/i2011-11131-3.
URL http://dx.doi.org/10.1140/epja/i2011-11131-3

[216] M. Schlarb, R. Gernhäuser, S. Klupp, R. Krücken, Pulse shape analysis for γ-ray tracking (part i): Pulse shape simulation with jass, The European Physical Journal A 47 (10) (2011) 132. doi:10.1140/epja/i2011-11132-2.
URL http://dx.doi.org/10.1140/epja/i2011-11132-2

[217] B. Bruyneel, B. Birkenbach, P. Reiter, Pulse shape analysis and position determination in segmented hpge detectors: The agata detector library, The European Physical Journal A 52 (3) (2016) 1–11. doi:10.1140/epja/i2016-16070-9.
URL http://dx.doi.org/10.1140/epja/i2016-16070-9

[218] B. Bruyneel, B. Birkenbach, P. Reiter, Pulse shape analysis and position determination in segmented hpge detectors: The agata detector library, The European Physical Journal A 52 (3) (2016) 70. doi:10.1140/epja/i2016-16070-9.
URL http://dx.doi.org/10.1140/epja/i2016-16070-9

[219] N. Goel, C. Domingo-Pardo, T. Habermann, F. Ameil, T. Engert, J. Gerl, I. Kojouharov, J. Maruhn, N. Pietralla, H. Schaffner, Characterisation of a symmetric {AGATA} detector using the imaging scanning technique, Nuclear Instruments and Methods in Physics Research Section A: Accelerators,

Spectrometers, Detectors and Associated Equipment 700 (2013) 10 – 21. doi:http://dx.doi.org/10.1016/j.nima.2012.10.028.
URL http://www.sciencedirect.com/science/article/pii/S0168900212011606

[220] A. Hernandez-Prieto, B. Quintana, S. Martín, C. Domingo-Pardo, Study of accuracy in the position determination with salsa, a γ-scanning system for the characterization of segmented {HPGe} detectors, Nuclear Instruments and Methods in Physics Research Section A: Accelerators, Spectrometers, Detectors and Associated Equipment 823 (2016) 98 – 106. doi:http://dx.doi.org/10.1016/j.nima.2016.03.103.
URL http://www.sciencedirect.com/science/article/pii/S0168900216301486

[221] F. Crespi, F. Camera, B. Million, M. Sassi, O. Wieland, A. Bracco, A novel technique for the characterization of a {HPGe} detector response based on pulse shape comparison, Nuclear Instruments and Methods in Physics Research Section A: Accelerators, Spectrometers, Detectors and Associated Equipment 593 (3) (2008) 440 – 447. doi:http://dx.doi.org/10.1016/j.nima.2008.05.057.
URL http://www.sciencedirect.com/science/article/pii/S0168900208007821

[222] S. Martín, B. Quintana, D. Barrientos, Wilcoxon signed-rank-based technique for the pulse-shape analysis of {HPGe} detectors, Nuclear Instruments and Methods in Physics Research Section A: Accelerators, Spectrometers, Detectors and Associated Equipment 823 (2016) 32 – 40. doi:http://dx.doi.org/10.1016/j.nima.2016.03.094.
URL http://www.sciencedirect.com/science/article/pii/S0168900216301255

[223] T. Ha, A. Korichi, F. L. Blanc, P. Désesquelles, N. Dosme, X. Grave, N. Karkour, S. Leboutelier, E. Legay, D. Linget, B. Travers, P. Pariset, New setup for the characterisation of the {AGATA} detectors, Nuclear Instruments and Methods in Physics Research Section A: Accelerators, Spectrometers, Detectors and Associated Equipment 697 (2013) 123 – 132. doi:http://dx.doi.org/10.1016/j.nima.2012.08.111.
URL http://www.sciencedirect.com/science/article/pii/S0168900212010157

[224] B. Bruyneel, P. Reiter, G. Pascovici, Characterization of large volume {HPGe} detectors. part i: Electron and hole mobility parameterization, Nuclear Instruments and Methods in Physics Research Section A: Accelerators, Spectrometers, Detectors and Associated Equipment 569 (3) (2006) 764 – 773. doi:http://dx.doi.org/10.1016/j.nima.2006.08.130.
URL http://www.sciencedirect.com/science/article/pii/S0168900206015166

[225] B. Birkenbach, B. Bruyneel, G. Pascovici, J. Eberth, H. Hess, D. Lersch, P. Reiter, A. Wiens, Determination of space charge distributions in highly segmented large volume hpge detectors from capacitance–voltage measurements, Nuclear Instruments and Methods in Physics Research Section A: Accelerators,

Spectrometers, Detectors and Associated Equipment 640 (1) (2011) 176 – 184. doi:https://doi.org/10.1016/j.nima.2011.02.109.
URL http://www.sciencedirect.com/science/article/pii/S0168900211005912

[226] B. Bruyneel, B. Birkenbach, P. Reiter, Space charge reconstruction in highly segmented hpge detectors through capacitance-voltage measurements, Nuclear Instruments and Methods in Physics Research Section A: Accelerators, Spectrometers, Detectors and Associated Equipment 641 (1) (2011) 92 – 100. doi:https://doi.org/10.1016/j.nima.2011.02.110.
URL http://www.sciencedirect.com/science/article/pii/S0168900211006085

[227] A. Wiens, B. Birkenbach, B. Bruyneel, J. Eberth, H. Hess, G. Pascovici, P. Reiter, D. Bazzacco, E. Farnea, C. Michelagnoli, F. Recchia, Improved energy resolution of highly segmented hpge detectors by noise reduction, The European Physical Journal A 49 (4) (2013) 1–10. doi:10.1140/epja/i2013-13047-2.
URL http://dx.doi.org/10.1140/epja/i2013-13047-2

[228] G. P. Contributors, GSL - GNU scientific library - GNU project - free software foundation (FSF), http://www.gnu.org/software/gsl/ (2010) [cited 2010-06-20 22:49:12].
URL http://www.gnu.org/software/gsl/

[229] W. Bangerth, R. Hartmann, G. Kanschat, deal.II – a general purpose object oriented finite element library, ACM Trans. Math. Softw. 33 (4) (2007) 24/1–24/27.

[230] G. Alzetta, D. Arndt, W. Bangerth, V. Boddu, B. Brands, D. Davydov, R. Gassmoeller, T. Heister, L. Heltai, K. Kormann, M. Kronbichler, M. Maier, J.-P. Pelteret, B. Turcksin, D. Wells, The deal.II library, version 9.0, Journal of Numerical Mathematics 26 (4) (2018) 173–183. doi:10.1515/jnma-2018-0054.

[231] B. S. Kirk, J. W. Peterson, R. H. Stogner, G. F. Carey, libMesh: A C++ Library for Parallel Adaptive Mesh Refinement/Coarsening Simulations, Engineering with Computers 22 (3–4) (2006) 237–254, http://dx.doi.org/10.1007/s00366-006-0049-3.

[232] M. Hatlo, F. James, P. Mato, L. Moneta, M. Winkler, A. Zsenei, Developments of mathematical software libraries for the lhc experiments, IEEE Transactions on Nuclear Science 52 (6) (2005) 2818–2822. doi:10.1109/TNS.2005.860152.

[233] E. Farnea, F. Recchia, D. Bazzacco, T. Kröll, Z. Podolyák, B. Quintana, A. Gadea, Conceptual design and monte carlo simulations of the {AGATA} array, Nuclear Instruments and Methods in Physics Research Section A: Accelerators, Spectrometers, Detectors and Associated Equipment 621 (1-3) (2010) 331 – 343. doi:http://dx.doi.org/10.1016/j.nima.2010.04.043.
URL http://www.sciencedirect.com/science/article/pii/S0168900210008922

[234] P. Désesquelles, Determination of the hit locations in segmented {HPGe} detectors without the use of simulations or scanning systems, Nuclear

Instruments and Methods in Physics Research Section A: Accelerators, Spectrometers, Detectors and Associated Equipment 654 (1) (2011) 324 – 329. doi:http://dx.doi.org/10.1016/j.nima.2011.06.099.
URL http://www.sciencedirect.com/science/article/pii/S0168900211013945

[235] P. Désesquelles, A. Boston, H. Boston, J. Cresswell, M. Dimmock, I. Lazarus, J. Ljungvall, L. Nelson, D.-T. Nga, P. Nolan, S. Rigby, J. Simpson, N.-T. Van-Oanh, Direct determination of the hit locations from experimental {HPGe} pulses, Nuclear Instruments and Methods in Physics Research Section A: Accelerators, Spectrometers, Detectors and Associated Equipment 729 (2013) 198 – 206. doi:http://dx.doi.org/10.1016/j.nima.2013.07.026.
URL http://www.sciencedirect.com/science/article/pii/S0168900213010024

[236] H. J. Li, J. Ljungvall, C. Michelagnoli, E. Clément, J. Dudouet, P. Désesquelles, A. Lopez-Martens, G. de France, Experimental determination of reference pulses for highly segmented hpge detectors and application to pulse shape analysis used in γ-ray tracking arrays, The European Physical Journal A 54 (11) (2018) 198. doi:10.1140/epja/i2018-12636-9.
URL https://doi.org/10.1140/epja/i2018-12636-9

[237] D. B. R. Venturelli, Adaptive grid search as pulse shape analysis algorithm for γ-tracking and results, Tech. rep., LNL (2004).

[238] P. Désesquelles, T. M. H. Ha, K. Hauschild, A. Korichi, F. Le Blanc, A. Lopez-Martens, A. Olariu, C. M. Petrache, Matrix formalism and singular-value decomposition for the location of gamma interactions in segmented hpge detectors, The European Physical Journal A 40 (2) (2009) 237–248. doi:10.1140/epja/i2008-10749-4.
URL http://dx.doi.org/10.1140/epja/i2008-10749-4

[239] T. Kröll, D. Bazzacco, A genetic algorithm for the decomposition of multiple hit events in the γ-ray tracking detector {MARS}, Nuclear Instruments and Methods in Physics Research Section A: Accelerators, Spectrometers, Detectors and Associated Equipment 565 (2) (2006) 691 – 703. doi:http://dx.doi.org/10.1016/j.nima.2006.06.036.
URL http://www.sciencedirect.com/science/article/pii/S0168900206011430

[240] F. Crespi, F. Camera, A. Bracco, B. Million, O. Wieland, V. Vandone, F. Recchia, A. Gadea, T. Kröll, D. Mengoni, E. Farnea, C. Ur, D. Bazzacco, Application of the recursive subtraction pulse shape analysis algorithm to in-beam {HPGe} signals, Nuclear Instruments and Methods in Physics Research Section A: Accelerators, Spectrometers, Detectors and Associated Equipment 604 (3) (2009) 604 – 611. doi:http://dx.doi.org/10.1016/j.nima.2009.03.203.
URL http://www.sciencedirect.com/science/article/pii/S0168900209006913

[241] M. Schlarb, R. Gernhäuser, R. Krücken, Simulation and real-time analysis of pulse shapes from hpge detectors, Tech. rep. (2008).

[242] Greta (gamma-ray energy tracking array) conceptual design report, Tech. rep. (2017).
URL http://greta.lbl.gov/documents/ConceptualDesignReport-071717.pdf

[243] T. Lauritsen, A. Korichi, S. Zhu, A. Wilson, D. Weisshaar, J. Dudouet, A. Ayangeakaa, M. Carpenter, C. Campbell, E. Clément, H. Crawford, M. Cromaz, P. Fallon, J. Greene, R. Janssens, T. Khoo, N. Lalović, I. Lee, A. Macchiavelli, R. Perez-Vidal, S. Pietri, D. Radford, D. Ralet, L. Riley, D. Seweryniak, O. Stezowski, Characterization of a gamma-ray tracking array: A comparison of gretina and gammasphere using a 60co source, Nuclear Instruments and Methods in Physics Research Section A: Accelerators, Spectrometers, Detectors and Associated Equipment 836 (2016) 46 – 56. doi:https://doi.org/10.1016/j.nima.2016.07.027.
URL http://www.sciencedirect.com/science/article/pii/S0168900216307434

[244] F. Recchia, D. Bazzacco, E. Farnea, A. Gadea, R. Venturelli, T. Beck, P. Bednarczyk, A. Buerger, A. Dewald, M. Dimmock, G. Duchêne, J. Eberth, T. Faul, J. Gerl, R. Gernhaeuser, K. Hauschild, A. Holler, P. Jones, W. Korten, T. Kröll, R. Krücken, N. Kurz, J. Ljungvall, S. Lunardi, P. Maierbeck, D. Mengoni, J. Nyberg, L. Nelson, G. Pascovici, P. Reiter, H. Schaffner, M. Schlarb, T. Steinhardt, O. Thelen, C. Ur, J. V. Dobon, D. Weiaahaar, Position resolution of the prototype {AGATA} triple-cluster detector from an in-beam experiment, Nuclear Instruments and Methods in Physics Research Section A: Accelerators, Spectrometers, Detectors and Associated Equipment 604 (3) (2009) 555 – 562. doi:http://dx.doi.org/10.1016/j.nima.2009.02.042.
URL http://www.sciencedirect.com/science/article/pii/S0168900209004124

[245] P.-A. Söderström, F. Recchia, J. Nyberg, A. Al-Adili, A. Ataç, S. Aydin, D. Bazzacco, P. Bednarczyk, B. Birkenbach, D. Bortolato, A. Boston, H. Boston, B. Bruyneel, D. Bucurescu, E. Calore, S. Colosimo, F. Crespi, N. Dosme, J. Eberth, E. Farnea, F. Filmer, A. Gadea, A. Gottardo, X. Grave, J. Grebosz, R. Griffiths, M. Gulmini, T. Habermann, H. Hess, G. Jaworski, P. Jones, P. Joshi, D. Judson, R. Kempley, A. Khaplanov, E. Legay, D. Lersch, J. Ljungvall, A. Lopez-Martens, W. Meczynski, D. Mengoni, C. Michelagnoli, P. Molini, D. Napoli, R. Orlandi, G. Pascovici, A. Pullia, P. Reiter, E. Sahin, J. Smith, J. Strachan, D. Tonev, C. Unsworth, C. Ur, J. Valiente-Dobón, C. Veyssiere, A. Wiens, Interaction position resolution simulations and in-beam measurements of the {AGATA} {HPGe} detectors, Nuclear Instruments and Methods in Physics Research Section A: Accelerators, Spectrometers, Detectors and Associated Equipment 638 (1) (2011) 96 – 109. doi:http://dx.doi.org/10.1016/j.nima.2011.02.089.
URL http://www.sciencedirect.com/science/article/pii/S016890021100489X

[246] F. Recchia, D. Bazzacco, E. Farnea, R. Venturelli, S. Aydin, G. Suliman, C. Ur, Performance of an agata prototype detector estimated by compton-imaging techniques, Nuclear Instruments and Methods in Physics Research Section A: Accelerators, Spectrometers, Detectors and Associated Equipment 604 (1) (2009) 60 – 63, pSD8.

doi:https://doi.org/10.1016/j.nima.2009.01.079.
URL http://www.sciencedirect.com/science/article/pii/S0168900209001168

[247] S. Paschalis, I. Lee, A. Macchiavelli, C. Campbell, M. Cromaz, S. Gros, J. Pavan, J. Qian, R. Clark, H. Crawford, D. Doering, P. Fallon, C. Lionberger, T. Loew, M. Petri, T. Stezelberger, S. Zimmermann, D. Radford, K. Lagergren, D. Weisshaar, R. Winkler, T. Glasmacher, J. Anderson, C. Beausang, The performance of the gamma-ray energy tracking in-beam nuclear array gretina, Nuclear Instruments and Methods in Physics Research Section A: Accelerators, Spectrometers, Detectors and Associated Equipment 709 (2013) 44 – 55. doi:https://doi.org/10.1016/j.nima.2013.01.009.
URL http://www.sciencedirect.com/science/article/pii/S0168900213000508

[248] D. Weisshaar, D. Bazin, P. Bender, C. Campbell, F. Recchia, V. Bader, T. Baugher, J. Belarge, M. Carpenter, H. Crawford, M. Cromaz, B. Elman, P. Fallon, A. Forney, A. Gade, J. Harker, N. Kobayashi, C. Langer, T. Lauritsen, I. Lee, A. Lemasson, B. Longfellow, E. Lunderberg, A. Macchiavelli, K. Miki, S. Momiyama, S. Noji, D. Radford, M. Scott, J. Sethi, S. Stroberg, C. Sullivan, R. Titus, A. Wiens, S. Williams, K. Wimmer, S. Zhu, The performance of the γ-ray tracking array gretina for γ-ray spectroscopy with fast beams of rare isotopes, Nuclear Instruments and Methods in Physics Research Section A: Accelerators, Spectrometers, Detectors and Associated Equipment 847 (2017) 187 – 198. doi:https://doi.org/10.1016/j.nima.2016.12.001.
URL http://www.sciencedirect.com/science/article/pii/S0168900216312402

[249] C. Lawson, R. Hanson, Solving Least Squares Problems, Classics in Applied Mathematics, Society for Industrial and Applied Mathematics, 1995.
URL https://books.google.fr/books?id=ROw4hU85nz8C

[250] M. R. Dimmock, A. J. Boston, J. R. Cresswell, I. Lazarus, P. Medina, P. Nolan, C. Parisel, C. Santos, J. Simpson, C. Unsworth, Validation of pulse shape simulations for an agata prototype detector, IEEE Transactions on Nuclear Science 56 (4) (2009) 2415–2425. doi:10.1109/TNS.2009.2021842.

[251] M. R. Dimmock, A. J. Boston, H. C. Boston, J. R. Cresswell, L. Nelson, P. J. Nolan, C. Unsworth, I. H. Lazarus, J. Simpson, Characterisation results from an agata prototype detector, IEEE Transactions on Nuclear Science 56 (3) (2009) 1593–1599. doi:10.1109/TNS.2009.2019103.

[252] X. Grave, R. Canedo, J. . Clavelin, S. Du, E. Legay, Narval a modular distributed data acquisition system with ada 95 and rtai, in: 14th IEEE-NPSS Real Time Conference, 2005., 2005, pp. 5 pp.–. doi:10.1109/RTC.2005.1547454.

[253] J. van der Marel, B. Cederwall, Backtracking as a way to reconstruct compton scattered γ-rays, Nuclear Instruments and Methods in Physics Research Section A: Accelerators, Spectrometers, Detectors and Associated Equipment 437 (2-3) (1999) 538 – 551. doi:http://dx.doi.org/10.1016/S0168-9002(99)00801-3.

URL http://www.sciencedirect.com/science/article/pii/S0168900299008013

[254] L. Milechina, B. Cederwall, Improvements in γ-ray reconstruction with positive sensitive ge detectors using the backtracking method, Nuclear Instruments and Methods in Physics Research Section A: Accelerators, Spectrometers, Detectors and Associated Equipment 508 (3) (2003) 394 – 403. doi:https://doi.org/10.1016/S0168-9002(03)01698-X.
URL http://www.sciencedirect.com/science/article/pii/S016890020301698X

[255] D. Bazzacco, mgt code developed within the tmr program 'gamma-ray tracking detectors'.

[256] G. Schmid, M. Deleplanque, I. Lee, F. Stephens, K. Vetter, R. Clark, R. Diamond, P. Fallon, A. Macchiavelli, R. MacLeod, A γ-ray tracking algorithm for the {GRETA} spectrometer, Nuclear Instruments and Methods in Physics Research Section A: Accelerators, Spectrometers, Detectors and Associated Equipment 430 (1) (1999) 69 – 83. doi:http://dx.doi.org/10.1016/S0168-9002(99)00188-6.
URL http://www.sciencedirect.com/science/article/pii/S0168900299001886

[257] A. Lopez-Martens, K. Hauschild, A. Korichi, J. Roccaz, J.-P. Thibaud, γ-ray tracking algorithms: a comparison, Nuclear Instruments and Methods in Physics Research Section A: Accelerators, Spectrometers, Detectors and Associated Equipment 533 (3) (2004) 454 – 466. doi:http://dx.doi.org/10.1016/j.nima.2004.06.154.
URL http://www.sciencedirect.com/science/article/pii/S0168900204014779

[258] S. Agostinelli, J. Allison, K. Amako, J. Apostolakis, H. Araujo, P. Arce, M. Asai, D. Axen, S. Banerjee, G. Barrand, F. Behner, L. Bellagamba, J. Boudreau, L. Broglia, A. Brunengo, H. Burkhardt, S. Chauvie, J. Chuma, R. Chytracek, G. Cooperman, G. Cosmo, P. Degtyarenko, A. Dell'Acqua, G. Depaola, D. Dietrich, R. Enami, A. Feliciello, C. Ferguson, H. Fesefeldt, G. Folger, F. Foppiano, A. Forti, S. Garelli, S. Giani, R. Giannitrapani, D. Gibin, J. G. Cadenas, I. González, G. G. Abril, G. Greeniaus, W. Greiner, V. Grichine, A. Grossheim, S. Guatelli, P. Gumplinger, R. Hamatsu, K. Hashimoto, H. Hasui, A. Heikkinen, A. Howard, V. Ivanchenko, A. Johnson, F. Jones, J. Kallenbach, N. Kanaya, M. Kawabata, Y. Kawabata, M. Kawaguti, S. Kelner, P. Kent, A. Kimura, T. Kodama, R. Kokoulin, M. Kossov, H. Kurashige, E. Lamanna, T. Lampén, V. Lara, V. Lefebure, F. Lei, M. Liendl, W. Lockman, F. Longo, S. Magni, M. Maire, E. Medernach, K. Minamimoto, P. M. de Freitas, Y. Morita, K. Murakami, M. Nagamatu, R. Nartallo, P. Nieminen, T. Nishimura, K. Ohtsubo, M. Okamura, S. O'Neale, Y. Oohata, K. Paech, J. Perl, A. Pfeiffer, M. Pia, F. Ranjard, A. Rybin, S. Sadilov, E. D. Salvo, G. Santin, T. Sasaki, N. Savvas, Y. Sawada, S. Scherer, S. Sei, V. Sirotenko, D. Smith, N. Starkov, H. Stoecker, J. Sulkimo, M. Takahata, S. Tanaka, E. Tcherniaev, E. S. Tehrani, M. Tropeano, P. Truscott, H. Uno, L. Urban, P. Urban, M. Verderi, A. Walkden, W. Wander, H. Weber, J. Wellisch, T. Wenaus, D. Williams, D. Wright, T. Yamada, H. Yoshida, D. Zschiesche, Geant4—a simulation toolkit, Nuclear

Instruments and Methods in Physics Research Section A: Accelerators, Spectrometers, Detectors and Associated Equipment 506 (3) (2003) 250 – 303. doi:https://doi.org/10.1016/S0168-9002(03)01368-8.
URL http://www.sciencedirect.com/science/article/pii/S0168900203013688

[259] N. Lalović, C. Louchart, C. Michelagnoli, R. Perez-Vidal, D. Ralet, J. Gerl, D. Rudolph, T. Arici, D. Bazzacco, E. Clément, A. Gadea, I. Kojouharov, A. Korichi, M. Labiche, J. Ljungvall, A. Lopez-Martens, J. Nyberg, N. Pietralla, S. Pietri, O. Stezowski, Performance of the {AGATA} γ-ray spectrometer in the prespec set-up at {GSI}, Nuclear Instruments and Methods in Physics Research Section A: Accelerators, Spectrometers, Detectors and Associated Equipment 806 (2016) 258 – 266. doi:http://dx.doi.org/10.1016/j.nima.2015.10.032.
URL http://www.sciencedirect.com/science/article/pii/S0168900215012395

[260] J. Ljungvall, R. Pérez-Vidal, A. Lopez-Martens, C. Michelagnoli, E. Clément, J. Dudouet, A. Gadea, H. Hess, A. Korichi, M. Labiche, N. Lalović, H. Li, F. Recchia, Performance of the advanced gamma tracking array at ganil, Nuclear Instruments and Methods in Physics Research Section A: Accelerators, Spectrometers, Detectors and Associated Equipment 955 (2020) 163297. doi:https://doi.org/10.1016/j.nima.2019.163297.
URL http://www.sciencedirect.com/science/article/pii/S0168900219315475

[261] Gammas emitted only after ion stopped (radioactivedecay physics).
URL http://hypernews.slac.stanford.edu:5090/HyperNews/geant4/get/hadronprocess/1275.html

[262] Ion gets a strange boost when emitting gamma ray (g4radioactivedecay).
URL http://hypernews.slac.stanford.edu:5090/HyperNews/geant4/get/hadronprocess/1295.html

[263] N. Lalović, D. Rudolph, Z. Podolyák, L. G. Sarmiento, E. C. Simpson, T. Alexander, M. L. Cortés, J. Gerl, P. Golubev, F. Ameil, T. Arici, C. Bauer, D. Bazzacco, M. A. Bentley, P. Boutachkov, M. Bowry, C. Fahlander, A. Gadea, J. Gellanki, A. Givechev, N. Goel, M. Górska, A. Gottardo, E. Gregor, G. Guastalla, T. Habermann, M. Hackstein, A. Jungclaus, I. Kojouharov, R. Kumar, N. Kurz, M. Lettmann, C. Lizarazo, C. Louchart, E. Merchán, C. Michelagnoli, T. Moeller, K. Moschner, Z. Patel, N. Pietralla, S. Pietri, D. Ralet, M. Reese, P. H. Regan, P. Reiter, H. Schaffner, P. Singh, C. Stahl, R. Stegmann, O. Stezowski, J. Taprogge, P. Thöle, A. Wendt, O. Wieland, E. Wilson, R. Wood, H.-J. Wollersheim, B. Birkenbach, B. Bruyneel, I. Burrows, E. Clément, P. Désesquelles, C. Domingo-Pardo, J. Eberth, V. González, H. Hess, J. Jolie, D. S. Judson, R. Menegazzo, D. Mengoni, D. R. Napoli, A. Pullia, B. Quintana, G. Rainovski, M. D. Salsac, E. Sanchis, J. Simpson, J. J. V. D. and, Study of isomeric states in 198,200,202,206pb and 206hg populated in fragmentation reactions, Journal of Physics G: Nuclear and Particle Physics 45 (3) (2018) 035105. doi:10.1088/1361-6471/aaa9df.
URL https://doi.org/10.1088%2F1361-6471%2Faaa9df

[264] A. R. Poletti, E. K. Warburton, J. W. Olness, Nuclear structure of high-spin states in ^{46}Ti and ^{46}V, Phys. Rev. C 23 (1981) 1550–1559. doi:10.1103/PhysRevC.23.1550.
URL https://link.aps.org/doi/10.1103/PhysRevC.23.1550

[265] S. Heil, S. Paschalis, M. Petri, On the self-calibration capabilities of $ \gamma$-ray energy tracking arrays, The European Physical Journal A 54 (10) (2018) 172. doi:10.1140/epja/i2018-12609-0.
URL https://doi.org/10.1140/epja/i2018-12609-0

[266] P. Napiralla, D. Brugnara, E. Clément, H. Egger, A. Goasduff, P. John, R. Kern, H. Li, N. Pietralla, J. Valiente-Dobón, Approach to a self-calibrating experimental γ-ray tracking algorithm, Nuclear Instruments and Methods in Physics Research Section A: Accelerators, Spectrometers, Detectors and Associated Equipment 955 (2020) 163337. doi:https://doi.org/10.1016/j.nima.2019.163337.
URL http://www.sciencedirect.com/science/article/pii/S0168900219315694

[267] Alpha, Beta, and Gamma-ray spectroscopy, Vol I and II, Amsterdam: NHPC, 1968.

[268] The Electromagnetic interaction in nuclear spectroscopy., Amsterdam: North-Holland, 1975.

[269] J. Cerny, Nuclear spectroscopy and reactions, Pure Appl. Phys., Academic Press, New York, NY, 1974.
URL https://cds.cern.ch/record/102345

[270] A. Dewald, S. Harissopulos, P. von Brentano, The differential plunger and the differential decay curve method for the analysis of recoil distance doppler-shift data, Zeitschrift für Physik A Atomic Nuclei 334 (2) (1989) 163–175. doi:10.1007/BF01294217.
URL http://dx.doi.org/10.1007/BF01294217

[271] P. Petkov, Errors arising from nuclear hyperfine interactions on lifetimes determined by the recoil distance doppler shift method, Nuclear Instruments and Methods in Physics Research Section A: Accelerators, Spectrometers, Detectors and Associated Equipment 349 (1) (1994) 289 – 291. doi:https://doi.org/10.1016/0168-9002(94)90636-X.
URL http://www.sciencedirect.com/science/article/pii/016890029490636X

[272] M. Hackstein, A. Dewald, Velocity distribution in recoil-distance doppler-shift experiments, Nuclear Instruments and Methods in Physics Research Section A: Accelerators, Spectrometers, Detectors and Associated Equipment 738 (2014) 93 – 98. doi:https://doi.org/10.1016/j.nima.2013.11.047.
URL http://www.sciencedirect.com/science/article/pii/S0168900213015866

[273] J. Valiente-Dobón, G. Jaworski, A. Goasduff, F. Egea, V. Modamio, T. Hüyük, A. Triossi, M. Jastrząb, P. Söderström, A. D. Nitto, G. de Angelis, G. de France,

N. Erduran, A. Gadea, M. Moszyński, J. Nyberg, M. Palacz, R. Wadsworth, R. Aliaga, C. Aufranc, M. Bézard, G. Baulieu, E. Bissiato, A. Boujrad, I. Burrows, S. Carturan, P. Cocconi, G. Colucci, D. Conventi, M. Cordwell, S. Coudert, J. Deltoro, L. Ducroux, T. Dupasquier, S. Ertürk, X. Fabian, V. González, A. Grant, K. Hadyńska-Klęk, A. Illana, M. Jurado-Gomez, M. Kogimtzis, I. Lazarus, L. Legeard, J. Ljungvall, G. Pasqualato, R. Pérez-Vidal, A. Raggio, D. Ralet, N. Redon, F. Saillant, B. Sayği, E. Sanchis, M. Scarcioffolo, M. Siciliano, D. Testov, O. Stezowski, M. Tripon, I. Zanon, Neda-neutron detector array, Nuclear Instruments and Methods in Physics Research Section A: Accelerators, Spectrometers, Detectors and Associated Equipment 927 (2019) 81 – 86. doi:https://doi.org/10.1016/j.nima.2019.02.021.
URL http://www.sciencedirect.com/science/article/pii/S0168900219301962

[274] J. Scheurer, M. Aiche, M. Aleonard, G. Barreau, F. Bourgine, D. Boivin, D. Cabaussel, J. Chemin, T. Doan, J. Goudour, M. Harston, A. Brondi, G. L. Rana, R. Moro, E. Vardaci, D. Curien, Improvements in the in-beam γ-ray spectroscopy provided by an ancillary detector coupled to a ge γ-spectrometer: the diamant-eurogam ii example, Nuclear Instruments and Methods in Physics Research Section A: Accelerators, Spectrometers, Detectors and Associated Equipment 385 (3) (1997) 501 – 510. doi:https://doi.org/10.1016/S0168-9002(96)01038-8.
URL http://www.sciencedirect.com/science/article/pii/S0168900296010388

[275] T. Konstantinopoulos, P. Petkov, A. Goasduff, T. Arici, A. Astier, L. Atanasova, M. Axiotis, D. Bonatsos, P. Detistov, A. Dewald, M. J. Eller, V. Foteinou, A. Gargano, G. Georgiev, K. Gladnishki, A. Gottardo, S. Harissopulos, H. Hess, S. Kaim, D. Kocheva, A. Kusoglu, A. Lagoyannis, J. Ljungvall, R. Lutter, I. Matea, B. Melon, T. J. Mertzimekis, A. Nannini, C. M. Petrache, A. Petrovici, G. Provatas, P. Reiter, M. Rocchini, S. Roccia, M. Seidlitz, B. Siebeck, D. Suzuki, N. Warr, H. De Witte, T. Zerrouki, Lifetime measurements in ^{100}Ru, Phys. Rev. C 95 (2017) 014309. doi:10.1103/PhysRevC.95.014309.
URL http://link.aps.org/doi/10.1103/PhysRevC.95.014309

[276] L. Sengelé, É. D. de PHYSIQUE ET CHIMIE-PHYSIQUE INSTITUT PLURIDISCIPLINAIRE HUBERT CURIEN UMR 7178 CNRS / IN2P3, Etude des modes octupolaires dans le noyau atomique de 156gd : recherche expérimentale de la symétrie tétraédrique. (2014).

[277] A. Stefanini, L. Corradi, G. Maron, A. Pisent, M. Trotta, A. Vinodkumar, S. Beghini, G. Montagnoli, F. Scarlassara, G. Segato, A. D. Rosa, G. Inglima, D. Pierroutsakou, M. Romoli, M. Sandoli, G. Pollarolo, A. Latina, The heavy-ion magnetic spectrometer prisma, Nuclear Physics A 701 (1) (2002) 217 – 221, 5th International Conference on Radioactive Nuclear Beams. doi:https://doi.org/10.1016/S0375-9474(01)01578-0.
URL http://www.sciencedirect.com/science/article/pii/S0375947401015780

[278] V. Modamio, J. J. Valiente-Dobón, S. Lunardi, S. M. Lenzi, A. Gadea, D. Mengoni, D. Bazzacco, A. Algora, P. Bednarczyk, G. Benzoni, et al., Lifetime

measurements in neutron-rich ^{63,65}co isotopes using the agata demonstrator, Phys. Rev. C 88 (2013) 044326. doi:10.1103/PhysRevC.88.044326.
URL http://link.aps.org/doi/10.1103/PhysRevC.88.044326

[279] F. Didierjean, D. Verney, G. Duchêne, J. Litzinger, K. Sieja, A. Dewald, A. Goasduff, R. Lozeva, C. Fransen, G. de Angelis, S. Aydin, D. Bazzacco, A. Bracco, S. Bottoni, L. Corradi, F. Crespi, E. Ellinger, E. Farnea, E. Fioretto, S. Franchoo, A. Gottardo, L. Grocutt, M. Hackstein, F. Ibrahim, K. Kolos, S. Leoni, S. Lenzi, S. Lunardi, R. Menegazzo, D. Mengoni, C. Michelagnoli, T. Mijatovic, V. Modamio, O. Möller, G. Montagnoli, D. Montanari, A. I. Morales, D. Napoli, M. Niikura, F. Recchia, E. Sahin, F. Scarlassara, L. Sengele, S. Szilner, J. F. Smith, A. M. Stefanini, C. Ur, J. J. Valiente-Dobón, V. Vandone, Neutron effective single-particle energies above ^{78}Ni: A hint from lifetime measurements in the $n = 51$ isotones ^{85}Se and ^{87}Kr, Phys. Rev. C 96 (2017) 044320. doi:10.1103/PhysRevC.96.044320.
URL https://link.aps.org/doi/10.1103/PhysRevC.96.044320

[280] E. Sahin, M. Doncel, K. Sieja, G. de Angelis, A. Gadea, B. Quintana, A. Görgen, V. Modamio, D. Mengoni, J. J. Valiente-Dobón, P. R. John, M. Albers, D. Bazzacco, G. Benzoni, B. Birkenbach, B. Cederwall, E. Clément, D. Curien, L. Corradi, P. Désesquelles, A. Dewald, F. Didierjean, G. Duchêne, J. Eberth, M. N. Erduran, E. Farnea, E. Fioretto, G. de France, C. Fransen, R. Gernhäuser, A. Gottardo, M. Hackstein, T. Hagen, A. Hernández-Prieto, H. Hess, T. Hüyük, A. Jungclaus, S. Klupp, W. Korten, A. Kusoglu, S. M. Lenzi, J. Ljungvall, C. Louchart, S. Lunardi, R. Menegazzo, C. Michelagnoli, T. Mijatović, B. Million, P. Molini, G. Montagnoli, D. Montanari, O. Möller, D. R. Napoli, A. Obertelli, R. Orlandi, G. Pollarolo, A. Pullia, F. Recchia, P. Reiter, D. Rosso, W. Rother, M.-D. Salsac, F. Scarlassara, M. Schlarb, S. Siem, P. P. Singh, P.-A. Söderström, A. M. Stefanini, O. Stézowski, B. Sulignano, S. Szilner, C. Theisen, C. A. Ur, M. Yalcinkaya, Shell evolution beyond $n = 40$: ^{69,71,73}Cu, Phys. Rev. C 91 (2015) 034302. doi:10.1103/PhysRevC.91.034302.
URL https://link.aps.org/doi/10.1103/PhysRevC.91.034302

[281] J. Litzinger, A. Blazhev, A. Dewald, F. Didierjean, G. Duchêne, C. Fransen, R. Lozeva, K. Sieja, D. Verney, G. de Angelis, D. Bazzacco, B. Birkenbach, S. Bottoni, A. Bracco, T. Braunroth, B. Cederwall, L. Corradi, F. C. L. Crespi, P. Désesquelles, J. Eberth, E. Ellinger, E. Farnea, E. Fioretto, R. Gernhäuser, A. Goasduff, A. Görgen, A. Gottardo, J. Grebosz, M. Hackstein, H. Hess, F. Ibrahim, J. Jolie, A. Jungclaus, K. Kolos, W. Korten, S. Leoni, S. Lunardi, A. Maj, R. Menegazzo, D. Mengoni, C. Michelagnoli, T. Mijatovic, B. Million, O. Möller, V. Modamio, G. Montagnoli, D. Montanari, A. I. Morales, D. R. Napoli, M. Niikura, G. Pollarolo, A. Pullia, B. Quintana, F. Recchia, P. Reiter, D. Rosso, E. Sahin, M. D. Salsac, F. Scarlassara, P.-A. Söderström, A. M. Stefanini, O. Stezowski, S. Szilner, C. Theisen, J. J. Valiente Dobón, V. Vandone, A. Vogt, Transition probabilities in neutron-rich ^{84,86}Se, Phys. Rev. C 92 (2015) 064322. doi:10.1103/PhysRevC.92.064322.
URL https://link.aps.org/doi/10.1103/PhysRevC.92.064322

[282] J. Litzinger, A. Blazhev, A. Dewald, F. Didierjean, G. Duchêne, C. Fransen, R. Lozeva, D. Verney, G. de Angelis, D. Bazzacco, B. Birkenbach, S. Bottoni, A. Bracco, T. Braunroth, B. Cederwall, L. Corradi, F. C. L. Crespi, P. Désesquelles, J. Eberth, E. Ellinger, E. Farnea, E. Fioretto, R. Gernhäuser, A. Goasduff, A. Görgen, A. Gottardo, J. Grebosz, M. Hackstein, H. Hess, F. Ibrahim, J. Jolie, A. Jungclaus, K. Kolos, W. Korten, S. Leoni, S. Lunardi, A. Maj, R. Menegazzo, D. Mengoni, C. Michelagnoli, T. Mijatovic, B. Million, O. Möller, V. Modamio, G. Montagnoli, D. Montanari, A. I. Morales, D. R. Napoli, M. Niikura, N. Pietralla, G. Pollarolo, A. Pullia, B. Quintana, F. Recchia, P. Reiter, D. Rosso, E. Sahin, M. D. Salsac, F. Scarlassara, P.-A. Söderström, A. M. Stefanini, O. Stezowski, S. Szilner, C. Theisen, J. J. Valiente-Dobón, V. Vandone, A. Vogt, Transition probabilities in neutron-rich ^{80,82}Se and the role of the $\nu g_{9/2}$ orbital, Phys. Rev. C 97 (2018) 044323. doi:10.1103/PhysRevC.97.044323.
URL https://link.aps.org/doi/10.1103/PhysRevC.97.044323

[283] M. Doncel, A. Gadea, J. J. Valiente-Dobón, B. Quintana, V. Modamio, D. Mengoni, O. Möller, A. Dewald, N. Pietralla, Determination of lifetimes of nuclear excited states using the recoil distance doppler shift method in combination with magnetic spectrometers, The European Physical Journal A 53 (10) (2017) 211. doi:10.1140/epja/i2017-12382-6.
URL https://doi.org/10.1140/epja/i2017-12382-6

[284] J. Van de Walle, V. Bildstein, N. Bree, J. Cederkäll, P. Delahaye, J. Diriken, A. Ekström, V. N. Fedosseev, R. Gernhäuser, A. Gustafsson, A. Herlert, M. Huyse, O. Ivanov, T. Kröll, R. Krücken, B. Marsh, N. Partronis, P. Van Duppen, D. Voulot, N. Warr, F. Wenander, K. Wimmer, S. M. Lenzi, In-trap decay of 61mn and coulomb excitation of 61mn/61fe, The European Physical Journal A 42 (3) (2009) 401–406. doi:10.1140/epja/i2009-10814-6.
URL http://dx.doi.org/10.1140/epja/i2009-10814-6

[285] A. Lemasson, H. Iwasaki, C. Morse, D. Bazin, T. Baugher, J. S. Berryman, A. Dewald, C. Fransen, A. Gade, S. McDaniel, A. Nichols, A. Ratkiewicz, S. Stroberg, P. Voss, R. Wadsworth, D. Weisshaar, K. Wimmer, R. Winkler, Observation of mutually enhanced collectivity in self-conjugate $^{\mathbf{76}}_{\mathbf{38}}\mathrm{sr}_{\mathbf{38}}$, Phys. Rev. C 85 (2012) 041303. doi:10.1103/PhysRevC.85.041303.
URL https://link.aps.org/doi/10.1103/PhysRevC.85.041303

[286] V. Vaquero, A. Jungclaus, P. Doornenbal, K. Wimmer, A. M. Moro, K. Ogata, T. Furumoto, S. Chen, E. Nácher, E. Sahin, Y. Shiga, D. Steppenbeck, R. Taniuchi, Z. Y. Xu, T. Ando, H. Baba, F. L. Bello Garrote, S. Franchoo, K. Hadynska-Klek, A. Kusoglu, J. Liu, T. Lokotko, S. Momiyama, T. Motobayashi, S. Nagamine, N. Nakatsuka, M. Niikura, R. Orlandi, T. Y. Saito, H. Sakurai, P. A. Söderström, G. M. Tveten, Z. Vajta, M. Yalcinkaya, In-beam γ-ray spectroscopy of ^{136}Te at relativistic energies, Phys. Rev. C 99 (2019) 034306. doi:10.1103/PhysRevC.99.034306.
URL https://link.aps.org/doi/10.1103/PhysRevC.99.034306

[287] V. Vaquero, A. Jungclaus, P. Doornenbal, K. Wimmer, A. Gargano, J. A. Tostevin, S. Chen, E. Nácher, E. Sahin, Y. Shiga, D. Steppenbeck, R. Taniuchi, Z. Y. Xu, T. Ando, H. Baba, F. L. B. Garrote, S. Franchoo, K. Hadynska-Klek, A. Kusoglu, J. Liu, T. Lokotko, S. Momiyama, T. Motobayashi, S. Nagamine, N. Nakatsuka, M. Niikura, R. Orlandi, T. Saito, H. Sakurai, P. A. Söderström, G. M. Tveten, Z. Vajta, M. Yalcinkaya, Gamma decay of unbound neutron-hole states in ^{133}Sn, Phys. Rev. Lett. 118 (2017) 202502. doi:10.1103/PhysRevLett.118.202502.
URL https://link.aps.org/doi/10.1103/PhysRevLett.118.202502

[288] D. Ralet, S. Pietri, T. Rodríguez, M. Alaqeel, T. Alexander, N. Alkhomashi, F. Ameil, T. Arici, A. Ataç, R. Avigo, T. Bäck, D. Bazzacco, B. Birkenbach, P. Boutachkov, B. Bruyneel, A. M. Bruce, F. Camera, B. Cederwall, S. Ceruti, E. Clément, M. L. Cortés, D. Curien, G. De Angelis, P. Désesquelles, M. Dewald, F. Didierjean, C. Domingo-Pardo, M. Doncel, G. Duchêne, J. Eberth, A. Gadea, J. Gerl, F. Ghazi Moradi, H. Geissel, T. Goigoux, N. Goel, P. Golubev, V. González, M. Górska, A. Gottardo, E. Gregor, G. Guastalla, A. Givechev, T. Habermann, M. Hackstein, L. Harkness-Brennan, G. Henning, H. Hess, T. Hüyük, J. Jolie, D. S. Judson, A. Jungclaus, R. Knoebel, I. Kojouharov, A. Korichi, W. Korten, N. Kurz, M. Labiche, N. Lalović, C. Louchart-Henning, D. Mengoni, E. Merchán, B. Million, A. I. Morales, D. Napoli, F. Naqvi, J. Nyberg, N. Pietralla, Z. Podolyák, A. Pullia, A. Prochazka, B. Quintana, G. Rainovski, M. Reese, F. Recchia, P. Reiter, D. Rudolph, M. D. Salsac, E. Sanchis, L. G. Sarmiento, H. Schaffner, C. Scheidenberger, L. Sengele, B. S. N. Singh, P. P. Singh, C. Stahl, O. Stezowski, P. Thoele, J. J. Valiente Dobon, H. Weick, A. Wendt, O. Wieland, J. S. Winfield, H. J. Wollersheim, M. Zielinska, Lifetime measurement of neutron-rich even-even molybdenum isotopes, Phys. Rev. C 95 (2017) 034320. doi:10.1103/PhysRevC.95.034320.
URL https://link.aps.org/doi/10.1103/PhysRevC.95.034320

[289] H. Iwasaki, A. Dewald, T. Braunroth, C. Fransen, D. Smalley, A. Lemasson, C. Morse, K. Whitmore, C. Loelius, The triple plunger for exotic beams triplex for excited-state lifetime measurement studies on rare isotopes, Nuclear Instruments and Methods in Physics Research Section A: Accelerators, Spectrometers, Detectors and Associated Equipment 806 (2016) 123 – 131. doi:https://doi.org/10.1016/j.nima.2015.09.091.
URL http://www.sciencedirect.com/science/article/pii/S0168900215011626

[290] A. Bracco, P. Chomaz, J. Gaardhøje, M. Makarow, P.-H. Heenen, G. Rosner, R. Kaiser, D. MacGregor, E. Widmann, G. Korner, Perspectives of nuclear physics in europe: Nupecc long range plan 2010, Discussion paper, European Science Foundation (2010).
URL http://eprints.gla.ac.uk/90049/

[291] J. Simpson, R. Krücken, Agata: The advanced gamma tracking array, Nuclear Physics News 13 (4) (2003) 15–18. arXiv:http://dx.doi.org/10.1080/10506890308232711, doi:10.1080/10506890308232711.
URL http://dx.doi.org/10.1080/10506890308232711

[292] Agata publications, http://npg.dl.ac.uk/agata_acc/AGATA_Publications.html, accessed: 2017-01-02.

[293] F. Crespi, V. Vandone, S. Brambilla, F. Camera, B. Million, S. Riboldi, O. Wieland, {HPGe} detectors timing using pulse shape analysis techniques, Nuclear Instruments and Methods in Physics Research Section A: Accelerators, Spectrometers, Detectors and Associated Equipment 620 (2-3) (2010) 299 – 304. doi:http://dx.doi.org/10.1016/j.nima.2010.02.273.
URL http://www.sciencedirect.com/science/article/pii/S0168900210005644

[294] S. C. Brenner, L. R. Scott, The Mathematical Theory of Finite ElementMethods, 2nd Edition, Vol. 15 of Texts in Applied Mathematics, Springer, 2002.

Part III

Appendices

Chapter 7

Selected publications

7.1 Shape Coexistence in Light Se Isotopes: Evidence for Oblate Shapes

Shape Coexistence in Light Se Isotopes: Evidence for Oblate Shapes

J. Ljungvall,[1] A. Görgen,[1] M. Girod,[2] J.-P. Delaroche,[2] A. Dewald,[3] C. Dossat,[1] E. Farnea,[4] W. Korten,[1] B. Melon,[3] R. Menegazzo,[4] A. Obertelli,[1] R. Orlandi,[5] P. Petkov,[3,6] T. Pissulla,[3] S. Siem,[7] R. P. Singh,[5,*] J. Srebrny,[8] Ch. Theisen,[1] C. A. Ur,[4,†] J. J. Valiente-Dobón,[5] K. O. Zell,[3] and M. Zielińska[1]

[1]*CEA-Saclay, DAPNIA/SPhN, F-91191 Gif-sur-Yvette Cedex, France*
[2]*CEA-DIF, DPTA/SPN, Bruyères-le-Châtel, F-91297 Arpajon Cedex, France*
[3]*Institut für Kernphysik, Universität zu Köln, D-50937 Köln, Germany*
[4]*INFN Sezione di Padova, I-35131 Padova, Italy*
[5]*INFN-Laboratori Nazionali di Legnaro, I-35020 Legnaro, Italy*
[6]*INRNE, Bulgarian Academy of Sciences, 1784 Sofia, Bulgaria*
[7]*Department of Physics, University of Oslo, N-0316 Oslo, Norway*
[8]*Heavy Ion Laboratory, Warsaw University, Warsaw, PL-02097, Poland*

(Received 17 December 2007; published 14 March 2008)

Lifetimes of states in the ground-state bands of ^{70}Se and ^{72}Se were measured using the recoil-distance Doppler shift method. The results deviate significantly from earlier measurements, requiring a revision of the conclusions drawn from a recent Coulomb excitation experiment concerning the shape of ^{70}Se. The new results lead to a coherent picture of shape coexistence in the neutron-deficient selenium and krypton isotopes. The coexistence and evolution of oblate and prolate shapes in this mass region is for the first time consistently described by new Hartree-Fock-Bogolyubov-based configuration-mixing calculations which were performed using the Gogny D1S interaction.

DOI: 10.1103/PhysRevLett.100.102502 PACS numbers: 21.10.Re, 21.10.Tg, 25.70.Hi, 27.50.+e

The nuclear shape is a very sensitive probe of the underlying nuclear structure and the interaction between the nucleons. Observables such as the electric quadrupole moment or the transition strength between excited nuclear states are hence important benchmarks for nuclear structure theory. Nuclei in the mass region $A \approx 70$ close to the $N = Z$ line are known to exhibit a variety of nuclear shapes, which can be attributed to large shell gaps at both prolate and oblate deformation for proton and neutron numbers 34 and 36. Coulomb excitation experiments have yielded the quadrupole moments for several low-lying states in ^{74}Kr and ^{76}Kr; their signs give firm evidence for the prolate character of the ground-state band coexisting with an excited oblate band built on a low-lying 0_2^+ state [1]. The analysis of the electromagnetic matrix elements and the properties of the 0_2^+ shape isomers [2] suggest an inversion of the prolate and oblate configurations with an oblate ground-state shape for ^{72}Kr. The relatively small $B(E2; 0_1^+ \rightarrow 2_1^+)$ value measured via intermediate-energy Coulomb excitation in ^{72}Kr [3] seems to support this interpretation. While many theoretical models predict the coexistence of prolate and oblate shapes [4–7], the inversion of oblate and prolate configurations in the light Kr isotopes is so far only correctly described by the so-called excited VAMPIR variational approach [8] and the Hartree-Fock-Bogoliubov (HFB) based configuration-mixing method using the Gogny D1S interaction, as described in Ref. [9].

The shape coexistence scenario in the neutron-deficient Se isotopes is less clear. Several theoretical investigations predict oblate ground-state configurations also for the Se isotopes near $N = Z$ [4,10,11]. The isotones ^{72}Se and ^{74}Kr show a similar structure with an isomeric excited 0_2^+ state just above the 2_1^+ state [12] and strongly decreasing $B(E2)$ strength for the transitions in the yrast cascade towards the ground state [13], which can be attributed to a strong mixing between prolate and oblate configurations at low spin. In neighboring ^{70}Se, on the other hand, a strong increase of the $B(E2)$ values was observed towards the ground state [13]. This behavior is very unusual, and the large $B(E2; 2_1^+ \rightarrow 0_1^+)$ value for ^{70}Se results in an unexplained discontinuity in the evolution of collectivity in the chain of Se isotopes. The best candidate for shape coexistence appears to be ^{68}Se, where two distinct rotational bands have been observed. The ground-state band has a lower moment of inertia and was interpreted as an oblate rotational band, while the excited band was found consistent with prolate shape [14]. The moments of inertia of the rotational structures observed in ^{68}Se and ^{70}Se show striking similarities [15], even though the presumed oblate rotation is not prevailing in ^{70}Se. Consequently, ^{70}Se was thought to show a rapid transition from oblate shape near the ground state to prolate shape at higher spins. A recent low-energy Coulomb excitation experiment with a ^{70}Se beam from REX-ISOLDE, however, found a negative diagonal $E2$ matrix element for the 2_1^+ state, indicating prolate shape for this state [16]. This result cast doubt on the existence of low-lying oblate states in ^{70}Se. As only the integral cross section was measured in the Coulomb excitation experiment, the result for the diagonal matrix element relies on the independently measured lifetime of the 2_1^+ state. This lifetime is hence a crucial parameter for the understanding of the shape coexistence in the light Se nuclei. In this Letter we report on a new lifetime measure-

ment with improved precision, and we interpret the results in the light of new configuration-mixing calculations beyond the mean-field approach.

Lifetimes of low-lying states in ^{70}Se and ^{72}Se were measured at the Laboratori Nazionali di Legnaro using the recoil-distance Doppler shift method [17]. The states were populated in the reactions ^{40}Ca(^{36}Ar, $\alpha 2p$)^{70}Se and ^{40}Ca(^{36}Ar, $4p$)^{72}Se at a beam energy of 136 MeV. Gamma rays were detected with the GASP detector array [18] comprising 38 escape-suppressed Ge detectors arranged in seven rings with respect to the beam axis. The isotopically enriched ^{40}Ca target had a thickness of 0.5 mg/cm^2 and was evaporated onto a 2.0 mg/cm^2 gold foil which was facing the beam. The recoils had an average velocity of 10.73(3) μm/ps and were stopped in a gold stopper foil of 10 mg/cm^2 thickness. The Cologne plunger device [19] was used to control the distance between the target and the stopper foils. Data were collected for 12 distances between 8 and 400 μm for an average of 10 h per distance. Events with at least two prompt γ rays detected in coincidence were recorded and sorted offline into $\gamma - \gamma$ matrices for further analysis.

To illustrate the quality of the data, spectra of the $2_1^+ \rightarrow 0_1^+$ transition in ^{70}Se and the $4_1^+ \rightarrow 2_1^+$ transition in ^{72}Se are shown in Fig. 1 for different distances between target and stopper foil. Similar spectra were obtained for all detector rings and plunger distances and for other transitions in both ^{70}Se and ^{72}Se. In all cases a coincidence gate was placed on the shifted component of the transition directly feeding the state of interest, so that effects of unknown side feeding were eliminated. The lifetimes of the states were extracted from the intensities of the stopped and Doppler-shifted components as a function of the plunger distance using the differential decay-curve method [17] following the procedure described in Ref. [20]. Since the lifetimes are relatively short, the contribution from γ rays emitted during deceleration in the stopper foil had to be considered. An average stopping time of 1.45(18) ps was found in a Monte Carlo simulation of the stopping process, which was also used to produce a set of line shape profiles for various lifetimes of the respective states [21]. The effect of the finite stopping time was included in the analysis by correcting for the fraction of γ rays emitted during deceleration. The results are shown in Table I.

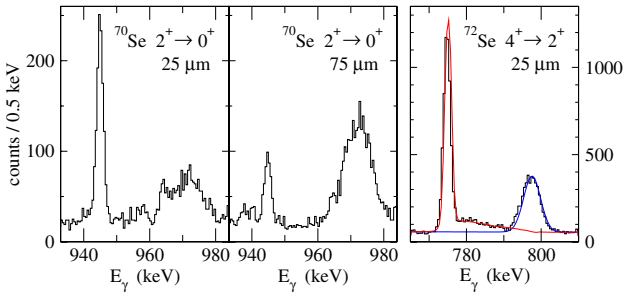

FIG. 1 (color online). Spectra showing the stopped and Doppler-shifted components observed in the forward detectors at 36° for the transitions and distances indicated. The simulated line shape of the stopped component (for a lifetime of 3.3 ps) and the Gaussian fit of the shifted component are shown for the transition in ^{72}Se.

While the new lifetimes for ^{72}Se are in reasonable agreement with the results of Heese *et al.* [13], the values for the 2_1^+ and 6_1^+ states in ^{70}Se deviate considerably. The most likely reason for this disagreement are effects from unknown side feeding in a singles measurement. It is interesting to note that significant deviations from older singles measurements were also observed in neighboring Kr isotopes [20], so that one might speculate about unusual feeding patterns in this mass region, which may not be correctly described by the feeding models employed in the older singles measurements. In the case of ^{70}Se, a delayed feeding component from the 13^- isomer with 2.3 ns lifetime [10] could have influenced the results of the previous measurement.

The experimental results in Table I are compared to HFB-based configuration-mixing calculations using the Gogny D1S interaction. The calculations contain no free parameters other than the globally derived parameters of the D1S nucleon-nucleon interaction [22,23]. The configuration mixing of the constrained HFB wave functions is calculated using the generator coordinate method with Gaussian overlap approximation. The five-dimensional generator coordinate comprises the collective quadrupole coordinates q_0 and q_2, which can be expressed in terms of the axial and triaxial deformation parameters β and γ, and the three Euler angles. It has been shown recently that the inclusion of the triaxial degree of freedom is crucial for the correct description of shape coexistence in the light Kr isotopes [1,24]. The procedure to calculate the energy spectra, reduced transition probabilities, and spectroscopic quadrupole moments is described in detail in Ref. [9].

TABLE I. Comparison of the new lifetimes with literature values. The resulting $B(E2)$ values and the energies of the states are compared to the theoretical calculations. The theoretical spectroscopic quadrupole moments are also given.

I^π	τ (ps)		E_{ex} (keV)		$B(E2;\downarrow)$ (e^2 fm^4)		Q_S
	New	[13]	Exp.	Theo.	Exp.	Theo.	(e fm^2)
^{70}Se							
2_1^+	3.2(2)	1.5(3)	945	818	342(19)	549	+16
4_1^+	1.4(1)	1.4(3)	2038	1800	370(24)	955	+12
6_1^+	1.9(3)	3.9(9)	3002	2703	530(96)	1404	−35
^{72}Se							
2_1^+	4.2(3)	4.3(5)	862	742	405(25)	678	+6
4_1^+	3.3(2)	2.7(4)	1637	1660	882(50)	1277	−33
6_1^+	1.7(1)	2.3(2)	2467	2266	1220(76)	2123	−77

The $B(E2)$ transition strength in ^{72}Se strongly decreases from the 6_1^+ to the ground state. The same behavior has been observed in the light Kr isotopes, where it is understood by an increased mixing of oblate and prolate configurations for the low-spin states [20]. The overall collectivity is higher in the Kr isotopes, which can be attributed to the deformation-driving effect of the $g_{9/2}$ proton orbital. The collectivity in ^{70}Se is much smaller than in ^{72}Se (due to less occupation of the $g_{9/2}$ neutron orbital), but a similar trend is observed: the $6_1^+ \rightarrow 4_1^+$ transition is more collective than the transitions below, which are similar in strength. The configuration-mixing calculations reproduce the energies of the states very well; the theoretical $B(E2)$ values, however, are systematically too large. On the other hand, the systematic trend, i.e., the lower collectivity of ^{70}Se, and the reduction of the $B(E2)$ values towards the ground state is qualitatively reproduced by the calculations.

With the new values from the present measurement, the systematics of the $B(E2)$ values in the chain of light Se isotopes shows a smooth decreasing trend from the most collective isotopes ^{76}Se and ^{74}Se at midshell to a small value for ^{68}Se [25], resolving the unexplained staggering caused by the very large $B(E2)$ value previously assigned to ^{70}Se.

The revised lifetime of the 2_1^+ state in ^{70}Se has important consequences for the interpretation of the results obtained in the recent Coulomb excitation experiment [16]. This is illustrated in Fig. 2, which shows the $B(E2; 2_1^+ \rightarrow 0_1^+)$ value as a function of the spectroscopic quadrupole moment Q_s. The full sloping lines represent the 1σ limits obtained from the measured Coulomb excitation cross section, which is sensitive to the quadrupole moment via the reorientation effect [26]. The dashed horizontal lines mark the 1σ limit of the $B(E2)$ value based on the old lifetime measurement by Heese *et al.* [13]. Only negative values of Q_s are consistent with both the old lifetime and the Coulomb excitation measurements, and it was concluded that the shape associated with the 2_1^+ state in ^{70}Se is prolate [16]. The present lifetime measurement requires a revision of this conclusion. The 1σ limits for the $B(E2)$ value from the new measurement are shown by the full horizontal lines. The intersection of the areas of possible values clearly favors a positive value of the spectroscopic quadrupole moment, i.e., oblate shape. Even though the precision of the lifetime measurement is significantly improved, it does not yet permit a precise determination of the quadrupole moment due to the large uncertainty of the Coulomb excitation cross section and its relatively weak dependence on the quadrupole moment. A more stringent constraint would require a more precise Coulomb excitation experiment. While the theoretical $B(E2)$ value is too large, the calculation also favors a moderately oblate shape for the state, as indicated by the asterisk in Fig. 2.

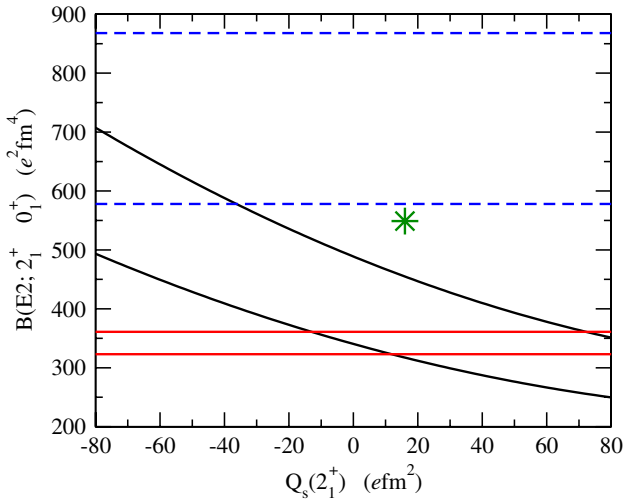

FIG. 2 (color online). $B(E2)$ value as a function of the spectroscopic quadrupole moment Q_s for the 2_1^+ state in ^{70}Se. The sloping lines indicate the 1σ range of values compatible with the Coulomb excitation measurement [16]. The horizontal solid (red) and dashed (blue) lines represent the 1σ ranges from the present and the earlier [13] lifetime measurements, respectively. The asterisk indicates the theoretical value.

The spectroscopic quadrupole moments for the low-lying states in ^{70}Se and ^{72}Se obtained in the calculations are given in Table I, and they are plotted in Fig. 3 as a function of spin. In addition, calculations were also performed for ^{68}Se, and the resulting quadrupole moments are included in Fig. 3. The agreement between the calculated and experimental excitation energies of the states in ^{68}Se is equally satisfying as for ^{70}Se and ^{72}Se. The 2_1^+ states of all three Se isotopes can be associated with oblate shapes of moderate deformation. The ground-state band in ^{72}Se evolves quickly into a highly collective prolate rotational

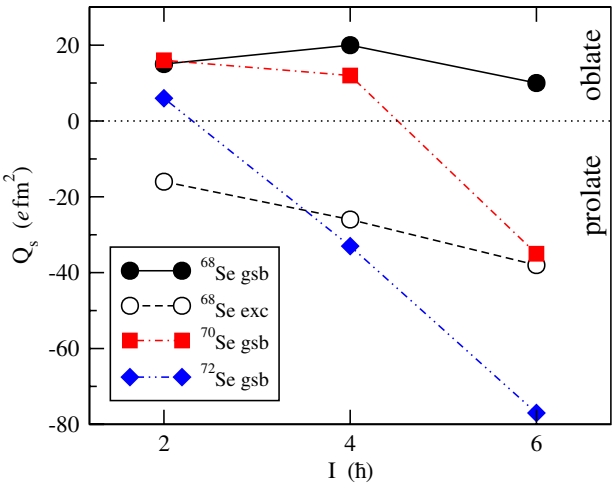

FIG. 3 (color online). Spectroscopic quadrupole moments obtained from the configuration-mixing calculations as a function of spin for the low-lying states in ^{68}Se, ^{70}Se, and ^{72}Se.

band. This is consistent with the rapid increase of the $B(E2)$ with spin, found both experimentally and theoretically. The ground-state band in ^{70}Se, on the other hand, stays oblate up to the 4_1^+ state and turns prolate only with the 6_1^+ state. This is consistent with the relatively small experimental $B(E2; 4_1^+ \rightarrow 2_1^+)$ and $B(E2; 2_1^+ \rightarrow 0_1^+)$ values, and the lower overall collectivity found in ^{70}Se. Finally, in ^{68}Se the ground-state band stays oblate, as already concluded by Fischer *et al.* from its low moment of inertia [14]. The quadrupole moments of the states in the excited band in ^{68}Se are negative, confirming the previous interpretation of shape coexistence in this nucleus. It is interesting to note in this context that the calculations find the lowest excited 0_2^+ state at 2.5 MeV excitation energy, which would explain why it has escaped observation so far, despite considerable experimental effort [14,15,25]. It also shows that the picture of two rotational bands built on oblate and prolate 0^+ states is too simplistic to describe the shape coexistence scenario in this mass region. This has already been pointed out based on the experimental results in the light Kr isotopes, which show not only a complex mixing of prolate and oblate shapes, but also mixing between rotational and vibrational states [1]. It has also become evident that triaxial shapes play a crucial role in this mass region; a correct description of the shape coexistence is only achieved if the triaxial degree of freedom is included in the beyond-mean-field calculations [24].

From the totality of experimental and theoretical results found in the light Se and Kr nuclei, a consistent picture seems to emerge in which oblate shapes become more and more favored near the ground state as one approaches $N = Z$. In the chain of Se isotopes ^{68}Se remains the best example for coexistence between oblate and prolate configurations. The conclusions drawn from the Coulomb excitation of ^{70}Se, which contradicted this picture, have to be revised based on the new lifetime measurement. The shape coexistence in ^{70}Se and ^{72}Se is, however, more delicate than in ^{68}Se or in the Kr isotopes, as the coexisting shapes do not prevail in collective bands to higher spin. Further experimental evidence for the shape coexistence scenario could come from multistep Coulomb excitation experiments.

In summary, a new RDDS lifetime measurement in ^{70}Se and ^{72}Se revealed considerable discrepancies with the literature values, requiring a revision of the conclusions drawn from the recent Coulomb excitation experiment on the shape of ^{70}Se. HFB-based configuration-mixing calculations have been performed through solving a five-dimensional, microscopic collective Hamiltonian. The calculated energies are in rather good agreement with the experimental results, while the $B(E2)$ values are systematically too large. The calculations support the interpretation of an oblate rotational ground-state band in ^{68}Se. Both theoretical and experimental results indicate that the energy of the oblate configuration increases with neutron number, so that prolate shapes are prevailing more and more in the heavier isotopes.

This work was partly supported by the European Community FP6—Structuring the ERA—Integrated Infrastructure Initiative—Contract EURONS No. RII3-CT-2004-506065.

*Permanent address: Inter University Accelerator Centre, New Delhi 110067, India.
†On leave from IFIN-HH Bucharest, R-077125, Romania.

[1] E. Clément *et al.*, Phys. Rev. C **75**, 054313 (2007).
[2] E. Bouchez *et al.*, Phys. Rev. Lett. **90**, 082502 (2003).
[3] A. Gade *et al.*, Phys. Rev. Lett. **95**, 022502 (2005).
[4] W. Nazarewicz *et al.*, Nucl. Phys. **A435**, 397 (1985).
[5] P. Bonche *et al.*, Nucl. Phys. **A443**, 39 (1985).
[6] M. Yamagami *et al.*, Nucl. Phys. **A693**, 579 (2001).
[7] M. Bender *et al.*, Phys. Rev. C **74**, 024312 (2006).
[8] A. Petrovici *et al.*, Nucl. Phys. **A665**, 333 (2000).
[9] J. Libert *et al.*, Phys. Rev. C **60**, 054301 (1999).
[10] T. Mylaeus *et al.*, J. Phys. G **15**, L135 (1989).
[11] A. Petrovici *et al.*, Nucl. Phys. **A728**, 396 (2003).
[12] J. E. Draper *et al.*, Phys. Rev. C **9**, 948 (1974).
[13] J. Heese *et al.*, Z. Phys. A **325**, 45 (1986).
[14] S. M. Fischer *et al.*, Phys. Rev. Lett. **84**, 4064 (2000).
[15] S. M. Fischer *et al.*, Phys. Rev. C **67**, 064318 (2003).
[16] A. M. Hurst *et al.*, Phys. Rev. Lett. **98**, 072501 (2007).
[17] A. Dewald *et al.*, Z. Phys. A **334**, 163 (1989).
[18] D. Bazzacco, in *Proceedings of the International Conference on Nuclear Structure at High Angular Momentum, Ottawa* (AECL Report No. 10613, 1992), Vol. 2, p. 376.
[19] A. Dewald, in *Ancillary Detectors and Devices for Euroball*, edited by H. Grawe (GSI and the Euroball Ancillary Group, Darmstadt, 1998), p. 70.
[20] A. Görgen *et al.*, Eur. Phys. J. A **26**, 153 (2005).
[21] P. Petkov *et al.*, Nucl. Instrum. Methods Phys. Res., Sect. A **431**, 208 (1999).
[22] J. Dechargé and D. Gogny, Phys. Rev. C **21**, 1568 (1980).
[23] J.-F. Berger *et al.*, Comput. Phys. Commun. **63**, 365 (1991).
[24] M. Girod *et al.* (to be published).
[25] E. Clément *et al.*, Nucl. Instrum. Methods Phys. Res., Sect. A doi:10.1016/j.nima.2008.01.059 (2008).
[26] K. Alder and A. Winther, *Electromagnetic Excitation: Theory of Coulomb Excitation with Heavy Ions* (North-Holland, Amsterdam, 1975).

7.2 Onset of collectivity in neutron-rich Fe isotopes: Toward a new island of inversion?

PHYSICAL REVIEW C **81**, 061301(R) (2010)

Onset of collectivity in neutron-rich Fe isotopes: Toward a new island of inversion?

J. Ljungvall,[1,2,3] A. Görgen,[1] A. Obertelli,[1] W. Korten,[1] E. Clément,[2] G. de France,[2] A. Bürger,[4] J.-P. Delaroche,[5] A. Dewald,[6] A. Gadea,[7] L. Gaudefroy,[5] M. Girod,[5] M. Hackstein,[6] J. Libert,[8] D. Mengoni,[9] F. Nowacki,[10] T. Pissulla,[6] A. Poves,[11] F. Recchia,[12] M. Rejmund,[2] W. Rother,[6] E. Sahin,[12] C. Schmitt,[2] A. Shrivastava,[2] K. Sieja,[10] J. J. Valiente-Dobón,[12] K. O. Zell,[6] and M. Zielińska[13]

[1]*CEA Saclay, IRFU, Service de Physique Nucléaire, F-91191 Gif-sur-Yvette, France*
[2]*GANIL, CEA/DSM-CNRS/IN2P3, Bd Henri Becquerel, BP 55027, F-14076 Caen, France*
[3]*CSNSM, CNRS/IN2P3, F-91405 Orsay, France*
[4]*Department of Physics, University of Oslo, PO Box 1048 Blindern, N-0316 Oslo, Norway*
[5]*CEA, DAM, DIF, F-91297 Arpajon, France*
[6]*Institut für Kernphysik, Universität zu Köln, D-50937 Köln, Germany*
[7]*Instituto de Fisica Corpuscular, CSIC-Universidad de Valencia, E-46071 Valencia, Spain*
[8]*Institut de Physique Nucléaire, CNRS/IN2P3-Université Paris-Sud, F-91406 Orsay, France*
[9]*Dipartimento di Fisica dell'Università and INFN Sezione di Padova, I-35131 Padova, Italy*
[10]*IPHC, CNRS/IN2P3 and Université Louis Pasteur, F-67037 Strasbourg, France*
[11]*Departamento de Física Teórica, IFT-AM/CSIC, Universidad Autónoma, E-28049 Madrid, Spain*
[12]*INFN, Laboratori Nazionali di Legnaro, I-35020 Legnaro, Italy*
[13]*Heavy Ion Laboratory, Warsaw University, Warsaw, PL-02097, Poland*

(Received 8 March 2010; published 15 June 2010)

The lifetimes of the first excited 2^+ states in ^{62}Fe and ^{64}Fe have been measured for the first time using the recoil-distance Doppler shift method after multinucleon transfer reactions in inverse kinematics. A sudden increase of collectivity from ^{62}Fe to ^{64}Fe is observed. The experimental results are compared with new large-scale shell-model calculations and Hartree-Fock-Bogolyubov–based configuration-mixing calculations using the Gogny D1S interaction. The results give a deeper understanding of the mechanism leading to an onset of collectivity near ^{68}Ni, which is compared with the situation in the so-called *island of inversion* around ^{32}Mg.

DOI: 10.1103/PhysRevC.81.061301 PACS number(s): 21.10.Re, 21.10.Tg, 27.50.+e

It is a common feature of systems of interacting fermions to form a shell structure. In atomic nuclei the spin-orbit interaction lowers the energy of the orbitals with the highest angular momentum into the next lower oscillator shell with opposite parity, leading to the well-known sequence of magic numbers. While the shell structure and the resulting energy gaps between the orbitals explain many general properties of nuclei across the nuclear chart, it has become evident that the shell structure and magic numbers change for nuclei with large neutron excess. As protons and neutrons in such exotic nuclei occupy different orbitals compared to their stable counterparts, the effective single-particle energies are shifted. As a consequence, some shell gaps vanish and new ones emerge [1]. It is important to find experimental signatures for the changing shell structure in order to advance the theoretical description of exotic nuclei, e.g., by finding better shell-model interactions or better energy functionals for mean-field based models.

The region of neutron-rich nuclei between $Z = 20$ (Ca) and $Z = 28$ (Ni) is of particular interest for understanding the evolution of the shell structure for nuclei with large neutron excess. Adding protons to the $1f_{7/2}$ orbital changes the relative energies of the neutron $2p_{3/2}$, $2p_{1/2}$, and $1f_{5/2}$ orbitals due to the strongly attractive proton-neutron spin-flip interaction [2]. With the gradual filling of the neutron fp harmonic oscillator shell, excitations into the $1g_{9/2}$ intruder orbital become increasingly important. Subtle effects related to the energy gap between the fp shell and the $1g_{9/2}$ orbital lead to a strong variation of collectivity for nuclei with $N \approx 40$. The nucleus $^{68}_{28}$Ni$_{40}$ has many features of a doubly magic nucleus with high excitation energy of the 2^+_1 state [3] and a small $B(E2; 0^+_1 \rightarrow 2^+_1)$ value [4]. Mass measurements, on the other hand, show that the $N = 40$ gap is weak for ^{68}Ni [5,6], and it has been argued that the small $B(E2)$ value does not necessarily indicate a shell gap at $N = 40$, but that it reflects the character of the 2^+_1 state as a predominant neutron excitation [7]. The fragility of the $N = 40$ subshell gap is further evidenced by the developing collectivity in the neutron-rich Zn and Ge isotopes, for which the energy of the 2^+_1 state drops sharply from $N = 38$ to $N = 42$ while the $B(E2)$ values increase [8,9]. The removal of protons from the $f_{7/2}$ orbital has a similar effect. The 2^+_1 energies in the Fe isotopes drop sharply above $N = 36$. The removal of only two protons changes the energy of the 2^+_1 state from 2033 keV in ^{68}Ni to 573 keV in ^{66}Fe [10]. The 2^+_1 energy drops even further to 517 keV in ^{68}Fe [11]. A similar behavior is observed in the Cr isotopes, where the 2^+_1 energies decrease gradually beyond the $N = 32$ subshell closure [12]. Inelastic proton-scattering experiments [13] and shell-model studies [14] corroborate the development of substantial collectivity and deformation in the neutron-rich Cr isotopes.

The role of the $\nu g_{9/2}$ orbital for the onset of collectivity in the region below ^{68}Ni has been discussed controversially in the past. The excitation spectrum of ^{64}Fe was established by Hoteling *et al.* and compared to shell-model calculations restricted to the fp model space [15]. Since the calculations

reproduced the energy of the 2^+ state reasonably well, it was concluded that the $\nu g_{9/2}$ orbital is not responsible for the low 2_1^+ energy and that it becomes important only at higher energies, where the calculations could not reproduce the observed states. Lunardi *et al.* have studied neutron-rich Fe isotopes of both even and odd mass [16]. Comparing the results to shell-model calculations in the fpg model space it was concluded that the occupation of the $g_{9/2}$ orbital influences the structure of the neutron-rich Fe isotopes considerably. The increasing role of the $g_{9/2}$ orbital is also consistent with the decreasing excitation energy of $9/2^+$ isomers in odd-mass Fe nuclei [17]. In studies of the odd-mass Mn isotopes, Valiente-Dobón *et al.* have argued that including the effects of the $g_{9/2}$ orbital improves the shell-model description of $^{61}Mn_{36}$ and $^{63}Mn_{38}$ [18], while Crawford *et al.* have interpreted the level structure in ^{61}Mn with a low-level density below 1 MeV without the need to invoke neutron excitations into the $g_{9/2}$ orbital [19]. In the Cr isotopes there is clear evidence for the influence of the $g_{9/2}$ orbital already for $^{59}Cr_{35}$ [20].

A deeper understanding of how collectivity develops in this region of the nuclear chart can come from experimental $B(E2)$ values. For the even-even nuclei $B(E2)$ values have been measured up to $^{58}Cr_{34}$ [21], $^{60}Fe_{34}$ [22], and $^{70}Ni_{40}$ [23]. Here we report on a lifetime measurement for the 2_1^+ states in ^{62}Fe and ^{64}Fe performed at the Grand Accélérateur National d'Ions Lourds (GANIL) using the recoil-distance Doppler shift (RDDS) method [24] in combination with multinucleon transfer reactions in inverse kinematics. The technique is similar to the one used in a recent lifetime measurement in ^{50}Ca and ^{51}Sc in direct kinematics at Legnaro [25]. Excited states in a wide range of neutron-rich nuclei were populated in multinucleon transfer reactions between a ^{238}U beam at 6.5A MeV and a ^{64}Ni target of 1.5 mg/cm^2 thickness. The targetlike reaction products were detected and identified event by event in the large-acceptance spectrometer VAMOS [26]. The optical axis of the spectrometer was positioned at 45° with respect to the beam axis, close to the grazing angle of the reaction. The focal plane detection system of the spectrometer allows the full reconstruction of the trajectories through the spectrometer and an unambiguous identification of the reaction products in mass, charge, and atomic number (see Fig. 1). The magnetic rigidity of the spectrometer was optimized for the transmission of ^{64}Fe.

The target was surrounded by nine large, segmented germanium clover detectors of the Exogam array [27], one at 180°, three at 135°, and five at 90° relative to the spectrometer axis. The typical average recoil velocity of the targetlike reaction products exiting the target foil was 37 μm/ps. In order to apply the RDDS technique the velocity of the recoils was slowed to approximately 32 μm/ps in a 4.7-mg/cm^2-thick magnesium foil placed at micrometer distances behind the target. The different Doppler shifts of γ rays emitted before and after the degrader foil were measured in the germanium detectors under backward angles. The distance between target and degrader was adjusted and controlled by a compact *plunger* device [28]. Data was collected for six distances between 40 and 750 μm. An additional measurement was performed without degrader to determine the exact recoil velocities after the target.

The spectra of Fig. 2 show γ rays recorded in coincidence with ions identified as ^{62}Fe and ^{64}Fe for selected target-

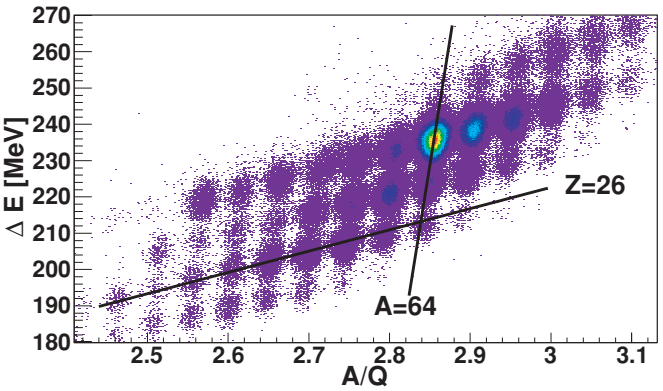

FIG. 1. (Color online) Typical identification plot showing the energy loss of the ions in the ionization chamber of VAMOS as a function of the mass-over-charge ratio, which is determined from the time of flight through the spectrometer and the magnetic rigidity. The lines indicate the loci of ions with $A = 64$ and $Z = 26$, respectively. The most intense peak corresponds to elastically scattered ^{64}Ni target nuclei. The data is shown for only one of 21 silicon detectors mounted in VAMOS and for one single charge state ($Q = 23$). The identification of the ions was performed in the same way for all detectors and all charge states reaching the focal plane.

degrader distances. A Doppler correction was performed using the recoil velocity measured in VAMOS after the degrader foil and the relative angle between the γ ray and the recoil vector. Two peaks are observed for the $2_1^+ \rightarrow 0_1^+$ transitions in both ^{62}Fe and ^{64}Fe, corresponding to the different recoil velocities before and after the degrader foil, respectively. The peaks are well separated for relative angles greater than 135°. Spectra were produced and analyzed separately for two angular ranges between 135° and 150° and between 160° and 180°, respectively. Decay curves $I_d/(I_d + I_f)$ were constructed from the intensities of the degraded (I_d) and fully Doppler shifted (I_f) components of the transitions as a function of target-degrader distance. The normalization factors $(I_d + I_f)$ were found to be consistent with the number of ions identified in VAMOS for each distance. Lifetimes of the 2_1^+ states in ^{60}Fe, ^{62}Fe, and ^{64}Fe were extracted separately for the two angular ranges from the decay curves of the 2_1^+ and 4_1^+ states using the differential decay curve (DDC) method [24] and then combined into a weighted average. In the DDC method the lifetime of a state is determined for each target-degrader distance from the slope of

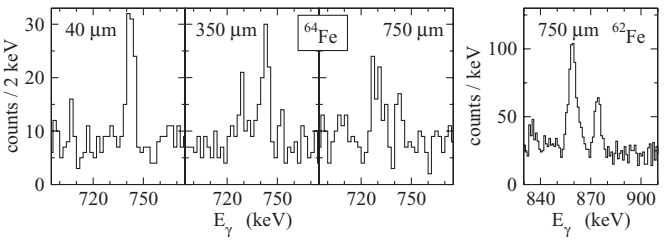

FIG. 2. Spectra showing the fully Doppler shifted and degraded components of the $2_1^+ \rightarrow 0_1^+$ transitions for three target-degrader distances in ^{64}Fe and for one distance in ^{62}Fe. The γ rays were observed at angles ranging from 160° to 180° with respect to the recoil direction.

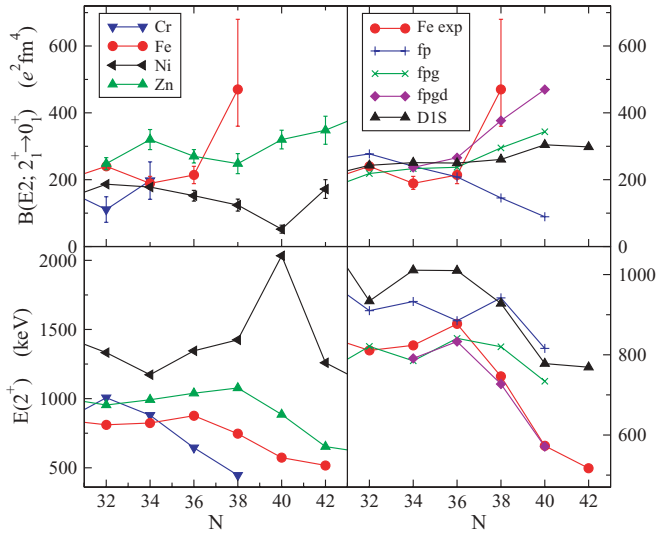

FIG. 3. (Color online) Systematic of $B(E2; 2_1^+ \rightarrow 0_1^+)$ and $E(2_1^+)$ values for even-even nuclei around ^{68}Ni. The data are taken from the compilation of Raman *et al.* [29] complemented by newer results for Cr [12,21], Fe [11], Ni [23], and Zn [8] isotopes. The panels on the right compare the experimental results for the chain of Fe isotopes with theoretical calculations (see text).

the decay curves, i.e., from the intensity curves as a function of distance. Distances were converted into flight times by using the average velocities measured separately for the different nuclides without degrader foil. In this way the lifetime of the 2_1^+ state in ^{60}Fe was determined to be 11.4(12) ps, which is in good agreement with the literature value of 11.6(22) ps [22]. Lifetimes for the 2_1^+ states in ^{62}Fe and ^{64}Fe were determined for the first time and found to be similar with 7.4(9) and 7.4(26) ps, respectively. The observed feeding times from the 4^+ states were found to be slightly different in ^{62}Fe and ^{64}Fe. The decay curves are consistent with the assumption of equal feeding times from the observed $4^+ \rightarrow 2^+$ and other unobserved transitions. Systematic deviations of the lifetimes derived at individual distances would appear if the feeding times for observed and unobserved transitions were different. The measured lifetimes yield $B(E2; 2_1^+ \rightarrow 0_1^+)$ values of 214(26) and 470^{+210}_{-110} e^2 fm^4 for ^{62}Fe and ^{64}Fe, respectively.

The $B(E2; 2_1^+ \rightarrow 0_1^+)$ values and excitation energies of the 2_1^+ states in this mass region are shown as a function of neutron number in the left part of Fig. 3. The large 2_1^+ energy and small $B(E2)$ value for ^{68}Ni could be interpreted as a sign for a subshell closure at $N = 40$. However, the chains of Zn and Fe isotopes above and below the proton shell closure, respectively, show a different behavior compared to the Ni isotopes. The drop in excitation energy of the 2_1^+ states, which is observed for all isotopic chains except Ni, illustrates that the nuclei become more collective and deformed with increasing neutron number. The $B(E2)$ values show that collectivity develops more gradually in the Zn compared to the Fe isotopes, where the new data indicate a steep increase from ^{62}Fe to ^{64}Fe.

To understand the rapid onset of collectivity in ^{64}Fe we have performed new shell-model calculations beyond the scope of previous calculations in this mass region [30]. A large valence space was used comprising the fp shell for protons and the $fpgd$ shell for neutrons outside a ^{48}Ca core. The effective interaction was based on a realistic CD-Bonn potential adapted to the model space by many-body perturbation techniques [31] and modified in its monopole part. The interaction reproduces the global evolution of single-particle energies along the nickel and $N = 40$ isotopic and isotonic chains, respectively. Transition probabilities were obtained using a standard polarization effective charge of $0.5\,e$. The shell-model diagonalizations accommodate for up to 14 particle-hole excitations across the $Z = 28$ and $N = 40$ gaps in the case of ^{64}Fe. The largest dimensionality tackled in the study was 7×10^9 for ^{64}Fe. More details of the shell-model calculations and the new effective interaction will be discussed in a forthcoming article [32].

To illustrate the importance of including the $\nu g_{9/2}$ and $d_{5/2}$ orbitals, calculations restricted to the neutron fpg and fp valence spaces are also shown in Fig. 3. The comparison suggests that the fpg valence space is sufficient to describe the 2_1^+ states in the Fe isotopes up to $N = 36$. The large $B(E2; 2_1^+ \rightarrow 0_1^+)$ value measured for ^{64}Fe clearly demonstrates the influence of neutron excitations across the gap at $N = 40$. In fact, the $B(E2)$ value can only be explained if the $d_{5/2}$ orbital is also included in the model space. The effect becomes even more evident in ^{66}Fe: Only the calculations in the full $fpgd$ model space reproduce the low excitation energies of the 2_1^+ state. It is well understood that the valence space should contain quasi-SU(3) partners, in this case the $g_{9/2}$ and $d_{5/2}$ orbitals, to allow the development of quadrupole collectivity [33].

For the ground state of ^{64}Fe the $fpgd$ shell-model calculations find average occupancies for the $\nu g_{9/2}$ and $d_{5/2}$ orbitals of 1.76 and 0.21, respectively, and this state is characterized by an intruder configuration with a strong two-particle two-hole component. Such intruder configurations become completely dominant in ^{66}Fe$_{40}$ and also in ^{62}Cr$_{38}$. In the latter case the occupancies of the $g_{9/2}$ and $d_{5/2}$ orbitals increase to 2.2 and 0.72, respectively, which drives the nucleus to an intrinsically deformed prolate shape (with $\beta \approx 0.35$) and causes a more rotational yrast sequence consistent with experimental observations [13]. The transition from spherical ^{68}Ni to more proton deficient $N \approx 40$ isotones with deformed intruder configurations seems to have some similarity to the situation in the so-called *island of inversion* of Na and Mg isotopes with $N \approx 20$ (see, e.g., Ref. [1] for a review). In both cases the developing quadrupole collectivity can be related to the occupation of neutron intruder orbitals from the next oscillator shell, which are at the same time quasi-SU(3) partners: ($f_{7/2}$, $p_{3/2}$) for ^{32}Mg and ($g_{9/2}$, $d_{5/2}$) in the present case. Active quadrupole partners are also available for the protons: ($d_{5/2}$, $s_{1/2}$) for Mg and ($f_{7/2}$, $p_{3/2}$) for Fe and Cr. The shell-model calculations furthermore find a reduction in the harmonic oscillator gap at $N = 40$ from ^{68}Ni to ^{60}Ca. The sudden increase of collectivity from ^{62}Fe to ^{64}Fe can thus be understood in a similar way as the increase of collectivity from ^{30}Mg to ^{32}Mg.

It is clear, on the other hand, that there is no shell closure at $N = 40$ comparable to the one at $N = 20$. At this point the analogy between the island of inversion, which is situated at

the end of a long chain of spherical $N = 20$ isotones, and the $N = 40$ region breaks down. With the exception of ^{68}Ni with closed proton shell, all $N = 40$ isotones develop collectivity and deformation (see left-hand part of Fig. 3). In a recent study within a microscopic collective model, the low-lying states in the $N = 40$ isotones (except ^{68}Ni) were described as prolate deformed ground-state bands and quasi-γ bands with good overall agreement between the calculations and experimental data [34]. We have extended these studies along the chain of Fe isotopes. The 2_1^+ energies and $B(E2)$ values were obtained in Hartree-Fock-Bogolyubov–based configuration mixing calculations using the the Gogny D1S force [35,36] and the generator coordinate method with Gaussian overlap approximation, treating axial and triaxial quadrupole deformations [37]. The calculations use a triaxial harmonic oscillator basis including 11 major shells. The collective masses are calculated as described in Ref. [38]. Albeit the 2_1^+ energies are on average 30% too high, the systematic trend is reasonably well reproduced, considering that the model contains no free parameters (and no effective charges). The calculated $B(E2)$ values show only a small increase at $N = 40$, which can also be attributed to the occupancy of the $\nu g_{9/2}$ orbital. This occupancy is found to increase from approximately 0.6 in in the ground state of ^{60}Fe to 2.5 in ^{64}Fe [39]. The occupancy of the $d_{5/2}$ orbital in the ground state of ^{64}Fe is found to be 0.06, i.e., smaller than in the shell model. A more important difference, however, is the fact that the $N = 40$ gap remains more or less constant in the Gogny mean-field calculation, performed at deformation zero, with $\Delta E \approx 4$ MeV from $Z = 20$ to $Z = 40$ (see Fig. 1 in Ref. [34]), whereas in the shell model the gap is strongly reduced for $Z < 28$. Although it is not obvious that single-particle energies from shell model and spherical mean-field calculations can be directly compared, since the latter do not contain any correlations beyond the mean field, the different development of the $N = 40$ shell gap could explain the more gradual increase of $B(E2)$ values in the Gogny calculation. On the other hand, proton excitations and the size of the $Z = 28$ gap could also contribute to the difference in collectivity. More theoretical work is needed to understand the origin of the differences between the shell-model and mean-field predictions. While experimental data on ^{60}Ca remain out of reach with present-day techniques, the measurement of $B(E2)$ values in neutron-rich Cr isotopes will already shed more light on this question and allow making better predictions for a possible doubly magic nature of ^{60}Ca.

In summary, the lifetimes of the 2_1^+ states in ^{62}Fe and ^{64}Fe have been measured using the RDDS technique in combination with multinucleon transfer reactions in inverse kinematics. A steep increase of the $B(E2; 2_1^+ \rightarrow 0_1^+)$ value is observed from ^{62}Fe to ^{64}Fe. The comparison with both shell-model calculations and a microscopic collective model based on the Gogny force allows relating the increase in collectivity to the occupation of neutron intruder orbitals. The mechanism causing this onset of collectivity below ^{68}Ni is found to be similar to the one responsible for the island of inversion around ^{32}Mg. The two theoretical approaches predict a different structure of the more exotic nuclei with $N \approx 40$.

The authors thank the technical staff at GANIL for excellent support and A. Navin for fruitful discussions. This work was partly supported by DFG (Germany) under Contract No. DE1516/-1, MICINN (Spain) under project FPA2009-13377, and Comunidad de Madrid (Spain) under project HEPHACOS S2009/ESP-1473.

[1] O. Sorlin and M.-G. Porquet, Prog. Part. Nucl. Phys. **61**, 602 (2008).
[2] T. Otsuka, T. Suzuki, R. Fujimoto, H. Grawe, and Y. Akaishi, Phys. Rev. Lett. **95**, 232502 (2005).
[3] R. Broda *et al.*, Phys. Rev. Lett. **74**, 868 (1995).
[4] O. Sorlin *et al.*, Phys. Rev. Lett. **88**, 092501 (2002).
[5] C. Guénaut *et al.*, Phys. Rev. C **75**, 044303 (2007).
[6] S. Rahaman *et al.*, Eur. Phys. J. A **34**, 5 (2007).
[7] K. Langanke, J. Terasaki, F. Nowacki, D. J. Dean, and W. Nazarewicz, Phys. Rev. C **67**, 044314 (2003).
[8] J. Van de Walle *et al.*, Phys. Rev. Lett. **99**, 142501 (2007).
[9] E. Padilla Rodal *et al.*, Phys. Rev. Lett. **94**, 122501 (2005).
[10] M. Hannawald *et al.*, Phys. Rev. Lett. **82**, 1391 (1999).
[11] P. Adrich *et al.*, Phys. Rev. C **77**, 054306 (2008).
[12] O. Sorlin *et al.*, Eur. Phys. J. A **16**, 55 (2003).
[13] N. Aoi *et al.*, Phys. Rev. Lett. **102**, 012502 (2009).
[14] K. Kaneko, Y. Sun, M. Hasegawa, and T. Mizusaki, Phys. Rev. C **78**, 064312 (2008).
[15] N. Hoteling *et al.*, Phys. Rev. C **74**, 064313 (2006).
[16] S. Lunardi *et al.*, Phys. Rev. C **76**, 034303 (2007).
[17] M. Block *et al.*, Phys. Rev. Lett. **100**, 132501 (2008).
[18] J. J. Valiente-Dobón *et al.*, Phys. Rev. C **78**, 024302 (2008).
[19] H. L. Crawford *et al.*, Phys. Rev. C **79**, 054320 (2009).
[20] S. J. Freeman *et al.*, Phys. Rev. C **69**, 064301 (2004).
[21] A. Bürger *et al.*, Phys. Lett. B **622**, 29 (2005).
[22] E. K. Warburton, J. W. Olness, A. M. Nathan, J. J. Kolata, and J. B. McGrory, Phys. Rev. C **16**, 1027 (1977).
[23] O. Perru *et al.*, Phys. Rev. Lett. **96**, 232501 (2006).
[24] A. Dewald, S. Harissopulos, and P. von Brentano, Z. Phys. A **334**, 163 (1989).
[25] J. J. Valiente-Dobón *et al.*, Phys. Rev. Lett. **102**, 242502 (2009).
[26] S. Pullanhiotan *et al.*, Nucl. Instrum. Methods A **593**, 343 (2008).
[27] J. Simpson *et al.*, Acta Phys. Hung. N. S. **11**, 159 (2000).
[28] T. Pissulla, A. Dewald *et al.*, Nucl. Instrum. Methods A (to be published).
[29] S. Raman *et al.*, At. Data Nucl. Data Tables **78**, 1 (2001).
[30] E. Caurier *et al.*, Eur. Phys. J. A **15**, 145 (2002).
[31] M. Hjorth-Jensen, T. T. S. Kuo, and E. Osnes, Phys. Rep. **261**, 125 (1995).
[32] S. M. Lenzi *et al.* (to be published).
[33] A. P. Zuker, J. Retamosa, A. Poves, and E. Caurier, Phys. Rev. C **52**, R1741 (1995).
[34] L. Gaudefroy *et al.*, Phys. Rev. C **80**, 064313 (2009).
[35] J. Dechargé and D. Gogny, Phys. Rev. C **21**, 1568 (1980).
[36] J.-F. Berger, M. Girod, and D. Gogny, Comput. Phys. Commun. **63**, 365 (1991).
[37] J.-P. Delaroche *et al.*, Phys. Rev. C **81**, 014303 (2010).
[38] M. Zielińska *et al.*, Phys. Rev. C **80**, 014317 (2009).
[39] J. M. Daugas *et al.* (to be published).

7.3 The Orsay Universal Plunger System

Nuclear Instruments and Methods in Physics Research A 679 (2012) 61–66

Contents lists available at SciVerse ScienceDirect

Nuclear Instruments and Methods in Physics Research A

journal homepage: www.elsevier.com/locate/nima

The Orsay Universal Plunger System

J. Ljungvall [a,*], G. Georgiev [a], S. Cabaret [a], N. Karkour [a], D. Linget [a], G. Sedes [a], R. Chevrier [b], I. Matea [c], M. Niikura [c], M.-D. Salsac [d], B. Sulignano [d]

[a] CSNSM, Bâtiments 104 et 108, 91405 Orsay Cedex, France
[b] CEA, DAM, DIF, F-91297 Arpajon, France
[c] Institut de Physique Nucléaire, IN2P3-CNRS and Université Paris-Sud, F-91406 Orsay Cedex, France
[d] CEA Saclay, IRFU, SPHN, F-91191 Gif-sur-Yvette, France

ARTICLE INFO

Article history:
Received 8 February 2012
Received in revised form
26 March 2012
Accepted 27 March 2012
Available online 4 April 2012

Keywords:
In-beam γ−ray spectroscopy
Recoil-Distance Doppler Shift
Lifetimes

ABSTRACT

A new plunger device for Recoil-Distance Doppler Shift and Time-Differential Recoil-In-Vacuum measurements has been developed at the CSNSM in collaboration with the IPN Orsay. It is conceived to be easily adapted to different experimental setups and facilities, in particular to the future radioactive beam facility Spiral2. An electronic feedback system keeping the distance between target and stopper foils constant, imperative for precision measurements of short lifetimes, was also developed.

The plunger device was commissioned with an experiment performed at the IPN Orsay Tandem accelerator laboratory using the Orgam germanium detector array. Excited states in ^{76}Kr were populated using the reaction ^{45}Sc(^{35}Cl,2p2n)^{76}Kr. The lifetime τ of the 4_1^+ state was determined to 4.3(6) ps, in accordance with previous measurement, confirming the functionality of the new plunger device. The commissioning experiment showed in particular that the electronic feed back system works as foreseen.

1. Introduction

Detailed spectroscopic information is, together with the nuclear mass, the experimentally accessible observables used to understand the many-body nuclear problem. The energies of excited states, although fundamental, give an incomplete picture of the nuclear-state wave function and are therefore by themselves insufficient for detailed scrutinizing of nuclear structure models. An additional sensitive probe of the nuclear wave function is the electromagnetic transition strength $B(E/ML: J_i \rightarrow J_f)$. Here $J_{i(f)}$ is the spin of the initial (final) nuclear state, L is the multipolarity of the emitted γ ray, and E/M indicates an electric- or a magnetic transition. The $B(E/ML: J_i \rightarrow J_f)$ is accessible via several different methods based either on the observation of the excitation, e.g. Coulomb excitation [1], or the decay of an excited state via γ−ray emission, e.g. methods based on the observed Doppler shift of the energy of the emitted γ ray [1] or fast timing measurements [2]. The measurement of the lifetime of an excited state gives a completely model-independent result given that the transition de-exciting the state in question is not of mixed multipolarity.

In this paper a so-called "plunger device" [3] will be described. The "plunger" consists of a thin target foil for the production of recoiling exited nuclei and a "stopper" foil at a well defined distance from the target and is used with the Recoil Distance Doppler Shift (RDDS) method [4]. This method is based on the observation of the γ−rays emitted when the nuclear states de-excite. By stopping the recoiling nuclei in a "stopper" foil two distinctive velocity regimes are created, and hence the γ rays emitted before or in the stopper foil can be separated using the observed Doppler shift of the γ−ray energies. γ−Rays emitted before the stopper foil will be observed with a "shifted" energy due to the Doppler shift. If the nuclei have been stopped the γ rays will be observed without a Doppler shift of their energy, i.e. "unshifted". By comparing the relative intensities of the "shifted" and "unshifted" components of the γ−ray line, the lifetime τ can be extracted. Using the RDDS method together with a plunger device lifetimes of about one to a few hundreds of picoseconds can be measured with a precision comparable to that of the statistical uncertainty. Such experiments therefore deliver high quality data on electromagnetic transition strengths. The distance between the target and stopper foil used for RDDS experiments is approximately given by the product of the lifetime of the excited state and the recoil velocity of the nuclei. This corresponds in many cases to less than a few tens of micrometers. A major technical challenge for a plunger device is therefore to keep the

* Corresponding author.
E-mail address: joa.ljungvall@csnsm.in2p3.fr (J. Ljungvall).

0168-9002/$ - see front matter © 2012 Elsevier B.V. All rights reserved.
http://dx.doi.org/10.1016/j.nima.2012.03.041

target- and stopper-foil parallel and at a fixed distance while they are heated by the beam.

Because of the sensitivity of the $B(E/ML : J_i \rightarrow J_f)$ value to the wave function, and the model independent determination of electromagnetic transition strengths given by plunger measurements, this technique will play an important role in the physics campaigns at future radioactive beam facilities, such as Spiral2 at GANIL [5]. Traditionally used together with heavy-ion fusion evaporation reactions recent developments have shown that the RDDS technique is also suited to measure lifetimes of excited states populated in multi-nucleon transfer reactions [6,7], intermediate-energy Coulomb excitation studies [8], low-energy multistep Coulomb excitation studies [9], as well as together with induced fission reactions to measure lifetimes of excited states in fission fragments.

The design of the new plunger will be described in Section 2. This will be followed in Section 3 by the description of a successful commissioning experiment performed at the IPN Orsay tandem. Future plans will be discussed in Section 4, to finally conclude in Section 5.

2. Design

In designing a plunger device a set of characteristics/problems have to be considered such as

- the possibility to vary the distances between target and stopper foil from a few micrometers to some tens of millimeters with a sub-micrometer precision,
- transparency of the device to minimize the absorption of the γ rays emitted from the de-exciting nuclei,
- a mechanism to stretch target and stopper foils,
- and an active feedback to compensate for changes in the target–stopper foil distance induced by the target-beam interaction.

The solutions used to address these concerns will be discussed in the following paragraphs.

The heart of any plunger device is the motor that positions the stopper foil relative to the target foil. There is a need to combine high precision, i.e. the ability to position the stopper foil within some tens of nanometers, with mechanics that are rigid enough to allow for feedback movements. At the same time one has to minimize the material around the target to keep the plunger device transparent to γ rays. For traditional plunger devices, designed to be used with fusion evaporation experiments, this problem is usually solved by placing the mechanics far away from the target using a coaxial geometry (e.g. see the plunger device in Ref. [10]). Such a design has the disadvantage that the plunger often becomes part of the beam line and hence difficult to adapt to different experimental setups. A more severe problem with the coaxial geometry is that it is best suited for experiments were the reaction products leave the target with a relatively small angle relative to the beam axis. An alternative is to use a linear piezo motor assembly on which the mechanics for target and stopper foils are mounted. It can be made very compact and allows for large angles between incoming beam and outgoing reaction products. This is the choice made for the Orsay Plunger. The base of the plunger is the PI N-661 Miniature Linear Stage (see Fig. 1). It is a piezo-electric linear motor with a movement range of 20 mm. The size of this industrially available assembly is 70 mm × 50 mm × 20 mm. Its linear motor can generate a force of up to 10 N. The movement is performed by the upper half of the PI N-661, which can be positioned with a precision of 40 nm. The Orsay Plunger is literally built around the PI N-661 linear motor. Its core is shown in Fig. 2. By the means of pre-threaded

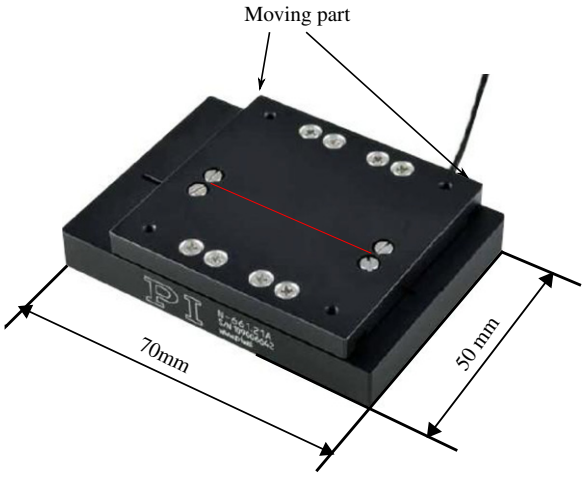

Fig. 1. The PI N-661 Miniature Linear Stage.

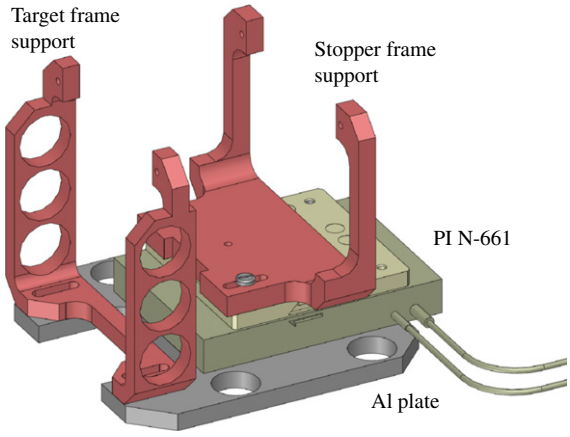

Fig. 2. Main components of the Orsay Plunger.

holes a stopper-foil support is mounted on the moving upper half of the piezo motor. The PI N-661 itself is mounted on an aluminum support plate, to which the target-holder support is also attached. This structure is supposed to remain the same independently of the type of experiment performed. Due to the relative thickness of the PI linear motor assembly the amount of material in the direction orthogonal to the beam and opposing the target- and stopper-foil holders is quite large, but this is of lesser importance since the observed Doppler shift of the energy of the emitted γ rays usually is too small for RDDS measurements at angles close to 90°.

The Orsay Plunger uses a target- and stopper-foil stretching system based on pulling the foils over metallic cones that are machined with high precision. This ensures that the foils can be considered as planar surfaces allowing a precise definition of the distance between them. In Fig. 3 the target stretcher assembly is shown. The target foil is glued onto the target frame, that in turn is positioned over the cone and attached with three screws. Stretching the foil is done by tightening the screws forcing the foil to slightly deform over the cone. The stretcher cone itself is attached with three screws to a ring, which is firmly attached to the plunger via the target-frame support. An identical assembly is used to mount the stopper foil. This allows the adjustment of the parallelism of the two foils by means of the three screws mentioned above attaching the stretcher cone to the rings used to fix the target- and stopper assemblies to the their respective

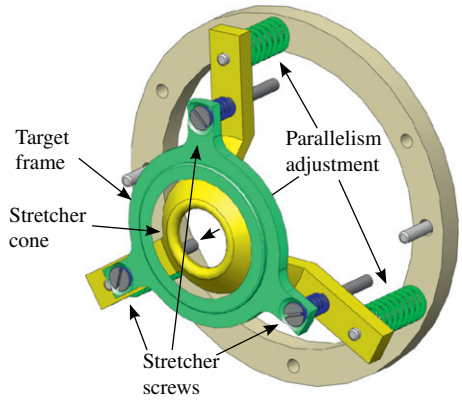

Fig. 3. Target frame and stretch cone shown without a target foil in place.

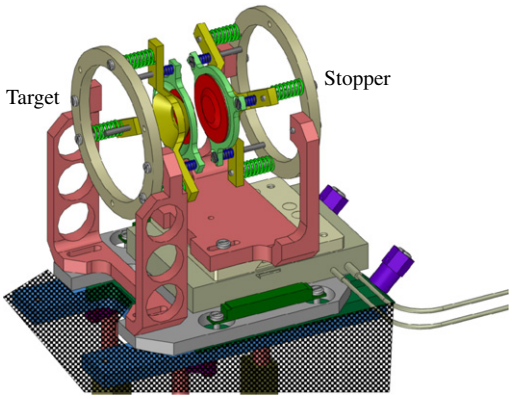

Fig. 4. Three dimensional view of the Orsay Plunger. The target and stopper foils are in place. The shaded part is a support structure specific for the commissioning experiment.

supports. The chosen target size of 10 mm and, with it, the size of the target frames and cones, can easily be changed if needed, e.g. for a multi-nucleon transfer reaction experiment or a reaction with a secondary beam. In Fig. 4 the complete assembly as used during the commissioning experiment is shown. The target and stopper foil sides are indicated in the figure. The shaded structure in the figure are specific for the use at the IPN Orsay Tandem.

When measuring short lifetimes the variations of the target–stopper distance, due to heating from the beam, might be significant compared to the distance and they have to be corrected for. An electronic feed-back system was developed for this purpose, correlating the distance between the foils with the capacitance measured between them: the two foils are used as a capacitor whose value changes as function of the distance between the two foils. A schematic of the electronics setup is shown in Fig. 5. The feed-back system consists of a high-precision pulser of type BNC Model PB-5, a spectroscopic amplifier Ortec 571, an impedance matcher circuit, a National Instruments BNC-2110 BNC adapter, and a National Instruments PCIE-6361 X Series DAQ—a PCI express card mounted in the control PC. The electronics chain was tested off-line for stability during a period of 64 h, showing a FWHM variation of 2.5‰, correlated with changes in the ambient temperature. The PI N-661 linear stage was controlled by the PI E-861 Controller, connected to the control PC via a USB interface. The electronics were controlled by an application developed under LabVIEW. The application provided the following functionality:

- sampling of the output of the Ortec 571 amplifier via the PCIE-6361 DAQ board,

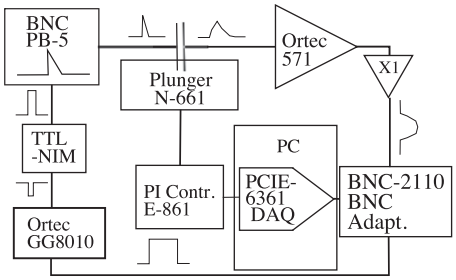

Fig. 5. Schematics of the electronics used to control the Orsay Plunger.

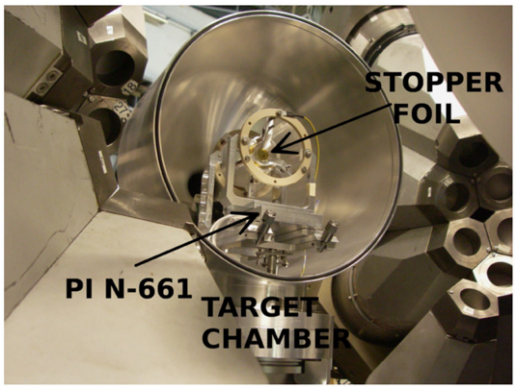

Fig. 6. A photo of the Orsay Plunger in the Orgam target chamber.

- online processing to extract the pulse-height at the output of the Ortec 571 amplifier,
- a closed loop feedback controlling the PI N-661 to keep the capacitance as stable as possible,
- slow control of the plunger system, i.e. adjustment of target–stopper foil distance, starting and stopping of the feedback, loading and saving configurations, and security functions.

3. Commissioning experiment

A commissioning experiment was performed at the IPN Orsay Tandem accelerator laboratory in order to verify that the Orsay Plunger device performs as foreseen. In particular the electronic feedback system, designed to keep the target–stopper foil distance constant, had to be proven reliable. The Orsay Plunger was mounted in the Orgam target chamber, surrounded by the 24 n-type HPGe detectors of the Orgam detector array. The Germanium detectors were equipped with BGO Compton suppression shields. A photo of the plunger in the chamber is shown in Fig. 6. The detectors were organized into three rings, according to their angle relative to the beam axis. Rings 1–3 were located at 46.5°, 133.5°, and 157.6°, respectively.

The main criteria to choose the reaction for the commissioning experiment were

- a high cross-section to allow for $\gamma\gamma$ coincidences,
- well known lifetimes of the lowest-laying yrast states to be able to cross-check the results,
- a high beam intensity from the IPN Orsay Tandem,
- and a target material suitable for a plunger experiment.

For the commissioning experiment the ^{45}Sc(^{35}Cl,2p2n)^{76}Kr reaction, with a beam energy of 126 MeV, was found suitable. Targets

of 1.1 mg/cm^2 ^{45}Sc, protected by thin layers of gold ($\ll 1$ mg/cm^2) evaporated on each side, were used during the experiment. A 5 mg/cm^2 thick gold foil was used as a stopper foil.

Data were collected for a total of five days with beam intensities between 10 and 40 pnA. Two different targets were used, one during the first two days, and a second target during the last three days. The first target was used for measuring distances longer than 50 μm. Before measuring shorter distances the target was changed as it was estimated that the second target was of higher quality. During the experiment it was (wrongly) estimated that the data from the first and second target could be use together by matching the normalized intensities for one overlapping distance. During the analysis, the data from the longer distances measured with the first target turned out to be incoherent, an effect most likely due to an insufficiently stretched target foil, which gave ill-defined target–stopper distances. Because of this only distances shorter than 50 μm were used in the lifetime analysis.

Problems with the spectroscopic amplifiers used during the experiment reduced the number of germanium detectors from 24 to 7, thus drastically reducing the statistics in $\gamma\gamma$ coincidence mode. The working detectors were partitioned as one in ring 1 and ring 3, respectively, and five in ring 2. Since the reaction had several open reaction channels of comparable strengths increasing the statistics by analyzing the data in singles mode was not possible due to too many overlapping $\gamma-$ray lines. A singles spectrum from ring 2 is shown in Fig. 7 where the γ rays from the transitions $2_1^+ \rightarrow 0_1^+$ (424 keV), $4_1^+ \rightarrow 2_1^+$ (611 keV), and $6_1^+ \rightarrow 4_1^+$ (824 keV) in ^{76}Kr are marked with arrows.

One of the main goals of the commissioning experiment was to verify the feed-back mechanism imperative for accurate measurements at short distances. All values read by the Orsay Plunger control computer were stored on disk to be used during the analysis of the experiment. A calibration was made by tracing the distance as a function of the pulse height at the output of the spectroscopic amplifier read by the DAQ in the control computer. This was done before the second target was exposed to beam, and redone after about 24 h of target irradiation with a beam intensity of 30 pnA. A calibration function was then fitted to the combined calibration data set. Shown in Fig. 8 are the calibration points together with the fitted function. The difference between electrical contact and

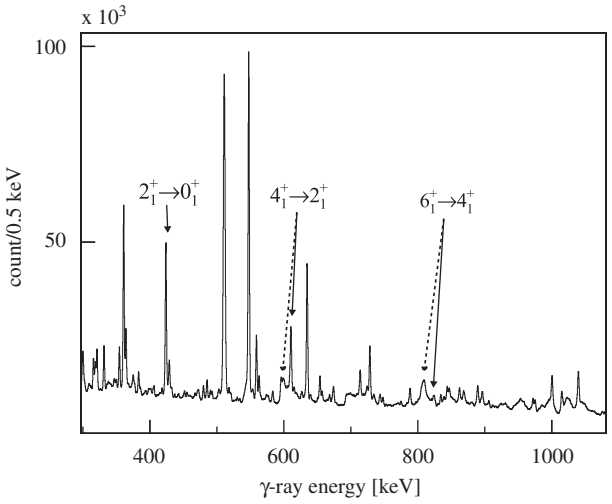

Fig. 7. Zoom on the region on interest for ^{76}Kr, taken with ring number 2 in Orgam in singles. The first three transitions in the ground-state band, 424 keV, 611 keV, and 824 keV, respectively, are marked with arrows. In-flight components are marked with thicker dashed arrows. The lifetime of the 2_1^+ state is too long to have an in-flight component.

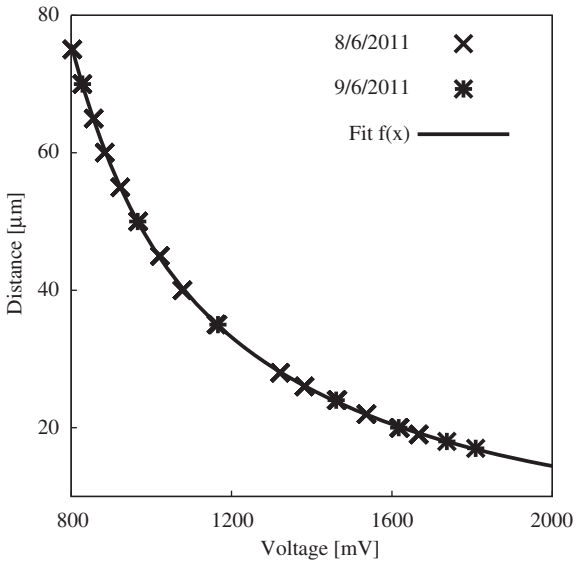

Fig. 8. Calibration curves for the capacitive measurement of the target–stopper distance for the plunger taken one day apart, showing the stability of the system. The distance scale on the *y*-axis has an arbitrary offset of about 5 μm. A fit to the measured points is also shown.

Table 1
Distances as determined using the function are shown in Fig. 8. The quoted uncertainties are the RMS's of the distance distributions.

Distance	Dist. (μm)
1	11.24(8)
2	15.67(2)
3	21.03(2)
4	25.40(2)
5	34.23(3)
6	44.59(4)

so-called optical contact, i.e. when no light could be observed between the two foils, was 9 μm. During the analysis of the experiment the calibration function was used to find the relative distances with a high precision. These distances are shown in Table 1. Given in the table are the mean distances together with the RMS of the distance distributions. For the shortest distance, some minor variation can be seen with a RMS of 0.1 μm, corresponding to about 1%. This is because the distance was at the limit considering the quality of the target and stopper foils, and, relative to the distance, a large tolerance for the feed-back system had to be used. It is, however, clear that the feed-back is capable of keeping the target–stopper foil distance constant.

Data from the experiment were sorted into four $\gamma\gamma$ matrices corresponding to the four possible permutations of coincidences given the angle of the different Ge detectors relative to the beam direction. $\gamma-$Ray spectra were produced by gating in the $\gamma\gamma$ matrices on the $\gamma-$ray peak corresponding to the emission in flight of the γ ray feeding the state of interest. Spectra in which the γ ray de-exciting the state of interest was observed at the same energy were summed, giving three spectra to analyse for each distance. In each spectrum the intensity of the unshifted and shifted peak of the transition of interest was determined. The intensities for each distance were normalized using the total number of $\gamma-$rays observed from the Coulomb excitation of the gold stopper. Lifetimes were then extracted using the methods

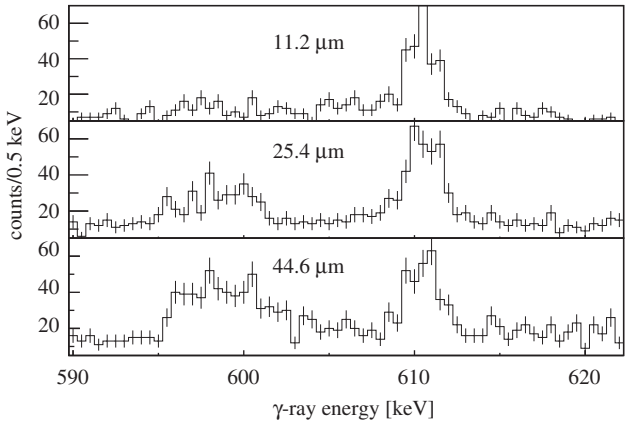

Fig. 9. γ-Ray spectra for the $4_1^+ \rightarrow 2_1^+$ transition in ring 2 gated on the shifted component of the $6_1^+ \rightarrow 4_1^+$ transition. The broad peaks to the left are the shifted peaks of the γ rays from the $4_1^+ \rightarrow 2_1^+$ transition, whereas the unshifted component is at the energy corresponding to that of the γ−ray transition (611 keV).

outlined in Ref. [3]. The expression

$$I(\gamma_1^{sh},\gamma_2^{us},x) = \tau v \frac{d}{dx} I(\gamma_1^{sh},\gamma_2^{sh},x) \quad (1)$$

is fitted to the experimental data consisting of the normalized γ−ray peak intensities $I(\cdots)$, using the χ^2 method with τ as a parameter together with four parameters describing a piecewise differential function for $I(\gamma_1^{sh},\gamma_2^{sh},x)$, in this case a quadratic spline. In the expression $I(\cdots)$ the first argument γ_1^{sh} refers to the gate used to extract the γ−ray intensity, i.e. the in-flight component of the $6_1^+ \rightarrow 4_1^+$, and the second argument refers to the transition de-exciting the state of interest. In this case the 4_1^+ state whose lifetime was measured. The superscript sh(us) on the second argument refers to the shifted(unshifted) component of the γ−ray intensity. The velocity v is determined from the observed Doppler shifts of the energies of the γ rays. In Fig. 9 example spectra used to fit the intensities are shown. All spectra were obtained by gating on the shifted component of the feeding $6_1^+ \rightarrow 4_1^+$ transition. By analyzing spectra gated on the in-flight component of the feeding transition systematical errors related to feeding times and the angular distributions of γ rays can be minimized [3]. Systematical errors arising from the so-called de-orientation effect can also be avoided [11]. The intensities of the shifted(in-flight) and unshifted(stopped) components were fitted by assuming fixed positions and widths for the γ−ray peaks, varying only the amplitude for each distance. The fits of Eq. (1) to the data are shown in Fig. 10 for the different rings in Orgam. The lifetime has been fitted for each ring separately, as well as using the data from all rings simultaneously giving a lifetime of 4.1(15) ps, 4.9(11) ps, 3.6(8) ps, and 4.3(6) ps, respectively. These values are consistent with the most recent and precise measurement of Görgen et al. [12], as well as other literature values as quoted in Table 2.

One should note that the large error in our measurement is not only due to low statistics, but also because the distances from which good data could be extracted were all quite short compared to the product of the lifetime of interest and the recoil velocity. Had the data taken with longer target–stopper distances been of the same quality as the data taken for the short distances the error would have been reduced.

4. Future development

The Orsay Plunger has been developed with future needs at GANIL and Spiral2 in mind. Apart from the classical use of RDDS

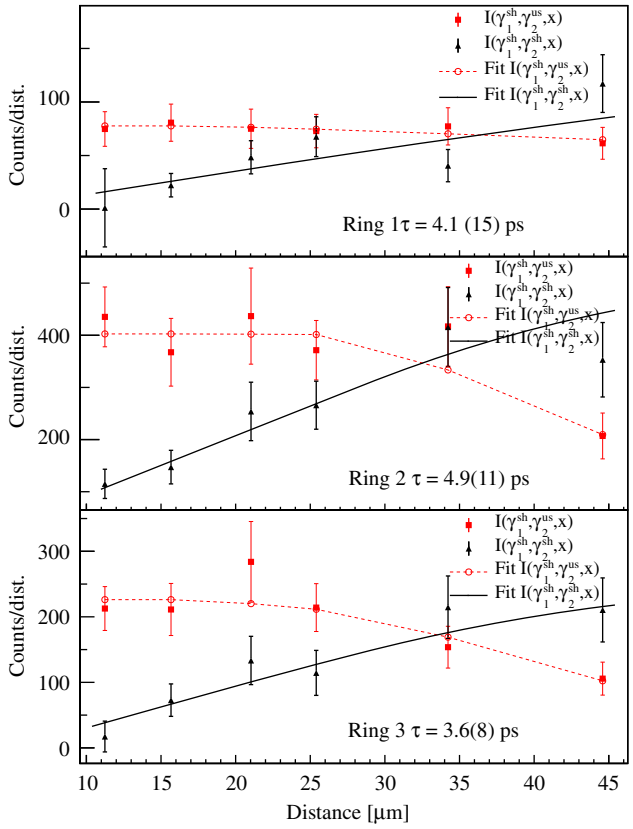

Fig. 10. Normalized intensity curves ($I(\gamma_1^{sh},\gamma_2^{us},x)$ and $I(\gamma_1^{sh},\gamma_2^{sh},x)$) for the $4_1^+ \rightarrow 2_1^+$ transition gated on the in-flight component of $6_1^+ \rightarrow 4_1^+$ for rings 1–3. The lifetime deduced from all data is $\tau = 4.3(6)$ ps.

Table 2
Comparison of literature values with the present work. Görgen et al. is the most recent value.

Ref.	τ (ps)
This work	4.3(6)
Görgen et al. [12]	3.67(9)
Wörrman et al. [13]	4.9(4)
Piercey et al. [14]	5(2)
Nolte et al. [15]	8.2(23)

together with fusion-evaporation reactions an extensive physics program using RDDS measurements together with high-intensity radioactive beams is also foreseen. Such experiments will often be performed using spectrometers such as VAMOS [16] and LISE [17] to identify the reaction products on an event-by-event basis. This will require the use of a degrader foil instead of a stopper foil and the modification of the target and stopper foil frames. As an example, a multi-nucleon transfer experiment using a light radioactive beam on a heavy neutron rich target will require that the beam hits the target at an angle of about 60°.

Another foreseen development is the use of the Orsay Plunger for high-precision gyromagnetic (g) factor measurements of excited states with lifetimes of the order of picoseconds. For states with such short lifetimes a very strong magnetic field is needed to achieve an observable modification of the angular distribution of the emitted γ rays within the lifetime of the excited state. One way to obtain such strong fields is to use the Transient Field technique. However, it has the shortcoming that the strength of the obtained magnetic field cannot be estimated using first principles and hence it relies on reference measurements to extract the g factor for the state of interest. Using a

plunger device together with the so-called "Time-Differential Recoil-In-Vacuum" (TDRIV) technique this problem can be overcome. This method uses the interaction of the nuclear magnetic moment with the magnetic field created by the electrons orbiting the recoiling ion as described by Goldring [18]. This interaction creates a time-dependent pattern in the angular distribution of the emitted γ-rays. The frequency of this pattern is directly proportional to the gyromagnetic factor of the nuclear state and to the magnetic field created at by the electrons orbiting the nucleus. For highly ionized light ions (e.g. with a single 1 s electron) this magnetic field can be calculated from first principles with high precision. A plunger device, by which one can obtain a precise time-control and measurements on a picosecond scale, is an essential tool in a similar type of measurements. TDRIV measurements on short-lived states in light nuclei have provided a number of precise g-factor measurements. A development if this technique, to be applied with radioactive beams, has been proposed by Stuchbery et al. [19]. The essential part of it is that the nuclei of interest are not stopped in the second plunger foil but are to fly through it into vacuum. It is estimated that the integral de-orientation of the nuclear spins, due to the RIV effects, would not impede the measurement. Provided that this technique works in the "differential-plunger" regime it would allow for model-independent high-precision measurements of g factors in light exotic nuclei.

5. Conclusions

A new plunger device has been developed in collaboration between CSNSM and IPN Orsay. Named The Orsay Universal Plunger System (Oups) it is intended for, but not limited to, use at radioactive and stable-beam facilities like GANIL and Spiral2. The flexible design allows simple adaptation to most facilities with a $\gamma-$ray spectrometer.

The device has been commissioned at the Tandem facility at IPN Orsay. Excited states in the nucleus ^{76}Kr were populated using the heavy-ion fusion evaporation reaction ^{45}Sc(^{35}Cl,2p2n)^{76}Kr. A lifetime of 4.3(6) ps for the 4_1^+ state in ^{76}Kr, compatible with recent lifetime measurements, could be extracted. The electronic feed back system designed to keep the distant constant between the target and stopper foils was proven to function to full satisfaction. It is therefore concluded that the Oups is ready for performing RDDS measurements.

Acknowledgment

The use of detectors from the Gammapool European Spectroscopy and France–UK (IN2P3/STFC) Loan-Pool Resources through the ORGAM (Orsay Gamma Array) project is gratefully acknowledged.

References

[1] A. Görgen, Journal of Physics G: Nuclear and Particle Physics 37 (2010) 103101.
[2] H. Mach, et al., Journal of Physics G: Nuclear and Particle Physics 31 (2005) S1421.
[3] A. Dewald, S. Harissopulos, P. von Brentano, Zeitschrift Physik A 334 (1989) 163.
[4] T.K. Alexander, K.W. Allen, Canadian Journal of Physics 43 (1965) 1563.
[5] M. Lewitowicz, Nuclear Physics A 805 (1–4) (2008) 519c.
[6] J.J. Valiente-Dobón, et al., Physical Review Letters 102 (2009) 242502.
[7] J. Ljungvall, et al., Physical Review C 81 (2010) 061301(R).
[8] A. Dewald, et al., Physical Review C 78 (2008) 051302(R).
[9] W. Rother, et al., Nuclear Instruments and Methods in Physics Research Section A 654 (2011) 196.
[10] A. Dewald, in: H. Grawe (Ed.), Ancillary Detectors and Devices for Euroball, GSI and the Euroball Ancillary Group, Darmstadt, 1998, p. 70.
[11] P. Petkov, A. Dewald, P. von Brentano, Nuclear Instruments and Methods in Physics Research Section A 457 (2001) 527.
[12] A. Görgen, et al., The European Physical Journal A 26 (2) (2005) 153–157.
[13] B. Wörmann, et al., Nuclear Physics A 431 (1984) 170.
[14] R.B. Piercey, et al., Physical Review C 25 (1982) 1941.
[15] E. Nolte, et al., Zeitschrift Physik A 268 (1974) 267.
[16] S. Pullanhiotan, et al., Nuclear Instruments and Methods in Physics Research Section A 593 (2008) 343.
[17] R. Anne, et al., Nuclear Instruments and Methods in Physics Research Section A 257 (1987) 215.
[18] G. Goldring, in: R. Bock (Ed.), Heavy Ion Collisions, vol. 3, North-Holland, Amsterdam, 1982, p. 483.
[19] A. Stuchbery, et al., Physical Review C 71 (2005) 047302.

7.4 Investigation of high-K states in ^{252}No

PHYSICAL REVIEW C **86**, 044318 (2012)

Investigation of high-K states in ^{252}No

B. Sulignano,[1] Ch. Theisen,[1] J.-P. Delaroche,[2] M. Girod,[2] J. Ljungvall,[3] D. Ackermann,[4,5] S. Antalic,[6] O. Dorvaux,[7] A. Drouart,[1] B. Gall,[7] A. Görgen,[8] P. T. Greenlees,[9] K. Hauschild,[3] R.-D. Herzberg,[10] F. P. Heßberger,[4,5] U. Jakobsson,[9] P. Jones,[9] R. Julin,[9] S. Juutinen,[9] S. Ketelhut,[9] W. Korten,[1] M. Leino,[9] A. Lopez-Martens,[3] M. Nyman,[9] A. Obertelli,[1] J. Pakarinen,[11] P. Papadakis,[10] E. Parr,[10] P. Peura,[9] J. Piot,[7] P. Rahkila,[9] D. Rostron,[10] P. Ruotsalainen,[9] J. Sarén,[9] C. Scholey,[9] J. Sorri,[9] J. Uusitalo,[9] M. Venhart,[12,6] and M. Zielińska[1]

[1]*CEA, Centre de Saclay, IRFU/Service de Physique Nucléaire, F-91191 Gif-sur-Yvette, France*
[2]*CEA, DAM, DIF, F-91297 Arpajon, France*
[3]*CSNSM, IN2P3-CNRS, F-91405 Orsay Campus, France*
[4]*GSI Helmholtzzentrum für Schwerionenforschung, D-64291 Darmstadt, Germany*
[5]*Helmholtz Institut Mainz, D-55099 Mainz, Germany*
[6]*Department of Physics and Biophysics, Comenius University, Bratislava 842 48, Slovakia*
[7]*Institut Pluridisciplinaire Hubert Curien, F-67037 Strasbourg, France*
[8]*SAFE Kjemibygningen, Sem Sælandsvei 26, 0371 Oslo, Norway*
[9]*Department of Physics, University of Jyväskylä, FIN-40014 Jyväskylä, Finland*
[10]*Department of Physics, University of Liverpool, Liverpool L69 7ZE, United Kingdom*
[11]*Isolde, CERN*
[12]*Institute of Physics, Slovak Academy of Sciences, Bratislava 845 11, Slovakia*

(Received 3 April 2012; revised manuscript received 19 July 2012; published 16 October 2012)

In this paper we investigate the rotational band built upon a two-quasiparticle 8^- isomeric state of ^{252}No up to spin $I^\pi = 22^-$. The excited states of the band were populated with the ^{206}Pb(^{48}Ca, $2n$) fusion-evaporation reaction. An unambiguous assignment of the structure of the 8^- isomer as a $7/2^+[624]_\nu \otimes 9/2^-[734]_\nu$ configuration has been made on the basis of purely experimental data. Comparisons with triaxial self-consistent Hartree-Fock-Bogoliubov calculations using the D1S force and breaking time-reversal as well as z-signature symmetries are performed. These predictions are in agreement with present measurements. Mean-field calculations extended to similar states in ^{250}Fm support the interpretation of the same two-neutron quasiparticle structure as the bandhead in both $N = 150$ isotones.

DOI: 10.1103/PhysRevC.86.044318 PACS number(s): 21.10.−k, 23.20.Lv, 23.35.+g, 27.90.+b

I. INTRODUCTION

In the past few decades exhaustive investigations of deformed nuclei in the transfermium region around $N = 152$ and $Z = 100$, where enhanced stability is observed, have been performed using in-beam and decay spectroscopy [1]. Nuclei in this region are produced with cross sections ranging from nanobarns to microbarns, high enough for detailed spectroscopic studies. Moreover, this region is characterized by the presence of K isomerism, which may enhance the stability of such nuclei against spontaneous fission [2], as in ^{270}Ds [3], in ^{254}No [4], and in ^{250}No [5].

K isomers are due to the presence near the Fermi surface of either neutron or proton orbitals with a large angular momentum projection K along the symmetry axis. Excitation of particles into such an orbital leads to a K state for which the decay is strongly hindered according to the ΔK selection rule. Therefore these states with a strong signature represent a new prolific ground for experimental investigations. The study of K isomers and collective bands built on them provides a detailed probe of single-particle states and their coupling to the collective degrees of freedom. Famous examples are located around $Z = 72$, $N = 106$ and include the textbook example of the $K^\pi = 16^+$ isomer in ^{178}Hf with a half-life of 31 yr (see for instance the review articles [6–8]). In the same way, the investigations of the nobelium isotopes ($Z = 102$), thus, deliver data in a region close to the domain of superheavy nuclei, where our knowledge of single-particle spectra and of pairing correlations is particularly limited. These studies can provide information relevant for the next shell closure, which is expected to be at $Z = 114$, 120, or 126 and $N = 184$ for spherical superheavy elements depending on the model (see [9–11] and references therein).

Ghiorso *et al.* were the first to discover K isomers in this region 39 years ago in ^{250}Fm and ^{254}No [12]. The decay of ^{254}No was recently revisited by Herzberg *et al.* [13] and by Tandel *et al.* [14], where a second isomer was found. In the nucleus ^{252}No, a new K isomer with a half-life of 110 ± 10 ms at an excitation energy of 1254 keV was discovered at SHIP (GSI, Darmstadt) [15] and confirmed at FMA (Argonne National Laboratory) [16], both experiments using decay spectroscopy techniques.

The isomer in ^{252}No has been interpreted as a two-quasineutron state with the configuration $7/2^+[624]_\nu \otimes 9/2^-[734]_\nu$ with spin and parity $I^\pi = 8^-$. This assignment was made by analogy with other $N = 150$ isotones. In fact, $K^\pi = 8^-$ isomers have been found in ^{244}Pu [16,17], ^{246}Cm [16,18], ^{248}Cf [19], and ^{250}Fm [20]. Very similar level schemes are observed in ^{246}Cm and ^{250}Fm, where the $I^\pi = 8^-$ isomer decays into the ground-state rotational bands via an intermediate excited band.

According to previous calculations, using Hartree-Fock-Bogoliubov (HFB) mean-field calculations with the Gogny

D1S force [21], the two-quasineutron $K^\pi = 8^-$ excitation in ^{252}No was predicted to lie at 1070 keV (without breaking time-reversal symmetry in the mean field [22]), in agreement with the experimental excitation energy $E_x = 1254$ keV. This result is in agreement with HFB calculations using the SLy4 interaction, which predict the two-quasineutron $K^\pi = 8^-$ excitation at ∼1300 keV [23]. On the other hand, both HFB models predict the two-quasiproton states at higher excitation energies (i.e., $E_x \sim 2000$ keV). In contrast, the macroscopic-microscopic Woods-Saxon calculations predict $K^\pi = 8^-$ isomers at ∼1 MeV for both two-quasineutron and two-quasiproton configurations [2,16,20]. Recent random phase approximation (RPA) calculations predict a two-neutron quasiparticle state at 1300 keV [24]. The differences between these predictions are related to different single-particle level schemes underlying the models.

The goal of this work is to deduce the structure of the $K^\pi = 8^-$ isomer in ^{252}No with purely experimental data and to understand how this structure changes with the rotational frequency. Together with previous data on ^{250}Fm [20], this will provide valuable reference points for theoretical models.

Strong constraints on the configuration assignment and models is provided (for $K^\pi \neq 0$ states) by the magnetic moment or gyromagnetic factor, which can be determined by measuring the $M1/E2$ intensity ratio within the band. While the $K^\pi = 8^-$ isomer in ^{252}No has been investigated using decay spectroscopy, this work extends the study to a rotational band built above this state via in-beam γ-ray spectroscopy, allowing for firm configuration assignments of the 8^- isomer.

II. EXPERIMENT

The experiment was carried out at the Accelerator Laboratory of the University of Jyväskylä. A $^{48}Ca^{+10}$ beam, with an energy of 218 MeV and an average current of 30 pnA, impinged on 452 μg/cm^2 thick ^{206}PbS (with an enrichment of 98.6%) targets mounted on a rotating wheel. The fusion-evaporation residues were selected by the gas-filled separator RITU [25] and implanted into the focal plane spectrometer GREAT [26]. GREAT consists of a multi-wire proportional counter (MWPC) to measure the time of flight and energy loss ΔE of the incoming ions and double-sided silicon strip detectors (DSSSD) to measure the energy and time of the ions and subsequent decays. The DSSSD are surrounded by germanium detectors (clover and planar) and PIN diodes for the detection of γ rays and conversion electrons from the decay of the implanted recoil. Prompt γ rays were detected in the 41 Compton-suppressed germanium detectors of the JUROGAM array. A γ-ray efficiency of 4.2% at 1332 keV was determined using calibration sources. The JUROGAM detector preamplifier signals were digitized with TNT2 digital pulse processor units [27]. This allowed a counting rate of up to 35 kHz for each germanium detector while retaining good energy and time resolution. Compared to standard analog shaping amplifiers and peak-sensing analog-to-digital converters (ADCs), the use of digital electronics allowed an increase of the average beam current by approximately a factor of 2. A time-stamped system total data readout (TDR) data acquisition system was used [28]. Data analysis was carried out using the GRAIN software package [29].

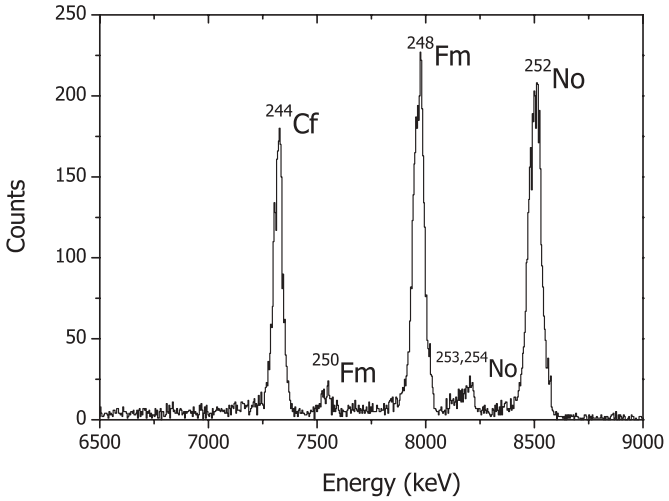

FIG. 1. Energy spectrum of α particles detected at the focal plane.

A total of 198 h of irradiation yielded 1.5×10^4 recoils detected at the focal plane correlated with the decay of ^{252}No and/or its daughters. The identification of the recoils was performed by demanding a signal (ΔE) in the MWPC detector in coincidence with an energy signal in the double-sided silicon strip implantation detector. Correlations between the time of flight and total energy were used to discriminate against scattered beam and target-like reaction products. The lifetime of the ^{252}No ground state was determined by correlating evaporation residues (ERs) with the subsequent alpha decay (α) or spontaneous fission (SF). Since the gain of the silicon detector electronics was optimized for the evaporation residues, events rendering overflow in the energy ADC and in anticoincidences with the MWPC were identified as SF events. The measured branching ratios for the different decay modes of the ^{252}No ground state, namely, $b_\alpha = 65.3(5)\%$ and $b_{SF} = 33.9(3)\%$, are found to be in good agreement with the literature values [30]. The electron capture decay path could not be measured directly so the previously measured value of $b_\epsilon = 0.8\%$ [31] was assumed. The α-particle energy spectrum in anticoincidence with MWPC events is shown in Fig. 1. From the time distribution a half-life of 2.43 ± 0.13 s was obtained for the ground state, in agreement with the evaluated data of 2.44 ± 0.04 s [32].

A. Delayed spectroscopy

Isomeric states in heavy nuclei often decay to the ground-state band via strongly converted electromagnetic transitions. Correlating such electrons, detected in the DSSSD and identified via their energy, with the implanted ERs allows selection of the recoils which were implanted prior to the decay of the isomeric state. For details see, e.g., Jones [33]. The measured electron sum signals of the isomer decays detected in the same pixel as an ER event within a time window of 700 ms after the implantation are shown in Fig. 2. The insert in Fig. 2 shows the logarithm of the time difference between implantation of the recoil and its subsequent electron

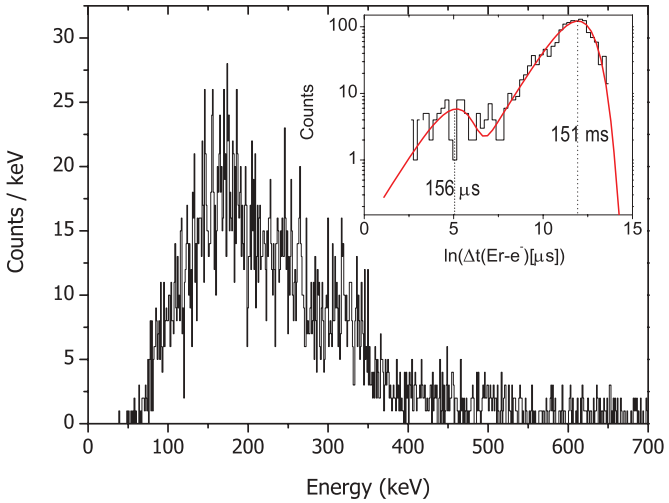

FIG. 2. (Color online) Energy spectrum of conversion electrons observed within 700 ms after a fusion-evaporation residue was implanted in the same pixel of the DSSSD. The inset shows the logarithmic decay time distribution of conversion electrons correlated with ER recoils detected at the focal plane; no correlation with α decay or SF of ^{252}No is required. The smaller contribution at 156 μs is ascribed to a short-lived isomer in ^{253}No.

decay. The red curve represents the time density distribution of electrons correlated to the evaporation residue of ^{252}No, and the peak position determines the lifetime via the $\ln(\tau)$ relation. This method [34,35] allows the discrimination of contributions from sources having different lifetimes. The distinct cluster with a lifetime of 156 μs corresponds most likely to the de-excitation of an isomeric state in ^{253}No. This is confirmed by the observation of the characteristic x rays of nobelium and few γ rays with energies similar to that reported recently by Antalic *et al*. [36]. ^{253}No nuclei have been produced via the $2n$ evaporation channel from reactions on the ^{207}Pb contaminant present in the ^{206}Pb target. The α decay of this channel is also visible in Fig. 1.

For an unambiguous identification and to remove the contribution from ^{253}No, an additional requirement of α decay or SF of ^{252}No observed subsequently in the same pixel was demanded. We should point out that among all possible open channels, ^{252}No is the only nucleus having a SF branch; SF is therefore an unambiguous signature of this nucleus. A total of 3833 conversion electrons (ER-e^- correlation) signals were detected in the DSSSD. A half-life of 109 $\pm$ 3 ms was found, in perfect agreement with 110 $\pm$ 10 ms quoted in [15].

Delayed γ rays from the de-excitation of isomeric states were detected in the germanium detectors surrounding the focal plane. A coincidence with the conversion electrons from the decay of the isomeric state using the conditions 2 ms $< \Delta t$(ER-e^-) $<$ 700 ms and $E_e^- <$ 700 keV was demanded. See Fig. 3 for the γ-ray spectra. The deduced decay pattern from the isomeric state is found to be in perfect agreement with the previous measurements [15], as shown in Fig. 4.

Moreover, it was possible to confirm the transitions observed in earlier experiments. Indeed, the $6^- \rightarrow 5^-$ (75 keV) $M1$ transition is clearly visible in Fig. 3, as are the $5^- \rightarrow 3^-$ at 107 keV, $7^- \rightarrow 5^-$ at 156 keV, $6^- \rightarrow 4^-$ at 133 keV, and

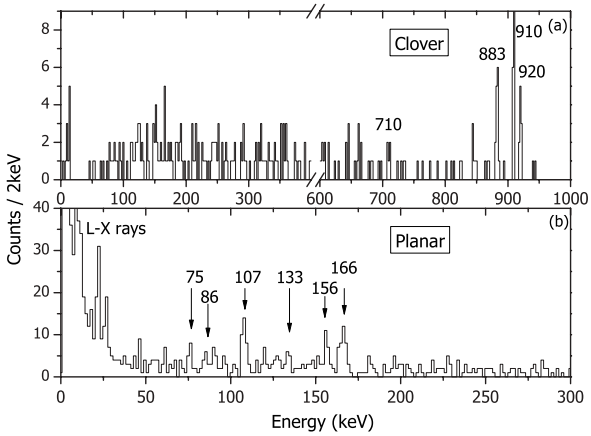

FIG. 3. Gamma rays detected in prompt coincidence with conversion electrons in the clover detector (a) and in the planar germanium detector (b) of the GREAT spectrometer.

$4^- \rightarrow 2^-$ at 86 keV $E2$ transitions. Other peaks are also visible in the spectra, although at present status it is not possible to fit them into our decay scheme.

B. Prompt spectroscopy at the target position

The de-excitation of states lying above the isomer was studied [see Fig. 5(a)] by correlating prompt γ rays in the

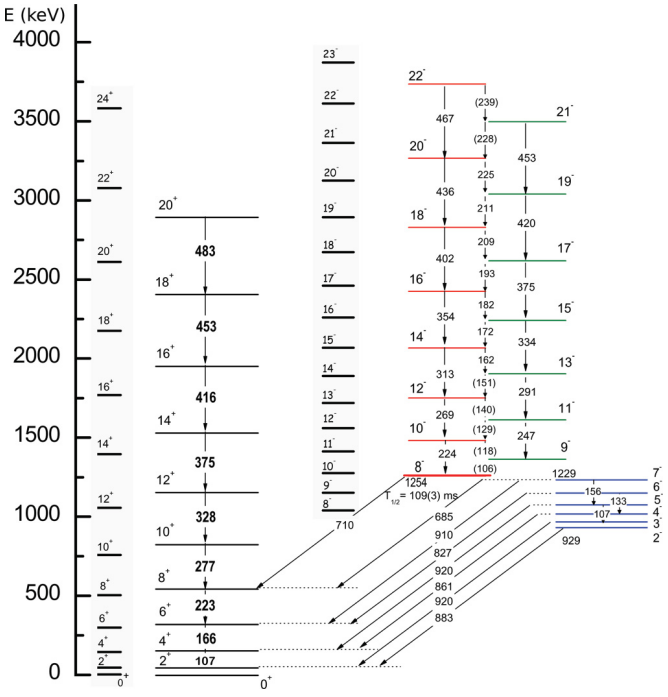

FIG. 4. (Color online) ^{252}No level scheme. Ground-state band measured up to spin $I^\pi = 20^+$ and comparison to HFB predictions to spin 24^+ (gray box) are shown on the left-hand side. The rotational band measured on top of the $K^\pi = 8^-$ neutron isomer is shown (up to spin $I^\pi = 22^-$) in red and green colors for even and odd spin sequences, respectively. HFB level predictions for this band to spin $I^\pi = 23^-$ are shown inside the gray box. The $K^\pi = 2^-$ collective band observed at lower excitation energy is marked in blue.

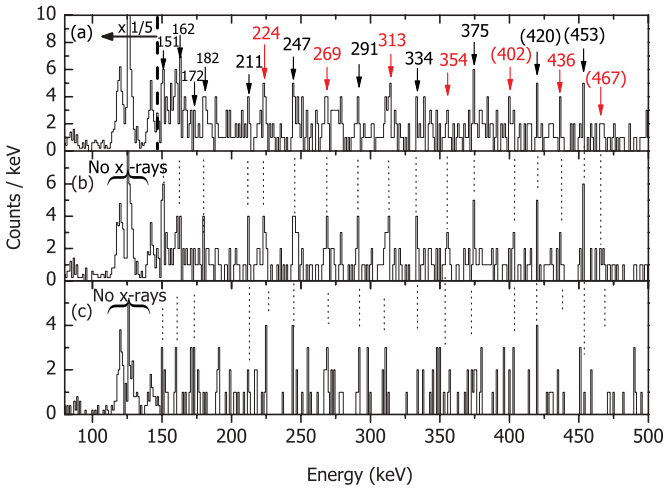

FIG. 5. (Color online) (a) Prompt γ-rays measured in JUROGAM in coincidence with an ER-e^- ($E_{e^-} < 700$ keV) pair observed at the same position in the DSSSD within 700 ms. (b) Same spectrum with the additional requirement that an α particle or SF is correlated with the evaporation residue. (c) Projection of the γ-γ coincidences matrix using electrons and α/SF correlations. The region of nobelium x rays has been scaled down by a factor of 5 in all three spectra.

JUROGAM array with fusion-evaporation residues observed in the focal plane of RITU. The additional requirement that an electron sum event was observed within 700 ms after a recoil at the same position in the DSSSD was made. Higher selectivity was reached by detecting the characteristic α or SF decay following the evaporation residue within ΔT(ER–α/SF) < 12 s [see Fig. 5(b)]. Support for the assignment of the rotational band is given by the investigation of recoil-gated γ-γ coincidences. Figure 5(c) shows the projection of the recoil-gated γ-γ coincidence matrix using electrons and α/SF correlations. Although the statistics are rather weak, each (presumed) transition is in coincidence with at least one of the other transitions. The corresponding level scheme including also transitions from previous work [15,37] is shown in Fig. 4.

C. Spin assignment

The spin I of the states in the rotational band built on top of the isomer can be assigned using a method extensively applied to superdeformed rotational bands in the mass 190 region [38,39]. The technique known as the Harris fit [40] consists in expanding the dynamic moment of inertia $\mathcal{J}^{(2)}$ in even powers of the rotational frequency $\hbar\omega = E_\gamma/2$ averaged over two consecutive γ-ray transitions,

$$\mathcal{J}^{(2)} = 4/\Delta E_\gamma = dI/d\omega = A + B\omega^2 + C\omega^4. \quad (1)$$

The resulting function is integrated with respect to ω to obtain the spin I, namely,

$$I_\gamma(\omega) - I_{\gamma 0} = A\omega + (B/3)\omega^3 + (C/5)\omega^5 + 1/2. \quad (2)$$

The basic assumption of the technique is that of no alignment at rotational frequency $\omega \sim 0$, i.e., $I_{\gamma 0} = 0$. This is indeed in perfect agreement with our HBF calculations, as discussed below in Sec. IV. The dynamic moment of inertia is displayed in Fig. 6(b). Let us first make a comment on the procedure used to calculate the moment of inertia. Although the band is characterized by a sequence of $\Delta I = 1\hbar$ transitions, this band is divided for convenience into two $\Delta I = 2\hbar$ branches when calculating the moment of inertia. Looking at the moment of inertia, one notes the presence of a shallow minimum at a rotational frequency of $\hbar\omega \sim 0.19$ MeV, a feature that will be commented upon later. Obviously, the two points in the vicinity of this minimum, which strongly deviate from the otherwise smooth pattern, should be excluded from the Harris fit. The low statistics in the γ-ray spectra measurements (see Fig. 5) leads to uncertainties in the determination of the parameters entering the fitted expression [Eq. (2)]. The best fit leads to the estimate $I_0 = 8.1 \pm 1.9\hbar$ for the bandhead level. In addition, the spin-fitting method introduced by Wu *et al.* [41] has been used as a cross-check of the above spin determination. The method gives for integer I_0 a minimum in the χ^2 function at $I_0 = 8\hbar$. Finally, both methods are fully consistent with spin $I_0 = 8\hbar$ for the bandhead.

D. Structure assignment

In the $N = 150$ (^{246}Cm and ^{248}Cf) isotones the presence of the 8^- isomeric states is a common feature of this region, as was already pointed out in the introduction. The neutron $7/2^+[624]_\nu \otimes 9/2^-[734]_\nu$ nature of this state has then been firmly established on the basis of different experimental means, e.g., transfer reactions and β decay. The similarity of the level schemes between ^{252}No and those for the other isotones makes the assumption that also in this case the decay proceeds through the two-neutron components of the wave functions. A direct measurement of the structure of the isomeric states found in ^{252}No produced via the fusion-evaporation reaction can be performed via the study of the γ rays emitted during the de-excitation of the band built on the isomeric state. The electromagnetic properties of the states were deduced and the magnetic moment, or the g_K gyromagnetic factor, was inferred. The g_K factor depends on the two-quasiparticle configuration and depends in general on the scenario. It is therefore a crucial quantity for understanding the isomer structure and for a comparison with the models. As mentioned in the introduction, the $K^\pi = 8^-$ isomeric state can be interpreted either as a two-quasiproton $(9/2^+[624]_\pi \otimes 7/2^-[514]_\pi)$ or two-quasineutron $(7/2^+[624]_\nu \otimes 9/2^-[734]_\nu)$ configuration. Although new HFB calculations are presented in this article, the complex formalism for calculating rigorously the magnetic moment has not yet been implemented in the HFB code. Therefore the gyromagnetic factor inferred from Woods-Saxon-based calculations will be used. According to [42], the g_K factor for these two 8^- configurations are 0.01 $(7/2^+[624]_\nu \otimes 9/2^-[734]_\nu)$ and 1.01 $(9/2^+[624]_\pi \otimes 7/2^-[514]_\pi)$, respectively. It is interesting to note that these values are very close to the asymptotic limit for singlet states ($\Sigma = 0$) which are energetically favored according to the Gallagher rule [43]. In this case the gyromagnetic factor of the spin cancels and one has only a contribution from the angular momentum I of the two protons ($g_K = g_l^p = 1$) or neutrons ($g_K = g_l^n = 0$). To determine the experimental g_K factor, the well-known relationship between the observed

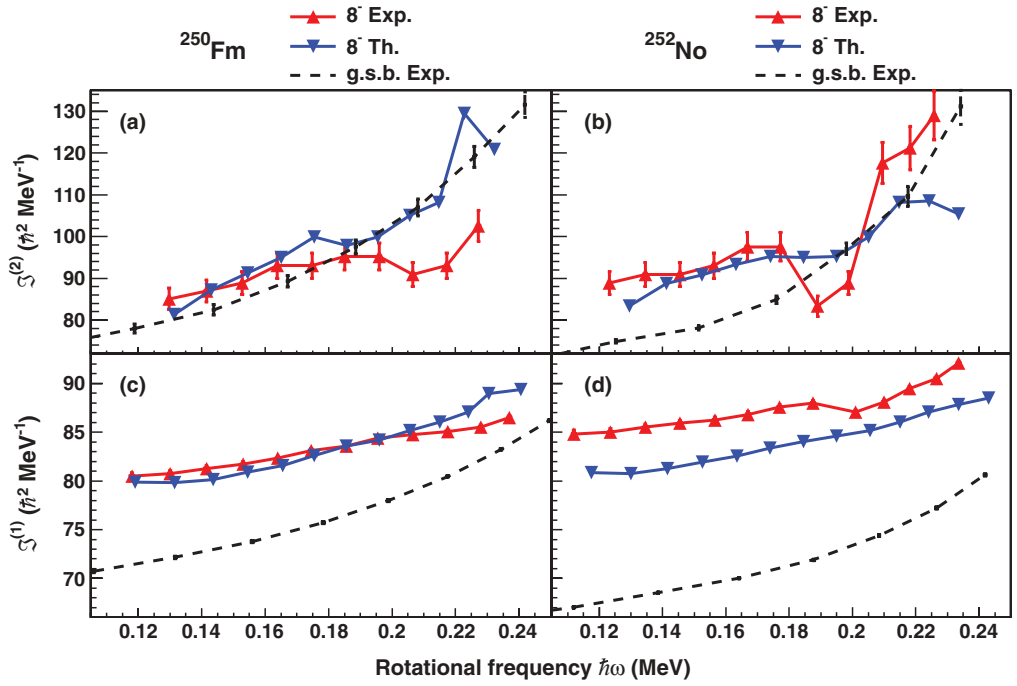

FIG. 6. (Color online) (a) and (b) Dynamic moment of inertia $\mathcal{J}^{(2)}$ vs $\hbar\omega$ for the ground-state rotational band (dashed black lines) and for the isomeric $K^\pi = 8^-$ band, for the ^{250}Fm and ^{252}No (red triangles) isotones. (c) and (d) Same as (a) and (b) but for the kinematic moments of inertia. Triangular blue marks represent theoretical calculations using the D1S Gogny force. See text for details.

γ-ray branching ratio, the g_K factor, and decay probabilities was used, i.e.,

$$R^{the} = \frac{I(M1; J \to J-1)}{I(E2; J \to J-2)} = \frac{1.76[E_\gamma(M1)]^3 B(M1)\ \mathrm{s}^{-1}}{1.22[E_\gamma(E2)]^5 B(E2)\ \mathrm{s}^{-1}}, \quad (3)$$

where the reduced transition probabilities $B(E2)$ and $B(M1)$ are

$$B(E2, J \to J-2) = \frac{5}{16\pi} e^2 Q_0^2 \langle JK20|(J-2)K\rangle^2 \quad (4)$$

and

$$B(M1, J \to J-1) = \frac{3}{4\pi}\left(\frac{e\hbar}{2Mc}\right)^2 (g_K - g_R)^2 K^2 \langle JK10|(J-1)K\rangle^2. \quad (5)$$

The core gyromagnetic factor is taken to be $g_R = Z/A = 0.4$ in the hydrodynamic limit. While the g_K factor changes strongly from one configuration to another, the electric quadrupole moment Q_o does not exhibit large differences and is accurately predicted by the models. We have here taken that for the neutron two-quasiparticle HFB value, namely, $Q_o = 13.75\ e$ b. The experimental branching ratios are given in Table I for the three initial states for which both interband $M1$ and intraband $E2$ transitions were measured. We have assumed a small mixing ratio for the $\Delta I = 1\hbar$ transition according to [44]. Unfortunately, the γ-ray transitions are observed with low intensity, which translates into large error bars for the experimental ratio. According to Eq. (3), the branching ratio is a parabolic function of g_K, as shown in Fig. 7 in the case of the $I^\pi = 14^-$ initial level. Decay probabilities lie on this parabola: $7/2^+[624]_\nu \otimes 9/2^-[734]_\nu$ with $g_K = 0.01$ (square symbol) and $9/2^+[624]_\pi \otimes 7/2^-[514]_\pi$) with $g_K = 1.01$ (circle symbol). The experimental intensity ratio is shown with the yellow area. The intersection of the experimental intensity ratio value with the parabola gives two possible g_K values. It is clear that only the $K^\pi = 8^-$ neutron configuration agrees well with the measured ratio. The same conclusion can be drawn for the 15^- and 16^- initial states.

However, using single intensity ratios from low-statistic spectra can lead to large uncertainties. It is therefore more appropriate in this case to apply the analytical method described in detail in [45]. The technique is based on the idea that the transitions in a strongly coupled band will have easily visible stretched $E2$ transitions and interband $\Delta I = 1\hbar$ transitions clustered at low energies. As the band is built on a particular configuration the branching ratios in the band are easily modeled by using this configuration as input. This gives an estimate of the number of counts one would expect to find in this $\Delta I = 1\hbar$ region in the spectrum, even if the statistics are not large enough to analyze individual peaks. An "integral branching ratio" is therefore extracted, and this may often take

TABLE I. Experimental intensity ratios $I(M1)/I(E2)$.

Initial level	$I(M1)/I(E2)$	R_{exp}
16^-	$I_\gamma(182)/I_\gamma(354)$	0.49 ± 0.41
15^-	$I_\gamma(172)/I_\gamma(334)$	0.37 ± 0.37
14^-	$I_\gamma(162)/I_\gamma(313)$	0.65 ± 0.37

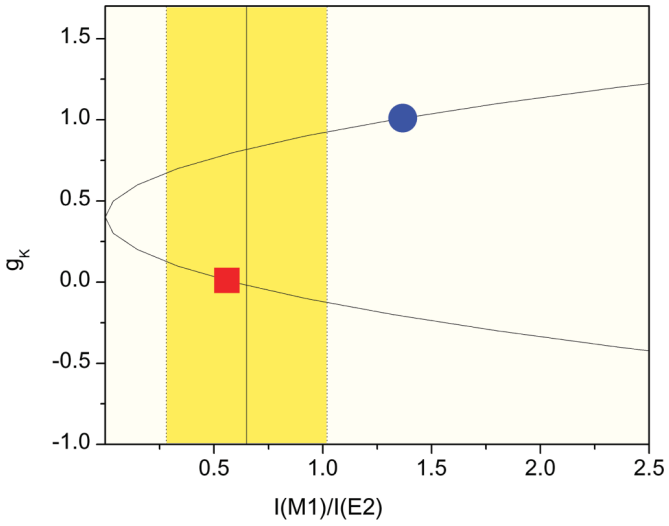

FIG. 7. (Color online) The relationship between intensity ratio $I(M1)/I(E2)$ and g_K, showing the values for the expected neutron (red square) and proton (blue circle) configurations compared with the experimental ratio (yellow area) for the decay of the $I^\pi = 14^-$ level. See text for details.

the form of an upper limit to compare the experimental spectral shape to that predicted by the rotational model based on the different possible configurations. The details are explained in [45].

The number of experimentally deduced counts is denoted with N_0 and the number of expected counts in the same region for both candidate configurations with N_n (two-quasineutron state $7/2^+[624]_\nu \otimes 9/2^-[734]_\nu$) or N_p (two-quasiproton state $9/2^+[624]_\pi \otimes 7/2^-[514]_\pi$), using the easily observed intensity of the $E2$ transitions as normalization. This method was applied for the intraband transitions $I^\pi = 14^-$ to $I^\pi = 19^-$. The comparison between the deduced values N_0 and the Gaussian probability distribution found for the two different scenarii shown in Fig. 8 favors the neutron structure being about 3 times as probable as the proton structure (56% versus 14%) [45].

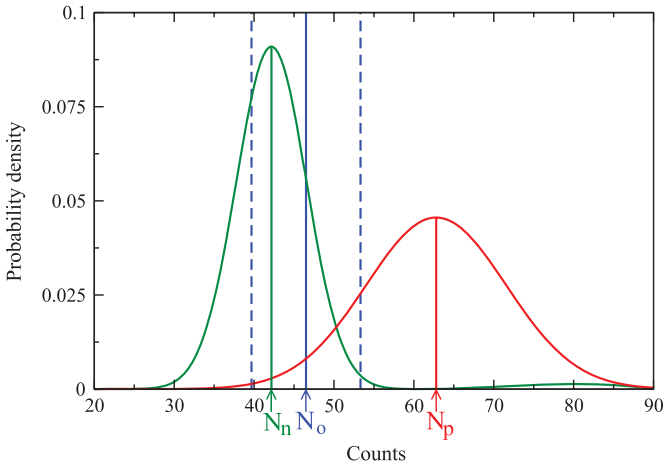

FIG. 8. (Color online) Expected total counts N_n for the two-quasiparticle neutron configuration (green) and N_p for the two-quasiparticle proton configuration (red) and observed counts N_o (blue line) along with attached uncertainties (dashed blue lines).

This technique was also applied to the rotational band built on top of the $K^\pi = 8^-$ isomer in ^{250}Fm [45], the result being fully consistent with the interpretation of Greenlees *et al.* [20].

This method combined with the measurement of the $M1/E2$ ratio provides a strong experimental indication of the isomeric structure as a spin singlet two-quasineutron state. With $K^\pi = 8^-$ as the bandhead, the likely configuration is $7/2^+[624]_\nu \otimes 9/2^-[734]_\nu$.

E. Hindrance factor

Long-lived K isomers occur because the decay via transitions with a large ΔK is strongly hindered: there is no state with similar wave function available for the decay. These states with a high degree of K purity can only be obtained for axially symmetric nuclei. The reduced hindrance factor f_ν gives an indication on the "goodness" of the quantum number K, or the K purity of the state. It is defined as

$$f_\nu = \left(T^\gamma_{1/2}/T^W_{1/2}\right)^{1/\nu}, \tag{6}$$

where $T^\gamma_{1/2}$ is the partial γ-ray half-life and $T^W_{1/2}$ is the Weisskopf single-particle estimate. The exponent $1/\nu = 1/(\Delta K - \lambda)$ represents the degree of forbiddenness with λ being the multipolarity of the decay radiation. A value of $f_\nu \sim 100$ is expected according to the systematics of Löbner [46]. In ^{252}No, the reduced hindrance factor can be obtained from the decay to the $K^\pi = 0^+$ ground-state band ($8^- \to 8^+$ $E1$ transition at 710 keV) or from the decay to the $K^\pi = 2^-$ octupole band ($8^- \to 7^-$ $M1$ transition at 25 keV). Using a branching ratio of 4% for the $E1$ transition at 710 keV [15], one obtains f_ν ($E1$, $8^- \to 8^+$) = 178 and f_ν ($M1$, $8^- \to 7^-$) = 218. The high value of the reduced hindrance factor testifies to the high purity of the two-quasiparticle $K^\pi = 8^-$ isomer and the small degree of mixing with both the ground-state band and the $K^\pi = 2^-$ excited band. This value favorably compares with the $K^\pi = 8^-$ isomer in the $N = 150$ isotones: f_ν (^{250}Fm, $E1$, $8^- \to 8^+$) = 213, f_ν (^{250}Fm, $M1$, $8^- \to 7^-$) = 192 [20], f_ν (^{246}Cm, $E1$, $8^- \to 8^+$) = 212 [47], and f_ν (^{244}Pu, $E1$, $8^- \to 8^+$) ~200 [17].

III. THEORETICAL FRAMEWORK

Mean-field calculations were performed in triaxial oscillator bases including 14 shells using the D1S Gogny force [21,22]. The neutron and proton single-particle states obtained at equilibrium deformation are shown in Fig. 9, where single neutron gaps are predicted at $N = 150$ and $N = 152$ while the proton main gaps are predicted to be at $Z = 98$ and 104. The deformed shell gaps indicated by the experiments are $N = 152$ and $Z = 100$ [1]. The present neutron and proton level schemes at equilibrium deformation differ from those in previous publications [9,16,48,49].

To establish our notation we first define the quasiparticle vacuum HFB energy from minimization of the functional

$$\delta \langle \Phi | \widehat{H} - \lambda_Z \widehat{Z} - \lambda_N \widehat{N} | \Phi \rangle = 0, \tag{7}$$

where $\widehat{H}$ is the nuclear Hamiltonian, and

$$\langle \Phi | \widehat{N} | \Phi \rangle = N; \ \langle \Phi | \widehat{Z} | \Phi \rangle = Z, \tag{8}$$

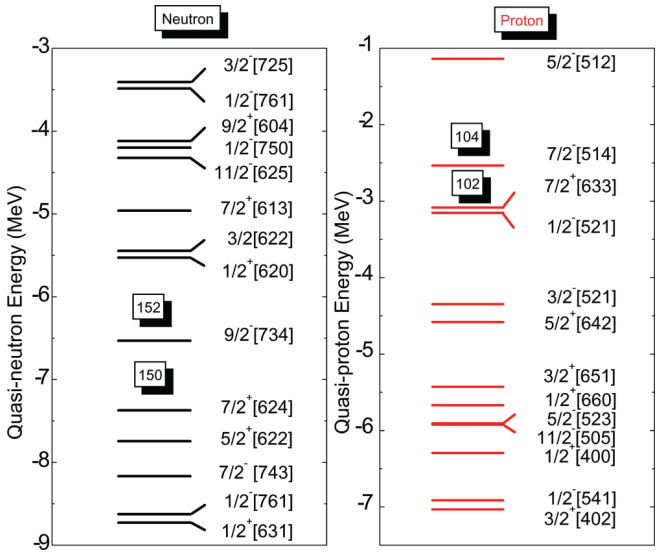

FIG. 9. (Color online) Single-particle energies for neutron and proton states in ^{252}No at axial equilibrium deformation of the HFB energy, where the charge quadrupole moment is $Q_0 = 13.75\,e$ b. The labels $[Nn_z\Lambda]$ are assigned by analogy with a Nilsson diagram.

with $\widehat{Z}$ and $\widehat{N}$ as the proton and neutron number operators, respectively, and λ_Z and λ_N Lagrange multipliers.

The two-quasiparticle excitations are sought for using blocking calculations also performed in the same HFB framework. Here, a trial state $|\Phi'_{ij}\rangle = \eta_i^+ \eta_j^+ |\Phi_{ij}\rangle$ is defined, in which η_i^+ is a quasiparticle creation operator. The index i (respectively j) refers to the set of quantum numbers of a one-quasiparticle orbital labeled i (respectively j) and located in the vicinity of the Fermi energy of the unblocked HFB solution $|\Phi\rangle$. Then the equation

$$\delta\langle\Phi'_{ij}|\widehat{H} - \lambda_N\,\widehat{N} - \lambda_Z\,\widehat{Z}|\Phi'_{ij}\rangle = 0 \qquad (9)$$

is solved, and the two-quasiparticle excitation energy is obtained as the difference [22]:

$$E^{ij}_{2qp} = \langle\Phi'_{ij}|\,\widehat{H}\,|\Phi'_{ij}\rangle - \langle\Phi|\,\widehat{H}\,|\Phi\rangle. \qquad (10)$$

If time-reversal symmetry is assumed, the signature partner pairs with angular momentum projections on the z axis, $K_- = K_1 - K_2$ and $K_+ = K_1 + K_2$, and parity $\pi = \pi_1 \cdot \pi_2$ are degenerate in energy.

The wave functions in the rotating frame actually are subject to fulfilment of spacial symmetries, namely, (i) parity operator $\widehat{\Pi}$, (ii) z signature $\hat{S}_z = i\hat{R}_3$ (π) with $\hat{R}_3$ as the operator for rotation around the z axis, and (iii) the product $\hat{K}\cdot\widehat{\Pi}_2$ of operators, where $\hat{K}$ stands for time-reversal symmetry and $\widehat{\Pi}_2$ for reflectiion with respect to the x-z plane. These symmetries form a set of self-consistent symmetries which are commuting only for the vacuum HFB solutions of a system rotating around the z axis [50]. Furthermore, two-quasiparticle excitations rotating along the x axis do break the signature symmetry here taken along the z axis and defined as

$$\hat{S}_z = ie^{-i\pi\hat{J}_z}, \qquad (11)$$

where $\hat{J}_z$ is the projection of angular momentum onto the z axis. The z-signature is broken because $\hat{J}_x$, the projection of angular momentum onto the x-axis, and $\hat{S}_z$ do not commute [51].

Within the HFB theory expressed in the rotating frame, the aligned two-quasiparticle internal structure of a nucleus with total angular momentum I, neutron number N, and proton number Z is determined by solving the equation for the dynamical quasiparticle vacuum $|\Phi'^{\omega}_{ij,+}\rangle$:

$$\delta\left\langle\Phi'^{\omega}_{ij,+}\right|\,\widehat{H} - \omega\,\widehat{J}_x - \lambda_N\,\widehat{N} - \lambda_Z\,\widehat{Z}\,\left|\Phi'^{\omega}_{ij,+}\right\rangle = 0, \qquad (12)$$

with the dynamical constraint on the x component J_x of the total angular momentum I defined by

$$J_x = \left\langle\Phi'^{\omega}_{ij,+}\right|\hat{J}_x|\Phi'^{\omega}_{ij,+}\rangle = \sqrt{I\,(I+1) - \langle J_z\rangle^2}, \qquad (13)$$

where the indexes ij stand for the blocked orbitals and the plus sign indicates aligned configurations.

In ^{250}Fm and ^{252}No, the two-quasiparticle signature partner bandheads with $\langle J_z\rangle^\pi = K^\pi_+ = 8^-$ and $\langle J_z\rangle^\pi = K^\pi_- = 1^-$ quantum numbers are built from the neutron $9/2^-$ and $7/2^+$ levels closest to the Fermi energies (see Fig. 9). For both nuclei, breaking time-reversal symmetry removes the energy degeneracy of the signature partner $K^\pi_- = 1^-$ and $K^\pi_+ = 8^-$ head levels. The two head levels display intrinsic excitation energies which differ by 200 keV. The aligned $K^\pi = 8^-$ two-quasiparticle head levels are lowest in energy. Excitation energies of the $K^\pi_- = 1^-$ and $K^\pi_+ = 8^-$ solutions are as follows: $E_x(K^\pi_- = 1^-) = 1.138$ MeV, $E_x(K^\pi_+ = 8^-) = 0.920$ MeV and $E_x(K^\pi_- = 1^-) = 1.195$ MeV, $E_x(K^\pi_+ = 8^-) = 0.982$ MeV, for ^{250}Fm and ^{252}No, respectively. The arithmetic mean energies of these signature-partner pairs are $E_{m,2qp} = 1.029$ MeV and $E_{m,2qp} = 1.031$ MeV for ^{250}Fm and ^{252}No, respectively. Both mean energies are close to those obtained previously in blocking calculations without breaking time-reversal symmetry, namely, 1.010 MeV (^{250}Fm) and 1.070 MeV (^{252}No) [22]. These results are in qualitative agreement with expectations based on the Gallagher rule [43]. After correcting for zero-point energy $E_0 = 8\hbar^2/2\mathcal{J}^{(1)}$, that is, $E_0 = 49$ keV (51 keV) for ^{252}No (^{250}Fm) as inferred from the kinematic moments of inertia $\mathcal{J}^{(1)}$ shown in Fig. 9, the calculated $I^\pi = 8^-$ head level energies are $E_x(I^\pi = 8^-) = 0.971$ MeV and $E_x(I^\pi = 8^-) = 1.031$ MeV for ^{250}Fm and ^{252}No, respectively. These calculated excitation energies are reasonably close to those found in experiments, namely, $E_x = 1.199$ MeV and $E_x = 1.254$ MeV for ^{250}Fm and ^{252}No, respectively.

IV. MOMENT OF INERTIA

A. General trend

The moments of inertia provide a tool to quantify the robustness and rigidity of the K isomer and the rotational band. The experimental kinematic and dynamic moments of inertia $\mathcal{J}^{(1)}$ and $\mathcal{J}^{(2)}$, respectively, are shown in Fig. 6 for the ground-state band (dashed black lines) and the $K^\pi = 8^-$ bands in the ^{250}Fm and ^{252}No (red triangles) isotones. Blue triangles represent theoretical results using the D1S Gogny force. Excellent agreement has been found for the ground-state bands [22] using the same theoretical framework. It is worth

noting that a good degree of accuracy is also obtained for the $K^\pi = 8^-$ two-quasiparticle isomeric band as far as the moment of inertia and the excitation energies are concerned. The agreement is in particular very good at low frequency, especially for ^{250}Fm. One should again note some irregularities in the moment of inertia that will be discussed in Sec. IV B.

In general, the moment of inertia of the ground-state band increases with increasing frequency under the influence of the Coriolis antipairing force, which slowly aligns the angular momentum along the rotation axis. On the other hand, the two-quasiparticle configuration of the excited band blocks the neutron pairing, increasing the kinematic moment of inertia already at low frequencies. At $\hbar\omega \sim 0.12$ MeV, the gain is $\sim$10% for ^{250}Fm and reaches $\sim$30% for ^{252}No. This effect is well known in odd-mass nuclei compared to their even-even neighbors. More generally, the moment of inertia is expected to increase with the number of quasiparticles involved. It is important to stress that the difference in the moment of inertia between the ground-state and the $K^\pi = 8^-$ bands reflects a change in pairing energy, not in deformation. Indeed, the neutron pairing energy has been found null in the present blocking HFB calculations while a quadrupole moment of 13.75 e b is predicted for the ground state close to 13.84 e b for the $K^\pi = 8^-$ isomeric state. In ^{250}Fm, the values are 13.39 e b (ground state) and 13.47 e b ($K^\pi = 8^-$).

In the $K^\pi = 8^-$ bands, the rotor is not only more rigid but also more stable with the rotation than the ground-state band. This can be inferred from the comparison of $\mathcal{J}^{(1)}$ and $\mathcal{J}^{(2)}$. Indeed, (i) the kinematic moment of inertia is almost constant as a function of the rotational frequency, and (ii) the difference between $\mathcal{J}^{(1)}$ and $\mathcal{J}^{(2)}$ is small (at least at low rotational frequency). In other words, there is little contribution from the unpaired nucleons as soon as the nucleus rotates. The alignment of the angular momentum along the rotation axis is small because of the robustness of the high-K configuration.

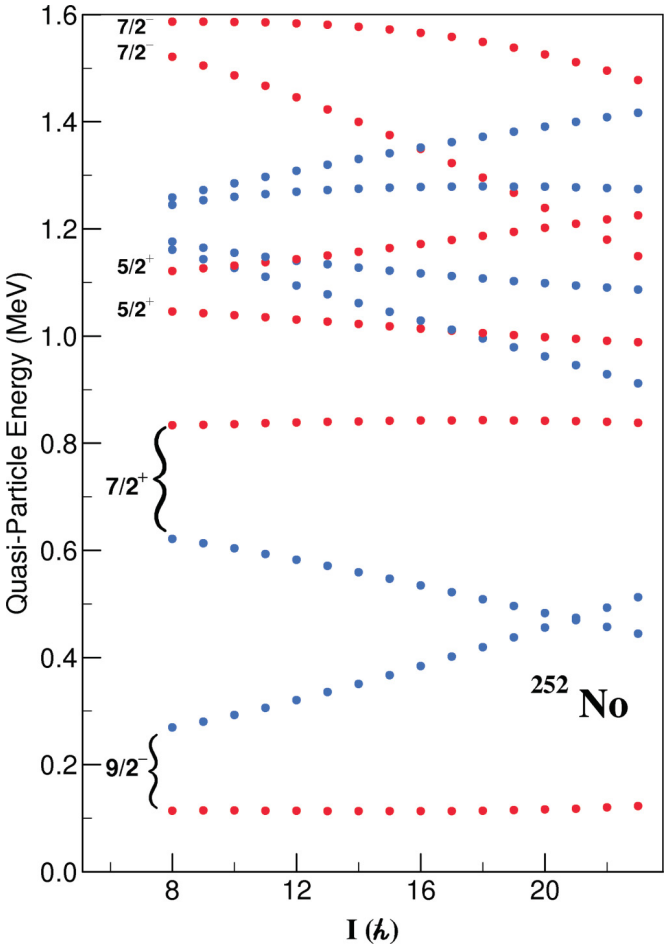

FIG. 10. (Color online) Quasiparticle energies calculated vs spin I for neutrons. The color code is for the occupation probabilities. Occupied orbitals are shown in red and empty ones in blue. States are labeled with quantum numbers π (parity) and Ω (projection onto the x axis of quasiparticle angular momentum).

B. Anomaly in the moment of inertia

As mentioned above, the regularity of rotational bands changes at $\hbar\omega \sim 0.19$ MeV for ^{252}No but also for ^{250}Fm at a slightly higher frequency: the moment of inertia decreases and seems to recover its initial trend at higher frequency. The theoretical moments of inertia also display irregularities but they are less pronounced.

Irregularities in the moment of inertia often result from the crossing of bands having the same spin and parity. When the bands get closer in energy, they repel mutually, inducing some perturbations of the level energies, displacements that are magnified in the dynamic moment of inertia. One of the bands displays a bump in the moment of inertia while the interacting partner displays a dip. As another consequence of the adiabatic interaction, the two bands exchange their single-particle configuration along the crossing. In a more general context, the time-dependent interaction of quantum systems is known as a Landau-Zener crossing [52]. Many examples of band crossings are found along the nuclear chart, for instance in superdeformed bands [53].

1. *Theoretical analysis*

To test the hypothesis of band crossing the investigation of Routhian properties has been carried out. The neutron quasiparticle energies in the rotating frame (Routhians) are shown in Fig. 10. They are labeled with quantum number π (parity) and Ω (projection onto the x axis of quasiparticle angular momentum at $I = 8\hbar$). Let us first note that the occupied quasiparticle orbitals labeled with the quantum numbers $\Omega^\pi = 9/2^-, 7/2^+$ display energies that are almost constant as a function of spin at least up to spin $I = 25\hbar$. This is consistent with the robustness of the $K^\pi = 8^-$ quasiparticle configuration as a function of the rotation. Also, these calculations did not show any orbital crossing among occupied orbitals with $\pi = -$.

The irregularities in the calculated moments of inertia should be correlated to the evolution of another parameter. Inspection of the proton pairing energy as a function of spin (see Fig. 11) does not reveal any changes or a pairing collapse that could induce the anomalies in the theoretical moments of inertia.

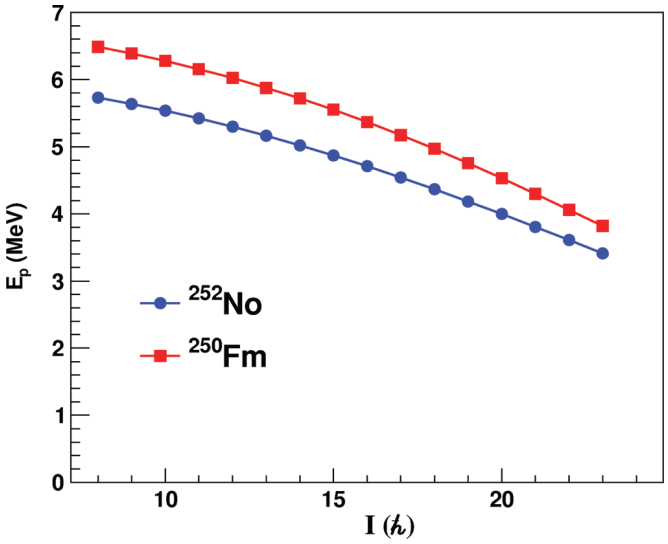

FIG. 11. (Color online) Proton pairing energy for ^{250}Fm and ^{252}No.

As customary in nuclear structure calculations, the axial and triaxial quadrupole deformations β and γ are defined as functions of the mass quadrupole moments Q_{20} and Q_{22}, respectively, as

$$\beta = \sqrt{\frac{\pi}{5}}\frac{\sqrt{Q_{20}^2 + 3Q_{22}^2}}{A\langle r^2\rangle} \tag{14}$$

and

$$\gamma = \arctan\sqrt{3}\frac{Q_{22}}{Q_{20}}, \tag{15}$$

where A and $\langle r^2\rangle$ are the nuclear mass numbers and mean square radius of the mass distribution, respectively, and where

$$\langle r^2\rangle = \tfrac{3}{5}(r_0 A^{1/3})^2 \tag{16}$$

with $r_0 = 1.2$ fm. The deformation parameters have here been calculated using the above equations for Q_{20} and Q_{22} values calculated for each spin value from $I = 8\hbar$ to $I = 24\hbar$. Over this spin sequence β and γ values remain constant to less than 3% and 1%, respectively, for ^{252}No and ^{250}Fm. These features suggest no shape evolution through the bands, which may explain the irregular pattern displayed by the calculated dynamic moments of inertia (see Fig. 6).

2. *Experimental band crossing*

We next investigate whether the irregularities observed in the $\mathcal{J}^{(2)}$ measurements stem from band crossing. One of the possible candidates to cross the $K^\pi = 8^-$ band at $\hbar\omega \sim 0.19$ MeV is the side band $K^\pi = 2^-$. It is not excluded that the $K^\pi = 8^-$ band could instead cross an unobserved band such as $K^\pi = 7^-$ predicted by Delaroche *et al.* [22] and observed in the isotone ^{248}Cf [54] at 1.5 MeV. Returning to the first hypothesis for which we have experimental information, we see that both bands have the same $\pi = -$ parity and similar bandhead excitation energies (see Fig. 4). To illustrate such a scenario we have plotted in Fig. 12 experimental excitation energies as a function of spin for the ground-state band (black

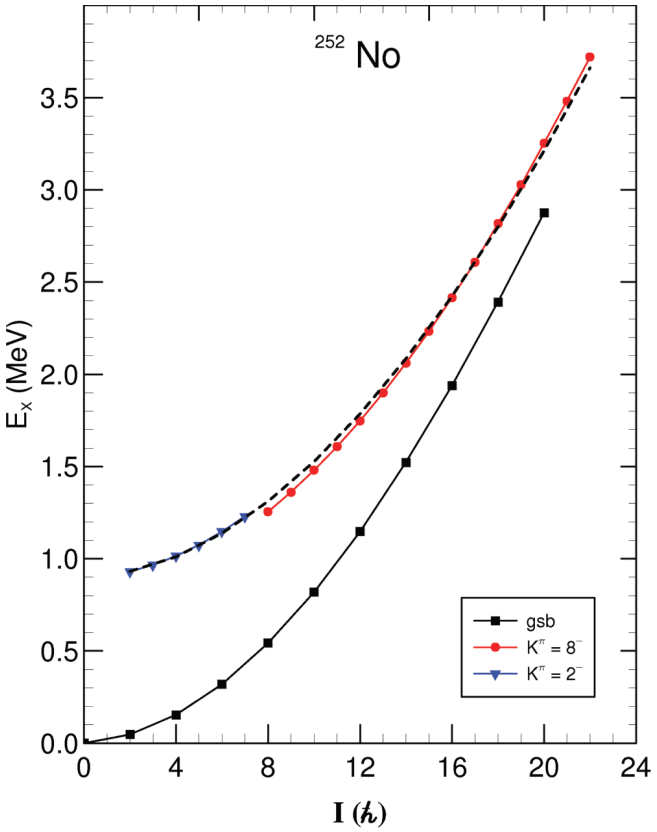

FIG. 12. (Color online) Energy vs spin for the ground-state rotational band (black dots), $K^\pi = 2^-$ excited band (blue triangles), and isomeric rotational band (red dots) for ^{252}No. The dashed line is for an extrapolation of the observed $K^\pi = 2^-$ band to spins higher than $I = 7\hbar$.

squares), the $K^\pi = 8^-$ band (red dots), the $K^\pi = 2^-$ band (blue triangles), as well as a smooth extrapolation of this latter band to spins higher than $I = 8\hbar$ (dashed line). As can be seen, the dashed curve crosses the red curve in the vicinity of the spin value $I = 17\hbar$, which is close to the rotational frequency $\hbar\omega \sim 0.19$ MeV where the shallow minima in the $\mathcal{J}^{(2)}$ values is observed. Due to the lack of statistics and to hindered feeding, the higher frequency portion of the $K^\pi = 2^-$ band is not observed. It is therefore impossible to check whether this band would display a bump in $\mathcal{J}^{(2)}$ values at approximately the same frequency where $\mathcal{J}^{(2)}$ values of the $K^\pi = 8^-$ band are showing a bump. One should remember also that the $K^\pi = 2^-$ band is observed at low spin because it is fed by a decay-out branch of the $K^\pi = 8^-$ level. If the assumption of band crossing holds correct, the observed $K^\pi = 8^-$ band crosses the $K^\pi = 2^-$ band at $\hbar\omega \sim 0.19$ MeV, and the band configurations will get exchanged: the $K^\pi = 2^-$ configuration becomes energetically favored and preferentially fed at higher frequencies. Such an interpretation holds too for the excited bands in ^{250}Fm where the crossing takes place at slightly different spin and frequency, namely, $I \sim 16\hbar$ and $\hbar\omega \sim 0.21$ MeV. Although K is no longer a good quantum number at higher spins, our scenario would require almost degenerate unperturbed states. Hence the suggested scenario will remain tentative until new data collected in higher statistic measurements are available.

3. Discussion

The presence of side bands with spin and parity 2^- seems to be a common feature in $N = 150$ isotones (e.g., ^{252}No, ^{250}Fm [20], ^{248}Cf [19], and ^{246}Cm [16,18]). The similar and low excitation energy ($E_x \sim 1$ MeV) of the $K^\pi = 2^-$ bandhead level suggests a collective character (namely, octupole correlations). On the theoretical side, structure models are predicting $\pi = -$ levels at low excitation energy for this mass region [24,55]. Within the RPA the low-energy $K^\pi = 2^-$ level is calculated for ^{252}No at $E_x = 0.998$ MeV [24], close to the experimental value. This study did not provide the major components of the $K^\pi = 2^-$ state wave function. Such structure information is available for ^{246}Cm, another $N = 150$ isotone, for which the two-neutron $9/2^-[734]_\nu \otimes 5/2^+[622]_\nu$ and two-proton $3/2^-[521]_\pi \otimes 7/2^+[633]_\pi$ quasiparticle excitations form the dominant components of the lowest $K^\pi = 2^-$ state [55]. More recently, projected shell-model calculations performed for $N = 150$ isotones (including ^{252}No) have focused on nonaxial octupole correlations [56]. It is interesting to note that the excitation energy range $E_x \sim 2.7$–3.2 MeV for states with spins from $I^\pi = 16^-$ to $I^\pi = 18^-$ in the calculated $K^\pi = 2^-$ band of ^{252}No is in qualitative agreement with the energy $E_x \sim 2.7$ MeV where crossing between the $K^\pi = 2^-$ and $K^\pi = 8^-$ bands is expected to occur (see Fig. 12).

Obviously, the next generation of HFB calculation in the rotating frame would consist in breaking time-reversal symmetry, z-signature, as well as left-right symmetry. This task is beyond the scope of the present work.

If the interpretation as an octupole character for the $K^\pi = 2^-$ band and interpretation of the band crossing are correct, it would induce an interesting feature at high angular momentum. The $K^\pi = 0^-$ octupole vibration predicted close to the $K^\pi = 2^-$ component [24] contains only the $\alpha = 1$ signature sequence. The Coriolis mixing between $\alpha = 1$ states in $K^\pi = 0^-$ and $K^\pi = 2^-$ bands induces an odd-even signature splitting (see, for instance, [57]). As discussed previously the top of the $K^\pi = 8^-$ isomeric band should mutate to a $K^\pi = 2^-$ character with therefore an odd-even signature splitting feature. Evidence for such a staggering has been found in both ^{250}Fm and ^{252}No but the statistical uncertainties are too large to draw any conclusions. More statistics and/or extension of measurements to higher spins would clarify this assumption and more generally the anomalies in the moments of inertia.

V. SUMMARY AND CONCLUSION

In this paper we reported on a detailed investigation of nonyrast states in ^{252}No. In-beam γ-ray spectroscopy was performed at the University of Jyväskylä using the recoil-decay tagging technique, with an emphasis on collective states built on the two-quasiparticle $K^\pi = 8^-$ isomer. The study of this rotational band and decay toward the ground state provides valuable information on the single-particle structure, collectivity, and K isomerism. The large reduced hindrance factor and the strong stability of the rotational band support high purity of the K isomeric state, which persists with increasing rotational frequency. The single-particle configuration component in the $K^\pi = 8^-$ level is probed by the interband $M1$ and intraband $E2$ experimental γ-ray intensity ratios that provide an indirect measurement of the g_K gyromagnetic factor. As deduced from the data a two-quasiparticle neutron state $7/2^+[624]_\nu \otimes 9/2^-[734]_\nu$ is suggested for the $K^\pi = 8^-$ band. The $K^\pi = 8^-$ isomers in other $N = 150$ isotones with lower masses, i.e., ^{246}Cm, ^{248}Cf, and ^{250}Fm, are thought to be built on the same two-neutron configuration.

The $\mathcal{J}^{(2)}$ values inferred from γ-ray measurements for the ^{252}No and ^{250}Fm $K^\pi = 8^-$ bands were compared with HFB calculations in the rotating frame that break time-reversal and z-signature self-consistent symmetries. A good overall agreement between measurements and calculations is obtained for bandhead energies and moments of inertia. However, the calculations failed in reproducing $\mathcal{J}^{(2)}$ values which display a shallow minimum observed at frequency $\hbar\omega \sim 0.18$–0.22 MeV for ^{252}No. This feature is tentatively interpreted as a crossing between the $K^\pi = 8^-$ and $K^\pi = 2^-$ bands, the latter band not being observed for spins beyond $I = 7\hbar$. We do not exclude the possibility that the $K^\pi = 8^-$ band might instead cross another unobserved band. Measurements with higher statistics would be a valuable asset to clarify the issue. The systematic occurrence of low-energy $K^\pi = 2^-$ excitations in $N = 150$ isotones is strongly suggestive of octupole correlations. Such correlations are ignored in the present microscopic model. However, they could be handled by breaking one more self-consistent symmetry, namely, the left-right symmetry. The hope is that extended cranking HFB calculations would (i) shed light on the interpretation of irregularity observed in the $\mathcal{J}^{(2)}$ moment of inertia of the $K^\pi = 8^-$ band at frequency $\hbar \approx 0.18$–0.22 MeV and (ii) provide a guide to infer quantum numbers of the quasiparticle components of the $\pi = -$ crossing band. Such calculations are under consideration. It would also be a valuable task to challenge predictions based on quasiparticle random phase approximation (QRPA) calculations [58], provided that the theory is extended to the rotating frame. Such an approach proved successful previously for the interpretation of back-bending phenomena observed in $\pi = -$ superdeformed bands of Hg isotopes [59,60]. Running QRPA calculations in the rotating frame with the D1S force as sole input would be a formidable task that most likely is manageable with the availability of algorithms and computers of the next generation.

Finally, it would be interesting to extend the present measurement of $K^\pi = 8^-$ band at high spin in other $N = 150$ isotones, e.g., ^{246}Cm and ^{248}Cf, and obviously in the heavier ^{254}Rf nuclide. Extension of the $K^\pi = 8^-$ rotational bands in ^{250}Fm and ^{252}No to spins higher than $I^\pi = 22^-$ would also help to clarify the anomalies in the moment of inertia.

ACKNOWLEDGMENTS

We thank the accelerator staff at the University of Jyväkylä for the excellent performance of the ion source and accelerator. H. Goutte is acknowledged for involvement in developing the cranking HFB code. This work has been supported by the EU-FP6-I3 Project EURONS No. 506065, the Academy of Finland [CoE Nuclear and Accelerator Based Physics Programme at JYFL, grants to PTG (111965) and CS (209430)], the EC "Marie Curie Actions grant," the UK STFC, and the US

Department of Energy (Contract No. DE- AC02-06CH11357). MV appreciates support from the Slovak grant agency VEGA (Contract No. 2/0105/11). SA was supported by the Slovak Research and Development Agency Contract No. APVV-0105-10 and VEGA Contract No. 1/0613/11. We thank the UK-France (STFC/IN2P3) Loanpool and the GAMMAPOOL European Spectroscopy Resource for the loan of detectors for JUROGAM. This work has benefited from the use of TNT2 cards, developed and financed by CNRS/IN2P3 for the GABRIELA project.

[1] R.-D. Herzberg and P. T. Greenlees, Prog. Part. Nucl. Phys. **61**, 674 (2008).
[2] F. R. Xu, E. G. Zhao, R. Wyss, and P. M. Walker, Phys. Rev. Lett. **92**, 252501 (2004).
[3] S. Hofmann *et al.*, Eur. Phys. J. A **10**, 5 (2001).
[4] F. P. Heßberger *et al.*, Eur. Phys. J. A **43**, 55 (2010).
[5] D. Peterson *et al.*, Phys. Rev. C **74**, 014316 (2006).
[6] P. M. Walker and G. D. Dracoulis, Hyperfine Interact. **135**, 83 (2001).
[7] P. Chowdhury *et al.*, in Proceedings of the DAE Symp. on Nucl. Phys. **55**, 13 (2010), www.sympnp.org/proceedings.
[8] R.-D. Herzberg and D. M. Cox, Radiochim. Acta **99**, 441 (2011).
[9] A. Sobiczewski and K. Pomorski, Prog. Part. Nucl. Phys. **58**, 292 (2007).
[10] J. F. Berger *et al.*, Nucl. Phys. **685**, 1c (2001).
[11] M. Bender, K. Rutz, P.-G. Reinhard, J. A. Maruhn, and W. Greiner, Phys. Rev. C **60**, 034304 (1999).
[12] A. Ghiorso *et al.*, Phys. Rev. C **7**, 2032 (1973).
[13] R.-D. Herzberg *et al.*, Nature (London) **442**, 896 (2006).
[14] S. K. Tandel *et al.*, Phys. Rev. Lett. **97**, 082502 (2006).
[15] B. Sulignano *et al.*, Eur. Phys. J. A **33**, 327 (2007).
[16] A. P. Robinson *et al.*, Phys. Rev. C **78**, 034308 (2008).
[17] P. Chowdhury *et al.*, in *Proceedings of the 3rd International Conference on Frontiers in Nuclear Structure, Astrophysics, and Reactions: FINUSTAR 3, Rhodes, Greece*, edited by P. Demetriou, R. Julin, and S. Harissopulos, AIP Conf. Proc. 1377 (AIP, Melville, NY, 2010), pp. 13–17.
[18] L. G. Multhauf *et al.*, Phys. Rev. C **3**, 1338 (1971).
[19] K. Katori, I. Ahmad, and A. M. Friedman, Phys. Rev. C **78**, 014301 (2008).
[20] P. T. Greenlees *et al.*, Phys. Rev. C **78**, 021303 (2008).
[21] J. F. Berger, M. Girod, and D. Gogny, Comput. Phys. Commun. **63**, 365 (1991); J. Dechargé and D. Gogny, Phys. Rev. C **21**, 1568 (1980).
[22] J.-P. Delaroche *et al.*, Nucl. Phys. A **771**, 103 (2006).
[23] P. H. Heenen (private communication).
[24] R. V. Jolos, L. A. Malov, N. Yu. Shirikova, and A. V. Sushkov, J. Phys. G **38**, 115103 (2011).
[25] M. Leino *et al.*, Nucl. Instrum. Methods B **99**, 653 (1995).
[26] R. D. Page *et al.*, Nucl. Instrum. Methods B **204**, 634 (2003).
[27] L. Arnold *et al.*, IEEE Trans. Nucl. Sci. **53**, 723 (2006).
[28] I. Lazarus *et al.*, IEEE Trans. Nucl. Sci. **48**, 567 (2001).
[29] P. Rahkila, Nucl. Instrum. Methods Phys. Res. A **595**, 637 (2008).
[30] A.-P. Leppanen *et al.*, Eur. Phys. J. A **28**, 301 (2006).
[31] B. Sulignano, Ph.D. thesis, University of Mainz, 2007.
[32] N. Nica, Nucl. Data Sheets **106**, 813 (2005).
[33] G. D. Jones, Nucl. Instrum. Methods Phys. Res. A **488**, 471 (2002).
[34] K.-H. Schmidt *et al.*, Eur. Phys. J. A **8**, 141 (2000).
[35] H. Bartsch, K. Huber, U. Kneissl, and H. Sattler, Nucl. Instrum. Methods **121**, 185 (1974).
[36] S. Antalic *et al.*, Eur. Phys. J. A **47**, 301 (2011).
[37] R.-D. Herzberg *et al.*, Phys. Rev. C **65**, 014303 (2001).
[38] J. A. Becker *et al.*, Phys. Rev. C **41**, R9 (1990).
[39] J. E. Draper *et al.*, Phys. Rev. C **42**, R1791 (1990).
[40] S. M. Harris, Phys. Rev. **138**, B509 (1965).
[41] C. S. Wu, J. Y. Zeng, Z. Xing, X. Q. Chen, and J. Meng, Phys. Rev. C **45**, 261 (1992).
[42] S. Cwiok *et al.*, Comput. Phys. Commun. **46**, 379 (1987); W. Nazarewicz, J. Dudek, R. Bengtsson, T. Bengtsson, and I. Ragnarsson, Nucl. Phys. A **435**, 397 (1985).
[43] C. J. Gallagher, Phys. Rev. **126**, 1525 (1962).
[44] A. Bohr and B. R. Mottelson, *Nuclear Structure*, Vol. II (Benjamin, New York, 1969).
[45] E. Parr *et al.*, Eur. Phys. J. A (to be published).
[46] K. E. G. Löbner, Phys. Lett. B **26**, 369 (1968).
[47] U. Shirwadkar *et al.* (private communication); U. Shirwadkar, Ph.D. thesis, University of Massachusetts Lowell, 2009.
[48] A. V. Afanasjev, T. L. Khoo, S. Frauendorf, G. A. Lalazissis, and I. Ahmad, Phys. Rev. C **67**, 024309 (2003).
[49] M. Bender, P. Bonche, T. Duguet, and P.-H. Heenen, Nucl. Phys. A **723**, 354 (2003).
[50] M. Girod, J. P. Delaroche, J. F. Berger, and J. Libert, Phys. Lett. B **325**, 1 (1994).
[51] H. Dancer, Ph.D. thesis, Lyon 1, 2000, http://hola.univ-lyon1.fr/.
[52] L. D. Landau, Phys. Z. Sowjetunion **1**, 88 (1932); **2**, 46 (1932) [English translation in *Collected Papers of L. D. Landau* (Pergamon, New York, 1965)]; C. Zener, Proc. R. Soc. London A **137**, 696 (1932).
[53] B. Singh, R. Zywina, and R. B. Firestone, Nucl. Data Sheets **97**, 241 (2002).
[54] S. W. Yates *et al.*, Phys. Rev. C **12**, 442 (1975).
[55] V. G. Soloviev and T. Siklos, Nucl. Phys. **59**, 145 (1964).
[56] Y.-S. Chen, Y. Sun, and Z.-C. Gao, Phys. Rev. C **77**, 061305 (2008).
[57] R. F. Casten, W.-T. Chou, and N. V. Zamfir, Nucl. Phys. A **555**, 563 (1993).
[58] S. Peru, G. Gosselin, M. Martini, M. Dupuis, S. Hilaire, and J.-C. Devaux, Phys. Rev. C **83**, 014314 (2011).
[59] T. Nakatsukasa, K. Matsuyanagi, S. Mizutori, and Y. R. Shimizu, Phys. Rev. C **53**, 2213 (1996).
[60] J. Kvasil, N. Lo Iudice, F. Andreozzi, F. Knapp, and A. Porrino, Phys. Rev. C **75**, 034306 (2007).

7.5 Musett: A segmented Si array for Recoil-Decay-Tagging studies at VAMOS

Nuclear Instruments and Methods in Physics Research A 747 (2014) 69–80

Contents lists available at ScienceDirect

Nuclear Instruments and Methods in Physics Research A

journal homepage: www.elsevier.com/locate/nima

Musett: A segmented Si array for Recoil-Decay-Tagging studies at VAMOS

Ch. Theisen [a,*], F. Jeanneau [a], B. Sulignano [a], F. Druillole [a], J. Ljungvall [b], B. Paul [a], E. Virique [a], P. Baron [a], H. Bervas [a], E. Clément [c], E. Delagnes [a], A. Dijon [c,1], E. Dossat [a], A. Drouart [a], F. Farget [c], Ch. Flouzat [a], G. De France [c], A. Görgen [a,2], Ch. Houarner [c], B. Jacquot [c], W. Korten [a], G. Lebertre [c], B. Lecornu [c], L. Legeard [c], A. Lermitage [d], S. Lhenoret [a], C. Marry [c], C. Maugeais [c], L. Menager [c], O. Meunier [a], A. Navin [c], F. Nizery [a], A. Obertelli [a], E. Rauly [d], B. Raine [c], M. Rejmund [c], J. Ropert [c], F. Saillant [c], H. Savajols [c], Ch. Schmitt [c], M. Tripon [c], E. Wanlin [d], G. Wittwer [c]

[a] CEA, Centre de Saclay, IRFU, F-91191 Gif-sur-Yvette, France
[b] CSNSM, F-91405 Orsay Campus, France
[c] GANIL, Boulevard Henri Becquerel, BP 55027 – F-14076 CAEN Cedex 05, France
[d] IPNO, 15 rue Georges Clémenceau, F-91406 Orsay, France

ARTICLE INFO

Article history:
Received 18 July 2013
Received in revised form
6 February 2014
Accepted 6 February 2014
Available online 17 February 2014

Keywords:
Recoil separator
Alpha spectroscopy
Silicon detector
Recoil decay tagging
Wien filter

ABSTRACT

A new segmented silicon-array called MUSETT has been built for the study of heavy elements using the Recoil-Decay-Tagging technique. MUSETT is located at the focal plane of the VAMOS spectrometer at GANIL and is used in conjunction with a γ-ray array at the target position. This paper describes the device, which consists of four 10×10 cm^2 Si detectors and its associated front-end electronics based on highly integrated ASICs electronics. The triggerless readout electronics, the data acquisition and the analysis tools developed for its characterization are presented. This device was commissioned at GANIL with the EXOGAM γ-ray spectrometer using the fusion–evaporation reaction ^{197}Au(^{22}Ne,5n)^{214}Ac. Additionally, the performance of the VAMOS Wien filter used during the in-beam commissioning is also reported.

1. Introduction

The study of the heaviest elements having extreme mass and charge is a major topic in nuclear physics. These elements are artificially produced using fusion–evaporation reactions and suffer from low production cross-sections, which decrease dramatically with atomic number. While decay studies have been performed for decades, prompt γ-ray or conversion-electron spectroscopy of transfermium elements (atomic number larger than 100) is more difficult and the associated challenges have been overcome since 1998, with the pioneering study of ^{254}No at the Argonne National Laboratory (USA) and at the University of Jyväskylä, Finland (see Ref. [1] for a recent review).

These studies require highly efficient and selective devices to detect and unambiguously identify the rare isotopes produced in an overwhelming background of unwanted reactions. The optical elements of a zero degree separator or spectrometer provide the basic selection needed. Since the rejection of projectiles and parasitic reactions is never ideal, the focal plane (FP) detection setup provides the additional identification of the transmitted reaction products. Prompt spectroscopy experiments are possible thanks to the Recoil-Tagging (RT) and Recoil-Decay-Tagging (RDT) techniques [2]. In the former case, the prompt transitions emitted around the target are filtered when a recoil having the expected characteristics (for instance energy, Time-of-Flight (ToF), energy loss, etc.) is identified at the FP of the spectrometer/separator. The RDT technique provides an additional and in most cases univocal identification, exploiting the decay characteristics of implanted nuclei. This technique uses time and position correlations between the implanted nuclei and its subsequent decays (e.g. α-decay).

At GANIL, the VAMOS (VAriable MOde Spectrometer) high acceptance ray-tracing spectrometer was initially designed for the study of exotic nuclei produced with SPIRAL1 radioactive

* Corresponding author.
E-mail address: christophe.theisen@cea.fr (Ch. Theisen).
[1] Present address: CEA Bruyères-le-Châtel, DIF/DPTA/SPN, F-91297 Arpajon, France.
[2] Present address: Department of Physics, University of Oslo, Oslo, Norway.

http://dx.doi.org/10.1016/j.nima.2014.02.016
0168-9002

beams, for a wide range of reactions such as transfer or deep-inelastic [3–5]. A zero degree operation for fusion–evaporation reaction studies was not a primary focus of VAMOS. However, a separation between the fusion–evaporation residues and the direct beam can be obtained either with its Wien Filter (WF), or in a gas-filled mode [6].

VAMOS can be coupled to the prompt γ-ray spectrometer EXOGAM [7,8]. EXOGAM is made of germanium clover detectors assembled in a close geometry around the target. The 12-clover configuration compatible with VAMOS provides a large efficiency of ~11% at 1.33 MeV, and is ideal for detecting medium-spin cascades emitted by heavy nuclei. In the near future the coupling with the γ-tracking array AGATA [9] will provide a further increase in efficiency and sensitivity. The coupling of EXOGAM and AGATA scheduled in 2014–2016 is expected to reach a photopeak efficiency of ~15% at 1.33 MeV along with an improved Doppler correction. The VAMOS zero degree mode combined with EXOGAM/AGATA will be suited and efficient for spectroscopic studies using fusion–evaporation reactions. A series of in-beam tests have been consequently conducted to characterize VAMOS for RT and RDT studies.

A first test of VAMOS as a zero degree separator was performed using the reaction ^{208}Pb(^{18}O, $3-4n$) $^{222-223}$Th. The α decay of ^{223,223}Th and their daughters could be measured. The known level scheme of the ^{222}Th octupole band could be built using γ–γ coincidences.

A second characterization of VAMOS and its WF was performed, using the idea[3] to direct the beam "straight through" thus allowing a better control of the beam (see details in Section 4.2). During this test the transmission for the fusion–evaporation reaction ^{197}Au(^{22}Ne, $5n$)^{214}Ac was measured.

In parallel, the VAMOS gas-filled mode was successfully tested [6]. Unprecedented transmissions have been deduced for the ^{40}Ca+^{152}Sm reaction (80% for α *xn* and above 95% for *xn yp* channels).

Finally, the FP array MUSETT (*MUr de Silicium pour l'Etude des Transfermiens par Tagging* - Silicon wall for the study of transfermium by tagging) segmented Si wall built for RDT studies at VAMOS was commissioned. The segmented Si wall and its new electronics and data acquisition system were tested at VAMOS (using the WF mode) coupled to EXOGAM using mainly the ^{197}Au (^{22}Ne, $5n$)^{214}Ac reaction.

This article describes the technical aspects of the MUSETT Si wall and the results of the in-beam commissioning. It is organized as follows: MUSETT is described in the next section. The test-bench and characterization are then detailed in Section 3. Section 4 is devoted to the in-beam commissioning, including the performance of the VAMOS WF. Finally, a summary and perspectives are given in Section 5. Supplementary material related to this article can be found online.

2. The MUSETT Si array

2.1. Specifications and constraints

MUSETT is originally designed for the VAMOS FP and has therefore to be adapted as much as possible to its ion optics, which is dispersive in the horizontal plane. Since the fusion–evaporation residues produced in the most asymmetric reactions carry low kinetic energy (typically 0.05 MeV/A or less), the implantation depth is shallow (a few μm). The dead layer at the entrance of the detector should therefore be minimized. As mentioned earlier, using the RDT technique requires energy, time and position measurement of the recoil and its subsequent decay. This is usually achieved using Double-sided Silicon Strip Detectors (DSSDs).

The large number of electronics channels required (for about 1000 strips) rules-out the choice of Font-End Electronics (FEE) preamplifiers using discrete components not only because of the volume constraints, but also due to the large number of corresponding feedthroughs. ASICs with multiplexed output are the only viable solution.

The energy resolution is a critical requirement and is necessary to resolve α-decay fine structures (i.e. better than 1%). On the other hand, the time resolution is not a critical issue in the present application. In the case of RDT experiments, the electronic deadtime is not only constrained by the average detection rate (typically a maximum of a few kHz) but a more severe constraint is related to the minimum lifetime of the nuclear states of interest. We would like to measure the times between the implantation and subsequent decay in the same detector element as low as few tens of μs. In the case of RDT experiments, events separated by long periods of time, up to minutes or more need to be correlated in time. This can be achieved using a universal clock.

It should be pointed out that the above-mentioned specifications overlap to a large extend with that of the MUST II array [10] designed mainly for direct reaction studies at GANIL. MUSETT capitalized extensively on the MUST II developments.

2.2. Technical description

We present below the silicon detectors and their FEE. The infrastructure needed and the integration performed to operate the detector modules is then described.

2.2.1. Si detectors

The MUSETT silicon array is made of four modules of ~10 × 10 cm^2 each, to obtain a total detection area of ~40 × 10 cm^2, which covers the recoil implantation profile in both VAMOS WF and gas-filled modes. The detectors are to a large extent based on the MUST II detectors with substantial improvements to cope with the implantation and detection of very heavy nuclei and their subsequent decay.

Each n-type, DC coupled DSSD is 300 μm thick and has 128 strips on each side (*X*-*Y* readout) : see Fig. 1. The crystal orientation is ⟨100⟩. *X* (*Y*) strips correspond to the front junction (back ohmic) side of the detector. Particles enter the detector from the junction side. The junction p+ implantation is made of a shallow Boron implantation of less than 0.25 μm (typically 0.1 μm). The front side segmentation is made with an aluminium contact grid 3000 Å thick whose total area is of 2.73% coverage only. There is no other metallic or oxide layer on the front side in order to reduce the energy loss for the incoming heavy nuclei. On the back ohmic side, the contacts consist of Al strips. The strip width on both sides is 700 μm with a pitch of 760 μm. The strip separation (interstrip) is therefore 60 μm. The thickness of the SiO_2 layer between the p+ front strips is 1 μm. The isolation between the n+ back strips is made with p-stop structures. The strip length is 97.220 mm for each side. The Si detector is mounted on a 2.4 mm epoxy (FR4) printed circuit board. The guard rings are kept floating. The Si detectors were provided by Micron Semiconductors, UK [13] and are known as "TTT3 design" in the catalogue.

The high voltage (negative) is applied on the front junction face of the Si detectors, which is therefore AC coupled to the FEE through polarization circuits. The depletion voltage of all detectors is less than −60 V for which the leakage current does not exceed 1 μA at room temperature for a new detector. Fig. 2 shows examples of capacitance as a function of the bias voltage (courtesy of Micron Semiconductors). A typical value is ~4 nF above the

[3] Suggested by M.R.

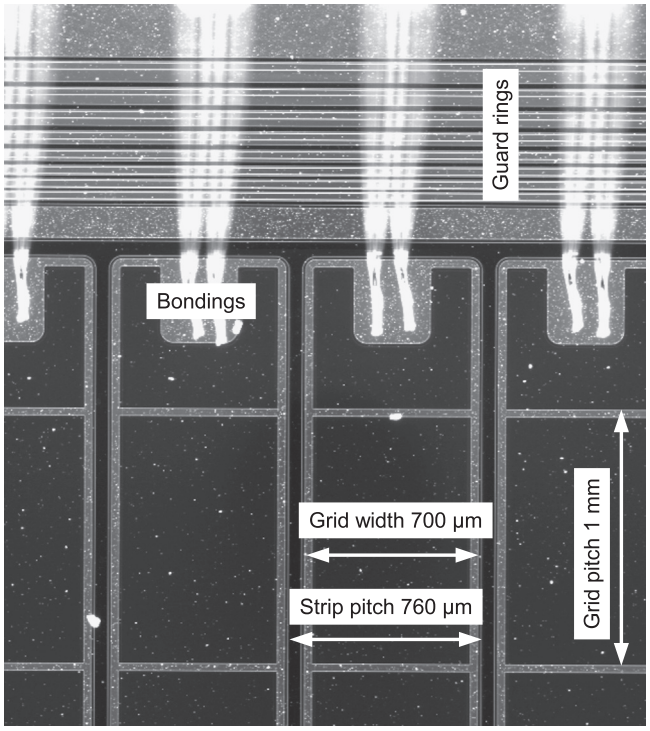

Fig. 1. Close view of the front p+ face (*X* strips) of a MUSETT DSSD taken with a microscope.

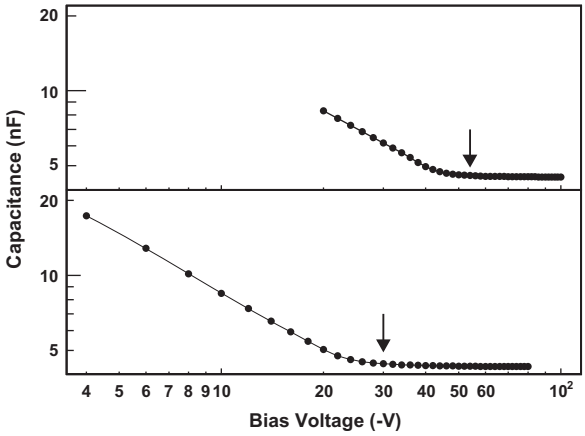

Fig. 2. Capacitance as a function of the bias voltage for two MUSETT detectors having a depletion voltage of −54 V (serial number 2577-10, top) and −30 V (serial number 2501-16, bottom). Arrows indicate the nominal depletion voltages. Results provided by Micron Semiconductors [13].

depletion voltage. Fig. 3 shows examples of leakage currents as a function of the bias voltage measured for different temperatures.

2.2.2. *ATHED ASICs and COFEE board*

Given the high number of electronics channels needed and the space constraints, highly integrated ASICs electronics have been used. The ATHED chip (ASICs for Time and High Energy Deposit) is the latest version of the MATE chip [12] developed for the MUST II project. The ASICs that operate 16 strips are grouped by 4 units on the COFEE[4] mother boards (designed by IPN Orsay), which provide

[4] COFEE stands for COulex Front-End Electronics; besides MUSETT, one of our goals is to use this multipurpose electronics with annular Si detectors for Coulomb excitation studies.

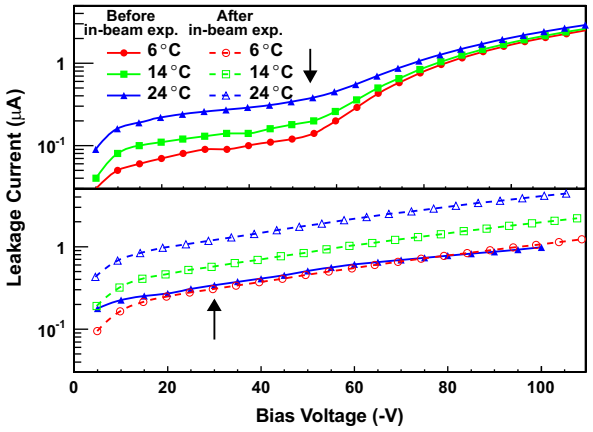

Fig. 3. Leakage current as a function of the bias voltage for two MUSETT detectors (the same detectors as in Fig. 2: serial number 2577-10 on the top, serial number 2501-16 on the bottom) for three different temperatures. The measurement for detector 2501-16 was performed before and after an in-beam measurement (fluence of approximately 10^6 heavy-ions/cm^2, mainly ^{22}Ne ions in the energy range 10–110 MeV). Arrows indicate the nominal depletion voltages.

the power supply, input/output and slow control interfaces. Consequently, four COFEE boards are needed to operate a DSSD.

ATHED delivers three types of analogue information per channel: time, energy and the leakage DC detector current (see Fig. 4). ATHED also gives a trigger logic signal corresponding to the cross-over above an adjustable threshold value.

The first stage is a Charge Sensitive Amplifier (CSA), based on a single-ended folded cascode architecture designed to convert both polarities (for both sides of the DSSD) of the input signal. The Rf specific block in parallel to the feedback capacitor Cf defines the value of a 60 MΩ equivalent feedback resistor, and the DC voltage level of the amplifier output. Four different values of the feedback capacitance can be selected, leading to different energy ranges. The most used ranges are ±45 MeV (Cf = 2.6 pF) and ±0.5 GeV (Cf = 27.6 pF). The output signal is processed in two separate blocks: energy and timing. The energy stage is composed of a CR-RC filter with two different possible values of the peaking time (1 or 3 μs). The amplitude of the shaped signal is memorized on the external hold signal managed by the readout card, via a track and hold stage.

The timing stage incorporates a fast shaper, a discriminator and a Time to Amplitude Converter (TAC). The shaper has a differential structure, with a CR-RC filter for a 22 ns peaking time. The threshold voltage is given by an internal 8 bit programmable Digital to Amplitude Converter, common to the 16 channels. The discriminator output delivers the start signal to the TAC. The OR between the 16 individual start signals alerts the readout card that an event has been detected. The TAC is stopped by an external stop signal. Two TAC ranges can be selected: 300 or 600 ns. Any of the 16 channels can be independently inhibited.

In the readout process, the analogue energy and timing information of the 16 channels are multiplexed and transmitted serially at a rate of 2 MHz through a voltage to current converter to the external Analogue to Digital Converter (ADC) inputs (analogue bus, differential signals). The triggering of the ATHED readout is common to the COFEE board (64 channels): all channels are read-out if any of the channels initiated the sequence (request mode). It is also possible to trigger the read-out by an external source, namely the readout electronics without any discriminator response. This so-called "Trig event" mode is used e.g. in pedestal calibration, leakage current measurement, and detection chain characterization. The slow control of ATHED is defined and carried on a standard serial I2C bus. ATHED is manufactured using the AMS BICMOS 0.8 μm technology. The die area is 42 mm^2 for a number of ~16,000 transistors.

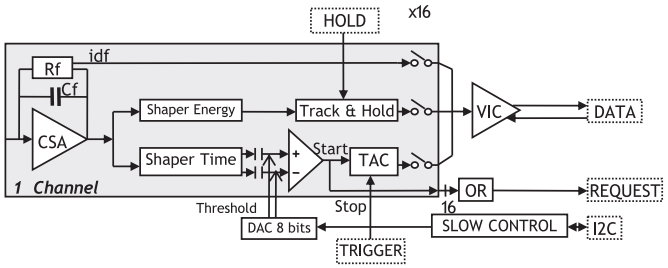

Fig. 4. Schematic view of ATHED.

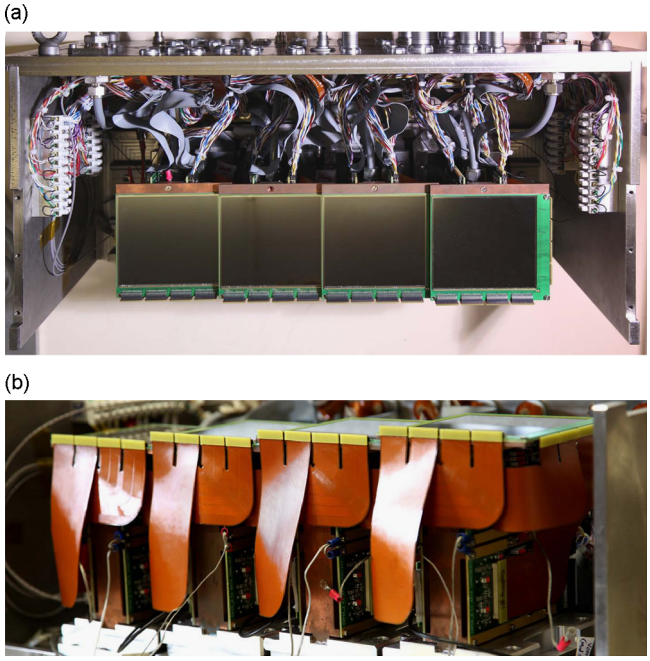

Fig. 5. (a) Picture of the MUSETT silicon array consisting of 65,536 pixels with the cabling for the slow control, voltages and acquisition signals. (b) View of the tile structure with kapton cables, the electronics and the copper cooling structures.

The slow control of each ASIC also allows controlling a multiplexer, selecting the inspection line of a channel, and controlling an internal generator to test all inputs from the ASICs. Each ASIC is read out on a separate analogue bus to reduce the transfer time to 16 μs. Since only the junction side of the Si detector is biased, only two of the four COFEE boards need to be AC coupled to the detector. This function is realized with daughter board polarization circuits. The value of the coupling capacitances is 10 nF. In the Saclay test bench environment, each COFEE board is connected to a CVM card to manage the configuration and the data, while in the GANIL environment, four COFEE boards are connected to a MUVI VXI card (see Sections 3.1.1 and 4.1).

2.2.3. Detector module and integration

The Si wall has been designed as a set of four identical detector modules (see Fig. 5). The idea of identical detector modules is to simplify the wall integration and to have interchangeable modules. All modules include the components needed to operate the Si detector: the FEE, the connectors, the mechanics, etc. The frame of a module is made of a copper structure in which a cooling fluid circulates to dissipate the ASICs power and to keep it at a constant temperature. The Si detector performance also improves due to the cooling. The connection between the detector and the COFEE electronics is made by kapton flex cables (see Fig. 5). In order to reduce the dead zones (Si detector printed circuit board), the detectors are arranged in a tile geometry.

2.2.4. Infrastructure of the Si array

The MUSETT array needs to be as far as possible remotely controlled since access to the experimental room is not possible during in-beam experiments. The high and low voltages are provided by a CAEN [11] SY 2527 system. The COFEE FEE require 5 low voltage lines (± 2.5 V, ± 5 V, $+3.3$ V) supplied by four CAEN floating low voltage A1517B and A1518B boards. These boards provide the voltage stability using remote sensing lines. The high voltage is supplied by a A1837N CAEN module. A LAUDA low-temperature thermostat RP845 [14] is used for the detectors and FEE cooling. The WINTHERM® Plus software [15] is used to control and monitor the cooling system.

3. Characterization

This section describes the environment developed to characterize the Si detector modules. Besides the FEE described previously in Section 2.2.2, the test bench (Section 3.1) installed at Saclay using VME electronics (Section 3.1.1) with its DAQ system (Section 3.1.2) is described. Analysis procedures and examples of detector characterization are given in subsections 3.1.3 and 3.2.

3.1. Test bench

3.1.1. Readout: the CVM boards

The CVM board "*Carte VME Multi-Application*" (multi-application VME Board) has been designed as a multipurpose and "light" electronics for characterization, integration or eventually in-beam experiments. The idea is to have a unique hardware but different firmwares adapted to the various operating modes.

The architecture of the laboratory test bench is sketched in Fig. 6. One MUSETT module is read-out by 4 COFEE boards each including 4 ATHED. Each COFEE board is controlled and acquired by one CVM board. Hence, the full MUSETT test bench is made of four slave CVM boards plus one CVM board in the VME master mode. A common trigger is not used, therefore the four CVM slave cards acquire data independently. A windows-based PC controls the entire system through the USB interface of the CVM master card, namely the STUC ("*Sonde de Test USB Configurable*" - Configurable USB Test Probe) generic USB daughter card interface.

A CVM is connected to the four serial analogue buses and digitizes the energy and time information from each ASIC. The most complex function on the board consists of four 14 bit ADC channels corresponding to the 4 ASICs analogue bus of a COFEE board. After digitization at a 2 MHz rate (16 μs for the 16 energy and time amplitudes), CVM data are pushed into a FIFO.

Data are time-stamped using a common 48 bit 50 MHz clock. The CVM master VME interface is connected to the PC via the USB link; it interfaces with the slave modules, which communicate with the master board through the VME bus.

3.1.2. DAQ

To control the CVM system, a data acquisition system has been developed using a client/server architecture: see Fig. 7. The experiment control and monitoring is made using the LabVIEW [16] framework. It includes the hardware slow control (CVM, COFEE, ATHED) and the monitoring part of the data flow. The data communication is made through a daemon server that waits for the LabVIEW client requests, and converts the commands into USB functions for the hardware configuration.

The multithread daemon also handles the data flow. It scans whether the CVM slave boards have available data in their FIFO

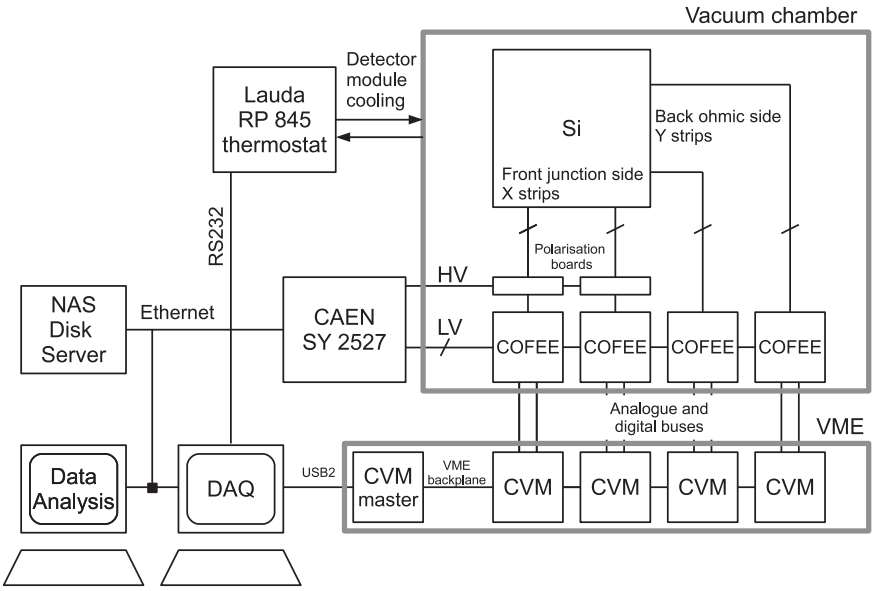

Fig. 6. Layout of the MUSETT test bench.

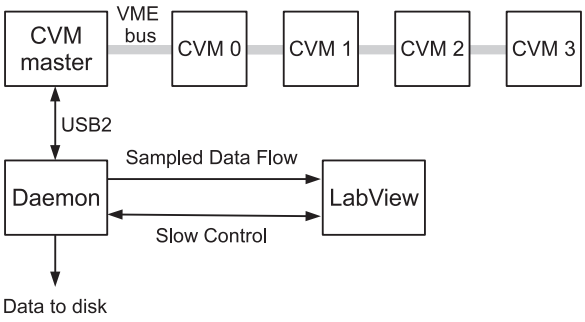

Fig. 7. Test bench DAQ architecture.

and if so, initiates a direct memory access sequence to read out the data. An event corresponds, at this level, to the digitized signals from 64 strips with its associated time-stamp. Part of the data flow can be sent to the LabVIEW program for monitoring.

3.1.3. Data analysis

Data analysis tools have been developed on linux using the ROOT [17] framework. The analysis is performed in different steps using as an initial input the data provided by the DAQ: raw data decoding, pedestal calibration, time ordering, α calibration, gain matching, and event building. Since the number of detector channels is relatively large, automatic procedures have been implemented for pedestal alignment, α calibration, data quality diagnostics, etc. Since the four CVM slave boards are triggerless, an event-builder based on time correlations has been implemented. Diagnostics are also provided to characterize the system e.g. missing channels, anomalous pedestal or width of an α peak. Examples of detector performance resulting from the data analysis are given in the next section.

3.2. Detector performance

We summarize in this section the representative characteristics of the detectors and electronics using the Saclay test bench. Measurements for only one detector (serial number 2501-16, depletion voltage $V_{dep} = -30$ V) are presented in this section (other detectors behave in a similar manner). All measurements presented in this section were obtained using the ASICs preamplifier with a feedback capacitance Cf = 2.6 pF ($\pm$45 MeV range). All source measurements were performed in the vacuum at a pressure less than 10^{-5} mbar.

3.2.1. Energy response, noise level

The noise of the whole chain can be evaluated measuring the pedestal width. This measurement is performed using the "trigger mode" i.e. the electronics readout is triggered using a logic pulse generator, without the need of any detector response. Without a detector, the pedestal width is $\sim$1.0 bit rms. With a detector, the value is $\sim$1.2 bits rms with only small changes as a function of temperature (from 6 to 24 °C), bias voltage or peaking time for a fully depleted detector but not over-biased (up to -120 V for the detector presented in this section). Thus, the intrinsic chain resolution is $\sim$20 keV FWHM. The minimum threshold measured at 6 °C with the MUSETT detection chain is $\sim$200 keV ($\sim$300) keV for the X (Y) detector side.

The detector resolution has been measured using a triple α source (^{239}Pu, ^{241}Am, ^{244}Cm) illuminating the junction side. The source was positioned $\sim$10 cm above the detector. Measurements were performed as a function of the temperature, bias voltage, for both 1 and 3 μs peaking times. Again, small variations are observed as a function of the bias voltage (for a given temperature and peaking time) for a fully depleted detector (the parallel noise is negligible). For a very high voltage (or current), not only does the resolution increase because of the parallel noise, but also some strips begin to malfunction with e.g. asymmetric peaks, spurious peaks, and coupling between neighbouring strips.

Table 1 summarizes the resolutions at a bias voltage of $2V_{dep} = -60$ V, T = 6 and 24 °C with 1 and 3 μs peaking times for the ^{244}Cm α energy at 5804.8 keV. In the analysis, the peaks corresponding to the transitions of ^{239}Pu at 5105.5, 5144.3 and 5156.6 keV, of ^{241}Am at 5442.8 and 5485.6 and keV, and of ^{244}Cm at 5762.6 and 5804.8 keV were fitted simultaneously with 7 Gaussian curves. Single spectra were used without any coincidence condition or cut. The X junction side is superior compared to the Y ohmic (back) side. The resolution is better for a peaking time of 3 μs, where the serial noise is lower. This is true only if the detector current is low: when the current is above $\sim$3 μA, the parallel noise increases and becomes the main contribution. In this case, it is better to use a 1 μs peaking time.

Table 1
Resolution obtained at 5804.8 keV for different temperatures and peaking times, at a bias voltage of $2V_{dep} = -60$ V.

Peaking time	$T=24$ °C	$T=6$ °C
$\tau = 1$ μs	$\overline{FWHM}(X) = 41.4$ keV	$\overline{FWHM}(X) = 32.6$ keV
	$\overline{FWHM}(Y) = 44.1$ keV	$\overline{FWHM}(Y) = 34.8$ keV
$\tau = 3$ μs	$\overline{FWHM}(X) = 33.6$ keV	$\overline{FWHM}(X) = 27.3$ keV
	$\overline{FWHM}(Y) = 37.1$ keV	$\overline{FWHM}(Y) = 31.3$ keV

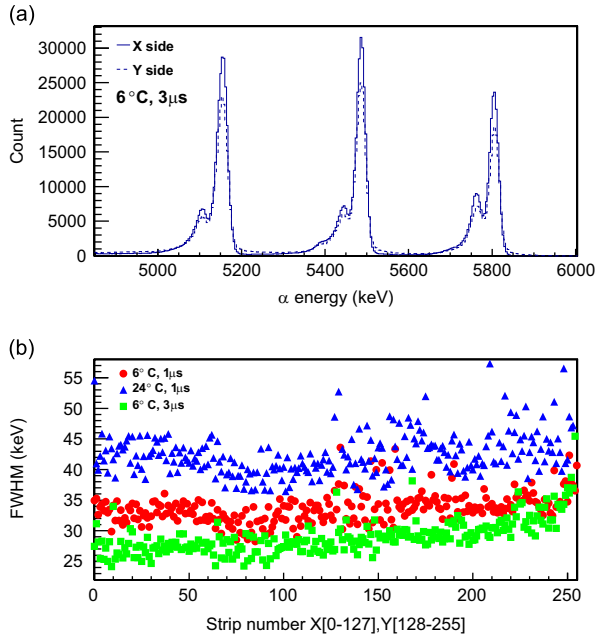

Fig. 8. (a) Example of α spectra. Full (doted) lines correspond to the X (Y) detector side. The measurement was performed at $T=6$ °C and 3 μs peaking time. (b) FWHM strips resolution for the ^{244}Cm peak at 5805 keV. Blue triangles: $T=24$ °C, 1 μs peaking time. Red circles: $T=6$ °C, 1 μs peaking time. Green squares: $T=6$ °C, 3 μs peaking time. All measurements were performed at a bias voltage of $2V_{dep} = -60$ V. (For interpretation of the references to color in this figure caption, the reader is referred to the web version of this article.)

As shown in Fig. 8b a small dispersion between strips is obtained. For a peaking time of 3 μs and at $T=6$ °C, the resolution worsens at one edge of the detector (large Y strip number). This is actually due to the kapton cables, which are the longest for these strips, increasing the capacitance and therefore both $1/f$ and serial noises. This effect is lower when using a 1 μs peaking time and unobservable when the detector current is larger. It is worth noting that all strips perform properly. The total α spectra for both sides ($T=6$ °C, HT=-60 V, $\tau = 3$ μs) are shown in Fig. 8a, where one clearly sees the fine structures of the α decays.

Tests were also performed with a prototype detector from the S3 collaboration (Super Separator Spectrometer [18]). This detector is known as "TTT5" in the Micron Semiconductors catalogue. It is inspired to a large extent from MUSETT with a lower capacitance and lower leakage current. With a peaking time of 3 μs, an average resolution of 25.5 keV is obtained on the X side, while the best strips have a resolution of ~ 22 keV. Detailed results will be reported elsewhere.

3.2.2. Cross-talk

A cross-talk corresponds to the influence of a particular strip on its neighbouring strips and/or neighbouring electronics channels. With the MUSETT FEE, neighbouring strips do not necessarily correspond to neighbouring FEE channels. This dissimilarity between strips and electronics channels was made to facilitate the COFEE card rooting. This feature allows us to disentangle the strips and electronics cross-talk as well as to deduce the cross-talks from α-source measurements.

The electronics cross-talk is found only between a responding channel n and the next one (channel $n+1$) of each ASIC. It is interpreted as a multiplexing residue in the serial analogue bus. In the worst case a value of 0.4% has been measured. Should it be necessary, electronics cross-talk can be corrected off-line. It is important to point-out that the electronics channels n and $n+1$ are not supposed to respond simultaneously in physical events.

The strips cross-talk corresponds to the pedestal shift of the two neighbours of the firing strip. In contrast to the electronics cross-talk, this effect is symmetric and affects equally both neighbours. The strip cross-talk is negligible on the Y ohmic back side, and is measured to be 0.5% of the main amplitude on the X junction front side, which indicates that it is related to the AC coupling mode on the junction side: the collected charge is split between the decoupling and interstrip capacitances. The pedestal shift depends neither on the temperature, nor on the detector, since the detector capacitances are geometric features that do not change significantly as soon as the detector is depleted. Note again the small cross-talk level ($\sim$0.5%). Moreover, it influences neighbours that in most cases do not respond simultaneously, except in the case of interstrip events discussed in the following section.

3.2.3. Interstrip events

When electron–hole pairs are generated in the X or Y interstrip regions, signals can be collected on adjacent strips. The detector response for these events can be visualized using the two dimensional plot ($E1$, $E2$), where $E1$ and $E2$ are the energies detected in the two neighbouring strips: see Fig. 9. Such events have been discussed in several papers e.g. [19–26] as charge carrier sharing and/or trapping in the interstrip SiO_2 region, but with somehow different interpretations or formalisms. Basically, electron–hole pairs are separated by the electric field and consequently move toward the electrodes. The signal amplitude and shape results from the migration of both electrons and holes. The observed interstrip patterns (Fig. 9) result actually from two effects. First, charge carriers can be collected on adjacent electrodes (charge sharing). Second, the front and/or back signals amplitude can be lowered if electrons and/or holes trapping occurs. Charge trapping corresponds to losses close to the Si–SiO_2 interface, resulting from a high-density electron accumulation layer. Details of the trapping and consequences on the signals are given in Ref. [26]. In the following, we outline briefly the main features of interstrip events and their consequences on the data analysis.

On the X side, the plots are characteristic of incomplete charge collection. Region (1) shown in Fig. 9 corresponds to hits near the edge of the interstrip. Holes are collected on the nearest strip, but electrons are partially trapped close to the Si–SiO_2 interface, which reduces the signal on the adjacent X strips by $-\Delta Q_t$ (remember that the total signal results from both holes and electrons moving to the strips). One therefore measures $(Q_{particle} - \Delta Q_t, -\Delta Q_t)$. This region extends in principle up to $(Q_{particle}/2, -Q_{particle}/2)$ when all electrons are trapped. It should be noted that only a fraction of the total energy is measured on the Y side for those events, which corroborates electron trapping. When increasing the bias voltage, the fraction of events in region (1) decreases as shown in Fig. 10, which corresponds to less electron trapping. This trend is also discussed in Ref. [26]. Fig. 10 corresponds to measurements performed at $T=6$ °C and 1 μs peaking time. Counts in the different regions of Fig. 9 were obtained setting 2D gates on the

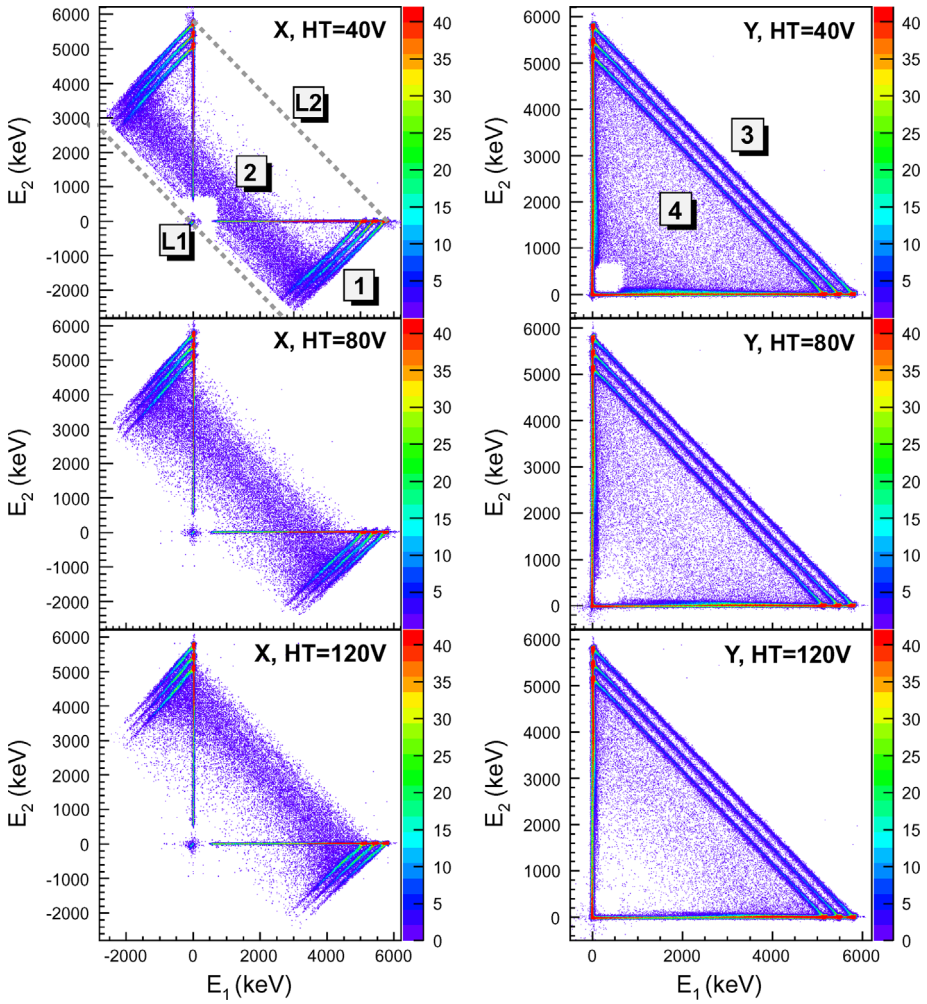

Fig. 9. Interstrip events for the *X* and *Y* side for three different bias voltages. See text for the explanation of the region labels.

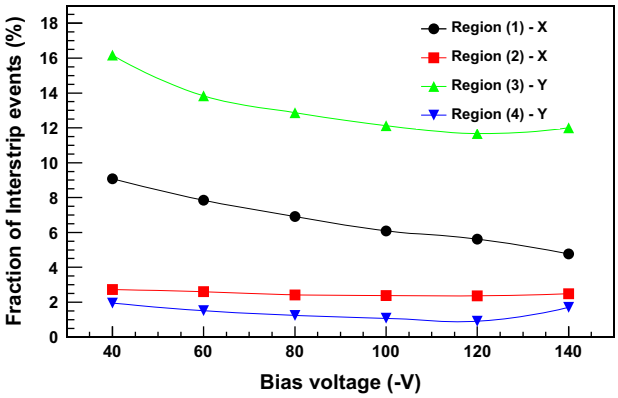

Fig. 10. Fraction of interstrip events. See text for details.

(*E*1, *E*2) plots. Very close figures were obtained at other temperatures or with a 3 μs peaking time.

In Refs. [20,19,22], the L1 or L2 lines were observed and interpreted as hits in the middle of the interstrip. In both L1 and L2 cases, holes diffuse to neighbouring *X* strips (charge sharing) with all electrons moving toward the rear side (L2) or fully trapped in the region of the Si–SiO_2 interface (L1). Note that in Refs. [20,19] only the L1 line is observed, while mainly L2 is observed in Ref. [22]. This can be related to the nature of particles illuminating the interstrip: α particles in the first case and 59.5 keV photons in the second case. The half-thickness for the 59.5 keV photons absorbtion in Si is ∼8 mm therefore electron–hole pairs can be created deeply in the detector without consequent electron trapping. On the contrary, α particles have a range of 25–30 μm therefore electron–hole pairs are created close to the Si–SiO_2 interface with consequently electron trapping prevailing. In the case of MUSETT detectors we are in an intermediate configuration between the L1 and L2 extreme cases (region (2) in Fig. 9) with electrons partially trapped. Region (2) moves towards the L2 line with increasing bias voltage, the fraction of these events being almost constant as a function of the bias voltage (see Fig. 10). Also, the energy is only partially detected on the back side with an average signal increasing as a function of the bias voltage when the number of electrons trapped decreases.

When electrons drift to the ohmic back side, the transverse size of the electrons cloud increases with the depth. Therefore the track can overlap between two strips: the signal is shared between these strips with $E_1+E_2=E_{particle}$ (if the hit did not occur simultaneously in the *X* interstrip region). It corresponds to region (3) in Fig. 9. Charge sharing in silicon strip detectors has been discussed in Ref. [21] considering the diffusion and drift in the electric field. More exhaustive interpretations include the diffusion and drift in the plasma column resulting from the large electron–hole pair concentration: see e.g. Refs. [23,25,24]. As shown in Fig. 10, the fraction of region (3) events decreases when the bias voltage increases, since the transverse cloud size is smaller for a larger

electric field. The fraction should also decrease with the implantation depth, increase with the particle energy and temperature.

Charge sharing on the *Y* side may also occur when electrons are partially trapped on the *X* interstrip (regions (1) and (2) discussed above). Such events correspond to region (4) in Fig. 9. It should be noted that the probability to have electron trapping in the *X* interstrip (regions (1) and (2)) and at the same time *Y* charge sharing results in region (4). Indeed, one can check that Fraction(4) = (Fraction(1) + Fraction(2)) × Fraction(3). Therefore, the total fraction of interstrip events is not the sum of the fractions in the four regions. As another consequence, the fraction of region (4) decreases with the bias voltage.

From the above discussion, it turns out that the deposited energy is only partially detected in regions (2) and (4) for which it cannot be recovered. On the contrary, shared charges on the *Y* side (region (3)) can be added to recover the total energy; see Fig. 11. Because signals are summed, the resolution is only ∼45 keV compared to ∼32 keV for a single hit. In region (1) the total energy can be recovered using $E_1 - E_2$ for the left bottom branch and $E_2 - E_1$ for the right top branch. This holds if all holes are collected on a single strip regardless of the fraction of electrons trapped. The reconstruction has however a poor resolution of ∼120 keV and is shifted downward by about 110 keV (see Fig. 11), which corresponds approximately to the energy loss of α particles in the SiO_2 layer.

All effects taken into account, it turns out that the full particle energy is better detected on the *Y* side, although the resolution is slightly worse compared to the junction side. Contrary to Ref. [20], we do not suggest to reject off-line the events for which two adjacent strips exhibit a non-zero charge. The fraction of such events is, as shown above, significant and cannot be ignored at least in low statistics experiments such as heavy elements studies.

It should be noted that we have performed a similar study with the S3 detector prototype, which has among characteristics a reduced strip separation on the junction side (30 μm compared to 60 μm for MUSETT). In brief, the fraction of events in region (1) decreases by a factor about 3. As expected, the interstrip *Y* charge sharing is very close because the strip width and pitch are unchanged on this side. Detailed results will be published elsewhere.

Finally, it should be noted that we have not observed with the MUSETT detector time-dependent effects like in Ref. [27]. This is probably because the measurements were performed after reaching stable conditions. On the other hand, time-dependent effects were noticed with the S3 prototype, and are being investigated.

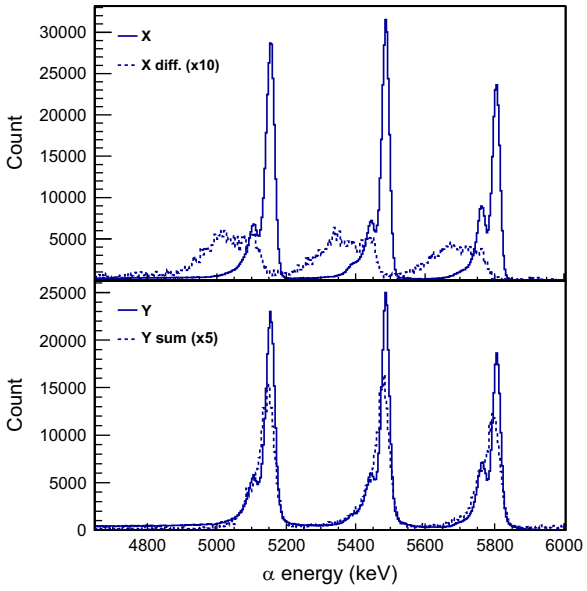

Fig. 11. Top: Spectra for the *X* front side. Full lines correspond to single strip events. The dashed lines correspond to the difference $E_i - E_j$ when charges are induced on two neighbouring strips. Bottom: Spectra for the *Y* back side, full lines corresponding to single strip events. The dashed lines correspond to the sum energy of two neighbouring strips. The interstrip dashed spectra have been scaled for better visibility. Data are taken at $T = 6$ °C, 3 μs peaking time, −60 V bias voltage.

4. In-beam commissioning

This section is devoted to the in-beam commissioning of MUSETT performed at GANIL. VAMOS in the WF mode is an important aspect of the experiment therefore Section 4.2 discusses the WF performance. The MUSETT in-beam performance is reported in Section 4.3.

4.1. Experimental conditions

Although references to the two first in-beam tests mentioned in Section 1 are made, we concentrate here on the experimental conditions of the MUSETT commissioning.

The $^{22}Ne^{10+}$ beam at an energy of 114 MeV was delivered by the CIME cyclotron with an intensity of 4.5 pnA (about 3×10^{10} particles per second). A ^{197}Au target (250 μg/cm^2) followed by a ^{12}C equilibrium foil (30 μg/cm^2) was used. This last foil is added to ensure that the ions reach a charge state close to their equilibrium value : see e.g. Ref. [28] and references therein. The targets were installed in the center of the EXOGAM array consisting during this experiment of 7 clover detectors with a target to crystal distance of 11.4 cm. VAMOS was used in its Q-Q-WF optics mode (two electric quadrupoles followed by the Wien Filter). The magnetic dipole after the WF was not used except for specific measurements, e.g. a scan of the beam charge states. The position of MUSETT was chosen according to ions optics calculations maximizing the transmission of the recoils deflected at an angle of 6° by the WF. The flight path between the target and MUSETT was 7.4 m for central trajectories. More details of the WF and optics are given in Section 4.2.

Although all DSSDs were available, we used MUSETT in a 2-detector configuration in order to (i) minimize the radiation damage and (ii) simplify the complexity of the electronics and acquisition chain. MUSETT was operated with a cooling fluid temperature of ∼20°. The beam was dumped at 0° in a Faraday cup whose current was monitored and recorded by the acquisition system.

The standard GANIL electronics and data acquisition system were used. MUSETT was read-out using the MUVI VXI cards [29] initially designed by the MUST II collaboration. These cards with their associated softwares and firmwares were upgraded to operate MUSETT in a triggerless mode. Data from the EXOGAM, VAMOS and MUSETT subsystems were time-stamped using a common 100 MHz clock. Upgrades of the DAQ were also made: new implementation of the data flow based on the NARVAL framework [30], of the GANIL Central Run Control, and of the Graphical User Interfaces. The on-line data control and off-line data analysis were made using the GRU (GANIL Root Utilities) and ViGRU (Visualization of GRU) packages [31], which are to a large extent based on the ROOT framework [17].

4.2. The VAMOS Wien filter

With a WF, the separation between the ions of interest from the beam and other unwanted reactions is based on their velocity. In very asymmetric reactions, the velocity difference between the recoil and the beam is large. This is therefore an ideal for the

specificities of the VAMOS WF. The reaction ^{197}Au(^{22}Ne,5n)^{214}Ac is relevant in that respect with a beam (recoil) velocity of $\sim$3.17 cm/ns ($\sim$0.31 cm/ns).

This section summarizes the VAMOS WF characteristics and performance determined using ion optics simulations compared with experimental results. The simulations and optimization of the electric quadrupole settings have been performed using the Zgoubi package [32,33]. We do not intend to show here fully realistic simulations since many parameters like the recoil angular distribution after the target, the charge state distribution, scattering inside the spectrometer, etc., were not calculated using a realistic physics generator. Our goal is to show the main characteristics relevant for the MUSETT commissioning at VAMOS and to a certain extent for future heavy element studies.

The VAMOS WF has inner dimensions of length $\times$ width $\times$ height $=1$ m $\times 1$ m $\times 0.15$ m. The WF is dispersive in the horizontal plane. The maximum fields available are $E=300$ kV/m and $B=0.2$ T. A safe electric field of 250 kV/m was used to avoid electric discharges. The electric and magnetic fields are oriented such that an accidental voltage breakdown after e.g. a spark would move the beam in a direction opposite to the detectors.

Requiring a maximum residues transmission, a WF is traditionally tuned with $E/B=v_0$(residues), driving the recoils at 0° independent of their charge state: see Fig. 12(a). However, as soon as the ions do not fulfil the condition $v=E/B$, a WF is not charge-state independent anymore, and thus it is dispersive in the horizontal plane. This traditional mode therefore disperses the beam, which potentially increases the probability of beam scattering into the detectors. We investigated an unusual WF mode tuned with $E/B=v_0$(beam), thus driving the beam at 0° regardless of its charge state, to allow a better focussing of the beam onto the beam dump: see Fig. 12(b). This mode may be of great interest in the case of radioactive beams where dumping radioactive species is a key experimental issue. Ion optics simulations show that the recoil transmissions are similar in both modes. Fig. 13 shows a simulation of a ^{214}Ac recoil distribution at the focal plane of VAMOS. The transmission has been optimized for the 10^+ charge state.

It should be noted that when the VAMOS optics is tuned for a given magnetic rigidity (or charge state), it defocuses all other magnetic rigidities. This is true, not only for the recoils, but also for the beam. As an example, the ion optics optimized for ^{214}Ac^{10+} focuses also ^{22}Ne^{10+} which has a similar $B\rho$, but disperses other beam and recoil charge states.

4.2.1. Effective length

While the geometric length of the WF is 1 m, the electric field acts on a smaller length. An effective length of 0.90 m has been determined in the first in-beam test using a ^{18}O beam where the position was precisely measured using secondary electron detectors [34,35]. All results of simulations shown in this paper have been obtained with an effective length of 0.9 m, the MUSETT array being centered around the ^{214}Ac central trajectories.

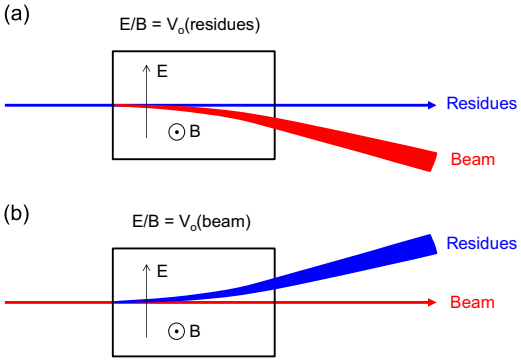

Fig. 12. Wien filter modes. (a) Traditional WF with nuclei of interest driven at 0°. (b) Beam "straight through" mode tried for the first time in this work.

4.2.2. Transmission

The transmission is calculated as the ratio of the number of recoils detected at the focal plane to the predicted number of recoils produced at the target. Experimentally, the number of recoils is obtained using their α decay. Note that the transmission, using the above definition, is a function of the detector size and efficiency (it is in fact a transmission-detection efficiency). The transmission has been measured for the ^{197}Au(^{22}Ne,5n)^{214}Ac reaction. At the beam energy of interest, a value of the cross-section of 2.87 mb was taken from Ref. [36].

A transmission of $36\pm2\%$ and $21\pm2\%$[5] was deduced in the second and third in-beam experiments, respectively. The difference is due to the spacial coverage of the detection system that was different between the two experiments. Our simulations using an optics optimized for ^{214}Ac^{10+} transmission lead on the other hand to transmissions of $\sim$66% and $\sim$45%, respectively. Comparison between our measurements and simulations has to be taken with care. There is indeed a factor of $\sim$2 between the measurements and the simulation, which suggests a systematic error that may be ascribed to two different sources:

- Recoil velocity and angular distribution: These distributions arise from two effects: particle evaporation (neutrons) and straggling in the target, which can be estimated using e.g. the PACE [37] and SRIM [38] codes, respectively. While the contribution from neutron emission can easily be estimated, less confidence can be associated to the contribution arising from the straggling in the target. The latter part is estimated to be the dominant contribution with $\Delta v/v\sim15\%$ and $\Delta\theta\sim100$ mrad (compared to $\Delta v/v\sim6\%$ and $\Delta\theta\sim50$ mrad from the neutron emission).
- The uncertainty in the cross-section taken from Ref. [36] is $\pm40\%$.

The deduced transmission should therefore be taken as an estimate and not as an accurate value. We should nonetheless stress that a transmission of $\sim$40% for very asymmetric reactions such as ^{197}Au(^{22}Ne,5n)^{214}Ac is larger than the value obtained with other recoil separators coupled to a large efficiency Ge array: see for instance [1,39] and references therein. To give another example, our simulations indicate a transmission of $\sim$50% for the fusion–evaporation reaction ^{238}U(^{22}Ne,5n)^{255}No.

4.2.3. Rejection

The beam rejection factor can be obtained from the ratio of beam intensity impinging on the target to the event rate (excluding the fusion–evaporation events) detected at the focal plane.

A rejection of $\sim10^7$ has been obtained in both recoil or beam straight through WF modes. As shown in Fig. 14, both direct (full energy) and scattered beam are detected with MUSETT.

While the presence of the full energy beam contamination does not overlap with the recoil energy, nor their decay, and therefore is at an acceptable level, the major part is made of a continuum spectrum interpreted as beam scattered inside the VAMOS spectrometer. To our knowledge, such events would be difficult to simulate. Also, our simulations predict that no direct beam should reach the focal plane detection. At this stage, we do not have yet a convincing explanation for the origin of the background sources. As a comparison, a beam suppression of about 2×10^{10} has been measured for the LISE WF [40] for the ^{209}Bi(^{48}Ca,2n)^{255}Lr

[5] Statistical error only; the error on the reference cross-section is not included.

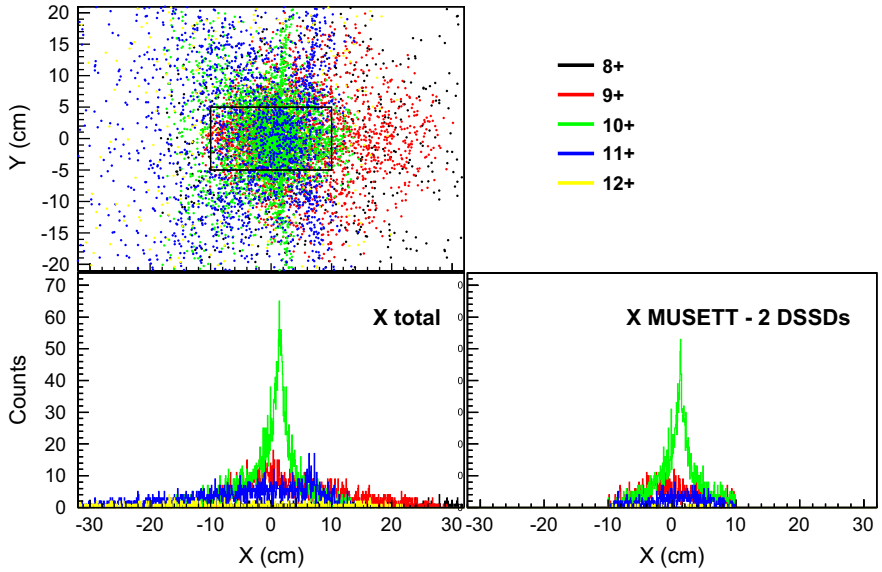

Fig. 13. Simulation of the ^{214}Ac residues detected at the focal plane of VAMOS. Top: recoil distribution (X,Y) at the focal plane. The rectangle corresponds to the area of the 2-MUSETT detector configuration used during the in-beam commissioning. Bottom left: projection of the recoil distribution on the X axis. Bottom right: same if detected in the two MUSETT detectors.

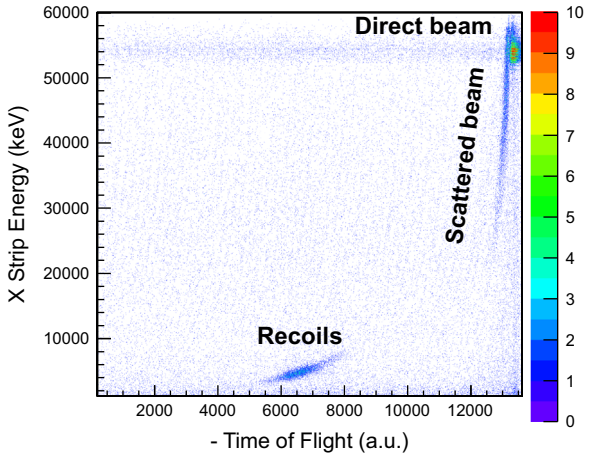

Fig. 14. ToF (arbitrary units) versus energy (on the X front side) identification matrix. Note that the time increases from right to left.

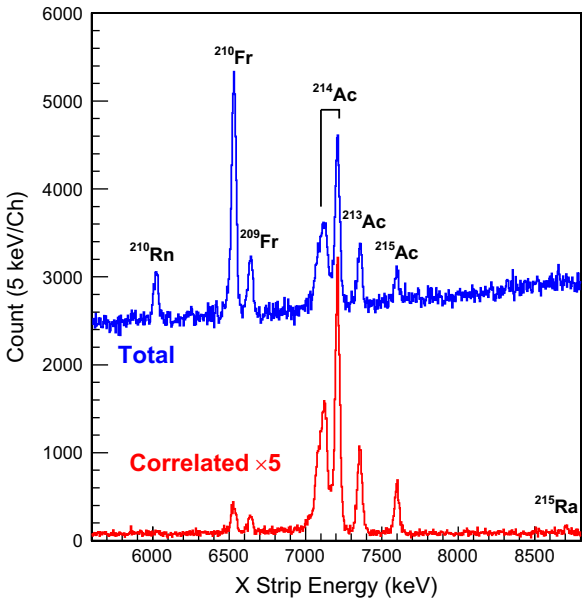

Fig. 15. Energy spectra. The total X front-side spectrum is obtained without any condition on position and time. The spectrum resulting from position and time correlations is scaled by a factor 5. See text for details.

fusion–evaporation reaction [41]. The LISE WF has however a total length of 12 m and the beam is stopped at mid filter ~8 m far away from the focal plane detection.

To summarize this section, the study of very asymmetric fusion–evaporation reactions at the mb level is feasible according to the measured rejection of the VAMOS WF. The main advantage of VAMOS in the context of fusion–evaporation reactions is its transmission, especially large for very asymmetric reactions.

4.3. RDT using the $^{22}Ne+^{197}Au$ reaction

Finally, we present in this section representative results obtained during the MUSETT in-beam commissioning.

Fig. 14 shows a ToF versus energy identification matrix. The ToF measured between MUSETT (start) and EXOGAM (stop) is given in arbitrary units and increases from right to left. Using the X (front side), the direct beam saturates the preamplifiers hence the calibration is incorrect for these events. Direct beam (full energy) corresponds to the area on the top right part of the matrix. The horizontal line starting from this area corresponds to a direct beam randomly correlated with EXOGAM. The parabola portion on the left corresponds to scattered beam. Scattered beam can also be random correlated with EXOGAM (mostly associated with the wrong cyclotron beam pulse): it corresponds to the background filling the plot and overlapping with the recoils of interest. It is possible to avoid such loci using a beam repetition period longer than the ToF inside the spectrometer. Finally, evaporation residues correspond to the region around a ToF ~6500 channels and E_x=5 MeV. Note that the energy is not corrected for any pulse height defect.

The total X (front side) energy spectrum is shown in Fig. 15. The α decay of nuclei populated in the fusion–evaporation reaction and of their daughters grows on a large background of scattered beam and to a smaller extent of fusion–evaporation residues. The spectrum resulting from recoil-α correlations is also shown in Fig. 15. Recoils were selected using a 2D gate set on the ToF versus energy identification matrix. A decay was then

searched in the same pixel within an interval of 1 min. This procedure reduces the background dramatically and removes long-lived daughter nuclei and grand-daughter nuclei like ^{210}Rn.

In ^{214}Ac, the energy of the most intense α peak at 7208 $\pm$ 3 keV corresponds to the ground-state feeding of ^{210}Fr (energy of 7215 $\pm$ 3 keV reported in [42]). We find that the peak on its left is a doublet with energies of 7083 $\pm$ 9 keV and 7128 $\pm$ 6 keV. The 7083 keV peak corresponds to the 7082 $\pm$ 4 keV line of [42] and 7080 $\pm$ 15 keV line of [43], feeding a level at 128 keV in ^{210}Fr. The 7128 keV line is not reported in Ref. [42], but interpreted in Ref. [43] ($E_\alpha \approx 7125$ keV) as resulting from the summing of the 7083 keV line with conversion electrons. Note that the summed intensity of the 7083 and 7128 keV lines (46 $\pm$ 3%) fits well with the 42 $\pm$ 2% intensity reported in Ref. [42] for the 7082 keV transition.

Half-lives can be measured using the recoil-α correlation procedure. A plot representing the decay time (in natural logarithm scale) versus the α-decay energy is shown in Fig. 16. The ^{215}Ra α peak ($p4n$ fusion–evaporation channel) with a half-life of $\sim$ 1.67 ms can clearly be seen, while it was hardly visible in Fig. 15. The ^{209,210}Fr decays are present in Fig. 16. Since the plot results from recoil-α correlations, it turns out that these two nuclei can be populated directly by fusion–evaporation (α2n and αn channels). The ^{209,210}Fr α-decay peaks shown in the total spectrum of Fig. 15, result therefore from the direct feeding after fusion–evaporation but also from the ^{213,214}Ac α decay.

As an example, the decay curve of ^{214}Ac is shown in Fig. 17. The half-lives are deduced fitting the decay plot with two exponential taking into account the random correlations: see e.g. Ref. [44].

The measured half-lives are summarized in Table 2 where they are compared with values from the literature. The agreement is excellent for ^{213}Ac and ^{215}Ra with the most recent results of Heßberger et al. [43]. Evaluated half-lives for ^{214}Ac and ^{215}Ac are about 45 years old [45]. We re-confirmed the ^{215}Ac half-life. We have improved the accuracy for ^{214}Ac and find a slightly lower value. Tabulated half-lives for ^{209}Fr and ^{210}Fr were obtained 40–50 years ago and display large dispersions. Because of the low statistics and uncertainty due to the long lifetime, we were unable to improve the accuracy. Our value for ^{210}Fr is compatible with those of Griffioen and Macfarlane [46] and Valli et al. [47] within 1σ. On the other hand, we find a value for ^{209}Fr lower compared to Griffioen and Macfarlane [46], Hornshøj et al. [48] and Valli et al. [47].

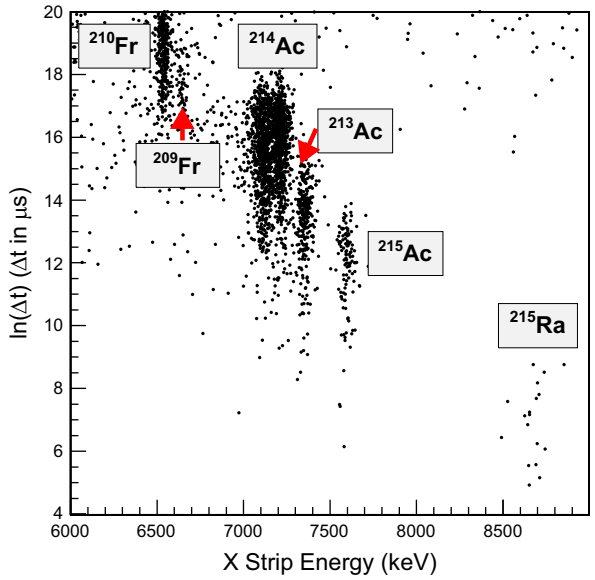

Fig. 16. Matrix representing the decay time in natural logarithm scale as a function of the α-decay energy.

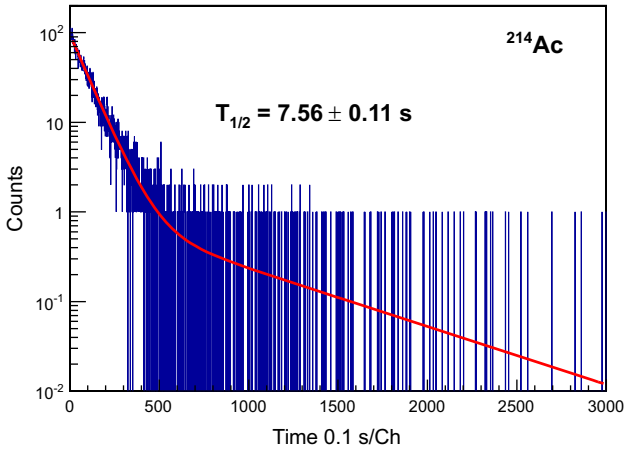

Fig. 17. Decay plot of ^{214}Ac.

Table 2
Half-lives measured in this work compared with data in the literature.

Isotope	Half-life, this work	Half-life, literature
^{209}Fr	40 $\pm$ 6 s	54.7 $\pm$ 1 [46] 50 $\pm$ 0.3 s [48] 52 $\pm$ 2 s [47]
^{210}Fr	163 $\pm$ 30 s	159 $\pm$ 5 [46] 191 $\pm$ 4 s [47]
^{213}Ac	723 $\pm$ 23 ms	731 $\pm$ 17 ms [43]
^{214}Ac	7.56 $\pm$ 0.11 s	8.2 $\pm$ 0.2 s [45]
^{215}Ac	175 $\pm$ 20 ms	170 $\pm$ 10 ms [45]
^{215}Ra	1.65 $\pm$ 0.16 ms	1.67 $\pm$ 0.01 ms [43]

Recoil-Decay-Tagged γ-ray spectra were obtained for the most intense fusion–evaporation channels: see Fig. 18 for ^{213,214}Ac. A level scheme has been proposed for ^{213}Ac by Heßberger et al. [49], based on ^{217}Pa decay studies. Using prompt γ-ray spectroscopy, we also observed the proposed transitions at 613.0 and 820.5 keV. Heßberger et al. observed in ^{214}Ac a transition at 91.8 keV after α decay of ^{218}Pa [43]. We are unable to confirm this transition but we have found several new transitions. Because of the modest statistics and complexity of odd-odd nuclei, an improved level scheme cannot be suggested. Gamma-rays were observed to deexcite the $29/2^+$ isomer of ^{215}Ac, previously studied using the fusion–evaporation reaction ^{204}Pb(^{15}N,4n)^{215}Ac [50]. Several tentative transitions were observed in the present study, but none of them corresponds to the proposed decay of the $29/2^+$ isomer.

To conclude this section, our data representing a few hours of beam time provide new results and point out the need for high-statistics and high-quality data sets in the region of neutron-deficient isotopes near the magic number N=126.

5. Summary and perspectives

The segmented Si wall MUSETT has been developed for Recoil-Decay-Tagging studies at VAMOS, GANIL. The array includes a Front End Electronics based on ASICs. A test bench has been developed at Saclay for tests and characterization of the detectors. Multipurpose VME cards, a data acquisition system and analysis tools have been developed. An energy resolution as low as 25 keV has been measured at 5.8 MeV. The detector and test bench developments have been made with a wider perspective. For instance, the test bench is used to characterise Double-sided Silicon Strip Detectors and preamplifier prototypes for the S3 collaboration.

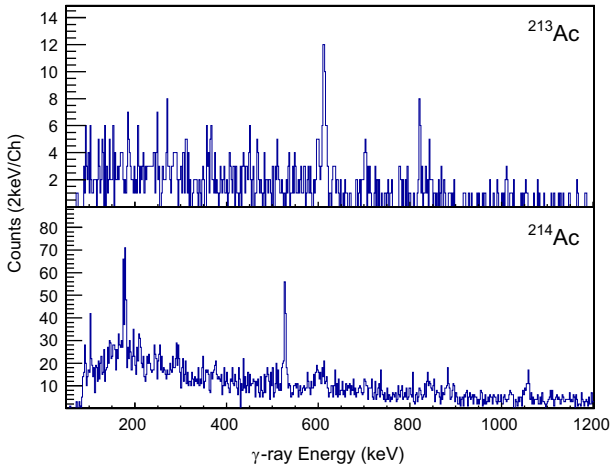

Fig. 18. Recoil-decay-tagged γ-ray spectra of ^{213,214}Ac.

The MUSETT array has been commissioned at GANIL with VAMOS in the Wien Filter vacuum mode, in conjunction with EXOGAM and using the fusion–evaporation reaction ^{22}Ne + ^{197}Au. The Recoil-Decay-Tagging technique has been successfully tested. Alpha-tagged prompt γ-ray spectra from $^{213–215}$Ac were obtained.

Performance of the VAMOS Wien Filter was studied for very asymmetric fusion–evaporation reactions. A large transmission has been deduced and the beam rejection allows studies at the mb level. For less asymmetric reactions, the VAMOS gas-filled mode recently tested provides a superior performance in terms of transmission and rejection [6].

The coupling of VAMOS with EXOGAM, its electronics upgrade (EXOGAM2), AGATA [9] or PARIS [51] will cover a large physics program: spectroscopy of heavy elements, study of exotic shapes, reaction mechanism studies, etc. Radioactive beams from SPIRAL2 (see e.g. [52]) foreseen by the end of the decade will open even greater perspectives.

Acknowledgments

MUSETT has been funded by an ANR (Agence Nationale de la Recherche) grant (ANR-05-BLAN-0150 MUSETT). This work has been supported by the EU-FP5 EXOTAG (contract HPRI-CT-1999-50017) and EU-FP6 INTAG (contract RII3-CT-2004-506065) projects. We are grateful to the GANIL staff for the support during the experiments: accelerator division, G. Frémont for making the targets. M. Kmiecik, A. Lopez-Martens, R. Lozeva, A. Maj, W. Męczyński, M. Zięblíński and M. Zielińska are acknowledged for their help during data taking.

Appendix A. Supplementary material

Supplementary data associated with this article can be found in the online version, at http://dx.doi.org/10.1016/j.nima.2014.02.016.

References

[1] R.-D. Herzberg, P.T. Greenlees, Progress in Particle and Nuclear Physics 61 (2008) 674.
[2] E.S. Paul, et al., Physical Review C 51 (1995) 78.
[3] H. Savajols, Nuclear Instruments and Methods in Physics Research Section B 204 (2003) 146.
[4] S. Pullanhiotan, M. Rejmund, A. Navin, W. Mittig, S. Bhattacharyya, Nuclear Instruments and Methods in Physics Research Section A 593 (2008) 343.
[5] M. Rejmund, et al., Nuclear Instruments and Methods in Physics Research Section A 646 (2011) 184.
[6] C. Schmitt, et al., Nuclear Instruments and Methods in Physics Research Section A 621 (2010) 558.
[7] J. Simpson, et al., Acta Physica Hungarica—NS-H 11 (2000) 159.
[8] F. Azaiez, W. Korten, Nuclear Physics News 7 (1997) 21.
[9] S. Akkoyun, et al., Nuclear Instruments and Methods in Physics Research Section A 668 (2012) 26.
[10] E. Pollacco, et al., European Physical Journal A 25 (s01) (2005) 287.
[11] CAEN—Costruzioni Apparecchiature Elettroniche Nucleari S.p.A., ⟨http://www.caen.it⟩.
[12] P. Baron, et al., Nuclear Science Symposium Conference Record, 2003 IEEE, vol. 1, 2003, p. 386.
[13] Micron Semiconductor Ltd, ⟨http://www.micronsemiconductor.co.uk ⟩.
[14] LAUDA, Operating Instructions, PROLINE Low-Temperature Thermostats with SmartCool System RP845, RP855, RP870, RP890, RP1290 RP1840, RP1845, RP3530, 2005.
[15] LAUDA Manual, *WINTHERM*® Plus—Software, Version 2.2 Rev. 1, 2005.
[16] LabVIEW Software, ⟨http://www.ni.com/labview⟩.
[17] R. Brun, F. Rademaker, Nuclear Instruments and Methods in Physics Research Section A 389 (1997) 81.
[18] A. Drouart, et al., European Physical Journal Web Conferences 17 (2011) 14004.
[19] J. Yorkston, A.C. Shotter, D.B. Syme, G. Huxtable, Nuclear Instruments and Methods in Physics Research Section A 262 (1987) 353.
[20] Y. Blumenfeld, et al., Nuclear Instruments and Methods in Physics Research Section A 421 (1999) 471.
[21] I.E. Anokhin, O.S. Zinets, Nuclear Instruments and Methods in Physics Research Section A 477 (2002) 110.
[22] S. Takeda, et al., Nuclear Instruments and Methods in Physics Research Section A 579 (2007) 859.
[23] M. Campbell, et al., Nuclear Instruments and Methods in Physics Research Section A 591 (2008) 38.
[24] J. Becker, K. Gärtner, R. Klanner, R. Richter, Nuclear Instruments and Methods in Physics Research Section A 624 (2010) 716.
[25] J. Bouchami, et al., Nuclear Instruments and Methods in Physics Research Section A 633 (Supplement (1)) (2011) S117.
[26] T. Poehlsen, E. Fretwurst, R. Klanner, S. Schuwalow, J. Schwandt, J. Zhang, Nuclear Instruments and Methods in Physics Research Section A 700 (2013) 22.
[27] T. Poehlsen, E. Fretwurst, R. Klanner, J. Schwandt, J. Zhang, Nuclear Instruments and Methods in Physics Research Section A 731 (2013) 172.
[28] G. Schiwietz, P.L. Grande, Nuclear Instruments and Methods in Physics Research Section B 175–177 (2001) 125.
[29] GANIL, MUVI documentation, ⟨http://wiki.ganil.fr/gap/wiki/Documentation/VXI/MUVI⟩.
[30] X. Grave, R. Canedo, J.-F. Clavelin, S. Du, E. Legay, in: Real Time Conference, 2005. 14th IEEE-NPSS, 2005, p. 119.
[31] GANIL, GRU/ViGRU documentation, ⟨http://wiki.ganil.fr/gap/wiki/Documentation/Gru/Gru⟩.
[32] F. Méot, Nuclear Instruments and Methods in Physics Research Section A 427 (1999) 353.
[33] F. Méot, F. Valero, zgoubi code, ⟨http://sourceforge.net/projects/zgoubi ⟩.
[34] A. Drouart, et al., Nuclear Instruments and Methods in Physics Research Section A 477 (2002) 401.
[35] A. Drouart, et al., Nuclear Instruments and Methods in Physics Research Section A 579 (2007) 1090.
[36] A.N. Andreev, D.D. Bogdanov, A.V. Eremin, A.P. Kabachenko, O.A. Orlova, G. M. Ter-Akopyan, V.I. Chepigin, Soviet Journal of Nuclear Physics 50 (1989) 381.
[37] A. Gavron, Physical Review C 21 (1980) 230.
[38] J.F. Ziegler, M.D. Ziegler, J.P. Biersack, Nuclear Instruments and Methods in Physics Research Section B 268 (2010) 1818.
[39] C.E. Düllmann, Nuclear Instruments and Methods in Physics Research Section B 266 (2008) 4123.
[40] R. Anne, A.C. Mueller, Nuclear Instruments and Methods in Physics Research Section B 70 (1992) 276.
[41] A. Chatillon, et al., European Physical Journal A 30 (2006) 397.
[42] P. Kuusiniemi, F.P. Heßberger, D. Ackermann, S. Hofmann, I. Kojouharov, European Physical Journal A 22 (2004) 429.
[43] F.P. Heßberger, et al., European Physical Journal A 8 (2000) 521.
[44] M.E. Leino, S. Yashita, A. Ghiorso, Physical Review C 24 (1981) 2370.
[45] K. Valli, W.J. Treytl, E.K. Hyde, Physical Review 167 (1968) 1094.
[46] R.D. Griffioen, R.D. Macfarlane, Physical Review 133 (1964) B1373.
[47] K. Valli, E.K. Hyde, W.J. Treytl, Journal of Inorganic and Nuclear Chemistry 29 (1967) 2503.
[48] P. Hornshøj, P.G. Hansen, B. Jonson, Nuclear Physics A 230 (1974) 380.
[49] F.P. Heßberger, et al., European Physical Journal A 15 (2002) 335.
[50] D.J. Decman, H. Grawe, H. Kluge, K.H. Maier, Zeitschrift fur Physik B 310 (1983) 55.
[51] A. Maj, et al., Acta Physica Polonica B 40 (2009) 565.
[52] M. Lewitowicz, Acta Physica Polonica B 42 (2011) 877.

7.6 Magnetism of an Excited Self-Conjugate Nucleus: Precise Measurement of the g Factor of the 2_1^+ State in ^{24}Mg

Magnetism of an Excited Self-Conjugate Nucleus: Precise Measurement of the g Factor of the 2_1^+ State in ^{24}Mg

A. Kusoglu,[1,2] A. E. Stuchbery,[3,*] G. Georgiev,[1] B. A. Brown,[4,5] A. Goasduff,[1] L. Atanasova,[6,†] D. L. Balabanski,[7] M. Bostan,[2] M. Danchev,[8] P. Detistov,[6] K. A. Gladnishki,[8] J. Ljungvall,[1] I. Matea,[9] D. Radeck,[10] C. Sotty,[1,‡] I. Stefan,[9] D. Verney,[9] and D. T. Yordanov[9,11,12]

[1]*CSNSM, CNRS/IN2P3; Université Paris-Sud, UMR8609, F-91405 Orsay-Campus, France*
[2]*Department of Physics, Faculty of Science, Istanbul University, Vezneciler/Fatih, 34134 Istanbul, Turkey*
[3]*Department of Nuclear Physics, RSPE, Australian National University, Canberra, Australian Capital Territory 2601, Australia*
[4]*National Superconducting Cyclotron Laboratory, Michigan State University, East Lansing, Michigan 48824, USA*
[5]*Department of Physics and Astronomy, Michigan State University, East Lansing, Michigan 48824, USA*
[6]*Institute for Nuclear Research and Nuclear Energy, Bulgarian Academy of Sciences, BG-1784 Sofia, Bulgaria*
[7]*ELI-NP, Horia Hulubei National Institute of Physics and Nuclear Engineering, 077125 Magurele, Romania*
[8]*Faculty of Physics, St. Kliment Ohridski University of Sofia, 1164 Sofia, Bulgaria*
[9]*IPN, Orsay, CNRS/IN2P3, Université Paris-Sud, F-91406 Orsay Cedex, France*
[10]*Institute for Nuclear Physics, University of Cologne, Zülpicher Straße 77, D-50937 Köln, Germany*
[11]*Max-Planck-Institut für Kernphysik, Saupfercheckweg 1, D-69117 Heidelberg, Germany*
[12]*CERN European Organization for Nuclear Research, Physics Department, CH-1211 Geneva 23, Switzerland*

(Received 4 November 2014; published 12 February 2015)

A precise measurement of the g factor of the first-excited state in the self-conjugate ($N = Z$) nucleus ^{24}Mg is performed by a new time-differential recoil-in-vacuum method based on the hyperfine field of hydrogenlike ions. Theory predicts that the g factors of such states, in which protons and neutrons occupy the same orbits, should depart from 0.5 by a few percent due to configuration mixing and meson-exchange effects. The experimental result, $g = 0.538 \pm 0.013$, is in excellent agreement with recent shell-model calculations and shows a departure from 0.5 by almost 3 standard deviations, thus achieving, for the first time, the precision and accuracy needed to test theory. Proof of the new method opens the way for wide applications including measurements of the magnetism of excited states of exotic nuclei produced as radioactive beams.

DOI: 10.1103/PhysRevLett.114.062501 PACS numbers: 21.10.Ky, 21.60.Cs, 23.20.En, 27.30.+t

The g factor is an important observable in the study of the quantum mechanics of nuclear excitations, being sensitive to single-particle aspects of the wave function. Because alternative effective interactions in the shell-model approach can describe excitation energies equally well but predict significantly different configuration mixing in the wave functions and, hence, different g factors, measurements of nuclear magnetism play a critical role in building an accurate understanding of nuclear structure. The g factor g and magnetic moment μ are related by $\mu = gI$ where μ has the units of nuclear magnetons and the angular momentum I is in units of $\hbar$.

For many years, the g factors of the first-excited states of even-even nuclei with equal numbers of protons and neutrons ($N = Z$) were expected to depart little from $g = 0.5$ [1]. This behavior occurs for self-conjugate nuclei because protons and neutrons occupy the same orbits and the intrinsic-spin moments of the nucleons largely cancel, leaving the orbital motion of the protons to produce the nuclear magnetism. More recent shell-model calculations, however, predict departures from $g = 0.5$ by up to 10% for the first-excited 2^+ states in the $N = Z$ sd-shell nuclei from ^{20}Ne to ^{36}Ar [2]. These departures stem from three mechanisms. First, configuration mixing in the shell-model basis space does not fully quench the spin contributions to the nuclear moment. Second, the Coulomb interaction between protons leads to isospin mixing, which introduces isovector contributions to the nuclear moment. Third, within the nucleus, meson exchange and higher-order configuration mixing contributions modify the magnetic dipole operator from that of a free nucleon.

On the experimental side, the predicted departures from $g = 0.5$ have not previously been observed. The excited states in question are short lived, having lifetimes of a few picoseconds. Their g factors must be measured via the spin precession of the nucleus in an extremely strong magnetic field, of the order of 10 kT or more. Such fields can be produced at the nucleus only by hyperfine interactions. Experimental precision and accuracy for these measurements has been limited, in part, because the short nuclear

lifetimes require the measurement of small differences in count rate. A more fundamental limitation, however, has stemmed from the use of ions with complex atomic configurations, for which the net strength of the hyperfine field is an uncertain superposition of many components.

This Letter reports a new measurement of the g factor of the first-excited state in the $N = Z$ nucleus ^{24}Mg (excitation energy $E_x = 1.369$ MeV, mean lifetime $\tau = 1.97$ ps [3]) based on hyperfine fields of hydrogenlike Mg ions. By the use of these well-defined hyperfine fields, together with efficient particle and γ-ray detection, the new measurement achieves the accuracy and precision needed to test the predicted departures from $g = 0.5$.

The experimental method is based on the observation of the precession of the nuclear moment as hydrogenlike ^{24}Mg ions fly through vacuum. As illustrated in Fig. 1, excited nuclei emerge from a target foil as ions carrying one electron. The nuclear spin $\boldsymbol{I}$ is aligned by the reaction whereas the atomic spin $\boldsymbol{J}$ is oriented randomly. The hyperfine interaction couples the atomic spin to the nuclear spin, and together they precess about the total $\boldsymbol{F} = \boldsymbol{I} + \boldsymbol{J}$ with a frequency proportional to the nuclear g factor. Thus, the orientation of the nuclear spin is periodically reduced and restored during the flight through vacuum. As a consequence, the angular intensity pattern of the γ rays emitted by the nuclei varies periodically, in step with the orientation of the nuclear spin. In the traditional recoil-in-vacuum, or "plunger," technique [4], the ions travel a set distance through vacuum before being stopped in a thick stopper foil, which immediately quenches the hyperfine interaction and freezes the orientation of the nuclear spin. The nuclear precession frequency is determined by observing changes in the radiation pattern as the flight time is varied by changing the distance between the target and stopper foils.

Here, we report the first use of a new time-differential recoil-in-vacuum (TDRIV) method. Proposed by Stuchbery, Mantica and Wilson [5] as a method suited for radioactive beams, its novel feature is to replace the thick stopper foil by a thinner foil that simply resets the electron configuration. For radioactive beams, this change allows projectile-excitation experiments in which the radioactive beam ion is

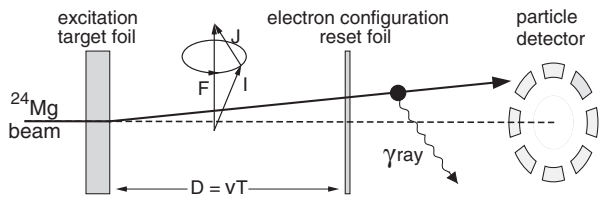

FIG. 1. Sketch of experiment. The "stopper" of the traditional plunger technique is replaced by a thin foil that resets the electron configuration of H-like ions. The particle detector, with segmentation around the beam axis, is located downstream of the γ-ray detectors.

detected at forward angles out of the view of the γ-ray detectors. In the present application to ^{24}Mg, the method enables experiments on high-velocity ions ($v/c \sim 0.1$) for which the optimal charge-state distribution of about 50% H-like can be achieved. The previous measurement [6], by the conventional TDRIV method following the ^{12}C(^{16}O, $\alpha\gamma$)^{24}Mg reaction, achieved a Mg recoil velocity of only $v/c \sim 0.056$ so that the H-like fraction was around 15%; most Mg ions carried three or four electrons.

A beam of ^{24}Mg at an energy of 120 MeV (5 MeV/nucleon) from the ALTO accelerator facility at IPN Orsay was excited in glancing collisions on a stretched foil of ^{93}Nb, 2.4 mg/cm^2 thick. Excited projectiles emerged from this target with ~93 MeV, corresponding to a velocity of $v/c = 0.0915(5)$. This velocity and its uncertainty were determined from experimental Doppler shifts and by evaluation of the reaction kinematics, taking into account the energy loss of the beam in the target. A 1.7 mg/cm^2 thick ^{197}Au foil served as the movable, stretched "reset" foil.

The experimental setup was comprised of the ORGAM hyperpure germanium (HPGe) detector array surrounding the Orsay plunger [7], on which the stretched foils were mounted, and an eightfold segmented plastic scintillation detector, located inside the beam line, 61 mm downstream from the target. Each segment had an azimuthal opening of $\Delta\phi_p = 30°$ and a polar opening angle from $\theta_p = 33°$ to $\theta_p = 38°$. The flight time of the excited ions T is related to the target-reset foil separation D by $T = D/\langle v \cos\theta_p \rangle$, where $\langle v \cos\theta_p \rangle$ represents an average over the angular acceptance of the particle detector.

ORGAM was populated with 13 HPGe detectors at the polar angles $\theta = 46.5°$, 72.1°, 85.8°, 94.2°, 108.0°, 133.6°, and 157.6°, relative to the beam axis. Gamma-ray detection angles near 90° were favored as these show the strongest anisotropy around the ϕ direction.

Data were taken in event-by-event mode, recording the arrival time and amplitude of the detected radiation from each particle and γ detector. Twenty-four target-reset foil distances from (near) the touching point of the foils to about 100 μm separation were measured. The beam intensity was about 0.3 pnA, and the running time was approximately 2 h for each distance.

Coincidence events corresponding to a γ-ray detection in the ORGAM array and a beam-particle detection in the plastic scintillator were sorted from the event data. Random coincidences were subtracted. An example of a resultant γ-ray spectrum is shown in Fig. 2. The intensity of the peak corresponding to the $2^+ \rightarrow 0^+$ transition of ^{24}Mg was determined for all particle-γ combinations.

In the presence of vacuum deorientation, the time-dependent particle-γ angular correlation takes the form (see e.g., Ref. [8] and references therein)

$$W(\theta_p, \theta_\gamma, \Delta\phi, t) = \sum_{kq} a_{kq}(\theta_p) G_k(t) D^{k*}_{q0}(\Delta\phi, \theta_\gamma, 0), \quad (1)$$

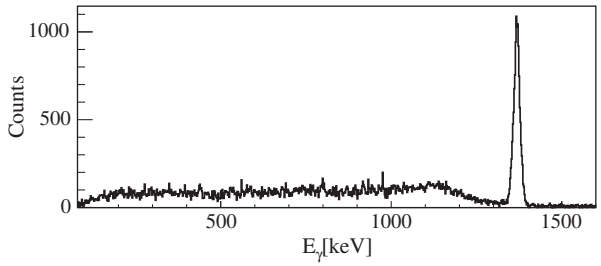

FIG. 2. Random-subtracted γ-ray spectrum collected at 80 μm plunger separation, showing the ^{24}Mg $2^+ \rightarrow 0^+$ 1368-keV photopeak. Data for all γ-ray detectors in coincidence with one particle detector segment are shown.

where θ_p and θ_γ are the polar detection angles for particles and γ rays, respectively; $\Delta\phi = \phi_\gamma - \phi_p$ is the difference between the corresponding azimuthal detection angles. $a_{kq}(\theta_p) = B_{kq}(\theta_p)Q_k F_k$, where $B_{kq}(\theta_p)$ is the statistical tensor, which defines the spin orientation of the initial state. F_k represents the F coefficient for the γ-ray transition, and Q_k is the attenuation factor for the finite size of the γ-ray detector. $D^{k*}_{q0}(\Delta\phi, \theta_\gamma, 0)$ is the Wigner-D matrix. For $E2$ excitation, $k = 0, 2, 4$ and $-k \leq q \leq k$. The attenuation coefficients $G_k(t)$ specify the time-dependent vacuum deorientation effect. For H-like $J = 1/2$ configurations, the $G_k(t)$ are cosine functions with a frequency determined by the nuclear g factor.

We refer to ions that decay between the target and the reset foil as "fast" and those that decay after the reset foil as "slow." The TDRIV method does not require that the γ-rays emitted from the fast and slow ions be separated in the observed energy spectrum. Decays of slow ions beyond the reset foil oscillate as $G_k(T)\bar{G}_k(\infty)$, where T is the flight time and $\bar{G}_k(\infty)$ is the average integral attenuation coefficient for slow ions that decay beyond the reset foil [5]. The fast component, however, is an average over decays taking place between the target and reset foils, so a range of precessions angles contribute and the oscillations are washed out [5]. Because the fast and slow components of the γ-ray line are not resolved, the net angular correlation shows damped oscillations, with the rate of damping determined by the nuclear lifetime.

With eightfold segmentation of the particle detector and 13 detectors in ORGAM, there are 104 individual particle-γ combinations. To analyze the data, the 104 time-dependent angular correlations were evaluated based on Eq. (1) and ordered according to the amplitude of the oscillations and whether the γ-ray intensity should initially increase, $W^\uparrow(T)$, or decrease, $W^\downarrow(T)$, with time. Forty-nine particle-γ combinations increase in magnitude initially. The remaining 55 particle-γ combinations initially decrease. Ratios of the coincidence γ-ray intensity corresponding to $W^\uparrow/W^\downarrow$ were formed in order, beginning with the pairing of the case showing strongest increase with the case of strongest decrease. These ratios were then formed into a geometric average

$$R(T) = \left(\prod_{i=1}^{n} \frac{W_i^\uparrow(T)}{W_i^\downarrow(T)}\right)^{1/n} \quad (2)$$

where n is the number of $W_i^\uparrow/W_i^\downarrow$ ratios included. The experimental geometric averages $R(T)$ largely factor out the detection efficiency for both γ-rays and particles.

Sensitivity is lost if $W^\uparrow/W^\downarrow$ ratios showing small amplitude oscillations are averaged with ratios showing large amplitude oscillations. The data set was therefore analyzed by forming geometric ratios in three groups, two of which are shown in Fig. 3. The $n = 14$ combinations showing the largest amplitude oscillations are labeled "strong," while the $n = 17$ ratios showing a moderate amplitude are labeled "intermediate." A further $n = 18$ pairs show a small amplitude. Because of the symmetry of the particle- and γ-detector arrays, certain particle-γ detector combinations should show the same angular correlation at all times. Ratios of such combinations should show a null effect. An example is shown in Fig. 3, labeled "null."

The g factor was determined from fits to the experimental data, as shown in Fig. 3. Fitting was performed using a computer code [9] that models the experimental conditions in detail based on Coulomb-excitation calculations, the formulas in Ref. [5], and Eq. (1) and then assembles $R(T)$ ratios in the same way that the experimental data are combined. The fitting procedures were broadly similar to those of Horstman *et al.* [6], the main difference being that the H-like K-shell hyperfine field is dominant in our measurement. Its value, $B_{1s}(0) = 29.09$ kT, was evaluated

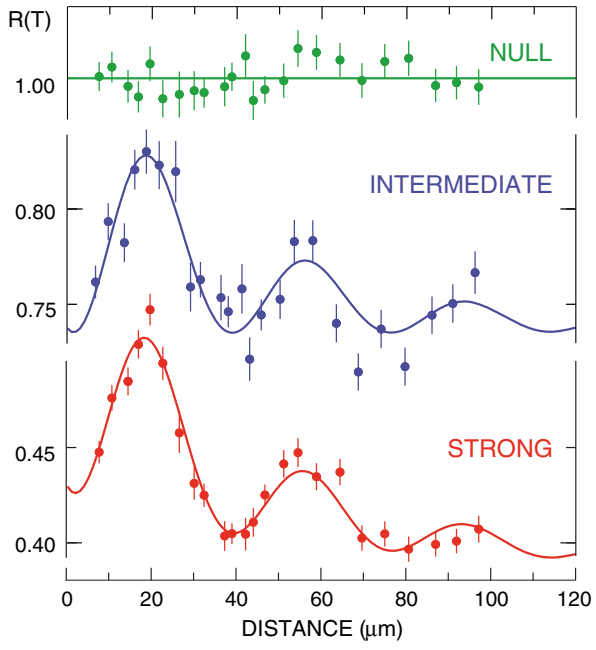

FIG. 3 (color online). $R(T)$ ratio data, Eq. (2), and fits based on detailed modeling of the experiment [9]. The distance is the separation of target and reset foils (22.4 μm = 1 ps flight time). The frequency of the oscillation determines the g factor.

with the General Relativistic Atomic Structure Package, GRASP2K [10]. Relativistic effects are of order 1%; the uncertainty in $B_{1s}(0)$ is negligible, which underpins the accuracy of the experimental g factor.

Results of the fits to the $R(T)$ data having strong, intermediate, and weak amplitude oscillations were $g = 0.538(13)$, 0.539(24), and 0.54(3), respectively, where the uncertainties are statistical only. The weighted average is $g = 0.538(11)$ (statistical error).

Systematic errors were evaluated as (i) $\delta g = \pm 0.0045$ from an uncertainty of ± 1.5 mm in the distance from the target to particle-detector face, (ii) $\delta g = \pm 0.0040$ from uncertainty in lifetime, $\tau = 1.97(5)$ ps [3], (iii) $\delta g = \pm 0.0035$ from the uncertainty in v/c, and (iv) $\delta g = \pm 0.0010$ from uncertainties in the distribution of hyperfine fields. The experimental g factor is therefore $g = 0.538 \pm 0.011(\text{statistical}) \pm 0.007(\text{systematic})$ or $g = 0.538(13)$, in reasonable agreement with, but more precise than, the previous measurement, $g = 0.51(2)$ [6]. The improvement stems in part from better statistical precision; however, systematic errors are also reduced. Uncertainty in the distribution of hyperfine fields has a small influence on the present measurement but was an important source of uncertainty in the previous measurement.

The first-excited state of ^{24}Mg is an isospin $T = 0$ state in a nuclide with $N = Z$. As such, it is useful to write the magnetic moment in terms of the isoscalar and isovector matrix elements

$$\mu = gI = g_{\ell_0}\langle \ell_0 \rangle + g_{\ell_1}\langle \ell_1 \rangle + g_{s_0}\langle s_0 \rangle + g_{s_1}\langle s_1 \rangle, \quad (3)$$

where ℓ and s represent the orbital and spin operators, and the subscripts 0 and 1 represent isoscalar and isovector, respectively. $I = \langle \ell_0 \rangle + \langle s_0 \rangle$. The free-nucleon values for the g factors are $g_{\ell_0} = (g_{\ell p} + g_{\ell n})/2 = 0.5$, $g_{\ell_1} = (g_{\ell p} - g_{\ell n})/2 = 0.5$, $g_{s_0} = (g_{sp} + g_{sn})/2 = 0.880$, and $g_{s_1} = (g_{sp} - g_{sn})/2 = 4.706$. (See Refs. [11–13] for further details.)

We first consider the sd shell-model space with isospin conserving Hamiltonians for which the isovector terms are zero: $\langle \ell_1 \rangle = \langle s_1 \rangle = 0$. Thus, if $\langle s_0 \rangle = 0$, $g(2^+) = g_{\ell_0} = 0.5$ for the bare $M1$ operator. However, the sd shell model gives small but nonzero values for $\langle s_0 \rangle$ [1]. For the ^{24}Mg case, $\langle s_0 \rangle = 0.069$ is obtained with the universal sd-shell interaction USDB. The USDA and USDB interactions with 30 and 56 parameters, respectively, update the universal sd-shell Hamiltonian USD to include additional data on neutron-rich nuclei [14]. USDB gives a slightly better rms deviation; however, there is little difference in the wave functions of stable nuclides. The following discussion is based on USDB, making reference to USD and USDA to give an indication of the theoretical uncertainty in the effective Hamiltonian. As will become evident below, this uncertainty affects the g factor at the level of ± 0.001. Taking USDB wave functions and bare nucleon values for g_{ℓ_0} and g_{s_0} gives $g(2^+) = 0.513$, which falls short of our experimental result.

Next we evaluate the effect of isospin mixing. In ^{24}Mg, the dominant contribution comes from mixing with the lowest $T = 1$, $I^\pi = 2^+$ state at $E_x \sim 10$ MeV. The isovector matrix elements were evaluated with the isospin non-conserving Hamiltonian of Ormand and Brown [15], obtaining $\langle \ell_1 \rangle = 0.020$ and $\langle s_1 \rangle = 0.0012$. Thus, with the addition of isospin mixing, $g(2^+) = 0.521$, which still falls short of the experimental value at the level of 1 standard deviation. The results with the USDA and USD interactions are 0.522 and 0.520, respectively.

It is well known that there are corrections to all of the matrix elements in Eq. (3) from mesonic exchange currents and higher-order configuration mixing. These corrections have been evaluated for the $d_{5/2}$ orbit at $A = 17$ by Towner and Khanna [11] and Arima *et al.* [12]. Because the magnetic moment of the predominantly $T = 0$ first-excited state in ^{24}Mg is dominated by the isoscalar orbital term, it is most sensitive to the corrections to g_{ℓ_0}, denoted δg_{ℓ_0}. The contribution to this correction coming from higher-order configuration mixing is $\delta g_{\ell_0} = 0.010$ according to Ref. [11] and $\delta g_{\ell_0} = 0.011$ according to Ref. [12], but there is disagreement for the mesonic-exchange contribution with Ref. [11] giving essentially zero and Ref. [12] giving $\delta g_{\ell_0} = 0.013$ (see Table 7.2 in Ref. [12]). Nevertheless, the resulting values of $g(2^+) = 0.531$ and 0.544, evaluated with the USDB Hamiltonian plus isospin nonconserving contributions and δg_{ℓ_0} corrections from Refs. [11,12], respectively, are both within the range of the experimental uncertainty.

An alternative approach is to determine the $M1$ operator empirically by performing a global fit to a wide range of data [2,13]. Our experimental g factor is shown in Fig. 4 along with previous results for $N = Z$ nuclei in the sd shell and NUSHELLX [16] calculations in the sd model space with the USDA and USDB interactions and the corresponding empirical $M1$ operators [2]. As is evident from Fig. 4, the new measurement is in very good agreement with these calculations; USDB gives $g(2^+) = 0.544(17)$. An uncertainty of about ± 0.017 in these theoretical g factors comes mainly from the δg_ℓ terms in the empirical $M1$ operator.

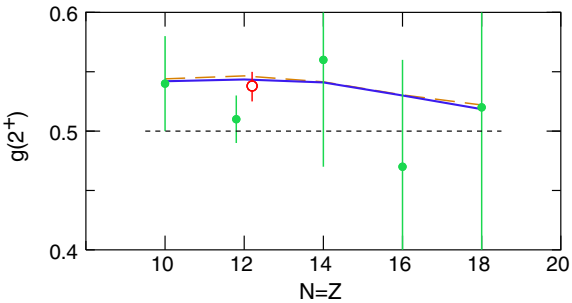

FIG. 4 (color online). Present result (open red circle) and previous results (filled green circles) [6,17–19] compared to shell-model calculations with USDA (dashed brown line) and USDB (solid blue line) calculations.

Thus, shell-model calculations consistently predict that the g factor of the first-excited state in the $N = Z$ nucleus ^{24}Mg is increased from $g = 0.5$, and our experiment confirms these predictions for the first time.

We have validated a new method for measuring the g factors of excited nuclear states with lifetimes in the picosecond regime. Measurements on stable isotopes like ^{24}Mg can reach new levels of precision and test nuclear model calculations in ways that were not previously possible. Moreover, as the method was designed for applications to radioactive beams, the present work prepares the way for a future measurement on the neutron-rich nucleus ^{32}Mg in the "island of inversion" [20].

The authors thank the technical staff of the ALTO facility for providing the beam and for assistance during the preparation and execution of the experiment. We also thank the UK/France (STFC/IN2P3) Loan Pool and GAMMAPOOL European Gamma-Ray Spectroscopy Pool for the loan of the detectors for ORGAM. This work was supported in part by the 2214-TUBITAK (Scientific and Technological Research Council of Turkey) Programme, the Scientific Research Projects Coordination Unit of Istanbul University under Project No. 46811, the European Community FP7 Capacities-Integrated Infrastructure Initiative-Contract ENSAR No. 262010, P2IO (Physique des 2 Infinis et des Origines) laboratory of excellence, Bulgarian NSF Grant No. DID-02/16, the Australian Research Council Grant No. DP0773273, and the U.S. National Science Foundation, NSF Grant No. PHY-1404442.

*Corresponding author.
andrew.stuchbery@anu.edu.au
†Present address: Department of Medical Physics and Biophysics, Medical University-Sofia, 1431 Sofia, Bulgaria.
‡Present address: KU Leuven, Instituut voor Kern-en Stralingsfysica, 3001 Leuven, Belgium.

[1] B. A. Brown, J. Phys. G **8**, 679 (1982).
[2] W. A. Richter, S. Mkhize, and B. A. Brown, Phys. Rev. C **78**, 064302 (2008).
[3] S. Raman, C. W. Nestor, Jr., and P. Tikkanen, At. Data Nucl. Data Tables **78**, 1 (2001).
[4] G. Goldring, in *Heavy Ion Collisions*, edited by R. Bock (North Holland, Amsterdam, 1982), Vol. 3, p. 483.
[5] A. E. Stuchbery, P. F. Mantica, and A. N. Wilson, Phys. Rev. C **71**, 047302 (2005).
[6] R. E. Horstman, J. L. Eberhardt, H. A. Doubt, C. M. E. Otten, and G. Van Middelkoop, Nucl. Phys. **A248**, 291 (1975).
[7] J. Ljungvall *et al.*, Nucl. Instrum. Methods Phys. Res., Sect. A **679**, 61 (2012).
[8] A. E. Stuchbery, Nucl. Phys. **A723**, 69 (2003).
[9] A. E. Stuchbery, computer code TDRIV_MODEL (unpublished).
[10] P. Jönsson, G. Gaigalas, J. Bieron, C. Froese Fisher, and I. P. Grant, Comput. Phys. Commun. **184**, 2197 (2013).
[11] I. S. Towner and F. C. Khanna, Nucl. Phys. **A399**, 334 (1983); I. S. Towner, Phys. Rep. **155**, 263 (1987).
[12] A. Arima, K. Shimizu, W. Bentz, and H. Hyuga, Adv. Nucl. Phys. **18**, 1 (1987).
[13] B. A. Brown and B. H. Wildenthal, Nucl. Phys. **A474**, 290 (1987).
[14] B. A. Brown and W. A. Richter, Phys. Rev. C **74**, 034315 (2006).
[15] W. E. Ormand and B. A. Brown, Nucl. Phys. **A491**, 1 (1989).
[16] B. A. Brown and W. D. M. Rae, Nucl. Data Sheets **120**, 115 (2014).
[17] J. L. Eberhardt, R. E. Horstman, H. A. Doubt, and G. van Middelkoop, Nucl. Phys. **A244**, 1 (1975).
[18] P. C. Zalm, A. Holthuizen, J. A. G. De Raedt, and G. Van Middelkoop, Nucl. Phys. **A315**, 133 (1979).
[19] K.-H. Speidel, S. Schielke, J. Leske, J. Gerber, P. Maier-Komor, S. J. Q. Robinson, Y. Y. Sharon, and L. Zamick, Phys. Lett. B **632**, 207 (2006).
[20] E. K. Warburton, J. A. Becker, and B. A. Brown, Phys. Rev. C **41**, 1147 (1990).

7.7 Measurement of lifetimes in ^{62,64}Fe , ^{61,63}Co, and ^{59}Mn

PHYSICAL REVIEW C **95**, 024312 (2017)

Measurement of lifetimes in ^{62,64}Fe, ^{61,63}Co, and ^{59}Mn

M. Klintefjord,[1,*] J. Ljungvall,[2] A. Görgen,[1] S. M. Lenzi,[3] F. L. Bello Garrote,[1] A. Blazhev,[4] E. Clément,[5] G. de France,[5] J.-P. Delaroche,[6] P. Désesquelles,[2] A. Dewald,[4] D. T. Doherty,[7] C. Fransen,[4] A. Gengelbach,[8] G. Georgiev,[2] M. Girod,[6] A. Goasduff,[9] A. Gottardo,[10] K. Hadyńska-Klęk,[1] B. Jacquot,[5] T. Konstantinopoulos,[2] A. Korichi,[2] A. Lemasson,[5] J. Libert,[10] A. Lopez-Martens,[2] C. Michelagnoli,[5] A. Navin,[5] J. Nyberg,[8] R. M. Pérez-Vidal,[11] S. Roccia,[2] E. Sahin,[1] I. Stefan,[10] A. E. Stuchbery,[12] M. Zielińska,[7] D. Barrientos,[13] B. Birkenbach,[4] A. Boston,[14] L. Charles,[15] M. Ciemala,[16] J. Dudouet,[17] J. Eberth,[4] A. Gadea,[11] V. González,[18] L. Harkness-Brennan,[14] H. Hess,[4] A. Jungclaus,[19] W. Korten,[7] R. Menegazzo,[20] D. Mengoni,[20,3] B. Million,[20] A. Pullia,[21,22] D. Ralet,[2,23,24] F. Recchia,[20,3] P. Reiter,[4] M. D. Salsac,[7] E. Sanchis,[18] O. Stezowski,[17] Ch. Theisen,[7] and J. J. Valiente Dobon[9]

[1]*Department of Physics, University of Oslo, N-0316 Oslo, Norway*
[2]*CSNSM, Univ. Paris-Sud, CNRS/IN2P3, Université Paris-Saclay, 91405 Orsay, France*
[3]*Dipartimento di Fisica e Astronomia dell'Università and INFN, Sezione di Padova, I-35131 Padova, Italy*
[4]*Institut für Kernphysik, Universität zu Köln, D-50937 Köln, Germany*
[5]*GANIL, CEA/DRF-CNRS/IN2P3, Bd. Henri Becquerel, BP 55027, F-14076 Caen, France*
[6]*CEA, DAM, DIF, F-91297 Arpajon, France*
[7]*Irfu, CEA, Université Paris-Saclay, F-91191 Gif-sur-Yvette, France*
[8]*Institutionen för fysik och astronomi, Uppsala Universitet, SE-751 05 Uppsala, Sweden*
[9]*INFN Laboratori Nazionali di Legnaro, Viale dell'Università, 2, I-35020 Legnaro, Italy*
[10]*Institut de Physique Nucléaire, CNRS/IN2P3-Université Paris-Sud, F-91406 Orsay, France*
[11]*Instituto de Física Corpuscular, CSIC-Universidad de Valencia, E-46071 Valencia, Spain*
[12]*Department of Nuclear Physics, Australian National University, Canberra ACT 0200, Australia*
[13]*CERN, CH-1211 Geneva 23, Switzerland*
[14]*Oliver Lodge Laboratory, The University of Liverpool, Liverpool, L69 7ZE, United Kingdom*
[15]*IPHC, UNISTRA, CNRS, 23 rue du Loess, 67200 Strasbourg, France*
[16]*The Henryk Niewodniczański Institute of Nuclear Physics, Polish Academy of Sciences, ul. Radzikowskiego 152, 31-342 Kraków, Poland*
[17]*Université de Lyon, Université Lyon-1, CNRS/IN2P3, UMR5822, IPNL, 4 Rue Enrico Fermi, F-69622 Villeurbanne Cedex, France*
[18]*Departamento de Ingeniería Electrónica, Universitat de Valencia, Burjassot, Valencia, Spain*
[19]*Instituto de Estructura de la Materia, CSIC, Madrid, E-28006 Madrid, Spain*
[20]*INFN Sezione di Padova, I-35131 Padova, Italy*
[21]*University of Milano, Dept. of Physics, I-20133 Milano, Italy*
[22]*INFN Milano, I-20133 Milano, Italy*
[23]*Institut für Kernphysik, Technische Universität Darmstadt, Darmstadt D-64289, Germany*
[24]*GSI Helmholtzzentrum für Schwerionenforschung GmbH, Planckstraße 1, D-64291 Darmstadt, Germany*

(Received 16 November 2016; revised manuscript received 3 January 2017; published 9 February 2017)

Lifetimes of the 4_1^+ states in ^{62,64}Fe and the $11/2_1^-$ states in ^{61,63}Co and ^{59}Mn were measured at the Grand Accélérateur National d'Ions Lourds (GANIL) facility by using the Advanced Gamma Tracking Array (AGATA) and the large-acceptance variable mode spectrometer (VAMOS++). The states were populated through multinucleon transfer reactions with a ^{238}U beam impinging on a ^{64}Ni target, and lifetimes in the picosecond range were measured by using the recoil distance Doppler shift method. The data show an increase of collectivity in the iron isotopes approaching $N = 40$. The reduction of the subshell gap between the $\nu 2p_{1/2}$ and $\nu 1g_{9/2}$ orbitals leads to an increased population of the quasi-SU(3) pair $(\nu 1g_{9/2}, \nu 2d_{5/2})$, which causes an increase in quadrupole collectivity. This is not observed for the cobalt isotopes with $N < 40$ for which the neutron subshell gap is larger due to the repulsive monopole component of the tensor nucleon-nucleon interaction. The extracted experimental $B(E2)$ values are compared with large-scale shell-model calculations and with beyond-mean-field calculations with the Gogny D1S interaction. A good agreement between calculations and experimental values is found, and the results demonstrate in particular the spectroscopic quality of the Lenzi, Nowacki, Poves, and Sieja (LNPS) shell-model interaction.

DOI: 10.1103/PhysRevC.95.024312

*malin.klintefjord@fys.uio.no

I. INTRODUCTION

A cornerstone of nuclear structure physics is the existence of "magic" nuclei with increased binding due to large gaps in the single-particle shell structure. Spectroscopy of exotic nuclei away from the line of β stability has shown that the magic numbers are not universal throughout the nuclear chart but depend on the ratio of neutron to proton numbers; that is, they may vary as a function of isospin [1]. Far from stability, the relative strength of the different terms in the nuclear force may vary and cause a modification of the shell structure. The theoretical description of the changing shell structure is challenging and requires appropriate valence spaces and effective interactions for shell-model calculations and improved energy functionals for mean-field-based models.

Regions in the nuclear chart with rapid changes in collectivity as a function of Z or N are of particular interest because they allow stringent testing of theoretical models. The neutron-rich nuclei close to ^{68}Ni show a rapid variation in collectivity, which is understood in the shell model as the combination of the effect of the monopole part of the central and tensor force [2,3], leading to a reduced shell gap at $N = 40$ as protons are removed, and quadrupole correlations arising from the multipole part. This favors a substantial gain in correlation energy via the excitation of neutrons across the $N = 40$ gap to the quasi-SU(3) partner orbitals $\nu g_{9/2}$ and $\nu d_{5/2}$. It should also be noted that, for protons, this is accompanied by an increase in excitations across the $Z = 28$ gap to the $p_{3/2}$ orbital, which is the quasi-SU(3) partner of the $f_{7/2}$ orbital. This mechanism has been theoretically investigated and compared with available experimental data for cobalt, iron, manganese, and chromium isotopes. It was concluded that the arising collective structures can only be reproduced by including the $\nu d_{5/2}$ together with the $\nu g_{9/2}$ orbital in the model space as one approaches $N = 40$ [4–7]. It was shown that the wave functions of the low-lying states contain a large contribution from these intruder states, while the configurations that correspond to "normal" shell filling lie higher in energy. This is the same mechanism that causes the disappearance of the $N = 8$ and $N = 20$ shell closures for neutron-rich nuclei, giving rise to so-called islands of inversion not only at the $N = 8$ and $N = 20$, but also at the $N = 40$ harmonic-oscillator shell closure [8].

A substantial amount of experimental data exist for the region, starting with $^{68}_{28}$Ni$_{40}$ with a high excitation energy of the 2^+_1 state and a small $B(E2; 2^+_1 \rightarrow 0^+_1)$ value, suggesting a closed-shell nucleus [9,10]. On the other hand, no strong $N = 40$ shell gap is seen in mass measurements [11,12], and the weak $B(E2; 2^+_1 \rightarrow 0^+_1)$ value in ^{68}Ni is understood as being due to a strong neutron component in the 2^+_1 excitation [13]. Spectroscopic studies of neutron-rich cobalt isotopes have shown that the $N = 40$ subshell gap inhibits the development of low-lying collective structures up to $^{65}_{27}$Co$_{38}$. Here, increasing neutron occupation of orbitals above the $N = 40$ gap manifests itself through the coexistence of spherical and deformed structures at low excitation energy. Even in ^{67}Co the yrast states can be reasonably well described as a proton particle (hole) weakly coupled to the 2^+_1 state in the corresponding iron (nickel) isotones [14–18].

Spectroscopy experiments following β decay [19–21], multinucleon transfer [22,23], and knock-out reactions [24] have found a sudden drop in the excitation energy of the 2^+_1 states in neutron-rich iron isotopes from $N = 38$. This is consistent with lifetime measurements [8,25] and intermediate-energy Coulomb excitation experiments [26] that show a strong increase of the $B(E2)$ values. Recent measurements performed at RIKEN have extended the systematics of excitation energies in chromium and iron isotopes towards the $N = 50$ shell gap [27], indicating a continuation of the $N = 40$ island of inversion toward $N = 50$. Extensive spectroscopic studies of manganese isotopes up to ^{63}Mn indicate an increase in collectivity already at lower neutron numbers [28,29]. Recent collinear laser spectroscopy of odd-even manganese isotopes up to ^{65}Mn and the measurement of the g factor of the ground state indicate that there is an increasing fraction of neutron excitation across the $N = 40$ subshell gap for manganese isotopes with $N \geqslant 36$ [30].

The enhanced collectivity of even-even nuclei around ^{66}Fe and ^{64}Cr was also the subject of theoretical investigations using mean-field-based approaches [31–34]. Hartree–Fock–Bogoliubov (HFB) calculations with the Gogny D1S interaction found the $N = 40$ subshell gap to be almost constant in size between $Z = 20$ and $Z = 40$ [35]. The potential-energy surfaces for ^{64}Cr and ^{66}Fe were found with a spherical minimum that is soft toward prolate deformation. Applying the generator coordinate method with a five-dimensional collective Hamiltonian (5DCH) yielded $B(E2; 2^+_1 \rightarrow 0^+_1)$ values for ^{64}Cr and ^{66}Fe that are in relatively good agreement with the experimental values, whereas the excitation energies were significantly overestimated [35].

While a coherent picture of nuclear structure around ^{68}Ni starts to emerge, there are still only few electromagnetic transition probabilities known in the region. Experimental $B(E2)$ values for the neutron-rich iron isotopes are only known for the $2^+_1 \rightarrow 0^+_1$ transitions [8,25,26], but not for higher-lying transitions. For the cobalt isotopes, lifetimes were reported for the $9/2^-$ and $11/2^-$ states in ^{61}Co [36], the $3/2^-$ and $9/2^-$ states in ^{63}Co [16], the $11/2^-$ state in ^{63}Co [18], and the $11/2^-$ and $13/2^-$ states in ^{65}Co [18]. For the manganese isotopes some transition strengths are known from Coulomb excitation of ^{61}Mn [37], and lifetimes were very recently reported for the $7/2^-$, $9/2^-$, and $11/2^-$ states in ^{63}Mn [38]. No transition strengths have been reported for ^{59}Mn so far. As theoretical descriptions of this region, in particular recent shell-model calculations [27], are showing an impressive agreement for excitation energies over a large range of isotopes, it is of great interest to challenge these models with experimental transition strengths, which are more sensitive to details of the wave functions than excitation energies alone. The measurements of additional experimental electromagnetic transition probabilities therefore provide important benchmarks for both shell-model and beyond-mean-field calculations.

The recoil-distance Doppler shift (RDDS) technique has been successfully applied in recent years in combination with multinucleon transfer reactions and the identification of reaction products in magnetic spectrometers [39]. Here, we report on the first RDDS lifetime measurement with AGATA

coupled to VAMOS++ at GANIL. New lifetimes were measured in ^{62,64}Fe, ^{61,63}Co, and ^{59}Mn by using multinucleon transfer reaction between ^{238}U projectiles and ^{64}Ni target nuclei. The article is organized as follows: Experimental details and the data analysis are described in Secs. II and III, respectively. The results are presented in Sec. IV and discussed and compared with theoretical calculations in Sec. V.

II. EXPERIMENTAL DETAILS

Excited states of nuclei in the $A \approx 60$ region were populated in multinucleon transfer-reactions from a 6.5A MeV ^{238}U beam with an intensity of 0.2–0.5 pnA impinging on a 1.25-mg/cm^2-thick ^{64}Ni target at GANIL. The VAMOS++ spectrometer [40–42] was used to detect and identify the target-like transfer products. It was positioned at 45° with respect to the beam axis, close to the grazing angle of the reaction. During this experiment the detection system of VAMOS++ consisted of a set of dual position-sensitive multiwire proportional counter detectors at the entrance of the spectrometer used for the time-of-flight measurement and giving the direction of the ions for Doppler correction, two sets of drift chambers used to determine the trajectory of the ions after the dipole magnet followed by multiwire proportional chambers to give the time of flight, and finally ionization chambers for measuring the total energy and energy loss of the ions at the focal plane. This focal plane detection in VAMOS++ allows for the reconstruction of the particle trajectories and the magnetic rigidity. In this experiment two settings of the magnetic rigidity were used with $B\rho = 0.97$ T m and $B\rho = 0.92$ T m.

Gamma rays were detected in the AGATA germanium γ-ray tracking array [43], which at the time of the experiment consisted of 19 crystals placed 23.5 cm from the target position. The detectors covered the backward angles from 145° to 180° with respect to the spectrometer axis. Count rates in each crystal were about 6–10 kHz depending on current beam intensity, and trapezoidal shaping with a rise time of 2.5 μs and a peak time of 3 μs was used. A γ-particle coincidence rate between AGATA and VAMOS++ of a few hundred hertz allowed for pulse-shape analysis of the signals from the segmented AGATA detectors to be performed online. The γ-ray tracking procedure was performed after each run (typically 12 hours of data taking) during the experiment reading data from disk. The high position resolution of AGATA, together with the reconstruction of the velocity vector for the ions in VAMOS++, resulted in a γ-ray resolution of 5.6 keV for the Doppler corrected 1345 keV γ-ray line in ^{64}Ni. The data, including the digitized germanium detector signals, were written to disk for further improved analysis [44].

The Orsay universal plunger system (OUPS) [45] was used for the lifetime measurements using the RDDS method. Particles recoiling out of the target were slowed down by a 3.0-mg/cm^2-thick ^{24}Mg degrader before entering the VAMOS++ spectrometer with a mean recoil velocity after the degrader of 10.7% of the speed of light. Target and degrader foils were mounted orthogonal to the entry axis of VAMOS++. Data were taken with six different target-degrader distances, $d_0 + 10.1(4)$ μm, $d_0 + 19.9(2)$ μm, $d_0 + 40.0(2)$ μm, $d_0 + 59.9(3)$ μm, $d_0 + 80.3(5)$ μm, and $d_0 + 206(4)$ μm, for about 24 h per distance. The offset d_0 was determined by using known lifetimes; see Sec. III. For the five shortest distances an active feedback system was used to control the distance.

III. DATA ANALYSIS

The target-like reaction products were identified in mass, charge, and atomic number with the VAMOS++ spectrometer. Nuclei with the same atomic number Z were identified by their characteristic energy loss from the ΔE-E energy spectrum, shown in Fig. 1. The mass-over-charge ratio of the ions was determined from the time of flight, the path through the spectrometer, and the magnetic rigidity. Combined with the total energy of the ions the mass can be determined, and the mass distributions for the manganese, iron, and cobalt chains are shown in Fig. 2. Gamma rays detected with AGATA in coincidence with ^{62,64}Fe, ^{61,63}Co, and ^{59}Mn, summed over all six distances, are shown in Fig. 3.

Gamma rays from the decaying excited states in the recoiling nuclei are emitted in flight. Due to the energy loss in the degrader, Doppler shifts are different for decays before and after the degrader, respectively. The spectra were incremented with γ rays that were Doppler corrected event by event by using the velocity vector of the recoiling ions after the degrader measured with the VAMOS++ spectrometer. Gamma rays emitted before the degrader have a higher velocity than those used in the Doppler correction and appear at lower energies when observed under backward angles. In the cases where the lifetime is comparable to the time of flight between the target and degrader, this procedure results in two distinct peaks for each decay, with decays occurring before the degrader contributing to the *shifted* peak (at lower energy) and decays occurring after the degrader contributing to the *unshifted* peak.

The effect of γ rays emitted during deceleration of the ions in the degrader foil was investigated for the different distances by using the AGATA Monte Carlo simulations package [46] and found negligible compared with the statistical and other

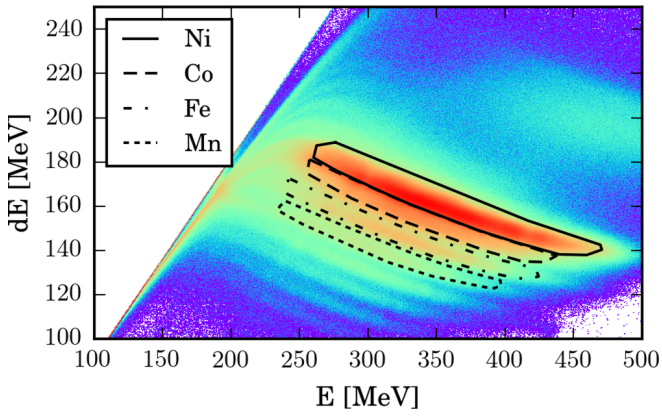

FIG. 1. Energy loss of the target-like reaction products in VAMOS++ as a function of total energy detected, with cuts on manganese (dotted), iron (dash-dotted), cobalt (dashed), and nickel (solid) isotopes.

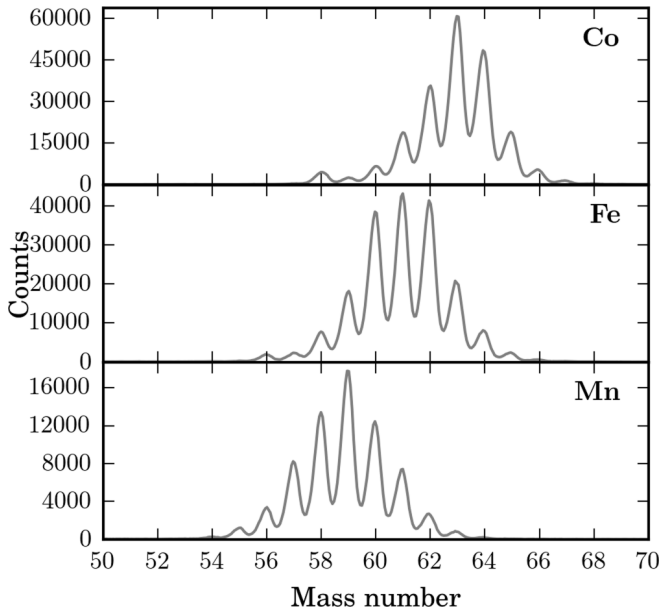

FIG. 2. Mass distributions for the manganese, iron, and cobalt isotopic chains.

systematic errors, except for the 2^+ state in ^{64}Ni, where systematic uncertainties from this effect dominates the statistical ones, and are of the order of 10%.

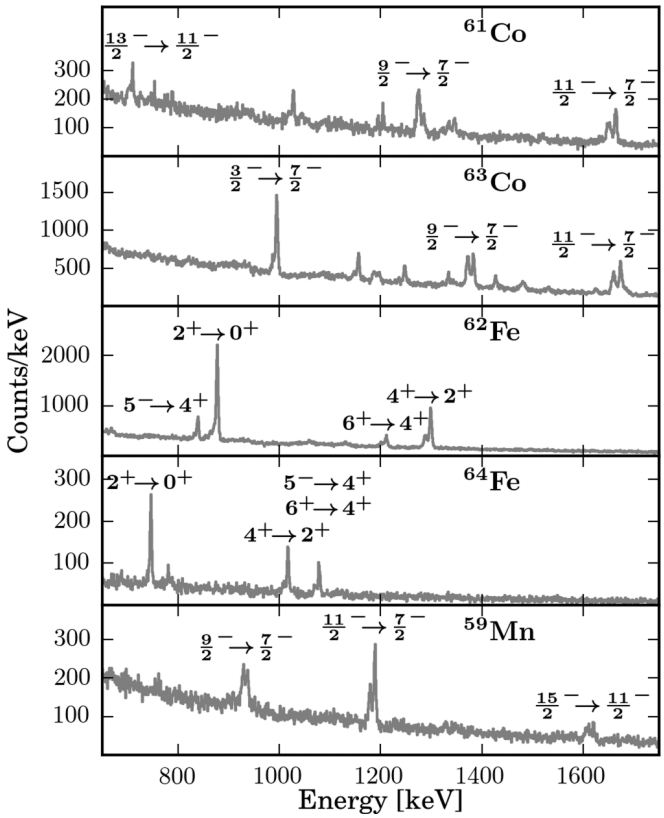

FIG. 3. γ-ray spectra in coincidence with ions identified as ^{59}Mn, ^{62,64}Fe, and ^{61,63}Co, summed over all six distances.

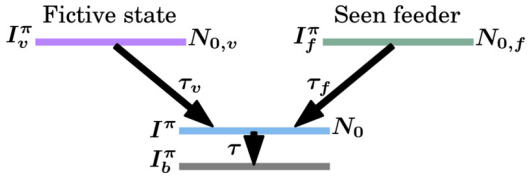

FIG. 4. Schematic level scheme illustrating the feeding and decay of the level of interest. Unobserved feeding is accounted for by introducing a fictive level (marked with v).

Decay curves $R(x)$ for the level of interest and for observed feeding transitions, $R_f(x)$, were constructed according to

$$R^{(\mathrm{expt})}(x) = \frac{I_u^{(\mathrm{expt})}(x)}{I_s^{(\mathrm{expt})}(x) + I_u^{(\mathrm{expt})}(x)},$$
$$R_f^{(\mathrm{expt})}(x) = \frac{1}{\epsilon_{\mathrm{rel.}}^{(\mathrm{expt})}} \frac{I_{u,\mathrm{f}}^{(\mathrm{expt})}(x)}{I_s^{(\mathrm{expt})}(x) + I_u^{(\mathrm{expt})}(x)}, \quad (1)$$

where $I_s^{(\mathrm{expt})}(x)$ and $I_u^{(\mathrm{expt})}(x)$ are the measured shifted and unshifted intensities, respectively, of the decay transition from the level of interest, $I_{u,\mathrm{f}}^{(\mathrm{expt})}(x)$ is the intensity of the unshifted component of the observed feeder, and $\epsilon_{\mathrm{rel.}}^{(\mathrm{expt})}$ is the relative detection efficiency for the feeding transition relative to the decay transition.

Lifetimes were fit to the observed γ decays by solving the coupled linear differential equations arising from the decay of the level of interest and its feeders, as illustrated in Fig. 4. The model for the level schemes used in this work consists of the level of interest, any observed transitions from feeder states, and *unseen feeding*, which is treated by introducing a fictive level approximating possible delayed feeding to the level of interest from other levels. More complicated feeding schemes have been tried, giving compatible results but with a higher χ^2/N_{dof} by a factor two or more. Therefore, the simplest scheme has been used. Given the proportion of decays coming from the feeders, $N_{0,\mathrm{f}}$ and $N_{0,\mathrm{v}}$, and the lifetimes, τ, τ_f, and τ_{v}, the fitted decay curves are

$$R(t) = e^{-t/\tau} + N_{0,\mathrm{f}}\tau_f \frac{e^{-t/\tau_f} - e^{-t/\tau}}{\tau_f - \tau} + N_{0,\mathrm{v}}\tau_{\mathrm{v}} \frac{e^{-t/\tau_{\mathrm{v}}} - e^{-t/\tau}}{\tau_{\mathrm{v}} - \tau},$$
$$F(t) \equiv 1 - R(t), \quad (2)$$
$$R_f(t) = N_{0,\mathrm{f}} e^{-t/\tau_f},$$

where F is called the flight curve. Note that $N_{0,\mathrm{v}}$ only includes the delayed unseen feeding. Any prompt unseen feeding, given by $1 - N_{0,\mathrm{f}} - N_{0,\mathrm{v}}$, does not influence the lifetime measurement.

Experimental data were obtained for $N_{\mathrm{dist}} = 6$ different distances $d_n^{(\mathrm{expt})}$ between target and degrader. The corresponding time of flight to the degrader is

$$t_n^{(\mathrm{expt})} = \frac{d_n^{(\mathrm{expt})} - d_{\mathrm{off.}}^{(\mathrm{expt})}}{v^{(\mathrm{expt})}}, \quad (3)$$

where $v^{(\mathrm{expt})}$ is the velocity of the particles before the degrader. The velocity $v^{(\mathrm{expt})}$ was obtained from the VAMOS++

spectrometer and corrected for the energy loss in the degrader by using the Doppler shift of the γ transition under study. The offset $d_{\text{off.}}^{(\text{expt})}$ was not measured during the experiment. Therefore, a value for the offset was obtained from the well-constrained fit of the lifetime of the 2_1^+ state in ^{64}Ni [47], resulting in $d_{\text{off.}}^{(64\text{Ni})} = -16.5 \pm 0.7\ \mu m$.

The intensities need to be normalized to allow for a direct comparison with experimental intensities. This is done by fitting normalization constants $I_{s+u,n}$, one for each distance of the degrader. By using both the shifted and unshifted components from the level of interest, the normalization constants $I_{s+u,n}$ are constrained by the total number of detected γ decays from this level; namely, $I_{s,n}^{(\text{expt})} + I_{u,n}^{(\text{expt})}$.

The lifetimes that best describe the data are found by using a nonlinear least-square minimization,

$$\begin{aligned}\chi^2(\tau,\tau_f,\tau_v,N_{0,\text{f}},N_{0,\text{v}},\vec{I}_{s+u},v,\epsilon_{\text{rel.}},d_{\text{off.}},\vec{d}\,) &= \sum_{n=1}^{N_{\text{dist}}}\left[\left(\frac{I_{u,n}^{(\text{expt})}-I_{s+u,n}R(t_n)}{\sigma_{I_{u,n}^{(\text{expt})}}}\right)^2+\left(\frac{I_{s,n}^{(\text{expt})}-I_{s+u,n}F(t_n)}{\sigma_{I_{s,n}^{(\text{expt})}}}\right)^2\right.\\ &\left.+\left(\frac{I_{u,n,\text{f}}^{(\text{expt})}-\epsilon_{\text{rel.}}I_{s+u,n}R_f(t_n)}{\sigma_{I_{u,n,\text{f}}^{(\text{expt})}}}\right)^2\right]\\ &+\left(\frac{v^{(\text{expt})}-v}{\sigma_{v^{(\text{expt})}}}\right)^2+\left(\frac{\epsilon_{\text{rel.}}^{(\text{expt})}-\epsilon_{\text{rel.}}}{\sigma_{\epsilon_{\text{rel.}}^{(\text{expt})}}}\right)^2+\left(\frac{d_{\text{off.}}^{(64\text{Ni})}-d_{\text{off.}}}{\sigma_{d_{\text{off.}}^{(64\text{Ni})}}}\right)^2\\ &+\sum_{n=1}^{N_{\text{dist}}}\left(\frac{d_n^{(\text{expt})}-d_n}{\sigma_{d_n^{(\text{expt})}}}\right)^2, \qquad (4)\end{aligned}$$

where $t_n = (d_n - d_{\text{off.}})/v$. By fitting the velocity, distances, distance offset, γ efficiency and normalization coefficients, the systematical uncertainties from these quantities were taken into account in the fitting procedure. Thus, the uncertainties in the obtained lifetimes incorporate all of these sources of experimental uncertainties. This also makes it possible to determine how much the different sources of experimental uncertainties influence the values and uncertainties of the obtained lifetimes, which we demonstrate in the following section. Here statistical errors refer to the errors extracted from the fit using Eq. (4) excluding the four last terms whereas the statistical errors are extracted from the increase in error on the lifetime using the full expression.

IV. RESULTS

The analysis procedure was tested by applying it to the lifetime of the first 2^+ state in ^{64}Ni. The resulting lifetime of $1.537(76)_{\text{stat}}(150)_{\text{sys}}$ ps agrees well with 1.570(50) ps obtained in Ref. [48] and the adopted value of 1.469(75) ps from Ref. [47]. However, it is in disagreement with the value of 1.287(52) ps from a recent Coulomb excitation experiment by Allmond *et al.* [49].

Because the lifetime of the 2^+ state in ^{64}Ni was used to constrain the offset parameter d_{off} for the distance, it was investigated how much the choice of its value influences the results for other nuclides. Using the newer value of Allmond *et al.* to determine the offset parameter yields shorter lifetimes for the other nuclides, but differences are within the error bars and would not change any conclusions; e.g., for ^{62}Fe the lifetime of the 4_1^+ states goes from 0.86(25) to 0.58(16) ps. For other nuclei the changes are similar. Constraining the distance parameter with the longer lifetime value of $1.537(76)_{\text{stat}}(150)_{\text{sys}}$ ps results in a lower χ^2 ($\chi^2/N_{\text{dof}} = 9$ vs $\chi^2/N_{\text{dof}} = 37$) of the fit and was therefore chosen. Approximately 8% of the uncertainty for the 2^+ state in ^{64}Ni originates from the measured intensities of the shifted and unshifted transitions, 68% from the statistical uncertainty in the velocity, and 19% from the distance offset. Applying the analysis method to the 4_1^+ state in ^{60}Fe results in a lifetime of 1.20(30) ps, with $\chi^2/N_{\text{dof}} = 1.29$ and 21% population from the seen $6_1^+ \to 4_1^+$ and $5_1^- \to 4_1^+$ transitions, with an effective lifetime of 15(15) ps. In the fit, 24% of the decay occurred via the long-lived (>9 ps) unseen feeder. In this case the statistical uncertainty is 98% of the total error. The obtained lifetime is in agreement with the result in Ref. [50].

For ^{62}Fe, the shifted and unshifted components of the $4_1^+ \to 2_1^+$ transition at 1299 keV are shown in Fig. 5. For this nucleus, the statistics allowed the inclusion of the $6_1^+ \to 4_1^+$ transition and the $5_1^- \to 4_1^+$ transition as seen feeding transitions, while unobserved feeding was taken into account by introducing a fictive feeding state. The corresponding decay curves are presented in Fig. 6. The fit yields a lifetime of $\tau_{4_1^+} = 0.86(25)$ ps with $\chi^2/N_{\text{dof}} = 1.72$, where $N_{\text{dof}} = 11$. In the fit, 27% of the intensity of the 4_1^+ state comes via the $6_1^+ \to 4_1^+$ transition with an effective lifetime of 9.5(24) ps, 25% via the $5_1^- \to 4_1^+$ transition with an effective lifetime of 58(50) ps, and 14% is attributed to unseen transitions with an effective lifetime of 75(75) ps. In this fit 97% of the error is statistical.

In ^{64}Fe, the lifetime of the 4_1^+ state was obtained from the shift of the $4_1^+ \to 2_1^+$ γ-ray transition at 1017 keV, shown in Fig. 5. The unresolved transitions at 1079 keV (from $6_1^+ \to 4_1^+$) and at 1078 keV (from $5_1^- \to 4_1^+$) were included as seen feeding in the fit, and the decay curves are shown in Fig. 6. As the 5_1^- state is more strongly populated than the 6_1^+ state and has a substantial lifetime it will be the main contributor to long-lived feeding. Subtracting the observed feeding, in combination with poor statistics, results in large uncertainties and hence very weak constraints on the fitting parameters. With unobserved feeding included in the fitting procedure, a short lifetime of 0.19(98) ps was obtained for the 4_1^+ state with $\chi^2/N_{\text{dof}} = 0.63$. The low χ^2 suggest a under-constrained fit, and such a short value lies outside the sensitivity range of the experiment. Assuming no unobserved feeding will always lead to a longer lifetime for the state of interest, providing only an upper limit for the lifetime. In case of the 4^+ state in ^{64}Fe an upper limit of $\tau < 1.8$ ps was found and adopted. In this case the fit yields $\chi^2/N_{\text{dof}} = 1.15$ with $N_{\text{dof}} = 9$, and 57% of the feeding was observed with an effective lifetime of 32(29) ps.

The γ-ray spectra gated on ^{63}Co, shown in Fig. 5, were used to extract the lifetime from the $11/2_1^- \to 7/2_1^-$ transition at 1674 keV γ-ray energy. Figure 6 shows the best fit of the decay curve with an unseen feeder of the order of 7 ps, resulting in $\tau_{11/2_1^-} = 0.55(19)$ ps with $\chi^2/N_{\text{dof}} = 1.6$ and $N_{\text{dof}} = 3$. Here, the relative strength of the unobserved feeding is 62%. This result is consistent, within the joint error bars, with the result found in Ref. [18]. In ^{61}Co, the $11/2_1^- \to (9/2)_1^-$ transition

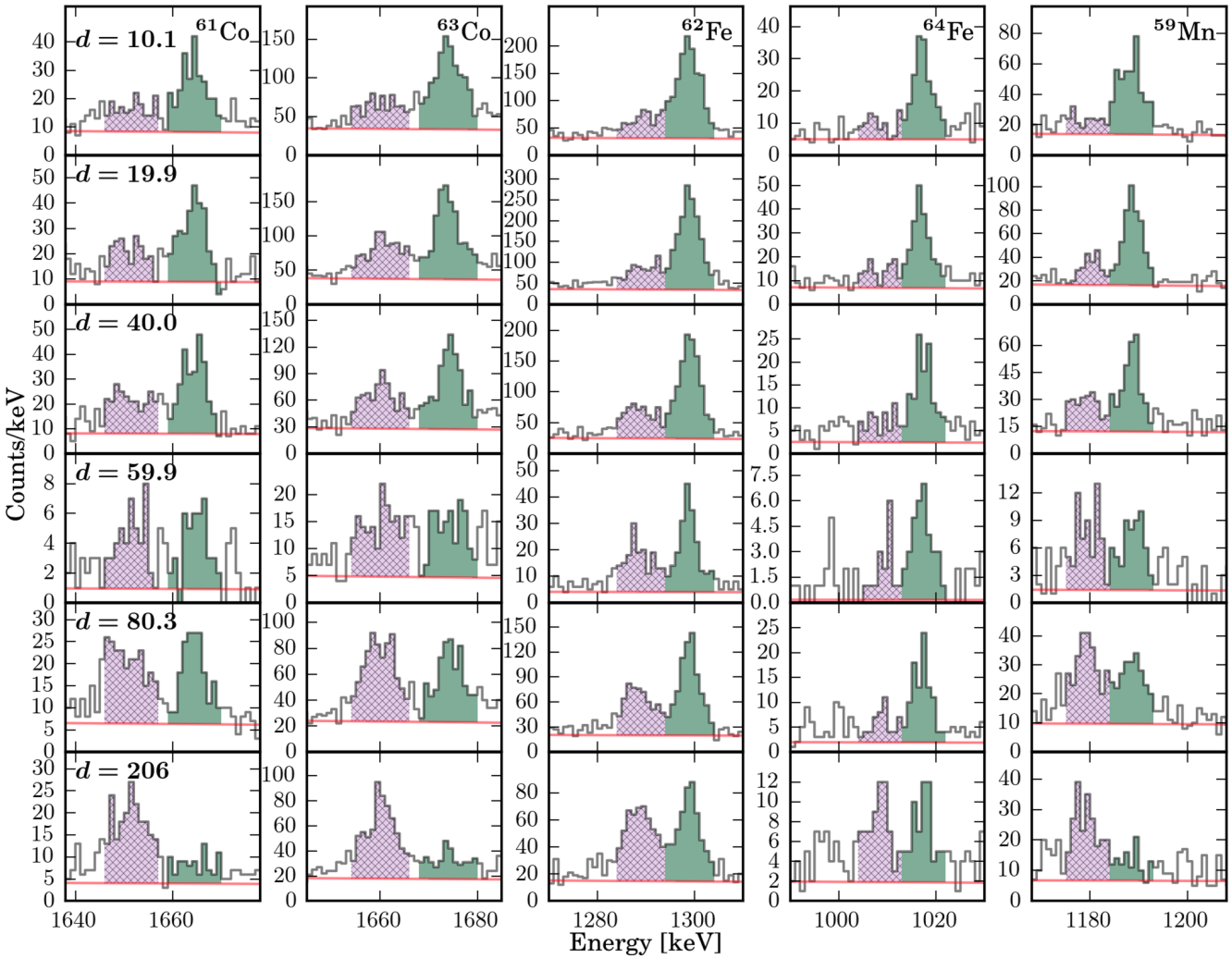

FIG. 5. The spectra used to extract the lifetime of the $11/2_1^-$ state in ^{59}Mn and ^{61,63}Co and the 4_1^+ in ^{62,64}Fe for the different distances d (in μm). Shown as color coded areas are the intensities used for determining the decay curves. The area to the left is the shifted component while the right area is the unshifted component.

at 1664 keV (see Fig. 5) was used to investigate the lifetime of the $11/2_1^-$ state. Seen feeding from the $(13/2)_1^- \rightarrow 11/2_1^-$ transition was included in the fit. Similar to the case of ^{64}Fe, the statistics were not sufficient to extract a precise value of the lifetime, and only an upper limit of $\tau < 2$ ps is found assuming no unobserved feeding. The $\chi^2/N_{\rm dof}$ for this fit is 2.3 with nine degrees of freedom.

Finally, the lifetime from the $11/2_1^- \rightarrow 7/2_1^-$ transition [28] at 1189 keV γ-ray energy in ^{59}Mn was extracted from the spectra shown in Fig. 5. Fitting the lifetime with an assumed long-lived unobserved feeder ($\tau_v > 7$ ps), where 17% of the decay proceeds via this feeder, resulted in a lifetime of $\tau_{11/2_1^-} = 2.63(40)$ ps with $\chi^2/N_{\rm dof} = 0.39$ and $N_{\rm dof} = 3$. The fit to the decay curve is shown in Fig. 6.

V. DISCUSSION

In Fig. 7 experimental and theoretical values for the reduced transition strengths in the iron isotopes $^{56-68}$Fe are shown for the $2_1^+ \rightarrow 0_1^+$ and $4_1^+ \rightarrow 2_1^+$ transitions. The new data points from this work are shown with stars. A small increase in the $B(E2)$ value for the $4_1^+ \rightarrow 2_1^+$ transition from $N = 34$ to $N = 36$ is observed. The upper limit for the lifetime of the 4_1^+ state in ^{64}Fe indicates a larger increase in the $B(E2)$ value from $N = 36$ to $N = 38$. Experimentally, the iron isotopes with $R_{42} = E(4^+)/E(2^+)$ ratios between the harmonic vibrator limit of 2 and the rotational limit of 3.3 [51] while having $B(E2; 4_1^+ \rightarrow 2_1^+)/B(E2; 2_1^+ \rightarrow 0_1^+)$ ratios smaller than 2 can be characterized as soft rotors, as already suggested by Daugas *et al.* [52].

Large-scale shell-model calculations using the modified LNPS interaction [4,27], also shown in Fig. 7, accurately reproduce the $B(E2; 4_1^+ \rightarrow 2_1^+)$ values within the experimental errors. For the effective charges, we have adopted those deduced in Ref. [53]: $e_n = 0.46$ and $e_p = 1.31$. This increase in collectivity can be explained by a decrease of the subshell gap at $N = 40$, driven by the monopole proton-neutron part of the effective interaction, favoring neutron excitations into the quasi-SU(3) partners $\nu 1g_{9/2}$-$\nu 2d_{5/2}$. The occupation number for the $\nu 1g_{9/2}$ orbital increases from 1.14 for the 4_1^+ state

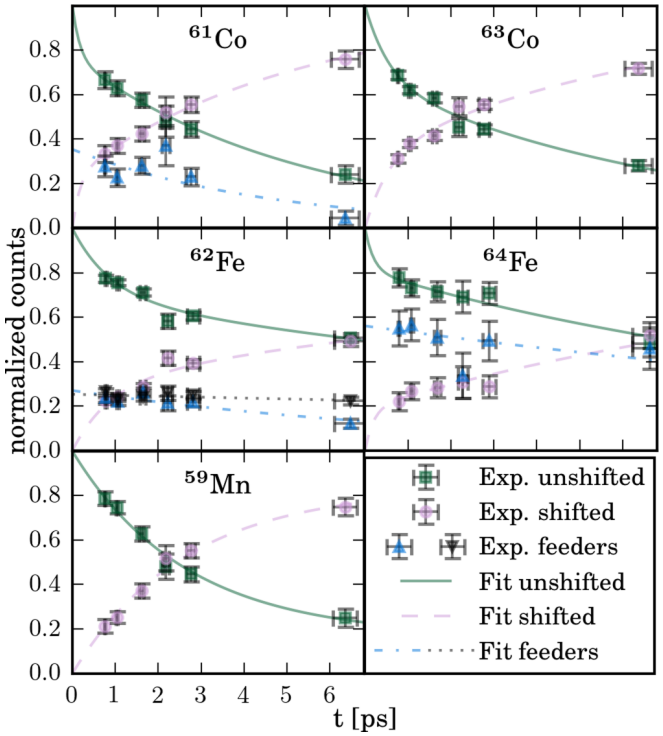

FIG. 6. The decay curves used to extract the lifetime of the $11/2^-_1$ states in ^{59}Mn and ^{61,63}Co and the 4^+_1 state in ^{62,64}Fe. Note that, for ^{62}Fe, two observed feeder states have been included in the fit. For ^{64}Fe the fit used to extract the upper limit on the lifetime is shown.

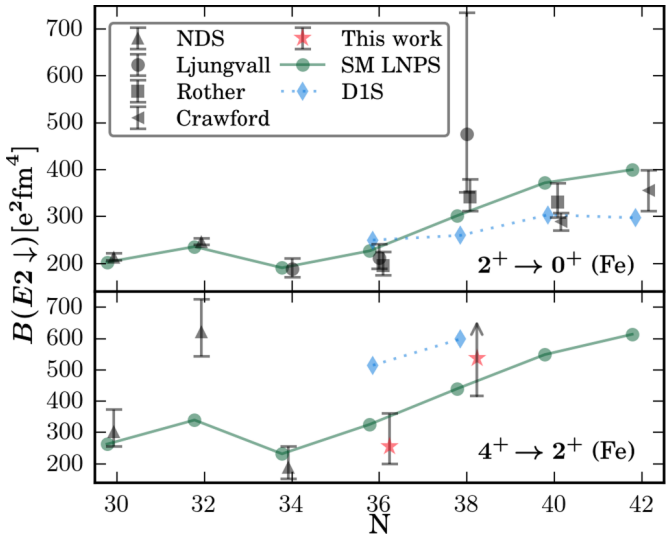

FIG. 7. $B(E2\downarrow)$ values for even iron isotopes for transitions from the first 2^+ and the first 4^+ state. The solid green lines with circles are shell-model calculations and the blue dashed lines with diamonds are D1S calculations, both a part of the present work. Previous experimental results with error bars are from Refs. [8,25,26] and Nuclear Data Sheets (NDS) [54–56], while the red stars are the new experimental results presented here.

in ^{62}Fe to 2.13 in ^{64}Fe. In relative terms the increase of occupation in the $\nu 2d_{5/2}$ orbital from $N = 36$ to $N = 38$ is even larger, going from 0.1 to 0.35 for the 4^+_1 states. On the proton side this is accompanied by an increase in the occupation of the $2p_{3/2}$ orbital, which is a quasi-SU(3) partner of the $1f_{7/2}$ orbital. The gain in energy due to the quadrupole correlations largely exceeds the energy needed to excite nucleons to the higher-lying orbitals.

We have also performed microscopic calculations based on constrained Hartree–Fock–Bogoliubov (CHFB) theory using the Gogny D1S interaction [57,58] and mapping to the five-dimensional collective Hamiltonian (5DCH). The method is described in detail in Ref. [59]. Worth noticing is that the CHFB + 5DCH calculations contain no free parameters except for those specifying the phenomenological D1S interaction, which is used across the entire nuclear chart. As can be seen in Fig. 7, these calculations give a relative increase in the $B(E2; 4^+_1 \rightarrow 2^+_1)$ values with neutron number that is very similar compared with the increase found in the shell-model calculations, but the absolute values are approximately twice as large. While the calculated $B(E2; 4^+_1 \rightarrow 2^+_1)$ value for ^{64}Fe is consistent with the experimental limit, the value for ^{62}Fe is too large. The $B(E2; 2^+_1 \rightarrow 0^+_1)$ values obtained with the 5DCH approach, on the other hand, are in good agreement with both experiment and shell-model calculations. Based on the transition strengths the results of the 5DCH calculations indicate a vibrational rather than rotational character for the neutron-rich Fe isotopes. The occupation numbers for the $\pi 1f_{7/2}$ and $\pi 2p_{3/2}$ orbitals are constant for the iron isotopes, with the latter remaining small, showing no increase of proton excitations across the $Z = 28$ shell gap, contrary to the shell-model predictions. Furthermore, at the mean-field level there are no signs of a weakening of the $N = 40$ subshell gap [35,52]. A similar result was found for neutron-rich zinc isotopes, where the 5DCH calculations also overestimated the $B(E2; 4^+_1 \rightarrow 2^+_1)$ values by a factor of two to three [60]. The 5DCH calculations provide dynamical deformed shapes for the ground state, 2^+, 4^+, and 6^+ yrast levels that are not strong enough. These discrepancies could be due to the missing of an explicit tensor term in the effective NN interaction in the Gogny D1S force. Work on implementation of such a term is currently in progress [61]. It should also be mentioned that the collective behavior assumed in the generator coordinate method (GCM) with the Gaussian overlap approximation (GOA) may not be valid close to the $Z = 28$ shell closure. The potential-energy surface obtained from the CHFB calculations shows softness in both β and γ deformation parameters, indicating no deformed minima in the iron region.

In neutron-rich cobalt isotopes a set of low-lying states has been interpreted as the $7/2^-$ proton hole weakly coupled to the 2^+ excitation in the corresponding nickel isotope; see, e.g., Refs. [16,17] and references therein. In particular it is expected that the first $11/2^-$ state belongs to this multiplet and, therefore, the $B(E2; 11/2^-_1 \rightarrow 7/2^-_1)$ values in the chain of cobalt isotopes should closely follow the $B(E2; 2^+_1 \rightarrow 0^+_1)$ values in the respective nickel isotones. In Fig. 8 the reduced transition strengths for the decay of the first 2^+ state in nickel isotopes are compared with that of the decay of the first $11/2^-$ state in the cobalt isotopes. Also shown are large-scale shell-model calculations based on the modified LNPS

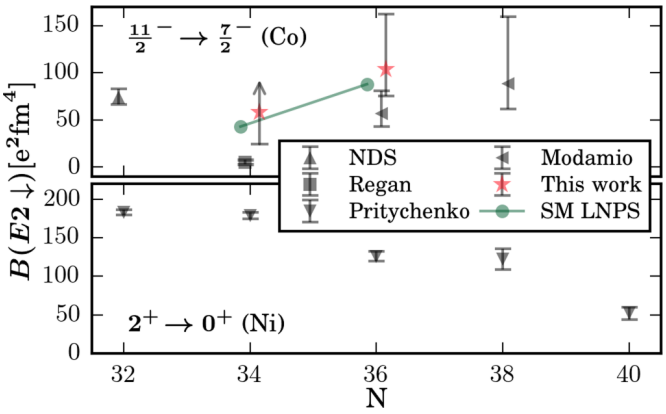

FIG. 8. $B(E2\downarrow)$ values for odd cobalt isotopes for transitions from the first $11/2^-$ to the ground state. The green solid line with circles represents shell-model calculations performed within this work. Previous experimental results with error bars are from Refs. [18,36] and the compilations [47,62] while the red stars are the new experimental results presented here. For comparison, the $B(E2\downarrow)$ values for the first 2^+ state in the even nickel isotopes are shown also.

interaction [4,27]. The new data points in this work are marked with stars. Although it was only possible to extract a lower limit for the transition probability in ^{61}Co ($N = 34$), it is clear that the result is incompatible with the older measurement from the work of Regan *et al.* who deduced 10^{+10}_{-3} ps [36]. Taking this into consideration, the hypothesis that the first $11/2^-$ state in the neutron-rich cobalt isotopes belongs to the multiplet generated by the coupling of the $7/2^-$ proton hole to the 2^+ state in the nickel isotopes is a good first-order understanding of their structure. The shell-model calculations reproduce very well the experimental data. Analyzing them in detail shows that both ^{61}Co and ^{63}Co lie outside the island of inversion below ^{68}Ni, where an increased population of quasi-SU(3) partner orbitals ($\nu 1g_{9/2}$-$\nu 2d_{5/2}$) generates quadrupole correlations. The occupation numbers for the $\nu 1g_{9/2}$ orbital remain small, around 0.1 for ^{61}Co and 0.5 for ^{63}Co for the first $11/2^-$ states. The $\nu 2d_{5/2}$ orbital is very weakly populated as well. Calculations restricted to a fp model space reproduce the excitation energies, and to a lesser extent also the transition strengths. This suggests that ^{61,63}Co can be viewed as being on the limit of the fp space, as was already concluded by Recchia *et al.* [17].

Only few transition strengths are known for the manganese isotopes, in particular for the $11/2^-_1 \rightarrow 7/2^-_1$ transition. The systematics of the $11/2^-_1$ level in the neutron-rich manganese isotopes ($A = 55$–61) shows rather constant energies with no signs of rapid changes in its structure. In ^{55}Mn the $B(E2; 11/2^-_1 \rightarrow 7/2^-_1)$ has been determined to be 167(20) e^2 fm^4 [63], to be compared with 110^{+15}_{-12} e^2 fm^4 in ^{59}Mn as measured in this work. Our calculations overestimate the $B(E2; 11/2^-_1 \rightarrow 7/2^-_1)$ value in ^{59}Mn, but remain smaller than the $B(E2; 11/2^-_1 \rightarrow 7/2^-_1)$ value in ^{55}Mn. Hence, neither the experimental nor the theoretical result show any sign of enhanced collectivity for ^{59}Mn. This is consistent with recent collinear laser spectroscopy studies of Babcock *et al.* [30], which suggest an increase of collectivity due to a weakening of the $N = 40$ subshell closure beyond $N = 36$.

TABLE I. Summary of experimental and theoretical lifetimes and $B(E2)$ values obtained in this work. Previously measured lifetimes are also given with corresponding reference.

Nuc.	State	γ energy	τ [ps]		$B(E2\downarrow)$ [e^2 fm^4]		
		[keV]	Expt.	Prev.	Expt.	SM	D1S
^{59}Mn	$11/2^-_1$	1189	2.63(40)		111^{+21}_{-15}	152	
^{62}Fe	4^+_1	1299	0.86(25)		256^{+105}_{-58}	326	515
^{64}Fe	4^+_1	1017	<1.8		>420	441	599
^{61}Co	$11/2^-_1$	1664	<2	10^{+10}_{-3} [36]	>24	43	
^{63}Co	$11/2^-_1$	1672	0.55(19)	1.0(3) [18]	104^{+58}_{-28}	88	

VI. SUMMARY

In the present work, lifetimes of excited states in moderately-neutron-rich cobalt, iron, and manganese isotopes have been measured by using the recoil distance Doppler shift method. The nuclei ^{61,63}Co, ^{62,64}Fe, and ^{59}Mn were produced in an experiment at GANIL via multinucleon transfer reactions of a ^{238}U beam on a ^{64}Ni target, identified on an event-by-event basis in the large-acceptance spectrometer VAMOS++, and γ rays were detected using the AGATA γ-ray spectrometer. It was possible to determine the lifetime of the 4^+_1 state in ^{62}Fe and give an upper limit for ^{64}Fe. For the odd-Z neighbor isotopes, lifetimes for the $11/2^-$ states in ^{59}Mn and ^{63}Co were determined, whereas for ^{61}Co again only an upper limit could be given. Theoretical calculations have been performed and compared with the experimental results, as summarized in Table I. Large-scale shell-model calculations using the modified LNPS interaction [4,27] give a very good description of the low-energy nuclear structure in the region. They show an increase in quadrupole collectivity when approaching $N = 40$. Quadrupole correlations induce the excitation of neutrons to the $\nu 1g_{9/2}$ and $\nu 2d_{5/2}$ orbitals. For the even-even iron isotopes, a rotational-like behavior emerges as $N = 40$ is approached. In the case of ^{59}Mn, the predicted transition probability for the $11/2^-_1 \rightarrow 7/2^-_1$ transition is larger than the measured one. It should be pointed out that our shell-model calculations are capable of reproducing both excitation energies and transition probabilities for nuclei both inside and outside of the island of inversion found at $N = 40$.

Beyond-mean-field CHFB + 5DCH calculations using the D1S interaction were also compared with the experimental data. Although the overall trend of increasing collectivity with increasing neutron number for the iron isotopes is clearly seen, the beyond-mean-field calculations suggest a vibrational-like structure and no clear change in structure close to $N = 38$. This might originate from the lack of an explicit tensor term in the force.

ACKNOWLEDGMENTS

We are grateful for the help from Johan Goupil and the GANIL technical staff. The authors would also like to thank M. Loriggiola, Laboratori Nazionali di Legnaro, and

G. Fremont, GANIL, for preparing the target and degrader foils. This project received funding from the European Union's Horizon 2020 research and innovation programme under grant agreement n°654002. Support from the Norwegian Research Council, project grant 213442, is acknowledged. The project has received funding from the Swedish Research Council. This work is supported by the Spanish Ministerio de Economía y Competitividad under contract FPA2014-57196-C5-4-P. One of the authors, A. Gadea, was partially supported by MINECO and Generalitat Valenciana, Spain, under the grants FPA2014-57196-C5 and PROMETEOII/2014/019, and by EU FEDER funds.

[1] O. Sorlin and M.-G. Porquet, Prog. Part. Nucl. Phys. **61**, 602 (2008).
[2] T. Otsuka, R. Fujimoto, Y. Utsuno, B. A. Brown, M. Honma, and T. Mizusaki, Phys. Rev. Lett. **87**, 082502 (2001).
[3] T. Otsuka, T. Suzuki, R. Fujimoto, H. Grawe, and Y. Akaishi, Phys. Rev. Lett. **95**, 232502 (2005).
[4] S. M. Lenzi, F. Nowacki, A. Poves, and K. Sieja, Phys. Rev. C **82**, 054301 (2010).
[5] P. C. Srivastava and V. K. B. Kota, Phys. At. Nucl. **74**, 971 (2011).
[6] J. Kotila and S. M. Lenzi, Phys. Rev. C **89**, 064304 (2014).
[7] L. Coraggio, A. Covello, A. Gargano, and N. Itaco, Phys. Rev. C **89**, 024319 (2014).
[8] J. Ljungvall, A. Görgen, A. Obertelli, W. Korten, E. Clément, G. de France, A. Bürger, J.-P. Delaroche, A. Dewald, A. Gadea *et al.*, Phys. Rev. C **81**, 061301 (2010).
[9] R. Broda, B. Fornal, W. Królas, T. Pawłat, D. Bazzacco, S. Lunardi, C. Rossi-Alvarez, R. Menegazzo, G. de Angelis, P. Bednarczyk, J. Rico, D. De Acuña, P. J. Daly, R. H. Mayer, M. Sferrazza, H. Grawe, K. H. Maier, and R. Schubart, Phys. Rev. Lett. **74**, 868 (1995).
[10] O. Sorlin, S. Leenhardt, C. Donzaud, J. Duprat, F. Azaiez, F. Nowacki, H. Grawe, Z. Dombrádi, F. Amorini, A. Astier, D. Baiborodin, M. Belleguic, C. Borcea, C. Bourgeois, D. M. Cullen, Z. Dlouhy, E. Dragulescu, M. Górska, S. Grévy, D. Guillemaud-Mueller, G. Hagemann, B. Herskind, J. Kiener, R. Lemmon, M. Lewitowicz, S. M. Lukyanov, P. Mayet, F. de Oliveira Santos, D. Pantalica, Y.-E. Penionzhkevich, F. Pougheon, A. Poves, N. Redon, M. G. Saint-Laurent, J. A. Scarpaci, G. Sletten, M. Stanoiu, O. Tarasov, and C. Theisen, Phys. Rev. Lett. **88**, 092501 (2002).
[11] C. Guénaut, G. Audi, D. Beck, K. Blaum, G. Bollen, P. Delahaye, F. Herfurth, A. Kellerbauer, H.-J. Kluge, J. Libert, D. Lunney, S. Schwarz, L. Schweikhard, and C. Yazidjian, Phys. Rev. C **75**, 044303 (2007).
[12] S. Rahaman, J. Hakala, V. V. Elomaa, T. Eronen, U. Hager, A. Jokinen, A. Kankainen, I. D. Moore, H. Penttilä, S. Rinta-Antila, J. Rissanen, A. Saastamoinen, C. Weber, and J. Äystö, Eur. Phys. J. A **34**, 5 (2007).
[13] K. Langanke, J. Terasaki, F. Nowacki, D. J. Dean, and W. Nazarewicz, Phys. Rev. C **67**, 044314 (2003).
[14] D. Pauwels, O. Ivanov, N. Bree, J. Büscher, T. E. Cocolios, J. Gentens, M. Huyse, A. Korgul, Y. Kudryavtsev, R. Raabe, M. Sawicka, I. Stefanescu, J. Van de Walle, P. Van den Bergh, P. Van Duppen, and W. B. Walters, Phys. Rev. C **78**, 041307(R) (2008).
[15] D. Pauwels, O. Ivanov, N. Bree, J. Büscher, T. E. Cocolios, M. Huyse, Y. Kudryavtsev, R. Raabe, M. Sawicka, J. Van de Walle, P. Van Duppen, A. Korgul, I. Stefanescu, A. A. Hecht, N. Hoteling, A. Wöhr, W. B. Walters, R. Broda, B. Fornal, W. Krolas, T. Pawlat, J. Wrzesinski, M. P. Carpenter, R. V. F. Janssens, T. Lauritsen, D. Seweryniak, S. Zhu, J. R. Stone, and X. Wang, Phys. Rev. C **79**, 044309 (2009).
[16] A. Dijon, E. Clément, G. de France, P. Van Isacker, J. Ljungvall, A. Görgen, A. Obertelli, W. Korten, A. Dewald, A. Gadea *et al.*, Phys. Rev. C **83**, 064321 (2011).
[17] F. Recchia, S. M. Lenzi, S. Lunardi, E. Farnea, A. Gadea, N. Mărginean, D. R. Napoli, F. Nowacki, A. Poves, J. J. Valiente-Dobón, M. Axiotis, S. Aydin, D. Bazzacco, G. Benzoni, P. G. Bizzeti, A. M. Bizzeti-Sona, A. Bracco, D. Bucurescu, E. Caurier, L. Corradi, G. de Angelis, F. Della Vedova, E. Fioretto, A. Gottardo, M. Ionescu-Bujor, A. Iordachescu, S. Leoni, R. Mărginean, P. Mason, R. Menegazzo, D. Mengoni, B. Million, G. Montagnoli, R. Orlandi, G. Pollarolo, E. Sahin, F. Scarlassara, R. P. Singh, A. M. Stefanini, S. Szilner, C. A. Ur, and O. Wieland, Phys. Rev. C **85**, 064305 (2012).
[18] V. Modamio, J. J. Valiente-Dobón, S. Lunardi, S. M. Lenzi, A. Gadea, D. Mengoni, D. Bazzacco, A. Algora, P. Bednarczyk, G. Benzoni *et al.*, Phys. Rev. C **88**, 044326 (2013).
[19] M. Hannawald, T. Kautzsch, A. Wöhr, W. B. Walters, K.-L. Kratz, V. N. Fedoseyev, V. I. Mishin, W. Böhmer, B. Pfeiffer, V. Sebastian, Y. Jading, U. Köster, J. Lettry, H. L. Ravn, and ISOLDE Collaboration, Phys. Rev. Lett. **82**, 1391 (1999).
[20] S. N. Liddick, B. Abromeit, A. Ayres, A. Bey, C. R. Bingham, B. A. Brown, L. Cartegni, H. L. Crawford, I. G. Darby, R. Grzywacz, S. Ilyushkin, M. Hjorth-Jensen, N. Larson, M. Madurga, D. Miller, S. Padgett, S. V. Paulauskas, M. M. Rajabali, K. Rykaczewski, and S. Suchyta, Phys. Rev. C **87**, 014325 (2013).
[21] G. Benzoni, A. Morales, H. Watanabe, S. Nishimura, L. Coraggio, N. Itaco, A. Gargano, F. Browne, R. Daido, P. Doornenbal, Y. Fang, G. Lorusso, Z. Patel, S. Rice, L. Sinclair, P.-A. Söderström, T. Sumikama, J. Wu, Z. Xu, R. Yokoyama, H. Baba, R. Avigo, F. B. Garrote, N. Blasi, A. Bracco, F. Camera, S. Ceruti, F. Crespi, G. de Angelis, M.-C. Delattre, Z. Dombradi, A. Gottardo, T. Isobe, I. Kuti, K. Matsui, B. Melon, D. Mengoni, T. Miyazaki, V. Modamio-Hoybjor, S. Momiyama, D. Napoli, M. Niikura, R. Orlandi, H. Sakurai, E. Sahin, D. Sohler, R. Taniuchi, J. Taprogge, Z. Vajta, J. Valiente-Dobón, O. Wieland, and M. Yalcinkaya, Phys. Lett. B **751**, 107 (2015).
[22] N. Hoteling, W. B. Walters, R. V. F. Janssens, R. Broda, M. P. Carpenter, B. Fornal, A. A. Hecht, M. Hjorth-Jensen, W. Królas, T. Lauritsen, T. Pawlat, D. Seweryniak, X. Wang, A. Wöhr, J. Wrzesiński, and S. Zhu, Phys. Rev. C **74**, 064313 (2006).
[23] S. Lunardi, S. M. Lenzi, F. Della Vedova, E. Farnea, A. Gadea, N. Marginean, D. Bazzacco, S. Beghini, P. G. Bizzeti, A. M. Bizzeti-Sona, D. Bucurescu, L. Corradi, A. N. Deacon, G. de Angelis, E. Fioretto, S. J. Freeman, M. Ionescu-Bujor, A. Iordachescu, P. Mason, D. Mengoni, G. Montagnoli, D. R. Napoli, F. Nowacki, R. Orlandi, G. Pollarolo, F. Recchia, F. Scarlassara, J. F. Smith, A. M. Stefanini, S. Szilner, C. A. Ur,

J. J. Valiente-Dobón, and B. J. Varley, Phys. Rev. C **76**, 034303 (2007).
[24] P. Adrich, A. M. Amthor, D. Bazin, M. D. Bowen, B. A. Brown, C. M. Campbell, J. M. Cook, A. Gade, D. Galaviz, T. Glasmacher, S. McDaniel, D. Miller, A. Obertelli, Y. Shimbara, K. P. Siwek, J. A. Tostevin, and D. Weisshaar, Phys. Rev. C **77**, 054306 (2008).
[25] W. Rother, A. Dewald, H. Iwasaki, S. M. Lenzi, K. Starosta, D. Bazin, T. Baugher, B. A. Brown, H. L. Crawford, C. Fransen, A. Gade, T. N. Ginter, T. Glasmacher, G. F. Grinyer, M. Hackstein, G. Ilie, J. Jolie, S. McDaniel, D. Miller, P. Petkov, T. Pissulla, A. Ratkiewicz, C. A. Ur, P. Voss, K. A. Walsh, D. Weisshaar, and K.-O. Zell, Phys. Rev. Lett. **106**, 022502 (2011).
[26] H. L. Crawford, R. M. Clark, P. Fallon, A. O. Macchiavelli, T. Baugher, D. Bazin, C. W. Beausang, J. S. Berryman, D. L. Bleuel, C. M. Campbell, M. Cromaz, G. de Angelis, A. Gade, R. O. Hughes, I. Y. Lee, S. M. Lenzi, F. Nowacki, S. Paschalis, M. Petri, A. Poves, A. Ratkiewicz, T. J. Ross, E. Sahin, D. Weisshaar, K. Wimmer, and R. Winkler, Phys. Rev. Lett. **110**, 242701 (2013).
[27] C. Santamaria, C. Louchart, A. Obertelli, V. Werner, P. Doornenbal, F. Nowacki, G. Authelet, H. Baba, D. Calvet, F. Château, A. Corsi, A. Delbart, J.-M. Gheller, A. Gillibert, T. Isobe, V. Lapoux, M. Matsushita, S. Momiyama, T. Motobayashi, M. Niikura, H. Otsu, C. Péron, A. Peyaud, E. C. Pollacco, J.-Y. Roussé, H. Sakurai, M. Sasano, Y. Shiga, S. Takeuchi, R. Taniuchi, T. Uesaka, H. Wang, K. Yoneda, F. Browne, L. X. Chung, Z. Dombradi, S. Franchoo, F. Giacoppo, A. Gottardo, K. Hadynska-Klek, Z. Korkulu, S. Koyama, Y. Kubota, J. Lee, M. Lettmann, R. Lozeva, K. Matsui, T. Miyazaki, S. Nishimura, L. Olivier, S. Ota, Z. Patel, N. Pietralla, E. Sahin, C. Shand, P.-A. Söderström, I. Stefan, D. Steppenbeck, T. Sumikama, D. Suzuki, Z. Vajta, J. Wu, and Z. Xu, Phys. Rev. Lett. **115**, 192501 (2015).
[28] J. J. Valiente-Dobón, S. M. Lenzi, S. J. Freeman, S. Lunardi, J. F. Smith, A. Gottardo, F. D. Vedova, E. Farnea, A. Gadea, D. R. Napoli *et al.*, Phys. Rev. C **78**, 024302 (2008).
[29] D. Steppenbeck, A. N. Deacon, S. J. Freeman, R. V. F. Janssens, S. Zhu, M. P. Carpenter, P. Chowdhury, M. Honma, T. Lauritsen, C. J. Lister *et al.*, Phys. Rev. C **81**, 014305 (2010).
[30] C. Babcock, H. Heylen, J. Billowes, M. Bissell, K. Blaum, P. Campbell, B. Cheal, R. G. Ruiz, C. Geppert, W. Gins, M. Kowalska, K. Kreim, S. Lenzi, I. Moore, R. Neugart, G. Neyens, W. Nörtershäuser, J. Papuga, and D. Yordanov, Phys. Lett. B **750**, 176 (2015).
[31] Z. H. Wang, J. Xiang, W. H. Long, and Z. P. Li, J. Phys. G **42**, 045108 (2015).
[32] K. Yoshida and N. Hinohara, Phys. Rev. C **83**, 061302 (2011).
[33] K. Sato, N. Hinohara, K. Yoshida, T. Nakatsukasa, M. Matsuo, and K. Matsuyanagi, Phys. Rev. C **86**, 024316 (2012).
[34] C. F. Jiao, J. C. Pei, and F. R. Xu, Phys. Rev. C **90**, 054314 (2014).
[35] L. Gaudefroy, A. Obertelli, S. Péru, N. Pillet, S. Hilaire, J. P. Delaroche, M. Girod, and J. Libert, Phys. Rev. C **80**, 064313 (2009).
[36] P. H. Regan, J. W. Arrison, U. J. Hüttmeier, and D. P. Balamuth, Phys. Rev. C **54**, 1084 (1996).
[37] J. Van de Walle, V. Bildstein, N. Bree, J. Cederkäll, P. Delahaye, J. Diriken, A. Ekström, V. N. Fedosseev, R. Gernhäuser, A. Gustafsson, A. Herlert, M. Huyse, O. Ivanov, T. Kröll, R. Krücken, B. Marsh, N. Partronis, P. Van Duppen, D. Voulot, N. Warr, F. Wenander, K. Wimmer, and S. M. Lenzi, Eur. Phys. J. A **42**, 401 (2009).
[38] T. Baugher, A. Gade, R. V. F. Janssens, S. M. Lenzi, D. Bazin, M. P. Carpenter, C. J. Chiara, A. N. Deacon, S. J. Freeman, G. F. Grinyer, C. R. Hoffman, B. P. Kay, F. G. Kondev, T. Lauritsen, E. M. Lunderberg, S. McDaniel, K. C. Meierbachtol, A. Ratkiewicz, S. R. Stroberg, K. A. Walsh, D. Weisshaar, and S. Zhu, Phys. Rev. C **93**, 014313 (2016).
[39] A. Dewald, O. Möller, and P. Petkov, Prog. Part. Nucl. Phys. **67**, 786 (2012).
[40] S. Pullanhiotan, M. Rejmund, A. Navin, W. Mittig, and S. Bhattacharyya, Nucl. Instrum. Methods Phys. Res., Sect. A **593**, 343 (2008).
[41] M. Rejmund, B. Lecornu, A. Navin, C. Schmitt, S. Damoy, O. Delaune, J. Enguerrand, G. Fremont, P. Gangnant, L. Gaudefroy, B. Jacquot, J. Pancin, S. Pullanhiotan, and C. Spitaels, Nucl. Instrum. Methods Phys. Res., Sect. A **646**, 184 (2011).
[42] M. Vandebrouck, A. Lemasson, M. Rejmund, G. Fremont, J. Pancin, A. Navin, C. Michelagnoli, J. Goupil, C. Spitaels, and B. Jacquot, Nucl. Instrum. Methods Phys. Res., Sect. A **812**, 112 (2016).
[43] S. Akkoyun, A. Algora, B. Alikhani, F. Ameil, G. de Angelis, L. Arnold, A. Astier, A. Ataç, Y. Aubert, C. Aufranc *et al.*, Nucl. Instrum. Methods Phys. Res., Sect. A **668**, 26 (2012).
[44] E. Clément (unpublished).
[45] J. Ljungvall, G. Georgiev, S. Cabaret, N. Karkour, D. Linget, G. Sedes, R. Chevrier, I. Matea, M. Niikura, M.-D. Salsac, and B. Sulignano, Nucl. Instrum. Methods Phys. Res., Sect. A **679**, 61 (2012).
[46] E. Farnea, F. Recchia, D. Bazzacco, T. Kröll, Z. Podolyák, B. Quintana, and A. Gadea, Nucl. Instrum. Methods Phys. Res., Sect. A **621**, 331 (2010).
[47] B. Pritychenko, J. Choquette, M. Horoi, B. Karamy, and B. Singh, At. Data Nucl. Data Tables **98**, 798 (2012).
[48] O. Kenn, K.-H. Speidel, R. Ernst, J. Gerber, N. Benczer-Koller, G. Kumbartzki, P. Maier-Komor, and F. Nowacki, Phys. Rev. C **63**, 021302 (2000).
[49] J. M. Allmond, B. A. Brown, A. E. Stuchbery, A. Galindo-Uribarri, E. Padilla-Rodal, D. C. Radford, J. C. Batchelder, M. E. Howard, J. F. Liang, B. Manning, R. L. Varner, and C.-H. Yu, Phys. Rev. C **90**, 034309 (2014).
[50] E. K. Warburton, J. W. Olness, A. M. Nathan, J. J. Kolata, and J. B. McGrory, Phys. Rev. C **16**, 1027 (1977).
[51] L. Grodzins, Phys. Lett. **2**, 88 (1962).
[52] J. M. Daugas, I. Matea, J.-P. Delaroche, M. Pfützner, M. Sawicka, F. Becker, G. Bélier, C. R. Bingham, R. Borcea, E. Bouchez, A. Buta, E. Dragulescu, G. Georgiev, J. Giovinazzo, M. Girod, H. Grawe, R. Grzywacz, F. Hammache, F. Ibrahim, M. Lewitowicz, J. Libert, P. Mayet, V. Méot, F. Negoita, F. de Oliveira Santos, O. Perru, O. Roig, K. Rykaczewski, M. G. Saint-Laurent, J. E. Sauvestre, O. Sorlin, M. Stanoiu, I. Stefan, C. Stodel, C. Theisen, D. Verney, and J. Żylicz, Phys. Rev. C **83**, 054312 (2011).
[53] M. Dufour and A. P. Zuker, Phys. Rev. C **54**, 1641 (1996).
[54] H. Junde, H. Su, and Y. Dong, Nucl. Data Sheets **112**, 1513 (2011).
[55] C. D. Nesaraja, S. D. Geraedts, and B. Singh, Nucl. Data Sheets **111**, 897 (2010).
[56] E. Browne and J. Tuli, Nucl. Data Sheets **114**, 1849 (2013).
[57] J. Dechargé and D. Gogny, Phys. Rev. C **21**, 1568 (1980).

[58] J. Berger, M. Girod, and D. Gogny, Comput. Phys. Commun. **63**, 365 (1991).
[59] J. P. Delaroche, M. Girod, J. Libert, H. Goutte, S. Hilaire, S. Péru, N. Pillet, and G. F. Bertsch, Phys. Rev. C **81**, 014303 (2010).
[60] C. Louchart, A. Obertelli, A. Görgen, W. Korten, D. Bazzacco, B. Birkenbach, B. Bruyneel, E. Clément, P. J. Coleman-Smith, L. Corradi, D. Curien, G. de Angelis, G. de France, J.-P. Delaroche, A. Dewald, F. Didierjean, M. Doncel, G. Duchêne, J. Eberth, M. N. Erduran, E. Farnea, C. Finck, E. Fioretto, C. Fransen, A. Gadea, M. Girod, A. Gottardo, J. Grebosz, T. Habermann, M. Hackstein, T. Huyuk, J. Jolie, D. Judson, A. Jungclaus, N. Karkour, S. Klupp, R. Krücken, A. Kusoglu, S. M. Lenzi, J. Libert, J. Ljungvall, S. Lunardi, G. Maron, R. Menegazzo, D. Mengoni, C. Michelagnoli, B. Million, P. Molini, O. Möller, G. Montagnoli, D. Montanari, D. R. Napoli, R. Orlandi, G. Pollarolo, A. Prieto, A. Pullia, B. Quintana, F. Recchia, P. Reiter, D. Rosso, W. Rother, E. Sahin, M.-D. Salsac, F. Scarlassara, M. Schlarb, S. Siem, P. P. Singh, P.-A. Söderström, A. M. Stefanini, O. Stézowski, B. Sulignano, S. Szilner, C. Theisen, C. A. Ur, J. J. Valiente-Dobón, and M. Zielinska, Phys. Rev. C **87**, 054302 (2013).
[61] R. N. Bernard and M. Anguiano, Nucl. Phys. A **953**, 32 (2016).
[62] C. M. Baglin, Nucl. Data Sheets **95**, 215 (2002).
[63] A. M. Nathan, J. W. Olness, E. K. Warburton, and J. B. McGrory, Phys. Rev. C **16**, 192 (1977).

7.8 Experimental determination of reference pulses for highly segmented HPGe detectors and application to Pulse Shape Analysis used in gamma-ray tracking arrays

Eur. Phys. J. A (2018) **52**: 198
DOI 10.1140/epja/i2018-12636-9

THE EUROPEAN PHYSICAL JOURNAL A

Regular Article – Experimental Physics

Experimental determination of reference pulses for highly segmented HPGe detectors and application to Pulse Shape Analysis used in γ-ray tracking arrays

H.J. Li[1], J. Ljungvall[2,a], C. Michelagnoli[3,1], E. Clément[1], J. Dudouet[2,4], P. Désesquelles[2], A. Lopez-Martens[2], and G. de France[1]

[1] GANIL, CEA/DRF-CNRS/IN2P3, BP 55027, 14076 Caen Cedex 5, France
[2] CSNSM, Université Paris-Sud, CNRS/IN2P3, Université Paris-Saclay, 91405 Orsay, France
[3] Institut Laue-Langevin, B.P. 156, F-38042 Grenoble Cedex 9, France
[4] Université Lyon 1, CNRS/IN2P3, IPN-Lyon, F-69622 Villeurbanne, France

Received: 26 January 2018 / Revised: 25 September 2018
Published online: 26 November 2018

Communicated by C. Ur

Abstract. For the first time, bases of signals delivered by highly segmented HPGe detectors, for identified hit locations, have been determined *in situ*, that is in the actual accelerator-target-detection system conditions corresponding to data acquisition during a physics experiment. As a consequence, these bases include all the genuine features and alterations of the signals induced by the experimental setup, *e.g.* diaphony, electronic response, specificity of individual crystals. The present pulse shape bases were constructed using calibration source data taken at the beginning of the AGATA campaign at GANIL. An experiment performed at GANIL using the AGATA γ-ray detector together with the VAMOS spectrometer was used to validate the bases. The performance of the bases when used for pulse-shape analysis has been compared to the performance of the standard bases, composed of pulse shapes generated by a computer simulation used for AGATA. This is done by comparing the Doppler correction capability. The so-called Jacobian method used to generate the *in situ* bases also produces correlations that can be applied to locate in a direct way (no search algorithm) the location where a γ-ray interacted given that only one segment is hit. As about 50% of all pulse-shape analysis is performed on crystals with only one segment hit this will allow for a large reduction in the needed computer power. Different ways to improve the results of this prospective work are discussed.

1 Introduction

A new generation of γ-ray tracking spectrometers, the Advanced Gamma Tracking Array (AGATA) [1] in Europe and the Gamma Ray Energy Tracking Array (GRETA) [2] in the USA, open new possibilities for nuclear structure studies with their excellent energy resolution, good peak-to-total and high efficiency for γ-ray energies in the range of tens of keV up to ten MeV. The concept of γ-ray tracking has motivated a long effort of Research and Development worldwide. In Europe the AGATA spectrometer is under construction to reach (in the next decades) an angular coverage of 4π. Meanwhile several AGATA campaigns have been performed with up to 35 High-Purity Segmented Germanium crystals at the laboratories of Legnaro National Laboratory [3], GSI [4], and GANIL [5]. AGATA has shown its advantage of high energy resolution at large recoil-velocities as compared to the traditional Germanium detector array like CLARA [6], EXOGAM [7] or the RISING setup [8].

The performance of γ-ray tracking arrays depends on the γ-ray tracking algorithm, which requires an accurate determination of the energies and positions of the γ-ray interactions. The positions and energies are given by Pulse Shape Analysis (PSA) on the digitized signals from each AGATA HPGe detector crystal. Each crystal has 36 segments and one central contact for a total of 37 output signals. Currently, AGATA uses the Adaptive Grid Search (AGS) [9] method. The pulse shape basis used for each detector has to be an accurate representation of the response of the detectors to achieve high position accuracy and resolution. Pulse-shape bases presently used within the AGATA collaboration are created using the AGATA Detector Library (ADL) [10]. The code calculates the electric field in the detector and generates signals by transporting

[a] e-mail: joa.ljungvall@csnsm.in2p3.fr

the charge carriers in this field and calculating the signals induced on the segments and central contact using the Shockley-Ramo theorem. The ADL takes into consideration the detector geometry, the impurity distribution, and the charge carrier mobilities. A considerable effort has been put into the experimental determination of physical parameters of importance to the pulse-shape generation in the AGATA detectors [11–13], reducing the uncertainties in a significant way as compared to the situation at the beginning of the AGATA project. Cross talk between electric channels is corrected using experimentally measured values on an event-by-event basis [14,15]. The response of the electronics is modeled in a realistic way but not on a channel by channel basis. This work has been successful and the PSA of AGATA gives an interaction position resolution of 5 mm Full Width at Half Maximum (FWHM) [16–18]. This is the needed resolution in order to construct a γ-ray tracking array with good performance [19].

However, the position resolution as determined from in-beam data using Doppler broadening [16] or from imaging methods [17,18,20] are not in accordance with the position resolution that would maximize the performance of γ-ray tracking. This is observed, when using the Orsay Forward Tracking algorithm [21], by the need to increase the parameter corresponding to the position resolution by a factor of 3 as compared to the value used for simulations where a position resolution of 5 mm FWHM was assumed. As the actual shape of the distribution of the errors of the PSA is not known it is not possible to make a direct connection between this factor 3 and the position resolution. A tempting interpretation is that a non-Gaussian position error distribution would require a larger effective position resolution for γ-ray tracking, while still giving a FWHM of Doppler corrected γ-ray peaks corresponding to a Gaussian position error distribution. If the bases were perfect the error distribution should be close to Gaussian and the error estimates from direct methods looking at the first interaction point and that from the parameter in the γ-ray tracking algorithm should coincide. Moreover, the hit-position distributions given by pulse-shape analysis performed on highly segmented HPGe detectors tend to show strong clustering effects, not reflecting the homogeneity of the γ-ray radiation field. There is no other mechanism than PSA that can generate an apparent clustering of γ-ray interactions. Using computer simulations of the pulse shapes to calculate both the signal basis and signals based on interaction position given by Geant4 simulations it is possible to verify that the clustering effect is not an artefact of the chosen PSA algorithms. This effect is therefor attributed to the fidelity of the basis. It is possible to build a complete experimental basis using 3D position scanning of the detectors [22–29], which should give a very accurate basis. However, as the electronic response function in principle changes with a specific set of electronics used for a detector and considering possible effects from the aging (neutron damage and annealing of the crystal) of the detector, the experimental data bases would in principle have to be redone more frequently than is practically possible if these effects are to be included in full detail.

A basis generation method that circumvents these problems was proposed by Désesquelles in refs. [30–32]. The idea is that a correlation is constructed between the known theoretical distribution of interaction points in a detector and experimental raw estimators of the positions valid for events with a single γ-ray interaction in the crystal. This could allow to build an experimental basis of pulse shapes in the same manner as energy calibrations are prepared. Before the experiment, a ^{60}Co source centered at the target position is used to acquire data and build experimental data bases for the experiment. As an additional bonus, correlations between interaction positions and raw estimators can be used for online PSA for events with only one segment having a net charge, under the assumption of a single γ-ray interaction point. The validity of this method has been evaluated using both five sets of simulated signals [31] and experimental pulses from the scanning system at the University of Liverpool [32]. As the real interaction position is known for data from a scanning table the mean error in position determination could be estimated to be less than 5 mm, hence fulfilling the resolution condition needed for γ-ray tracking. In the present paper, the method proposed by Désesquelles is applied using data taken for energy calibration with a non collimated γ source and tested on real in-beam data using the AGATA electronics chain and detectors in experimental conditions. To the knowledge of the authors this has not been done before. The work reported on in this paper had as goals to investigate the feasibility and performance of this method.

An additional important problem faced by γ-ray tracking arrays is the correct determination of the number of γ-ray interactions in a detector segment. This problem is outside the scope of the present work, and the number of segments that has been hit is identified with the number of γ-ray interactions. Work performed within the AGATA and GRETA/GRETINA Collaborations underlines the need for high fidelity bases in order to improve on this determination [33].

The paper is organized as follows: in sect. 2 the method, referred to in this paper as *in situ*, is described in detail and the choices of the experimental raw estimators are presented together with examples of database pulses generated with this method. Comparisons are made in sect. 3 between the PSA done with experimental and with calculated data bases. The comparison is based on the Doppler correction capabilities using experimental in-beam data from an AGATA experiment performed at GANIL. Using PSA based on the experimental correlations directly without passing by the Adaptive Grid Search is also explored. Conclusions and outlooks are given in sect. 4.

2 In situ method for pulse shape basis construction and hit location

In the following, we make the usual approximation that the signal in a segment is induced by a single γ-ray interaction. This is often not the case for γ rays with an energy

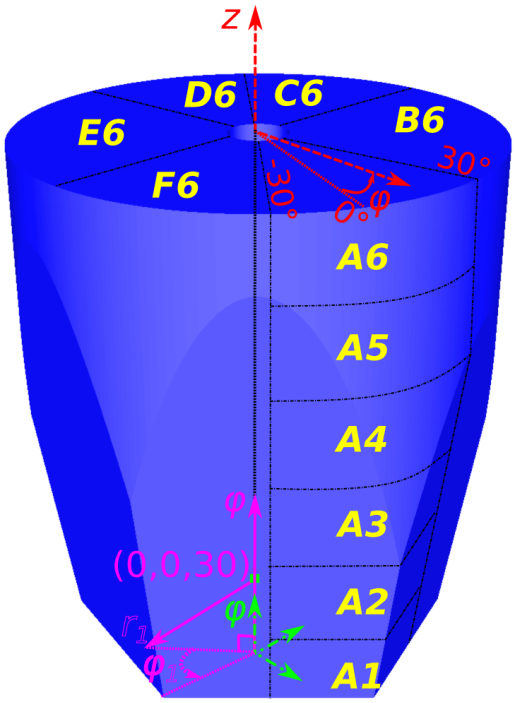

Fig. 1. (Color online) Schematic diagram of one AGATA crystal with the three different coordinate systems used in this paper shown in different colors. The top system (dashed lines) shows the coordinates used for all but the first ring. Note that the origin of the coordinate system is at the front of the crystal, not at the back as could be suggested by the figure. For the first ring, a system with r_1, ϕ_1, and z is used (solid lines), having an origin at $(0, 0, 30)$ mm in the crystal reference system shown with x', y', and z' axes (dash-dotted lines). The latter system is also the coordinate system used for Geant4 simulations.

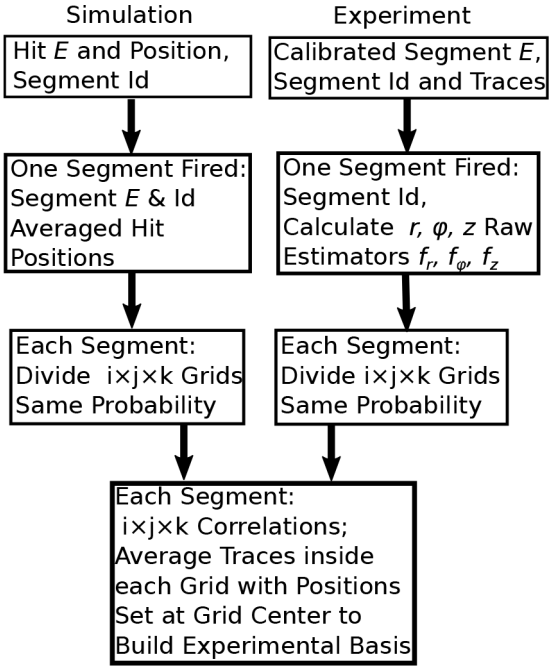

Fig. 2. Scheme describing the *in situ* method to produce an experimental basis of pulse shape. For details, see text.

above a few hundred keV. Geant4 simulation performed within the scope of this work of a ^{60}Co source, however, shows that if an energy condition of $E_{segment} > 200$ keV is used together with the condition that only one segment has been hit the energy weighted average position of the interactions in this segment is on average located within 0.8 mm of the position of the largest single interaction. The largest interaction also contains, on average, 85% of the deposited energy. These distances are smaller than the expected sensitivity showing that the identification between the number of hit segments and number of γ-ray interactions does not render the method presented in the paper a priori invalid. The conditions of a hit segment multiplicity of one and a minimum energy $E_{segment} > 200$ keV have been applied to both the simulated and experimental data used for the construction of the data bases.

Both the construction of an experimental basis using the *in situ* method as well as the application to real-time pulse shape analysis require the construction of good correlations between the theoretical γ-ray interaction point distributions, *e.g.* r, ϕ, and z in fig. 1, and experimental raw estimators of the same quantities. Note the use of two different coordinate systems, depending on the ring number, for the experimental estimators, this because the electric field gradient should be as parallel as possible to the r coordinate to simplify the experimental raw estimator. The theoretical γ-ray interaction distributions are given by AGATA Geant4 simulations [34] with a source at the same position as used to collect the experimental source data. Raw estimators, described in previous work by Désesquelles *et al.* [31,32] and later in this paper, are then calculated using the signals from a ^{60}Co source centered at the target position. The raw estimators use both the net-charge signal from the segment in which the γ-ray interacted and the transient signals from neighboring segments. For example, if a γ-ray interaction is in segment A4, see the schematic diagram in fig. 1, the pulses in segments A3, A4, A5, B4, and F4 are used to produce the raw estimators.

The steps needed to construct an experimental basis (which gives the correlations needed for real-time PSA as a part of the process) are shown in fig. 2. The simulations should give an accurate description of the geometry used for the source measurements, *i.e.* all detectors should be included in the simulation. The Geant4 simulation used in this work is capable of reproducing the measured efficiency within 3% [35]. A total of 3 billion events were simulated to generate a statistics of 30 million selected events in a detector. Calibrated energies E and traces for all the segments were recorded for a ^{60}Co source centered at the target position during the measurement. For this work, data was collected for a total of 12 hours with an event rate of about 400 Hz per crystal, taken at the beginning of the AGATA Campaign at GANIL, with the AGATA detectors at their nominal position. The experimental signals used have been processed in the same way as is done in AGATA before the signals are used for PSA, *e.g.* they are

gain-matched and time aligned. The segment multiplicity has been determined as done by the AGATA preprocessing codes [1]. No further processing was done. Only data where one segment has been hit by the γ ray can be used. This condition is applied on both experimental and simulated data. For each interaction, the energy deposited by the γ-ray and the three spatial Cartesian coordinates (see the green coordinates in fig. 1) are obtained from the simulation. In the case of multiple interactions in one segment, the energy-weighted average position is used. This is the standard procedure to emulate the effects of pulse-shape analysis in simulations within the γ-ray tracking community. The extraction of the correlations between the experimental traces and the hit averaged positions is done in three steps. First r is defined as the distance between the hit position and the center line of the core contact in the xy-plane for the last five rings (*i.e.*, rings 2–6), see the cylindrical coordinate system (dashed lines) in fig. 1, *i.e.*

$$r = \sqrt{x^2 + y^2}. \tag{1}$$

This definition is used for backwards rings (2 to 6) only. Because of the special shape of the electric field lines in the first ring (A1-F1), r is redefined to be

$$r_1 = \sqrt{x^2 + y^2 + (z - 30)^2}, \tag{2}$$

which is the distance between the hit position and a point at $(0, 0, 30)$ mm, see the coordinate system with solid lines in fig. 1. The raw estimator for r, noted f_r, which was optimized using simulated detector pulses as a part of this work, is given by a combination of the estimators suggested in ref. [31],

$$f_r = \frac{\sum_i (i - \langle i \rangle)^3 s_i}{\sum_i s_i} - 400 \times \frac{\sum_i S_{\mathrm{t}i} + S_{\mathrm{b}i} + S_{\mathrm{l}i} + S_{\mathrm{r}i}}{\sum_i s_i}, \tag{3}$$

using both the net-charge signal and the transient signals from the neighboring segments in the source measurement. Here, i is the index of the signal trace, S is the signal from the hit segment (S_i is one sample of the signal), $s_i = (S_{i+1} - S_{i-1})/2$ is the derivative of the signal and

$$\langle i \rangle = \sum_i i\, s_i \Big/ \sum_i s_i$$

is the average sample of the derivative of the pulse with $\sum_i s_i = E$ the calibrated energy of the signal. Finally S_{t}, S_{b}, S_{l} and S_{r} are signals from the four direct neighbors of the hit segment. Using the previous example, with a γ-ray interaction in segment A4, its top S_{t}, bottom S_{b}, left S_{l} and right neighbor S_{r} are A5, A3, B4, and F4, respectively. Then, for each segment, the distributions of both r and its raw estimator f_r are divided into intervals with the condition that each interval has the same probability, *e.g.* interval r_i and f_{ri} both hold $X\%$ of the total number of counts. This procedure is illustrated in fig. 3. Finally, using this so-called Jacobian correspondence, one can deduce, from the measurement of f_r, an estimate of r. The new version of the f_r estimator was developed using signals of the ADL base, and gives better results.

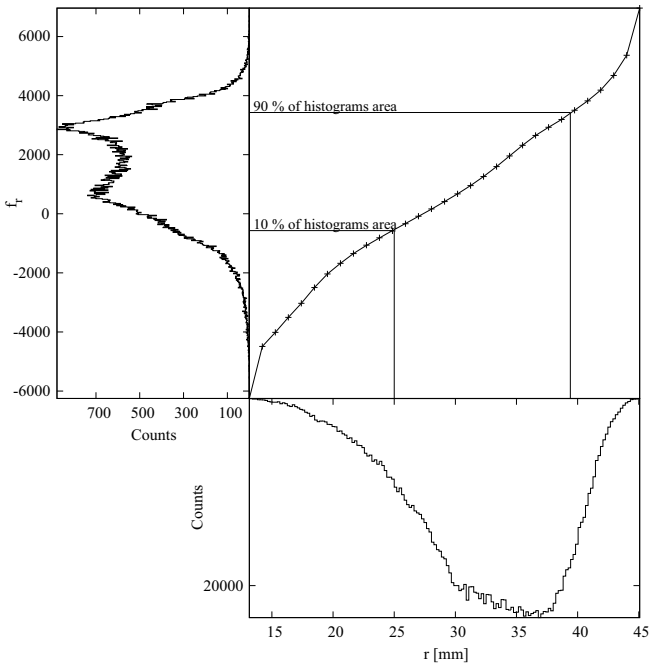

Fig. 3. Example showing how the r-f_r correlation is constructed for segment A1 in detector A002. In the top left corner the distribution of the experimental raw estimator f_r is shown, with the raw estimator on the y axis and the number of counts on the inverted x axis. The simulated r distribution is shown at the bottom with an inverted y axis. A correlation is constructed by identifying the coordinate value and raw estimator value that corresponds to the same fraction of the integral of each distribution, respectively. Explicit examples are given for 10% and 90%.

The second step is to calculate φ and its raw estimator f_φ. φ is the azimuthal angle with origin along the symmetry plane of the segment, as shown in fig. 1 with φ_1 for the first ring and φ for the other rings. Hence, φ is an angle in the range between around $-30°$ and $30°$, but the exact values vary with detector type and segment. The raw estimator of φ we have used is

$$f_\varphi = \frac{(\max S_{\mathrm{l}} - \min S_{\mathrm{l}}) - (\max S_{\mathrm{r}} - \min S_{\mathrm{r}})}{(\max S_{\mathrm{l}} - \min S_{\mathrm{l}}) + (\max S_{\mathrm{r}} - \min S_{\mathrm{r}})}. \tag{4}$$

It is calculated from the transient signals of the direct neighbors in the same ring. This estimator was found to perform better than the one used in ref. [31]. Then, the Jacobian correspondence between φ and its raw estimator f_φ is calculated as previously, except that the calculation is not done in the whole segment but inside small $r_i \pm \Delta r$ intervals (corresponding to $f_{ri} \pm \Delta f_r$ for the raw estimator), see fig. 4. Inside each r_i interval, the length of the φ steps varies roughly as $\propto r$. This is to keep the volume of the voxels close to constant inside the detector volume.

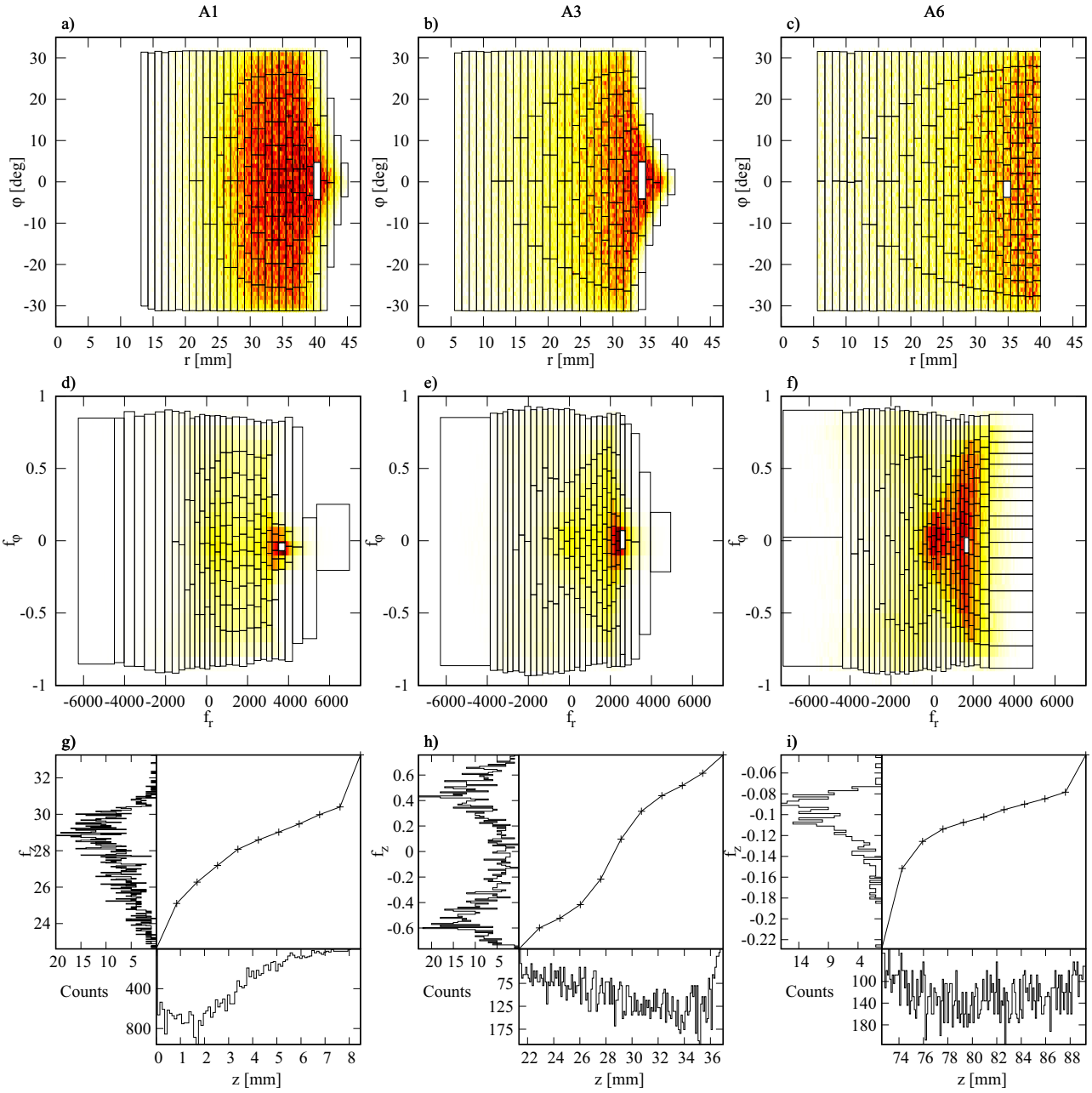

Fig. 4. (Color online) First row: simulated r-φ distribution for segments A1 (a), A3 (b) and A6 (c). Second row, raw estimator f_r-f_φ distribution for segments A1 (d), A3 (e) and A6 (f). For each pair of simulated and experimental data (*i.e.* (a)–(d), (b)–(e), and (c)–(f)) the squares show the used divisions in r, f_r and φ, f_φ and each pair of squares contains the same fraction of events thus allowing the correspondence between the raw estimators and the coordinates. The third row explicitly shows the correlations between the raw estimators f_z and the z coordinates when constrained to the white filled squares shown in the first two rows. That is, the upper-left histogram in figure (g) is filled when f_r and f_φ are within the white square in figure (d), the bottom histogram of figure (g) is filled when r and φ in the simulations is within the white square in figure (a). The line shows the correlation between the raw estimator f_z and z coordinate for this r, φ grid point. This is repeated for segments A3 and A6 in figure (h) and (i), respectively.

The last step is to calculate the correspondence between the depth z and its raw estimator f_z, which is

$$f_{z1} = \frac{\sum_i i s_i}{\sum_i s_i}\,, \tag{5}$$

for the first ring using the net-charge signal as used in ref. [31],

$$f_{z2} = \frac{(\max S_\mathrm{t} - \min S_\mathrm{t}) - (\max S_\mathrm{b} - \min S_\mathrm{b})}{(\max S_\mathrm{t} - \min S_\mathrm{t}) + (\max S_\mathrm{b} - \min S_\mathrm{b})} \tag{6}$$

for the middle four rings using the transient signals in the same column, and

$$f_{z3} = -\frac{\max S_\mathrm{b} - \min S_\mathrm{b}}{\sum_i s_i}\,, \tag{7}$$

for the last ring using the transient signal from its bottom neighbor in ring 5 and normalized by segment energy $E = \sum_i s_i$. The estimators for the last five rings have also been modified with respect to what was used in ref. [31]. Then, the Jacobian correspondence between z and its raw estimator f_z is calculated separately for each segment, each r interval, and each φ interval, see fig. 4.

In this way, we obtain a one-to-one mapping, coming from the equal probability condition, between (x, y, z) and the measured (f_r, f_φ, f_z). In order to validate our codes, the method was first tested using an ADL basis with a grid size of $2 \times 2 \times 2\,\mathrm{mm}^3$. This gave a precision of $\sigma = 2.8\,\mathrm{mm}$ ($\sigma_x = 1.7$, $\sigma_y = 1.7$, and $\sigma_z = 1.5$) for the difference between the known ADL positions and the reconstructed positions. This is in accordance with what was found for simulated pulses by Désesquelles *et al.* [31].

Figure 4 illustrates the procedure to generate the needed correlations between simulated distributions of interaction positions and experimental distributions of the raw estimators. Examples of simulated and experimental distributions for an A type detector are shown. The simulated 2D distribution of φ *vs.* r is shown for segments A1, A3, and A6 in figs. 4(a), 4(b), and 4(c), respectively. Also shown are the divisions used for the r and φ coordinates. In figs. 4(d), 4(e), and 4(f) the corresponding 2D raw estimator distributions are shown. For each square in the simulated distributions there is a square in the experimental distributions containing the same fraction of events. In figs. 4(g), 4(h), and 4(i) the z-f_z correlations created for the squares that are filled with white in figures (a)–(f) are shown. These are examples of the correlations used for real-time PSA where the three raw estimators f_r, f_φ and f_z are calculated and the γ-ray interaction point is given by linear interpolation in the corresponding voxel.

The results of our work can be used in two ways for the location of γ-ray interactions in the crystal.

1) When only one segment in a crystal is hit, the x, y, z position of the hit can be deduced from the determination of f_r, f_φ, f_z (through the Jacobian correspondences shown *e.g.* in figs. 3 and 4). This procedure will be referred to as the Direct Method (DM) in the following.
2) When multiple hits induce pulse overlaps, the locations of the hits can only be obtained using a deconvolution code, in our case an Adaptative Grid Search algorithm. This code needs as input a basis of signals corresponding to identified locations covering the volume of the detector. In the next paragraph, we show how such a signal basis can be built using the $(f_r, f_\varphi, f_z) \rightarrow (x, y, z)$ mapping. This basis will be referred to as the *in situ* basis.

To build the experimental basis, all signals giving raw estimators leading to the same voxel are averaged after normalization. The center x, y, and z of the voxel is considered as the corresponding hit position. Figure 5 shows ten ^{60}Co experimental pulses after normalization by the hit energy. They are all calculated to belong to the voxel at $x = 4.7\,\mathrm{mm}$, $y = 25.2\,\mathrm{mm}$, $z = 41.8\,\mathrm{mm}$ in segment B4. One can see that both the net-charge signal from segment B4 and the transient signals from the direct neighbors B3, B5, A4 and C4 used for the calculations of the estimators have very similar shapes. The pulses are however not identical, which is not to be expected as the voxels used have a finite volume. The number of experimental samples per voxel varies from 10 to 400.

Examples from the experimental basis generated using the *in situ* method are shown in fig. 6. The basis signals for the same position ($x = 31\,\mathrm{mm}$, $y = 5.5\,\mathrm{mm}$, $z = 63\,\mathrm{mm}$) in three different detectors are shown. Two of the detectors have the same geometrical shape (type A) while the third detector is of type B. It is encouraging to see that the signals from the two type A detectors are very similar while the signal from the type B detector is different.

3 Application to in-beam γ-ray spectroscopy from fusion-fission reactions

The width of a γ-ray peak in a spectrum after Doppler correction can be deduced from the Doppler shift formula

$$E_\gamma = E_{\gamma 0}\,\frac{\sqrt{1-\beta^2}}{1-\beta\cos\theta}\,, \tag{8}$$

where E_γ is the energy detected in the detector, $E_{\gamma 0}$ is the energy of the γ ray in the rest frame of the nucleus, β is the velocity of the nucleus emitting the γ ray and θ is the angle between the velocity of the emitting nucleus and the γ ray in the laboratory frame. From this formula one gets a γ-ray peak width $\Delta E_{\gamma 0}$ of

$$(\Delta E_{\gamma 0})^2 = \left(\frac{\partial E_{\gamma 0}}{\partial E_\gamma}\Delta E_\gamma\right)^2 + \left(\frac{\partial E_{\gamma 0}}{\partial \beta}\Delta\beta\right)^2 + \left(\frac{\partial E_{\gamma 0}}{\partial \theta}\Delta\theta\right)^2. \tag{9}$$

This can be used to evaluate the performance of the PSA via the relation

$$\cos\theta = \frac{\boldsymbol{v}\cdot\boldsymbol{r}}{|\boldsymbol{v}||\boldsymbol{r}|}\,, \tag{10}$$

where $\boldsymbol{v}$ is the velocity of the nucleus and $\boldsymbol{r}$ is the first interaction position of the γ ray as determined from PSA.

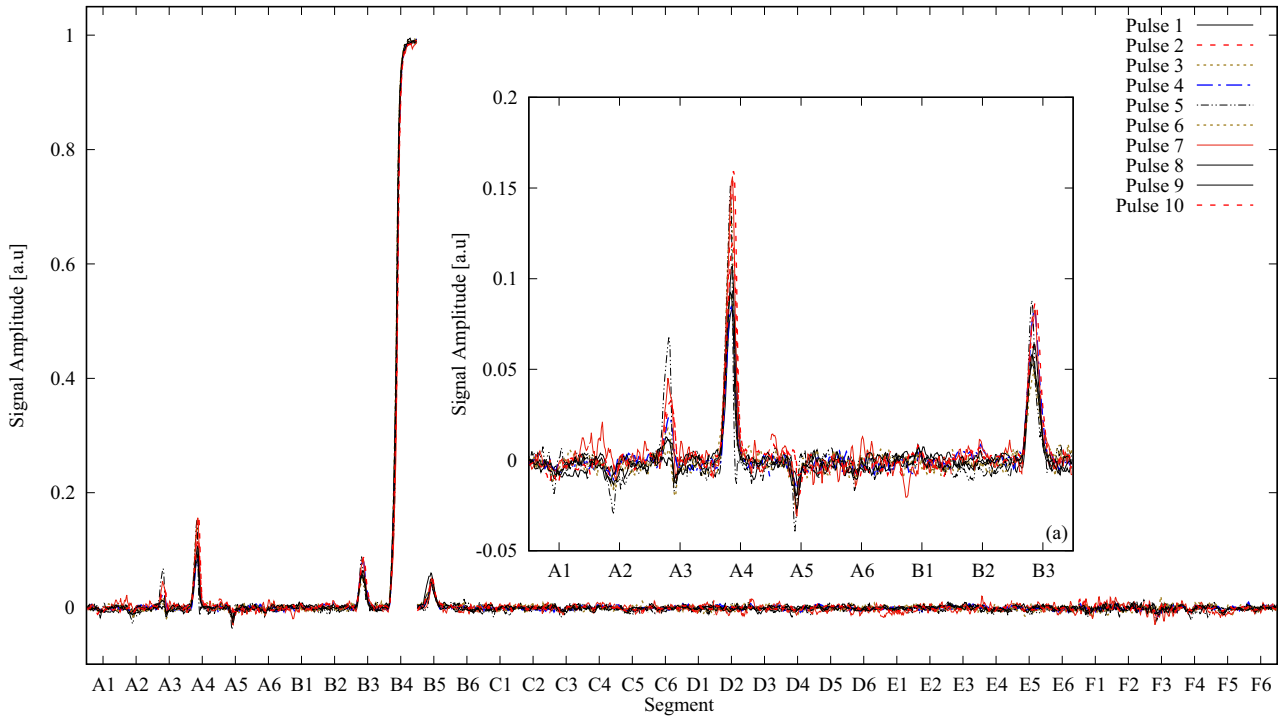

Fig. 5. (Color online) Ten experimental signals that are found to belong to the same voxel by present method. The average of the pulses is used as the experimental basis pulse for the grid position corresponding to the center of the voxel. The inset (a) is an enlargement on the transient signals.

This was used to assess the performance of PSA using the experimental *in situ* data bases and to investigate the precision that could be achieved using the correlations to extract the γ-ray interaction position in the case a crystal had only one segment hit. Data from an in-beam experiment was analyzed in three different ways producing three different sets of data corresponding to:

- Adaptive Grid Search using the ADL bases (1).
- Adaptive Grid Search using the ADL bases + the Direct method for one net-charge segment events (2).
- Adaptive Grid Search using the *in situ* bases (3).

The analysis was performed using the AGATA data analysis chain as described in ref. [1] with a modification to the PSA code to give the possibility to treat one-hit-segment events with the Direct Method. This means that all γ-ray energies are tracked γ-ray energies and that all calibrations, pre- and post-processing of data are identical for all three cases. Experimental bases for six different detectors were constructed.

The data used is from an experiment performed for the spectroscopy of neutron-rich nuclei in the mass 80–100 region. An ^{238}U beam with an energy of 6.2 MeV/u impinged on a 10 μm-thick ^{9}Be target. Excited nuclei were produced by either fusion-fission or induced fission of the beam, and they were fully identified in the VAMOS spectrometer [36–38]. The γ rays were detected by AGATA configured in its compact mode [5], *i.e.* moved 88 mm closer to the target. Details of the experiment can be found in ref. [39]. Clusters 12 and 13 at circa 112° to the recoil direction were used for the PSA test as they allowed maximum Doppler broadening for this experimental setup. The recoil velocity v/c of about 10% was also sufficiently high for the Doppler broadening of the γ-ray peaks to be sensitive to the PSA. This experiment was performed within 2 months of collecting the ^{60}Co data used to construct the experimental data bases.

The strongly populated channel ^{98}Zr [40] was used for the investigations, as its 1223 keV γ ray de-exciting the 2_1^+ state provides good sensitivity to the position resolution via the angle used for Doppler correction, and hence the PSA. Lower energy γ rays are also emitted in the reaction, but as the impact of the position resolution in terms of Doppler correction is proportional to the γ-ray energy they were not analyzed. Furthermore, a recent lifetime measurement [41] gives an upper limit for the lifetime of the 2_1^+ of $\tau < 11$ ps. This is in a range that will not give any line shape effects comparable to those from pulse-shape analysis. Estimates of the different components of the peak width for a γ ray at 1.2 MeV have been made using eq. (9). A recoil with a velocity β of around 10%, and a $\Delta\beta = 0.4\%$ [42] produces a Doppler broadening $\Delta E_{\gamma 0}/E_{\gamma 0}$ of 0.11% at 112° (term 2 in eq. (9)). An uncertainty of $\Delta\theta = 1°$ (6°) for the determined angle between the recoil and emitted γ ray will give a 0.16% (0.97%) Doppler broadening in the energy spectra (term 3 in eq. (9)). For our case, $\Delta\theta = 1°$ corresponds to a PSA resolution of about 2.3 mm FWHM. Given that a reasonable estimate for the intrinsic energy resolution of the detectors in the conditions of the experiment is $\Delta E_\gamma = 0.2\%$, a perfect position determination would give a $\Delta E_{\gamma 0}/E_{\gamma 0} = \sqrt{0.11^2 + 0.2^2} = 0.23\%$ whereas the use

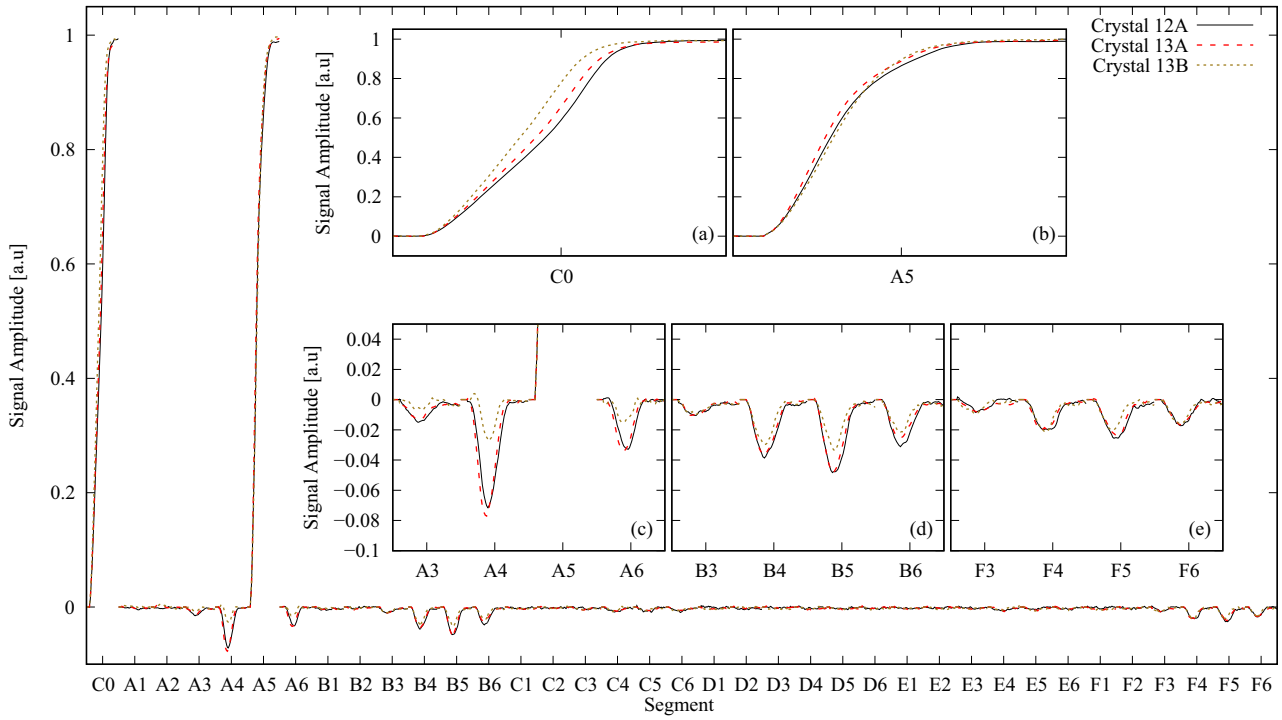

Fig. 6. (Color online) Pulse shapes coming from two same shaped detectors of type A and one type B detector for the same position ($x = 31\,\text{mm}$, $y = 5.5\,\text{mm}$, $z = 63\,\text{mm}$) in the detectors. The core signal is shown in more detail in inset (a), the net-charge signal in inset (b), and the transient signals from the nearest neighbours are shown in detail in insets (c)–(e).

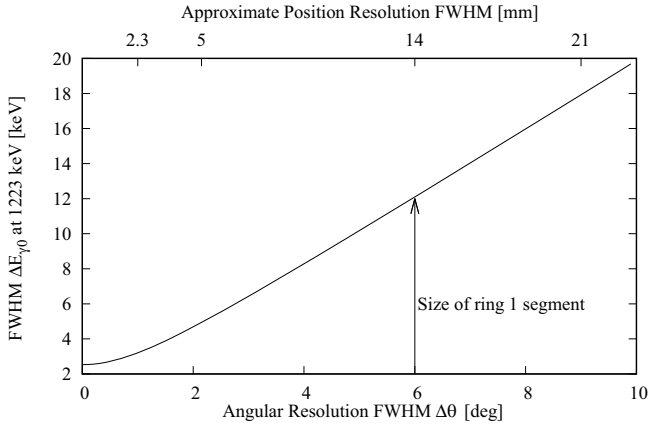

Fig. 7. Approximate width of the 1223 keV γ ray de-exciting the 2_1^+ state as a function of angular and position resolution. On the upper scale are indicated the approximate linear resolutions for 1° angular resolution, the stated design goal of AGATA, the size corresponding to a segment, and finally the linear resolution corresponding to 9° angular resolution.

of the segment center for Doppler correction would give $\Delta E_{\gamma 0}/E_{\gamma 0} = \sqrt{0.11^2 + 0.2^2 + 0.97^2} = 0.996\%$. Therefore, PSA can improve the energy resolution by at most a factor of 4 as compared to Doppler correction only using the segment centers for γ-ray hit locations in this particular experiment. In fig. 7, an estimate of the FWHM as a function of position resolution is shown for the 1223 keV γ ray given the experimental setup used for this work. The size of a segment is also indicated.

The hit distributions in the xy-plane and z direction for events with only one net-charge segment are shown in figs. 8 and 9, respectively. In the columns of fig. 8 the xy-plane hit distributions for the six rings for detector 13A are shown for PSA performed using the Adaptive Grid Search (AGS) and the ADL basis, PSA performed using the Direct Method, and finally PSA performed using AGS and the *in situ* basis. The distributions are clearly different but none is very homogeneous, which could indicate a better PSA. For the Direct Method, one can see a ring-like cluster near the core in ring 1 and six clusters in ring 2 and ring 3 in the corners of the hexagonal part of the crystal. This is because for small or large r, φ is divided into only one interval, causing the small clusters. For the z distributions shown in fig. 9, the present method tends to assign the z coordinate at the center of the segment as compared to AGS, which clusters points closer to the segment boundaries.

To, tentatively, compare the position resolution for the three different cases, two different sets of γ-ray spectra were produced with Doppler corrected γ-ray energies emitted from ^{98}Zr. The first set, referred to as set I, is made with all tracked γ rays, and the resulting spectra are shown in fig. 10. The strong transitions populated from ^{98}Zr are marked in fig. 10(a) with the information taken from ref. [40]. Here, the solid line is the result from the simulated ADL bases using AGS, dashed is from combining the direct method with AGS and an ADL bases, dotted is for AGS using *in situ* bases, and dash-dotted when corrected with the segment center (*i.e.*, without PSA). As PSA performance and basis fidelity vary from crys-

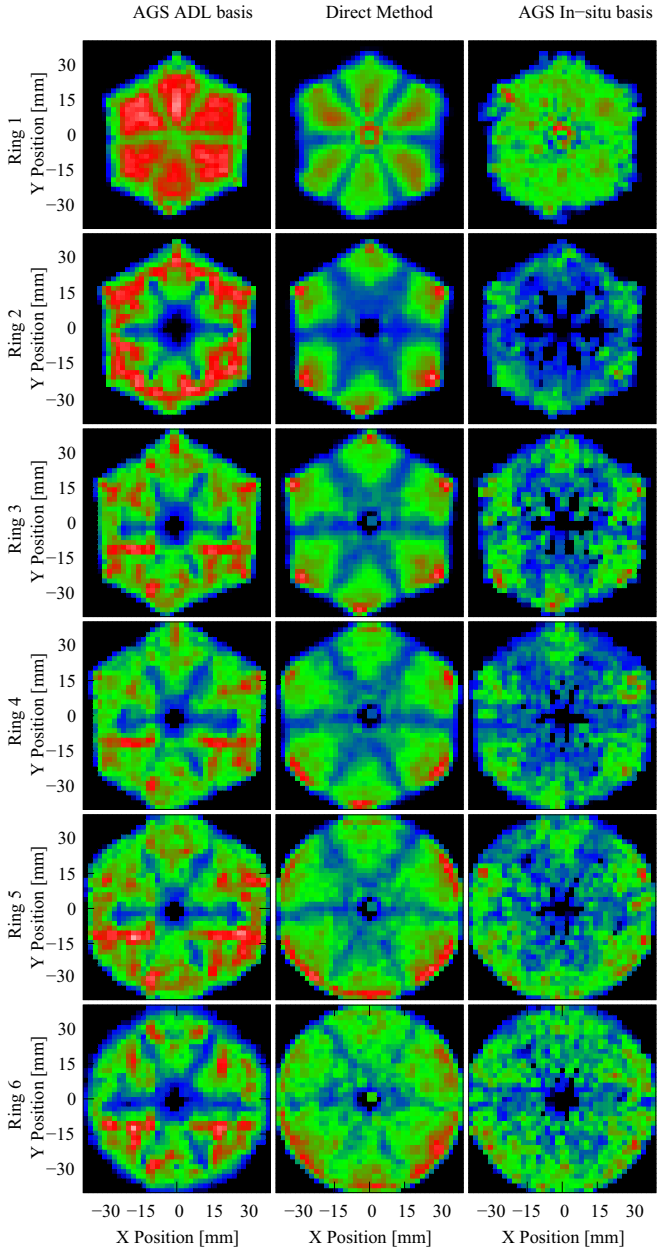

Fig. 8. (Color online) Comparisons of hit distributions in xy-plane between PSA performed with AGS and ADL basis (left), PSA performed with the Direct Method (center), and PSA performed with AGS using the *in situ* basis (right) for the six rings in detector 13A. Events with only one net charge segment were used. The color scale goes from black (0 counts), via blue (10 counts), green (100 counts), red (250 counts), and finally white (500 counts).

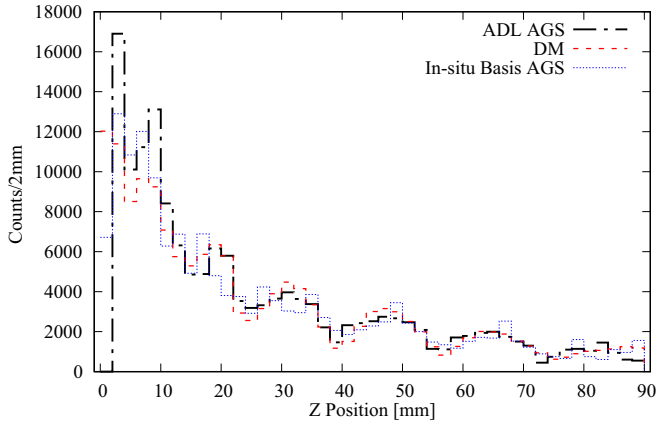

Fig. 9. (Color online) Comparisons of z hit distributions between AGS using the ADL basis, AGS using the *in situ* basis, and the Direct Method. Events from detector 13A with only one segment hit have been used.

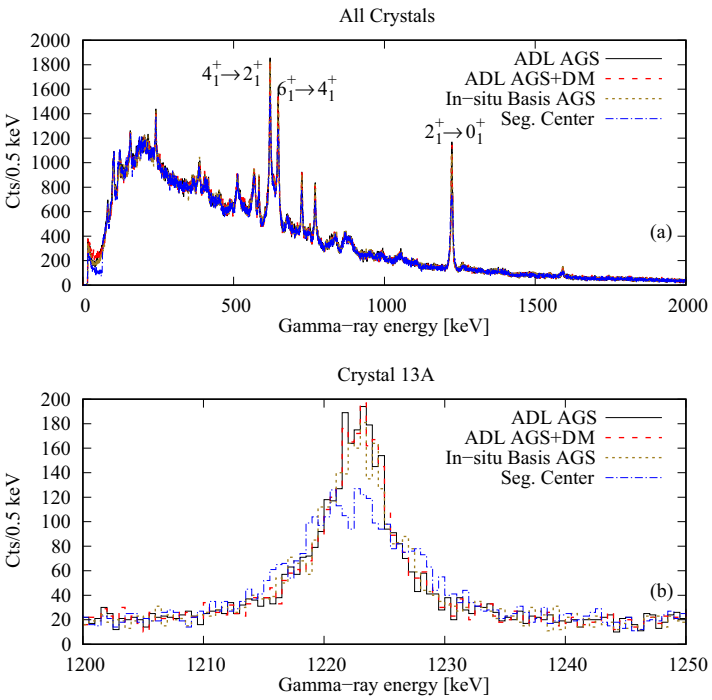

Fig. 10. (Color online) (a) Doppler corrected γ-ray spectra of ^{98}Zr for all events. Solid line is the result using the AGS with the ADL bases, dashed is from combining the Direct Method with the AGS using the ADL bases, dotted is for the AGS using the *in situ* bases, and dash-dotted when corrected with the segment center (*i.e.*, without PSA). (b) Same as (a) with the energy zoomed in on the $2_1^+ \rightarrow 0_1^+$ transition of ^{98}Zr and only when the interaction position used for Doppler correction was in crystal 13A (see text for details).

tal to crystal the performance was evaluated individually for each crystal, this by demanding that the interaction whose position was used for Doppler correction was in the investigated crystal. An example of such spectra for one out of six studied crystals is shown in fig. 10(b). In this way the six different sets of bases could be compared. A second set of γ-ray spectra produced to highlight the performance of the Direct Method, referred to as set II, were created by demanding that the interaction position used for Doppler correction was in a crystal with only one net-charge segment. In these spectra, the statistics is reduced by a factor of ≈ 3.5 for the peak at 1.223 MeV. This reduction comes from the preference of absorbed γ rays of this energy to interact more than once in one crystal.

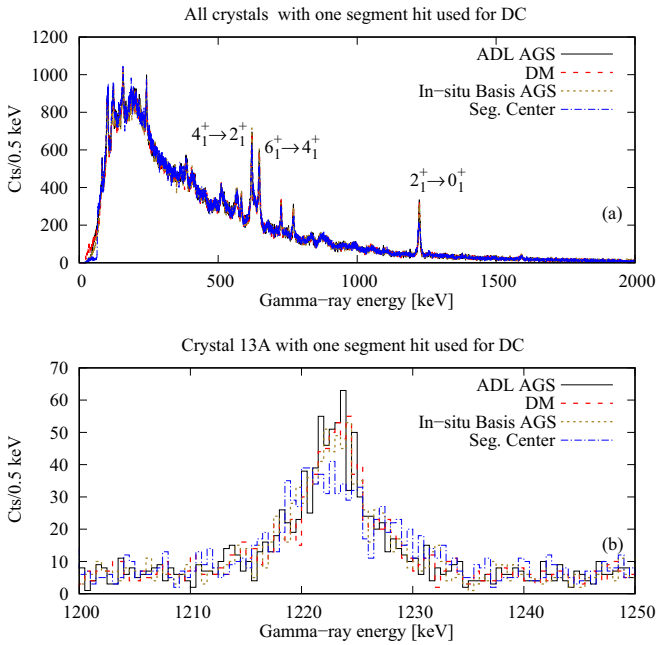

Fig. 11. (Color online) (a) Doppler corrected γ-ray spectra of ^{98}Zr for events where the interaction point used for Doppler correction was in a crystal with only one segment hit. Solid line is the result using the AGS with the ADL bases, dashed is from the Direct Method, dotted is for the AGS using the *in situ* bases, and dash-dotted when corrected with the segment center (*i.e.* without PSA). (b) Same as (a) with the energy zoomed in on the $2_1^+ \rightarrow 0_1^+$ transition of ^{98}Zr and only when the interaction position used for Doppler correction was in crystal 13A (see text for details).

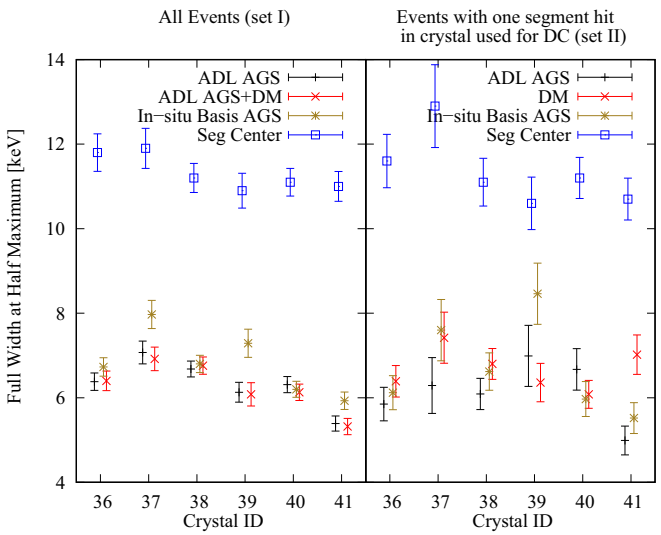

Fig. 12. (Color online) The full width at half maximum from Gaussian fits to the peaks in the data, crystal by crystal. The left panel is for all data (set I), and crystal number indicates the crystal in which the interaction position used to define the angle for Doppler correction was recorded. For the right panel, there is the additional constraint that there was only one segment with a net charge in the crystal with the interaction used for Doppler correction (set II).

The reduction factor is smaller for lower γ-ray energies as they are more likely to be absorbed within one segment. Spectra produced with this extra condition are shown in fig. 11, where the top panel marked with an (a) shows the full energy range whereas the bottom panel shows a zoom on the region of interest. The interest of investigating the Direct Method comes from the fact that before γ-ray tracking about 50% of the events can be expected as one segment hit events, and hence the use of the Direct Method can reduce the CPU demand for PSA considerably. In the present architecture of AGATA, where each crystal is physically connected via optical fibers to a computer for the PSA this gain will not allow a reduction of the same order (*i.e.*, 50%) for the needed computer hardware. For the future, where data from crystals will be transported on a standard TCP/IP computer network before the PSA, this decrease of needed computing hardware can be capitalized on. It should be noted that the choice of PSA method does not affect the statistics after γ-ray tracking, as can be seen in the full-range spectra in figs. 10 and 11.

For all data sets the FWHM has been extracted, giving a total of 48 values. The data is summarized in fig. 12. First comparing the FWHM for set I, the difference between using AGS with the ADL bases or AGS with the ADL bases and the Direct Method is small, reflecting the small fraction of events where the Doppler correction was made with an interaction position determined with the Direct Method. For all crystals the difference is smaller than the uncertainty in the determination of the FWHM. Looking at the difference using AGS with the ADL bases and the *in situ* bases, the latter is performing worse for three of the crystals, 37 (12B), 39 (13A), and 41 (13C), but still about a factor of two better than when using the segment center as interaction position. Turning the attention to data set II, the pattern is repeated with the exception of crystal 41 (13C) where AGS with *in situ* basis is performing better than the Direct Method. However, considering the larger error bars from the decreased statistics, statistical scattering cannot be excluded as the reason for this.

4 Conclusions and outlook

Using experimental data from the AGATA@GANIL campaign, we have demonstrated the possibility to use the Jacobian method to both produce an experimental pulse-shape *in situ* basis and to perform PSA by the so-called Direct Method for events with only one net-charge segment in a crystal. Both give comparable performance for PSA as if a basis calculated with the ADL package had been used. The Direct Method is of particular interest as it allows a considerable reduction in needed computing for events with only one net-charge segment in a crystal. The results for the *in situ* experimental basis require some more comments. There is no improvement in performance, neither for the position resolution nor in the reduction of

computing power needed for the *in situ* basis as compared to the ADL basis. The slightly worse PSA performance of the *in situ* bases suggests that they are less accurate than the ADL bases. There are several possible reasons for this. In the first step of creating an *in situ* basis, the theoretical interaction point distributions are determined. To do this, assumptions about the effective segmentation of the Ge crystals are made. In this work, the segmentation used in the AGATA Geant4 package was used. An alternative would be to use a code such as ADL to better determine the segmentation borders in a hybrid approach to construct the basis for a crystal. We note that the neutron damage correction methods developed within the AGATA community, see Bruyneel *et al.* [43], depend on the trajectories of the charge carriers as calculated by ADL, showing the need for pulse-shape calculations even in the case of improved PSA performance with an *in situ* basis. However, an *in situ* approach still allows for effects not easily modeled to be included.

An issue not touched upon in this work, because of the effort to construct a basis from a calibration like measurement, is that of time aligning the traces before averaging. This is a critical issue for the pulse-shape analysis where a time resolution of less than the 10 ns sampling time is needed for optimal performance [31]. There is also an open question on the type of events to use to construct an *in situ* basis. In this work events (simulated and experimental) with one net-charge segment were used with an assumption of equality between number of net-charge segments and γ-ray interactions. This is clearly wrong for many γ-ray energies and an improvement in this selection process is well worth exploring. Experimental bases using gates on the Compton back-scattering edge have been produced within the context of this work but the strong reduction in statistics prohibited any conclusion as to whether this is an improvement or not.

The above mentioned issues could be corrected using a coincidence measurement between AGATA and an external fast scintillator detector (time resolution), combined with a more restrictive selection of the used events (favouring one γ-ray interaction). While technically not difficult the increase in needed measuring time is at least a factor of 20, *i.e.* from about a night to about a week. Remaining less time consuming then the full scanning of individual crystals, the increase in required time, together with the need of additional detectors, removes the "calibration" aspect of the method. The use of the *in situ* method for "characterisation" measurement before experimental campaigns, however, remains an interesting option to explore.

One possible approach for improving the *in situ* basis is in the choice of the grid used in the final basis. In this work, the grid for each detector was dictated by the condition of similar voxel volumes in the grid, available statistics, and the natural polar coordinate system of the crystal. However, other choices are possible [44] and several possibilities should be systematically explored and choosing a grid more closely connected to the intrinsic sensitivity of the detector is interesting.

Given the encouraging results presented in this paper, continued work exploring the *in situ* method with its inherent inclusion of electronic responses and experimental conditions is needed.

The authors would like to thank the AGATA Collaboration and the GANIL technical staff. We are also grateful to Dino Bazzacco and Francesco Recchia for fruitful discussion. Gilbert Duchêne is thanked for providing the in-beam data set.

References

1. S. Akkoyun *et al.*, Nucl. Instrum. Methods Phys. Res. A **668**, 26 (2012).
2. I. Lee *et al.*, Nucl. Phys. A **746**, 255 (2004).
3. A. Gadea *et al.*, Nucl. Instrum. Methods Phys. Res. A **654**, 88 (2011).
4. N. Pietralla *et al.*, EPJ Web of Conferences **66**, 02083 (2014).
5. E. Clément *et al.*, Nucl. Instrum. Methods Phys. Res. A **855**, 1 (2017).
6. A. Gadea *et al.*, Eur. Phys. J. A **20**, 193 (2003).
7. J. Simpson *et al.*, Acta Phys. Hung. **11**, 159 (2000).
8. H. Wollersheim *et al.*, Nucl. Instrum. Methods Phys. Res. A **537**, 637 (2005).
9. R. Venturelli, D. Bazzacco, LNL Annual Report (2004) p. 220.
10. B. Bruyneel, B. Birkenbach, P. Reiter, Eur. Phys. J. A **52**, 70 (2016).
11. B. Bruyneel, P. Reiter, G. Pascovici, Nucl. Instrum. Methods Phys. Res. A **569**, 764 (2006).
12. B. Bruyneel, B. Birkenbach, P. Reiter, Nucl. Instrum. Methods Phys. Res. A **641**, 92 (2011).
13. B. Birkenbach *et al.*, Nucl. Instrum. Methods Phys. Res. A **640**, 176 (2011).
14. B. Bruyneel *et al.*, Nucl. Instrum. Methods Phys. Res. A **599**, 196 (2009).
15. A. Wiens *et al.*, Eur. Phys. J. A **49**, 47 (2013).
16. F. Recchia *et al.*, Nucl. Instrum. Methods Phys. Res. A **604**, 555 (2009).
17. P.-A. Söderström *et al.*, Nucl. Instrum. Methods Phys. Res. A **638**, 96 (2011).
18. T. Steinbach *et al.*, Eur. Phys. J. A **53**, 23 (2017).
19. G. Schmid *et al.*, Nucl. Instrum. Methods Phys. Res. A **430**, 69 (1999).
20. F. Recchia *et al.*, Nucl. Instrum. Methods Phys. Res. A **604**, 60 (2009).
21. C. Michelagnoli *et al.*, in preparation.
22. A. Boston *et al.*, Nucl. Instrum. Methods Phys. Res. B **261**, 1098 (2007).
23. L. Nelson *et al.*, Nucl. Instrum. Methods Phys. Res. A **573**, 153 (2007).
24. T. Ha *et al.*, Nucl. Instrum. Methods Phys. Res. A **697**, 123 (2013).
25. S. Martín, B. Quintana, D. Barrientos, Nucl. Instrum. Methods Phys. Res. A **823**, 32 (2016).
26. F. Crespi *et al.*, Nucl. Instrum. Methods Phys. Res. A **593**, 440 (2008).
27. C. Domingo-Pardo *et al.*, Nucl. Instrum. Methods Phys. Res. A **643**, 79 (2011).

28. N. Goel *et al.*, Nucl. Instrum. Methods Phys. Res. A **652**, 591 (2011).
29. M. Ginsz, *Characterization of high-purity, multi-segmented germanium detectors*, PhD Thesis, Université de Strasbourg, Ecole doctorale de physique et chimie physique, Institut Pluridisciplinaire Hubert Curien, UMR 7178 CNRS/IN2P3 (2015).
30. P. Désesquelles *et al.*, Phys. Rev. C **62**, 024614 (2000).
31. P. Désesquelles, Nucl. Instrum. Methods Phys. Res. A **654**, 324 (2011).
32. P. Désesquelles *et al.*, Nucl. Instrum. Methods Phys. Res. A **729**, 198 (2013).
33. *Second AGATA-GRETINA tracking arrays collaboration meeting*, private communication (2018).
34. E. Farnea *et al.*, Nucl. Instrum. Methods Phys. Res. A **621**, 331 (2010).
35. N. Lalović *et al.*, Nucl. Instrum. Methods Phys. Res. A **806**, 258 (2016).
36. S. Pullanhiotan, M. Rejmund, A. Navin, W. Mittig, S. Bhattacharyya, Nucl. Instrum. Methods Phys. Res. A **593**, 343 (2008).
37. M. Vandebrouck *et al.*, Nucl. Instrum. Methods Phys. Res. A **812**, 112 (2016).
38. M. Rejmund *et al.*, Nucl. Instrum. Methods Phys. Res. A **646**, 184 (2011).
39. J. Dudouet *et al.*, Phys. Rev. Lett. **118**, 162501 (2017).
40. B. Singh, Z. Hu, Nucl. Data Sheets **98**, 335 (2003).
41. L. Bettermann *et al.*, Phys. Rev. C **82**, 044310 (2010).
42. Y.H. Kim *et al.*, Eur. Phys. J. A **53**, 162 (2017).
43. B. Bruyneel *et al.*, Eur. Phys. J. A **49**, 61 (2013).
44. I. Doxas, C. Nieter, D. Radford, K. Lagergren, J.R. Cary, Nucl. Instrum. Methods Phys. Res. A **580**, 1331 (2007).

7.9 B(E2) anomalies in the yrast band of ^{170}Os

$B(E2)$ anomalies in the yrast band of ^{170}Os

A. Goasduff,[1,2,*] J. Ljungvall,[1] T. R. Rodríguez,[3] F. L. Bello Garrote,[4] A. Etile,[1] G. Georgiev,[1] F. Giacoppo,[5,6] L. Grente,[7] M. Klintefjord,[4] A. Kuşoğlu,[1,8,9] I. Matea,[10] S. Roccia,[1] M.-D. Salsac,[7] and C. Sotty[1,11]

[1]*CSNSM, Université Paris-Sud, CNRS/IN2P3, Université Paris-Saclay, 91405 Orsay, France*

[2]*Dipartimento di Fisica and INFN, Sezione di Padova, I-35131 Padova, Italy*

[3]*Departamento de Física Teórica and Centro de Investigación Avanzada en Física Fundamental-CIAFF, Universidad Autónoma de Madrid, E-28049 Madrid, Spain*

[4]*Department of Physics, University of Oslo, N-0316 Oslo, Norway*

[5]*Helmholtz Institute Mainz, 55099 Mainz, Germany*

[6]*GSI Helmholtzzentrum für Schwerionenforschung, 64291 Darmstadt, Germany*

[7]*Irfu, CEA, Université Paris-Saclay, F-91191 Gif-sur-Yvette, France*

[8]*Department of Physics, Faculty of Science, Istanbul University, Vezneciler/Fatih, 34134 Istanbul, Turkey*

[9]*ELI-NP, Horia Hulubei National Institute of Physics and Nuclear Engineering, 077125 Magurele, Romania*

[10]*Institut de Physique Nucléaire, CNRS-IN2P3, Université Paris-Sud, Université Paris-Saclay, 91406 Orsay Cedex, France*

[11]*Horia Hulubei National Institute of Physics and Nuclear Engineering-IFIN HH, 077125 Bucharest, Romania*

(Received 11 March 2019; revised manuscript received 30 July 2019; published 5 September 2019)

Background: The neutron-deficient osmium isotopic chain provides a great laboratory for the study of shape evolution, with the transition from the soft triaxial rotor in ^{168}Os to the well-deformed prolate rotor in ^{180}Os, while shape coexistence appears around $N = 96$ in ^{172}Os. Therefore, the study of the Os isotopic chain should provide a better understanding of shape changes in nuclei and a detailed scrutiny of nuclear structure calculations. In this paper, the lifetimes of the low-lying yrast states of ^{170}Os have been measured for the first time to investigate the shape evolution with neutron number.

Purpose: Lifetimes of excited states in the ground-state band of ^{170}Os are measured to investigate the shape evolution with neutron number in osmium isotopes and compare with state-of-the-art calculations.

Methods: The states of interest were populated via the fusion-evaporation reaction ^{142}Nd(^{32}S, $4n$) at a bombarding energy of 170 MeV at the ALTO facility from IPN (Orsay, France). Lifetimes of the 2_1^+ and 4_1^+ states in ^{170}Os were measured with the recoil-distance Doppler-shift method using the Orsay universal plunger system.

Results: Lifetimes of the two first excited states in ^{170}Os were measured for the first time. A very small $B(E2; 4_1^+ \rightarrow 2_1^+)/B(E2; 2_1^+ \rightarrow 0_1^+) = 0.38(11)$ was found, which is very uncharacteristic for collective nuclei. These results were compared to state-of-the-art beyond-mean-field calculations.

Conclusions: Although theoretical results give satisfactory results for the energy of the first few excited states in ^{170}Os and the $B(E2; 2_1^+ \rightarrow 0_1^+)$ they fail to reproduce the very small $B(E2; 4_1^+ \rightarrow 2_1^+)$, which remains a puzzle.

DOI: 10.1103/PhysRevC.100.034302

I. INTRODUCTION

The mechanisms of shape transitions remain a challenging topic in nuclear structure calculations, but are becoming experimentally more accessible. While the transition between shapes is generally gradual, the systems of interest are those that exhibit abrupt changes in observables with the addition or subtraction of a few nucleons. The osmium isotope chain provides such a test case, as it goes from a soft triaxial rotor in ^{168}Os to a mid-shell well-deformed prolate rotor in ^{180}Os, with the appearance of shape coexistence close to $N = 96$ in ^{172}Os. The osmium isotopic chain is the longest continuous chain of even-even isotopes with available spectroscopic data on the low-lying yrast states covering a mass range from $A = 162$ to $A = 198$. The evolution of the energies of the yrast 2^+ and 4^+ for those isotopes is reported in the upper panel of Fig. 1 together with the structural benchmark $E_{4_1^+}/E_{2_1^+}$ ($R_{4/2}$) in the lower panel. A transition from vibratorlike structures for the most neutron-rich nuclei to deformed prolate rotors close to the mid-neutron shell passing by γ-unstable or triaxial shapes is suggested by the data [1–4]. Moving close to the $N = 82$ shell closure at $A = 158$, the collectivity decreases and neutron-deficient osmium isotopes pass through shape coexistence at $A = 172$ [5] to a single-particle-like excitation in ^{162}Os [6].

Osmium isotopes with $N \approx 96$ lie at the edge of the region of neutron-deficient nuclei close to the $Z = 82$ shell closure where a large number of nuclei with shape coexistence [7] are found, making it fertile ground for nuclear structure research.

*alain.goasduff@pd.infn.it

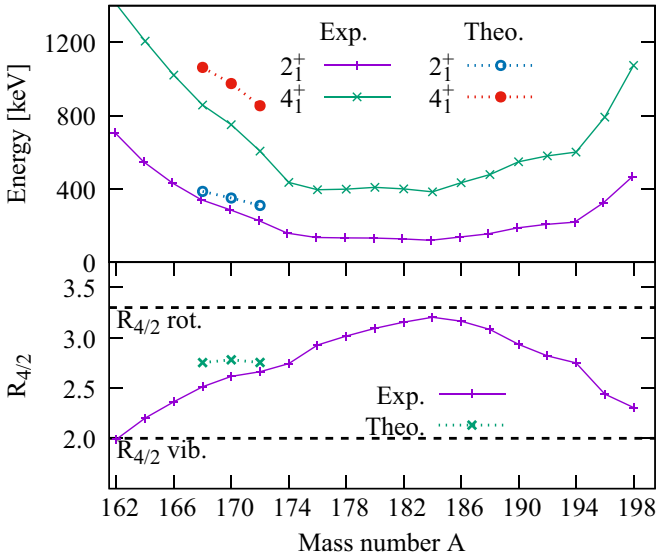

FIG. 1. The excitation energy systematic of the 2^+ and 4^+ yrast states in the osmium isotopes in the upper panel. The structural benchmark $R_{4/2} = E_{4_1^+}/E_{2_1^+}$ is presented in the lower panel together with the empirical limits for rotation and vibrational nuclei. The theoretical values for ^{168,170,172}Os are a part of this work.

A good example is ^{186}Pb with three 0^+ states close in energy [8]. Shape-coexistence phenomena have been evidenced in several nuclei in the lead region and recent lifetime measurements in Po [9], Pb [10–12], Hg [13–15], and Pt [16]. These discoveries have allowed a deeper understanding of the shape-coexistence origins. The model-independent measurements of the $B(E2)$ values in the yrast bands have given firm experimental evidence of several low-energy configurations highly mixed at low spins.

The question of shape coexistence in the neutron-deficient osmium isotopes has been addressed several times over the last few decades. The yrast sequence of ^{172}Os shows a sharp backbend near spin $14\hbar$ originated from the $i_{13/2}$ neutron alignment [17]. At a spin of $6\hbar$, an up-bend can be observed. The shape coexistence in ^{170,172}Os was discussed based on a three-band mixing model [18] reproducing level energies and moments of inertia. The work suggested that shape coexistence is as well present in ^{170}Os although the deformed structure responsible for the anomaly seen in the moments of inertia in ^{172}Os is shifted upwards in ^{170}Os, making its influence on the kinematic moments of inertia significantly smaller. To explain this variation in the moments of inertia around ^{172}Os several approaches were employed based on either particle alignment or phenomenological shape coexistence [17]. Although no firm conclusions could be drawn, shape coexistence is presented as a plausible explanation. The question of shape coexistence in ^{172}Os [19] was also addressed by means of lifetime measurements using the recoil-distance Doppler-shift (RDDS) method giving access to the transition quadrupole moment Q_t. A strong variation in the Q_t with increasing spin in the ground-state band was observed. This behavior could be explained by the model of three bands with strong mixing. Studying the spectroscopy of ^{168}Os [20] and using a similar theoretical approach of the three-band mixing model, a conclusion similar to that for ^{170}Os is reached concerning the presence of shape coexistence as the shaping force of the low-spin spectroscopy.

More recent studies concerning neutron-deficient Os isotopes such as ^{162}Os [21], including a lifetime measurement of the $17/2^+$ state in ^{167}Os [22] and of yrast and non-yrast states in ^{168}Os [23], give evidence for a shape transition from prolate deformation via γ-soft nuclei to spherical shapes close to the $N = 82$ shell gap. It is worth pointing out that for ^{168}Os Grahn *et al.* [23] measured a reduced transition probability for the yrast 4^+ resulting in $B_{4/2} = B(E2; 4_1^+ \rightarrow 2_1^+)/(B(E2; 2_1^+ \rightarrow 0_1^+) = 0.34(18)$. A $B_{4/2} < 1$ is very rare throughout the nuclear chart, with only a handful of examples away from closed shell nuclei, e.g., ^{48,50}Cr [24], ^{72,74}Zn [25], ^{114}Te [26], ^{114}Xe [27], ^{166}W [28], ^{168}Os [23], and ^{172}Pt [29]. These observations have not been reproduced so far by any type of state-of-the-art nuclear structure calculations, neither large-scale shell models nor beyond-mean-field models.

Beyond-mean-field calculations using the Gogny D1S force, allowing for triaxial shapes, have been used to investigate the shape coexistence phenomenon. For lighter nuclei such as Kr [30] and Se [31], it has been shown that triaxial shapes have to be included in the A $\sim$ 70 region for a correct reproduction of the observable. The importance of the triaxial degree of freedom has also been demonstrated in neutron-rich osmium [1].

The work presented here was initiated to elucidate the question of shape coexistence and shape evolution in neutron-deficient osmium isotopes. In this paper the result of an experiment where the lifetimes of yrast states in ^{170}Os have been measured via the RDDS method are presented. The results are compared to the state-of-the-art beyond-mean-field calculations.

II. EXPERIMENT AND RESULTS

The experiment was performed at the ALTO facility (IPN Orsay, France) using the Tandem accelerator. Excited states in ^{170}Os were populated in the reaction ^{142}Nd(^{32}S, $4n$)^{170}Os at a beam energy of 170 MeV. The isotopically enriched ^{142}Nd target had a thickness of 1 mg/cm^2. The Nd was evaporated onto a 2 mg/cm^2 thick Ta fronting facing the beam. The energy loss of the beam inside the Ta backing was taken into account in the determination of the bombarding energy. A 5 mg/cm^2 Au thick foil was used as a stopper foil for the fusion-evaporation fragments. Target and stopper were mounted on the Orsay universal plunger system (OUPS) plunger [32]. The γ rays were detected by the ORGAM germanium detector array composed of 10 Compton-suppressed high-purity germanium (HPGe) detectors distributed over two rings at backward angles (133.5° and 157.6°) and two additional detectors at forward angle (43°). The recoil velocity of the ^{170}Os nuclei was deduced from the Doppler shift of γ rays emitted in flight to be $\beta = v/c = 1.62 \pm 0.02\%$.

Data were collected for eight target-stopper separations between 18 and 740 μm. The normalization of the data for the different distances was obtained using the 278-keV line of ^{197}Au, resulting from the Coulomb excitation of the

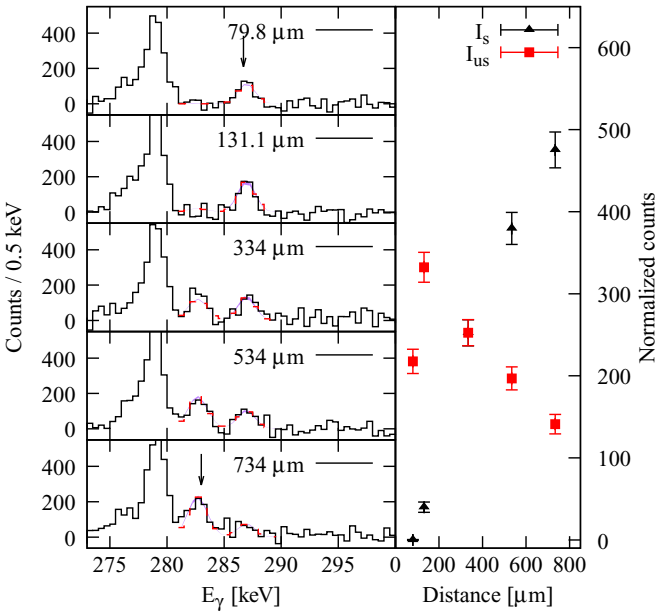

FIG. 2. Left: Background subtracted γ-ray spectra obtained by gating on the in-flight transition of the $4_1^+ \rightarrow 2_1^+$ for the detectors at 157.6°. The γ-ray spectra show the stopped and in-flight components of the $2_1^+ \rightarrow 0_1^+$. Only the distances in the sensitive range are presented. The stopped component is indicated by an arrow in the uppermost panel, and the in-flight component with an arrow in the lowest panel. The large peak at 279 keV is the Coulomb excitation of the gold stopper. Spectra are background subtracted. The fit used to extract the integral of the two components is displayed for each distance with the red dashed line. The purple curves correspond to the variations performed by the MINOS package to find the two-sided error on τ. Right: Normalized number of counts for the distances in the sensitive range used to extract the lifetime of the 2^+ state.

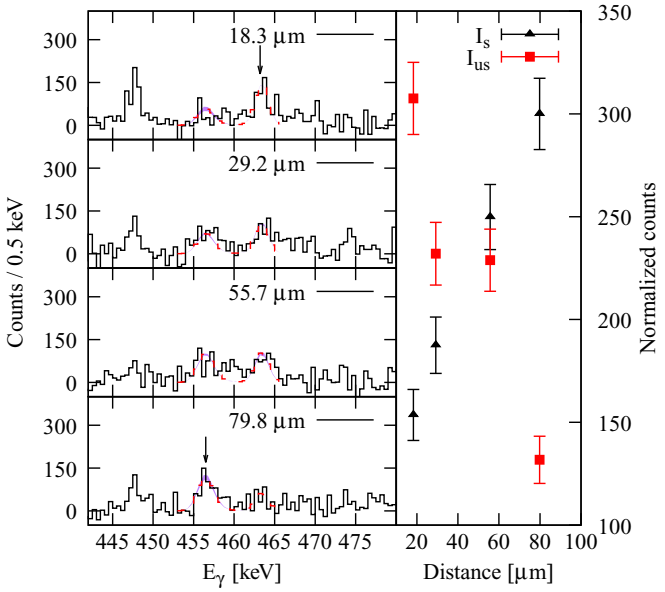

FIG. 3. Same as Fig. 2 for the $4_1^+ \rightarrow 2_1^+$ transition at 157.6° obtained by gating on the $6_1^+ \rightarrow 4_1^+$ in-flight transition.

stopper foil. The normalization is thus directly proportional to the integrated beam current on the target. The γ-γ coincidences were reconstructed and used to avoid the side-feeding effect on the lifetime determinations. Lifetimes of the two first excited states were obtained using γ-γ coincidence and the differential decay-curve method (DDCM) [33,34] gating on the in-flight component of the feeding transition. The γ-γ coincidences were sorted ringwise and the background subtracted projection was then summed and used to extract the lifetimes of interest. The background subtracted spectra obtained by gating on the in-flight component of the 4_1^+ and 6_1^+ are presented in Figs. 2 and 3 for the detectors at 157.6° and in Figs. 4 and 5 for the ones at 133.5°, respectively. Because the spectra were contaminated with peaks from other nuclei and there was not sufficient statistics to work with triple coincidences, two independent methods were used to extract the lifetimes of interest: the traditional method, in which the intensities of the peaks were extracted from the in-flight gated spectrum using analytic functions, and a Monte Carlo–based approach. For the latter, GEANT4 Monte Carlo simulations taking into account all the relevant aspects of the experimental setup such as the position and resolution of individual detectors, target and degrader thickness, reaction kinematics, etc., were used to determine the line shapes of the peaks. These line shapes were later used to extract the intensities of the stopped (I_{us}) and in-flight (I_s) intensities in the spectra as a function of the lifetime (τ) via the relation

$$I_{us} = \frac{dI_s}{dt}\tau. \quad (1)$$

I_{us} (red square) and Is (black triangle), after renormalization to the Coulomb excitation of the Au stopper, are given in the right-hand panels of Figs. 2 and 3 for the 2^+ and 4^+ states, respectively, and for the detectors placed at 157.6°. The same analysis was performed independently for the detectors at

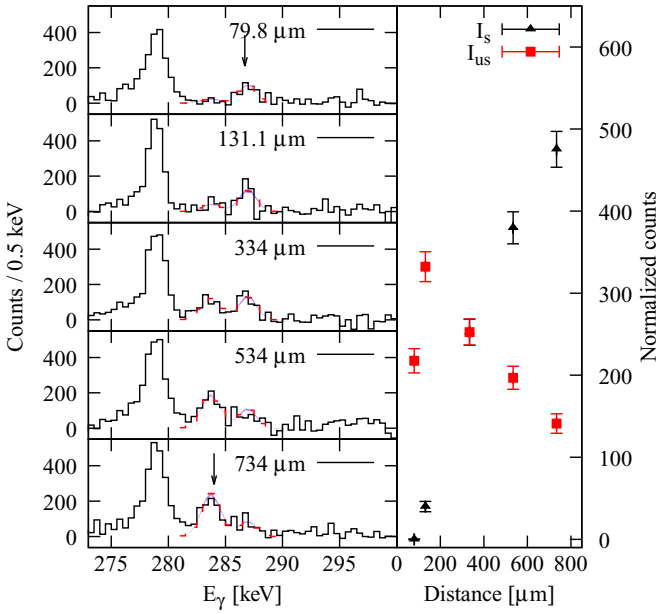

FIG. 4. Same as Fig. 2 for the $2_1^+ \rightarrow 0_1^+$ transition gated on the in-flight transition of the $4_1^+ \rightarrow 2_1^+$ for the detectors at 133.5°.

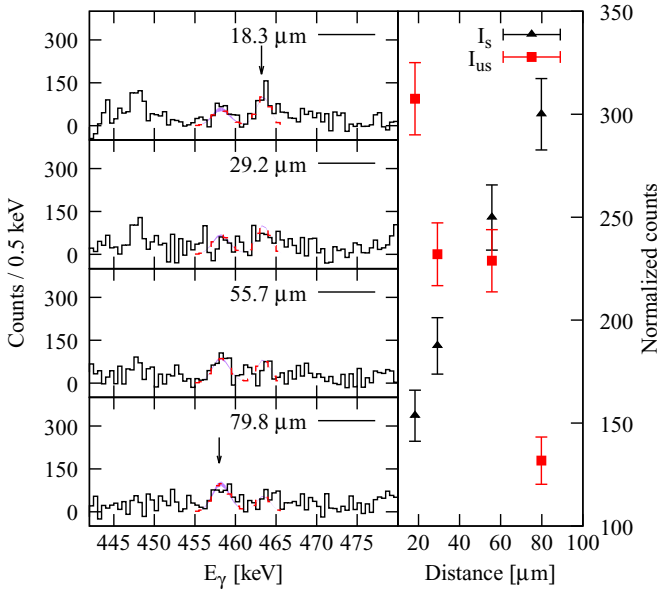

FIG. 5. Same as Fig. 3 for the $4_1^+ \rightarrow 2_1^+$ transition at 133.5° obtained by gating on the $6_1^+ \rightarrow 4_1^+$ in-flight transition.

133.5° and the results are presented in Figs. 4 and 5. Lifetimes were extracted using background subtracted spectra gated on the in-flight component of the feeding transition. Using such a gated approach allows one to get rid of the problem with long lived unseen feeding. Moreover, the second approach presents the advantage of taking into account the non-Gaussian shape of the peaks due to the angular aperture of the detectors, the velocity distribution, and slowing down of the recoiling nuclei in the target or stopper. For these reasons the more robust fit given by the second approach gives a more reliable determination of the lifetimes. The lines shapes were fitted to the experimental spectra using the MINUIT2 package [35] and the asymmetric errors were extracted using the MINOS function included in MINUIT2, leaving as free parameters only the number of counts in the two components. MINOS extracts the error on either side by varying the lifetime such that $\Delta\chi^2 = 1$ while minimizing the χ^2 on all other free parameters. In Figs. 2 and 3 the γ-ray spectra obtained by projecting the γ-γ matrices on the in-flight component of the feeding transition ($4_1^+ \rightarrow 2_1^+$ and $6_1^+ \rightarrow 4_1^+$, respectively) are presented (solid black line) for the distance in the sensitive range for the lifetime measurement. The corresponding fits are shown (dashed red line) for γ-ray spectra with detectors at the most backward angle, representing about half of the total statistic. Purple bands corresponding to the variations done by MINOS to find the two-sided errors are also shown. It should be noted that the two methods yielded compatible results using the same background subtracted spectra. While the results using the second methods are reported in Table I, the ones employing the first methods correspond to 80^{+11}_{-13} ps for the 2_1^+ and 20^{+8}_{-5} ps for the 4_1^+.

Reduced electromagnetic transition probabilities were obtained from the measured lifetime (τ) using the formula

$$\tau = 8.13 \times 10^{13} E_\gamma^{-5} [B(E2)\downarrow]^{-1} (1+\alpha)^{-1}, \qquad (2)$$

TABLE I. Spin and parities of the yrast states in ^{170}Os together with their excitation energies, lifetimes, and reduced electromagnetic transition probabilities (experimental and theoretical). The reported theoretical values are the ones obtained in this work using the symmetry-conserving configuration mixing method.

				$B(E2)\downarrow$ (e^2b^2)	
J^π	E (keV)	τ (ps)	$I_i^\pi \rightarrow I_f^\pi$	Expt.	Theor.
2_1^+	287	70^{+6}_{-6}	$2_1^+ \rightarrow 0_1^+$	$0.54^{+0.05}_{-0.05}$	0.53
4_1^+	750	18^{+6}_{-4}	$4_1^+ \rightarrow 2_1^+$	$0.21^{+0.07}_{-0.04}$	0.81

where E_γ is in units of keV, $B(E2)\downarrow$ in e^2b^2, τ in picoseconds, and α the total internal conversion coefficient evaluated using Ref. [36]. The results are summarized in Table I.

As this is a very unusual result the validity of the measured lifetime of the 4_1^+ state can be questioned. The data were analyzed in an independent manner by several of the authors using more than one way of estimating the peak intensities. Results scatter slightly but within errors and the anomaly of a $B_{4/2} < 1$ remains valid.

III. DISCUSSION

The measured B(E2; $2_1^+ \rightarrow 0_1^+$) of 0.54(0.05) e^2b^2 (97(8) W.u.) is in agreement with extrapolation from less neutron-deficient osmium isotopes. It is also in good agreement with earlier theoretical estimates [37]. The variable-moment-of-inertia (VMI) model [38] with the fitted parameters [18] gives an estimate of the $B(E2; 2_1^+ \rightarrow 0_1^+)$ of ^{170}Os, which is ∼40% lower than the experimental value. A similar underestimate is obtained for ^{172}Os; however, the VMI model reproduces correctly the evolution of the $B(E2; 2_1^+ \rightarrow 0_1^+)$ going from ^{172}Os to ^{170}Os. Looking at the 2_1^+ state the ^{170}Os behaves as a transitional nucleus with the normal decrease in collectivity moving away from the neutron mid-shell.

The $B(E2; 4_1^+ \rightarrow 2_1^+)$ of 0.21(0.05) e^2b^2 is, in contrast to the "normal" $B(E2; 2_1^+ \rightarrow 0_1^+)$, surprisingly small, resulting in a $B_{4/2}$ ratio of 0.38(11). Similar results were obtained in ^{166}W [28], ^{168}Os [23], and ^{172}Pt [29]. Based on those measurements, Cederwall *et al.* [29] proposed a transition at $N = 94$ from a collective regime into a senioritylike scheme as a possible explanation for the $B_{4/2} < 1$, despite the presence of a large number of valence nucleons. The position of such a phase transition at $N = 94$ is supported by the present data. However, as ^{170}Os is rather collective the suggested explanation, i.e., a transition into a senioritylike scheme, is very surprising. Band-mixing calculations for ^{170}Os [18] cannot explain this phenomenon, as the ground-state band should be pure at such low spins. Moreover, it is worth noticing that the 2_1^+ states of these four nuclei follow the expected correlations between the $E(4_1^+)/E(2_1^+)$ or the product of the number of valence protons and neutrons and the $B(E2; 2_1^+ \rightarrow 0_1^+)$ [39].

To try to understand the small $B_{4/2}$ ratio, symmetry-conserving configuration mixing (SCCM) calculations were performed using the generator coordinate method framework with Hartree-Fock-Bogoliubov states found with variation after particle number projection (PN-VAP) [40,41]. In general

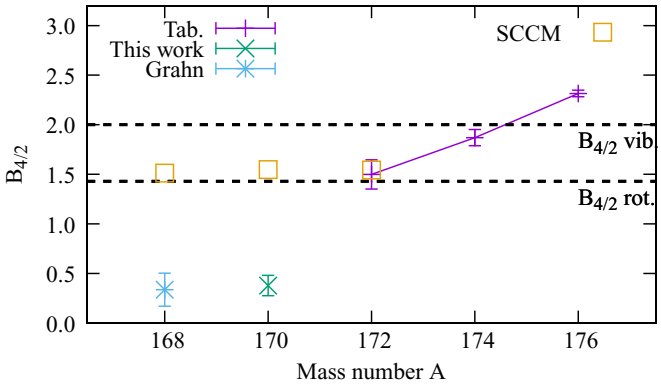

FIG. 6. The ratio between $B(E2;4_1^+ \rightarrow 2_1^+)$ and the $B(E2;2_1^+ \rightarrow 0_1^+)$ ($B_{4/2}$) for the neutron-deficient osmium isotopes. The tabulated values for ^{172,174}Os values were taken from National Nuclear Data Center and from Refs. [43,44] for ^{176}Os. The value reported for ^{168}Os is the one from the work of Grahn *et al.* [23]. The experimental value for ^{170}Os as well as the theoretical values for ^{168,170,172}Os are part of this work.

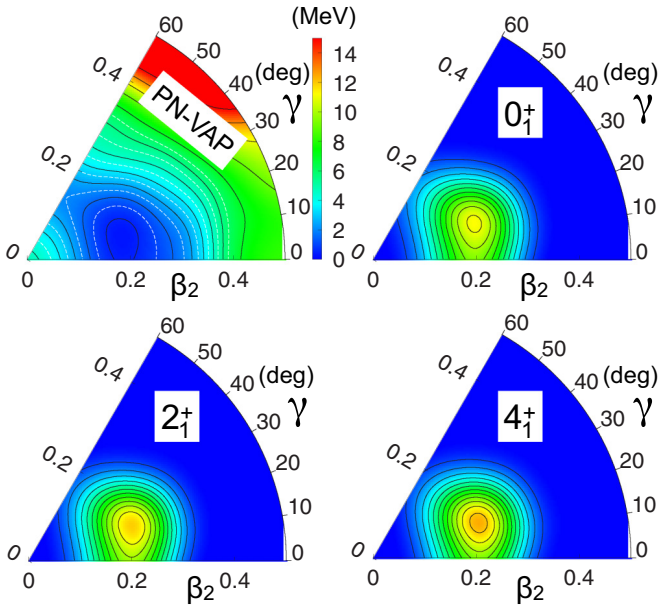

FIG. 7. The PN-VAP potential energy surface for ^{170}Os (top left) and collective wave functions for the ground state (top right) as well as the yrast 2^+ (bottom left) and 4^+ (bottom right) states. All calculated wave functions display a very similar structure.

the yrast states are given as close to prolate with $\beta \approx 20°$ and $\gamma \leqslant 20°$. For ^{172}Os, the yrast band is, however, triaxial with $\gamma \approx 30°$. The energies for the lowest yrast and non-yrast states for ^{168,170,172}Os are presented in Fig. 1. The agreement between experimental and theoretical excitation energies is satisfactory (see Ref. [42] and references therein). In Fig. 6 experimentally known $B_{4/2}$ are shown together with the results of the calculations. The experimental $B_{4/2}$ are presented in Fig. 6 for $^{169-176}$Os and compared for $^{168-172}$Os to the present theoretical calculations. The $B_{4/2}$ for ^{172}Os is well reproduced by the model; however, the ones of ^{168,170}Os are overestimated by a factor of ∼4. As shown in Table I, the $B(E2;2_1^+ \rightarrow 0_1^+)$ of ^{170}Os is very well reproduced, as well as those of ^{168,172}Os. Thus the observed discrepancy on the $B_{4/2}$ for ^{168,170}Os is solely originated by the $B(E2;4_1^+ \rightarrow 2_1^+)$. Indeed a similar factor of ∼4 is found between the experimental and theoretical $B(E2;4_1^+ \rightarrow 2_1^+)$. While the experimental $B_{4/2}$ ratio is small, the resulting theoretical ratios are ∼1.5, close to that of a deformed rotor. The experimental $B_{4/2}$ ratio for ^{172}Os is 1.5(2), compatible with the present theoretical approach. The present results show that the structural change is more sudden than previously observed. Indeed the large drop in $B_{4/2}$ is already evidenced in ^{170}Os.

A possible explanation for the observed $B_{4/2}$ ratio is that the yrast 4^+ state does not belong to the same band as the 2_1^+ state. The origin for this mismatch could be the presence of a shape-coexistent rotational band whose 4^+ member would be below the 4^+ level of the ground-state band. The SCCM method calculations performed in this work show no evidence for such a sideband. In Fig. 7 the potential energy surface (PES) obtained using the PN-VAP method, and the collective wave functions for the 0_1^+, 2_1^+, and 4_1^+ states are plotted in the (β_2, γ) plane. The PES exhibits only one minimum at a slightly triaxial deformation $(\beta_2, \gamma) \sim (0.2, 15°)$ and the collective wave functions have all the same structure, revealing that they belong to the same rotational band. The second 4^+ in the calculations (not shown) corresponds to a state in a γ band. Another possibility is that the experimental yrast 4^+ has a single-particle nature that could be produced, e.g., by the alignment of a pair at low spin as it was found in ^{44}S [42]. In order to search for such a state, calculations were expanded by performing PN-VAP calculations including cranking and by extending the range of triaxial quadrupole deformations to $-60° < \gamma < 120°$ as done in Ref. [42]. The full configuration mixing was not performed due to the large computational burden. Nevertheless, a 4^+ state with the sought-after characteristics to reproduce the low $B(E2;4_1^+ \rightarrow 2_1^+)$ value would manifest itself as a minimum for the projected $J \geqslant 4$ PES's not present in the $J = 0, 2$ PES's computed at non-zero intrinsic rotation (cranking) frequency, $\omega \neq 0$. Such a feature has not been found in the calculations and the origin of the observed transition probability remains unexplained within the employed formalism and/or variational space.

IV. CONCLUSION

The lifetimes of the first excited 2^+ and 4^+ states in ^{170}Os were measured for the first time using the RDDS method at the ALTO facility with the ORGAM γ-ray array coupled to the OUPS plunger. A surprisingly small $B(E2;4_1^+ \rightarrow 2_1^+)$ value was found. To understand this value, the results were compared to the state-of-the-art beyond-mean-field calculations. The model accurately reproduced the energies of the lowest-lying yrast states and the 2^+ reduced transition probabilities in ^{168,170,172}Os. Although the model described correctly the properties of the yrast 4^+ state of ^{172}Os, the sudden structural change observed when removing two neutrons is not present in the calculation. The question of the origin of the small $B_{4/2}$ in ^{168,170}Os remains open and merits experimental efforts

in order to validate these surprising results and expand the known lifetimes to higher spin yrast and yrare states.

ACKNOWLEDGMENTS

The authors would like to thank the ALTO technical team for the good quality beam that was provided during the experiment. Dr. K. O. Zell and Dr. A. Blazhev from IKP Köln are thanked for the excellent quality Nd targets. We also thank the UK/France (STFC/IN2P3) Loan Pool and GAMMAPOOL European Gamma-Ray Spectroscopy Pool for the loan of the detectors for ORGAM. This work was supported in part by the 2214-TUBITAK (Scientific and Technological Research Council of Turkey) Programme, the Scientific Research Projects Coordination Unit of Istanbul University under Project No. 46811, and the European Community FP7 Capacities-Integrated Infrastructure Initiative-Contract ENSAR No. 262010. This work has been partly funded (A.G.) by the P2IO LabEx (ANR-10-LABX-0038) in the framework Investissements d'Avenir (ANR-11-IDEX-0003-01) managed by the French Agence Nationale de la Recherche (ANR). T.R.R. acknowledges support from Spanish Grants No. FIS-2014-53434-P MINECO and Programa Ramon y Cajal 2012 No. 11420, and computing time at GSI-Darmstadt.

[1] P. R. John, V. Modamio, J. J. Valiente-Dobón, D. Mengoni, S. Lunardi, T. R. Rodríguez, D. Bazzacco, A. Gadea, C. Wheldon, T. Alexander, G. de Angelis, N. Ashwood, M. Barr, G. Benzoni, B. Birkenbach, P. G. Bizzeti, A. M. Bizzeti-Sona, S. B. M. Bowry, A. Bracco, F. Browne, M. Bunce, F. Camera, B. Cederwall, L. Corradi, F. C. L. Crespi, P. Désesquelles, J. Eberth, E. Farnea, E. Fioretto, A. Görgen, A. Gottardo, J. Grebosz, L. Grente, H. Hess, A. Jungclaus, T. Kokalova, A. Korichi, W. Korten, A. Kuşoğlu, S. Lenzi, S. Leoni, J. Ljungvall, G. Maron, W. Meczynski, B. Melon, R. Menegazzo, C. Michelagnoli, T. Mijatović, B. Million, P. Molini, G. Montagnoli, D. Montanari, D. R. Napoli, P. Nolan, C. Oziol, Z. Podolyák, G. Pollarolo, A. Pullia, B. Quintana, F. Recchia, P. Reiter, O. J. Roberts, D. Rosso, E. Sahin, M.-D. Salsac, F. Scarlassara, M. Sferrazza, J. Simpson, P.-A. Söderström, A. M. Stefanini, O. Stezowski, S. Szilner, C. Theisen, C. A. Ur, and J. Walshe, Phys. Rev. C **90**, 021301 (2014).

[2] Z. Podolyák, S. J. Steer, S. Pietri, F. R. Xu, H. L. Liu, P. H. Regan, D. Rudolph, A. B. Garnsworthy, R. Hoischen, M. Górska, J. Gerl, H. J. Wollersheim, T. Kurtukian-Nieto, G. Benzoni, T. Shizuma, F. Becker, P. Bednarczyk, L. Caceres, P. Doornenbal, H. Geissel, J. Grebęosz, A. Kelic, I. Kojouharov, N. Kurz, F. Montes, W. Prokopowicz, T. Saito, H. Schaffner, S. Tashenov, A. Heinz, M. Pfützner, A. Jungclaus, D. L. Balabanski, C. Brandau, A. M. Bruce, W. N. Catford, I. J. Cullen, Z. Dombrádi, E. Estevez, W. Gelletly, G. Ilie, J. Jolie, G. A. Jones, M. Kmiecik, F. G. Kondev, R. Krücken, S. Lalkovski, Z. Liu, A. Maj, S. Myalski, S. Schwertel, P. M. Walker, E. Werner-Malento, and O. Wieland, Phys. Rev. C **79**, 031305 (2009).

[3] C. Wheldon, G. D. Dracoulis, R. T. Newman, P. M. Walker, C. J. Pearson, A. P. Byrne, A. M. Baxter, S. Bayer, T. Kibédi, T. R. McGoram, S. M. Mullins, and F. R. Xu, Nucl. Phys. A **699**, 415 (2002).

[4] P. D. Bond, R. F. Casten, D. D. Warner, and D. Horn, Phys. Lett. B **130**, 167 (1983).

[5] P. M. Davidson, G. D. Dracoulis, T. Kibédi, A. P. Byrne, S. S. Anderssen, A. M. Baxter, B. Fabricius, G. J. Lane, and A. E. Stuchbery, Nucl. Phys. A **568**, 90 (1994).

[6] D. T. Joss, K. Lagergren, D. E. Appelbe, C. J. Barton, J. Simpson, B. Cederwall, B. Hadinia, R. Wyss, S. Eeckhaudt, T. Grahn, P. T. Greenlees, P. M. Jones, R. Julin, S. Juutinen, H. Kettunen, M. Leino, A.-P. Leppänen, P. Nieminen, J. Pakarinen, P. Rahkila, C. Scholey, J. Uusitalo, R. D. Page, E. S. Paul, and D. R. Wiseman, Phys. Rev. C **70**, 017302 (2004).

[7] K. Heyde and J. L. Wood, Rev. Mod. Phys. **83**, 1467 (2011).

[8] A. N. Andreyev, M. Huyse, P. V. Duppen, L. Weissman, D. Ackermann, J. Gerl, F. P. Hessberger, S. Hofmann, A. Kleinbohl, G. Munzenberg, S. Reshitko, C. Schlegel, H. Schaffner, P. Cagarda, M. Matos, S. Saro, A. Keenan, C. Moore, C. D. O'Leary, R. D. Page, M. Taylor, H. Kettunen, M. Leino, A. Lavrentiev, R. Wyss, and K. Heyde, Nature (London) **405**, 430 (2000).

[9] T. Grahn, A. Dewald, P. T. Greenlees, U. Jakobsson, J. Jolie, P. Jones, R. Julin, S. Juutinen, S. Ketelhut, T. Kröll, R. Krücken, M. Leino, P. Maierbeck, B. Melon, M. Nyman, R. D. Page, P. Peura, T. Pissulla, P. Rahkila, J. Sarén, C. Scholey, J. Sorri, J. Uusitalo, M. Bender, and P. H. Heenen, Phys. Rev. C **80**, 014323 (2009).

[10] A. Dewald, R. Peusquens, B. Saha, P. von Brentano, A. Fitzler, T. Klug, I. Wiedenhöver, M. P. Carpenter, A. Heinz, R. V. F. Janssens, F. G. Kondev, C. J. Lister, D. Seweryniak, K. A. Saleem, R. Krücken, J. R. Cooper, C. J. Barton, K. Zyromski, C. W. Beausang, Z. Wang, P. Petkov, A. M. Oros-Peusquens, U. Garg, and S. Zhu, Phys. Rev. C **68**, 034314 (2003).

[11] T. Grahn, A. Dewald, O. Möller, R. Julin, C. W. Beausang, S. Christen, I. G. Darby, S. Eeckhaudt, P. T. Greenlees, A. Görgen, K. Helariutta, J. Jolie, P. Jones, S. Juutinen, H. Kettunen, T. Kröll, R. Krücken, Y. Le Coz, M. Leino, A.-P. Leppänen, P. Maierbeck, D. A. Meyer, B. Melon, P. Nieminen, M. Nyman, R. D. Page, J. Pakarinen, P. Petkov, P. Rahkila, B. Saha, M. Sandzelius, J. Sarén, C. Scholey, and J. Uusitalo, Phys. Rev. Lett. **97**, 062501 (2006).

[12] T. Grahn, A. Dewald, O. Möller, R. Julin, C. W. Beausang, S. Christen, I. G. Darby, S. Eeckhaudt, P. T. Greenlees, A. Görgen, K. Helariutta, J. Jolie, P. Jones, S. Juutinen, H. Kettunen, T. Kröll, R. Krcüken, Y. L. Coz, M. Leino, A.-P. Leppänen, P. Maierbeck, D. A. Meyer, B. Melon, P. Nieminen, M. Nyman, R. D. Page, J. Pakarinen, P. Petkov, P. Rahkila, B. Saha, M. Sandzelius, J. Sarén, C. Scholey, J. Uusitalo, M. Bender, and P.-H. Heenen, Nucl. Phys. A **801**, 83 (2008).

[13] L. P. Gaffney, M. Hackstein, R. D. Page, T. Grahn, M. Scheck, P. A. Butler, P. F. Bertone, N. Bree, R. J. Carroll, M. P. Carpenter, C. J. Chiara, A. Dewald, F. Filmer, C. Fransen, M. Huyse, R. V. F. Janssens, D. T. Joss, R. Julin, F. G. Kondev, P. Nieminen, J. Pakarinen, S. V. Rigby, W. Rother, P. Van Duppen,

H. V. Watkins, K. Wrzosek-Lipska, and S. Zhu, Phys. Rev. C **89**, 024307 (2014).

[14] T. Grahn, A. Petts, M. Scheck, P. A. Butler, A. Dewald, M. B. Gómez Hornillos, P. T. Greenlees, A. Görgen, K. Helariutta, J. Jolie, P. Jones, R. Julin, S. Juutinen, S. Ketelhut, R. Krücken, T. Kröll, M. Leino, J. Ljungvall, P. Maierbeck, B. Melon, M. Nyman, R. D. Page, T. Pissulla, P. Rahkila, J. Sarén, C. Scholey, A. Semchenkov, J. Sorri, J. Uusitalo, R. Wadsworth, and M. Zielinska, Phys. Rev. C **80**, 014324 (2009).

[15] M. Scheck, T. Grahn, A. Petts, P. A. Butler, A. Dewald, L. P. Gaffney, M. B. Gómez Hornillos, A. Görgen, P. T. Greenlees, K. Helariutta, J. Jolie, P. Jones, R. Julin, S. Juutinen, S. Ketelhut, T. Kröll, R. Krücken, M. Leino, J. Ljungvall, P. Maierbeck, B. Melon, M. Nyman, R. D. Page, J. Pakarinen, E. S. Paul, T. Pissulla, P. Rahkila, J. Sarén, C. Scholey, A. Semchenkov, J. Sorri, J. Uusitalo, R. Wadsworth, and M. Zielińska, Phys. Rev. C **81**, 014310 (2010).

[16] K. A. Gladnishki, P. Petkov, A. Dewald, C. Fransen, M. Hackstein, J. Jolie, T. Pissulla, W. Rother, and K. O. Zell, Nucl. Phys. A **877**, 19 (2012).

[17] R. A. Bark, G. D. Dracoulis, and A. E. Stuchbery, Nucl. Phys. A **514**, 503 (1990).

[18] G. D. Dracoulis, R. A. Bark, A. E. Stuchbery, A. P. Byrne, A. M. Baxter, and F. Riess, Nucl. Phys. A **486**, 414 (1988).

[19] A. Virtanen, N. R. Johnson, F. K. McGowan, I. Y. Lee, C. Baktash, M. A. Riley, J. C. Wells, and J. Dudek, Nucl. Phys. A **591**, 145 (1995).

[20] D. T. Joss, S. L. King, R. D. Page, J. Simpson, A. Keenan, N. Amzal, T. Back, M. A. Bentley, B. Cederwall, J. F. C. Cocks, D. M. Cullen, P. T. Greenlees, K. Helariutta, P. M. Jones, R. Julin, S. Juutinen, H. Kankaanpaa, H. Kettunen, P. Kuusiniemi, M. Leino, M. Muikku, A. Savelius, J. Uusitalo, and S. J. Williams, Nucl. Phys. A **689**, 631 (2001).

[21] D. T. Joss, N. Amzal, D. E. Appelbe, T. Bäck, C. J. Barton, M. A. Bentley, B. Cederwall, J. F. C. Cocks, D. M. Cullen, S. Eeckhaudt, T. Grahn, P. T. Greenlees, B. Hadinia, K. Helariutta, P. M. Jones, R. Julin, S. Juutinen, H. Kankaanpää, A. Keenan, H. Kettunen, S. L. King, P. Kuusiniemi, K. Lagergren, M. Leino, A. P. Leppänen, M. Muikku, P. Nieminen, R. D. Page, J. Pakarinen, E. S. Paul, P. Rahkila, C. Scholey, A. Savelius, J. Simpson, M. J. Taylor, J. Uusitalo, S. J. Williams, D. D. Warner, D. R. Wiseman, and R. Wyss, J. Phys. G **31**, S1593 (2005).

[22] D. O'Donnell, T. Grahn, D. T. Joss, J. Simpson, C. Scholey, K. Andgren, L. Bianco, B. Cederwall, D. M. Cullen, A. Dewald, E. Ganioglu, M. B. Gómez Hornillos, P. T. Greenlees, B. Hadinia, H. Iwasaki, U. Jakobsson, J. Jolie, P. Jones, D. S. Judson, R. Julin, S. Juutinen, S. Ketelhut, M. Labiche, M. Leino, N. M. Lumley, P. J. R. Mason, O. Möller, P. Nieminen, M. Nyman, R. D. Page, J. Pakarinen, E. S. Paul, M. Petri, A. Petts, P. Peura, N. Pietralla, T. Pissulla, P. Rahkila, P. Ruotsalainen, M. Sandzelius, P. J. Sapple, J. Saren, J. Sorri, J. Thomson, J. Uusitalo, and H. V. Watkins, Phys. Rev. C **79**, 064309 (2009).

[23] T. Grahn, S. Stolze, D. T. Joss, R. D. Page, B. Sayğı, D. O'Donnell, M. Akmali, K. Andgren, L. Bianco, D. M. Cullen, A. Dewald, P. T. Greenlees, K. Heyde, H. Iwasaki, U. Jakobsson, P. Jones, D. S. Judson, R. Julin, S. Juutinen, S. Ketelhut, M. Leino, N. Lumley, P. J. R. Mason, O. Möller, K. Nomura, M. Nyman, A. Petts, P. Peura, N. Pietralla, T. Pissulla, P. Rahkila, P. J. Sapple, J. Sarén, C. Scholey, J. Simpson, J. Sorri, P. D. Stevenson, J. Uusitalo, H. V. Watkins, and J. L. Wood, Phys. Rev. C **94**, 044327 (2016).

[24] D. Hertz-Kintish, L. Zamick, and S. J. Q. Robinson, Phys. Rev. C **90**, 034307 (2014).

[25] C. Louchart, A. Obertelli, A. Görgen, W. Korten, D. Bazzacco, B. Birkenbach, B. Bruyneel, E. Clément, P. J. Coleman-Smith, L. Corradi, D. Curien, G. de Angelis, G. de France, J.-P. Delaroche, A. Dewald, F. Didierjean, M. Doncel, G. Duchêne, J. Eberth, M. N. Erduran, E. Farnea, C. Finck, E. Fioretto, C. Fransen, A. Gadea, M. Girod, A. Gottardo, J. Grebosz, T. Habermann, M. Hackstein, T. Huyuk, J. Jolie, D. Judson, A. Jungclaus, N. Karkour, S. Klupp, R. Krücken, A. Kusoglu, S. M. Lenzi, J. Libert, J. Ljungvall, S. Lunardi, G. Maron, R. Menegazzo, D. Mengoni, C. Michelagnoli, B. Million, P. Molini, O. Möller, G. Montagnoli, D. Montanari, D. R. Napoli, R. Orlandi, G. Pollarolo, A. Prieto, A. Pullia, B. Quintana, F. Recchia, P. Reiter, D. Rosso, W. Rother, E. Sahin, M.-D. Salsac, F. Scarlassara, M. Schlarb, S. Siem, P. P. Singh, P.-A. Söderström, A. M. Stefanini, O. Stézowski, B. Sulignano, S. Szilner, C. Theisen, C. A. Ur, J. J. Valiente-Dobón, and M. Zielinska, Phys. Rev. C **87**, 054302 (2013).

[26] O. Möller, N. Warr, J. Jolie, A. Dewald, A. Fitzler, A. Linnemann, K. O. Zell, P. E. Garrett, and S. W. Yates, Phys. Rev. C **71**, 064324 (2005).

[27] G. de Angelis, A. Gadea, E. Farnea, R. Isocrate, P. Petkov, N. Marginean, D. R. Napoli, A. Dewald, M. Bellato, A. Bracco, F. Camera, D. Curien, M. D. Poli, E. Fioretto, A. Fitzler, S. Kasemann, N. Kintz, T. Klug, S. Lenzi, S. Lunardi, R. Menegazzo, P. Pavan, J. L. Pedroza, V. Pucknell, C. Ring, J. Sampson, and R. Wyss, Phys. Lett. B **535**, 93 (2002).

[28] B. Sayğı, D. T. Joss, R. D. Page, T. Grahn, J. Simpson, D. O'Donnell, G. Alharshan, K. Auranen, T. Bäck, S. Boening, T. Braunroth, R. J. Carroll, B. Cederwall, D. M. Cullen, A. Dewald, M. Doncel, L. Donosa, M. C. Drummond, F. Ertuğral, S. Ertürk, C. Fransen, P. T. Greenlees, M. Hackstein, K. Hauschild, A. Herzan, U. Jakobsson, P. M. Jones, R. Julin, S. Juutinen, J. Konki, T. Kröll, M. Labiche, A. Lopez-Martens, C. G. McPeake, F. Moradi, O. Möller, M. Mustafa, P. Nieminen, J. Pakarinen, J. Partanen, P. Peura, M. Procter, P. Rahkila, W. Rother, P. Ruotsalainen, M. Sandzelius, J. Sarén, C. Scholey, J. Sorri, S. Stolze, M. J. Taylor, A. Thornthwaite, and J. Uusitalo, Phys. Rev. C **96**, 021301 (2017).

[29] B. Cederwall, M. Doncel, O. Aktas, A. Ertoprak, R. Liotta, C. Qi, T. Grahn, D. M. Cullen, B. S. Nara Singh, D. Hodge, M. Giles, S. Stolze, H. Badran, T. Braunroth, T. Calverley, D. M. Cox, Y. D. Fang, P. T. Greenlees, J. Hilton, E. Ideguchi, R. Julin, S. Juutinen, M. K. Raju, H. Li, H. Liu, S. Matta, V. Modamio, J. Pakarinen, P. Papadakis, J. Partanen, C. M. Petrache, P. Rahkila, P. Ruotsalainen, M. Sandzelius, J. Sarén, C. Scholey, J. Sorri, P. Subramaniam, M. J. Taylor, J. Uusitalo, and J. J. Valiente-Dobón, Phys. Rev. Lett. **121**, 022502 (2018).

[30] E. Clément, A. Gorgen, W. Korten, E. Bouchez, A. Chatillon, J.-P. Delaroche, M. Girod, H. Goutte, A. Hurstel, Y. Le Coz, A. Obertelli, S. Peru, C. Theisen, J. N. Wilson, M. Zielinska, C. Andreoiu, F. Becker, P. A. Butler, J. M. Casandjian, W. N. Catford, T. Czosnyka, G. de France, J. Gerl, R.-D. Herzberg, J. Iwanicki, D. G. Jenkins, G. D. Jones, P. J. Napiorkowski, G. Sletten, and C. N. Timis, Phys. Rev. C **75**, 054313 (2007).

[31] J. Ljungvall, A. Gorgen, M. Girod, J.-P. Delaroche, A. Dewald, C. Dossat, E. Farnea, W. Korten, B. Melon, R. Menegazzo, A. Obertelli, R. Orlandi, P. Petkov, T. Pissulla, S. Siem, R. P. Singh, J. Srebrny, C. Theisen, C. A. Ur, J. J. Valiente-Dobón, K. O. Zell, and M. Zielinska, Phys. Rev. Lett **100**, 102502 (2008).

[32] J. Ljungvall, G. Georgiev, S. Cabaret, N. Karkour, D. Linget, G. Sedes, R. Chevrier, I. Matea, M. Niikura, M.-D. Salsac, and B. Sulignano, Nucl. Instrum. Methods Phys. Res. Sect. A **679**, 61 (2012).
[33] A. Dewald, S. Harissopulos, and P. von Brentano, Z. Phys. A **334**, 163 (1989).
[34] A. Dewald, O. Möller, and P. Petkov, Prog. Part. Nucl. Phys. **67**, 786 (2012).
[35] M. Hatlo, F. James, P. Mato, L. Moneta, M. Winkler, and A. Zsenei, IEEE Trans. Nucl. Sci. **52**, 2818 (2005).
[36] T. Kibédi, T. W. Burrows, M. B. Trzhaskovskaya, P. M. Davidson, and C. W. Nestor, Jr., Nucl. Instrum. Methods Phys. Res. Sect. A **589**, 202 (2008).
[37] W. Nazarewicz, M. Riley, and J. Garrett, Nucl. Phys. A **512**, 61 (1990).
[38] M. A. J. Mariscotti, G. Scharff-Goldhaber, and B. Buck, Phys. Rev. **178**, 1864 (1969).
[39] R. F. Casten and N. V. Zamfir, Phys. Rev. Lett. **70**, 402 (1993).
[40] T. R. Rodríguez and J. L. Egido, Phys. Rev. C **84**, 051307(R) (2011).
[41] T. R. Rodríguez and J. L. Egido, Phys. Lett. B **705**, 255 (2011).
[42] J. L. Egido, M. Borrajo, and T. R. Rodríguez, Phys. Rev. Lett. **116**, 052502 (2016).
[43] O. Möller, P. Petkov, B. Melon, A. Dewald, A. Fitzler, J. Jolie, D. Tonev, S. Christen, B. Saha, K. O. Zell, and M. Heidemann, Phys. Rev. C **72**, 034306 (2005).
[44] B. Melon, Ph.D. thesis, University of Cologne, 2011 (unpublished).

7.10 Performance of The Advanced GAmma Tracking Array at GANIL

Nuclear Inst. and Methods in Physics Research, A 955 (2020) 163297

Contents lists available at ScienceDirect

Nuclear Inst. and Methods in Physics Research, A

journal homepage: www.elsevier.com/locate/nima

Performance of the Advanced GAmma Tracking Array at GANIL

J. Ljungvall [a,*], R.M. Pérez-Vidal [b], A. Lopez-Martens [a], C. Michelagnoli [c,d], E. Clément [c], J. Dudouet [a,i], A. Gadea [b], H. Hess [f], A. Korichi [a], M. Labiche [j], N. Lalović [e], H.J. Li [c], F. Recchia [g,h], and the AGATA collaboration

[a] CSNSM, Université, Paris-Sud, CNRS/IN2P3, Université Paris-Saclay, 91405 Orsay, France
[b] Instituto de Física Corpuscular, CSIC - Universidad de Valencia, E-46980 Paterna, Valencia, Spain
[c] GANIL, CEA/DRF-CNRS/IN2P3, BP 55027, 14076 Caen cedex 5, France
[d] Institut Laue-Langevin, B.P. 156, F-38042 Grenoble cedex 9, France
[e] Department of Physics, Lund University, SE-22100, Lund, Sweden
[f] IKP, University of Cologne, D-50937 Cologne, Germany
[g] INFN Sezione di Padova, I-35131 Padova, Italy
[h] Dipartimento di Fisica e Astronomia dell'Università di Padova, I-35131 Padova, Italy
[i] Institut de Physique Nucléaire de Lyon, Université de Lyon, Université Lyon 1, CNRS-IN2P3, F-69622 Villeurbanne, France
[j] STFC Daresbury Laboratory, Daresbury, Warrington WA4 4AD, United Kingdom

ARTICLE INFO

Keywords:
AGATA spectrometer
GANIL facility
γ-ray tracking
Nuclear structure
HPGe detectors

ABSTRACT

The performance of the Advanced GAmma Tracking Array (AGATA) at GANIL is discussed, on the basis of the analysis of source and in-beam data taken with up to 30 segmented crystals. Data processing is described in detail. The performance of individual detectors are shown. The efficiency of the individual detectors as well as the efficiency after γ-ray tracking are discussed. Recent developments of γ-ray tracking are also presented. The experimentally achieved peak-to-total is compared with simulations showing the impact of back-scattered γ rays on the peak-to-total in a γ-ray tracking array. An estimate of the achieved position resolution using the Doppler broadening of in-beam data is also given.

Angular correlations from source measurements are shown together with different methods to take into account the effects of γ-ray tracking on the normalization of the angular correlations.

1. Introduction

In order to perform γ-ray spectroscopy nuclear structure studies in conditions of extreme neutron/proton asymmetry and/or extreme angular momentum the so-called γ-ray tracking arrays are considered as indispensable tools. Two international collaborations, Advanced-GAmma-Tracking-Array (AGATA) [1] in Europe and Gamma-Ray Energy Tracking Array (GRETA) in the US [2] are presently building such arrays. Position sensitive High-Purity Germanium (HPGe) detectors will cover close to 4π of solid angle and track the path of the γ rays inside the detector medium giving maximum efficiency and an excellent energy resolution. The technique of γ-ray tracking allows both the high efficiency needed for high-fold coincidences and the excellent position resolution needed for Doppler Correction at in-flight fragmentation facilities.

Gamma-ray tracking starts from the digitally recorded wave-forms of the pre-amplified signals of the highly-segmented HPGe detectors. The wave-forms are treated with Pulse Shape Analysis (PSA) techniques to extract the position of the interaction points of the γ rays in the detector, presently with a position resolution of about 5 mm FWHM [3–5]. The interaction points (*hits*) are grouped into events on the basis of their *timestamp*, *i.e.* the absolute time of the γ-ray interaction. The sequence of interaction points of the γ rays in the same event is reconstructed from the hits via *tracking* algorithms. A higher efficiency with a high peak-to-total is expected as the solid angle taken by Anti-Compton shields is now occupied by HPGe crystals and the Compton event suppression is performed by the γ-ray tracking algorithm. The use of digital electronics allows a higher count-rate with maintained energy resolution, and rates up to 50 kHz per crystals are routinely used during experiments. The almost continuous measurement of γ-ray emission angles, via the PSA and tracking, allows for the excellent Doppler correction seen in γ-ray tracking arrays and opens up a new degree of sensitivity in the determination of nuclear structure observables such as electromagnetic moments (e.g. lifetimes measurements based on Doppler shift and perturbed angular correlations). This paper is meant as both a snapshot in time of the capacities of AGATA and as a reference paper to be used when analyzing data from AGATA experiments performed at GANIL.

* Corresponding author.
E-mail address: joa.ljungvall@csnsm.in2p3.fr (J. Ljungvall).

https://doi.org/10.1016/j.nima.2019.163297
Received 9 May 2019; Received in revised form 6 December 2019; Accepted 12 December 2019
Available online 16 December 2019

The first experimental campaign with the demonstrator AGATA sub-array was at LNL (2009–2011) [6] where it was coupled to the PRISMA spectrometer for the study of neutron-rich nuclei produced in fusion–fission and neutron-transfer reactions. This was followed by a campaign at GSI (2012–2014). Here a larger AGATA sub-array was coupled to the FRS separator [7] for the first campaign with radioactive ion beams. The performance of the AGATA sub-array at GSI has been extensively studied [8], with focus on the efficiency of the AGATA sub-array as a function of energy and data treatment. Other performance aspects such as the peak-to-total ratio were also investigated.

Since 2015, AGATA has been operating [9] at GANIL, Caen, France, where it has been coupled to VAMOS (a variable mode high acceptance spectrometer) [10,11]. Three campaigns of measurements have been performed with focus mainly on neutron-rich nuclei populated using multi-nucleon transfer reactions or via fusion–fission or induced fission. In 2018, a campaign with AGATA coupled to the NEDA [12] neutron detector and the DIAMANT [13,14] charged particle detector was performed. AGATA is foreseen to stay at GANIL until the middle of 2021. A campaign of source measurements was performed during 2016 to, together with in-beam data, quantify the performance of AGATA at the GANIL site as well. Basic performance data such as efficiencies are needed to analyze the data taken during the campaigns, but a careful follow-up of the evaluation of the AGATA performance as the size of the array changes, detectors and electronics age and/or are changed is also of considerable interest. It allows one to ensure that the performance is in accordance with expectations. Furthermore, it helps understand where efforts to improve are important — this both at a fundamental level, e.g. Pulse-shape analyses or γ-ray tracking, and on a more practical level learning how to best maintain the system at a high level of performance. Extensive Monte Carlo simulations of AGATA are performed as well in order to predict the performance in different experimental configurations and with different number of AGATA crystals. A thorough evaluation of the performance of such a detection system allows for the bench-marking of the Monte Carlo simulations, further helping the analysis of experimental data.

There is an extensive literature on the performance of γ-ray tracking arrays (e.g. [15–17]) that address the questions of efficiency, peak-to-total, and, Doppler correction capabilities of γ-ray tracking arrays. As this paper aims at giving a snap shot in time of AGATA and its capabilities during the AGATA at GANIL campaign no detailed comparisons are made with the literature as in most cases significant differences in setups and methodology would require extensive discussion to make sense of such comparisons.

In this paper we will describe the performance of AGATA as of mid 2016, when it was equipped with 30 crystals. In Sections 2 and 3 the experimental set up and data acquisition are presented. The performance of individual crystals is discussed in Section 4. In Section 5 the performance of AGATA as an array is discussed, using the Orsay Forward Tracking algorithm. Estimates of the position resolution achievable in a typical experiment are given in Section 6. As the angular coverage of AGATA increases the capabilities in terms of measuring angular correlations increase and this is discussed in Section 7. Conclusions are given in Section 8.

2. Experimental setup and data taking

In 2016 the AGATA array consisted of 10 triple clusters (Agata Triple Cluster, or ATC) [18] and one double cluster (Agata Double Cluster or ADC) arranged as schematically represented in Fig. 1. Two of the detectors present in the frame where not connected to an electronics channel, giving a total of 30 active detectors. One detector showed varying performance, related to the electronics that was used, and is excluded form the efficiency determinations. Measurements were performed both at what is referred to as “nominal position” *i.e.* the front surfaces of all AGATA crystals are positioned at 23.5 cm from the target position, and at “compact position” with a distance of 13.5 cm between

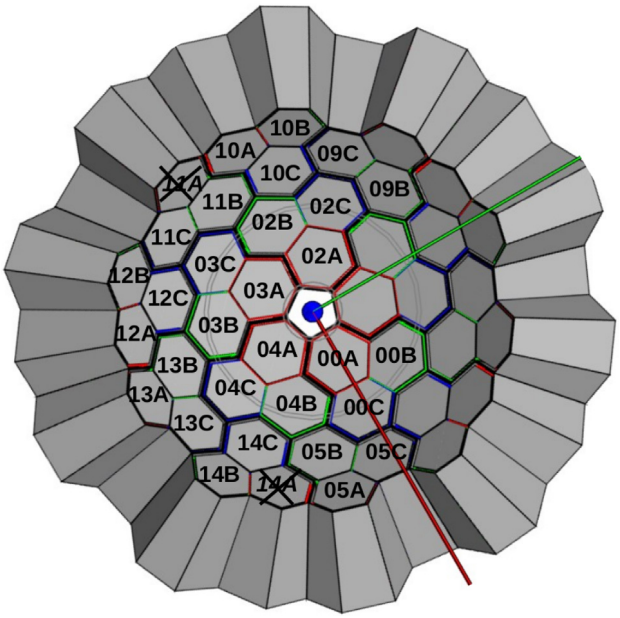

Fig. 1. AGATA detectors seen from the reaction chamber point of view, labeled according to their position in the honeycomb. The two crossed over detectors are physically present, but not connected to an electronic channel. Positions with no labeling are empty. The red and green line are the x-, and, *y*-axis, respectively, for the installation in Legnaro and GSI, showing the rotation made of the structure at GANIL. (For interpretation of the references to color in this figure legend, the reader is referred to the web version of this article.)

Table 1
Radioactive sources used for the measurement.

Source	Activity [kBq]	t_0
^{152}Eu	19.1	05/01/2016
^{60}Co	8.7	05/01/2016

the closest part of the imaginary sphere that touches the front of the AGATA crystals and the target position. Different standard radioactive sources were placed at the target position, see Table 1. The Aluminum materials surrounding the target position, *i.e.* reaction chamber and target holder, were the same as in most of the experimental setups of the campaign. These aluminum structures are included in the Geant4 simulations [19,20] presented in this work.

For each detector, the data were collected from the 36 segments as well as for two different gains of the central contact (ranges of ≈8 and 20 MeV). The segment signals are referred to with a letter A–F and a number 1–6 where the letter gives the sector of the crystal and the number the slice, *i.e.* the segmentation orthogonal to the bore hole for the central contact. The AGATA raw data for each crystal in an event consist of, for each segment and for the central contact, the amplitude and 100 samples (10 ns time between samples, ≈40 pre-trigger and ≈60 post-trigger) of the rise-time of the waveform and a time-stamp, used for the event building. For the source data used in this paper the amplitude was extracted from a trapezoidal filter with a shaping time of 10 μs followed by a flat top of 1 μs. The online and offline data processing is done using the same computer codes, and are described in detail in Section 3.

The preamplifier outputs were digitized and pre-processed by two different generations of electronics. The ATCA phase 0 electronics was developed at an early stage of the project for the AGATA Demonstrator, described in Ref. [1]. For the GANIL Phase a second generation of electronics was developed referred to as the GGP’s [21]. The two generations of electronics use the same algorithms for determining the energy. However, for the determination of the time of a signal, the ATCA phase 0 electronics use a digital constant fraction (CFD) whereas

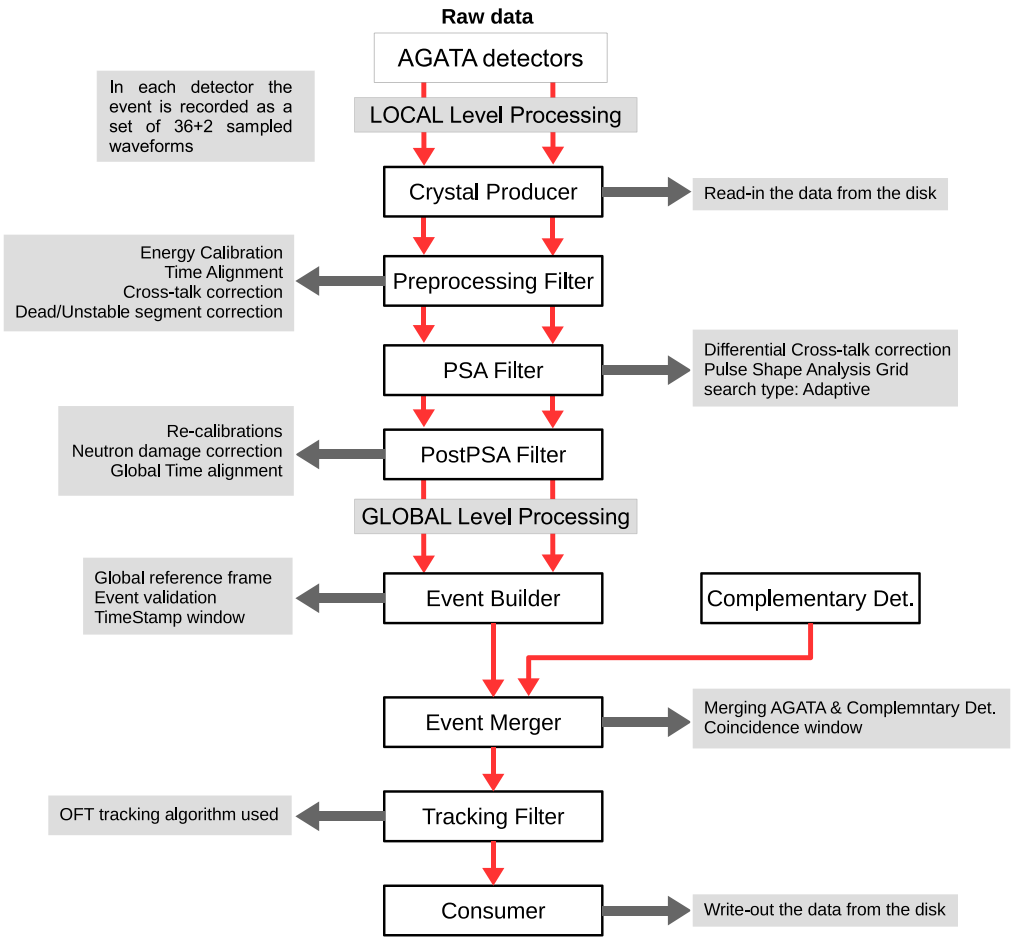

Fig. 2. Chains of Narval actors used for data processing. For details see text.

the GGPs use a low-level leading edge algorithm. These times are used for triggering purposes only. For both generations of the electronics discussed above digital CFDs are used for proper timing when analyzing the data. A time signal is also extracted directly from the digitizer in order to provide a γ-ray trigger for the VME electronics of VAMOS.

3. Data processing

The raw data (event-by-event amplitude, timestamp and traces for segments and central contact) are treated with the chain of Narval actors as depicted in Fig. 2. Starting at the top we have data coming from the front-end electronics into the computer farm with the first Narval actor [1], the "Crystal Producer" that puts the data of the crystal into the Agata Data Flow. The next step, done in the "Pre-processing Filter" is to perform energy calibrations, time alignments, cross-talk corrections and the reconstruction of data in crystals, which are missing a segment (in case of several missing segments this is no longer possible), see Section 4. Following the preprocessing comes the pulse-shape analysis where the γ-ray interaction positions are extracted using an adaptive grid search algorithm [22] where the experimental pulses are compared to pulses calculated using the Agata Detector Library [23]. Tests allowing to search for more than one interaction per segment of an AGATA crystal have been performed. These tests have shown no improvement in terms of efficiency and peak-to-total after γ-ray tracking so presently the search is limited to one interaction per segment. From this point on the traces are removed from the data flow. In a typical experiment the result from the PSA are also written to disk at this point as this allows redoing the subsequent steps in the analysis offline without the time consuming PSA. The final step where the data from each crystal is treated individually (Local Level Processing) is the "Post PSA", in which, apart from timestamp realignments, several energy correction procedures described in Section 4 are performed. After this, data from all AGATA crystals are merged in the "Event Builder" on the basis of a coincidence condition using the individual time stamps of each crystal. This is the start of what is referred to as the Global Level Processing. Complementary detectors are added into the Agata Data Flow in the "Event Merger". This is done before γ-ray tracking because complementary data from these detector, e.g. data from a beam tracking detector in case of a very large beam spot, are potentially of use for the tracking of the γ rays. Finally γ-ray tracking is performed. In this work the OFT γ-ray tracking algorithm has been used [24]. Finally the data is written to disk by a "Consumer". This procedure is performed online for monitoring of the experiments (data processing) but also performed as a part of the data analysis (data replay) starting from the raw traces or from the interaction points given by the online PSA. The possibility to also store the experimental traces to disk depends on the experimental conditions, and is in practice only possible if the number of validated events is lower than about 3 kHz per crystal (inducing a dead time of about 15%). Automatic procedures have been developed, both for energy calibration purposes and for the preparation of the configuration files that the actors use allowing error free and fast analyses of experimental data.

4. Crystal performance

In this section the performance in terms of energy and resolution for each crystal is discussed, named with their position in the AGATA frame at GANIL. The performance of the individual detectors was determined using measurements with ^{60}Co and ^{152}Eu sources, see Table 1. A set of standard procedures are performed to minimize the FWHM for each

crystal. These procedures consist of cross-talk corrections and neutron-damage correction. The energies for events with more than one segment with net charge have to be corrected for cross talk, mainly between the central contact and the segments, as the energy calibration is performed mainly with events with segment multiplicity 1. Correction coefficients are extracted from source data either by looking at the shift of the full-energy peak made by the summing of segments in fold two events or by looking at the base-line shift in fold one events. This procedure has been described in detail by Bruyneel et al. [25,26]. The correction for the effects of the neutron damage on the detection of the γ rays of interest has been performed following the theoretical approach described by Bruyneel and coauthors [27]. Two calibration coefficients for every detector channel, used to correct for the electron and hole trapping, are determined. This is done using a grid-search based minimization of the FWHM and the left tail of the peaks in the spectra for each channel, *i.e.* 37 per detector. In Fig. 3 the effect of the correction is shown for one detector. This correction is more important for the segments as they are more sensitive to hole trapping, but it is also done for the central contact, and it is thus important also when the sum energy of hits inside a crystal for an event is normalized to the value measured by the central contact. This correction is particularly important for measurements of lifetimes via line-shape analysis techniques, where the symmetry of the detector response function is extremely important to minimize systematical errors in the lifetime determination.

4.1. Energy resolution

The energy resolution has been determined for each segment and central contact for the crystals in the array at the moment of taking source data (2016). After the exposure to fast neutrons produced in deep inelastic collisions, fission and fusion evaporation reactions in the first campaign at GANIL in 2015, several AGATA crystals were damaged by the charge traps created by neutron radiation damage in the Ge crystal. For the most exposed detectors the integrated flux exceeds 10^9 n/cm^2. This is based on the deterioration of the uncorrected FWHM [28]. These traps are lattice defects that lead to a reduction of the charge collection efficiency which appears as a low energy tailing on the energy line shape (red line in Fig. 3). In position sensitive Ge detectors, like the AGATA ones, it is possible to apply an empirical correction to the neutron damage effects [27]. These corrections were applied to 20 of the AGATA crystals in this work (see Table A.3 in Appendix). As an example of the effect of neutron damage correction the original spectra and the ones after the corrections, for one detector, are shown in Fig. 3. For the other 10 detectors good energy resolution was achieved without the neutron-damage correction procedure.

In Fig. 4 the resolutions for the central contacts and sum of segments for the used detectors are reported. The average FWHM resolution found for the central contacts before the neutron damage correction is 2.93 keV and is improved to 2.57 keV after correction. In the case of the sum of segments the average FWHM is improved from 5.22 keV to 3.08 keV, showing the difference in sensitivity to charge trapping. The comparison with the resolutions taken from detector data sheets or factory measurements is reported in Fig. 5. In general all the measured FWHM resolutions for the crystals agree with the original ones, except for the detector 11C (B013), which apart from being neutron damaged had a resolution problem during the measurements, in both central contact and segments, due to problems with the electronics.

4.2. Crystal efficiency

The efficiency of each crystal has been determined first from the central contact signal. Although this is not the normal operation mode when performing γ-ray spectroscopy with AGATA, the crystal central contact efficiency allows easier diagnostic of the Data Acquisition Chain and easier comparison to Geant4 simulations. For these reasons, it is of great value. Two sets of data for efficiency measurement at

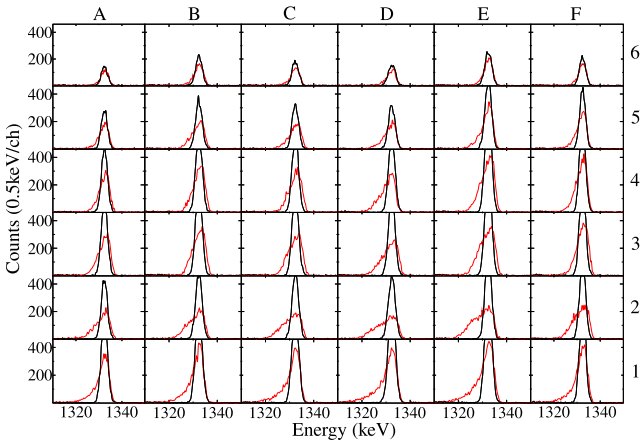

Fig. 3. Example of the peak line shapes for the 1332 keV ^{60}Co γ-ray before (red) and after (black) the neutron damage correction for the 36 segments of the crystal A002 position 12A ATC3. (For interpretation of the references to color in this figure legend, the reader is referred to the web version of this article.)

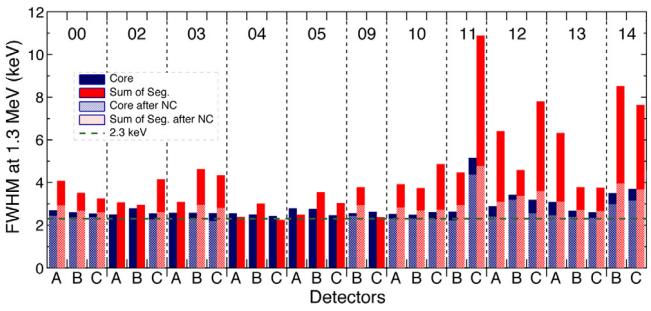

Fig. 4. FWHM at 1.332 MeV (^{60}Co) of the central contact (blue) and the sum of segments (red) before (dark colors) and after (light colors) the neutron damage correction for 20 out of the 30 capsules individually named with its position labels. (For interpretation of the references to color in this figure legend, the reader is referred to the web version of this article.)

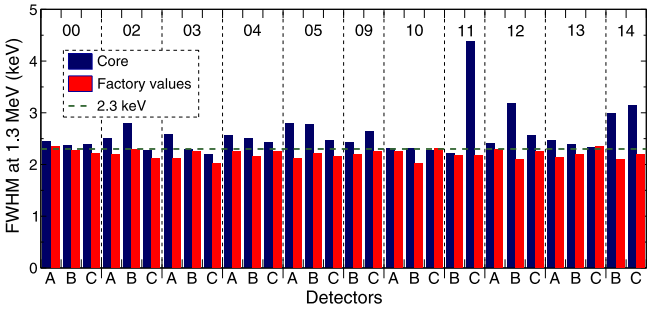

Fig. 5. FWHM at 1.332 MeV (^{60}Co) of the central contact (blue) after the neutron damage correction compared with the original FWHM measured by Canberra (red) for the 30 capsules individually named with its position labels. (For interpretation of the references to color in this figure legend, the reader is referred to the web version of this article.)

the nominal and compact position of AGATA have been taken. All efficiency numbers quoted in this section are corrected for dead time of the data acquisition system.

The efficiency has been determined both from γ-γ coincidences, corrected for the angular correlation effects for the given geometry, and from singles central contact data taken with ^{60}Co and ^{152}Eu sources. The coincidence data are not affected by dead-time of the processing chain. The singles central contact measurement is. To bypass this effect, the latter have been recorded in coincidence with the VME/VXI

electronic of the GANIL acquisition system coupled to AGATA via the AGAVA board [1,9]. The GANIL acquisition system is triggered by the OR of the AGATA digitizers CFDs, triggering the AGAVA board. The individual AGATA channels are then validated by the AGAVA request within a 300 ns coincidence time window. At the source rate, the VME/VXI GANIL electronic has a dead-time of 40 μs per read-out event, greater than the AGATA electronic system, and it can be precisely quantified and used for live time correction in the single central contact efficiency measurement. For the γ-γ coincidence, the 1332 keV–1173 keV from the ^{60}Co source and 121.8 keV–1408 keV, 121.8 keV–244.7 keV and 344.3 keV–778.9 keV coincidences from the ^{152}Eu source were used. For fitting the γ-ray peak areas used to extract the efficiency values, the Radware software package was used [29]. A background subtraction was made by evaluating the correlated background on both sides of the gating energy for the γ-γ coincidences analysis.

Using the 1.3 MeV transition from the decay of ^{60}Co the efficiency relative to a 3 in × 3 in NaI detector (*i.e.*, 1.2×10^{-3} cps/Bq at 25 cm) for each detector at nominal position was extracted and is reported in Fig. 6. In the same picture, the value at 1.3 MeV as measured at the factory or during the customer acceptance tests is shown. The average measured value is 79% with a sample standard deviation of 5%, close to the factory values average of 81%. Crystal 02C suffered from oscillations during the measurement and is therefore excluded in the efficiency numbers discussed below.

The absolute central contact efficiency for the whole array, composed of 29 operational crystals, is reported in Fig. 7 for the nominal position of AGATA and Fig. 8 for the compact position of AGATA. Here each crystal is treated as a single detector like in a standard γ-ray detector array. The values obtained in the singles measurement are compared with the γ-γ results and simulations and overlap well. For the nominal geometry, the efficiency measured using singles is 2.95(6)% at 1332 keV whereas for the compact geometry it is 5.5(1)% at 1332 keV. Geant4 simulations using the AGATA simulation package [20] have been performed. These simulations include a realistic implementation of the reaction chamber used during the experimental campaign at GANIL [9], a steel block to emulate the effect of the VAMOS quadrupole, as well as the two crystals that were present but not used during the measurements. There is 12% discrepancy between the simulation and the experimental results. This difference is larger than the 2.5% average discrepancy for the individual crystals, as shown in Fig. 6, between factory measurements and measurements made within the AGATA collaboration. However, Geant4 simulations of the three differently shapes crystals used by AGATA give a relative efficiency of 86%, 86%, and 87%, for type A, B, and C, respectively. The average measured value is 79%, or 8% lower. This is in reasonable agreement with the 12% of efficiency missing when compared with simulations, as is illustrated in Figs. 7 and 8 (green line) where the efficiency of each crystal has been scaled to its measured value. Here the question of how the 12% of effective germanium is lost has to be raised. The presence of a dead layer or missing germanium will have an impact on the PSA as the pulse shapes depend on the active volume and shape of the germanium diode. Simulations assuming a thicker dear layers improve the correspondence with experimental data. It is however difficult to pin down the contribution from different surfaces of the detectors, *i.e.*, one can reproduce experimental data with different combination of dead layers around the central contact and at the back of the detector. Moreover, the mismatch of the efficiencies at low energies cannot be corrected reducing the active volume around the central contact or at the back of the detector. In Figs. 7 and 8 simulations with a dead layer of 2.5 mm around the central contact and 3 mm at the back are also shown. For estimates of dead layers in HPGe detectors see, e.g., the work of Eberth and Simpson [30] or Utsunomiya et al. [31]

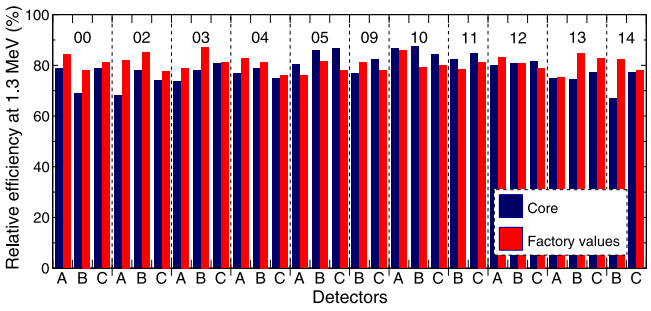

Fig. 6. Relative central contact efficiency at 1.3 MeV (^{60}Co) in comparison with the initial relative efficiency as provided by manufacturer for the 29 capsules individually named with its position label.

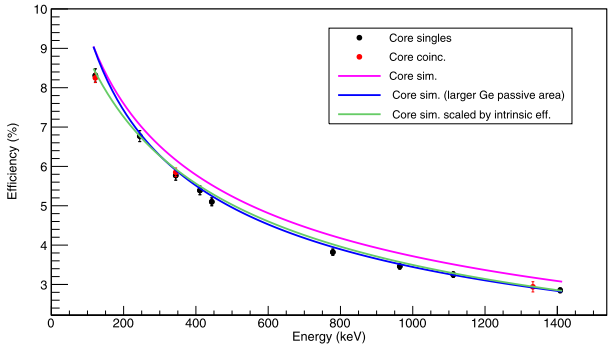

Fig. 7. Absolute central contact efficiency for the 29 capsules AGATA sub-array in **nominal position** (23.5 cm distance source to detectors) obtained with the data from ^{152}Eu and ^{60}Co in singles (black circles) and in coincidences (red circles) in comparison with the simulations (magenta, blue, and green lines). The green line corresponds to simulations where the efficiency has been scaled according to the difference between the simulated absolute efficiency and the measured absolute efficiency. Simulations performed with increased dead layers are also shown (blue line). See text for details. The rate per crystal at this position was around 200 Hz. (For interpretation of the references to color in this figure legend, the reader is referred to the web version of this article.)

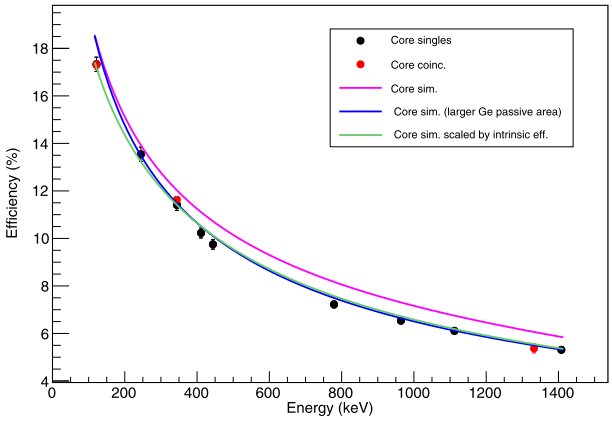

Fig. 8. Same as Fig. 7 for the compact configuration and with a data rate per between 300 and 500 Hz. (For interpretation of the references to color in this figure legend, the reader is referred to the web version of this article.)

5. Performance of the AGATA array with the Orsay Forward Tracking

Description of OFT. The Orsay Forward Tracking (OFT) algorithm [24] was developed with simulated data sets produced with the Geant4 AGATA code [20]. The output of the simulations was modified to emulate the expected experimental conditions, such as energy resolution

Table 2
Table summarizing the meaning and standard ranges of the main adjustable parameters of OFT.

Parameter	Definition	Typical value
σ_θ	Average interaction-point position resolution (cm)	0.3–3
P_{sing}	Minimum probability to accept single-interaction-point clusters	0.02–0.15
P_{track}	Minimum figure of merit to accept multiple-interaction-point clusters	0.02–0.05

and threshold and position resolution allowing the optimization of the algorithm using a realistic input. As all forward-tracking algorithms the OFT starts with clustering interaction points. These clusters are evaluated using a χ^2-like test where scattered energies after every interaction point as given by the energies in each interaction point are compared to scattered energies as given by the Compton scattering formula using the measured positions of the interaction points. The best permutation for each cluster is calculated and the clusters are sorted in order of best figure of merit. Clusters that pass a threshold called P_{track} are accepted as good γ rays. The most influential parameter in this is σ_θ corresponding to the error in scattered energy derived from the error in interaction positions from the PSA. Using simulations this parameter was optimized to $\sigma_\theta = 2.4$ mm corresponding to the assumed position resolution in the simulations of 5 mm FWHM at 100 keV interaction point energy. Single interaction points that are further away than 40 mm from the closest other interaction point are treated as a photo-electric absorption event. Here the probability for a γ ray to have penetrated to a given depth and been absorbed via the photo electric effect is evaluated and compared to the P_{sing} parameter. The single-interaction-point evaluation is an important part of the tracking algorithm since the efficiency loss when it is not included is very large for low-energy events, and non negligible at higher energies: ∼20% of 1.4 MeV total-absorption events in each individual detector are single interaction points. This last fact is due to the way PSA identifies interaction points in the AGATA detectors. As mentioned above, the Grid Search algorithm [22] used online only looks for 1 interaction point per segment. This is at variance with what is currently done at GRETINA [32] where the fits of the segment traces allow for more than one hit per segment. For a detailed explanation on the OFT algorithms see Lopez-Martens et al. [24].

OFT parameters. The definition and typical ranges of the main parameters of OFT are summarized in Table 2.

Tuning the parameters can affect the spectral quality and shape. As an example, a high value of σ_θ corresponds to nearly fully relaxing the comparison between scattered energies obtained from interaction positions and scattered energies obtained from energy differences. Basically, using a very large σ_θ reduces the cluster evaluation stage to finding the most likely sequence of interaction points in a cluster on the basis of ranges and interaction probabilities only. Increasing σ_θ increases the high-energy efficiency. However, it also decreases the low-energy efficiency in the case of medium to high photon-multiplicity events since single-interaction points are being accepted as members of multi-interaction point clusters and are therefore lost as potential γ rays absorbed in a single interaction. There is an optimal value of σ_θ, which maximizes the gain in efficiency at medium and high energy while minimizing the loss of efficiency at low energy. By analyzing source and in-beam data obtained at Legnaro, GSI and GANIL, the optimal value of σ_θ is found to be around ∼6 and 8 mm. This corresponds to an average experimental position resolution a factor of 2 to 3 worse than anticipated. This is consistent with measurements of the position resolution of an interaction point as a function of the deposited energy [5] as well as with the observed clusterization of interaction points in specific areas of the detector segments.

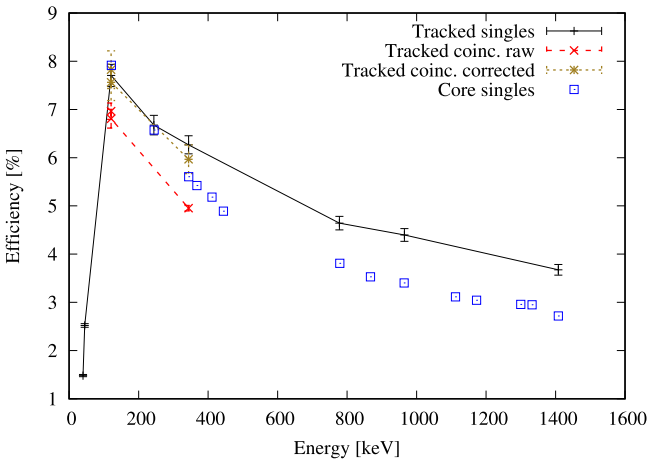

Fig. 9. Tracking efficiency of 29 AGATA detectors as a function of photon energy obtained with the standard OFT parameter set and using either the total singles tracked spectrum or the (121 keV–244 keV), (121 keV–1408 keV) and (344 keV–778 keV) γ-γ coincidences. The efficiency for 29 cores scaled from Fig. 7 is also shown. See text for details.

Another example is given by the energy range of the single-interaction spectrum, which grows when the threshold for validation of the corresponding clusters is lowered. For $P_{sing} = 0.15$, the spectrum extends to ∼600 keV, while for $P_{sing} = 0.02$, it goes beyond 2 MeV. Extending the spectrum increases the overall efficiency at high-energy. There is however a trade off in the form of a larger background: for $P_{sing} = 0.02$, the single-interaction points are responsible for nearly two thirds of the background present in the spectrum of tracked photon energies. Recent developments in the OFT code have improved on this point by using an empirically deduced energy-"distance in germanium" relationship instead of the single parameter P_{sing}, allowing an improved peak-to-total. The new single-interaction treatment, that is tailored not to have a negative impact on efficiency, is further discussed in Section 5.2.

The optimal value of P_{track} is found to be around 0.05. Some very slight adjustments can be made as a function of σ_θ, but the general trend is that a smaller value leads to more background and a larger value reduces the peak intensities.

5.1. Tracking efficiency measurements

The standard set of OFT parameters ($\sigma_\theta = 0.8$, $P_{track} = 0.05$ and $P_{sing} = 0.05$) were used to extract the tracking efficiency of AGATA at GANIL in a configuration with 29 capsules. The efficiencies to track the photons emitted by a ^{152}Eu source were obtained by comparing the detected peak areas to the expected intensities given the source activity, the measurement time interval and the electronics dead time. Since there are several 2-photon cascades in the radioactive decay of ^{152}Eu, the efficiencies at certain photon energies can also be measured by comparing the detected peak area of a transition when a coincidence with the transition of interest is required or not. The advantage of this second method is that no knowledge of the source activity or dead time of the system is required. The efficiencies obtained are shown in Fig. 9.

The efficiency to track a 1.4 MeV photon with 29 capsules is found to be 3.67(1)%. This corresponds to an add back factor with respect to the efficiency of the 29 detectors taken individually of 1.285(4).

In Fig. 9, the raw coincidence efficiencies at 121 and 344 keV lie below the singles tracking efficiency curve. This is because the tracking efficiency varies with the angle between the emitted photons; most notably it vanishes for small angles due to the deficiencies of the AGATA PSA algorithm and/or due to the fact that the tracking algorithm cannot disentangle the points belonging to the 2 coincident

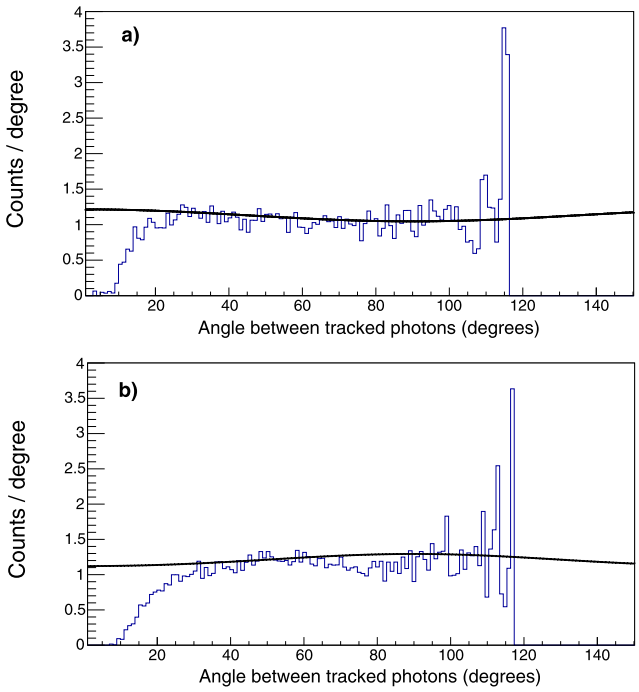

Fig. 10. (a) γ-γ angular correlations obtained for the 121.8 keV–244.7 keV cascade in ^{152}Sm using the OFT parameter $\sigma_\theta = 0.8$. (b) same as (a) for the 344.3 keV–778.9 keV cascade in ^{152}Gd and in the case of $\sigma_\theta = 2.0$. The solid lines represent the best adjustment of the theoretical curves to the data. The peaks at high angles are associated with large statistical errors not shown in order to keep the figure clear.

photons when these lie too close to each other. This is clearly seen in the plot of the γ-γ angular correlations for the 121.8–244.7 and 344.3–778.9 coincidences in ^{152}Sm and^{152}Gd shown in Fig. 10. By correcting the coincidence efficiencies by the missing fraction of the experimental angular correlations compared to the theoretical curve, the correct tracking efficiency values are recovered.

Using a larger value of σ_θ leads to a slightly lower tracking efficiency below 200 keV, but yields 13% more efficiency at 1.4 MeV, making the add back factor increase to ~1.4. It also changes the raw coincidence efficiencies for some coincidence couples. In the case of the 344.3 keV–778.9 keV cascade of Fig. 10, in particular, correlations are not only absent at small angles, but also at larger angles, when OFT most probably misinterprets all or a subset of the interaction points of the event as points belonging to a back-scatter sequence.

5.2. Tracking peak-to-total ratio

An important performance parameter for a γ-ray spectrometer is the peak to total ratio quantifying the fraction of events found in the full energy peak as compared to the total number of detected γ rays. Data was taken with a ^{60}Co source with an activity of 8.7 kBq. Gamma-ray tracking was then performed offline for 29 of the 30 AGATA detectors using the 30th as an external trigger. In the 30th detector a central contact energy of 1332.5 ± 5 keV was demanded. In this manner a γ-ray multiplicity of one can be guaranteed for the remaining 29 detectors. In Fig. 11 the γ-ray spectrum is shown, together with spectra made with the two different treatments of the single-interaction validation used in this work. The peak-to-total using the empirically fitted maximum distance in germanium for single interactions is 36.4(4)%. It is well known that the peak-to-total in a γ-ray tracking array is dominated by single-interaction points accepted as events corresponding to a direct absorption of the total γ-ray energy via the photoelectric effect. Excluding such events the peak-to-total is increased to 52.4(6)%, with a reduction in efficiency for the full energy peak of 17%. The variation

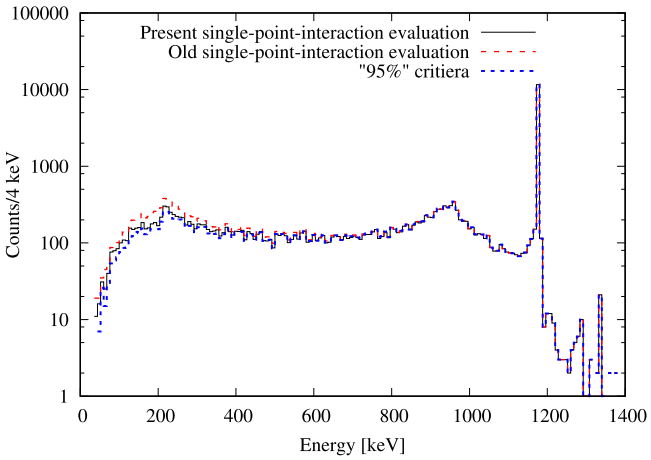

Fig. 11. Gamma-ray tracked spectra for 29 AGATA detectors for ^{60}Co data using a 30th AGATA detector as a external trigger by demanding the full absorption of the 1332.5 keV gamma in it. The solid line (black) is using the latest single-point interaction validation procedure, the dashed line (red) is using the old single-point interaction validation procedure, and finally the dotted line (blue) using the 95% absorption limit. (For interpretation of the references to color in this figure legend, the reader is referred to the web version of this article.)

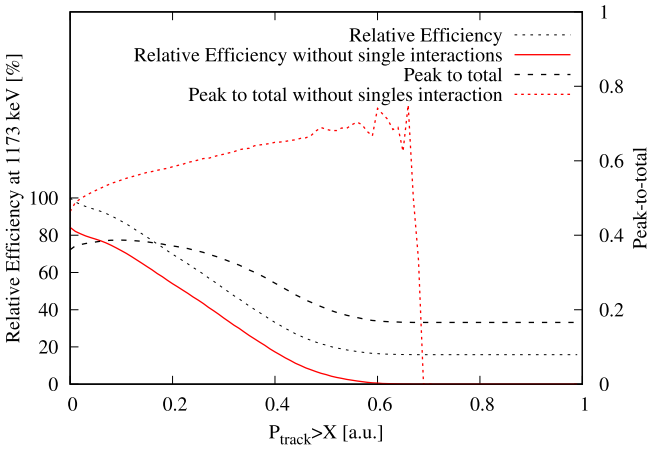

Fig. 12. Efficiency relative to $P_{track} = 0$ at 1173 keV and peak to total as a function of P_{track} used by the OFT algorithm to accept or not a γ-ray track. This for when including or excluding single point interactions.

of peak-to-total and efficiency at 1173 keV as a function of the P_{track} parameter is shown in Fig. 12, for the cases when single interactions are included or excluded. Note that above $P_{track} > 0.7$ no events with multiple interaction points are left. From Fig. 12 it is clear that for the OFT algorithm the peak-to-total has a weak dependence on the P_{track} parameter, again showing that it is σ_θ that is the most important parameter for OFT.

Monte Carlo simulations using the AGATA simulation package were made in order to compare the simulated γ-ray tracking performance with experimental data. In the simulations a ^{60}Co was simulated with a source strength of 5 kBq. An absolute time was used in the simulations allowing effects such as pile-up and random coincidences to be simulated. Gamma-ray interactions in the same segment were packed at their energy-weighted average positions. These were then written into the same data format as used to store experimental post-PSA data. This allowed the use of identical γ-ray tracking and data analyses codes for the experimental and simulated data, *i.e.* the simulated data was treated exactly as explained for the experimental data above. Four different simulations were performed. The first one including only the HPGe crystals and the aluminum end-caps. The second simulation

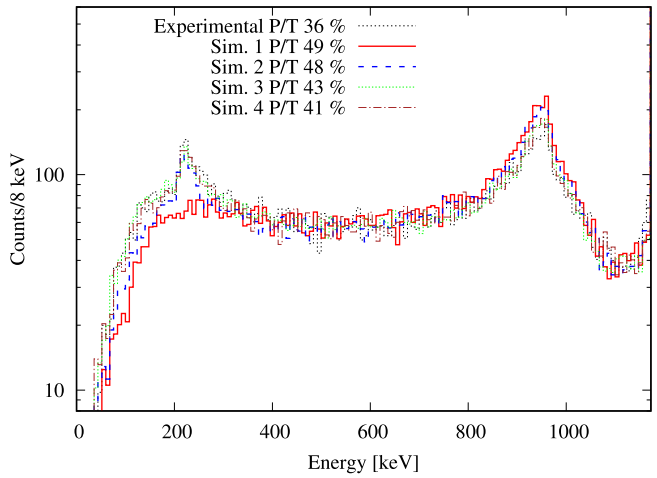

Fig. 13. Comparisons between experimental spectrum (in black) and spectra from four different simulations. The spectra are normalized to the same number of counts in the region 0–1165 keV. Simulation 1 includes only AGATA, simulation 2 also includes a schematic implementation of the VAMOS dipole magnet, simulation 3 further adds concrete walls around the experimental setup. Finally, simulation 4 has thicker dead layers added to the HPGe crystals. For further details on the simulations, see the text.

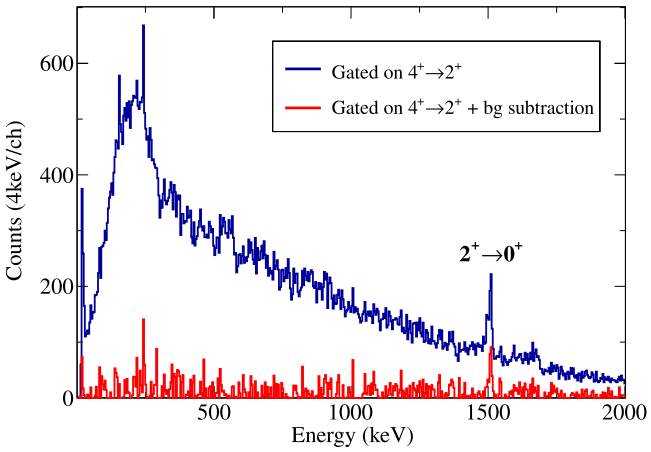

Fig. 14. Gamma-ray spectra showing the 1510 keV $2_1^+ \rightarrow 0_1^+$ transition in ^{92}Mo used to estimate the in beam efficiency.

included a large piece of steel to mimic the large quadrupole magnet of the VAMOS. The third simulation included both the large piece of steel mimicking VAMOS, concrete walls and the target chamber. A fourth simulation was also performed adding to the third simulations thicker dead layers to the HPGe crystals. The added dead layers were 3 mm at the back side of the detector and 2.5 mm around the central contact. The peak-to-total for the different simulations, when gating on the 1332.5 keV transition to look at the 1173 keV transition were 49%, 48%, 43%, and 41%, respectively. This is to be compared to the experimental value of 36%. In Fig. 13 the Compton scattering part of the 1332.5 keV gated ^{60}Co spectra is shown for experimental and simulated data. In the experimental spectrum a pronounced back-scattering peak can be seen just above 200 keV. The simulation labeled 1, only including AGATA itself, does not show such a back-scattering peak and consequently the peak-to-total is much better than for the experimental data. For simulation 2, where the VAMOS quadrupole has been included in a very schematic way a clear back-scattering peak emerges. However, at both lower and higher energies as compared to the back-scattering peak the experimental data contains more counts. In simulation 3, where the concrete walls are included together with the scattering chamber a shape of the spectrum very close to the experimental one is produced. This suggests that a significant fraction of the spectrum is not due to Compton scattering inside the HPGe crystals of AGATA, but from the scattering on the structures around AGATA into AGATA. Including thicker dead layers in the HPGe crystals in the simulation, as done for the fourth simulation, increases slightly the amount of background between the full-energy peak and the Compton edge, but does not change the shape of the spectrum in a significant way. However, the peak-to-total is decreased by about 5%. These "back scattered" γ rays are very difficult to properly discriminate against as they are from the point of view of γ-ray tracking perfectly good single interaction point events in the front of the crystals.

5.3. In-beam efficiency of AGATA coupled to VAMOS

The in-beam efficiency of AGATA is different from that of source measurements, as the efficiency is also a function of count rate in the individual detectors due to pile-up (rejected and non rejected) and rate limitations in the electronics. In-beam efficiency varies from experiment to experiment therefor exact numbers are both difficult to reliably produce and not of general interest. The aim of the section is to give a useful rule of thumb to allow consistency checks when analyzing data. The in-beam efficiency for events with a higher γ-ray fold than one also depends on the angular distribution of and correlation of the γ-ray transitions used to measure it. This both via pure geometrical effects and via the lowered γ-ray tracking efficiency for γ rays with a preference for being emitted in parallel. The in-beam efficiency has been estimated for AGATA coupled to VAMOS for an experiment where a ^{92}Mo beam impinged on a ^{92}Mo target, and the beam-like reaction products were unambiguously identified in VAMOS, also providing the velocity vector for Doppler correction. During this experiment 23 AGATA crystals were operational in the array, each counting at around 45 kHz with a shaping time of 2.5 μs. As the target and the beam both were ^{92}Mo, de-excitation of target-like and beam-like particles could be studied. The beam-like and target-like nuclei travel with a relative angle of about 90°, allowing an estimate of the effect of the angular distribution on the measured efficiency.

The coincidence method was used to determine the efficiency at 1510 keV, *i.e*, the number of detected $2_1^+ \rightarrow 0_1^+$ γ rays per detected γ ray from the $4_1^+ \rightarrow 2_1^+$ transition was determined. Peak intensities were extracted from singles spectra and from $\gamma\gamma$ coincidence matrices. The projected gate in the $\gamma\gamma$ coincidence matrix is shown in Fig. 14. The efficiency at 1510 keV extracted using this method is after γ-ray tracking 1.5(1)%, to be compared with the expected efficiency of about 2.5% for 23 AGATA crystals at an energy of 1.5 MeV. This loss of efficiency, some 40% lower, has several origins. In this section we will try to identify the sources of this reduction. At count rates of about 45 kHz and a shaping time of 2.5 μs there is a loss of the order of 20% due to the pile-up protection built in the AGATA pre-processing firmware [33]. There is also the loss in tracking efficiency for higher fold events. A lower limit for this can be estimated using the smallest used cluster angle in the OFT of 8° (as can be seen in Fig. 10 the efficiency to track two γ rays inside this cone is close to zero) which corresponds to approximately 6% of the solid angle of 23 AGATA detectors. These contributions add up to about 25% of losses (i.e. more than half of the lost efficiency) that are rate dependent, via the pile up, and related to the detector physics (*i.e.* the rise time of the HPGe crystals and average cluster size for typical γ rays) and therefore always will be present. There is an open question from where the remaining about 15% of efficiency loss is coming. Measurements suggests that 5% to 10% could come from overload beyond specification of the trigger distribution system related to the high total rate (more than 1MHz).

6. Position resolution of the PSA

The VAMOS allows for a very precise determination of the recoil vector of the identified ion. The direction can in this context be considered as exact whereas the velocity has an error in the order of a few per

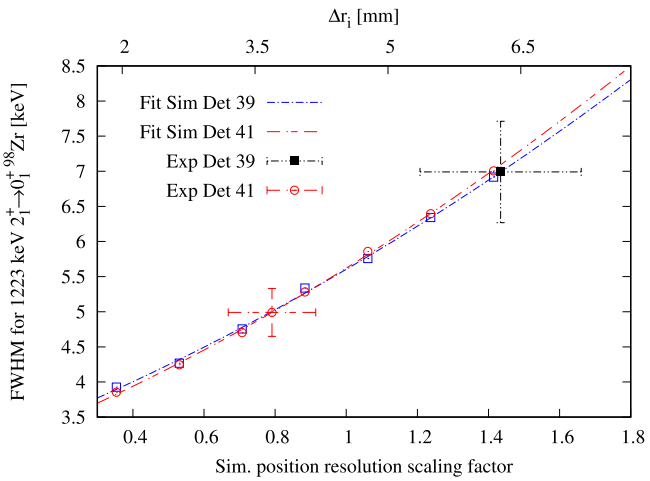

Fig. 15. Estimated position resolution for two detectors in the AGATA array. The lines are fits to the FWHM of simulated data sets for the two different detectors where the assumed position resolution has been varied. Large symbols show the measured FWHM for each detector (y-axis) and corresponding deduced position resolution (x-axis). For details on simulation and experiment, see text. Note that the lower x-axis is a scaling factor of the position resolution given in Söderström et al. [5] for the FWHM in one dimension. The upper x-axis shows the average resolution for the interaction points used for Doppler Correction.

mill. Given that the recoil velocity has a very small error the position resolution can be estimated by the Doppler Broadening of the γ-ray peaks via the Doppler Shift given by (for details see, e.g., Söderström et al. [5])

$$E_\gamma = E_{\gamma 0}\frac{\sqrt{(1-\beta^2)}}{(1-\beta cos\theta)} \tag{1}$$

where E_γ is the energy detected in the detector, $E_{\gamma 0}$ is the energy of the γ ray in the rest frame of the nucleus, β is the velocity of the nucleus emitting the γ ray and θ is the angle between the velocity of the emitting nucleus and the γ ray in the laboratory frame. From this we have a γ-ray peak width $\Delta E_{\gamma 0}$ of

$$(\Delta E_{\gamma 0})^2 = \left(\frac{\partial E_{\gamma 0}}{\partial E_\gamma}\Delta E_\gamma\right)^2 + \left(\frac{\partial E_{\gamma 0}}{\partial \beta}\Delta\beta\right)^2 + \left(\frac{\partial E_{\gamma 0}}{\partial \theta}\Delta\theta\right)^2. \tag{2}$$

This can be used to evaluate the performance of the PSA via the relation

$$\cos\theta = \frac{\vec{v}\cdot\vec{r}}{|\vec{v}||\vec{r}|} \tag{3}$$

where $\vec{v}$ is the recoil velocity as detected by VAMOS and $\vec{r}$ is the position vector of the first γ-ray interaction as given by γ-ray tracking. The method employed to determine the position resolution for six different AGATA crystals is to perform Geant4 simulations that in a realistic way take into account all experimental contributions to the FWHM of the γ-ray peaks while varying the assumed position resolution of the PSA. The experimental FWHM of the γ-ray peak can then be used to interpolate the actual position resolution of the PSA as done by, e.g., Recchia et al. [4].

In this case the experiment was a fusion–fission experiment populating, among other nuclei, ^{98}Zr. A beam of ^{238}U impinged on a 10 μm think ^{9}Be foil. The VAMOS was positioned at 28° relative to the beam axis. Six AGATA detectors close to 112° relative to the recoil direction were used to sample the position resolution of the detectors in the array, as they had the largest Doppler Broadening, increasing the sensitivity to the position resolution. As all data were analyzed after γ-ray tracking it was the interaction used for Doppler Correction that determined which detector was studied. The FWHM of the γ-ray peaks were determined using Gaussian fits. An error $\Delta\beta/\beta = 0.0045$ as deduced from the mass resolution of VAMOS gives a constant contribution to the FWHM of the γ-ray peak of 0.13%.

The simulations took into account the energy loss in the target and straggling as the reaction products leave the target as well as the acceptance of VAMOS. For these simulations the AGATA Geant4 simulations package was used [20]. In the simulations a perfect knowledge of the recoil velocity was assumed ($\Delta\vec{v} = 0$). An intrinsic resolution of the AGATA detectors of 2.6 keV at 1332 keV was assumed for all detectors. Peak widths as a function of position resolution were determined for seven different position resolutions. As a baseline the experimentally determined energy dependent position resolution from Söderström et al. [5]

$$\Delta r_i = 1.9 + 4.4 * \sqrt{100\ \text{keV}/E_i}\ \text{mm FWHM} \tag{4}$$

where E_i is the energy of the interaction point i. The resolution was scaled with a value ranging 0.36 to 1.41 for the different simulations. This procedure allows to correctly capture the variation in position resolution with the energy of the interaction point used for Doppler correction. From the simulations it was determined that the average position resolution for the interaction point used for the Doppler Correction when using the non-scaled function of Söderström et al. [5] is 4.3 mm FWHM. For each assumed position resolution the FWHM of the simulated γ-ray peak for each detector was determined by a Gaussian fit. The extra width coming from the error in recoil velocity was added quadratically. In Fig. 15 these values are shown with small symbols for detector 39 and 41 (which has the best and worst experimental position resolution, respectively). To each set of FWHM coming from the variation of position resolution a second degree polynomial function was fitted. Using the inverse of these functions the position resolution of the individual detectors can be determined (see large symbols in Fig. 15). Note that in Fig. 15 the x-axis is a scaling factor with the previously determined position resolution as base, *i.e.* 1 means the detector has the same PSA performance that was previously measured. The six detectors used to sample the position resolution are located in the span 0.79–1.4 (as compared to Söderström et al. [5]), with five detectors larger than 1.08 and a weighted average of 1.15. This corresponds to an average position resolutions used for Doppler Correction of 3.7 mm-6.1 mm FWHM, with a weighted average of 5.1 mm FWHM. The average error on the estimated position resolution is 1 mm. There is no obvious difference in how the detectors perform for other parameters than the PSA, nor in how they have been treated. It should be noted that the probability of having a maximum difference of 2.4 between six values randomly taken from a Gaussian distribution with a $\sigma = 1$ is in the order of 50%, i.e. our results is rather probable even if all the detectors are performing identically. It is however of interest in a future work to investigate the variance of detector performance with respect to PSA in AGATA.

7. Angular correlations in AGATA

The use of AGATA for angular correlation measurements to determine the multipolarity of γ decays has been investigated using source data. Two pairs of γ-γ cascades from the decay of ^{152}Eu were used: The first pair was the 1408 keV–121.8 keV coincidence in ^{152}Sm de-exciting the 2^-_1 level at 1530 keV to the ground state via the 2^+_1 level at 121.8 keV. The second pair is the 244.7 keV–121.8 keV de-exciting the 4^+_1 level at 366.5 keV and the 2^+_1 level, also in ^{152}Sm.

The tracking algorithm identifies the first interaction point of each γ ray and as the position of the source is known the angle between the γ rays in the 1408 keV–121.8 keV pair and the 244.7 keV–121.8 keV pair could be determined and histogramed, see lower panel in Fig. 16. The main features of the two pairs of γ rays are similar. The cut at about 8 degrees is a result of the tracking algorithm, whereas for larger angles the geometry of AGATA as used for the source measurement dominates the shape of the spectra. The slower rise in intensity for the 244.7–121.8 keV cascade at low angles comes from the intrinsic difficulty to track two low-energy γ rays emitted into a small solid angle, since they often will be reconstructed as one γ ray with sum energy. The angular

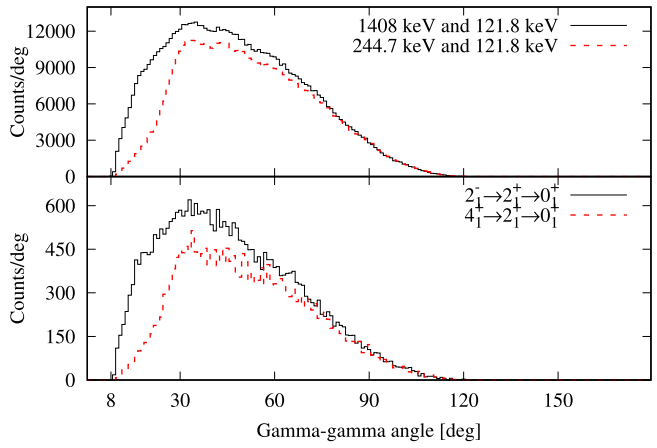

Fig. 16. Histograms used for angular correlation measurements using AGATA. The lower panel shows the angle between the two correlated γ rays detected in AGATA. The upper panel shows the angle between γ rays from uncorrelated events concatenated before tracking.

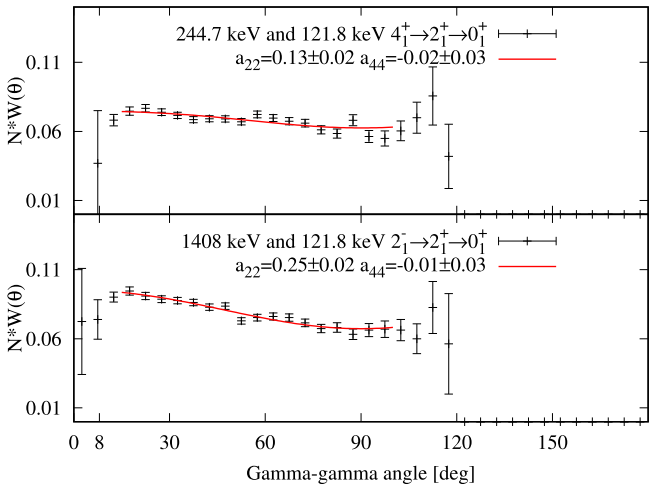

Fig. 17. Gamma–gamma angular correlations measured with AGATA. The upper panel shows the angular correlation for the $4_1^+\rightarrow2_1^+\rightarrow0_1^+$ pair of transitions in ^{152}Sm. The lower panel is for the $2_1^-\rightarrow2_1^+\rightarrow0_1^+$ transitions.

correlation is then extracted by normalizing for geometrical effects and the already mentioned decrease in efficiency for two low-energy γ rays absorbed close to each other. The normalization was created by tracking events consisting of the interaction points of two events each with a total energy corresponding to one of the γ rays in the cascade of interest concatenated into one event, thus generating pairs of γ rays with the correct energies, but with no angular correlation. From the tracked events the angle between the γ rays was then again extracted. The resulting histograms for the two pairs of γ rays are shown in the upper panel of Fig. 16.

By dividing the histograms in the lower panel in Fig. 16 by the upper panel the histograms shown in Fig. 17 are created. The upper panel is for the $4_1^+\rightarrow2_1^+\rightarrow0_1^+$ cascade, the lower panel for the $2_1^-\rightarrow2_1^+\rightarrow0_1^+$ cascade. For each angular correlation the expression

$$W(\theta) = 1 + a_{22}P_2(cos(\theta)) + a_{44}P_4(cos(\theta)) \quad (5)$$

where $a_{22,44}$ are the directional correlations coefficients and $P_{2/4}$ are the Legendre polynomials of order 2 and 4 respectively, have been fitted, and the a_{22} and a_{44} coefficients extracted. For the stretched $4_1^+\rightarrow2_1^+\rightarrow0_1^+$ cascade the fitted values are $a_{22} = 0.13 \pm 0.02$ and $a_{44} = -0.02 \pm 0.03$ to be compared with theoretical values of $a_{22} = 0.102$ and $a_{44} = 0.0091$. For the non-mixed the $2_1^-\rightarrow2_1^+\rightarrow0_1^+$ cascade our fit gives $a_{22} = 0.25 \pm 0.02$ and $a_{44} = -0.01 \pm 0.03$, for which the theoretical values are $a_{22} = 0.25$ and $a_{44} = 0$. With three out of four values within 1σ this is in agreement with what is expected if AGATA is correctly reproducing the angular correlations.

A particularity of a γ-tracking array as compared to a classical multi-detector γ-ray spectrometer is the continuous variation in efficiency with the angle between the detected γ rays. For angular correlations this means the normalization of the angular correlations need not only to consider geometrical coverage. This can be seen by looking at the difference between using uncorrelated hits that are concatenated and tracked or tracked uncorrelated γ rays concatenated into events when constructing the normalization used to extract the angular correlations from the experimental correlations. In the top panel of Fig. 18 the histogram drawn with a black solid line shows the distribution of θ angles between uncorrelated γ rays concatenated after tracking. The histogram drawn with red dashed line shows the θ angle distribution if one instead concatenates uncorrelated events using the individual hits and then preforms the tracking. The bottom panel shows the resulting angular correlations using the two different methods of generating the normalization. It is clear that the effects of γ-ray tracking, included when events are concatenated before tracking, are needed for a correct normalization over the entire angle range. This procedure works well

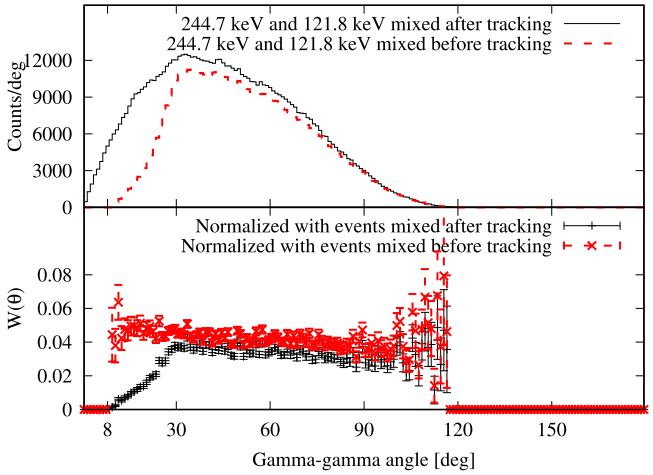

Fig. 18. Normalization histograms and angular correlations for $4_1^+\rightarrow2_1^+\rightarrow0_1^+$ using the "concatenate before tracking" and "concatenate after tracking" methods.

for source data where the peak-to-background ratio is high and γ rays from different decays have no correlations. The application of this method to in-beam data is however more problematic due too the lower peak-to-background ratio and cross-event angular correlations coming from aligned nuclei.

8. Conclusions and perspective

The performance of AGATA installed at GANIL, coupled to the VAMOS has been characterized. The efficiency of AGATA, as a whole as well as for individual crystals, has been determined using both singles measurements and coincidence methods. It has been done both using AGATA as a standard array and as a γ-ray tracking array. A total efficiency for AGATA of 3.8(1)% at 1332 keV for the nominal geometry when using γ-ray tracking was determined. This is to be compared to 2.9% at 1332 keV if AGATA is used as normal multi-detector array. It is also shown how the efficiency extracted from coincidence has to be corrected for angular correlation effects, as the increased probability to emit parallel γ rays combined with the clustering stage of γ-ray tracking generates a loss of efficiency that depends on the angle between the two γ rays. This correction has to be made on top of the typical correction made for angular correlations effects.

As the AGATA detectors have been used in different campaigns the segments of some of the detectors are showing clear signs of neutron damages. Annealing procedures are complicated for these detectors and ingenious neutron damage correction procedures have been developed allowing an almost full recovery of the intrinsic energy resolution. The average central contact energy resolution for AGATA (beginning of 2016) is 2.57 keV at 1332 keV and for the segments 3.08 keV at 1332 keV. Corresponding values before applying neutron damage correction are 3.08 keV and 5.22 keV for central contacts and segments, respectively. The neutron damage correction procedure is effective, but at some point the detectors will need to be annealed. Maintenance, such as annealing, are as important for the future of AGATA as the more appealing technical developments that can be made.

The position resolution given by the PSA for AGATA at GANIL has been estimated for 6 AGATA crystals using data from an experiment performed in the first half of the campaign. This was done by comparing experimental data with Monte Carlo simulations in which the position resolution was varied. It turns out that the average position resolution found was a factor of 1.16(5) larger than what was measured in a dedicated experiment [5].

As the number of crystals in AGATA increases the interest in using AGATA for angular correlations and distributions increases. Using a ^{152}Eu source angular correlations have been produced and methods to properly normalize for the combined effect of geometry and γ-ray tracking have been devised.

Finally, the AGATA detector system is performing very well, as proven by the physics results that have been produced. However, improvements in the PSA and further tuning of γ-ray tracking algorithms would be beneficial. A better understanding of the details of the signal generation in the segmented detectors is needed to improve the PSA. This would also allow for better handling of multiple interactions in one segment and removing the nonphysical clustering of interaction points. Such improvements would allow for an increased peak-to-total.

Declaration of competing interest

The authors declare that they have no known competing financial interests or personal relationships that could have appeared to influence the work reported in this paper.

CRediT authorship contribution statement

J. Ljungvall: Conceptualization, Data curation, Formal analysis, Writing - orginal draft, Writing review & editing. **R.M. Pérez-Vidal:** Data curation, Formal analysis, Writing - orginal draft, Writing review & editing. **A. Lopez-Martens:** Data curation, Formal analysis, Writing - orginal draft, Writing review & editing. **C. Michelagnoli:** Conceptualization, Data curation, Formal analysis, Methodology. **E. Clément:** Data curation, Formal analysis, Writing - orginal draft, Writing review & editing. **J. Dudouet:** Data curation, Formal analysis, Writing review & editing. **A. Gadea:** Data curation, Supervision, Writing - orginal draft, Writing review & editing. **H. Hess:** Data curation, Resources. **A. Korichi:** Data curation, Formal analysis, Writing - orginal draft, Writing review & editing. **M. Labiche:** Data curation, Formal analysis, Writing - orginal draft, Writing review & editing. **N. Lalović:** Data curation, Writing - orginal draft, Writing review & editing. **H.J. Li:** Data curation, Formal analysis, Writing - orginal draft, Writing review & editing. **F. Recchia:** Data curation, Formal analysis, Writing - orginal draft, Writing review & editing.

Acknowledgments

The authors would like to thank the AGATA collaboration and the GANIL technical staff. Gilbert Duchêne is thanked for providing the in-beam data set used to extract the position resolution of the pulse-shape analysis. The excellent performance of the AGATA detectors is assured by the AGATA Detector Working group. This work was partially supported by the Ministry of Science, Spain, under the Grants BES-2012-061407, SEV-2014-0398, FPA2017-84756-C4 and by the EU FEDER, Spain funds. The research and development on AGATA was supported by the German BMBF under Grants 06K-167, 06KY205I, 05P12PKFNE, 05P15PKFN9, and 05P18PKFN9. The AGATA project is supported in France by the CNRS and the CEA. The UK Science and Technology Facility Council (STFC) supports the AGATA project.

Table A.3
Crystal lookup table for the 32 crystals present in the set-up, although only 30 were used in the measurement. The capsules in position 11A and 14A were not operational and shown in italic. Neutron damage correction was performed on detectors marked in bold.

Cluster	Crystal A	Crystal B	Crystal C	Position array
ATC6	**A001**	**B004**	**C010**	00
ATC8	A009	B005	**C008**	02
ATC5	A005	**B002**	**C009**	03
ATC9	A004	B008	C013	04
ATC10	A010	B012	C012	05
ADC9	–	**B011**	C011	09
ATC2	**A003**	**B003**	**C005**	10
ATC7	*A006*	**B013**	**C006**	11
ATC3	**A002**	**B010**	**C001**	12
ATC4	**A007**	**B007**	**C007**	13
ATC1	*A008*	**B001**	**C003**	14

Appendix. Detector and crystal positions and ids

See Table A.3.

References

[1] S. Akkoyun, A. Algora, B. Alikhani, F. Ameil, G. de Angelis, L. Arnold, A. Astier, A. Ataç, Y. Aubert, C. Aufranc, A. Austin, S. Aydin, F. Azaiez, S. Badoer, D. Balabanski, D. Barrientos, G. Baulieu, R. Baumann, D. Bazzacco, F. Beck, T. Beck, P. Bednarczyk, M. Bellato, M. Bentley, G. Benzoni, R. Berthier, L. Berti, R. Beunard, G.L. Bianco, B. Birkenbach, P. Bizzeti, A. Bizzeti-Sona, F.L. Blanc, J. Blasco, N. Blasi, D. Bloor, C. Boiano, M. Borsato, D. Bortolato, A. Boston, H. Boston, P. Bourgault, P. Boutachkov, A. Bouty, A. Bracco, S. Brambilla, I. Brawn, A. Brondi, S. Broussard, B. Bruyneel, D. Bucurescu, I. Burrows, A. Bürger, S. Cabaret, B. Cahan, E. Calore, F. Camera, A. Capsoni, F. Carrió, G. Casati, M. Castoldi, B. Cederwall, J.-L. Cercus, V. Chambert, M.E. Chambit, R. Chapman, L. Charles, J. Chavas, E. Clément, P. Cocconi, S. Coelli, P. Coleman-Smith, A. Colombo, S. Colosimo, C. Commeaux, D. Conventi, R. Cooper, A. Corsi, A. Cortesi, L. Costa, F. Crespi, J. Cresswell, D. Cullen, D. Curien, A. Czermak, D. Delbourg, R. Depalo, T. Descombes, P. Désesquelles, P. Detistov, C. Diarra, F. Didierjean, M. Dimmock, Q. Doan, C. Domingo-Pardo, M. Doncel, F. Dorangeville, N. Dosme, Y. Drouen, G. Duchêne, B. Dulny, J. Eberth, P. Edelbruck, J. Egea, T. Engert, M. Erduran, S. Ertürk, C. Fanin, S. Fantinel, E. Farnea, T. Faul, M. Filliger, F. Filmer, C. Finck, G. de France, A. Gadea, W. Gast, A. Geraci, J. Gerl, R. Gernhäuser, A. Giannatiempo, A. Giaz, L. Gibelin, A. Givechev, N. Goel, V. González, A. Gottardo, X. Grave, J. Grebosz, R. Griffiths, A. Grint, P. Gros, L. Guevara, M. Gulmini, A. Görgen, H. Ha, T. Habermann, L. Harkness, H. Harroch, K. Hauschild, C. He, A. Hernández-Prieto, B. Hervieu, H. Hess, T. Hüyük, E. Ince, R. Isocrate, G. Jaworski, A. Johnson, J. Jolie, P. Jones, B. Jonson, P. Joshi, D. Judson, A. Jungclaus, M. Kaci, N. Karkour, M. Karolak, A. Kaşkaş, M. Kebbiri, R. Kempley, A. Khaplanov, S. Klupp, M. Kogimtzis, I. Kojouharov, A. Korichi, W. Korten, T. Kröll, R. Krücken, N. Kurz, B. Ky, M. Labiche, X. Lafay, L. Lavergne, I. Lazarus, S. Leboutelier, F. Lefebvre, E. Legay, L. Legeard, F. Lelli, S. Lenzi, S. Leoni, A. Lermitage, D. Lersch, J. Leske, S. Letts, S. Lhenoret, R. Lieder, D. Linget, J. Ljungvall, A. Lopez-Martens, A. Lotodé, S. Lunardi, A. Maj, J. van der Marel, Y. Mariette, N. Marginean, R. Marginean, G. Maron, A. Mather, W. Meczyński, V. Mendéz, P. Medina, B. Melon, R. Menegazzo, D. Mengoni, E. Merchan, L. Mihailescu, C. Michelagnoli, J. Mierzejewski, L. Milechina, B. Million, K. Mitev, P. Molini, D. Montanari, S. Moon, F. Morbiducci, R. Moro, P. Morrall, O. Möller, A. Nannini, D. Napoli, L. Nelson, M. Nespolo, V. Ngo, M. Nicoletto, R. Nicolini, Y.L. Noa, P. Nolan, M. Norman, J. Nyberg, A. Obertelli, A. Olariu, R. Orlandi, D. Oxley, C. Özben, M. Ozille, C. Oziol, E. Pachoud, M. Palacz, J. Palin, J. Pancin, C. Parisel, P. Pariset, G. Pascovici, R. Peghin, L. Pellegri, A. Perego, S. Perrier, M. Petcu, P. Petkov, C. Petrache, E. Pierre, N. Pietralla, S. Pietri, M. Pignanelli, I. Piqueras, Z. Podolyak, P.L. Pouhalec, J. Pouthas, D. Pugnére, V. Pucknell, A. Pullia, B. Quintana, R. Raine, G. Rainovski, L. Ramina, G. Rampazzo, G.L. Rana, M. Rebeschini, F. Recchia, N. Redon, M. Reese, P. Reiter, P. Regan, S.

Riboldi, M. Richer, M. Rigato, S. Rigby, G. Ripamonti, A. Robinson, J. Robin, J. Roccaz, J.-A. Ropert, B. Rossé, C.R. Alvarez, D. Rosso, B. Rubio, D. Rudolph, F. Saillant, E. Şahin, F. Salomon, M.-D. Salsac, J. Salt, G. Salvato, J. Sampson, E. Sanchis, C. Santos, H. Schaffner, M. Schlarb, D. Scraggs, D. Seddon, M. Şenyiğit, M.-H. Sigward, G. Simpson, J. Simpson, M. Slee, J. Smith, P. Sona, B. Sowicki, P. Spolaore, C. Stahl, T. Stanios, E. Stefanova, O. Stézowski, J. Strachan, G. Suliman, P.-A. Söderström, J. Tain, S. Tanguy, S. Tashenov, C. Theisen, J. Thornhill, F. Tomasi, N. Toniolo, R. Touzery, B. Travers, A. Triossi, M. Tripon, K. Tun-Lanoë, M. Turcato, C. Unsworth, C. Ur, J. Valiente-Dobon, V. Vandone, E. Vardaci, R. Venturelli, F. Veronese, C. Veyssiere, E. Viscione, R. Wadsworth, P. Walker, N. Warr, C. Weber, D. Weisshaar, D. Wells, O. Wieland, A. Wiens, G. Wittwer, H. Wollersheim, F. Zocca, N. Zamfir, M. Ziebliński, A. Zucchiatti, Agata-advanced {GAmma} tracking array, Nucl. Instrum. Methods Phys. Res. A 668 (2012) 26–58, http://dx.doi.org/10.1016/j.nima.2011.11.081, URL http://www.sciencedirect.com/science/article/pii/S0168900211021516.

[2] I.Y. Lee, M.A. Deleplanque, K. Vetter, Developments in large gamma-ray detector arrays, Rep. Progr. Phys. 66 (7) (2003) 1095, URL http://stacks.iop.org/0034-4885/66/i=7/a=201.

[3] F. Recchia, D. Bazzacco, E. Farnea, R. Venturelli, S. Aydin, G. Suliman, C. Ur, Performance of an agata prototype detector estimated by compton-imaging techniques, Nucl. Instrum. Methods Phys. Res. A 604 (1) (2009) 60–63, http://dx.doi.org/10.1016/j.nima.2009.01.079, pSD8. URL http://www.sciencedirect.com/science/article/pii/S0168900209001168.

[4] F. Recchia, D. Bazzacco, E. Farnea, A. Gadea, R. Venturelli, T. Beck, P. Bednarczyk, A. Buerger, A. Dewald, M. Dimmock, G. Duchûne, J. Eberth, T. Faul, J. Gerl, R. Gernhaeuser, K. Hauschild, A. Holler, P. Jones, W. Korten, T. Kröll, R. Krücken, N. Kurz, J. Ljungvall, S. Lunardi, P. Maierbeck, D. Mengoni, J. Nyberg, L. Nelson, G. Pascovici, P. Reiter, H. Schaffner, M. Schlarb, T. Steinhardt, O. Thelen, C. Ur, J.V. Dobon, D. Weisshaar, Position resolution of the prototype agata triple-cluster detector from an in-beam experiment, Nucl. Instrum. Methods Phys. Res. A 604 (3) (2009) 555–562, http://dx.doi.org/10.1016/j.nima.2009.02.042, URL http://www.sciencedirect.com/science/article/pii/S0168900209004124.

[5] P.-A. Söderström, F. Recchia, J. Nyberg, A. Al-Adili, A. Ataç, S. Aydin, D. Bazzacco, P. Bednarczyk, B. Birkenbach, D. Bortolato, A. Boston, H. Boston, B. Bruyneel, D. Bucurescu, E. Calore, S. Colosimo, F. Crespi, N. Dosme, J. Eberth, E. Farnea, F. Filmer, A. Gadea, A. Gottardo, X. Grave, J. Grebosz, R. Griffiths, M. Gulmini, T. Habermann, H. Hess, G. Jaworski, P. Jones, P. Joshi, D. Judson, R. Kempley, A. Khaplanov, E. Legay, D. Lersch, J. Ljungvall, A. Lopez-Martens, W. Meczynski, D. Mengoni, C. Michelagnoli, P. Molini, D. Napoli, R. Orlandi, G. Pascovici, A. Pullia, P. Reiter, E. Sahin, J. Smith, J. Strachan, D. Tonev, C. Unsworth, C. Ur, J. Valiente-Dobón, C. Veyssiere, A. Wiens, Interaction position resolution simulations and in-beam measurements of the {AGATA} {HPGe} detectors, Nucl. Instrum. Methods Phys. Res. A 638 (1) (2011) 96–109, http://dx.doi.org/10.1016/j.nima.2011.02.089, URL http://www.sciencedirect.com/science/article/pii/S016890021100489X.

[6] A. Gadea, E. Farnea, J. Valiente-Dobón, B. Million, D. Mengoni, D. Bazzacco, F. Recchia, A. Dewald, T. Pissulla, W. Rother, G. de Angelis, A. Austin, S. Aydin, S. Badoer, M. Bellato, G. Benzoni, L. Berti, R. Beunard, B. Birkenbach, E. Bissiato, N. Blasi, C. Boiano, D. Bortolato, A. Bracco, S. Brambilla, B. Bruyneel, E. Calore, F. Camera, A. Capsoni, J. Chavas, P. Cocconi, S. Coelli, A. Colombo, D. Conventi, L. Costa, L. Corradi, A. Corsi, A. Cortesi, F. Crespi, N. Dosme, J. Eberth, S. Fantinel, C. Fanin, E. Fioretto, C. Fransen, A. Giaz, A. Gottardo, X. Grave, J. Grebosz, R. Griffiths, E. Grodner, M. Gulmini, T. Habermann, C. He, H. Hess, R. Isocrate, J. Jolie, P. Jones, A. Latina, E. Legay, S. Lenzi, S. Leoni, F. Lelli, D. Lersch, S. Lunardi, G. Maron, R. Menegazzo, C. Michelagnoli, P. Molini, G. Montagnoli, D. Montanari, O. Möller, D. Napoli, M. Nicoletto, R. Nicolini, M. Ozille, G. Pascovici, R. Peghin, M. Pignanelli, V. Pucknell, A. Pullia, L. Ramina, G. Rampazzo, M. Rebeschini, P. Reiter, S. Riboldi, M. Rigato, C.R. Alvarez, D. Rosso, G. Salvato, J. Strachan, E. Sahin, F. Scarlassara, J. Simpson, A. Stefanini, O. Stezowski, F. Tomasi, N. Toniolo, A. Triossi, M. Turcato, C. Ur, V. Vandone, R. Venturelli, F. Veronese, C. Veyssiere, E. Viscione, O. Wieland, A. Wiens, F. Zocca, A. Zucchiatti, Conceptual design and infrastructure for the installation of the first agata sub-array at lnl, Nucl. Instrum. Methods Phys. Res. A 654 (1) (2011) 88–96, http://dx.doi.org/10.1016/j.nima.2011.06.004, URL http://www.sciencedirect.com/science/article/pii/S0168900211011132.

[7] C. Domingo-Pardo, D. Bazzacco, P. Doornenbal, E. Farnea, A. Gadea, J. Gerl, H. Wollersheim, Conceptual design and performance study for the first implementation of agata at the in-flight rib facility of gsi, Nucl. Instrum. Methods Phys. Res. A 694 (2012) 297–312, http://dx.doi.org/10.1016/j.nima.2012.08.039, URL http://www.sciencedirect.com/science/article/pii/S0168900212009102.

[8] N. Lalović, C. Louchart, C. Michelagnoli, R. Perez-Vidal, D. Ralet, J. Gerl, D. Rudolph, T. Arici, D. Bazzacco, E. Clément, A. Gadea, I. Kojouharov, A. Korichi, M. Labiche, J. Ljungvall, A. Lopez-Martens, J. Nyberg, N. Pietralla, S. Pietri, O. Stezowski, Performance of the {AGATA} γ-ray spectrometer in the prespec set-up at {GSI}, Nucl. Instrum. Methods Phys. Res. A 806 (2016) 258–266, http://dx.doi.org/10.1016/j.nima.2015.10.032, URL http://www.sciencedirect.com/science/article/pii/S0168900215012395.

[9] E. Clément, C. Michelagnoli, G. de France, H. Li, A. Lemasson, C.B. Dejean, M. Beuzard, P. Bougault, J. Cacitti, J.-L. Foucher, G. Fremont, P. Gangnant, J. Goupil, C. Houarner, M. Jean, A. Lefevre, L. Legeard, F. Legruel, C. Maugeais, L. Ménager, N. Ménard, H. Munoz, M. Ozille, B. Raine, J. Ropert, F. Saillant, C. Spitaels, M. Tripon, P. Vallerand, G. Voltolini, W. Korten, M.-D. Salsac, C. Theisen, M. Zielińska, T. Joannem, M. Karolak, M. Kebbiri, A. Lotode, R. Touzery, C. Walter, A. Korichi, J. Ljungvall, A. Lopez-Martens, D. Ralet, N. Dosme, X. Grave, N. Karkour, X. Lafay, E. Legay, I. Kojouharov, C. Domingo-Pardo, A. Gadea, R. Pérez-Vidal, J. Civera, B. Birkenbach, J. Eberth, H. Hess, L. Lewandowski, P. Reiter, A. Nannini, G.D. Angelis, G. Jaworski, P. John, D. Napoli, J. Valiente-Dobón, D. Barrientos, D. Bortolato, G. Benzoni, A. Bracco, S. Brambilla, F. Camera, F. Crespi, S. Leoni, B. Million, A. Pullia, O. Wieland, D. Bazzacco, S. Lenzi, S. Lunardi, R. Menegazzo, D. Mengoni, F. Recchia, M. Bellato, R. Isocrate, F.E. Canet, F. Didierjean, G. Duchêne, R. Baumann, M. Brucker, E. Dangelser, M. Filliger, H. Friedmann, G. Gaudiot, J.-N. Grapton, H. Kocher, C. Mathieu, M.-H. Sigward, D. Thomas, S. Veeramootoo, J. Dudouet, O. Stézowski, C. Aufranc, Y. Aubert, M. Labiche, J. Simpson, I. Burrows, P. Coleman-Smith, A. Grant, I. Lazarus, P. Morrall, V. Pucknell, A. Boston, D. Judson, N. Lalović, J. Nyberg, J. Collado, V. González, I. Kuti, B. Nyakó, A. Maj, M. Rudigier, Conceptual design of the agata 1π array at ganil, Nucl. Instrum. Methods Phys. Res. A 855 (Suppl. C) (2017) 1–12, http://dx.doi.org/10.1016/j.nima.2017.02.063, URL http://www.sciencedirect.com/science/article/pii/S0168900217302590.

[10] H. Savajols, Vamos: a variable mode high acceptance spectrometer, Nuclear Phys. A 654 (1) (1999) 1027c–1032c, http://dx.doi.org/10.1016/S0375-9474(00)88592-9, URL http://www.sciencedirect.com/science/article/pii/S0375947400885929.

[11] M. Rejmund, B. Lecornu, A. Navin, C. Schmitt, S. Damoy, O. Delaune, J. Enguerrand, G. Fremont, P. Gangnant, L. Gaudefroy, B. Jacquot, J. Pancin, S. Pullanhiotan, C. Spitaels, Performance of the improved larger acceptance spectrometer: Vamos++, Nucl. Instrum. Methods Phys. Res. A 646 (1) (2011) 184–191, http://dx.doi.org/10.1016/j.nima.2011.05.007, URL http://www.sciencedirect.com/science/article/pii/S0168900211008515.

[12] J. Valiente-Dobón, G. Jaworski, A. Goasduff, F. Egea, V. Modamio, T. Hüyük, A. Triossi, M. Jastrząb, P. Söderström, A.D. Nitto, G. de Angelis, G. de France, N. Erduran, A. Gadea, M. Moszyński, J. Nyberg, M. Palacz, R. Wadsworth, R. Aliaga, C. Aufranc, M. Bézard, G. Baulieu, E. Bissiato, A. Boujrad, I. Burrows, S. Carturan, P. Cocconi, G. Colucci, D. Conventi, M. Cordwell, S. Coudert, J. Deltoro, L. Ducroux, T. Dupasquier, S. Ertürk, X. Fabian, V. González, A. Grant, K. Hadyńska-Klęk, A. Illana, M. Jurado-Gomez, M. Kogimtzis, I. Lazarus, L. Legeard, J. Ljungvall, G. Pasqualato, R. Pérez-Vidal, A. Raggio, D. Ralet, N. Redon, F. Saillant, B. Sayği, E. Sanchis, M. Scarcioffolo, M. Siciliano, D. Testov, O. Stezowski, M. Tripon, I. Zanon, Neda-neutron detector array, Nucl. Instrum. Methods Phys. Res. A 927 (2019) 81–86, http://dx.doi.org/10.1016/j.nima.2019.02.021, URL http://www.sciencedirect.com/science/article/pii/S0168900219301962.

[13] J. Scheurer, M. Aiche, M. Aleonard, G. Barreau, F. Bourgine, D. Boivin, D. Cabaussel, J. Chemin, T. Doan, J. Goudour, M. Harston, A. Brondi, G.L. Rana, R. Moro, E. Vardaci, D. Curien, Improvements in the in-beam γ-ray spectroscopy provided by an ancillary detector coupled to a ge γ-spectrometer: the diamant-eurogam ii example, Nucl. Instrum. Methods Phys. Res. A 385 (3) (1997) 501–510, http://dx.doi.org/10.1016/S0168-9002(96)01038-8, URL http://www.sciencedirect.com/science/article/pii/S0168900296010388.

[14] J. Gál, G. Hegyesi, J. Molnár, B. Nyakó, G. Kalinka, J. Scheurer, M. Aléonard, J. Chemin, J. Pedroza, K. Juhász, V. Pucknell, The vxi electronics of the diamant particle detector array, Nucl. Instrum. Methods Phys. Res. A 516 (2) (2004) 502–510, http://dx.doi.org/10.1016/j.nima.2003.08.158, URL http://www.sciencedirect.com/science/article/pii/S0168900203025075.

[15] A. Korichi, T. Lauritsen, A. Wilson, J. Dudouet, E. Clément, N. Lalović, R. Perez-Vidal, S. Pietri, D. Ralet, O. Stézowski, Performance of a gamma-ray tracking array: Characterizing the agata array using a 60co source, Nucl. Instrum. Methods Phys. Res. A 872 (2017) 80–86, http://dx.doi.org/10.1016/j.nima.2017.08.020, URL http://www.sciencedirect.com/science/article/pii/S0168900217308781.

[16] T. Lauritsen, A. Korichi, S. Zhu, A.N. Wilson, D. Weisshaar, J. Dudouet, A.D. Ayangeakaa, M.P. Carpenter, C.M. Campbell, E. Clément, H.L. Crawford, M. Cromaz, P. Fallon, J.P. Greene, R.V.F. Janssens, T.L. Khoo, N. Lalović, I.Y. Lee, A.O. Macchiavelli, R.M. Perez-Vidal, S. Pietri, D.C. Radford, D. Ralet, L.A. Riley, D. Seweryniak, O. Stezowski, Characterization of a gamma-ray tracking array: A comparison of GRETINA and Gammasphere using a^{60}Co source, Nucl. Instrum. Methods Phys. Res. A 836 (2016) 46–56, http://dx.doi.org/10.1016/j.nima.2016.07.027, URL http://www.sciencedirect.com/science/article/pii/S0168900216307434.

[17] D. Weisshaar, D. Bazin, P.C. Bender, C.M. Campbell, F. Recchia, V. Bader, T. Baugher, J. Belarge, M.P. Carpenter, H.L. Crawford, M. Cromaz, B. Elman, P. Fallon, A. Forney, A. Gade, J. Harker, N. Kobayashi, C. Langer, T. Lauritsen, I.Y. Lee, A. Lemasson, B. Longfellow, E. Lunderberg, A.O. Macchiavelli, K. Miki, S. Momiyama, S. Noji, D.C. Radford, M. Scott, J. Sethi, S.R. Stroberg, C. Sullivan, R. Titus, A. Wiens, S. Williams, K. Wimmer, S. Zhu, The performance of the γ-ray tracking array GRETINA for γ-ray spectroscopy with fast beams of rare isotopes, Nucl. Instrum. Methods Phys. Res. A 847 (2017) 187–198, http://dx.doi.org/10.1016/j.nima.2016.12.001, URL http://www.sciencedirect.com/science/article/pii/S0168900216312402.

[18] A. Wiens, H. Hess, B. Birkenbach, B. Bruyneel, J. Eberth, D. Lersch, G. Pascovici, P. Reiter, H.-G. Thomas, The {AGATA} triple cluster detector, Nucl. Instrum. Methods Phys. Res. A 618 (1–3) (2010) 223–233, http://dx.doi.

org/10.1016/j.nima.2010.02.102, URL http://www.sciencedirect.com/science/article/pii/S0168900210003384.

[19] S. Agostinelli, J. Allison, K. Amako, J. Apostolakis, H. Araujo, P. Arce, M. Asai, D. Axen, S. Banerjee, G. Barrand, F. Behner, L. Bellagamba, J. Boudreau, L. Broglia, A. Brunengo, H. Burkhardt, S. Chauvie, J. Chuma, R. Chytracek, G. Cooperman, G. Cosmo, P. Degtyarenko, A. Dell'Acqua, G. Depaola, D. Dietrich, R. Enami, A. Feliciello, C. Ferguson, H. Fesefeldt, G. Folger, F. Foppiano, A. Forti, S. Garelli, S. Giani, R. Giannitrapani, D. Gibin, J.G. Cadenas, I. González, G.G. Abril, G. Greeniaus, W. Greiner, V. Grichine, A. Grossheim, S. Guatelli, P. Gumplinger, R. Hamatsu, K. Hashimoto, H. Hasui, A. Heikkinen, A. Howard, V. Ivanchenko, A. Johnson, F. Jones, J. Kallenbach, N. Kanaya, M. Kawabata, Y. Kawabata, M. Kawaguti, S. Kelner, P. Kent, A. Kimura, T. Kodama, R. Kokoulin, M. Kossov, H. Kurashige, E. Lamanna, T. Lampén, V. Lara, V. Lefebure, F. Lei, M. Liendl, W. Lockman, F. Longo, S. Magni, M. Maire, E. Medernach, K. Minamimoto, P.M. de Freitas, Y. Morita, K. Murakami, M. Nagamatu, R. Nartallo, P. Nieminen, T. Nishimura, K. Ohtsubo, M. Okamura, S. O'Neale, Y. Oohata, K. Paech, J. Perl, A. Pfeiffer, M. Pia, F. Ranjard, A. Rybin, S. Sadilov, E.D. Salvo, G. Santin, T. Sasaki, N. Savvas, Y. Sawada, S. Scherer, S. Sei, V. Sirotenko, D. Smith, N. Starkov, H. Stoecker, J. Sulkimo, M. Takahata, S. Tanaka, E. Tcherniaev, E.S. Tehrani, M. Tropeano, P. Truscott, H. Uno, L. Urban, P. Urban, M. Verderi, A. Walkden, W. Wander, H. Weber, J. Wellisch, T. Wenaus, D. Williams, D. Wright, T. Yamada, H. Yoshida, D. Zschiesche, Geant4-a simulation toolkit, Nucl. Instrum. Methods Phys. Res. A 506 (3) (2003) 250–303, http://dx.doi.org/10.1016/S0168-9002(03)01368-8, URL http://www.sciencedirect.com/science/article/pii/S0168900203013688.

[20] E. Farnea, F. Recchia, D. Bazzacco, T. Kröll, Z. Podolyák, B. Quintana, A. Gadea, Conceptual design and Monte Carlo simulations of the {AGATA} array, Nucl. Instrum. Methods Phys. Res. A 621 (1–3) (2010) 331–343, http://dx.doi.org/10.1016/j.nima.2010.04.043, URL http://www.sciencedirect.com/science/article/pii/S0168900210008922.

[21] D. Barrientos, M. Bellato, D. Bazzacco, D. Bortolato, P. Cocconi, A. Gadea, V. Gonzalez, M. Gulmini, R. Isocrate, D. Mengoni, A. Pullia, F. Recchia, D. Rosso, E. Sanchis, N. Toniolo, C.A. Ur, J.J. Valiente-Dobon, Digital FPGA-based front-end electronics for the GALILEO array, IEEE Trans. Nucl. Sci. 62 (6) (2015) 3134–3139, http://dx.doi.org/10.1109/tns.2015.2480243, URL https://doi.org/10.1109%2Ftns.2015.2480243.

[22] R. Venturelli, D. Bazzacco, Adaptive Grid Search as Pulse Shape Analysis Algorithm for γ-Tracking and Results, LNL Annual Report, 2004, p. 220.

[23] B. Bruyneel, B. Birkenbach, P. Reiter, Pulse shape analysis and position determination in segmented hpge detectors: The agata detector library, Eur. Phys. J. A 52 (3) (2016) 70, http://dx.doi.org/10.1140/epja/i2016-16070-9, URL http://dx.doi.org/10.1140/epja/i2016-16070-9.

[24] A. Lopez-Martens, K. Hauschild, A. Korichi, J. Roccaz, J.-P. Thibaud, γ-Ray tracking algorithms: a comparison, Nucl. Instrum. Methods Phys. Res. A 533 (3) (2004) 454–466, http://dx.doi.org/10.1016/j.nima.2004.06.154, URL http://www.sciencedirect.com/science/article/pii/S0168900204014779.

[25] B. Bruyneel, P. Reiter, A. Wiens, J. Eberth, H. Hess, G. Pascovici, N. Warr, D. Weisshaar, Crosstalk properties of 36-fold segmented symmetric hexagonal {HPGe} detectors, Nucl. Instrum. Methods Phys. Res. A 599 (2–3) (2009) 196–208, http://dx.doi.org/10.1016/j.nima.2008.11.011, URL http://www.sciencedirect.com/science/article/pii/S0168900208015921.

[26] B. Bruyneel, P. Reiter, A. Wiens, J. Eberth, H. Hess, G. Pascovici, N. Warr, S. Aydin, D. Bazzacco, F. Recchia, Crosstalk corrections for improved energy resolution with highly segmented hpge-detectors, Nucl. Instrum. Methods Phys. Res. A 608 (1) (2009) 99–106, http://dx.doi.org/10.1016/j.nima.2009.06.037, URL http://www.sciencedirect.com/science/article/pii/S0168900209012455.

[27] B. Bruyneel, B. Birkenbach, J. Eberth, H. Hess, G. Pascovici, P. Reiter, A. Wiens, D. Bazzacco, E. Farnea, C. Michelagnoli, F. Recchia, Correction for hole trapping in agata detectors using pulse shape analysis, Eur. Phys. J. A 49 (5) (2013) 61.

[28] T.J. Ross, C.W. Beausang, I.Y. Lee, A.O. Macchiavelli, S. Gros, M. Cromaz, R.M. Clark, P. Fallon, H. Jeppesen, J.M. Allmond, Neutron damage tests of a highly segmented germanium crystal, Nucl. Instrum. Methods Phys. Res. A 606 (3) (2009) 533–544, http://dx.doi.org/10.1016/j.nima.2009.04.024, URL http://www.sciencedirect.com/science/article/pii/S0168900209008250.

[29] D. Radford, Radware. URL https://radware.phy.ornl.gov/main.html.

[30] J. Eberth, J. Simpson, From ge(li) detectors to gamma-ray tracking arrays-50 years of gamma spectroscopy with germanium detectors, Prog. Part. Nucl. Phys. 60 (2) (2008) 283–337, http://dx.doi.org/10.1016/j.ppnp.2007.09.001, URL http://www.sciencedirect.com/science/article/pii/S0146641007000828.

[31] H. Utsunomiya, H. Akimune, K. Osaka, T. Kaihori, K. Furutaka, H. Harada, Surface channel effect on γ-ray response functions of coaxial germanium detectors, Nucl. Instrum. Methods Phys. Res. A 548 (3) (2005) 455–463, http://dx.doi.org/10.1016/j.nima.2005.04.062, URL http://www.sciencedirect.com/science/article/pii/S0168900205010508.

[32] S. Paschalis, I. Lee, A. Macchiavelli, C. Campbell, M. Cromaz, S. Gros, J. Pavan, J. Qian, R. Clark, H. Crawford, D. Doering, P. Fallon, C. Lionberger, T. Loew, M. Petri, T. Stezelberger, S. Zimmermann, D. Radford, K. Lagergren, D. Weisshaar, R. Winkler, T. Glasmacher, J. Anderson, C. Beausang, The performance of the gamma-ray energy tracking in-beam nuclear array gretina, Nucl. Instrum. Methods Phys. Res. A 709 (2013) 44–55, http://dx.doi.org/10.1016/j.nima.2013.01.009, URL http://www.sciencedirect.com/science/article/pii/S0168900213000508.

[33] F. Recchia, D. Bazzacco, M. Bellato, D. Borolato, E. Farnea, D. Mengoni, Efficency and Energy Resolution of the Agata Demonstartor at High Count Rate, Tech. rep. LNL, 2010.

7.11 Pulseshape calculations using the AGATAGeFEM code and applications

UNDER EDITING

EPJ manuscript No.
(will be inserted by the editor)

Pulseshape calculations using the AGATAGeFEM code and applications

J. Ljungvall[1]

CSNSM, Univ Paris-Sud, CNRS/IN2P3, F-91405 Orsay, France

Abstract. A code, AGATAGeFEM, that models segmented High-purity Gemernium detetectors is presented. It is discussed how the geometry is implemented, and how the electric and weighting fields are calculted. Further more are the models used for charge carrier velocity described and the solution for charge-carrier transport is shown. To code allows simple application of electroical response functions and linear and differential cross-talk. As an example of application the code is used to investigate the impact of noise and cross-talk on the achivied position resolution in AGATA detectors.

PACS. 21.10.Tg In-beam γ-ray spectroscopy

1 Introduction

In nuclear-structure physics, as in many other fields of research, the development of better instrumentation and the discoveries of new physics have been closely linked. One of the most powerful techniques to study atomic nuclei is and have been that of gamma-ray spectroscopy combined with in-beam production of the species of interest. However, the present stable-beam facilities using classical gamma-ray spectrometers based on Compton suppressed germanium detectors, such as EUROBALL [1] and GAMMASPHERE [2], have severe limitations as the nuclear physics community explores the atomic nuclei under more and more extreme conditions. In order too overcome these limitations several radioactive beam facilities are under construction, or have recently been constructed, in the world, e.g., Spiral2 , FAIR, RIKEN, FRIB and HEISOLDE. High intensity stable beams are also foreseen for the future. To maximize the return in terms of physics on these investments the detection systems also need to be improved. They need to be more efficient, have higher resolving power and withstand higher counting rates. For gamma-ray spectrometers the answer to these demands lie in co called gamma-ray tracking arrays. During the last decade the gamma-ray spectroscopy community has been deeply involved in the development of two gamma-ray tracking arrays, AGATA [3], and GRETA [4].

The use of digital electronics combined pulse-shape analysis (PSA) with will allow an increase of the solid angle covered by germanium and in the maximum count rate for each germanium crystal. This without a better peak-to-total and higher efficiency. The main characteristics of these spectrometers are the lack of Compton suppression shields, which has been replaced with gamma-ray tracking: The track of the gamma-ray through the arrays is reconstructed using interaction points given by pulse-shape analysis. For this method to by efficient and have a high probability to reject tracks from gamma-rays that were not fully absorbed it is crucial that the pulse-shape analysis giving the interaction positions and energies are accurate. The accuracy of the PSA will depend of how well the detector response is determined, and to a lesser degree to the algorithm used for the PSA. The characterisation of the used HPGe detectors are hence of great importance, and represents at the same time a difficult problem. In this paper a computer code written to model the 36 times segmented HPGe germanium detectors used in AGATA and GRETA will be described, together with the application of this code to the problem of detector characterisation and pulse-shape analysis.

Extensive work has been done to model the response of these highly segmented germanium detectors.

We will begin with describing the AGATAGeFEM code and the models and assumptions made in section 4. The use of the code to benchmark the effect of cross talk and noise for on two pulse-shape algorithms covered in section 6. Finally, conclusions will be drawn in section 7.

2 A short introduction to the generation of pulse shapes in semiconductor detectors

The pulse-shape formation in any detector based on the motion of charge carriers can be calculated using the Shockley-Ramo theorem [5,6], which states that the induced charge on an electrode due to moving charges can be calculated as

$$\frac{dQ(t)}{dt} = e\left[N_h\ \boldsymbol{v}_h(\boldsymbol{r}_h)\cdot\boldsymbol{W}(\boldsymbol{r}_h) - N_e\ \boldsymbol{v}_e(\boldsymbol{r}_e)\cdot\boldsymbol{W}(\boldsymbol{r}_e)\right] \quad (1)$$

where $\boldsymbol{W}(\boldsymbol{r}_{e,h}) = -\nabla\Phi_W(\boldsymbol{r}_{e,h})$ is the weighting field, $N_{e,h}$ are the number of charge carriers for electrons and holes, and $\boldsymbol{v_{e,h}}(\boldsymbol{r_{e,h}})$ are the charge carrier velocities, which are functions of the electric field $\boldsymbol{E}(\boldsymbol{r})$. The electric field is calculated from the electric potential as $\boldsymbol{E}(\boldsymbol{r}) = -\nabla\Phi(\boldsymbol{r})$. Since the electric and weighting fields are two fundamental quantities, the calculation of pulse shapes for any semiconductor detector begins with solving the two differential equations

$$\nabla^2\Phi(\boldsymbol{r}) = -\frac{\rho(\boldsymbol{r})}{\epsilon_{Ge}} \tag{2}$$

and

$$\nabla^2\Phi_W(\boldsymbol{r}) = 0 \tag{3}$$

known as the Poisson and Laplace equations. They describe the electric and weighting potentials, respectively. In equation 2, $\rho(\boldsymbol{r})$ is the free charge distribution in the detector and ϵ_{Ge} the dielectric constant for germanium. The weighting potential $\Phi_W(\boldsymbol{r})$ is not an electric potential but a “tool”\ used to calculate the current on the collecting electrode. It is calculated by setting it to one on the collecting electrode and zero on all other contacts and then solving the Laplace equation.

One of the major difficulties one trying to solve equation 1 is to find the correct dependence for the charge carrier velocities $\boldsymbol{v_{e,h}}(\boldsymbol{r_{e,h}})$ as a function of the electric field $\boldsymbol{E}(\boldsymbol{r})$. For detector cold to liquid nitrogen temperatures operating with electric field in the order of 10^5 V/m the charge carriers will no longer follow a trajectory parallel to the electric field, this due to the anisotropy of the charge carrier velocity. The physics and the models used in this work will be discussed in section 3.

The final part of producing a realistic detector response it the application of a filter to reproduce the effects of the limited band with of the electronics and other effects such as electronic cross talk. This could in principle be done by measuring the response of the system using a pulse generator. Such an approach is however often not practical since single germanium crystals can be used with different electronics. It is often sufficient and always more practical to approximate the true response of the electronics with analytical function.

3 Charge carrier motion in high purity germanium detectors

Several models are developed for carrier mobilities in germanium crystals cooled down to liquid nitrogen temperatures ($\approx -175^\circ$ Celsius). For the electrons the model of Nathan [7] as described by Mihailescu [8] is used in this work. This model describes the anisotropy of the electron drift velocity observed in germanium with high accuracy, and is used to model the drift of electrons in AGATAGeFEM.

Crucial for all pulse shape calculations are good models for the charge carrier velocities as a function of the electric field. A commonly used function [9] to describe the charge carrier velocity is

$$\boldsymbol{v}(\boldsymbol{r}) = \frac{\mu_0\boldsymbol{E}(\boldsymbol{r})}{\left(1 + (E(\boldsymbol{r})/E_0)^\gamma\right)^{1/\gamma}} - \mu_n\boldsymbol{E}(\boldsymbol{r}), \tag{4}$$

where E_0, γ, μ_n, and μ_0 are experimentally adjusted parameters. This parametrision is valid when the electric field is parallel to one of the symmetry axes <100>, <110> or <111>. In all other cases the charge carrier velocity will not be parallel to the electric field (the apparent breaking of the conservation of momentum is absorbed by crystal). For the hole mobility B. Bruyneel et al. [10] have developed a model based on the so-called "streaming motion" concept where the holes are accelerated to a threshold energy where the holes emit an optical phonon, losing most of its energy, and is then re-accelerated in the applied electric field to the threshold energy and so on. In this work however, another model based on the assumption that the variation in carrier velocity as a function of the electric field can be described by the fraction of holes populating the light-hole band and the heavy-hole band and a field dependent relaxation time. The anisotropy is given by the effective masses being the second derivative of the energy of the hole bands. While not completely founded to the much higher energy of the light compared to the heavy hole band, this model do reproduce experimental data for hole drift velocities. For holes the surfaces of equal energy in the conduction bands are not ellipsoids, which means that the reciprocal effective mass tensor will depend on the direction of the wave vector $\boldsymbol{k}$. Here the assumption was made that the wave vector is parallel to the applied electric field. The hole energy functions are [11]

$$\epsilon_h(k) = Ak^2 \pm \left[B^2k^4 + C^2\left(k_x^2k_y^2 + k_y^2k_z^2 + k_z^2k_x^2\right)\right]^{1/2} \tag{5}$$

where the positive (negative) sign is for the light (heavy) hole band. Using equation

$$\left(\frac{1}{m^*}\right)_{\mu\nu} = \frac{1}{\hbar^2}\frac{d^2\epsilon(k)}{dk_\mu dk_\nu} \equiv \bar{\bar{\Gamma}} \tag{6}$$

to calculate the reciprocal effective mass tensor, we have

$$\boldsymbol{v}_h = q\mathcal{T}(E)\left[\mathcal{F}(E)\,\bar{\bar{\Gamma}}_h^{heavy} + (1-\mathcal{F}(E))\,\bar{\bar{\Gamma}}_h^{light}\right]\boldsymbol{E}. \tag{7}$$

Comparing equation 7 with

$$\boldsymbol{v} = qt\bar{\bar{\Gamma}}\boldsymbol{E}, \tag{8}$$

the factor $\mathcal{T}(E)$ in the latter equation corresponds to t in the former and should thus be considered an electric-field dependent relaxation time. $\mathcal{F}(E)$ is the fraction of the holes moving in the heavy hole band and it is also assumed to be field dependent. Equation 4 can now, as in the case for electrons, be used to calculate the hole drift velocities in the $< 100 >$ and $< 111 >$ directions. Using these velocities one can solve for $\mathcal{T}(E)$ and $\mathcal{F}(E)$ for

the electric-field strength in question. A big difference for holes as compared to electrons is that the reciprocal effective mass tensor now will change as the direction of the electric field changes. In figure 1 the anisotropy of charge carrier transport is illustrated. Here a deficiency of the model can be noted looking at the v_{φ}^{h} shown in the bottom right corner. There should be no anisotropy in any of the <100>, <110>, or <111> directions as they are symmetry axis in germanium, as is the case for the electrons shown in the left column. If there has been no anisotropy the top row would have shown perfect spheres in one color and the second and third row have shown zero velocities. It should be noted that nor the drift model for electrons nor for holes tries to model the effects of crystal temperature or impurity concentrations on the charge carrier drift velocities although these effects do modify the drift velocity [12]. The effect of varying the hole drift velocities have been studied within the GRETINA collaboration [13] where it was concluded that for the moment the position resolution is not limited by how the hole mobility is modeled.

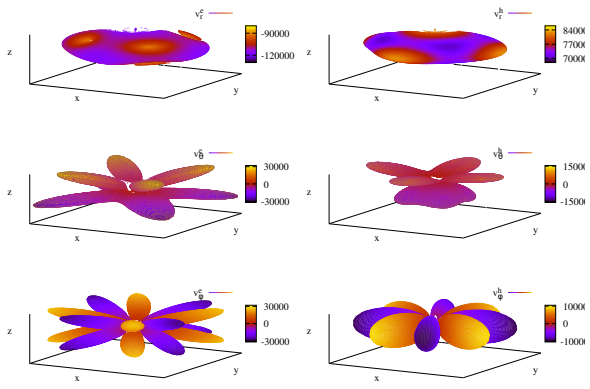

Fig. 1. Plot of charge carrier velocities as a function of the direction of the electric field. The column to the right is for electrons whereas the column to the right is for holes. The three rows show the $\hat{r}$, $\hat{\theta}$, $\hat{\phi}$ components of the velocities, respectively.

4 The AGATAGeFEM code

There are several codes and program packages that have been developed to calculate pulse shapes from HPGe detectors such as the detector elements that build up AGATA. Some examples are MGS [14], JASS [15,15,16] and ADL [17,10,18]. Although they differ in details they all have in common that they use methods based on finite difference to solve the partial differential equations (Laplace equation) needed to calculate the electric field in the detector and the weighting potentials used to calculate the pulse shapes from the different electrodes of the detector. However, the complex shapes of the AGATA crystals does not allow for an exact reproduction of their geometry using a finite difference scheme. This is a problem that can be circumvented using finite element methods (FEM). It is not within the scope of this paper to describe FEM, and we refer to [19] and references therein.

AGATAGeFEM is an effort to use FEM to calculate the electric and weighting potentials of AGATA type germanium detectors, relying heavily on high quality open source software. The program is written in C++ and leverage quite heavily both object orientation and the template features of C++ (but very little C++11). For charge carrier transport the ordinary differential equation solvers of the Gnu Scientific Library [20] were chosen. The geometry is describded to machine precision for charge transport and mesh genertion. Earlier versions of the program used mainly a library called dealii [21,22]. This is a very flexible code that allows an iterative refinement of the FEM mesh in a very simple way. However, the mesh cell geometry is limited to quadrilaterals and hexahedra. This is from solving the partial differential equations very good choices. However, as I not want to project down the solutions to a regular grid when using them in charge carrier transport process and calculations of the induced signals via the Shockley-Ramo theorem. Laying behind this is the idea that the refinement procedure tells where high granularity is needed and all projection to regular grid deteriorates this information. The problem is then that to find the correct cell in an irregular mesh requires at some point to ask cells if a points belongs to them and hexahedra cells have boundaries that are curved making these calculations quite complicated. As a result the first version of AGATAGeFEM was capable of calculating about 2-3 pulse shapes/s. While this is enough to calculate a basis for use with PSA it is far from enough for using the code in fitting of parameters used in the pulse shape calculations or to use it in a complete Monte Carlo simulation chain. I therefore moved the FEM part of the program into using the libmesh library [23]. It uses tetrahedra with each side defined by three points making the calculation whether a point is inside a cell or not much faster. I further more restrained to the use of only linear basis function in the solution. This way the code reproduced the results from before but a factor of almost 100 faster.

Other features of the AGATAGeFEM is that it is fully parallelized using both threads and the MPI interface to allow field calculations as well as for pulse-shape calculations and for fitting the parameters that enter into pulse-shape calculations using χ^2 fitting based on the Minuit and Minuit2 [24] that comes with ROOT [25]. It further has an interface allowing calculating both fields and pulses and displaying these inside the chosen detector geometry from the ROOT interpreter interface (the cint and cling interpreter). It has further a very simple server client mechanism allowing other programs to ask the server to calculate pulse shapes for it.

There further exsists needed miscellaneous codes for applying pre-amplifier response (defined in time domain), cross talk, to re-sample pulse shapes, compare pulse shapes,

calculate pulse shapes from the output of the Agata geant4 MC [26] etc.

4.1 AGATA Detector model

4.1.1 Geometry

The AGATA crystals are 90 mm long and have an diameter of 80 mm. They have been produces in four different shapes. Symmetric hexagonal prototypes and three different non-symmetric hexagonal shapes for use in the AGATA. The non-symmetric shapes are needed to be able to close pack the crystals in an spherical geometry. For details of the AGATA crystal geometries, see [3]. In figure 2 the geometry of a "A" type AGATA crystal is shown. For the generation of the FEM mesh OpenCASCADE models of the detectors where generated whereas for the charge transportation the detector geometries where implemented in C++ as the union of a cylinder and six planes or using the CSG geometry of geant4 [27]. The hole corresponding to the core contact was modeled with the possibility of changing the radius of at the bottom of the hole. The two different geometrical models of the detectors are equivalent, and both flexieble enouch to allow off-centered bore holes, bore holes with angles, etc if this would have to be tested. Examples of the geometry are shown in figures 3 and 4.

4.1.2 Calculations of the electric fields and weighting fields

AGATAGeFEM uses a total of 40 fields when calculating the pulse shapes. The first 37 corresponds to the weighting-fields for the 36 segments and the core. These are, expect for the central contact wich is trivial, defined either using the limiting depth values and start and stop angle or using the intersection between the detector surface and four planes. The segments to not have to cover the hole surface of the detector, but presently no implementation of suitable boundary conditions for the electric field calculations are present in the code limiting the value of this option.

To calculate the electric field while solving the charge transport equations AGATAGeFEM uses three fields. The first one is the solution to the Laplace equation with 0 V on the surface of the detector and V_bias V on the central contact. The second one is the solution of the Poisson equation assuming (\0\) V on both the surface and the central contact but with a impurity contribution of 1 at the front of the detector that decreases linearly as a function of depth to the back of the detector. The third and final field is like the second but reversing the slope of the impurity concentration. This allows varying the effective impurity concentration and its effect on the electric field in the detector without recalculating the fields, important when trying to fit detector parameters to experimental signals.

For solving the Laplace equation and the Poisson equation AGATAGeFEM uses the libmesh library [23].

4.1.3 Solving the charge transport equation

The detector pulses are calculated by first transporting the point representing electrons and the point representing holes from the point of origin using

$$\frac{d\boldsymbol{r_{e,h}}}{dt} = \boldsymbol{v_{e,h}}\left(\boldsymbol{E}\right). \tag{9}$$

This pair of equations are solved separately for the holes and the electrons using an solver algorithm with an adaptive time step. The program AGATAGeFEM allows the user to choose between any of the possible algorithms provided by GSL, but the default choice it that of the embedded Runge-Kutta Prince-Dormand method. The paths of the electrons and the paths are sampled at a given frequency, by default a timestep of 1 ns is used. As the charge carriers approaches the boundary of the detector this time step is adapted to allow an accurate description of the pulse shapes.

In the next step the charge on electrode i is calculated using

$$Q_i\left(t\right) = q\left(\Phi^i_W(\boldsymbol{r_e}(t)) - \Phi^i_W(\boldsymbol{r_h}(t))\right) \tag{10}$$

for all 37 signals. It should be noted that the core signal has the opposite polarity of the segment signals and that the sum of all signals should be identical to zero.

4.1.4 Convoluting with response function

The signals can the optionally be convoluted with the response of the electronics. In this work the response of the electronics have been modeled by convoluting the calculated signals with the function shown (in time-domain) in figure 5. The effect of so-called crosstalk, both linear and differential, can also be included in the response function if needed. For in-depth discussion concerning crosstalk in segmented germanium detectors, see [28,29]. An example of the signals calculated with and without response function is given in figure 6. The effect of linear and derivative cross talk is also shown.

5 Scan of parameter sensitivity

In order to understand the impact of different parameters that enter into the calculations of pulse shapes the sensitivity of the pulse shapes to each parameter was calculated for a large number of points inside a detector. In figure 7 the extraction of the sensitivity which is defined as the second derivative of the square sum of the difference between a reference pulse and the a pulse calculated with a parameter changed a fraction.

In figure 8 is shown at how many positions in the detector that each parameter has the largest sensitivity. It can be seen that at most points it is the parameters that parameterise the velocity of the charge carriers in the <100> direction that is dominating. Looking at figure 9 one can

notice however that the highest average sensitivity for the dominating positions is found for the crystal orientation followed by the parameterization of the hole mobility in the <111> direction. This would suggest that these parameters are most likely to make a signal change "net-charge segment". In figure 10 the sensitivity as a function of position in the detector volume is shown for the $\mu_e^{<100>}$ parameter. It is quite homogeneous inside the volume although the projection on the XY plane shows that, apart from the volume effect, is an increase in sensitivity close to the <100> directions. This is normal as the parameterization of the charge carrier velocity only depends on parameters corresponding to that direction. A similar pattern can be seen for the $\mu_h^{<100>}$ parameter in figure 11, but with the maximum shifted towards lower radii corresponding to pulses in which the hole drift contributes more to the pulse shapes. For the parameters $\mu_e^{<111>}$ and $\mu_h^{<111>}$, shown in figures 12 and 13 the situation is a bit different. For the electrons the pattern is what can be expected, i.e. parameters concerning the <111> direction show sensitivity in the region where charge transport is parallelle to the <111> direction. For the holes the situation seems less clear. The pattern is not reflecting the <111> direction in the crystal. This is not needed in the model as it, unlike the model for the electrons, do not impose that the charge carriers when the electric field is parallel to a symmetry axis are moving parallel with the axis, which by symmetry arguments has to be wrong. This can also be seen in figure 1 where the φ component of the hole velocity is non zero in the xy-plane <100> directions. It is based on this clear that the hole velocity model used should be changed for future work as comparisons with experimental in order to fit parameters would be difficult.

6 Evaluation of effects of cross talk and noise for different PSA using Monte Carlo simulation data

Using the code AGATAGeFEM the resolution for Gridsearch methods and the Singular Value Decomposition methods as a function of noise and inclusion of differential and linear crosstalk have also been investigated. Assuming that the detector physics of a segmented germanium detector is well known, the problem of determining the coordinates of an γ-ray interaction in a large volumes HPGe detector dependence closely on the knowledge of the response of the electronics and on the signal-to-noise ratio. These two aspects have been studies by performing PSA on a dataset calculated using the same code as that used to calculate the reference dataset of pulse shapes used by the PSA code. On this reference set of shapes different amount of noise have been added. Each position where then analysed 20 times, each time with different noise added. Also added are linear and differential crosstalk. This have been done both for the gridsearch method and for the matrix method [30]. The results are summarized in table 1. It should be noticed that according to this work the crosstalk has a very limited influence on the resolution, neither on the average reconstructed position nor by introducing systematic errors. In figures 14 and 15 two-dimensional projections of the by the two different PSA algorithms determined interaction positions are shown. For both cases both linear and differential crosstalk have been included in the simulated events but not in the database used for the PSA. Looking at figure 14 and 15 a striking difference shows up for large noises. The gridsearch algorithm tends to cluster points towards the segment boundaries whereas the matrix method seems to move the points towards the most likely point, i.e. the barycenter of the segment.

In the work by Söderström et al. [31], the experimental position resolution has been investigated as a function of the energy deposited at the interaction point. Data from the work of Söderström et al. work is presented together with the result of pulse shape analysis performed on simulated traces done with-in the scope of this work in figure 17. It is interesting to note that the extensive gridsearch is doing better on simulated data than what has been experimentally for energies above about 50 keV whereas the Matrix inversion using SVD decomposition to suppress increase the signal-to-noise ratio is performing better at very low interaction energies.

7 Conculsions

A C++ based code called AGATAGeFEM aimed at modeling segmented high-purity detectors has been developed. It allows the implementation of the detector geometry and segmentation schemes to with in machine precision and uses state-of-the-art Finite Element Methods to solve the Laplace and Poisson equations. The resulting fields are calculated using the basis functions and support points of the actual FEM grid, i.e. function evaluation rather than interpolation.

The charge transport equations are solved using time adaptive Runge-Kutta methods from the GNU Scientific Libraray. To the induced charge signals linear and differential cross talk is added together with the preamplifier response function modeled in time domain. The model use in AGATAGeFEM for hole charge carrier velocity has to be improved.

As an example of applications AGATAGeFEM is used to invesitgate the impact of cross talk and noise for the grid search pulse shape method and for the SVD PSA method. The result suggest that cross talk at the level of what is found in AGATA has no real impact on the result of the PSA.

Acknowledgement

The author would like to thank the AGATA collaboration.

References

1. J. Simpson, The euroball spectrometer, Zeitschrift für Physik A Hadrons and Nuclei 358 (2) (1997) 139–143.

Table 1. Full width at half maximum for different amount of noise for a inclusive gridsearch on a 1x1x1 mm^3 basis and using the SVD matrix method with the same basis.

	No crosstalk		
Noise		GS [mm]	
[% rms]	Δx	Δy	Δz
0.6	1.3	1.4	1.3
3.1	2.4	2.5	2.4
6.1	4.2	4.7	4.2
12	8.8	10	8.9
18	13	14	13
37	20	19	17
		SVD [mm]	
	Δx	Δy	Δz
0.6	2.4	2.5	1.8
3.1	5.5	5.7	4.2
6.1	7.5	7.8	5.9
12	10	10	8.4
18	12	12	10
37	16	16	13
	Full crosstalk		
Noise		GS [mm]	
[% rms]	Δx	Δy	Δz
0.6	1.4	1.4	1.3
3.1	2.4	2.5	2.4
6.1	4.3	4.7	4.2
12	8.8	10	8.9
18	13	14	13
37	20	20	17
		SVD [mm]	
	Δx	Δy	Δz
0.6	2.8	2.8	2.0
3.1	5.5	5.7	4.3
6.1	7.4	7.7	5.9
12	10	10	8.4
18	12	12	10
37	16	16	13

doi:10.1007/s002180050290.
URL http://dx.doi.org/10.1007/s002180050290

2. M. A. Deleplanque, R. M. e. Diamond, 1987 gammasphere proposal preprint lbnl-5202, Tech. rep., LBNL (1987).
3. S. Akkoyun, A. Algora, B. Alikhani, F. Ameil, G. de Angelis, L. Arnold, A. Astier, A. Ataç, Y. Aubert, C. Aufranc, A. Austin, S. Aydin, F. Azaiez, S. Badoer, D. Balabanski, D. Barrientos, G. Baulieu, R. Baumann, D. Bazzacco, F. Beck, T. Beck, P. Bednarczyk, M. Bellato, M. Bentley, G. Benzoni, R. Berthier, L. Berti, R. Beunard, G. L. Bianco, B. Birkenbach, P. Bizzeti, A. Bizzeti-Sona, F. L. Blanc, J. Blasco, N. Blasi, D. Bloor, C. Boiano, M. Borsato, D. Bortolato, A. Boston, H. Boston, P. Bourgault, P. Boutachkov, A. Bouty, A. Bracco, S. Brambilla, I. Brawn, A. Brondi, S. Broussard, B. Bruyneel, D. Bucurescu, I. Burrows, A. Bürger, S. Cabaret, B. Cahan, E. Calore, F. Camera, A. Capsoni, F. Carrió, G. Casati, M. Castoldi, B. Cederwall, J.-L. Cercus, V. Chambert, M. E. Chambit, R. Chapman, L. Charles, J. Chavas, E. Clément, P. Cocconi, S. Coelli, P. Coleman-Smith, A. Colombo, S. Colosimo, C. Commeaux, D. Conventi, R. Cooper, A. Corsi, A. Cortesi, L. Costa, F. Crespi, J. Cresswell, D. Cullen, D. Curien, A. Czermak, D. Delbourg, R. Depalo, T. Descombes, P. Désesquelles, P. Detistov, C. Diarra, F. Didierjean, M. Dimmock, Q. Doan, C. Domingo-Pardo, M. Doncel, F. Dorangeville, N. Dosme, Y. Drouen, G. Duchêne, B. Dulny, J. Eberth, P. Edelbruck, J. Egea, T. Engert, M. Erduran, S. Ertürk, C. Fanin, S. Fantinel, E. Farnea, T. Faul, M. Filliger, F. Filmer, C. Finck, G. de France, A. Gadea, W. Gast, A. Geraci, J. Gerl, R. Gernhäuser, A. Giannatiempo, A. Giaz, L. Gibelin, A. Givechev, N. Goel, V. González, A. Gottardo, X. Grave, J. Grebosz, R. Griffiths, A. Grint, P. Gros, L. Guevara, M. Gulmini, A. Görgen, H. Ha, T. Habermann, L. Harkness, H. Harroch, K. Hauschild, C. He, A. Hernández-Prieto, B. Hervieu, H. Hess, T. Hüyük, E. Ince, R. Isocrate, G. Jaworski, A. Johnson, J. Jolie, P. Jones, B. Jonson, P. Joshi, D. Judson, A. Jungclaus, M. Kaci, N. Karkour, M. Karolak, A. Kaşkaş, M. Kebbiri, R. Kempley, A. Khaplanov, S. Klupp, M. Kogimtzis, I. Kojouharov, A. Korichi, W. Korten, T. Kröll, R. Krücken, N. Kurz, B. Ky, M. Labiche, X. Lafay, L. Lavergne, I. Lazarus, S. Leboutelier, F. Lefebvre, E. Legay, L. Legeard, F. Lelli, S. Lenzi, S. Leoni, A. Lermitage, D. Lersch, J. Leske, S. Letts, S. Lhenoret, R. Lieder, D. Linget, J. Ljungvall, A. Lopez-Martens, A. Lotodé, S. Lunardi, A. Maj, J. van der Marel, Y. Mariette, N. Marginean, R. Marginean, G. Maron, A. Mather, W. Meczyński, V. Mendéz, P. Medina, B. Melon, R. Menegazzo, D. Mengoni, E. Merchan, L. Mihailescu, C. Michelagnoli, J. Mierzejewski, L. Milechina, B. Million, K. Mitev, P. Molini, D. Montanari, S. Moon, F. Morbiducci, R. Moro, P. Morrall, O. Möller, A. Nannini, D. Napoli, L. Nelson, M. Nespolo, V. Ngo, M. Nicoletto, R. Nicolini, Y. L. Noa, P. Nolan, M. Norman, J. Nyberg, A. Obertelli, A. Olariu, R. Orlandi, D. Oxley, C. Özben, M. Ozille, C. Oziol, E. Pachoud, M. Palacz, J. Palin, J. Pancin, C. Parisel, P. Pariset, G. Pascovici, R. Peghin, L. Pellegri, A. Perego, S. Perrier, M. Petcu, P. Petkov, C. Petrache, E. Pierre, N. Pietralla, S. Pietri, M. Pignanelli, I. Piqueras, Z. Podolyak, P. L. Pouhalec, J. Pouthas, D. Pugnére, V. Pucknell, A. Pullia, B. Quintana, R. Raine, G. Rainovski, L. Ramina, G. Rampazzo, G. L. Rana, M. Rebeschini, F. Recchia, N. Redon, M. Reese, P. Reiter, P. Regan, S. Riboldi, M. Richer, M. Rigato, S. Rigby, G. Ripamonti, A. Robinson, J. Robin, J. Roccaz, J.-A. Ropert, B. Rossé, C. R. Alvarez, D. Rosso, B. Rubio, D. Rudolph, F. Saillant, E. ¸Sahin, F. Salomon, M.-D. Salsac, J. Salt, G. Salvato, J. Sampson, E. Sanchis, C. Santos, H. Schaffner, M. Schlarb, D. Scraggs, D. Seddon, M. Şenyiğit, M.-H. Sigward, G. Simpson, J. Simpson, M. Slee, J. Smith, P. Sona, B. Sowicki, P. Spolaore, C. Stahl, T. Stanios, E. Stefanova, O. Stézowski, J. Strachan, G. Suliman, P.-A. Söderström, J. Tain, S. Tanguy, S. Tashenov, C. Theisen, J. Thornhill, F. Tomasi, N. Toniolo, R. Touzery, B. Travers, A. Triossi, M. Tripon, K. Tun-Lanoë, M. Turcato, C. Unsworth, C. Ur, J. Valiente-Dobon, V. Vandone, E. Vardaci, R. Venturelli, F. Veronese, C. Veyssiere, E. Viscione, R. Wadsworth, P. Walker, N. Warr, C. Weber, D. Weisshaar, D. Wells, O. Wieland, A. Wiens, G. Wittwer, H. Wollersheim, F. Zocca, N. Zamfir, M. Ziebliński, A. Zucchiatti, Agata-advanced {GAmma} tracking

array, Nuclear Instruments and Methods in Physics Research Section A: Accelerators, Spectrometers, Detectors and Associated Equipment 668 (2012) 26 – 58. doi:http://dx.doi.org/10.1016/j.nima.2011.11.081.
URL http://www.sciencedirect.com/science/article/pii/S0168900211021516

4. I. Y. Lee, M. A. Deleplanque, K. Vetter, Developments in large gamma-ray detector arrays, Reports on Progress in Physics 66 (7) (2003) 1095.
URL http://stacks.iop.org/0034-4885/66/i=7/a=201
5. S. Ramo, Proc. IRE 27 (1939) 584.
6. W. Shockley, J. Appl. Phys. 9 (1938) 635.
7. M. I. Nathan, Anisotropy of the conductivity of n-type germanium at high electric fields, Phys. Rev. 130 (1963) 2201–2204. doi:10.1103/PhysRev.130.2201.
URL http://link.aps.org/doi/10.1103/PhysRev.130.2201
8. L. Mihailescu, W. Gast, R. Lieder, H. Brands, H. Jäger, The influence of anisotropic electron drift velocity on the signal shapes of closed-end {HPGe} detectors, Nuclear Instruments and Methods in Physics Research Section A: Accelerators, Spectrometers, Detectors and Associated Equipment 447 (3) (2000) 350 – 360. doi:http://dx.doi.org/10.1016/S0168-9002(99)01286-3.
URL http://www.sciencedirect.com/science/article/pii/S0168900299012863
9. G. Knoll, Radiation Detection and Measurement, Wiley, 2000.
10. B. Bruyneel, P. Reiter, G. Pascovici, Characterization of large volume {HPGe} detectors. part i: Electron and hole mobility parameterization, Nuclear Instruments and Methods in Physics Research Section A: Accelerators, Spectrometers, Detectors and Associated Equipment 569 (3) (2006) 764 – 773. doi:http://dx.doi.org/10.1016/j.nima.2006.08.130.
URL http://www.sciencedirect.com/science/article/pii/S0168900206015166
11. C. Kittel, Introduction to Solid State Physics, Wiley, 1996.
URL https://books.google.fr/books?id=1X8pAQAAMAAJ
12. H. Mei, D.-M. Mei, G.-J. Wang, G. Yang, The impact of neutral impurity concentration on charge drift mobility in p-type germanium, Journal of Instrumentation 11 (12) (2016) P12021–P12021. doi:10.1088/1748-0221/11/12/p12021.
URL https://doi.org/10.1088%2F1748-0221%2F11%2F12%2Fp12021
13. V. Prasher, M. Cromaz, E. Merchan, P. Chowdhury, H. Crawford, C. Lister, C. Campbell, I. Lee, A. Macchiavelli, D. Radford, A. Wiens, Sensitivity of gretina position resolution to hole mobility, Nuclear Instruments and Methods in Physics Research Section A: Accelerators, Spectrometers, Detectors and Associated Equipment 846 (2017) 50 – 55. doi:https://doi.org/10.1016/j.nima.2016.11.038.
URL http://www.sciencedirect.com/science/article/pii/S0168900216311925
14. [link].
URL http://www.iphc.cnrs.fr/-MGS-.html
15. M. Schlarb, R. Gernhäuser, S. Klupp, R. Krücken, Pulse shape analysis for γ-ray tracking (part i): Pulse shape simulation with jass, The European Physical Journal A 47 (10) (2011) 132. doi:10.1140/epja/i2011-11132-2.
URL http://dx.doi.org/10.1140/epja/i2011-11132-2
16. M. Schlarb, R. Gernhäuser, R. Krücken, Simulation and real-time analysis of pulse shapes from hpge detectors, Tech. rep. (2008).
17. B. Bruyneel, B. Birkenbach, P. Reiter, Pulse shape analysis and position determination in segmented hpge detectors: The agata detector library, The European Physical Journal A 52 (3) (2016) 1–11. doi:10.1140/epja/i2016-16070-9.
URL http://dx.doi.org/10.1140/epja/i2016-16070-9
18. B. Bruyneel, B. Birkenbach, P. Reiter, Pulse shape analysis and position determination in segmented hpge detectors: The agata detector library, The European Physical Journal A 52 (3) (2016) 70. doi:10.1140/epja/i2016-16070-9.
URL http://dx.doi.org/10.1140/epja/i2016-16070-9
19. S. C. Brenner, L. R. Scott, The Mathematical Theory of Finite ElementMethods, 2nd Edition, Vol. 15 of Texts in Applied Mathematics, Springer, 2002.
20. G. P. Contributors, GSL - GNU scientific library - GNU project - free software foundation (FSF), http://www.gnu.org/software/gsl/ (2010) [cited 2010-06-20 22:49:12].
URL http://www.gnu.org/software/gsl/
21. W. Bangerth, R. Hartmann, G. Kanschat, deal.II – a general purpose object oriented finite element library, ACM Trans. Math. Softw. 33 (4) (2007) 24/1–24/27.
22. G. Alzetta, D. Arndt, W. Bangerth, V. Boddu, B. Brands, D. Davydov, R. Gassmoeller, T. Heister, L. Heltai, K. Kormann, M. Kronbichler, M. Maier, J.-P. Pelteret, B. Turcksin, D. Wells, The deal.II library, version 9.0, Journal of Numerical Mathematics 26 (4) (2018) 173–183. doi:10.1515/jnma-2018-0054.
23. B. S. Kirk, J. W. Peterson, R. H. Stogner, G. F. Carey, libMesh: A C++ Library for Parallel Adaptive Mesh Refinement/Coarsening Simulations, Engineering with Computers 22 (3–4) (2006) 237–254, http://dx.doi.org/10.1007/s00366-006-0049-3.
24. M. Hatlo, F. James, P. Mato, L. Moneta, M. Winkler, A. Zsenei, Developments of mathematical software libraries for the lhc experiments, IEEE Transactions on Nuclear Science 52 (6) (2005) 2818–2822. doi:10.1109/TNS.2005.860152.
25. I. Antcheva, M. Ballintijn, B. Bellenot, M. Biskup, R. Brun, N. Buncic, P. Canal, D. Casadei, O. Couet, V. Fine, L. Franco, G. Ganis, A. Gheata, D. G. Maline, M. Goto, J. Iwaszkiewicz, A. Kreshuk, D. M. Segura, R. Maunder, L. Moneta, A. Naumann, E. Offermann, V. Onuchin, S. Panacek, F. Rademakers, P. Russo, M. Tadel, Root — a c++ framework for petabyte data storage, statistical analysis and visualization, Computer Physics Communications 180 (12) (2009) 2499 – 2512, 40 YEARS OF CPC: A celebratory issue focused on quality software for high performance, grid and novel computing architectures. doi:https://doi.org/10.1016/j.cpc.2009.08.005.
URL http://www.sciencedirect.com/science/article/pii/S0010465509002550
26. E. Farnea, F. Recchia, D. Bazzacco, T. Kröll, Z. Podolyák, B. Quintana, A. Gadea, Conceptual design and monte carlo simulations of the {AGATA} array, Nuclear

Instruments and Methods in Physics Research Section A: Accelerators, Spectrometers, Detectors and Associated Equipment 621 (1-3) (2010) 331 – 343. doi:http://dx.doi.org/10.1016/j.nima.2010.04.043.
URL http://www.sciencedirect.com/science/article/pii/S0168900210008922

27. S. Agostinelli, J. Allison, K. Amako, J. Apostolakis, H. Araujo, P. Arce, M. Asai, D. Axen, S. Banerjee, G. Barrand, F. Behner, L. Bellagamba, J. Boudreau, L. Broglia, A. Brunengo, H. Burkhardt, S. Chauvie, J. Chuma, R. Chytracek, G. Cooperman, G. Cosmo, P. Degtyarenko, A. Dell'Acqua, G. Depaola, D. Dietrich, R. Enami, A. Feliciello, C. Ferguson, H. Fesefeldt, G. Folger, F. Foppiano, A. Forti, S. Garelli, S. Giani, R. Giannitrapani, D. Gibin, J. G. Cadenas, I. González, G. G. Abril, G. Greeniaus, W. Greiner, V. Grichine, A. Grossheim, S. Guatelli, P. Gumplinger, R. Hamatsu, K. Hashimoto, H. Hasui, A. Heikkinen, A. Howard, V. Ivanchenko, A. Johnson, F. Jones, J. Kallenbach, N. Kanaya, M. Kawabata, Y. Kawabata, M. Kawaguti, S. Kelner, P. Kent, A. Kimura, T. Kodama, R. Kokoulin, M. Kossov, H. Kurashige, E. Lamanna, T. Lampén, V. Lara, V. Lefebure, F. Lei, M. Liendl, W. Lockman, F. Longo, S. Magni, M. Maire, E. Medernach, K. Minamimoto, P. M. de Freitas, Y. Morita, K. Murakami, M. Nagamatu, R. Nartallo, P. Nieminen, T. Nishimura, K. Ohtsubo, M. Okamura, S. O'Neale, Y. Oohata, K. Paech, J. Perl, A. Pfeiffer, M. Pia, F. Ranjard, A. Rybin, S. Sadilov, E. D. Salvo, G. Santin, T. Sasaki, N. Savvas, Y. Sawada, S. Scherer, S. Sei, V. Sirotenko, D. Smith, N. Starkov, H. Stoecker, J. Sulkimo, M. Takahata, S. Tanaka, E. Tcherniaev, E. S. Tehrani, M. Tropeano, P. Truscott, H. Uno, L. Urban, P. Urban, M. Verderi, A. Walkden, W. Wander, H. Weber, J. Wellisch, T. Wenaus, D. Williams, D. Wright, T. Yamada, H. Yoshida, D. Zschiesche, Geant4—a simulation toolkit, Nuclear Instruments and Methods in Physics Research Section A: Accelerators, Spectrometers, Detectors and Associated Equipment 506 (3) (2003) 250 – 303. doi:https://doi.org/10.1016/S0168-9002(03)01368-8.
URL http://www.sciencedirect.com/science/article/pii/S0168900203013688
28. B. Bruyneel, P. Reiter, A. Wiens, J. Eberth, H. Hess, G. Pascovici, N. Warr, D. Weisshaar, Crosstalk properties of 36-fold segmented symmetric hexagonal {HPGe} detectors, Nuclear Instruments and Methods in Physics Research Section A: Accelerators, Spectrometers, Detectors and Associated Equipment 599 (2-3) (2009) 196 – 208. doi:http://dx.doi.org/10.1016/j.nima.2008.11.011.
URL http://www.sciencedirect.com/science/article/pii/S0168900208015921
29. A. Wiens, H. Hess, B. Birkenbach, B. Bruyneel, J. Eberth, D. Lersch, G. Pascovici, P. Reiter, H.-G. Thomas, The {AGATA} triple cluster detector, Nuclear Instruments and Methods in Physics Research Section A: Accelerators, Spectrometers, Detectors and Associated Equipment 618 (1-3) (2010) 223 – 233. doi:http://dx.doi.org/10.1016/j.nima.2010.02.102.
URL http://www.sciencedirect.com/science/article/pii/S0168900210003384
30. P. Désesquelles, T. M. H. Ha, K. Hauschild, A. Korichi, F. Le Blanc, A. Lopez-Martens, A. Olariu, C. M. Petrache, Matrix formalism and singular-value decomposition for the location of gamma interactions in segmented hpge detectors, The European Physical Journal A 40 (2) (2009) 237–248. doi:10.1140/epja/i2008-10749-4.
URL http://dx.doi.org/10.1140/epja/i2008-10749-4
31. P.-A. Söderström, F. Recchia, J. Nyberg, A. Al-Adili, A. Ataç, S. Aydin, D. Bazzacco, P. Bednarczyk, B. Birkenbach, D. Bortolato, A. Boston, H. Boston, B. Bruyneel, D. Bucurescu, E. Calore, S. Colosimo, F. Crespi, N. Dosme, J. Eberth, E. Farnea, F. Filmer, A. Gadea, A. Gottardo, X. Grave, J. Grebosz, R. Griffiths, M. Gulmini, T. Habermann, H. Hess, G. Jaworski, P. Jones, P. Joshi, D. Judson, R. Kempley, A. Khaplanov, E. Legay, D. Lersch, J. Ljungvall, A. Lopez-Martens, W. Meczynski, D. Mengoni, C. Michelagnoli, P. Molini, D. Napoli, R. Orlandi, G. Pascovici, A. Pullia, P. Reiter, E. Sahin, J. Smith, J. Strachan, D. Tonev, C. Unsworth, C. Ur, J. Valiente-Dobón, C. Veyssiere, A. Wiens, Interaction position resolution simulations and in-beam measurements of the {AGATA} {HPGe} detectors, Nuclear Instruments and Methods in Physics Research Section A: Accelerators, Spectrometers, Detectors and Associated Equipment 638 (1) (2011) 96 – 109. doi:http://dx.doi.org/10.1016/j.nima.2011.02.089.
URL http://www.sciencedirect.com/science/article/pii/S016890021100489X
32. M. R. Dimmock, A. J. Boston, J. R. Cresswell, I. Lazarus, P. Medina, P. Nolan, C. Parisel, C. Santos, J. Simpson, C. Unsworth, Validation of pulse shape simulations for an agata prototype detector, IEEE Transactions on Nuclear Science 56 (4) (2009) 2415–2425. doi:10.1109/TNS.2009.2021842.
33. M. R. Dimmock, A. J. Boston, H. C. Boston, J. R. Cresswell, L. Nelson, P. J. Nolan, C. Unsworth, I. H. Lazarus, J. Simpson, Characterisation results from an agata prototype detector, IEEE Transactions on Nuclear Science 56 (3) (2009) 1593–1599. doi:10.1109/TNS.2009.2019103.

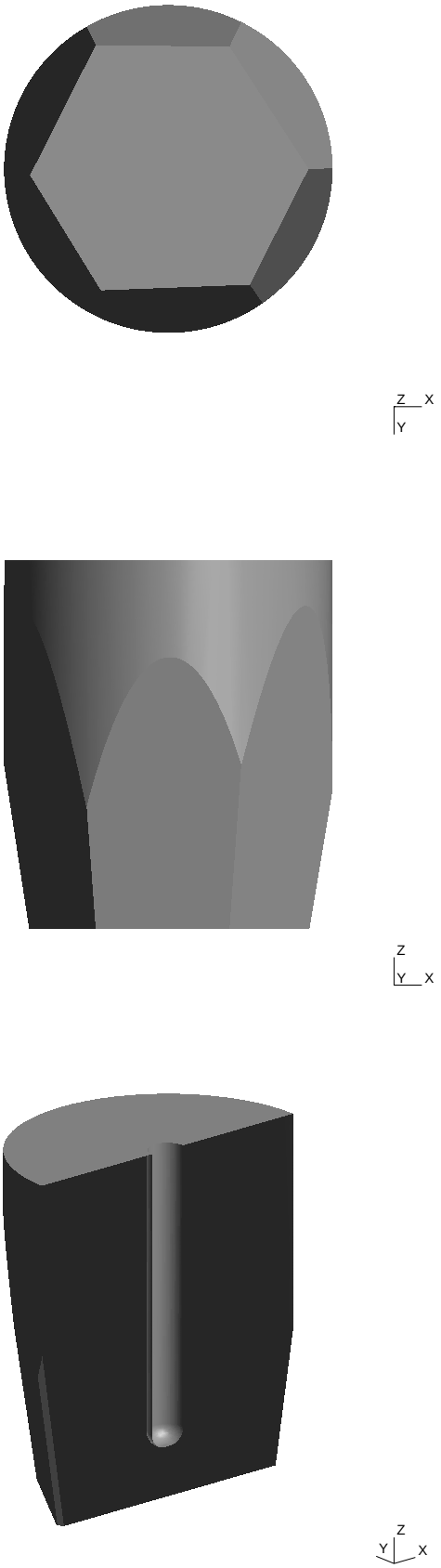

Fig. 2. Views of a "A" type AGATA crystal.

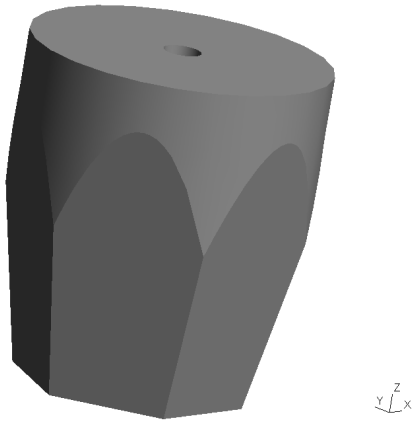

Fig. 3. A symmetric prototype crystal.

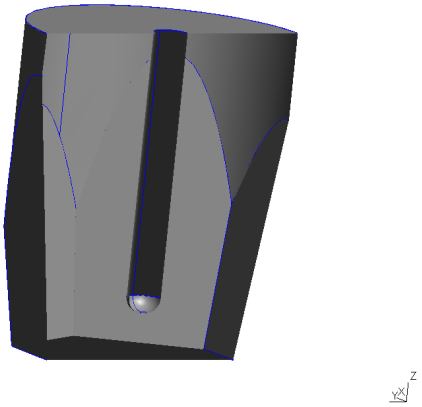

Fig. 4. A "C" type AGATA crystal. Half the volume is hidden to show the central contact.

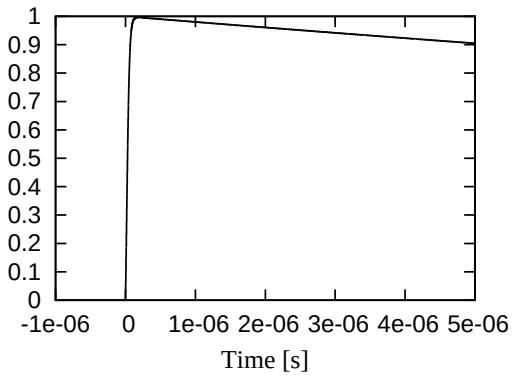

Fig. 5. Response function of the electronics shown in time domain.

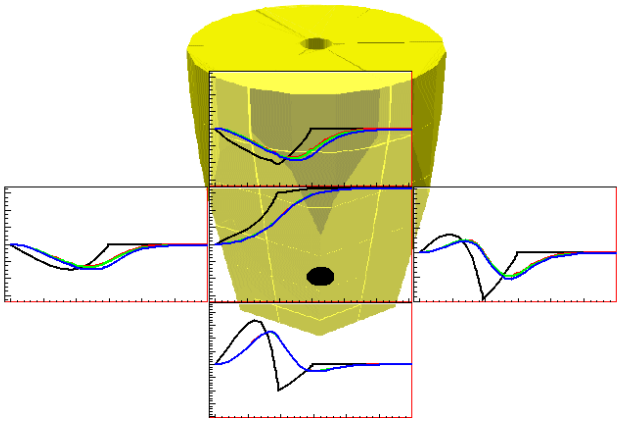

Fig. 6. Example of a pulse originating from R=24mm and z=23mm. The modulating effect of the response of the electronics is clearly seen. The effect of linear and derivative crosstalk is also shown. The netcharge segment is marked with a black circle.

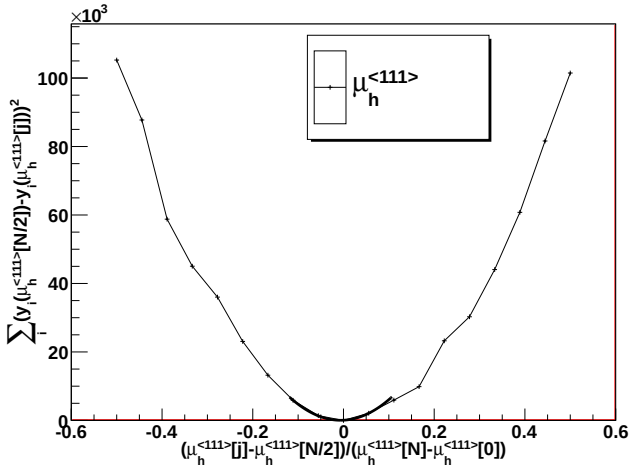

Fig. 7. Example of how the sensitivity of the pulse shapes to a specific parameter (in this case $\mu_h^{<111>}$) at a position in the detector is extracted.

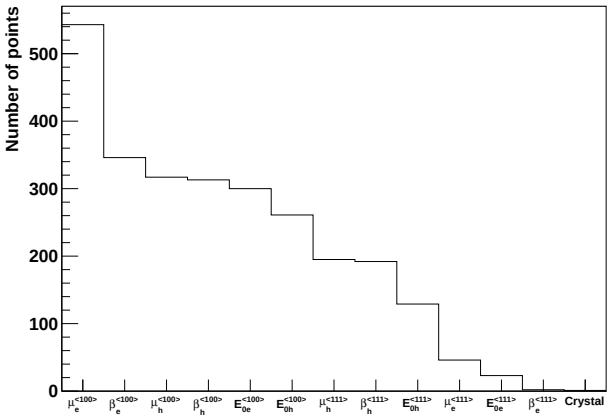

Fig. 8. Number of points in the crystal where a specific parameter had the largest influence

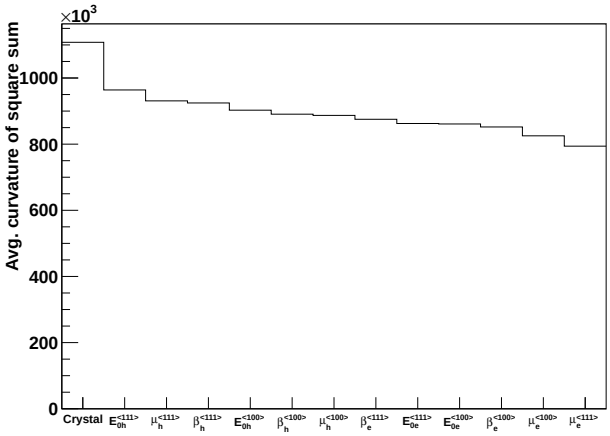

Fig. 9. The average sensitivity for different parameters taken over points where they had the largest sensitivity.

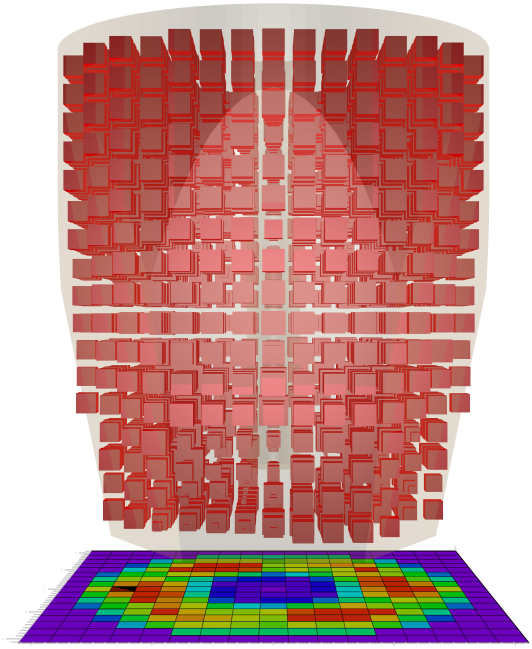

Fig. 10. The influence of the electron mobility in the <100> direction on the pulse shapes as a function of position

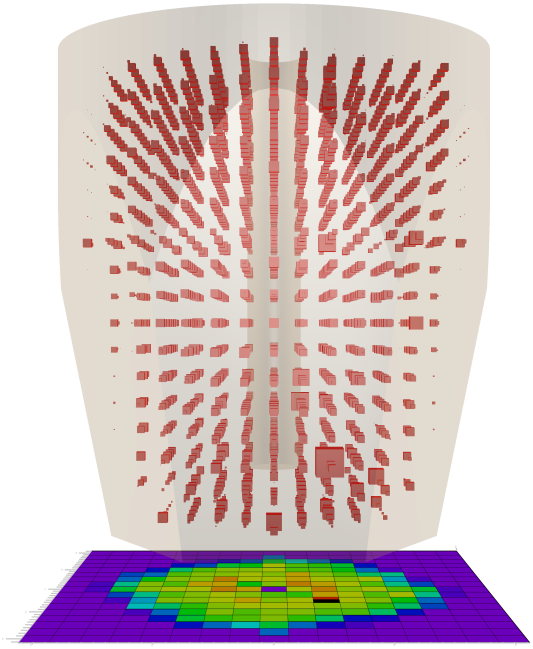

Fig. 11. The influence of the hole mobility in the <100> direction on the pulse shapes as a function of position

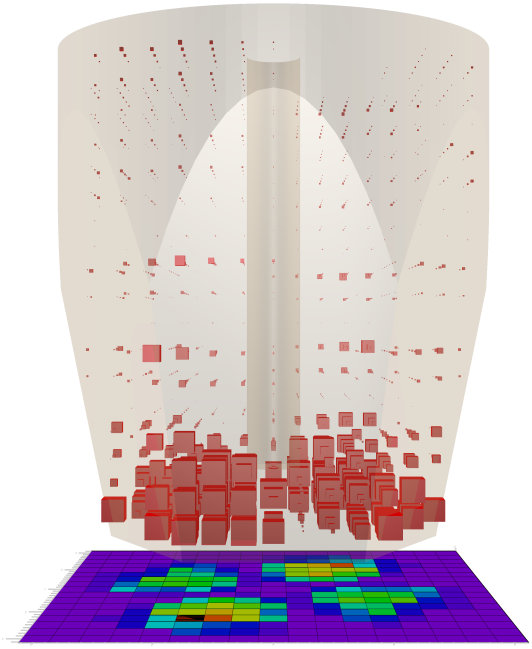

Fig. 12. The influence of the electron mobility in the <111> direction on the pulse shapes as a function of position.

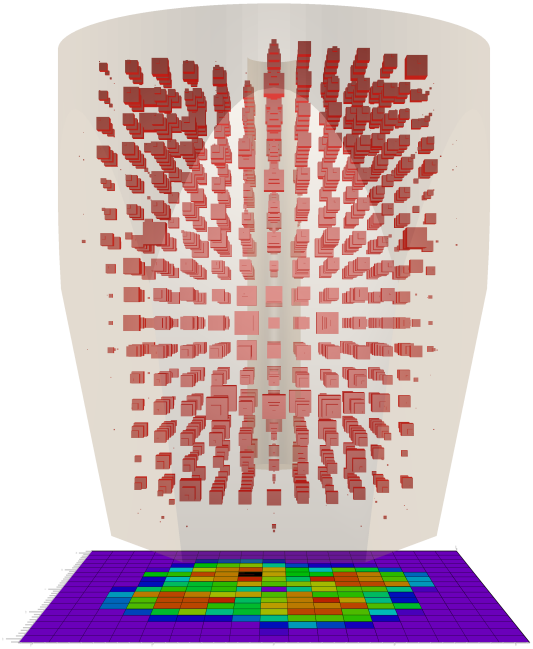

Fig. 13. The influence of the hole mobility in the <111> direction on the pulse shapes as a function of position

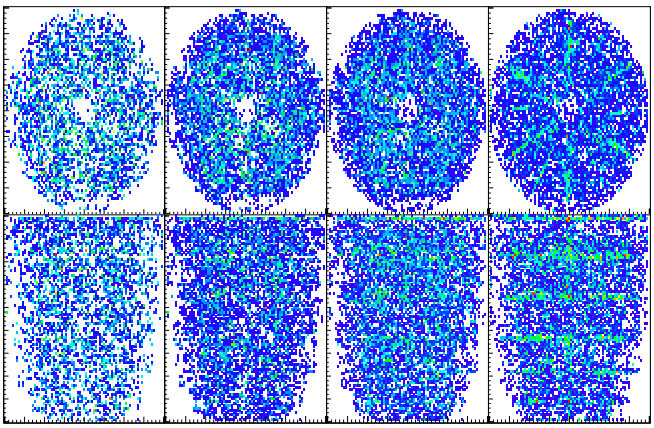

Fig. 14. Extensive gridsearch on the simulated dataset. 2D projections of positions as determined by PSA. The level of noise have been varied in the interval .6%→12%. Note clustering close to segment boundaries for bad signal-to-noise ratio.

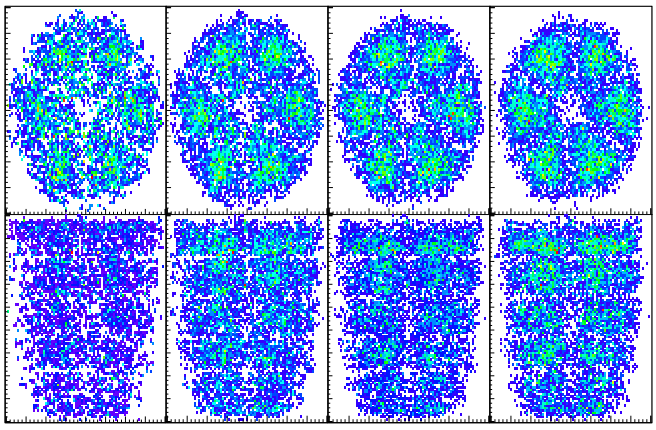

Fig. 15. SVD Matrix PSA on the simulated dataset. 2D projections of positions as determined by PSA. The level of noise have been varied in the interval .6%→12%. Note how larger noise drives the results towards the center of the segments.

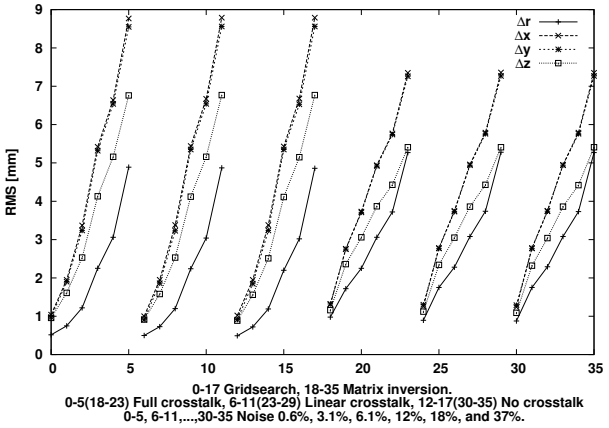

Fig. 16. RMS values for different amount of noise for a inclusive gridsearch on a 1x1x1 mm^3 basis and using the SVD matrix method with the same basis. Results without crosstalk, with only linear crosstalk, or with linear and differential crosstalk added to the test signals are shown.

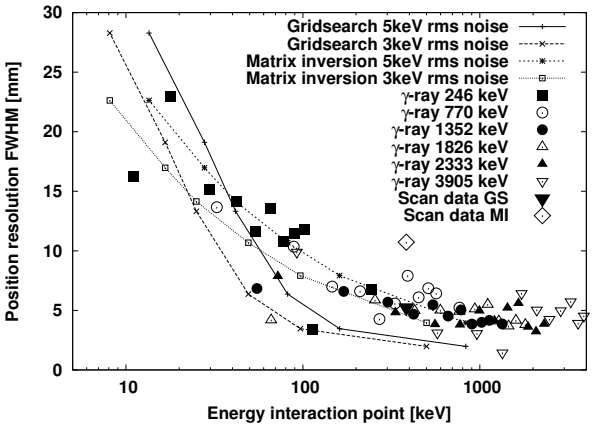

Fig. 17. Position resolution as a function of interaction energy for simluated data, for different γ-ray energies [31], and for data from the 3D-scanning of S002 at Liverpool [32,33] using extensive gridsearch (GS) or matrix inversion after SVD (MI).

7.12 Extended Geant4 simulations of the AGATA spectrometer

UNDER EDITING

EPJ manuscript No.
(will be inserted by the editor)

Extended Geant4 simulations of the AGATA spectrometer

J. Ljungvall[1]

CSNSM, Univ Paris-Sud, CNRS/IN2P3, F-91405 Orsay, France

Abstract. The AGATA geant4 Monte Carlo code has been extended with several new reaction kinematics included as well as the possibility to use continuous time in the simulation allowing the study of background and pile-up within time gates. These new features have been applied to the planning and analysing of experiments performed at the AGATA@GANIL campaign.

PACS. 21.10.Tg In-beam γ-ray spectroscopy

1 Introduction

Monte Carlo simulations have become an important tool in all experimental physics and many other domains of science. High resolution γ-ray spectroscopy is no exception and simulations are extensively used to design experimental apparatus, to plan experiments, and to analyse the experiments. Simulations are used to estimate efficiencies and response functions of the detectors as well as to include effects that are difficult to model analytically, e.g. slowing down in the target, non-regular angular coverage of the detectors. In this paper development of the AGATA geant4 simulation code [1] are discussed, and examples of applications of these developments are given.

In section 2 a short description of the AGATA geant4 code is given, followed by the description of some implemented bench marks used to verify the correctness of the code for each new version of Geant4 [2] in section 3. Section 4 is devoted to the description of how one can include realistic time structures in the simulations allowing the modeling of build up of activity, pile-up in detectors etc. This is followed by section 5 that discuss the implementation of reaction kinematics in the code where examples of simulations and comparisons with experimental data is also give. Monte Carlo simulations are used within the AGATA collaboration to compare experimental and simulated efficiencies for source measurements, and for this reason many simulations of source measurements have been made. In section 6 examples are given with specialization to inclusion of the source strengths in the simulations. Finally conclusions and an outlook is given in section 7.

2 A short description of the AGATA geant4 code

The AGATA geant4 Monte Carlo Simulation code [1] was developed by Farnea et al. to design the AGATA array and as a tool to develop γ-ray tracking algorithms. In the code the geometry of the detector system is defined using text input files giving the size and positions of the crystals, dead layers, aluminium in incapsulation and crystats. Scattering from material behind the crystals is modeled using a thicker than actual aluminum end of the triple clusters.

Photon transport and transport of charged particles and neutrons are done using the appropriate geant4 processes. The effect of the electrical segmentation, i.e. the possiblity to read out deposited energy and corresponding position with a identified segment, is done in a schematic but accurate way.

The code has built in event generators and can read events generated externally from ascii files. This allows for several different ways of generating events. The output of the code is a list mode file, containing information of which detectors that have been hit, the segment with net energy for each deposited energy. How the energy is deposited depends on the "tracking mode", where either the primary interaction of photons are used or the secondary electrons are tracked. There are options in the code to post-process this interaction points to emulate the finite resolution and resolving power of the PSA.

3 Tools to validate of physics processes

As AGATA was to move from Legnaro to GANIL I got involved in the simulations of the expected performances. This included simulations to estimate the efficiency as well as simulations of Recoil Distance Doppler shift experiments. The first step in this process was to benchmark the physics of the simulations and of the event generators I added. To do this I added a "test" geometry consisting of a sphere. All particles are stopped and the energy deposited locally when they intersect the sphere. This feature is implemented via the inheritance of a geant4 G4VProcess class that kills all particles when they enter the volume

named "TestSpherePhys". This allows for simple investigation of quantities such as attenuation coefficients for γ rays, energy loss for heavy ions in materials etc. As examples I've included the validation of the attenuation of γ rays in Germanium in figure 1, the stopping power of ions in metals in figure 2 and finally the validation of the lifetime of excited states in an ion shown in figure 3. During this phase an error in the inclusion of Compton and photoelectric cross section were found. Note that this error was introduced in the stage of simulations for the GSI phase and were not present in the code described by Farnea et al. [1]. These test allowed the validation of the physics

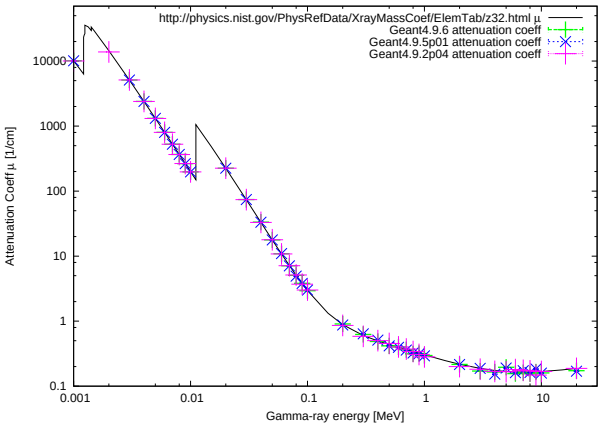

Fig. 1. Attenuation coefficient for γ rays in Germanium as given by different version of geant4.

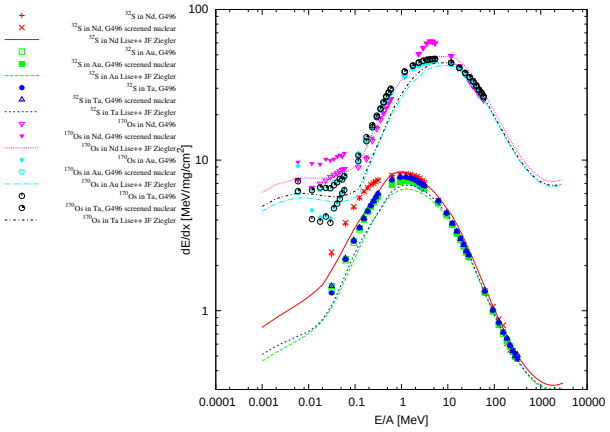

Fig. 2. Stopping powers for six different combination of ions. Geant4 simulations are compared to results form the LISE++ code [3].

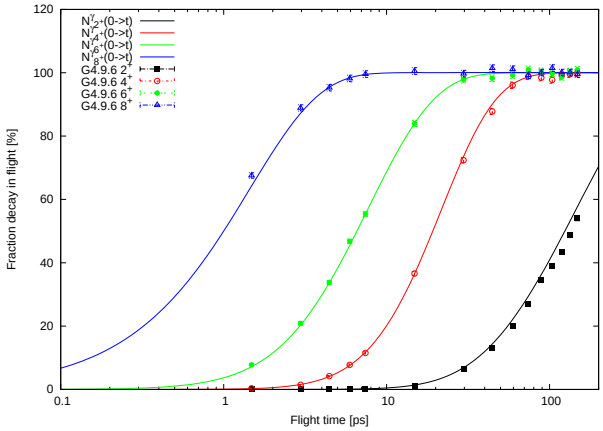

Fig. 3. Validation of the decay of exicsted states in ^{170}Os. Note that the lifetimes are not taken from experiment but just realistic values.

used in the AGATA simulations and the discovery of a few problems and bugs in the geant4 code [4,5].

4 Wall time simulations - including reaction rates

In many experiment the limit in sensitivity is a result of random background that leaks through time gates, this as a result of either finite time resolution of the experimental or that the studies states have lifetimes that are long compared to the random reaction rate. For high reaction rates there is also the issue of pile-up in the detectors; this both from randoms and multiple reactions with-in a time window too short for the detectors to resolve (in the case of AGATA this is about a few hundred nanoseconds). These situations are typically difficult to handle in Monte-Carlo simulations, especially the build up of activity, as one is dealing with 15 orders of magnitude in time scales. However, in the AGATA simulation code a continuous wall time clock has been included. This is controlled by giving the number of particles per second and the beam structure when simulating reactions, or by giving the source strength when simulating source measurements. The two can be combined. For beams the particles are assumed to be evenly distributed within the time bunches (this gives Poisson time statistics for a continuous beam). The list mode output file of the AGATA simulation then contains a universal time stamp allowing sorting the event and creating coincidences, pile-up events etc. If /(β\) decay is simulated this typically requires a divide and conquer procedure first sorting data into files containing time windows and then sorting events with in each file.

5 Simulation of reaction kinematics

In the preparation for experiments and proposals for AGATA(I've performed a large range of simulations of Recoil Distance Doppler Shifts experiments. These simulations include the correct kinematics, the possibility to populate the excited states in the reaction product as wanted etc. In the step of analysing the simulations the acceptance of VAMOS was also included. Examples are given in figure 4 and figure 5 where an experiment performed in 2008 at GANIL with the EXOGAM γ-ray spectrometer combined with the VAMOS stood as example and the improvements that could be gained from AGATA. This was done by reproducing the experimental spectra from the 2008 experiment and after this replacing the EXOGAM spectrometer with AGATA in the simulations.

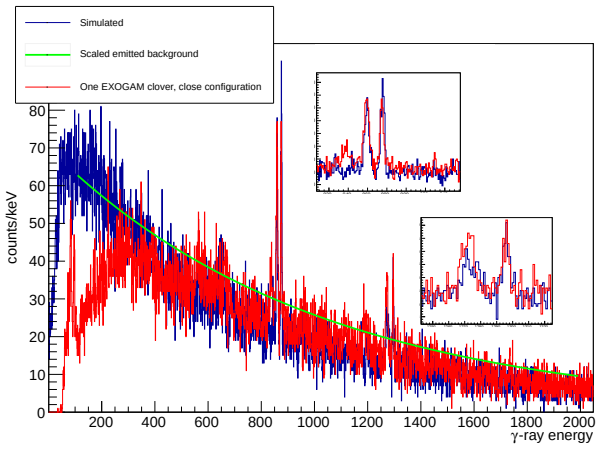

Fig. 4. Geant4 simulation of an experiment [6] where excited states in ^{62}Fe where populated using multi-nucleon transfer from a ^{238}U beam impinging on ^{64}Ni target. In the experiment the target like products where identified event by event in the VAMO Spectrometer. Gamma rays where detected in the EXOGAM γ-ray spectrometer. A plunger with a Mg degrader was used, giving rise to the double peak structure seen.

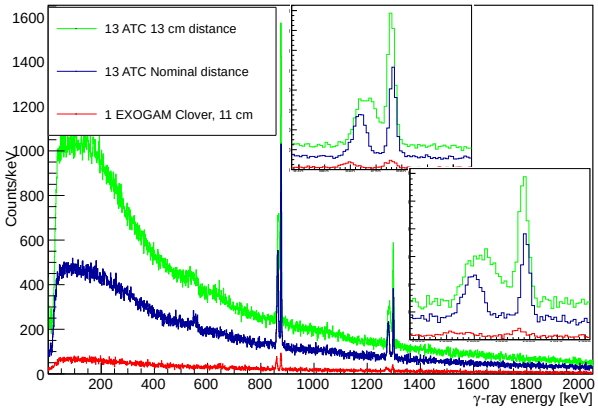

Fig. 5. Geant4 simulations comparing AGATA in different configurations for a lifetime measurement in ^{62}Fe using a plunger device with EXOGAM used in a previous experiment. The increased efficiency for similar peak separation is clear.

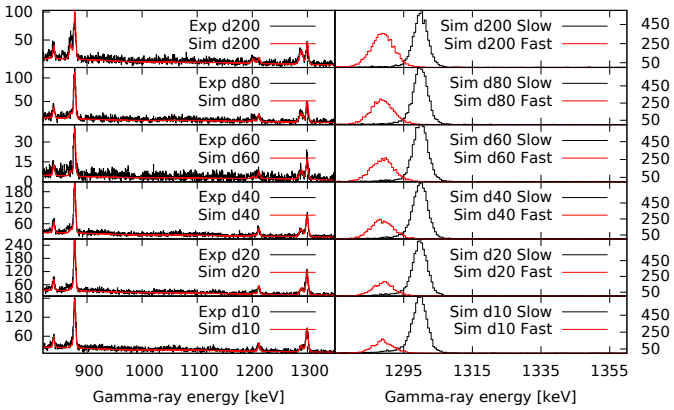

Fig. 6. Realistic simulation of the first AGATA@GANIL experiment. In these simulations the populations and lifetime of levels have been adapted to reproduce experimental spectra as a function of distance between the target and the degrader foil. The purpose of the simulations was to determine the peak shape of the "slow" component.

As a final example of simulations of AGATA that I have done is the reproduction of experimental spectra while analysing the data from the experiment published by Klintefjord et al. [7]. In these simulations as many factors as possible where taken into account in order to reproduce the experimental spectra. This in order to estimate the peak shapes of the two components seen in the RDDS experiment. This was needed as the lifetimes of the 4_1^+ states in the irons were not much longer than the transit time for the nuclei in the Mg degrader used. These simulations are shown in figure 6.

Having validated the basic physics of the simulations I've added to the already existing event generator to include the kinematics of fusion-fission reactions and Coulomb excitations. During this time I also introduced features to include radioactive sources with a specific source strength and model the experiments with given beam intensities and beam structures. This work was done to a large extent for reason not related to AGATA in an effort to model an experiment performed at GANIL in 2012.

In figures 7 to 11 I show the result of a simulation of Coulomb excitation of the ^{74}Kr with an energy of 350 MeV on a ^{208}Pb target. The target and beam like particles were detected in a DSSSD detector. A beam intensity of 1000 pps was assumed with beam frequency of 100 MHz and a pulse width of 2 ns. The last sentence means that the start time for each event moves forward with on average 1 ms per event, but limited to windows of 2 ns each 10 ns. This time, i.e. the start time of the event is a part of the event header in the output file. For each individual interaction in an event there is also the time relative the event start. This data has then been time sorted, i.e. interactions that are in coincidence in a detector are treated together. For a simulated low number of particles per second this can be

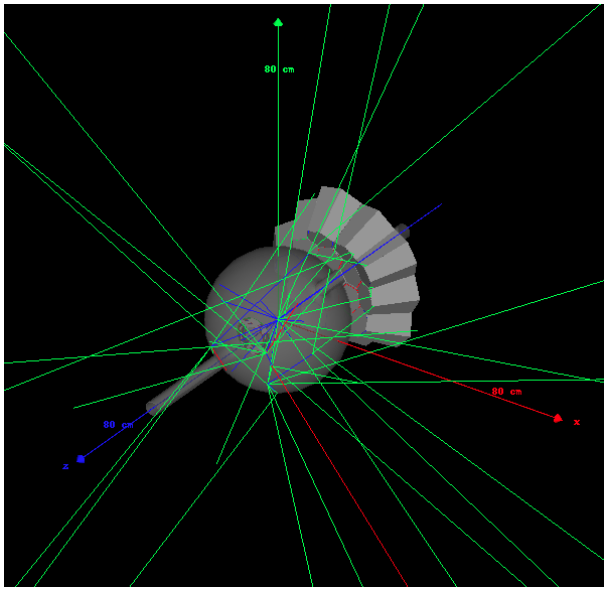

Fig. 7. Geant4 geomerty of a simulation of a Coulomb excitation of ^{74}Kr using a realistic time structre of the beam.

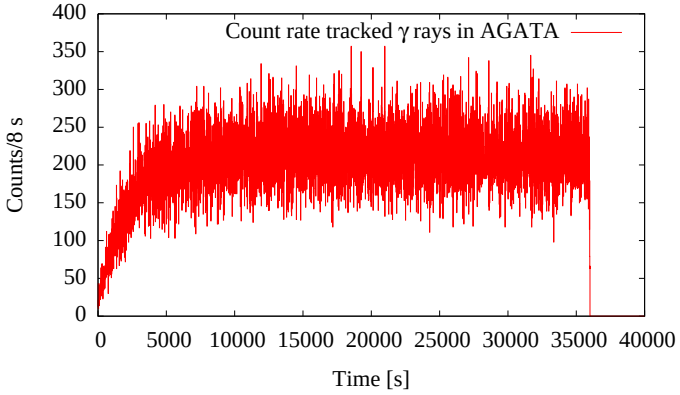

Fig. 8. Count-rate as a function of time. The build up of β activity can clearly be seen.

done by keeping a stack in memory but for more intense beams such as used in the simulation discussed in chapter intermediary steps such as writing files containing fixed times windows are needed. In this particular simulation the data was stored in the AGATA Data Flow format ADF, one file for each detector with time stamped data and analyzed using the tools used to analyse experimental data. As a consequence the number of γ rays that are detected per second increases due to the build up of ^{74}Kr in the target chamber as can be seen in figure 8. In figure 9 the energy versus angle in the DSSSD detector is shown, with the band of beam like particles and the target like particles at lower energies. If no coincidence gate is set on the time difference between the DSSSD and AGATA a γ-ray spectrum like what is shown in figure 10 is produced. If however a coincidence gate between the DSSSD and the tracked γ ray is used a clean γ-ray spectrum is produced, as shown in figure 11. While this feature of keeping track of the real time is rather neat it is not really useful. Consider

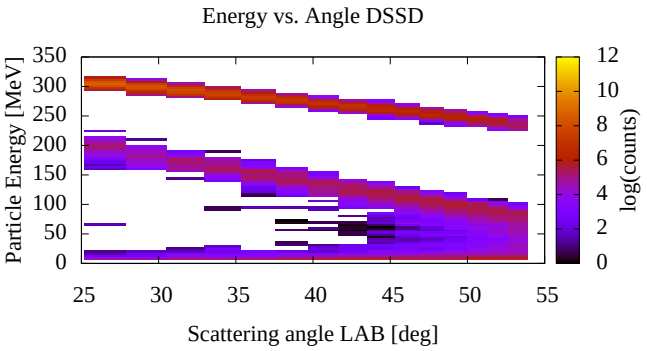

Fig. 9. Simulation of the detection of beam-like and target like particles in a silicon detector.

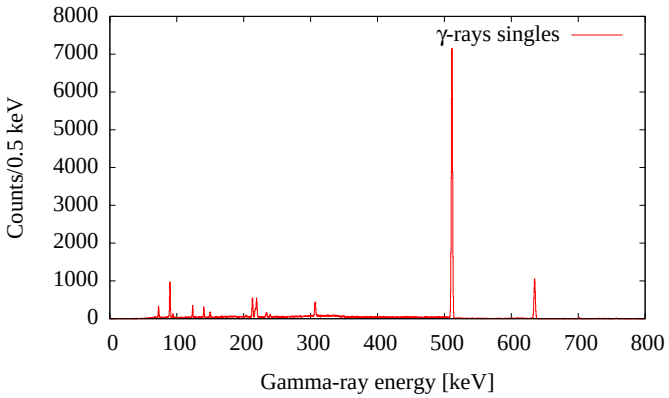

Fig. 10. Gamma rays as detected in AGATA without time gate on prompt γ rays in coincidence with detected particles. Note the γ rays from β decay.

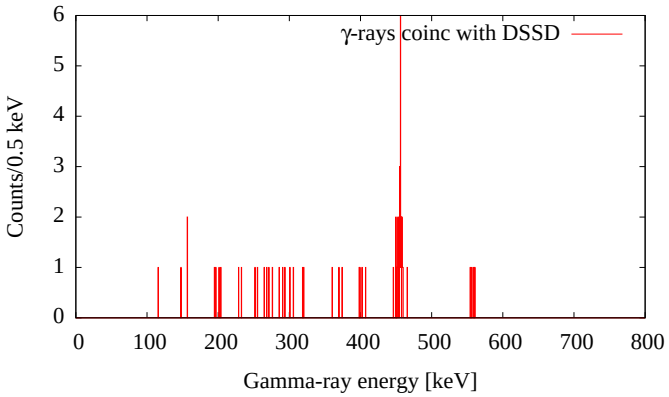

Fig. 11. Gamma rays as detected in AGATA with time gate on prompt γ rays in coincidence with detected particles. Note that the γ rays from β decay are absent.

a stable beam experiment with 10^{12} pps. It is possible to simulate some 10^4 pps in the best case on a single CPU. The factor of 10^8 would indicate that we would need some 10^{10} W of electric power to keep up with the experiment! Clearly one has to be more clever.

I've also performed similar simulations to show the expected increase in performance with AGATA for different type of experiments. In figure 12 the simulated comparison between an array representing JUROGAM and 1π of AGATA for a lifetime measurement using the RDDS technique with ^{186}Pb populated using heavy-ion fusion reactions. The choice of 1π AGATA comes from the idea to show the increase in efficiency given the same peak separation.

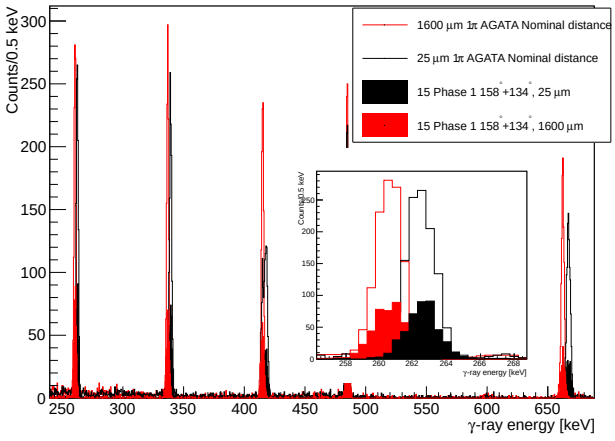

Fig. 12. Simulation of a lifetime measurement with a Plunger device with excited states in ^{186}Pb populated using heavy-ion fusion reactions. The background is estimated by reproducing experimental spectra from an experiment performed at Jyväskylä.

6 Simulation of sources

In order to investigate differences between measured and simulated efficiency for the sub-array of AGATA used for the first AGATA campaign at GSI [8] I did complete simulations of AGATA using a chain of Monte Carlo simulations with ^{60}Co sources of varying source strength. The energy deposition points were then fed into the pulse shape calculation code AGATAGeFEM that produces output files that can be read by the AGATA analyses tool chain. Noise, cross talk and realistic use of CFD threshold for the timing was applied before PSA being performed on the simulated traces. The same simulated interaction points were also treated in a more classic way where the PSA was simulated by packing and smearing (see for example explanation in Lopez et al. [9]). The conclusion from this work was, inline with all preliminary work done for AGATA and GRETA, that the tracking performance after PSA when using a correct data base of pulse shapes should be very good. Examples of simulations for ^{60}Co sources are shown in figures 13,14,15,16, and 17.

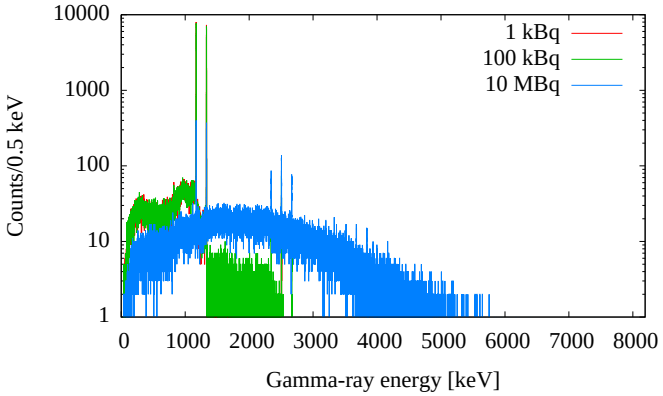

Fig. 13. Singles spectra for simulations of ^{60}Co with different source strengths (1 kBq, 100 kBq, and 10 MBq).

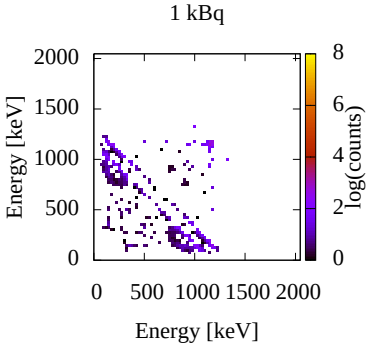

Fig. 14. Gamma-gamma matrix of ^{60}Co with different a source strengths of 1 kBq.

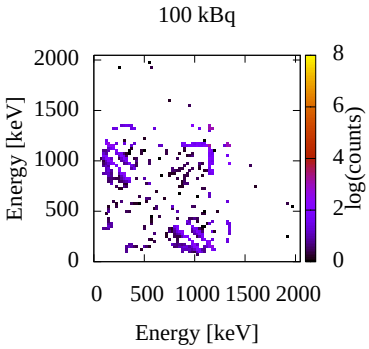

Fig. 15. Gamma-gamma matrix of ^{60}Co with different a source strengths of 100 kBq.

7 Conclusions

Several new features have been added to the AGATA geant4 simulation packages. These include reaction kinematics for Coulomb excitation reactions and for induced fission reactions. Further more a mechanism to simulate the passing of time and hence also model time background and coincidences has been developed and tested. All these

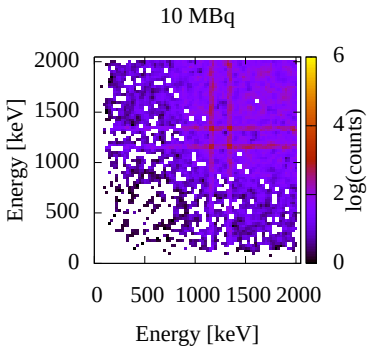

Fig. 16. Gamma-gamma matrix of ^{60}Co with different a source strengths of 10 MBq.

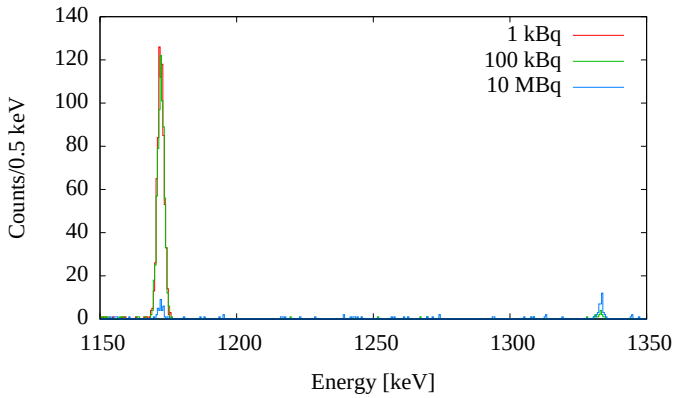

Fig. 17. Gated spectra for simulations of ^{60}Co with different source strengths (1kBq, 100 kBq, and 10 MBq).

features have been used to plan and analyze experiments during the AGATA@GANIL phase of the AGATA project.

Acknowledgement

The author would like to give special thanks to Marc Labiche, Caterina Michelagnoli, and the AGATA collaboration.

References

1. E. Farnea, F. Recchia, D. Bazzacco, T. Kröll, Z. Podolyák, B. Quintana, A. Gadea, Conceptual design and monte carlo simulations of the {AGATA} array, Nuclear Instruments and Methods in Physics Research Section A: Accelerators, Spectrometers, Detectors and Associated Equipment 621 (1-3) (2010) 331 – 343. doi:http://dx.doi.org/10.1016/j.nima.2010.04.043.
URL http://www.sciencedirect.com/science/article/pii/S0168900210008922
2. S. Agostinelli, J. Allison, K. Amako, J. Apostolakis, H. Araujo, P. Arce, M. Asai, D. Axen, S. Banerjee, G. Barrand, F. Behner, L. Bellagamba, J. Boudreau, L. Broglia, A. Brunengo, H. Burkhardt, S. Chauvie, J. Chuma, R. Chytracek, G. Cooperman, G. Cosmo, P. Degtyarenko, A. Dell'Acqua, G. Depaola, D. Dietrich, R. Enami, A. Feliciello, C. Ferguson, H. Fesefeldt, G. Folger, F. Foppiano, A. Forti, S. Garelli, S. Giani, R. Giannitrapani, D. Gibin, J. G. Cadenas, I. González, G. G. Abril, G. Greeniaus, W. Greiner, V. Grichine, A. Grossheim, S. Guatelli, P. Gumplinger, R. Hamatsu, K. Hashimoto, H. Hasui, A. Heikkinen, A. Howard, V. Ivanchenko, A. Johnson, F. Jones, J. Kallenbach, N. Kanaya, M. Kawabata, Y. Kawabata, M. Kawaguti, S. Kelner, P. Kent, A. Kimura, T. Kodama, R. Kokoulin, M. Kossov, H. Kurashige, E. Lamanna, T. Lampén, V. Lara, V. Lefebure, F. Lei, M. Liendl, W. Lockman, F. Longo, S. Magni, M. Maire, E. Medernach, K. Minamimoto, P. M. de Freitas, Y. Morita, K. Murakami, M. Nagamatu, R. Nartallo, P. Nieminen, T. Nishimura, K. Ohtsubo, M. Okamura, S. O'Neale, Y. Oohata, K. Paech, J. Perl, A. Pfeiffer, M. Pia, F. Ranjard, A. Rybin, S. Sadilov, E. D. Salvo, G. Santin, T. Sasaki, N. Savvas, Y. Sawada, S. Scherer, S. Sei, V. Sirotenko, D. Smith, N. Starkov, H. Stoecker, J. Sulkimo, M. Takahata, S. Tanaka, E. Tcherniaev, E. S. Tehrani, M. Tropeano, P. Truscott, H. Uno, L. Urban, P. Urban, M. Verderi, A. Walkden, W. Wander, H. Weber, J. Wellisch, T. Wenaus, D. Williams, D. Wright, T. Yamada, H. Yoshida, D. Zschiesche, Geant4—a simulation toolkit, Nuclear Instruments and Methods in Physics Research Section A: Accelerators, Spectrometers, Detectors and Associated Equipment 506 (3) (2003) 250 – 303. doi:https://doi.org/10.1016/S0168-9002(03)01368-8.
URL http://www.sciencedirect.com/science/article/pii/S0168900203013688
3. O. Tarasov, D. Bazin, Lise++: Exotic beam production with fragment separators and their design, Nuclear Instruments and Methods in Physics Research Section B: Beam Interactions with Materials and Atoms 376 (2016) 185 – 187, proceedings of the XVIIth International Conference on Electromagnetic Isotope Separators and Related Topics (EMIS2015), Grand Rapids, MI, U.S.A., 11-15 May 2015. doi:https://doi.org/10.1016/j.nimb.2016.03.021.
URL http://www.sciencedirect.com/science/article/pii/S0168583X1600224X
4. Gammas emitted only after ion stopped (radioactivedecay physics).
URL http://hypernews.slac.stanford.edu:5090/HyperNews/geant4/get/hadronprocess/1275.html
5. Ion gets a strange boost when emitting gamma ray (g4radioactivedecay).
URL http://hypernews.slac.stanford.edu:5090/HyperNews/geant4/get/hadronprocess/1295.html
6. J. Ljungvall, A. Görgen, A. Obertelli, W. Korten, E. Clément, G. de France, A. Bürger, J.-P. Delaroche, A. Dewald, A. Gadea, L. Gaudefroy, M. Girod, M. Hackstein, J. Libert, D. Mengoni, F. Nowacki, T. Pissulla, A. Poves, F. Recchia, M. Rejmund, W. Rother, E. Sahin, C. Schmitt, A. Shrivastava, K. Sieja, J. J. Valiente-Dobón, K. O. Zell, M. Zielińska, Onset of collectivity in neutron-rich fe isotopes: Toward a new island of inversion?, Phys. Rev. C 81 (2010) 061301. doi:10.1103/PhysRevC.81.061301.
URL http://link.aps.org/doi/10.1103/PhysRevC.81.061301
7. M. Klintefjord, J. Ljungvall, A. Görgen, S. M. Lenzi, F. L. Bello Garrote, A. Blazhev, E. Clément, G. de France, J.-P.

Delaroche, P. Désesquelles, A. Dewald, D. T. Doherty, C. Fransen, A. Gengelbach, G. Georgiev, M. Girod, A. Goasduff, A. Gottardo, K. Hadyńska-Klęk, B. Jacquot, T. Konstantinopoulos, A. Korichi, A. Lemasson, J. Libert, A. Lopez-Martens, C. Michelagnoli, A. Navin, J. Nyberg, R. M. Pérez-Vidal, S. Roccia, E. Sahin, I. Stefan, A. E. Stuchbery, M. Zielińska, D. Barrientos, B. Birkenbach, A. Boston, L. Charles, M. Ciemala, J. Dudouet, J. Eberth, A. Gadea, V. González, L. Harkness-Brennan, H. Hess, A. Jungclaus, W. Korten, R. Menegazzo, D. Mengoni, B. Million, A. Pullia, D. Ralet, F. Recchia, P. Reiter, M. D. Salsac, E. Sanchis, O. Stezowski, C. Theisen, J. J. Valiente Dobon, Measurement of lifetimes in ^{62,64}Fe,^{61,63} Co, and ^{59}Mn, Phys. Rev. C 95 (2017) 024312. doi:10.1103/PhysRevC.95.024312.
URL http://link.aps.org/doi/10.1103/PhysRevC.95.024312

8. Pietralla, N., Reese, M, Cortes, M.L., Ameil, F., Bazzacco, D., Bentley, M.A., Boutachkov, P., Domingo-Pardo, C., Gadea, A., Gerl, J., Goel, N., Golubev, P., Górska, M., Guastalla, G., Habermann, T., Kojouharov, I., Korten, W., Merchán, E., Pietri, S., Ralet, D., Reiter, P., Rudolph, D., Schaffner, H., Singh, P.P., Wieland, O., Wollersheim, H.J., On the road to fair: 1st operation of agata in prespec at gsi, EPJ Web of Conferences 66 (2014) 02083. doi:10.1051/epjconf/20146602083.
URL https://doi.org/10.1051/epjconf/20146602083
9. A. Lopez-Martens, K. Hauschild, A. Korichi, J. Roccaz, J.-P. Thibaud, γ-ray tracking algorithms: a comparison, Nuclear Instruments and Methods in Physics Research Section A: Accelerators, Spectrometers, Detectors and Associated Equipment 533 (3) (2004) 454 – 466. doi:http://dx.doi.org/10.1016/j.nima.2004.06.154.
URL http://www.sciencedirect.com/science/article/pii/S0168900204014779

7.13 OASIS ANR

Project summary

The OASIS project aims at optimizing the science production of the Advanced GAmma-ray Tracking Array (AGATA) γ-ray spectrometer. Presently installed at the Grand Accélérateur National d'Ions Lourds (GANIL) at Caen, France, AGATA has passed the demonstrator phase of its early implementation (15 high-purity germanium detectors) and now contains 32 such detectors with infrastructure to accommodate 45 detectors covering 1π of solid angle.

AGATA is a new generation γ-ray spectrometer designed to overcome the inherent limitation of the previous generation of Compton suppressed HPGe detector arrays. By replacing the Anti-Compton shields, which occupy a significant amount of solid angle, with HPGe detectors solid angle coverage, and hence efficiency, can be increased. However, for this approach to produce high quality γ-ray spectra an alternative Compton suppression technique has to be developed. This is γ-ray tracking: The energy and position of individual γ-ray interaction points inside the HPGe is determined using highly segmented detectors combined with digital electronics and pulse-shape analysis. These interaction points are then tested for the hypotheses that they belong to a fully absorbed γ ray. For the γ-ray tracking to work the γ-ray interaction points have to be located to within 5 mm inside the detectors. A very important additional increase in performance comes from the very high effective angular granulation of AGATA given by knowing the interaction positions giving very good Doppler Correction capabilities, something very important in modern experimental nuclear structure research. Because of the high performance of AGATA it is considered a very important detector for the future and present nuclear structure research facilities in Europe, such as FAIR, HIE-ISOLDE, SPES, and SPIRAL2.

Since the first physics campaign with AGATA started has showed its high performance in experimental situation where the sensitivity is dominated by the Doppler broadening of the γ-ray peaks, for high-count rate situations, and when it is beneficial to have a very compact γ-ray spectrometer - AGATA has proven to be a technical success in many ways.

During the work analyzing experimental data the AGATA collaboration, and the γ-ray tracking community, has however seen that the performance of AGATA in terms of Compton suppression from the γ-ray tracking is not what simulations suggests it should be. It is believed in the γ-ray tracking community that cause for this is related to problems with the pulse-shape analysis. Although the nominal position resolution from the pulse-shape analysis is within the required limits several indications points to that the pulse-shape analysis does not perform as good as is needed. The OASIS project aims at carefully investigating the reasons for this using computer simulations to try to reproduce and understand the deficiencies seen in experimental data. One particular problem that will be addressed within the OASIS project is that of correctly determining the number of actual interaction that a γ-ray has had with the AGATA. Several novel ideas are to be investigated.

Finally, many aspects of analyzing γ-ray spectroscopy data have to be reviewed when using AGATA. This mainly comes from the fact that there is more detailed information to look at offering new possibilities. What was previously simple calibration procedures using source data, such as efficiency calibrations, now has complex dependencies on the experimental situation and choices made for the γ-ray tracking algorithms. Other methods, e.g. to determine angular correlations and distributions,

also need to be developed specifically for γ-ray tracking. A part of OASIS is dedicated to this work, making sure that the γ-ray tracking community will have thoroughly tested and quantifies procedures.

Summary table of persons involved in the project:

Partner	Name	First name	Current position	Involvement (person.month)	Role & responsibilities in the project (4 lines max)
CSNSM	Ljungvall	Joa	CR1	18	Scientific coordinator Student supervisor
CSNSM	Lopez-Martens	Araceli	DR2	6	Coordination task 2 γ-ray tracking expert
CSNSM	Korichi	Amel	DR2	6	Responsible Scanning CSNSM
CSNSM	Dosme	Nicolas	IE1	1.5	Technical support Scanning and computing
CSNSM	Legay	Eric	IR2	1	”
CSNSM	Grave	Xavier	IRHC	1.5	”
CSNSM	Linget	Dennis	IR1	1	”
CSNSM	Gibelin	Laurent	TCS	1	”
GANIL	Clément	Emanuel	CR1	9	Supervisor Post doc 1 Coordination task 3
IRFU/SPhN	Theisen	Christophe	E6	9	Work together with post-doc on task 1 γ-ray spectroscopy expert
IRFU/SPhN	Zielińska	Magda	E3	6	Supervisor Post doc 2 Coordination task 1
IRFU/SEDI	Karolak	Marc	E2	3	HPGe detectors expert
IPHC	Duchêne	Gilbert	DR1	6	Responsible Scanning IPHC Coordination IPHC contribution task 1,2
IPHC	Sigward	Marie-Hélène	IE2	3	Perform Scanning
IPHC	Didierjean	François	IR2	3	γ-ray tracking
IPHC	De Canditiis	Bartolomeo	PhD	6	MC Simulations for PSA, Analyzing scanning data

Any change that have been made in the full proposal compared to the pre-proposal

Change of strategy to acquire AGATA electronics. This is of no consequence for the science program, and a potentially less expensive solution. Also the need to renew the radioactive sources for the CSNSM scanning table and the IPHC scanning table has been lifted to scientific coordinators attention, and funds for this will be included in the OASIS.

7.13.1 Proposal's context, positioning and objective(s)

1. Objectives and scientific hypotheses Modern nuclear structure physics aims at bridging the gap between QCD and the effective in-medium force felt by nucleons in nuclei, on one hand, and on the other hand creating a uniformed view of all phenomena observed over the Segré chart. Not only important in its own

right, a detailed understanding of nuclear structure is very important for, e.g. astrophysical applications where small variations, such as the ordering of states, can create large changes in production rates, or to constrain nuclear matrix elements involved in neutrino-less double β decay. It is therefore important to probe and understand terms in the nucleon-nucleon interaction that are "weak" for stable nuclei turning nuclear structure physics into a high-precision field, requiring high precision instrumentation with high sensitivity [290]. Gamma-ray spectroscopy is a very important part of this instrumentation, used in more than half of all nuclear structure physics experiments.

The OASIS project aims at greatly increasing the present performance of the Advanced GAmma Tracking Array (AGATA) [203] that is the next-generation γ-ray spectrometer for in-beam nuclear structure studies that is build in Europe. AGATA is recognized [290] as a key part of feature nuclear structure research in Europe, and our capacity to fully exploit the array will be of utmost importance to benefit from the opportunities given by new radioactive and high-intensity stable beam facilities being constructed in Europe such as FAIR, HIE-ISOLDE, SPES, and SPIRAL2. AGATA is presently installed at GANIL, Caen, France in a version that is about 1/5 of the full size of AGATA.

The conceptual design of AGATA, and its American counterpart GRETA, goes back to the end of the 1990's and the beginning of 2000's when simulations showed that a γ-ray spectrometer using so-called γ-ray tracking would provided unprecedented sensitivity, especially if combined with digital electronics allowing high count rates, i.e. high luminosity. For many physics cases the gain would be two orders in magnitude or more [291, 233]. This is illustrated in figure 7.1.

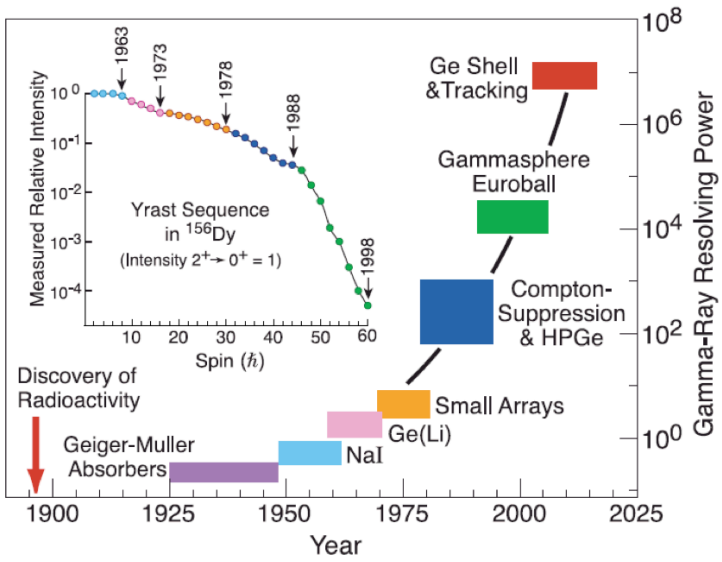

Figure 7.1: Figure showing the increased resolving power for γ-ray spectrometers. The resolving power is to be interpreted as inverse of the fraction of the total γ-ray intensity than can be seen.

Therefore the development of γ-ray tracking arrays was started using segmented

HPGe detectors that are closely packed allowing the coverage of up to 80% of the solid angle. Gamma-ray tracking is, as the name suggests, the reconstruction of a γ ray's path in a detector by determination of the positions of its energy depositions. The tracking is done under the hypothesis that the γ ray was fully absorbed, and a track is accepted or rejected based on a figure of merit that should be high for truly absorbed γ rays and low for γ rays that were only partially absorbed and Compton scattered out of the detector. This way a high efficiency can be achieved while suppressing the Compton background. Simulations show that that for γ-ray tracking to work the position of γ-ray interactions have to be determined within 5 mm. This also gives an effective angular opening for AGATA of 1° making the Doppler Correction capabilities excellent, important especially for experiments using inverse kinematics as is often the case for radioactive beam experiments.

Large resources have been invested in the AGATA project in Europe, and it is in many aspects a technical success. Both AGATA and GRETINA have proven to be excellent γ-ray spectrometers for physics were γ rays are emitted from nuclei moving faster than $\frac{v}{c} \approx 10\%$ of the speed of light. However, today the situation is that for experiments with high γ-ray multiplicity or when γ-ray coincidences are needed to identify the γ rays of interest both AGATA and GRETINA, scaled to the same solid angle coverage, perform worse than Gammasphere, i.e. the generation of γ-spectrometers they should replace. The expectations based on simulations is that AGATA should outperform Gammasphere with a factor of 2. This is understood within the γ-ray tracking community as due to a few specific issues that have not yet been resolved to satisfaction:

- The determination of the interaction positions within the detectors is not good enough.

The first objective of OASIS is to resolve this issue.

- The problem of correctly assigning the number of interactions inside a detector segment.

The second objective of OASIS is to mitigate this problem.

As the AGATA collaboration has started analyzing data from AGATA in detail it stands clear that data from a γ-ray tracking array challenges our understanding of γ-ray spectrometers. A striking example is the efficiency as a function of the multiplicity of detected γ rays where for a tracking array the situation is complex. Here the energy and geometrical separation of all absorbed γ rays have an impact on the actual efficiency. It therefore becomes important to be able to model the response of the detector array using simulations to deconvolute experimental data in a consistent way.
The third objective of OASIS is to fully characterize AGATA to allow all γ-ray spectroscopy methods to be applied and apply this to data in order to extract more physics.

If the objectives of OASIS are realized AGATA would gain a factor of 2 in performance

2. Originality and relevance in relation to the state of the art A block diagram of γ-ray tracking is shown in figure 7.2. It starts with highly segmented HPGe

detectors (in the case of AGATA the detectors are 36-fold segmented in 6x6 pattern) where the signals from all 37 (36 outer segments and the central contact) are digitized. The signals are then decomposed and the position and energy of every individual interaction are extracted. After this step interactions from all detectors that are in coincidence are used to perform the γ-ray tracking where all reasonable combinations of interaction points are tested in order to reconstruct fully absorbed γ rays. It is considered within the community that if the signal decomposition can provide the correct positions and number of interaction points in an event, the tracking algorithms will perform well.

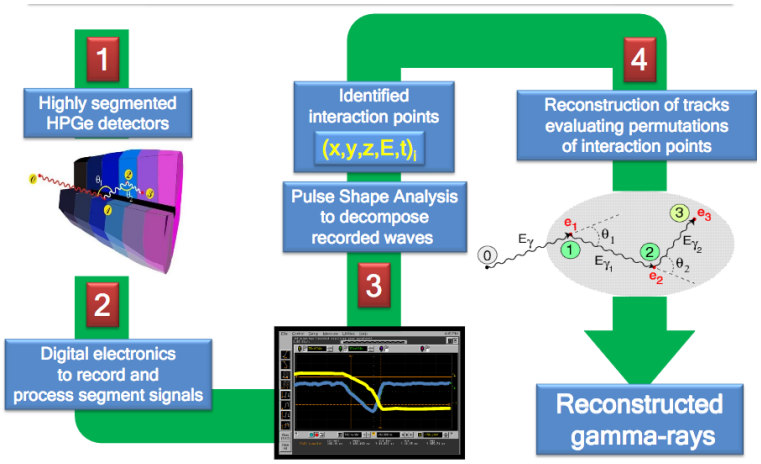

Figure 7.2: Block diagram showing the ingredients needed for γ-ray tracking.

The decomposition procedures, referred to as pulse shape analysis (PSA) are based on comparing a pre-calculated (or measured) set of signals to the experimental signals. This set, called the basis for the detector, contains signals for a 3D grid of interaction points inside the detector, typically some tens of thousands points for an AGATA crystal. In figure 7.3 an example is shown where a basis signal (red) corresponding to the best position in the base is overlaid on the experimental signal (black). The signals are composed of signals for each 36 segments and the central contact signal.

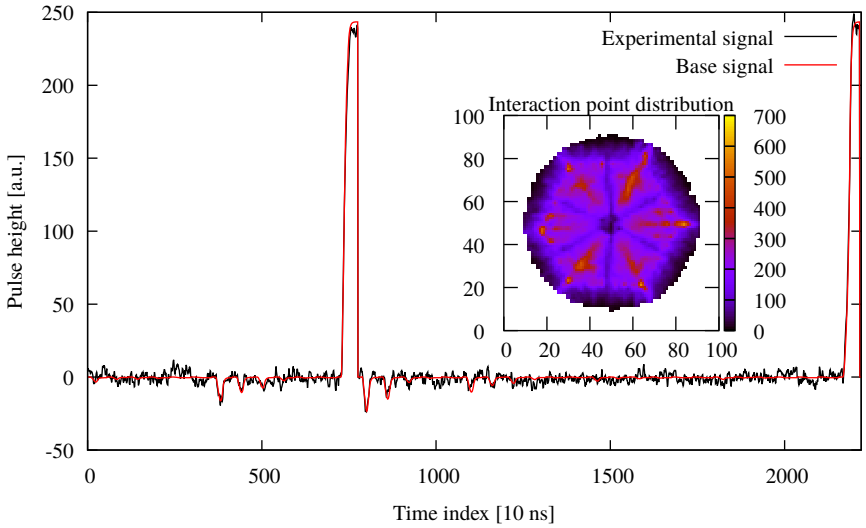

Figure 7.3: Example of pulse shape decomposition used in AGATA. The black signal is experimental and the red corresponds to the best match in the basis. The inset shows the distribution of interaction positions from grid search PSA.

At the time of planning the OASIS project all steps in this chain have been extensively tested and used for producing results published in peer-reviewed journals [292]. Dedicated experiments have been performed to test the PSA [244, 245] showing that the achieved position resolution is within specifications. Experiments have also been performed to characterize the performance of AGATA [259]. There it is shown that the γ-ray tracking performance expected from Monte Carlo simulations are not reproduced using experimental data. A too low efficiency, and more important too low peak-to-total in the spectra are found. The differences can partly be explained by a difference in active volume for the detectors between simulation and experiment. However the low experimental peak-to-total reflects the need to assume a larger error than the nominal 5 mm FWHM in the positions used in tracking to get a good efficiency. This reflects large tails on the errors in the positions determined by the PSA. The suspicion that the lower than expected performance comes from problem with the PSA is further enhanced looking directly at the output of the PSA. As shown in the inset of figure 7.3, the distribution of interaction points in one AGATA crystal shows clustering of the interaction points. This is clearly not physical since over the solid angle of one detector the γ-ray flux is homogeneous. Different algorithms have been tested to perform the PSA [237, 239, 238, 240, 215]. This extensive testing has shown that independently of the algorithm used the basis has to have an excellent fidelity, requiring a perfect understanding of not only the detector but also the electronics response function (methods to circumvent this problems have been proposed [234]). Extensive work has been done on modeling detectors, characterizing detectors and electronics [217, 235, 227, 219, 220, 293, 221, 240, 222, 244, 245, 224] in order to achieve this high fidelity of the bases but up to date the results are not fully satisfactory. Objective one of OASIS relates directly to this. A second general conclusion that has been drawn is that the determination of the actual num-

ber of interaction points in a detector is a very complicated problem since the signals of one large interaction often can be reproduced using two smaller interactions (e.g. see [238]). A direct result of this is the difficulty to properly discriminate between single Compton scattering events and Compton scattering plus photo electric effect absorption, lowering the quality of the γ-ray spectra. The improved treatment of this is objective 2 of OASIS.

3. Risk management and methodology To achieve the objectives described above this project has three well defined tasks:

   (a) Understand and model detectors (objective 1).

   (b) Improve algorithms for treating the signals from these detectors (objective 2).

   (c) Understand the response function of a γ-tracking array. This will be very important as the complexity of spectroscopic work done with AGATA will increase (objective 3).

   Task 1 will be addressed using numerical simulations. A code developed by the scientific coordinator during the last decade, called AGATAGeFEM solves the electric field and weighting potentials using Finite Element methods [294] with tetrahedral cells. This allows a definition of the geometry only limited by the numerical precision. The signals are generated using the Shockley-Ramo theorem, where the transport of the charge carriers in the electric field is done using an adaptive fourth order Runge-Kutta algorithm [228]. Examples of field calculations and pulse shapes calculated with the code are shown in figure 7.4.

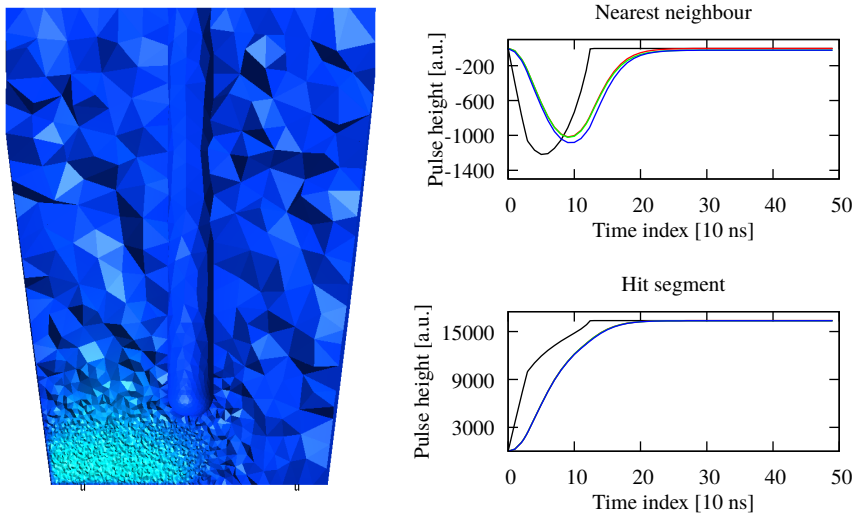

Figure 7.4: To the left the weighting potential of an A slice segment inside an AGATA A type crystal calculated using the AGATAGeFEM code. The refinement in regions where the potential changes fast is clearly visible. To the right, example of pulse shapes calculated using AGATAGeFEM. The example shows the pulse shapes before applying the response of the electronics (black), with a low pass filter (red) and including only linear cross talk or linear+differential cross talk (green and blue)

The AGATAGeFEM code will be used to investigate what deficiencies in the pulse-shape data base that are responsible for the problems encountered by the PSA. This will be done by generating a set of interaction points in AGATA using the AGATA Monte Carlo simulation package [233], and then calculating the corresponding pulse shapes with varying parameters (detector geometry, electronic response functions etc). These pulses will then be analyzed using the same code as used for data analysis in AGATA. The data base used will be calculated assuming the geometrical and electrical properties of the crystals used to calculate the data based used to analyze experimental data. It is hoped that this way the discrepancies between the modeled and real HPGe detectors used in AGATA can be revealed. Finally, what has been learned will be applied on real AGATA detectors, testing with experimental data. It is foreseen to perform this last step using data from scanning tables equipped with AGATA electronics to be able to perform scanning in parallel with validation and this way be able to address problem regions in the detectors during the scanning. Whereas the computer modeling part of task 1 is rather risk free in terms of its feasibility the accessibility to an AGATA crystal for scanning (with corresponding cryostat) is not guaranteed. Our mitigation strategy in the case of failing to have access to an AGATA crystal is the use of already existing scan data. However, this solution will not allow targeted scanning of the crystal.

Task 2 will be addressed by adding information to the PSA algorithms. In general the idea is to add information to pulse-shape decomposition step to allow a better determination of the number of interactions inside single segments. One possibility is to let PSA suggest several solutions varying the number of interaction points in a segment, and then let γ-ray tracking choose the best solution. A second road to follow would be to combine the PSA and γ-tracking steps into one minimization problem. One could even imagine calculating the pulse shapes used as a part of the minimization this way allowing a correct modeling of the charge-carrier cloud extension and diffusion.

As pointed out, a considerable amount of effort has already been spent on modelling HPGe detectors, PSA, and γ-ray tracking development. The success of OASIS is therefore far from given. The scientific coordinator does however believe that he is in a good position to really advance the field given his experience in the field. Even in the case of failure to reach the objectives within the OASIS project a few question marks concerning our lack of understanding of the HPGe detectors will have been answered.

Task 3, which corresponds one-to-one to objective three, is to fill this lack of knowledge. The methodology will be the use of concatenation of experimental data to create high multiplicity events combined with geant4 Monte Carlo simulations+Pulse shape calculations. By assuring that we can reproduce the response of AGATA using simulations, these will be a good tool to deconvolute

experimental spectra. The first part of this task is considerably smaller and is less complicated than task 1-2, and a good starting point for a student. It is associated with a very small risk. As for the exploitation of AGATA data in order to extract physical results, this is important as such a result most likely would be a part of the PhD students work. The ambition of OASIS is to push the performance of AGATA so that physical results that were not accessible before OASIS will be after. However in the case that this fails the scientific coordinator is in possession of data from which physical results can be extracted given the present performance of AGATA allowing a mitigation strategy for this part of task 3.

7.13.2 Project organization and means implemented

1. Scientific coordinator The scientific coordinator Joa Ljungvall has worked with AGATA and related issues since his PhD (defended in spring 2005). During this decade he has performed detector characterization, Monte Carlo simulations, pulse-shape calculations, pulse-shape analysis, and proposed and performed experiments and published results from AGATA. Most of the technical work has been presented during the AGATA collaboration meetings (AGATA weeks) where he has given more than 15 presentation related to these topics. He was also the first to integrate a pulse-shape analysis code into the AGATA data acquisition system and has an excellent understanding of information technology aspects of AGATA, as well as the detector physics and the demands on its performance to fulfill the physics programs depending on it.

2. Consortium The consortium is created to give large contact surfaces between the student, the post-docs and the permanent staff involved in the OASIS project. A second criteria is to involve most of the french expertise in the field in such a way that the complementary aspect is not only in terms of different expertise but different experiences working on the same subject. The idea behind this is that the field of research addressed by OASIS is already well investigated and by collecting as much experience as possible it will be possible to avoid repeating already performed work. In figure 7.5 a mind chart of how the objectives of OASIS are connected to the tasks and the competences needed to finish the tasks and accomplish the goals. The last part of the figure shows the major (but unique) different contributions from the different partners. Table 7.1 summaries the responsible person for each partner, the main resource that is asked for and to which task(s) the partner will mainly (but not uniquely) contribute.

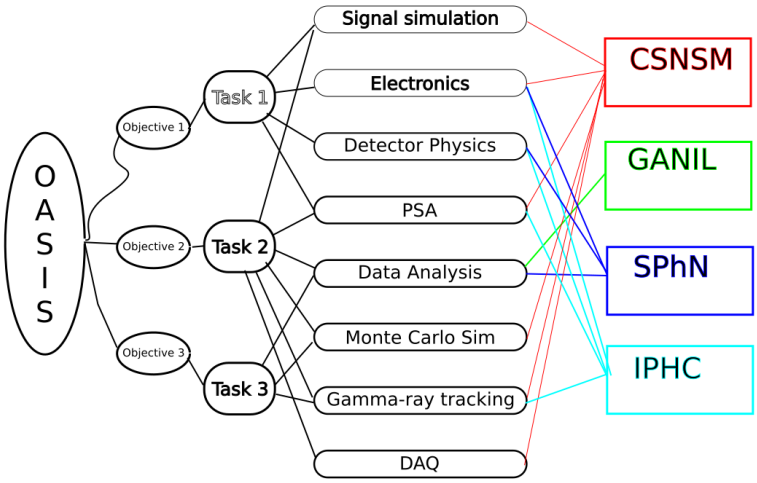

Figure 7.5: Figure showing how the different objectives, tasks, needed competences and how different members of the consortium contribute

Table 7.1: Table showing the partners of the consortium, the principal contact person and a first order distribution of the tasks and resources

Partner	Person	Resources	Task
CSNSM	Joa Ljungvall	Student+Equipment	1,2,3
GANIL	Emmanuel Clément	Post-doc 1	3
SPhN	Magda Zielińska	Post-doc 2	1
IPHC	Gilbert Duchêne	Equipment	1

The Centre de Sciences Nucléaires et de Sciences de la Matière (CSNSM) is a funding member of the AGATA collaboration which has been leading in the development of γ-ray tracking algorithms, pulse-shape analysis codes, and detector characterization using the Orsay Scanning table. A geographically close partner that has necessary complementary detector physics and "hands on" experience with AGATA type detectors is the Service de Physique Nucléaire/IRFU Cea (SPhN). They have a long time involvement in the AGATA project both in its conceptual phase, in the early and present exploitation phase and as one of the laboratories that are performing Customer Acceptance Tests (CAT's) for the AGATA collaboration. The SPhN also has an experienced γ-ray spectroscopy group. A post-doc working at SPhN will therefore profit from a strong local competence and close proximity to the CSNSM which should generate an excellent environment to advance OASIS towards its objectives. GANIL is the present host laboratory of AGATA and therefore a natural partner for a project that aims at pushing the exploration of AGATA data as far as possible. With a post-doc focusing on task 3, together with the student at CSNSM, a close to complete characterization of AGATA as a γ-ray spectrometer is possible. This will be combined with analyzing data with the goal of extracting nuclear-structure physics. The Institut Pluridisciplinaire Hubert CURIEN (IPHC) has a large experience in working with AGATA detectors, especially in comparing experi-

mental pulses coming from dedicated detector scanning setups with calculated pulses, with a recent thesis. Their presence within the consortium is thus of utmost value to ensure that to the work of especially task 1 can proceed from an advanced point. IPHC is also one of two french laboratories (the second being CSNSM) equipped to scan AGATA detectors allowing to measure the pulse shapes from a well defined location inside the crystal to allow a complete characterization of the crystal. This complementary and redundancy drastically reduced the risks if the OASIS project will have the possibility to scan an AGATA crystal.

3. Means of achieving the objectives

   As has been described the three objectives of OASIS will be reached by solving three different tasks. Table 7.1 shows the course partitioning of the tasks. The tasks are subdivided into smaller parts according to the present understanding of the scientific coordinator. More details of the planning for each task are given under respective head line below. The only real estimation of success for objective one and two of OASIS is the improvement in performance of AGATA. Task 1 and task 2 corresponding to objective 1 and 2 can however be broken down into smaller steps, with the possibility to define whether it was successfully or not. Towards the end of the second year it will be very beneficial to organize an international workshop for γ-ray tracking and PSA. Funds are thus requested for this and this workshop is one of the deliverables of OASIS. Objective three is a bit different in that the first part is less exploratory and more production like and can be planned with clear objectives and deliverables. For the second part of objective 3, i.e. the application to experimental data to extract more physics the scope depends heavily on the outcome of all tasks and therefore has to be left open ended, e.g. without a well defined sub-task or deliverable.

   The resources asked by each partner in the consortium to achieve the tasks are listed in table 7.2. The travel request are generic on the scale of 3.3 kEuro per year and partner. This is to allow frequent travel between the laboratories to be able to participate hands on in e.g. detector scanning or data taking with AGATA at GANIL (not experiments but to this project dedicated data, e.g. source data). Also it is our intentions to have 2 collaboration meetings per year of 2 days each. The assumption of four participants per laboratory is made in the cost estimation.

   - Detailing Task 1 In table 7.3 the sub tasks of task 1 are shown together with the contributing members and deliverables. The approximate time span for the completion of each task is also shown. Considering the time needed to write publications and a PhD thesis the tasks are to be finished some time before the end of the OASIS project. As task number one is based on the use of computer simulations the first step is to achieve the coupling between the AGATA Monte Carlo code simulations package, the AGATAGeFEM pulse-shape calculation-code package and the AGATA online data acquisition part. This is work that is partly already performed by the scientific coordinator, but it has to be completed and upgraded to be compatible with the latest developments made on all the different codes. This is the first step and has to be done before the task can proceed, and is a first deliverable - a short report showing how computer simulations have been used to produce data that has been treated using the AGATA

Table 7.2: Resources asked for for each partner to accomplish tasks

Partner	Resource	Demand [kEuro]
CSNSM	PhD student	98
CSNSM	Collimated ^{137}Cs source	10
CSNSM	CPU for cloud computing	5
CSNSM	Equipment for CSNSM scanning table	10
CSNSM	Workshop+Travel	20
CSNSM	Open Access Publishing	10
SPhN	2 year post-doc	126
SPhN	CAT Lab equipment	20
SPhN	Travel	11
IPHC	^{152}Eu source and Equipment for IPHC scanning table	20
IPHC	Travel	10
GANIL	2 year post-doc	115
GANIL	Travel	10
Total		465
	ANR funding asked for	**492**

online data acquisition and subsequent data analysis programs (already existing within the AGATA collaboration). The choice a FEM-based code to calculate the electric fields inside the AGATA crystal allows the possibility to investigate the effects of geometrical imperfection to an arbitrary small scale.

After this the computer modeling sub-tasks should be performed in parallel. This because much of the work analyzing the result of varying different aspect (i.e. detector geometry of the electronics response function) will be compared with each other. Typically the student and one of the post-docs will share this work with support from the scientific coordinator and permanent staff at CSNSM and SPhN. When all sub-tasks are finished short report will be written summarizing the influence of each change on position resolution, γ-ray tracking efficiency and peak-to-total in the γ-ray spectra. It will also clearly state if we have succeeded in pinning down the reasons for the less-than-perfect performance of the PSA algorithms, which is the measure of success for these sub-tasks. Here it should be noted the in2p3 project "Data flow for nuclear physics" will be able to provide the needed infrastructures for the computer based calculations. Therefore a small amount of money is asked for to contribute to the local computer infrastructure by buying additional computer power for the cloud. Access to a cloud computing facility is important as pulse-shape analysis and calculations are very CPU-time consuming activities.

If possible the result will be compared to and collaborated by the experimental scanning of an AGATA HPGe detector. Here is of extra interest the possibility to use a ^{152}Eu source as one will be able to study the impact of the charge carrier cloud size by using the different γ-ray energies available. Funds are therefore demanded for a ^{152}Eu source. This is work that has to be done on an ad-hoc time scale as it is impossible to foresee the availability of an AGATA crystal. An unavailability of an AGATA crystal during the project period is a real risk, with as only mitigation the use of

already existing scan data. It should here be pointed out that the access to two different scanning table setups and, via the consortium, different sets of scanning data, provides a very important redundancy to assure that the project can profit if a detector is available. However, for this redundancy there is a need to replace the collimated ^{137}Cs source at CSNSM, and funds will be asked for this within the OASIS project. There is also a request for funding to allow the use of an AGATA digitizer test-bench available at CSNSM together with the CSNSM scanning table make sure that the electronic response function is the correct one. The technical services of CSNSM (IT and electronics) will be solicited for this work. The possibility to scan the same detector using both the CSNSM and IPHC scanning table with different electronics would be of great interest and would enable us determining the pulse-shape alteration as a function of electronics.

Table 7.3: Table showing an overview of the sub tasks of task 1.

Sub task	Leader	Partners/ Contribution	Success indicator	Deliverable	Start month	End month
AGATAGeFEM MC Sim coupling	CSNSM	CSNSM, IPHC	Data injected in AGATA online code	Full simulation	0	6
Investigate geometrical effect	IRFU	CSNSM, SPhN, IPHC	Effect seen and quantified	Sensitivity estimate	6	30
Investigate effects from electronics	IRFU	CSNSM, SPhN, IPHC	Effect seen and quantified	Sensitivity estimate	6	30
Implement and investigate charge carrier cloud effects	CSNSM	CSNSM, IPHC	Effect seen and quantified	Sensitivity estimate	6	30
Scan AGATA detector crystal	CSNSM	CSNSM, IPHC	Data taken	Data set	0	24
Publish	CSNSM	CSNSM, SPhN, IPHC	Publication	Publication	18	36

- Detailing Task 2 In table 7.4 the sub tasks of task 2 are shown together with the contributing members and deliverables. The approximate time span for the completion of each task is also shown. Considering the time needed to write publications and a PhD thesis the tasks are to be finished some time before the end of the OASIS project. Task number two aims at better estimating the actual number of γ-ray interactions detected inside AGATA in each event, this way fulfilling the second objective of OASIS. Although this task of course is closely correlated to task 1, the principal difference is the abandoning of a logical separation between individual detectors and AGATA as a hole. This separation has no physical meaning and is a consequence of the assumption made that PSA (the subject of task 1 and objective 1) will not profit from any additional information outside the single crystal. It was therefore seen as not worth the considerable technical effort of the time when the electronics and DAQ of AGATA was design to consider all of AGATA at the level of PSA. The OASIS project takes the stand that this assumption should be questioned and that the inclusion of a global view into PSA will allow a better (although not exact) determination of the number of γ-ray interactions inside AGATA.

  The first step of task 2 will be to connect what is today called ”the local level” and ”the global level” of data in AGATA. The ”local level” refers to

data from one crystal without any time correlations to other detectors, whereas "the global level" unites time correlated data from all crystals, and if present, ancillary detectors. In the present form the codes used for PSA have only access to pulse-shapes from the crystals whereas γ-ray tracking only have access to the deduced positions and energy depositions. As a first step in this task the removal of the barrier between local and global level in the structure of the analysis is mandatory, and comes with a deliverable in form of reanalyzed data to prove that the new code is working.

Of utmost importance to reach the second objective of OASIS, and to finish task 2 is to have a reliable estimate of the position on an event by event basis from the PSA. Presently this information is not given by the PSA routines used in AGATA and the second sub-task of task 2, mandatory before continuing, is to implement a PSA routine that also provides errors. This can be done either using a classical $\chi^2 + 1$ approach in the case of using the present grid search method or using another PSA method where the errors also can be extracted, e.g. the Matrix method with Singular Value Decomposition. In order to see if the estimated errors are correct data with large Doppler Shifts will be used to correlate the error estimates to the Doppler Correction capability. The measure of success is to find such a correlation and that the increase in width of the Doppler Corrected peak corresponds to the given position uncertainties. There is potential technical risk here in that no reliable error estimate from the PSA can be found on an event-by-event basis. If this would be the case the project would have to proceed without but with a decreased chance of achieving objective 2. At the time of writing there is no reliable estimate to which extent.

As the sub-tasks related to joining the local and global level and the position error estimates have been finished the sub-tasks investigating different ways of improving the γ-ray tracking can be addressed. Although not separated as a sub-task there will be the need to put in place an efficient way of analyzing the results to access the success of each sub-task. These task will performed in parallel if possible. If one proves to be the correct way this will quickly be discovered and the consortium force can be directed towards it. A worst case scenario would be that none of the ideas tested within the OASIS project improves the performance of the γ-ray tracking. However, even in such a case OASIS will have helped by removing some possible routes to explore.

- Detailing Task 3 Task 3 is detailed in table 7.5. The approximate time span for the completion of each task is also shown. Since a large part of task 3 will be centred around a 24 month post-doc it has a more compact schedule than task 1 and 2. Here the first step will be to identify existing experimental data suitable for the work in question and put in place the corresponding simulations. During the years that AGATA has been taking data suitable data sets for the suggested investigation have been taken and are becoming available to the entire AGATA collaboration. This first sub-task has therefore only a small risk associated to it.

  The three consecutive named sub-tasks are to be performed in the enumerated order, as this in some way corresponds to the needs of the γ-ray

Table 7.4: Table showing an overview of the sub tasks of task 2.

Sub task	Leader	Partners/ Contribution	Success indicator	Deliverable	Start month	End month
Join local and global data flow	CSNSM	CSNSM	Reproduction of old result	Functional PSA+ γ-ray tracking code	0	12
Implement error	CSNSM	CSNSM	Correlation Doppler Broadening PSA error	PSA code	0	12
Gamma-ray tracking chooses solution	CSNSM	CSNSM, IPHC	Better figure of merit in γ-ray spectra	Functional code	12	30
PSA and γ-ray tracking in one step	CSNSM	CSNSM	Better figure of merit in γ-ray spectra	Functional code	12	30
Pre PSA estimation of number of hits	CSNSM	CSNSM	Better figure of merit in γ-ray spectra	Functional code	12	30
Publish	CSNSM	CSNSM, IPHC	Publication	Publication	18	36

spectroscopy community. For these tasks, as well as all of task 3, the indicators of success are reliable estimates of the errors made when extracting intensities from experimental spectra in different situations or deconvoluting a continuous spectrum. The tasks will be performed using standard γ-ray spectroscopy tools and are associated with a very small technical risk.

Table 7.5: Table showing an overview of the sub tasks of task 3.

Sub task	Leader	Partners/ Contribution	Success indicator	Deliverable	Start month	End month
Prepare data (sim and exp)	GANIL	GANIL, CSNSM		Data	0	6
Efficiency as function of fold and γ-ray energy	GANIL	GANIL, SPhN, CSNSM	Reliable error estimates	Recipe and code for collaboration	6	20
Determination of angular correlations and distributions	GANIL	GANIL, SPhN, CSNSM	Reliable error estimates	Recipe and code for collaboration	6	20
Deconvolution of continuous γ-ray distributions	GANIL	GANIL, SPhN, CSNSM	Reliable error estimates	Recipe and code for collaboration	6	20
Publish	GANIL	GANIL, SPhN, CSNSM	Publication	Publication	12	24

- CSNSM demand justification The CSNSM is asking for funds to finance one PhD student. Furthermore is the CSNSM asking for funds to complement existing AGATA electronics in order to have an AGATA electronics setup to perform detector scanning and to renew the collimated ^{137}Cs source and, if needed, minor upgrades of the scanning table hardware. The AGATA electronics are needed to remove the ambiguity coming from different electronics when working with PSA. CSNSM will also organize an international workshop during the end of the second year of OASIS, and funds are asked for this. The estimated cost for a 3 day workshop with 20 participants is 1000 euros. We would like to invite participants from the Gretina collaboration in the USA with an estimated cost of 1300 Euro/person. This gives an estimation of about 5000 euros for the workshop.

As all results from OASIS are to be published with open access the CSNSM is also asking for money to pay for this.

Finally the CSNSM asks for some money to be able to make a small contribution to the local cloud computing infrastructure that will be solicited by the OASIS project.

- GANIL demand justification GANIL is the present host-laboratory of AGATA and therefore an indispensable partner for OASIS. Having a qualified post-doc on site will allow rapid reaction, e.g., if complementary source data is needed. Physical access to AGATA will also help the post-doc in the understanding. Missions are required for the travel within the consortium for the post-doc and the permanent personnel.
- SPhN demand justification The tasks to be addressed by SPhN in OASIS is man hour demanding and hence the financing of a post-doc is asked for. The post-doc will work with the SPhN scientists on the PSA and simulation. He will be in close contact with the AGATA detector lab and therefore gain experience in the full readout chain from the crystals to the disks via the front-end electronics and digital electronics. Missions are required for the travel within the consortium for the post-doc and the two permanent physicists. Funds needed to upgrade and maintenance of the AGATA detector lab is also asked for.
- IPHC demand justification As one of the laboratories that can perform the complete scanning of a crystal IPHC are investigating the possibilities of performing scanning with a ^{152}Eu source to be able to study the impact of the charge carrier cloud size on the pulse shape generation. IPHC therefore request money to acquire such a source. This will also require an upgrade of the collimator used at the IPHC scanning table and if needed some minor refurbish of the table, which is included in the request. Missions are required for the travel within the consortium for the IPHC personnel.

7.13.3 Impact and benefits of the project

The OASIS project has as main goal to improve the performance of AGATA. This will allow increased scientific production not only from future experiments but also passed experiments. In the perspective of the future use of AGATA at large scale nuclear physics installations in Europe, it is important that AGATA performs at the highest level possible, as anything else would be an unacceptable waste of resources.

The investigations performed within the OASIS project will move forward our knowledge about HPGe detectors as it has become clear that in order for PSA to perform according to our expectations a very detailed understanding of the detectors is needed. This knowledge will be used to improve the performance of AGATA. We will furthermore publish all results with open access. As the goal is to provide solution to the γ-ray tracking community world wide all computer codes will be licensed using appropriate licences (CeCILL) to allow the world wide use of the computer codes.

An interesting application of detailed knowledge about segmented HPGe detectors is that of the detection of neutrino less double beta decay. Here HPGe detectors are made by enriched (^{76}Ge) material and used as both source and detector. Pulse-shape analysis is used to discriminate against background events.

If the improvements from OASIS for PSA and γ-ray tracking are substantial there exists applications outside γ-ray spectroscopy for nuclear structure. Environmen-

tal monitoring in the case of very complex radioactive contamination where γ-ray tracking would allow both identification of the nuclei as well mapping of its spatial distribution. Also safe guards application where segmented germanium detectors combined with PSA could allow collimator less tomography of spent nuclear fuel to assure its integrity.

Chapter 8

List of Publications

- *Isospin Properties of Nuclear Pair Correlations from the Level Structure of the Self-Conjugate Nucleus* ^{88}*Ru* B. Cederwall, X. Liu, Ö. Aktas, A. Ertoprak, W. Zhang, C. Qi, E. Clément, G. de France, D. Ralet, A. Gadea, A. Goasduff, G. Jaworski, I. Kuti, B. M. Nyakó, J. Nyberg, M. Palacz, R. Wadsworth, J. J. Valiente-Dobón, Al- H. Azri, A. Ataç Nyberg, T. Bäck, G. de Angelis, M. Doncel, J. Dudouet, A. Gottardo, M. Jurado, **J. Ljungvall**, D. Mengoni, D. R. Napoli, C. M. Petrache, D. Sohler, J. Timár, D. Barrientos, P. Bednarczyk, G. Benzoni, B. Birkenbach, A. J. Boston, H. C. Boston, I. Burrows, L. Charles, M. Ciemala, F. C. L. Crespi, D. M. Cullen, P Désesquelles, C. Domingo-Pardo, J. Eberth, N. Erduran, S. Ertürk, V. González, J. Goupil, H. Hess, T. Huyuk, A. Jungclaus, W. Korten, A. Lemasson, S. Leoni, A. Maj, R. Menegazzo, B. Million, R. M. Perez-Vidal, Zs. Podolyak, A. Pullia, F. Recchia, P. Reiter, F. Saillant, M. D. Salsac, E. Sanchis, J. Simpson, O. Stezowski, Ch. Theisen, and M. Zielińska , Phys.Rev.Lett. 124, 062501 (2020)
- *Performance of the Advanced GAmma Tracking Array at GANIL* **J. Ljungvall**, R.M. Pérez-Vidal, A. Lopez-Martens, C. Michelagnoli, E. Clément, J. Dudouet, A. Gadea, H. Hess, A. Korichi, M. Labiche, N. Lalović, H.J. Li, F. Recchia, Nuclear Instruments and Methods in Physics Research, Section A, volume 955, January 2020
- *Lifetime measurements in* ^{52,54}*Ti to study shell evolution toward N=32* A .Goldkuhle, C . Fransen, A. Blazhev, M. Beckers, B. Birkenbach, T. Braunroth, E. Clément, A. Dewald, J. Dudouet, J. Eberth, H. Hess, B. Jacquot, J.Jolie, Y.-H. Kim, A. Lemasson, S. M. Lenzi, H. J. Li, J. Litzinger, C. Michelagnoli, C. Müller-Gatermann, B. S. Nara Singh, R. M. Pérez-Vidal, D. Ralet, P. Reiter, A. Vogt, N. Warr, K. O. Zell, A. Ataç, D Barrientos, C Barthe-Dejean, G. Benzoni, A. J. Boston, H. C. Boston, P. Bourgault, I. Burrows, J. Cacitti, B. Cederwall, M. Ciemala, D. M. Cullen, G. De France, C. Domingo-Pardo, J.-L. Foucher, G. Fremont, A. Gadea, P. Gangnant, V. González, J. Goupil, C. Henrich, C. Houarner, M. Jean, D. S. Judson, A. Korichi, W Korten, M. Labiche, A. Lefevre, L. Legeard, F. Legruel, S. Leoni, **J. Ljungvall**, A. Maj, C. Maugeais, L. Ménager, N. Ménard, R. Menegazzo, D. Mengoni, B. Million, H. Munoz, D. R. Napoli, A. Navin, J. Nyberg, M. Ozille, Zs. Podolyak, A. Pullia, B. Raine, F. Recchia, J. Ropert, F. Saillant, M. D. Salsac, E. Sanchis, C. Schmitt, J. Simpson, C. Spitaels, O Stezowski,Ch. Theisen, M. Toulemonde, M. Tripon, J.-J. Valiente Dobón, G. Voltolini, and M. Zielińska, Phys. Rev. C 100, 054317

- *B(E2) anomalies in the yrast band of ^{170}Os* A. Goasduff, **J. Ljungvall**, T. R. Rodríguez, F. L. Bello Garrote, A. Etile, G. Georgiev, F. Giacoppo, L. Grente, M. Klintefjord, A. Kuşoğlu, I. Matea, S. Roccia, M.-D. Salsac, and C. Sotty, Phys. Rev. C 100, 034302 (2019)

- *Evidence of octupole-phonons at high spin in 207Pb* D. Ralet, E. Clément, G. Georgiev, A.E. Stuchbery, M. Rejmund, P. Van Isacker, G. de France , A. Lemasson, **J. Ljungvall**, C. Michelagnoli, A. Navin , D.L. Balabanski, L. Atanasova, A. Blazhev, G. Bocchi , R. Carroll, J. Dudouet, E. Dupont, B. Fornal, S. Franchoo, C. Fransen, C. Müller-Gatermann, A. Goasduff , A. Gadea, P.R. John, D. Kocheva, T. Konstantinopoulos , A. Korichi, A. Kuşoğlu, S.M. Lenzi, S. Leoni, R. Lozeva, A. Maj, R. Perez, N. Pietralla, C. Shand, O. Stezowski, D. Wilmsen, D. Yordanov, D. Barrientos, P. Bednarczyk, B. Birkenbach, A.J. Boston, H.C. Boston, I. Burrows, B. Cederwall, M. Ciemala, J. Collado, F. Crespi, D. Cullen, H.J. Eberth, J. Goupil, L. Harkness, H. Hess, A. Jungclaus, W. Korten, M. Labiche, R. Menegazzo, D. Mengoni, B. Million, J. Nyberg, Zs. Podolyák, A. Pullia, B. Quintana Arnés, F. Recchia, P. Reiter, F. Saillant, M.D. Salsac, E. Sanchis, C. Theisen, J.J. Valiente Dobon, O. Wieland, Phys. Lett. B. 797, (2019)

- *Experimental determination of reference pulses for highly segmented HPGe detectors and application to Pulse Shape Analysis used in γ-ray tracking arrays* H. J. Li, **J. Ljungvall**, C. Michelagnoli, E. Clément, J. Dudouet, P. Désesquelles, A. Lopez-Martens, G. de France, Eur. Phys. J. A (2018) 54: 198.

- *Pseudospin Symmetry and Microscopic Origin of Shape Coexistence in the ^{78}Ni Region: A Hint from Lifetime Measurements* C. Delafosse, D. Verney, P. Marevic, A. Gottardo, C. Michelagnoli, A. Lemasson, A. Goasduff, **J. Ljungvall**, E. Clement, A. Korichi, G. De Angelis, C. Andreoiu, M. Babo, A. Boso, F. Didierjean, J. Dudouet, S. Franchoo, A. Gadea, G. Georgiev, F. Ibrahim, B. Jacquot, T. Konstantinopoulos, S.M. Lenzi, G. Maquart, I. Matea, D. Mengoni, D.R. Napoli, T. Niksic, L. Olivier, R.M. Perez-Vidal, C. Portail, F. Recchia, N. Redon, M. Siciliano, I. Stefan, O. Stezowski, D. Vretenar, M. Zielinska, D. Barrientos, G. Benzoni, B. Birkenbach, A.J. Boston, H.C. Boston, B. Cederwall, L. Charles, M. Ciemala, J. Collado, D.M. Cullen, P. Desesquelles, G. de France, C. Domingo-Pardo, J. Eberth, V. Gonzalez, L.J. Harkness-Brennan, H. Hess, D.S. Judson, A. Jungclaus, W. Korten, A. Lefevre, F. Legruel, R. Menegazzo, B. Million, J. Nyberg, B. Quintana, D. Ralet, P. Reiter, F. Saillant, E. Sanchis, Ch. Theisen, J.J. Valiente Dobon, Phys.Rev.Lett. 121, 192502 (2018)

- *Lifetimes of excited states in triaxially deformed ^{107}Tc and $^{109,111,113}Rh$* T.W. Hagen, A. Gorgen, W. Korten, L. Grente, M.-D. Salsac, F. Farget, T. Braunroth, B. Bruyneel, I. Celikovic, E. Clement, G. de France, O.Delaune, A.Dewald, A.Dijon, M.Hackstein, B.Jacquot, J.Litzinger, **J. Ljungvall**, C. Louchart, C. Michelagnoli, D.R. Napoli, F. Recchia, W. Rother, E. Sahin, S. Siem, B. Sulignano, Ch. Theisen, J.J. Valiente-Dobon , Eur. Phys. J. **A** (2018) 54: 50

- *Evidence for Coexisting Shapes through Lifetime Measurements in ^{98}Zr* P. Singh, W. Korten, T.W. Hagen, A. Gorgen, L. Grente, M.-D. Salsac, F. Farget, E. Clement, G. de France, T. Braunroth, B. Bruyneel, I. Celikovic, O. Delaune, A. Dewald, A. Dijon, J.-P. Delaroche, M. Girod, M. Hackstein, B. Jacquot, J. Libert, J. Litzinger, **J.Ljungvall**, C. Louchart, A. Gottardo, C. Michelagnoli, C. Muller-Gatermann, D.R. Napoli, T. Otsuka, N. Pillet, F. Recchia, W. Rother, E. Sahin, S. Siem, B.

Sulignano, T. Togashi, Y. Tsunoda, Ch. Theisen, J. J. Valiente-Dobon , Phys.Rev.Lett. 121, 192501 (2018)

- *Prompt-delayed γ -ray spectroscopy with AGATA, EXOGAM and VAMOS++* Y. H. Kim, A. Lemasson, M. Rejmund, A. Navin, S. Biswas, C. Michelagnoli, I. Stefan, R. Banik, P. Bednarczyk, S. Bhattacharya, S. Bhattacharyya, E. Clément, H. , L. Crawford, G. De France, P. Fallon, J. Goupil, B. Jacquot, H. J. Li, **J. Ljungvall**, A. O. Macchiavelli, A. Maj, L. Ménager, V. Morel, R. Palit, R. M. Pérez-Vidal, J. Ropert, C. Schmitt , Eur. Phys. J. **A** (2017) 53: 162

- *Conceptual design of the AGATA 1π array at GANIL* E. Clément , C. Michelagnoli , G. de France , H.J. Li , A. Lemasson , C. Barthe Dejean , M. Beuzard , P. Bougault , J. Cacitti , J.-L. Foucher , G. Fremont , P. Gangnant , J. Goupil , C. Houarner , M. Jean , A. Lefevre , L. Legeard , F. Legruel , C. Maugeais , L. Ménager , N. Ménard , H. Munoz , M. Ozille , B. Raine , J.A. Ropert , F. Saillant , C. Spitaels , M. Tripon , Ph. Valler, , G. Voltolini , W. Korten , M.-D. Salsac , Ch. Theisen , M. Zielińska , T. Joannem , M. Karolak , M. Kebbiri , A. Lotode , R. Touzery , Ch. Walter , A. Korichi , **J. Ljungvall** , A. Lopez-Martens , D. Ralet , N. Dosme , X. Grave , N. Karkour , X. Lafay , E. Legay , I. Kojouharov , C. Domingo-Pardo , A. Gadea , R.M. Pérez-Vidal , J.V. Civera , B. Birkenbach , J. Eberth , H. Hess , L. Lewandowski , P. Reiter , A. Nannini , G. De Angelis , G. Jaworski , P. John , D.R. Napoli , J.J. Valiente-Dobón , D. Barrientos , D. Bortolato , G. Benzoni , A. Bracco , S. Brambilla , F. Camera , F.C.L. Crespi , S. Leoni , B. Million , A. Pullia , O. Wiel, , D. Bazzacco , S.M. Lenzi , S. Lunardi , R. Menegazzo , D. Mengoni , F. Recchia , M. Bellato , R. Isocrate , F.J. Egea Canet , F. Didierjean , G. Duchêne , R. Baumann , M. Brucker , E. Dangelser , M. Filliger , H. Friedmann , G. Gaudiot , J.-N. Grapton , H. Kocher , C. Mathieu , M.-H. Sigward , D. Thomas , S. Veeramootoo , J. Dudouet , O. Stézowski , C. Aufranc , Y. Aubert , M. Labiche , J. Simpson , I. Burrows , P.J. Coleman-Smith , A. Grant , I.H. Lazarus , P.S. Morrall , V.F.E. Pucknell , A. Boston , D.S. Judson , N. Lalović , J. Nyberg , J. Collado , V. González , I. Kuti , B.M. Nyakó , A. Maj , M. Rudigier , Nuclear Instruments and Methods in Physics Research, Section A, volume 855, February 2017, page 1-12

- $^{96}_{36}Kr_{60}$*-Low-Z Boundary of the Island of Deformation at N=60* J. Dudouet, A. Lemasson, G. Duchêne, M. Rejmund, E. Clément, C. Michelagnoli, F. Didierjean, A. Korichi, G. Maquart, O. Stezowski, C. Lizarazo, R. M. Pérez-Vidal, C. Andreoiu, G. de Angelis, A. Astier, C. Delafosse, I. Deloncle, Z. Dombradi, G. de France, A. Gadea, A. Gottardo, B. Jacquot, P. Jones, T. Konstantinopoulos, I. Kuti, F. Le Blanc, S. M. Lenzi, G. Li, R. Lozeva, B. Million, D. R. Napoli, A. Navin, C. M. Petrache, N. Pietralla, D. Ralet, M. Ramdhane, N. Redon, C. Schmitt, D. Sohler, D. Verney, D. Barrientos, B. Birkenbach, I. Burrows, L. Charles, J. Collado, D. M. Cullen, P. Désesquelles, C. Domingo Pardo, V. González, L. Harkness-Brennan, H. Hess, D. S. Judson, M. Karolak, W. Korten, M. Labiche, **J. Ljungvall**, R. Menegazzo, D. Mengoni, A. Pullia15, F. Recchia, P. Reiter, M. D. Salsac, E. Sanchis, Ch. Theisen, J. J. Valiente-Dobón, and M. Zielińska , Phys. Rev. Lett. 118, 162501 (2017)

- *Evolution of nuclear shapes in odd-mass yttrium and niobium isotopes from lifetime measurements following fission reactions* T. W. Hagen, A. Görgen, W. Korten, L. Grente, M.-D. Salsac, F. Farget, I. Ragnarsson, T. Braunroth, B. Bruyneel, I. Celikovic, E. Clément, G. de France, O. Delaune, A. Dewald, A. Dijon, M. Hackstein, B. Jacquot, J. Litzinger, **J. Ljungvall**, C. Louchart, C. Michelagnoli, D. R.

Napoli, F. Recchia, W. Rother, E. Sahin, S. Siem, B. Sulignano, Ch. Theisen, and J. J. Valiente-Dobon , Phys. Rev. C 95, 034302 (2017)

- *In-beam γ-ray spectroscopy of the neutron-rich platinum isotope ^{200}Pt toward the N=126 shell gap* P. R. John, J. J. Valiente-Dobón, D. Mengoni, V. Modamio, S. Lunardi, D. Bazzacco, A. Gadea, C. Wheldon, T. R. Rodríguez, T. Alexander, G. de Angelis, N. Ashwood, M. Barr, G. Benzoni, B. Birkenbach, P. G. Bizzeti, A. M. Bizzeti-Sona, S. Bottoni, M. Bowry, A. Bracco, F. Browne, M. Bunce, F. Camera, L. Corradi, F. C. L. Crespi, B. Melon, E. Farnea, E. Fioretto, A. Gottardo, L. Grente, H. Hess, Tz. Kokalova, W. Korten, A. Kuşoğlu, S. Lenzi, S. Leoni, **J. Ljungvall**, R. Menegazzo, C. Michelagnoli, T. Mijatović, G. Montagnoli, D. Montanari, D. R. Napoli, Zs. Podolyák, G. Pollarolo, F. Recchia, P. Reiter, O. J. Roberts, E. Şahin, M.-D. Salsac, F. Scarlassara, M. Sferrazza, P.-A. Söderström, A. M. Stefanini, S. Szilner, C. A. Ur, A. Vogt, and J. Walshe , Phys.Rev. C 95, 064321 (2017)

- *Anomalies in the Charge Yields of Fission Fragments from the $^{238}U(n, f)$ Reaction* J. N. Wilson, M. Lebois, L. Qi, P. Amador-Celdran, D. Bleuel, J. A. Briz, R. Carroll, W. Catford, H. De Witte, D. T. Doherty, R. Eloirdi, G. Georgiev, A. Gottardo, A. Goasduff, K. Hadyńska-Klęk, K. Hauschild, H. Hess, V. Ingeberg, T. Konstantinopoulos, **J. Ljungvall**, A. Lopez-Martens, G. Lorusso, R. Lozeva, R. Lutter, P. Marini, I. Matea, T. Materna, L. Mathieu, A. Oberstedt, S. Oberstedt, S. Panebianco, Zs. Podolyák, A. Porta, P. H. Regan, P. Reiter, K. Rezynkina, S. J. Rose, E. Sahin, M. Seidlitz, O. Serot, R. Shearman, B. Siebeck, S. Siem, A. G. Smith, G. M. Tveten, D. Verney, N. Warr, F. Zeiser, and M. Zielińska, Phys. Rev. Lett. 118, 222501 (2017)

- *Measurement of lifetimes in ^{62,64}Fe, ^{61,63}Co, and ^{59}Mn* M. Klintefjord, **J. Ljungvall**, A. Görgen, S. M. Lenzi, F. L. Bello Garrote, A. Blazhev, E. Clément, G. de France, J.-P. Delaroche, P. Désesquelles, A. Dewald, D. T. Doherty, C. Fransen, A. Gengelbach, G. Georgiev, M. Girod, A. Goasduff, A. Gottardo, K. Hadyńska-Klęk, B. Jacquot, T. Konstantinopoulos, A. Korichi, A. Lemasson, J. Libert, A. Lopez-Martens, C. Michelagnoli, A. Navin, J. Nyberg, R. M. Pérez-Vidal, S. Roccia, E. Sahin, I. Stefan, A. E. Stuchbery, M. Zielińska, D. Barrientos, B. Birkenbach, A. Boston, L. Charles, M. Ciemala, J. Dudouet, J. Eberth, A. Gadea, V. González, L. Harkness-Brennan, H. Hess, A. Jungclaus, W. Korten, R. Menegazzo, D. Mengoni, B. Million, A. Pullia, D. Ralet, F. Recchia, P. Reiter, M. D. Salsac, E. Sanchis, O. Stezowski, Ch. Theisen, and J. J. Valiente Dobon , Phys. Rev. C 95, 024312 (2017)

- *Lifetime measurements in ^{100}Ru* T. Konstantinopoulos, P. Petkov, A. Goasduff, T. Arici, A. Astier, L. Atanasova, M. Axiotis, D. Bonatsos, P. Detistov, A. Dewald, M. J. Eller, V. Foteinou, A. Gargano, G. Georgiev, K. Gladnishki, A. Gottardo, S. Harissopulos, H. Hess, S. Kaim, D. Kocheva, A. Kusoglu, A. Lagoyannis, **J. Ljungvall**, R. Lutter, I. Matea, B. Melon, T. J. Mertzimekis, A. Nannini, C. M. Petrache, A. Petrovici, G. Provatas, P. Reiter, M. Rocchini, S. Roccia, M. Seidlitz, B. Siebeck, D. Suzuki, N. Warr, H. De Witte, T. Zerrouki, Phys. Rev. C 95, 014309 (2017)

- *Low-energy Coulomb excitation of ^{96,98}Sr beams* E. Clément, M. Zielińska, S. Péru, H. Goutte, S. Hilaire, A. Görgen, W. Korten, D. T. Doherty, B. Bastin, C. Bauer, A. Blazhev, N. Bree, B. Bruyneel, P. A. Butler, J. Butterworth, J. Cederkäll, P. Delahaye, A. Dijon, A. Ekström, C. Fitzpatrick, C. Fransen, G. Georgiev, R.

Gernhäuser, H. Hess, J. Iwanicki, D. G. Jenkins, A. C. Larsen, **J. Ljungvall**, R. Lutter, P. Marley, K. Moschner, P. J. Napiorkowski, J. Pakarinen, A. Petts, P. Reiter, T. Renstrøm, M. Seidlitz, B. Siebeck, S. Siem, C. Sotty, J. Srebrny, I. Stefanescu, G. M. Tveten, J. Van de Walle, M. Vermeulen, D. Voulot, N. Warr, F. Wenander, A. Wiens, H. De Witte, K., Phys. Rev C 94, 054326 (2016)

- *Superdeformed and Triaxial States in* ^{42}Ca K. Hadyńska-Klęk, P. J. Napiorkowski, M. Zielińska, J. Srebrny, A. Maj, F. Azaiez, J. J. Valiente Dobón, M. Kicińska-Habior, F. Nowacki, H. Naïdja, B. Bounthong, T. R. Rodríguez, G. de Angelis, T. Abraham, G. Anil Kumar, D. Bazzacco, M. Bellato, D. Bortolato, P. Bednarczyk, G. Benzoni, L. Berti, B. Birkenbach, B. Bruyneel, S. Brambilla, F. Camera, J. Chavas, B. Cederwall, L. Charles, M. Ciemala, P. Cocconi, P. Coleman-Smith, A. Colombo, A. Corsi, F. C. L. Crespi, D. M. Cullen, A. Czermak, P. Désesquelles, D. T. Doherty, B. Dulny, J. Eberth, E. Farnea, B. Fornal, S. Franchoo, A. Gadea, A. Giaz, A. Gottardo, X. Grave, J. Grebosz, A. Görgen, M. Gulmini, T. Habermann, H. Hess, R. Isocrate„ J. Iwanicki, G. Jaworski, D. S. Judson, A. Jungclaus, N. Karkour, M. Kmiecik, D. Karpiński, M. Kisieliński, N. Kondratyev, A. Korichi, M. Komorowska„ M. Kowalczyk, W. Korten, M. Krzysiek, G. Lehaut, S. Leoni, **J. Ljungvall**, A. Lopez-Martens, S. Lunardi, G. Maron, K. Mazurek, R. Menegazzo, D. Mengoni, E. Merchán„ W. Meczyński, C. Michelagnoli, J. Mierzejewski, B. Million, S. Myalski, D. R. Napoli, R. Nicolini, M. Niikura, A. Obertelli, S. F. Özmen, M. Palacz, L. Próchniak, A. Pullia„ B. Quintana, G. Rampazzo, F. Recchia, N. Redon, P. Reiter, D. Rosso, K. Rusek, E. Sahin, M.-D. Salsac, P.-A. Söderström, I. Stefan, O. Stézowski, J. Styczeń, Ch. Theisen, N. Toniolo, C. A. Ur, V. Vandone„ R. Wadsworth, B. Wasilewska, A. Wiens, J. L. Wood, K. Wrzosek-Lipska, and M. Zieblíński , Phys. Rev. Lett. 117, 062501 (2016)
- *Pygmy dipole resonance in* ^{140}Ce *via inelastic scattering of* ^{17}O M. Krzysiek, M. Kmiecik, A. Maj, P. Bednarczyk, A. Bracco, F. C. L. Crespi, E. G. Lanza, E. Litvinova, N. Paar, R. Avigo, D. Bazzacco, G. Benzoni, B. Birkenbach, N. Blasi, S. Bottoni, S. Brambilla, F. Camera, S. Ceruti, M. Ciemala, G. de Angelis, P. Désesquelles, J. Eberth, E. Farnea, A. Gadea, A. Giaz, A. Görgen, A. Gottardo, J. Grebosz, H. Hess, R. Isocarte, A. Jungclaus, S. Leoni, **J. Ljungvall**, S. Lunardi, K. Mazurek, R. Menegazzo, D. Mengoni, C. Michelagnoli, B. Milion, A. I. Morales, D. R. Napoli, R. Nicolini, L. Pellegri, A. Pullia, B. Quintana, F. Recchia, P. Reiter, D. Rosso, M. D. Salsac, B. Siebeck, S. Siem, P.-A. Söderström, C. Ur, J. J. Valiente-Dobon, O. Wiel, K. Wrzosek-Lipska, M. Zieblíński, Phys. Rev. C 93, 044330 (2016)
- *Spectroscopic Quadrupole Moments in* $^{96,98}Sr$*: Evidence for Shape Coexistence in Neutron-Rich Strontium Isotopes at N=60* E. Clément, M. Zielińska, A. Görgen, W. Korten, S. Péru, J. Libert, H. Goutte, S. Hilaire, B. Bastin, C. Bauer, A. Blazhev, N. Bree, B. Bruyneel, P. A. Butler, J. Butterworth, P. Delahaye, A. Dijon, D. T. Doherty, A. Ekström, C. Fitzpatrick, C. Fransen, G. Georgiev, R. Gernhäuser, H. Hess, J. Iwanicki, D. G. Jenkins, A. C. Larsen, **J. Ljungvall**, R. Lutter, P. Marley, K. Moschner, P. J. Napiorkowski, J. Pakarinen, A. Petts, P. Reiter, T. Renstrøm, M. Seidlitz, B. Siebeck, S. Siem, C. Sotty, J. Srebrny, I. Stefanescu, G. M. Tveten„ J. Van de Walle, M. Vermeulen, D. Voulot, N. Warr, F. Wenander, A. Wiens, H. De Witte, and K. Wrzosek-Lipska, Phys. Rev. Lett. 116, 022701 (2016)
- *Performance of the AGATA* γ*-ray spectrometer in the PreSPEC set-up at GSI* N. Lalović, C. Louchart, C. Michelagnoli, R.M. Perez-Vidal, D. Ralet, J. Gerl, D.

Rudolph, T. Arici, D. Bazzacco, E. Clément, A. Gadea, I. Kojouharov, A. Korichi, M. Labiche, **J. Ljungvall**, A. Lopez-Martens, J. Nyberg, N. Pietralla, S. Pietri, O. Stezowski, For PreSPEC and AGATA Collaborations, Nuclear Instruments and Methods in Physics Research, Section A, volume 806, January 2016, page 258-266

- *Probing collectivity in Zn isotopes with one particle or hole outside the N=40 subshell closure* I. Čeliković, A. Dijon, E. Clément, G. de France, P. Van Isacker, **J. Ljungvall**, A. Dewald, C. Fransen, G. Georgiev, A. Görgen, A. Gottardo, M. Hackstein, T. W. Hagen, C. Louchart, P. Napiorkowski, A. Obertelli, F. Recchia, W. Rother, S. Siem, B. Sulignano, P. Ujić, J. J. Valiente-Dobón, and M. Zielińska, Phys. Rev. C 91, 044311 (2015)

- *Magnetism of an Excited Self-Conjugate Nucleus: Precise Measurement of the g Factor of the* 2_1^+ *State in* ^{24}Mg A. Kusoglu, A. E. Stuchbery, G. Georgiev, B. A. Brown, A. Goasduff, L. Atanasova, D. L. Balabanski, M. Bostan, M. Danchev, P. Detistov, K. A. Gladnishki, **J. Ljungvall**, I. Matea, D. Radeck, C. Sotty, I. Stefan, D. Verney, D. T. Yordanov, , Phys. Rev. Lett. 114. 062501 (2015)

- *Shell evolution beyond N=40:* ^{69,71,73}*Cu* E. Sahin, M. Doncel„ K. Sieja, G. de Angelis, A. Gadea, B. Quintana, A. Görgen, V. Modamio, D. Mengoni, J. J. Valiente-Dobón, P. R. John, M. Albers, D. Bazzacco, G. Benzoni, B. Birkenbach, B. Cederwall, E. Clément, D. Curien, L. Corradi, P. Désesquelles, A. Dewald, F. Didierjean, G. Duchêne, J. Eberth, M. N. Erduran, E. Farnea, E. Fioretto, G. de France, C. Fransen, R. Gernhäuser, A. Gottardo, M. Hackstein, T. Hagen, A. Hernández-Prieto, H. Hess, T. Hüyük, A. Jungclaus, S. Klupp, W. Korten, A. Kusoglu, S. M. Lenzi, **J. Ljungvall**, C. Louchart, S. Lunardi„ R. Menegazzo, C. Michelagnoli, T. Mijatović, B. Million, P. Molini, G. Montagnoli, D. Montanari, O. Möller, D. R. Napoli, A. Obertelli, R. Orlandi, G. Pollarolo, A. Pullia, F. Recchia, P. Reiter, D. Rosso, W. Rother, M.-D. Salsac, F. Scarlassara, M. Schlarb, S. Siem, Pushpendra P. Singh, P.-A. Söderström, A. M. Stefanini, O. Stézowski, B. Sulignano, S. Szilner, Ch. Theisen, C. A. Ur, and M. Yalcinkaya, Phys. Rev. C 91, 034302 (2015)

- *Shape evolution in the neutron-rich osmium isotopes: Prompt* γ*-ray spectroscopy of* ^{196}*Os* P.R.John, V.Modamio, J.J.Valiente-Dobon, D.Mengoni, S.Lunardi, T.R.Rodriguez, D.Bazzacco, A.Gadea, C.Wheldon, T.Alexander, G.de Angelis, N.Ashwood, M.Barr, G.Benzoni, B.Birkenbach, P.G.Bizzeti, A.M.Bizzeti-Sona, S.Bottoni, M.Bowry, A.Bracco, F.Browne, M.Bunce, F.Camera, B.Cederwall, L.Corradi, F.C.L.Crespi, P.Desesquelles, J.Eberth, E.Farnea, E.Fioretto, A.Gorgen, A.Gottardo, J.Grebosz, L.Grente, H.Hess, A.Jungclaus, Tz.Kokalova, A.Korichi, W.Korten, A.Kusoglu, S.Lenzi, S.Leoni, **J.Ljungvall**, G.Maron, W.Meczynski, B.Melon, R.Menegazzo, C.Michelagnoli, T.Mijatovic, B.Million, P.Molini, G.Montagnoli, D.Montanari, D.R.Napoli, P.Nolan, C.Oziol, Zs.Podolyak, G.Pollarolo, A.Pullia, B.Quintana, F.Recchia, P.Reiter, O.J.Roberts, D.Rosso, E.Sahin, M.-D.Salsac, F.Scarlassara, M.Sferrazza, J.Simpson, P.-A.Soderstrom, A.M.Stefanini, O.Stezowski, S.Szilner, Ch.Theisen, C.A.Ur, J.Walshe,Phys.Rev. C 90, 021301 (2014)

- *Musett: A segmented Si array for Recoil-Decay-Tagging studies at VAMOS* Ch. Theisen„ F. Jeanneau, B. Sulignano, F. Druillole, **J. Ljungvall**, B. Paul, E. Virique, P. Baron, H. Bervas, E. Clément, E. Delagnes, A. Dijon, E. Dossat, A. Drouart, F. Farget, Ch. Flouzat, G. De France, A. Görgen, Ch. Houarner, B. Jacquot, W.

Korten, G. Lebertre, B. Lecornu, L. Legeard, A. Lermitage, S. Lhenoret, C. Marry, C. Maugeais, L. Menager, O. Meunier, A. Navin, F. Nizery, A. Obertelli, E. Rauly, B. Raine, M. Rejmund, J. Ropert, F. Saillant, H. Savajols, Ch. Schmitt, M. Tripon, E. Wanlin, G. Wittwer,Nuclear Instruments and Methods in Physics Research, Section A, volume 747, May 21, 2014, page 69-80

- *Identification and rejection of scattered neutrons in AGATA* M. Şenyiğit, A. Ataç, S. Akkoyun, A. Kaşkaş, D. Bazzacco, J. Nyberg, F. Recchia S. Brambilla, F. Camera, F.C.L. Crespi, E. Farnea, A. Giaz, A. Gottardo, R. Kempley, **J. Ljungvall**, D. Mengoni, C. Michelagnoli, B. Million, M. Palacz, L. Pellegri, S. Riboldi, E. Sahin, P.A. Söderström, J.J. Valiente Dobon,Nuclear Instruments and Methods in Physics Research, Section A, volume 735, January 21, 2014, page 267-276

- *Direct determination of the hit locations from experimental HPGe pulses* P. Désesquelles, A.J. Boston, H.C. Boston, J.R. Cresswell, M.R. Dimmock, I.H. Lazarus, **J. Ljungvall**, L. Nelson, D.-T. Nga, P.J. Nolan, S.V. Rigby, J. Simpson, N.-T. Van-Oanh,Nuclear Instruments and Methods in Physics Research, Section A, volume 729, 21 November, 2013, page 198-206

- *Collectivity of light Ge and As isotopes* A.Corsi, J.-P.Delaroche, A.Obertelli, T.Baugher, D.Bazin, S.Boissinot, F.Flavigny, A.Gade, M.Girod, T.Glasmacher, G.F.Grinyer, W.Korten, J.Libert, **J.Ljungvall**, S.McDaniel, A.Ratkiewicz, A.Signoracci, R.Stroberg, B.Sulignano, D.Weisshaar,Phys.Rev. C 88, 044311 (2013)

- *Collective nature of low-lying excitations in ^{70,72,74}Zn from lifetime measurements using the AGATA spectrometer demonstrator* C.Louchart, A.Obertelli, A.Gorgen, W.Korten, D.Bazzacco, B.Birkenbach, B.Bruyneel, E.Clement, P.J.Coleman-Smith, L.Corradi, D.Curien, G.de Angelis, G.de France, J.-P.Delaroche, A.Dewald, F.Didierjean, M.Doncel, G.Duchene, J.Eberth, M.N.Erduran, E.Farnea, C.Finck, E.Fioretto, C.Fransen, A.Gadea, M.Girod, A.Gottardo, J.Grebosz, T.Habermann, M.Hackstein, T.Huyuk, J.Jolie, D.Judson, A.Jungclaus, N.Karkour, S.Klupp, R.Krucken, A.Kusoglu, S.M.Lenzi, J.Libert, **J.Ljungvall**, S.Lunardi, G.Maron, R.Menegazzo, D.Mengoni, C.Michelagnoli, B.Million, P.Molini, O.Moller, G.Montagnoli, D.Montanari, D.R.Napoli, R.Orlandi, G.Pollarolo, A.Prieto, A.Pullia, B.Quintana, F.Recchia, P.Reiter, D.Rosso, W.Rother, E.Sahin, M.-D.Salsac, F.Scarlassara, M.Schlarb, S.Siem, P.P.Singh, P.-A.Soderstrom, A.M.Stefanini, O.Stezowski, B.Sulignano, S.Szilner, Ch.Theisen, C.A.Ur, J.J.Valiente-Dobon, M.Zielinska, Phys.Rev. C 87, 054302 (2013)

- *Investigation of high-K states in ^{252}No* B. Sulignano, Ch. Theisen J.-P. Delaroche, M. Girod, **J. Ljungvall**, D. Ackermann, S. Antalic, O. Dorvaux, A. Drouart, B. Gall, A. Görgen, P. T. Greenlees, K. Hauschild, R.-D. Herzberg, F. P. Heßberger, U. Jakobsson, P. Jones, R. Julin, S. Juutinen, S. Ketelhut, W. Korten, M. Leino, A. Lopez-Martens, M. Nyman, A. Obertelli, J. Pakarinen, P. Papadakis, E. Parr, P. Peura, J. Piot, P. Rahkila, D. Rostron, P. Ruotsalainen, J. Sarén, C. Scholey, J. Sorri, J. Uusitalo, M. Venhart, and M. Zielińska, Phys. Rev. C 86, 044318 (2012)

- *Shell-Structure and Pairing Interaction in Superheavy Nuclei: Rotational Properties of the Z=104 Nucleus ^{256}Rf*, P. T. Greenlees, J. Rubert, J. Piot, B. J. P. Gall, L. L. Andersson, M. Asai, Z. Asfari, D. M. Cox, F. Dechery, O. Dorvaux, T. Grahn, K. Hauschild, G. Henning, A. Herzan, R.-D. Herzberg, F. P. Hessberger, U. Jakobsson, P. Jones, R. Julin, S. Juutinen, S. Ketelhut, T.-L. Khoo, M. Leino, **J. Ljungvall**, A. Lopez-Martens, R. Lozeva, P. Nieminen, J. Pakarinen, P. Papadakis, E.

Parr, P. Peura, P. Rahkila, S. Rinta-Antila, P. Ruotsalainen, M. Sandzelius, J. Saren, C. Scholey, D. Seweryniak, J. Sorri, B. Sulignano, Ch. Theisen, J. Uusitalo, M. Venhart,Phys. Rev. Lett. 109, 012501 (2012)

- *N=50 core excited states studied in the $^{96}_{46}Pd_{50}$ nucleus*, M. Palacz, J. Nyberg, H. Grawe, K. Sieja, G. de Angelis, P. Bednarczyk, A. Blazhev, D. Curien, Z. Dombradi, O. Dorvaux, J. Ekman, J. Galkowski, M. Gorska, J. Iwanicki, G. Jaworski, J. Kownacki, **J. Ljungvall**, M. Moszynski, F. Nowacki, D. Rudolph, D. Sohler, D. Wolski, M. Zieblinski, Phys. Rev. C 86, 014318 (2012)

- *The Orsay Universal Plunger System*, **J. Ljungvall**, G. Georgiev, S. Cabaret, N. Karkour, D. Linget, G. Sedes, R. Chevrier, I. Matea, M. Niikura, M.-D. Salsac, B. Sulignano, Nuclear Instruments and Methods in Physics Research, Section A, volume 679, July 1, 2012, page 61-66

- *In-beam spectroscopy with intense ion beams: Evidence for a rotational structure in ^{246}Fm*, J. Piot, B.J.-P. Gall, O. Dorvaux, P. T. Greenlees, N. Rowley, L. L. Andersson, D. M. Cox, F. Dechery, T. Grahn, K. Hauschild, G. Henning, A. Herzan, R.-D. Herzberg, F.P. Hessberger, U. Jakobsson, P. Jones, R. Julin, S. Juutinen, S. Ketelhut, T.-L. Khoo, M. Leino, **J. Ljungvall**, A. Lopez-Martens, P. Nieminen, J. Pakarinen, P. Papadakis, E. Parr, P. Peura, P. Rahkila, S. Rinta-Antila, J. Rubert, P. Ruotsalainen, M. Sandzelius, J. Saren, C. Scholey, D. Seweryniak, J. Sorri, B. Sulignano, J. Uusitalo, Phys.Rev. C 85, 041301 (2012)

- *AGATA-Advanced GAmma Tracking Array*, Nuclear Instruments and Methods in Physics Research, Section A, Volume 668, March 11, 2012, pages 26-58

- *First spectroscopy of ^{66}Se and ^{65}As: Investigating shape coexistence beyond the N=Z line*, A. Obertelli, T. Baugher, D. Bazin, S. Boissinot, J.-P. Delaroche, A. Dijon, F. Flavigny, A. Gade, M. Girod, T. Glasmacher, G.F. Grinyer, W. Korten, **J. Ljungvall**, S. McDaniel, A. Ratkiewicz, B. Sulignano, P. Van Isacker, D. Weisshaar,Phys. Lett. B. 701, issue 4 (2011)

- *Lifetime measurements in ^{63}Co and ^{65}Co*, A.Dijon, E.Clement, G.de France, P.Van Isacker, **J.Ljungvall**, A.Gorgen, A.Obertelli, W.Korten, A.Dewald, A.Gadea, L.Gaudefroy, M.Hackstein, D.Mengoni, Th.Pissulla, F.Recchia, M.Rejmund, W.Rother, E.Sahin, C.Schmitt, A.Shrivastava, J.J.Valiente-Dobon, K.O.Zell, M.Zielińska,Phys. Rev. C 83, 064321 (2011)

- *Interaction position resolution simulations and in-beam measurements of the AGATA HPGe detectors*, P.-A. Söderström, F. Recchia, J. Nyberg, A. Al-Adili, A. Ataç, S. Aydin, D. Bazzacco, P. Bednarczyk, B. Birkenbach, D. Bortolato, A.J. Boston, H.C. Boston, B. Bruyneel, D. Bucurescu, E. Calore, S. Colosimo, F.C.L. Crespi, N. Dosme, J. Eberth, E. Farnea, F. Filmer, A. Gadea, A. Gottardo, X. Grave, J. Grebosz, R. Griffiths, M. Gulmini, T. Habermann, H. Hess, G. Jaworski, P. Jones, P. Joshi, D.S. Judson, R. Kempley, A. Khaplanov, E. Legay, D. Lersch, **J. Ljungvall**, A. Lopez-Martens, W. Meczynski, D. Mengoni, C. Michelagnoli, P. Molini, D.R. Napoli, R. Orlandi, G. Pascovici, A. Pullia, P. Reiter, E. Sahin, J.F. Smith, J. Strachan, D. Tonev, C. Unsworth, C.A. Ur, J.J. Valiente-Dobón, C. Veyssierea, A. Wiens and The AGATA Collaboration, Nuclear Instruments and Methods in Physics Research, Section A, volume 638, Issue 1, May 11, 2011, page 96-109

- *Onset of collectivity in neutron-rich Fe isotopes: Toward a new island of inversion?*, **J.Ljungvall**, A.Görgen, A.Obertelli, W.Korten, E.Clément, G.de France, A.Bürger, J.-P.Delaroche, A.Dewald, A.Gadea, L.Gaudefroy, M.Girod, M.Hackstein, J.Libert, D.Mengoni, F.Nowacki, T.Pissulla, A.Poves, F.Recchia, M.Rejmund, W.Rother, E.Sahin, C.Schmitt, A.Shrivastava, K.Sieja, J.J.Valiente-Doón, K.O.Zell, and M.Zielińska, Phys. Rev. C 81, 061301(R) (2010)

- *Lifetimes of odd-spin yrast states in ^{182}Hg*, M.Scheck, T.Grahn, A.Petts, P.A.Butler, A.Dewald, L.P.Gaffney, M.B.Gomez Hornillos, A.Gorgen, P.T.Greenlees, K.Helariutta, J.Jolie, P.Jones, R.Julin, S.Juutinen, S.Ketelhut, T.Kroll, R.Krucken, M.Leino, **J.Ljungvall**, P.Maierbeck, B.Melon, M.Nyman, R.D.Page, J.Pakarinen, E.S.Paul, Th.Pissulla, P.Rahkila, J.Saren, C.Scholey, A.Semchenkov, J.Sorri, J.Uusitalo, R.Wadsworth, M.Zielińska, Phys.Rev. C 81, 014310 (2010)

- *Evolution of collectivity in ^{180}Hg and ^{182}Hg*, T.Grahn, A.Petts, M.Scheck, P.A.Butler, A.Dewald, M.B.Gomez Hornillos, P.T.Greenlees, A.Gorgen, K.Helariutta, J.Jolie, P.Jones, R.Julin, S.Juutinen, S.Ketelhut, R.Krucken, T.Kroll, M.Leino, **J.Ljungvall**, P.Maierbeck, B.Melon, M.Nyman, R.D.Page, Th.Pissulla, P.Rahkila, J.Saren, C.Scholey, A.Semchenkov, J.Sorri, J.Uusitalo, R.Wadsworth, M.Zielińska, Phys.Rev. C 80, 014324 (2009)

- *Position resolution of the prototype AGATA triple-cluster detector from an in-beam experiment*, F.Recchia, D.Bazzacco, E.Farnea, A.Gadea, R.Venturelli, T.Beck, P.Bednarczyk, A.Buerger, A.Dewald, M.Dimmock, G.Duchêne, J.Eberth, T.Faul, J.Gerl, R.Gernhaeuser, K.Hauschild, A.Holler, P.Jones, W.Korten, Th.Kröll, R.Krücken, N.Kurz, **J.Ljungvall**, S.Lunardi, P.Maierbeck, D.Mengoni, J.Nyberg,L.Nelson, G.Pascovici, P.Reiter, H.Schaffner, M.Schlarb,T.Steinhardt, O.Thelen, C.A.Ur, J.J.Valiente Dóbon and D.Weisshaar, Nuclear Instruments and Methods in Physics Research, Section A, Volume 604, Issue 3, 11 June 2009, Pages 555-562

- *γ-Ray Spectroscopy at the Limits: First Observation of Rotational Bands in ^{255}Lr*, S.Ketelhut, P.T.Greenlees, D.Ackermann, S.Antalic, E.Clement, I.G.Darby, O.Dorvaux, A.Drouart, S.Eeckhaudt, B.J.P.Gall, A.Gorgen, T.Grahn, C.Gray-Jones, K.Hauschild, R.-D.Herzberg, F.P.Hessberger, U.Jakobsson, G.D.Jones, P.Jones, R.Julin, S.Juutinen, T.-L.Khoo, W.Korten, M.Leino, A.-P.Leppanen, **J.Ljungvall**, S.Moon, M.Nyman, A.Obertelli, J.Pakarinen, E.Parr, P.Papadakis, P.Peura, J.Piot, A.Pritchard, P.Rahkila, D.Rostron, P.Ruotsalainen, M.Sandzelius, J.Saren, C.Scholey, J.Sorri, A.Steer, B.Sulignano, Ch.Theisen, J.Uusitalo, M.Venhart, M.Zielińska, M.Bender, P.-H.Heenen, Phys.Rev.Lett. 102, 212501 (2009)

- *Shape evolution in self-conjugate nuclei, and the transitional nucleus ^{68}Se*, A.Obertelli, T.Baugher, D.Bazin, J.-P.Delaroche, F.Flavigny, A.Gade, M.Girod, T.Glasmacher, A.Goergen, G.F.Grinyer, W.Korten, **J.Ljungvall**, S.McDaniel, A.Ratkiewicz, B.Sulignano, D.Weisshaar, Phys.Rev. C 80, 031304 (2009)

- *Shape of ^{44}Ar: Onset of deformation in neutron-rich nuclei near ^{48}Ca*, M.Zielińska, A.Gorgen, E.Clement, J.-P.Delaroche, M.Girod, W.Korten, A.Burger, W.Catford, C.Dossat, J.Iwanicki, J.Libert, **J.Ljungvall**, P.J.Napiorkowski, A.Obertelli, D.Pietak, R.Rodriguez-Guzman, G.Sletten, J.Srebrny, Ch.Theisen, K.Wrzosek,Phys.Rev. C 80, 014317 (2009)

- *Shape coexistence in light Se isotopes: Evidence for oblate shapes*, **J.Ljungvall**, A.Gorgen, M.Girod, J.-P.Delaroche, A.Dewald, C.Dossat, E.Farnea, W.Korten,

B.Melon, R.Menegazzo, A.Obertelli, R.Orlandi, P.Petkov, T.Pissulla, S.Siem, R.P.Singh, J.Srebrny, Ch.Theisen, C.A.Ur, J.J.Valiente-Dobon, K.O.Zell, M.Zielińska, Phys. Rev. Lett. 100, 102502 (2008)

- *Neutron interactions in AGATA and their influence on gamma-ray tracking* **Joa Ljungvall**, Johan Nyberg, Nuclear Instruments and Methods in Physics Research, Section A, volume 550, Issue 1-2, September 11, 2005, page 379-391

- *A study of fast neutron interactions in high-purity germanium detectors*, **Joa Ljungvall**, Johan Nyberg, Nuclear Instruments and Methods in Physics Research, Section A, volume 546, Issue 3, July 11, 2005, page 553-573

- *Monte Carlo Simulations of The Neutron Wall detector system*, **Joa Ljungvall**, Marcin Palacz, Johan Nyberg. Nuclear Instruments and Methods in Physics Research, Section A, volume 538, Issue 3, August 11, 2004, page 741-762

- *Observation of core-excited E4 isomer in* ^{98}Cd, Blazhev, A., Gorska, M, Grawe, H, Nyberg, J., Palacz, M., Caurier, E., Dorvaux, O., Gadea, A., Nowacki, F., Andreoiu, C., de Angelis, G., Balabanski, D., Beck, Ch., Cederwall, B., Curien, D., Doring, J., Ekman, J., Fahlander, C., Lagergren, K, **Ljungvall, J.**, Moszynski, M, Norlin, L.-O., Plettner, C., Rudolph, D, Sohler, D, Spohr, K.M. , Thelen, O., Weiszflog, M, Wisell, M, Wolinska, M, Wolski, W. Physical Review C (Nuclear Physics), volume 69, number 6, June 2004, page 64304-1-8

Conference proceedings

- Toward lifetime and g factor measurements of short-lived states in the vicinity of ^{208}Pb D.Ralet, G.Georgiev, A.E.Stuchbery, E.Cement, A.Lemasson, C.Michelagnoli, M.Rejmund, L.Atanasova, D.L.Balabanski, G.Bocchi, R.Carroll, A.Dewald, J.Dudouet, B.Fornal, G.de France, S.Franchoo, C.Fransen, C.Muller-Gatermann, A.Goasduff, A.Gadea, B.Jacquot, P.R.John, D.Kocheva, T.Konstantinopoulos, A.Korichi, A.Kusoglu, S.M.Lenzi, S.Leoni, J.Ljungvall, R.Lozeva, A.Maj, A.Navin, R.Perez, N.Pietralla, C.Shand, O.Stezowski, D.Yordanov , Phys.Scr. 92, 054004 (2017)

- PRODUCTION AND STUDY OF NEUTRON-RICH NUCLEI USING THE LICORNE DIRECTIONAL NEUTRON SOURCE J.N. Wilson, M. Lebois, L. Qi, P. Amador-Celdran D. Bleuel, J.A. Briz, R. Carroll, W. Catford, H. De Witte, D. Doherty, R. Eloirdi, G. Georgiev, A. Gottardo, A. Goasduff, K. Hadynska-Klek, K. Hauschild, M. Hess, V. Ingeberg, T. Konstantinopoulos, J. Ljungvall, A. Lopez-Martens, G. Lorusso, R. Lozeva, R. Lutter, P. Marini, I. Matea, T. Materna, L. Mathieu, A. Oberstedt, S. Oberstedt, S. Panebianco, Z. Podolyak, A. Porta, P.H. Regan, P. Reiter, K. Rezynkina, S.J. Rose, E. Sahin, M. Seidlitz, R. Shearman, B. Siebeck, S. Siem, A.G. Smith, G.M. Tveten, D. Verney, N. Warr, F. Zeiser, M. Zielinska , Acta Phys.Pol. B 48, 395 (2017)

- LIFETIME MEASURMENTS OF EXCITED STATES IN NEUTRON-RICH FISSION FRAGMENTS T.W. Hagen, L. Grente, A. Görgen, M.-D. Salsac, W. Korten, F. Farget, T. Braunroth, B. Bruyneel, I. Celikovic, E. Clément, G. de France, O. Delaune, A. Dewald, A. Dijon, M. Hackstein, B. Jacquot, J. Litzinger, J. Ljungvall , C. Louchart, C. Michelagnoli, D.R. Napoli, A. Navin, F. Recchia, M. Rejmund, W. Rother, E. Sahin, S. Siem, B. Sulignano, Ch. Theisen, J.J. Valiente-Dobon , Acta Phys.Pol. B 47, 903 (2016)

- STUDY OF OCTUPOLE COLLECTIVITY IN ^{146}Nd AND ^{148}Sm USING THE NEW COULOMB EXCITATION SET-UP AT ALTO M. Komorowska, M. Zielińska, P. Napiorkowski, D.T. Doherty, K. Wrzosek-Lipska, P.A. Butler, L. Próchniak, W. Korten, R. Briselet, H. De Witte, L.P. Gaffney, G. Georgiev, A. Goasduff, A. Görgen, A. Gottardo, E.T. Gregor, K. Hadyńska-Klęk, H. Hess, M. Klintefjord, T. Konstantinopoulos, J. Ljungvall, R. Lutter, I. Matea, P. Matuszczak, G.G. O'Neill, W. Piatek, P. Reiter, D. Rosiak, M. Scheck, M. Seidlitz, B. Siebeck, M. Thürauf, N. Warr , Acta Phys.Pol. B 47, 923 (2016)

- Nuclear g-factor measurement with time-dependent recoil in vacuum in radioactive-beam geometry A.Kusoglu, A.E.Stuchbery, G.Georgiev, A.Goasduff, L.Atanasova, D.L.Balabanski, M.Bostan, M.Danchev, P.Detistov, K.Gladnishki, J.Ljungvall, I.Matea, D.Radeck, C.Sotty, I.Stefan, D.Verney, D.T.Yordanov , Proc.NUBA Conference Series -1: Nuclear Physics and Astrophysics, Antalya, Turkey, 15-21 September 2014, p.012041 (2015); J.of Phy.:Conf.Seri. 590

- LICORNE: A new and unique facility for producing intense, kinematically focused neutron beams at the IPN Orsay J.N. Wilson, M. Lebois, P. Halipre, B. Leniau, I. Matea, D. Verney, S. Oberstedt, R. Billnert, A. Oberstedt, G. Georgiev and J. Ljungvall, EPJ Web of Conferences 62, 05006 (2013)

- Onset of collectivity in neutron-rich Sr and Kr isotopes: Prompt spectroscopy after Coulomb excitation at REX-ISOLDE, CERN E. Clément, A. Görgen, A. Dijon, G. de France, B. Bastin, A. Blazhev, N. Bree, P. Butler, P. Delahaye, A. Ekström, G. Georgiev, N. Hasan, J. Iwanicki, D. Jenkins, W. Korten, A.C. Larsen, J. Ljungvall, K. Moschner, P. Napiorkowski, J. Pakarinen, A. Petts, T. Renstrom, M. Seidlitz, S. Siem, C. Sotty, J. Srebrny, I. Stefanescu, G.M. Tveten, J. Van de Walle, N. Warr, K. Wrzosek-Lipska, M. Zielińska, C. Bauer, B. Bruyneel, J. Butterworth, C. Fitzpatrick, C. Fransen, R. Gernhäuser, H. Hess, R. Lutter, P. Marley, P. Reiter, B. Siebeck, M. Vermeulen, A. Wiens and H. De Witte,EPJ Web of Conferences 62, 01003 (2013)

- Lifetime measurements on fission fragments in the A $\sim$ 100 region, L. Grente, M.-D. Salsac, W. Korten, A. Görgen, T. W. Hagen, T. Braunroth, B. Bruyneel, I. Celikovic, E. Clément, O. Delaune, A. Dijon, A. Drouart, S. Ertürk, F. Farget, G. de France, A. Gottardo, M. Hackstein, B. Jacquot, J. Libert, J. Litzinger, J. Ljungvall, C. Louchart, C. Michelagnoli, D.R. Napoli, A. Navin, N. Pillet, A. Pipidis, F. Recchia, M. Rejmund, W. Rother, E. Sahin, C. Schmitt, S. Siem, B. Sulignano, J.J. Valiente-Dobon and K.O. Zell, EPJ Web of Conferences 62, 01002 (2013)

- Lifetime Measurements of Zn Isotopes Around N = 40 I.Celikovic, A.Dijon, E.Clement, G.de France, P.Van Isacker, **J.Ljungvall**, C.Fransen, G.Georgiev, A.Gorgen, A.Gottardo, M.Hackstein, T.W.Hagen, C.Louchart, P.Napiorkowski, A.Obertelli, F.Recchia, W.Rother, S.Siem, B.Sulignano, P.Ujic, J.J.Valiente-Dobon, M.Zielinska, Acta Phys.Pol. B44, 375 (2013)

- Odd-parity ^{100}Sn Core Excitations M.Palacz, J.Nyberg, H.Grawe, K.Sieja, G.de Angelis, P.Bednarczyk, A.Blazhev, D.Curien, Z.Dombradi, O.Dorvaux, J.Ekman, J.Galkowski, M.Gorska, J.Iwanicki, G.Jaworski, J.Kownacki, **J.Ljungvall**, M.Moszynski, F.Nowacki, D.Rudolph, D.Sohler, D.Wolski, M.Zieblinsk, Acta Phys.Pol. B44, 491 (2013)

- *Lifetime Measurements in Neutron-rich Fe and Co Isotopes*, A.Dijon, **J.Ljungvall**, E.Clement, G.de France, P.Van Isacker, A.Gorgen, A.Obertelli, W.Korten, J.P.Delaroche, A.Dewald, A.Gadea, L.Gaudefroy, M.Girod, M.Hackstein, J.Libert, D.Mengoni, T.Pissula, F.Recchia, M.Rejmund, W.Rother, E.Sahin, C.Schmitt, A.Shrivastava, J.J.Valiente-Dobon, K.O.Zell, M.Zielińska, Acta Physica Polonica B 42, 829 (2011)
- Onset of collectivity in Neutron-Rich iron isotopes: Toward a new island of inversion? **J. Ljungvall**, FRONTIERS IN NUCLEAR STRUCTURE, ASTROPHYSICS, AND REACTIONS: FINUSTAR 3. AIP Conference Proceedings, Volume 1377, pp. 386-388 (2011).
- *K Isomer in ^{252}No*, B.Sulignano, Ch.Theisen, **J.Ljungvall**, D.Ackermann, S.Antalic, O.Dorvaux, A.Drouart, A.Görgen, P.T.Greenlees, K.Hauschild, R.D.Herzberg, F.P.Hebetaberger, S.Hofmann, U.Jakobsson, P.Jones, R.Julin, S.Juutinen, S.Ketelhut, W.Korten, M.Leino, M.Nyman, A.Obertelli, J.Pakarinen, E,Parr, P.Papadakis, P.Peura, J.Piot, P.Rahkila, D.Rostron, P.Ruotsalainen, J.Saren, C.Scholeyb J.Sorri, J.Uusitalo, M.Venhart, and M.Zielińska, AIP Conf. Proc. / Volume 1224, pp. 322-331, INTERNATIONAL SYMPOSIUM ON EXOTIC NUCLEI (2009)
- *Evolution Of Shapes And Collectivity In Exotic Nuclei*, Andreas Görgen and **Joa Ljungvall**, AIP Conf. Proc. / Volume 1224, pp. 54-63, INTERNATIONAL SYMPOSIUM ON EXOTIC NUCLEI (2009)
- *Lifetime Measurements and Coulomb Excitation of Light Hg Nuclei*, A.Petts, P.A.Butler, T.Grahn, A.Blazhev, N.Bree, B.Bruyneel, J.Cederkall, E.Clement, T.E.Cocolios, A.Dewald, J.Eberth, L.Fraile, C.Fransen, M.B. GomezHornillos, P.T.Greenlees, A.Gorgen, M.Guttormsen, K.Hadynska, K.Helariutta, R.-D.Herzberg, M.Huyse, D.G.Jenkins, J.Jolie, P.Jones, R.Julin, S.Juutinen, S.Ketelhut, S.Knapen, T.Kroll, R.Krucken, A.C.Larsen, M.Leino, **J.Ljungvall**, P.Maierbeck, P.L.Marley, B.Melon, P.J.Napiorkowski, M.Nyman, R.D.Page, J.Pakarinen, G.Pascovici, N.Patronis, P.J.Peura, E.Piselli, Th.Pissulla, P.Rahkila, P.Reiter, J.Saren, M.Scheck, C.Scholey, A.Semchenkov, S.Siem, I.Stefanescu, J.Sorri, J.Uusitalo, J.Van de Walle, P.Van Duppen, D.Voulot, R.Wadsworth, N.Warr, D.Weisshaar, F.Wenander, M.Zielińska, Proc.13th Intern.Symposium on Capture Gamma-Ray Spectroscopy and Related Topics, Cologne, Germany, 25-29 Aug.2008, J.Jolie, A.Zilges, N.Warr, A.Blazhev, Eds., p.414 (2009); AIP Conf.Proc. 1090 (2009)
- *Probing collectivity in the vicinity of neutron deficient Pb nuclei*, T.Grahn, A.Dewald, M.B.Gomez Hornillos, P.T.Greenlees, A.Gorgen, K.Helariutta, J.Jolie, P.Jones, R.Julin, S.Juutinen, S.Ketelhut, R.Krucken, T.Kroll, M.Leino, **J.Ljungvall**, P.Maierbeck, B.Melon, M.Nyman, R.D.Page, A.Petts, Th.Pissulla, P.Rahkila, J.Saren, C.Scholey, J.Sorri, J.Uusitalo, R.Wadsworth, M.Zielińska, Proc.Frontiers in Nuclear Structure, and Reactions (FINUSTAR 2), Crete, Greece, 10-14 Sept. 2007, P.Demetriou, R.Julin, S.V.Harissopulos, Eds. p.260 (2008); AIP Conf.Proc 1012 (2008)
- *Coulomb Excitation of Neutron-Rich ^{44}Ar at SPIRAL*, M.Zielińska, A.Goergen, A.Burger, W.Catford, E.Clement, C.Dossat, J.Iwanicki, W.Korten, **J.Ljungvall**, P.J.Napiorkowski, D.Pietak, G.Sletten, J.Srebrny, Ch.Theisen, K.Wrzosek, Acta Physica Polonica B 39, 519 (2008)
- *A Monte Carlo Simulation of the EUROBALL Neutron Wall detector system: How to identify scattered neutrons*, **Joa Ljungvall**, Marcin Palacz, Johan Nyberg. Acta Physica Polonica, Series B, volume 34, number 4, April 2003, page 2453-2456

Chapter 9

Shape of the rare-earth nucleus ^{136}Sm via sub-barrier Coulomb excitation

9.1 Proposal (as sent to the GANIL PAC)

GANIL
PROPOSAL FOR EXPERIMENT

PAC date (fill in):	EXP # (Do not fill in):
March, 2010	**E**

- If Be or Ni production targets are to be used, indicate the maximum beam intensity the target can handle.
- Test runs which may be needed to commission new apparatus are encouraged, but should be presented as separate proposals.

Title*: **Shape of the rare-earth nucleus ^{136}Sm via sub-barrier coulomb excitation**

Is it a follow up experiment? [Yes/No]: **No** If yes, experiment number: **E** Is this just a TEST? [Yes/No]: **No**

Spokespersons (if several, please use capital letters to indicate the name of the contact person):
A. OBERTELLI (CEA Saclay), J. Ljungvall (CSNSM), E. Clément (GANIL)

Address of the contact person:
CEA Saclay, SPhN, 91191 Gif-sur-Yvette

Phone:01 69 08 74 86 Fax: 01 69 08 74 84 E-mail:alexandre.obertelli@cea.fr

Address of a backup contact person:
CSNSM, 91000 Orsay

Phone: Fax: E-mail: ljungall@csnsm.in2p3.fr

Other Participants or Organisations:
CEA Saclay: F. Dechery, A. Drouart, A. Goergen, W. Korten, C. Louchart, A. Obertelli, B. Sulignano, Ch. Theisen
GANIL: E. Clément, G. De France, H. Savajols, C. Stodel
CSNSM: J. Ljungvall

Short abstract:
We propose to investigate nuclear shapes in neutron-deficient rare earth nuclei below the N=82 shell closure by measuring the sub-barrier Coulomb excitation cross section of ^{136}Sm. By coupling the measured cross section with the experimentally known lifetime of the first 2^+ excited state in ^{136}Sm, we will determine its quadrupole moment. The nuclei with N=78 and Z=62 belong to one of the few regions of heavy nuclei in the nuclear chart where oblate-prolate coexistence near the ground state is predicted. Other models predict a triaxial ground state with γ=30°. Up to now, quadrupole moments in this region remain completely unexplored.

Beam line (G1–G4, D1–D6, etc.)**: D6** | If **LISE** is requested, do you need the **Wien Filter**? [Yes/No]: **YES**

Devices needed:														
(Mark with an **X** or no. of detectors needed)	VAMOS		EXOGAM	X	DIAMANT		N-WALL		SPEG		MAYA		TIARA	
	MUST2		DEMON		INDRA		LISE2000		LISED4		LISED6	X	SIRA	
	NAUTILIS		CHARISSA		ECLAN									
Other devices (specify):														

Fill in completely:	Ion(s)	Energy (A.MeV)	Intensity (nAe)	UT/beam
Primary beam(s)	**^{126}Xe** **^{82}Kr**	**1.20** **4.27**	**0.02** **5800 (10^{12} pps)**	**6** **15**
Secondary beam(s) if **SISSI** is requested	1. 2. 3.			
SPIRAL beam(s)	1. 2.			

Will you need **SISSI**? Yes/No: **NO** If yes, SISSI Target(s) and Thickness(es):
LISE production target? Yes/No: **YES** If yes, LISE Target(s) and Thickness(es): **^{58}Ni, 1 mg.cm^{-2}**

TOTAL number of beam UTs Requested: 21 | Time (UTs) required for setting up the apparatus: 21

* If needed, to unlock this form, point to "Unprotect Document" on the Tools menu

(1 UT=8 hours)	Time (UTs) needed for off-beam calibration and dismounting: 9

If you need to accelerate more than one beam or energy (stable or SPIRAL), *include the beam-change tuning time* in your requested number of beam UTs. If not, the experiment may not be scheduled to run all at one time. **1 CSS1 Beam (^{82}Kr), 1 CIME beam (^{126}Xe).**

Number of auxiliary (parasitic) beam UTs (if needed):
6

If you wish to split beam UTs into more than one run, please specify UTs per run and period requested between runs:
Auxiliary beam time should be scheduled at least 3 weeks before the experiment

On what date would you be ready to run: **September 2010**

Excluded periods during next 3 years (if any already known):

Acquisition system: **GANIL** Other (specify):

SAFETY: list any hazardous equipment or substances to be used, such as a radioactive target, liquid nitrogen, explosive gas, etc., even in SPEG chambers or germanium detectors:
none

Go to Page 2

Give the status of previous experiment(s) by this group in the last 3 years: e.g. results from of status of analysis of previous experiments at GANIL (or related experiments elsewhere):

A. Drouart, E533 (2008), analysed, publication to be submitted
W. Korten, E553 (2008), analysed, publication to be submitted
A. Goergen, E393S (2006), published

List publications, conference presentations, PhDs awarded, or other theses completed as a result of previous experiment(s) at GANIL (or related experiments elsewhere):
J. Ljungvall *et al.*, to be submitted (2010)
B. Avez *et al.*, to be submitted (2010)
M. Zielinska *et al.*, Phys. Rev. C 80, 014317 (2009)
E. Clément *et al.*, Phys. Rev. C 75, 054313 (2007)
A. Chatillon *et al.*, Phys. Rev. Lett. 98, 132503 (2007)
B. Avez, CEA Saclay, PhD thesis (2009)
E. Clément, CEA Saclay, PhD thesis (2006)
A. Chatillon, CEA Saclay, PhD thesis (2005)
A. Obertelli, CEA Saclay, PhD thesis (2005)

List any NEW devices needed for this experiment which still have to be bought or manufactured:
S2 Micron detector + mechanics (reaction chamber exists but needs some modifications)

At what date do you expect these to be available? **September 2010**

List any special devices needed for this experiment which would require to be mounted prior to the experiment (special target chambers, detector arrays, etc.:

1 mg.cm^{-2} and 0.5 mg.cm^{-2} ^{58}Ni targets to be built

How long will it take to mount the particular device(s) once the area is available to you?

Will this require opening the roof beams above the area? [Yes/No]: **No**

Additional comments:

Shape of the rare-earth nucleus ^{136}Sm *via* sub-barrier coulomb excitation

1-Motivations

The shape is one of the most fundamental properties of atomic nuclei. Calculations from deformed harmonic-oscillator potentials predict that prolate and oblate shapes should be equally probable across the nuclear chart. In the case of real nuclei, where the shell structure changes from a harmonic oscillator type to a Woods-Saxon+spin-orbit type with intruder orbitals, a strong dominance of prolate shapes is observed, which is related to the sharp surface of the nuclear potential [1]. Oblate shapes are expected when a major shell is almost filled due to the strong shape-driving effect of holes in the K=1/2 orbitals. This effect is seen for example in HFB calculations which predict oblate and prolate shapes to be equally favored just below the N=82 shell closure. Quadrupole deformation is not restricted to axial shapes : triaxiality may play an important role in connecting axially-deformed minima [2] or can even be prefered for the ground-state shape. The measurement of observables related to the nuclear shape represents a stringent test for theoretical models.

The HFB calculations with the Gogny D1S interaction predict deformed prolate shapes in the region above Z=50 and below N=82, except for a small region of oblate shapes for the most proton-rich N=78 and N=76 isotones [3]. The question of shape coexistence at low excitation energy, in the sense of two energy minima at different deformations, is raised but still unanswered in this mass region. Indeed, several studies in light Samarium nuclei showed several rotationnal bands associated to different intrinsic shapes. From lifetime measurements, a large deformation of β~0.3 has been deduced for the ground-state band of the lightest Sm isotopes [4].

To account for possible configuration mixing, correlations beyond the mean field have to be considered in the calculations. Such correlations can be accounted for through a mixing of HFB wave functions over collective degrees of freedom with the so-called Generator Coordinate Method (GCM). We have investigated HFB-based configuration mixing calculations for the chain of $^{134\text{-}138}$Sm isotopes *(i)* using the Gogny D1S and the GCM with Gaussian overlap approximation (GOA) comprising axial and non-axial quadrupole degrees of freedom [5] and *(ii)* using the Skyrme Sly4 interaction and the GCM with axial symmetry and projected particle number and angular momentum [6]. In all cases, the total energy surfaces constrained to axial symmetry show almost degenerated minima at oblate and prolate shapes in both Gogny and Skyrme cases. The 5DCH (5-Dimension Collective Hamiltonian) approach predicts that these two minima are connected together via non-axial quadrupole shapes and therefore do not predict any oblate-prolate shape coexistence a low-excitation energy. In ^{136,138}Sm, a trixial minimum is found, as suggested earlier from other models [7]. A purely triaxial nucleus with γ=30° has a much lower quadrupole moment than an axial oblate- or prolate-shaped nucleus. **The objective of this proposal is to determine the quadrupole moment of ^{136}Sm**, as a representative nucleus of this region where oblate-prolate shape coexistence is expected from axial treatment but not from a 5DCH approach. As detailed later, the choice of ^{136}Sm, among neighboring nuclei presenting also two axial energy minima, is motivated by the feasibility of the experiment.

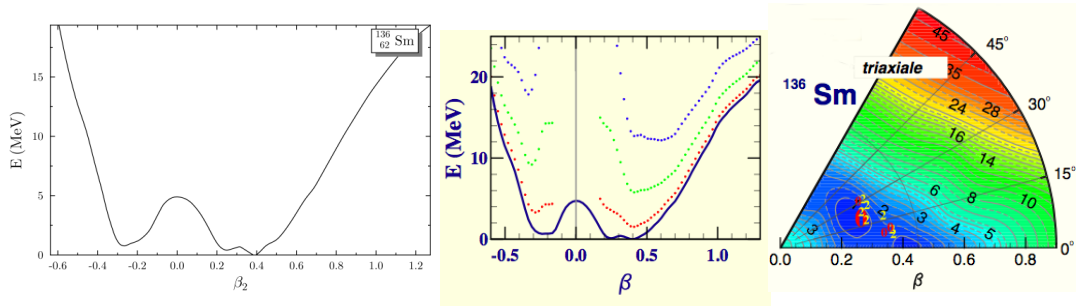

Figure 1: (Left) Total energy surfaces for ^{136}Sm as a function of axial symmetry from calculations performed with the Skyrme Sly4 interaction and particle-number projection (PAV). (Middle) Total energy of ^{136}Sm (blue line) as a function of imposed axial deformation from HFB calculations with the Gogny D1S interaction. Dotted lines represent total-energy curves at I=2,4,6 angular momentum. (Right) Total energy surface in the (β,γ) plane calculated with the Gogny D1S interaction.

In the case of ^{136}Sm, the resulting quadrupole moment is predicted to a rather small value of -99 efm^2 from 5DCH. Deformations where minima are observed in the energy surfaces restricted to axial symmetry occur at β =±0.3. This amplitude of deformation corresponds to a mean quadrupole deformation of Q=±255 efm^2. A low-energy Coulomb excitation, as detailed in the next section, can distinguish between these scenarii. It appears

therefore as a sensitive test of the scenario of shape coexistence in ^{136}Sm, and more generally in this mass region.

The neutron-deficient rare earth nuclei are accessible via heavy-ion induced fusion-evaporation reactions. However, experimental studies of shapes near the ground state are lacking completely in the considered region. Coulomb excitation experiments, which are sensitive to the spectroscopic quadrupole moments via the reorientation effect, are the most direct way to study shape transitions and shape coexistence. Some beams are expected to be soon available at REX-ISOLDE. The lightest Samarium isotope being accessible today for Coulomb excitation is ^{140}Sm. The technique of combining lifetime and Coulomb excitation measurements has been successfully employed recently to obtain quadrupole moments, such as in ^{70}Se [8].
In the rare-earth region where low-lying oblate deformations are expected, no Coulomb excitation has been performed due to the difficulty of producing such beams and identify incoming particles on an event-by-event method. The spectroscopy of ^{136}Sm is known and its first 2^+ excited state lies at 255 keV above the ground state. Its half-life has been measured at 88(9) ps [9]. The moment of inertia extracted from its high-spin spectroscopy [7,9,10] indicates a rather large deformation of $\beta \sim 0.3$, but no information is known about the low excitation-energy deformation, sensitive to the details of the total energy surface (see Fig. 1).
We propose an innovative setup to measure the Coulomb-excitation of ^{136}Sm produced by fusion evaporation and determine the number of incoming particles from a delayed measurement. This technique will allow to determine the absolute Coulomb-excitation cross section of ^{136}Sm on ^{58}Ni and, by combination with its known lifetime, one can estimate its quadrupole moment. This experiment, the first of its kind, can be seen as a pre-S3 experiment. The spectrometer S3 will indeed allow producing intense cocktail secondary beams via fusion-evaporation at SPIRAL2 with, unfortunately, no isobaric separation.

2-Experimental setup

The production of light Samarium isotopes via fusion-evaporation forbids to use a “heavy” primary beam (A>100) in order to ensure a clean rejection of beam particles with the LISE Wien filter. On the other hand, since we aim at using these fusion-evaporation products for a Coulomb-excitation secondary reaction, the residues should have a velocity large enough to use a high-Z target and reach a sizeable cross section.
These two reactions (fusion-evaporation for production and Coulomb excitation) are constrained in terms of incident energy: both should be performed around the Coulomb barrier.

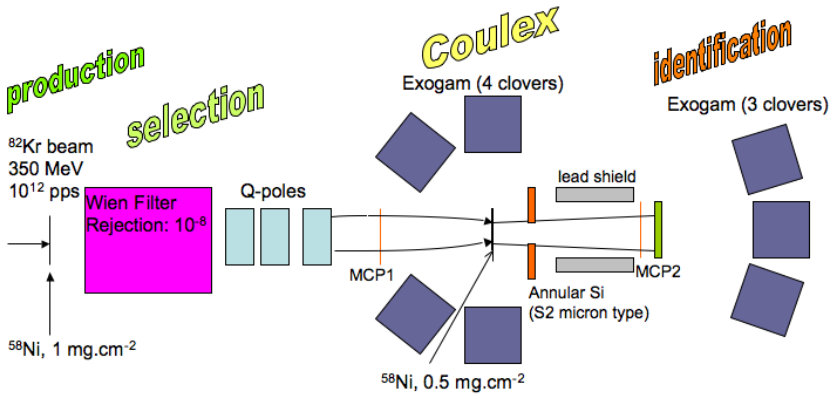

Figure 2: Experimental setup.

According to available stable beams at GANIL, we found that an optimized setup to study ^{136}Sm is as follow. The fusion-evaporation residues will be formed from a ^{82}Kr incident beam accelerated at 350 MeV (4.27 MeV/u) with the CSS1 cyclotron, at an intensity of 10^{12} pps, impinging on a ^{58}Ni target (68 % abundance) of 1 mg.cm^{-2}. The Paquerette rotative target will be used to maintain the target temperature under 900 degrees. The maximum of the excitation function for ^{136}Sm is found for an incident energy of 340 MeV. The total fusion-evaporation cross section is calculated with PACE4 to be 576 mb at the entrance of the production target, among which ^{136}Sm is produced at 83 mb (purity of 15 %) via the alpha-evaporation channel. At the exit of the

target, the fusion-evaporation cross section is 294 mb and ^{136}Sm is produced at 64 mb (22 %). The incident energy is chosen to place the maximum of the excitation function in the middle of the target. Similar calculations performed with the HIVAP code from GSI predict that the maximum of the excitation function is at an incident energy close to the PACE4 value. The total fusion-evaporation cross section is also similar to the PACE4 prediction but the purity of the beam is 10% of ^{136}Sm. Finally, the compound-recoil velocity at the exit of the target ranges from 0.0492 c and 0.0534 c (beam=0.091 c at the exit of the target), which corresponds to energies from 154 MeV to 181 MeV for ^{136}Sm. The velocity spread will be reduced to ±5% (from 162 to 178 MeV) at the exit of the Wien filter with slits. In the following, we consider the most pessimistic predictions of a 10% purity and a mean fusion-evaporation cross section of 500 mb. The angular distribution of ^{136}Sm nuclei due to particle evaporation is calculated to be peaked around 1.5 degrees in the laboratory frame.
In the recent E533 experiment, Xe+Sn and Xe+Zr have been measured [12]. The LISE Wien filter was shown to reach a rejection of 2. 10^{-8}, resulting in the present case to a 10^4 pps contamination of beam particles in the secondary beam (*i.e.* 1%). From these experiments, we expect a transmission of ^{136}Sm better than 20%. Expectations from calculations are worst : Zgoubi calculations predict that the 27^+ charge state has the larger transmission with 35%. The charge state distribution of ^{136}Sm convoluted with calculated transmissions give a global transmission of 10% for ^{136}Sm.

The above uncertainties on (i) the primary beam rejection, (ii) transmission and (iii) relative production of ^{136}Sm lead us to request auxiliary beam in LISE to measure these quantities. Details on this preliminay test will be further exposed during the oral presentation.

In the following, the intensity of the secondary beam is calculated assuming a total transmission of 20%. The total intensity on the secondary target is calculated to be around 1. 10^6 pps containing 1. 10^5 pps (lower limit of 10% for the purity) of ^{136}Sm at 1.25 MeV/nucleon. The time of flight from the production target to the secondary target will be of several hundreds of nanoseconds.

Shape	Qs (efm^2)	$\sigma[50_{cm}°;160_{cm}°]$ (mb)
Spherical	0	542^{+62}_{-53}
Prolate	- 255 efm^2	449^{+51}_{-40}
Oblate	+255 efm^2	649^{+74}_{-57}

Table 1: Coulomb-excitation cross sections for ^{136}Sm+^{58}Ni at 160 MeV (mid-target energy) integrated over the whole angular range covered by the annular Si detector.

As mentioned earlier, the first 2^+ excited state of ^{136}Sm has been measured at 255 keV with a lifetime of 88 (9) ps. Predictions for the Coulomb excitation cross section of ^{136}Sm on ^{58}Ni has been performed using the GOSIA code [13], assuming three different shapes for the first 2^+ state of ^{136}Sm : *(i)* spherical, *(ii)* prolate and *(iii)* oblate. Integrated cross sections (from 50 to 160 degrees in the center of mass) have been calculated and are displayed in Table 1. All three values differ from each other with a sizeable difference of >20%. Te quoted error bars contain uncertainties from the lifetime measurement. Note that multistep excitations vanish at such low incident energy. Only the first 2^+ excited state will be populated.

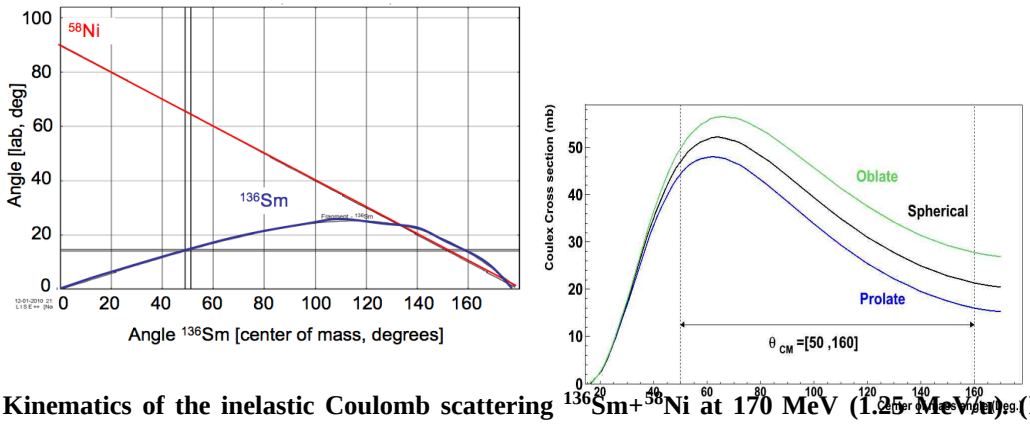

Figure 3: (Left) Kinematics of the inelastic Coulomb scattering ^{136}Sm+^{58}Ni at 170 MeV (1.25 MeV/u). (Right) Differential angular distribution of the Coulomb excitation of ^{136}Sm on ^{58}Ni as a function of the scattering angle in the center of mass. The angular range covered by the Si stripped detector is shown.

Considering the experimental uncertainties on the lifetime of $^{136}Sm(2^+)$ measured at 88(9) ps, an uncertainty of 15% in the cross section measurement should allow us to distinguished between a prolate, and an oblate shape for $^{136}Sm(2^+)$ in case the deformation amplitude exceeds 150 e fm^2.
Four Exogam clovers will be placed at 15 centimeters from the target center, leading to a total *photopeak efficiency* of 9 % for a 300 keV transition. Depending on available electronics and mechanical constrains, we may add other clovers around the secondary target, increasing linearly the final statistics. Assuming a 0.5 mg.cm^{-2} secondary ^{58}Ni target, one gets 1000 photopeak events per day of experiment. Considering the above-mentioned Coulomb-excitation cross section typical for all nuclei present in the beam, the low incident energy that prevent multiple scattering and a detection efficiency (Compton or photopeak) of 20% per clover for gamma-ray energies around 300 keV, we expect a rate of 1 Hz per crystal at the secondary target position. We plan to place a segmented Silicon annular detector (Micron S2 type, 48 mm inner radius, 96 mm outer radius) at 90 mm to detect scattered particles from 15_{lab}° to 28_{lab}°, which correspond to large center-of-mass angles from 50° to 160° (see kinematics in Fig. 3), where the differential cross section is more sensitive to the quadrupole moment, as displayed in Table 1 and the right panel of Fig. 3. At least three different angular bins will be made to increase the analysis sensitivity to the quadrupole moment. To give an idea of the sensitivity, we shall reach an uncertainty of about ±100 efm^2 in the range of discussed quadrupole moments including all uncertainties (mainly 15% from normalization, 10% from the lifetime measurement). The energy resolution of the Si detector will allow disentangling scattered Ni and Sm isotopes. The angular cone defined by the inner radius is large enough (15°) to let the secondary beam go through with no damage risk for the internal strips.

Incident ^{136}Sm nuclei will be implanted downstream the secondary target in an aluminium foil backed by three Exogam detectors. Appropriate shielding will be placed between the implantation foil and the Exogam detectors located around the secondary target. The counting of decay gamma-transitions of ^{136}Pm (daughter of ^{136}Sm via electron conversion, $T_{1/2}$=47 s) will determine the incident rate of ^{136}Sm. This measurement will provide an absolute normalization for the Coulomb excitation cross section for ^{136}Sm. A 114.2 keV line in ^{136}Pm gathers 36% of the decay strength, leading to a clear identification of implanted ^{136}Sm. This absolute normalization to determine the Coulomb-excitation cross section is possible because the beta-decay of ^{136}Sm and all branching ratios are known. No nuclei populating ^{136}Sm via its radioactive decay is expected to be significantly produced in the secondary beam. The father nucleus ^{136}Eu has a half life of 3.3 s (an isomer with an half life of 3.8 s), short compared to ^{136}Sm. The residual influence, if any, of the implantation of ^{136}Eu could be corrected from time correlations between prompt and delayed gammas in the implantation Exogam detectors. We do not expect any line close to 114 keV in the decay chain of implanted nuclei that could pollute the rate estimate. The Exogam clovers for decay-tagging will be placed behind the reaction chamber where the implantation foil will be located. A geometrical efficiency close to 50% could be reached. Nevertheless, we plan to position the detector at 30 cm from the foil to reduce the solid angle and therefore the counting rate. Being at 30 cm from the implantation foil reduces also the effect the gamma efficiency of the implantation profile. We estimate the gamma counting rate produced in the detector by the decay of beam particles to be around 10^3-10^4 Hz. The accumulated statistics will be extremely large and will allow γ-γ coincidences between crystals of the Exogam clovers to properly determine the number of implanted ^{136}Sm isotopes.

An additional separation from ^{78}Kr primary-beam not rejected via the Wien-Filter will be performed by a time-of-flight measurement between two Micro-Channel plates (MCPs). The MCP #2 will provide a start signals for time coincidences between prompt events and delayed signals from decays that will allow rejecting prompt gamma decays of nuclei excited during their implantation. In case a residual part of the beam particles impinging on the secondary target are not implanted on the Al foil, a correction factor to deduce the total ^{136}Sm will be determined from the ratio #MCP1/#MCP2.

A stable-beam measurement is required to tune and start operating the setup in “easy” conditions. We propose to perform the Coulomb excitation of the stable ^{126}Xe. The lifetime of its first 2^+ state (388 keV) has been measured at 40.8(13) ps. Its quadrupole moment is not known but it is expected to be well deformed at a prolate ground state. The beam will be delivered from the CIME cyclotron at a velocity close to the one expected for ^{136}Sm at the exit of the Wien filter (energy of 1.20 MeV/u). Since the two different stable beams are accelerated from separate cyclotrons (Kr in CSS1, Xe in CIME), no extra time is needed for the beam tuning. We expect an integrated cross section of about 500 mb. A one-day measurement at 10^6 pps gives about 2. 10^4 photopeak events, enough for a differencial cross section measurement. This reference measurement will provide a global validation of the efficiency of EXOGAM (around the Coulomb-excitation target), the

segmented silicon annular detector, the target thickness and the efficiency of the MCPs. The gamma spectrum obtained with the detector from the implantation area will give a reference for background. Th eXe beam will be used also for a first tune of the Wien filter.

4-Beam-time request

We need for this experiment 2 days to tune the setup (^{126}Xe primary beam and ^{136}Sm secondary beam), 1 day for the reference measurement with ^{126}Xe and 4 days for the secondary beam experiment. The information used for beam time estimate are summarized in Table 2.

Table 2: Summary of ingredients considered for the beam time request.

Primary beam (^{82}Kr @ 350 MeV / CSS1)	10^{12} pps
Production target (^{58}Ni, 1 mg.cm^{-2})	1.4 10^{19} cm^{-2}
Mean fusion-evaporation cross section	400 mb (10 % of ^{136}Sm, lower limit)
Wien Filter transmission	30 %
Secondary beam intensity	1.5 10^{6} pps (1.5 10^{5} pps of ^{136}Sm)
Secondary target (^{58}Ni, 0.5 mg.cm^{-2})	5.2 10^{18} cm^{-2}
Coulomb-excitation cross section	600 mb (from 50° to 160° deg. cm)
Photopeak efficiency @ 300 keV (4 clovers)	9 %
Beam time (fusion-evap. beam)	4 days
Statistics (photopeak events + ^{136}Sm in annular Si)	3. 10^{4} >4 angular bins possible with <2% statistical errors

Finally, we request 7 days of beam time to measure to perform the Coulomb-excitation of ^{136}Sm and access the quadrupole deformation of its first excited 2^{+} state. The requested 21 UTs of beam time are decomposed in *(i)* 8 UTs of a ^{126}Xe stable beam at 1.2 MeV/u delivered by CIME and *(ii)* 15 UTs of a ^{82}Kr beam at 350 MeV delivered by CSS1.

Prior the experiment, we request 6 UTs of ^{82}Kr at 350 MeV to verify the Wien-filter correct operation under our experimental conditions, and measure *(i)* the beam rejection, *(ii)* the beam purity in ^{136}Sm and *(iii)* the Wien Filter transmission.

References

[1] I. Hamamoto and B. R. Mottelson, ArXiv:0903.0973v1 [nucl-th] (2009).
[2] M. Girod *et al.*, Phys. Lett. B **676**, 39 (2009).
[3] http://www-phynu.cea.fr/science_en_ligne/carte_potentiels_microscopiques
[4] M. A. Coardona *et al.*, Phys. Rev. C **44**, 891 (1991).
[5] M. Girod, private communication (2010).
[6] J. Sadoudi, private communication (2010). Codes from M. Bender (CENBG).
[7] E. S. Paul *et al.*, J. Phys. G : Nucl. Part. Phys. **20**, 1405 (1994).
[8] J. Ljungvall *et al.*, Phys. Rev. Lett. **100**, 102502 (2008).
[9] F. Soramel *et al.*, Phys. Rev. C **38**, 537 (1988).
[10] F. Falla-Soleto, LNL annual report (2005).
[11] A. A. Sonzogni, Nuclear Data Sheets **95**, 837 (2002).
[12] B. Avez, CEA Saclay, PhD thesis (2009).
[13] T. Czosnyka, D. Cline and C. Y. Wu, Bull. Am. Phys. Soc. **28**, 745 (1983).

9.2 Experiment, a two stage rocket into the void

In order to validate the production rate of ^{136}Sm and the possibility to reject the primary beam an initial test was performed. The date from this test experiment was analyzed by me, and a report was written and send to GANIL in order to have the actual experiment programmed. The optimistic conclusions from this test was that the measurement was feasible.

9.2.1 Report on test experiment for E614

Results from the test part of E614, "Shape of rare-earth nucleus ^{136}Sm via sub-barrier Coulomb excitation"

J. Ljungvall[a], A. Obertelli[b], B. Bruyneel[b], L. Caceres[d], E. Clement[d], A. M. Corsi[b], A. Drouart[b], L. Gaudefroy[c], B. Jacqout[d], O. Kamalou[d], C. Santamaria[b], J.-C. Thomas[d]

[a] *CSNSM*
[b] *CEA Saclay*
[c] *CEA DAM*
[d] *GANIL*

1. Introduction

The experiment "Shape of rare-earth nucleus ^{136}Sm via sub-barrier Coulomb excitation"was accepted by the GANIL PAC in spring 2010, together with 6 UTs of beam time to test and verify some crucial aspects for the experiment to work:

1. Primary beam rejection.
2. Transmission of evaporation residues.
3. Production rate of ^{136}Sm.

Furthermore, we have, closely related to the question of rejection of the primary beam, the issue of the absolute count rate in the angular silicon detector that will be used to detect the scattered ^{136}Sm nuclei in the experiment.

2. Experimental setup

The setup used to perform the test part of the E614 experiment is shown in figure 1. The secondary target and the zero degree Silicon detector are removable. The main purpose of the MCP2 detector is to count the incoming particles and to allow for the determination of the scattering angle. MCP1 is used to estimate the amount of beam particles downstream the secondary target. The $LaBr_3$ detectors are used to identify the γ rays from the β decay of ^{136}Sm. The zero degree Silicon detector is used for the tuning of LISE.

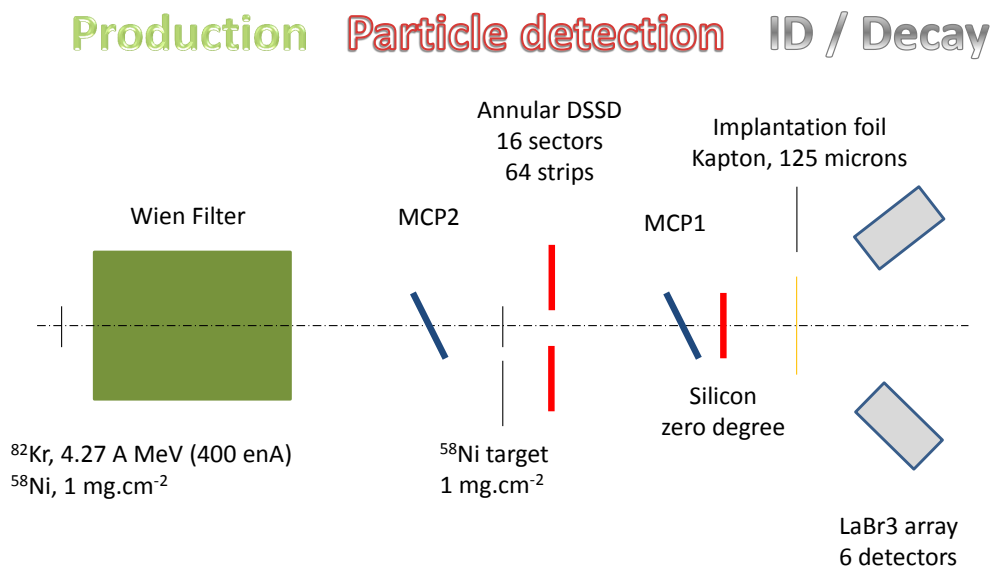

Figure 1: Setup for the test experiment.

3. Results from test experiment

3.1. Rejection of primary beam/transmission of products

We did not manage to reject sufficiently the primary beam while transmitting the fusion residues.

During the test, we encountered issues to align the beam in the LISE beam line, upstream and inside the WF. After optics measurements performed after the test, it appeared that quadrupoles upstream the Wien Filter were dis-aligned by some millimeters. A PPAC was also off centered. We believe that these misalignments were responsible of our experimental difficulties to transmit the fusion products and reject the primary beam with the Wien Filter.

To identify the primary beam and transmission of ERs a silicon detector at zero degrees was used together with a time of flight measurement between the two MCP detectors. This identification is shown in figure 2. As the effective area of the zero degree silicon detector is much smaller than that of the two MCP detectors, there is a large fraction of events that has a zero

energy. In figure 2 a gate used to estimate the number of ERs is shown. Everything outside this gate is considered to be scattered primary beam.

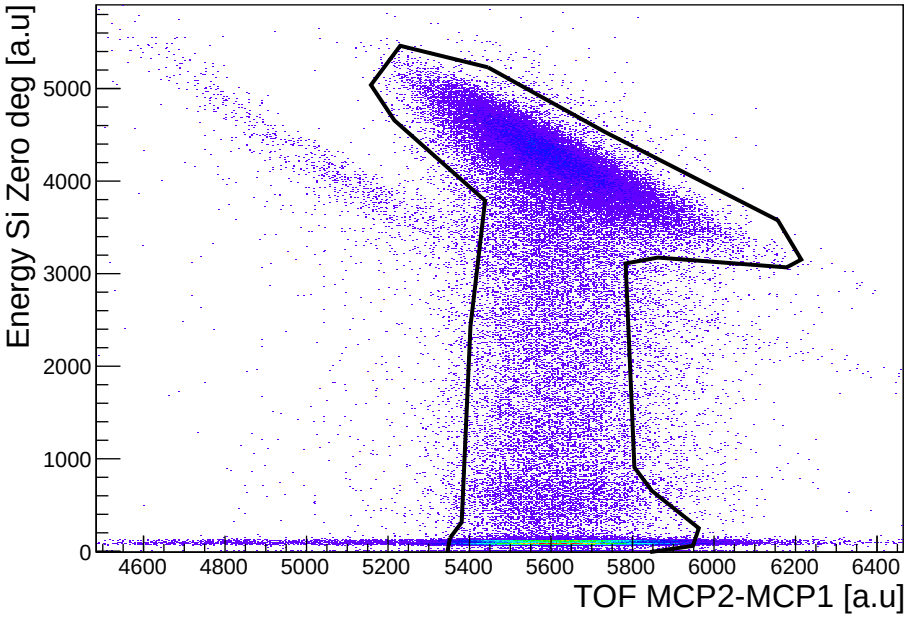

Figure 2: Identification of evaporation residues using in beam Si detector. Everything inside the black gate is considered to be ERs. A band corresponding to scattered beam can clearly be seen lower in energy as compared to the ERs.

It was not possible to get a decent ^{136}Sm transmission when the primary beam is fully rejected.

3.2. Count rates in Si detector

One limiting factor for the experiment is the amount of scattered primary beam that will hit the DSSD detector used for the Coulomb excitation. A large amount of time was used during the experiment to try to optimize, i.e. minimize, the count rate in the DSSD. These measurements were of course affected by the previously mentioned issues regarding the optics misalignment.

In figure 3 the hit pattern in the DSSD is shown together with the hit pattern in MCP2, without or with one of two different gates on the position in the DSSD. Gate 1 is interpreted as being fusion evaporation residues, whereas gate 2 is thought to be scattered beam. This data was taken with a primary beam intensity of 100 nAe and the DSSD trigger rate was 1500 Hz, with the most hit strip counting at 300 Hz. As can be seen they are physically separated. However, the situation shown in figure 3 is the best compromise that we could find. In figure 4 the energy as measured in the DSSD is shown, both total and when gated with gate 1 or 2. The distinctly different energy distribution supports the interpretation of the two different structures seen in figure 3. To further investigate the origin of the two structures seen in both figure 3 and 4 data that was taken without a secondary Coulomb excitation target was also analysed. In figure 5(a) the hit pattern on the Spider Si is shown, indicating a weaker scattered primary beam component. This can also be seen in the Spider energy spectra shown in figure 5(b). This suggest a large fraction of the scattered primary beam comes from interactions with the secondary target or its frame.

These results illustrate that we have difficulties producing an experimental condition that allows the use a primary beam intensity that is high enough. Again, these problems are believed to be a result from the alignment problems mentioned in section 3.1.

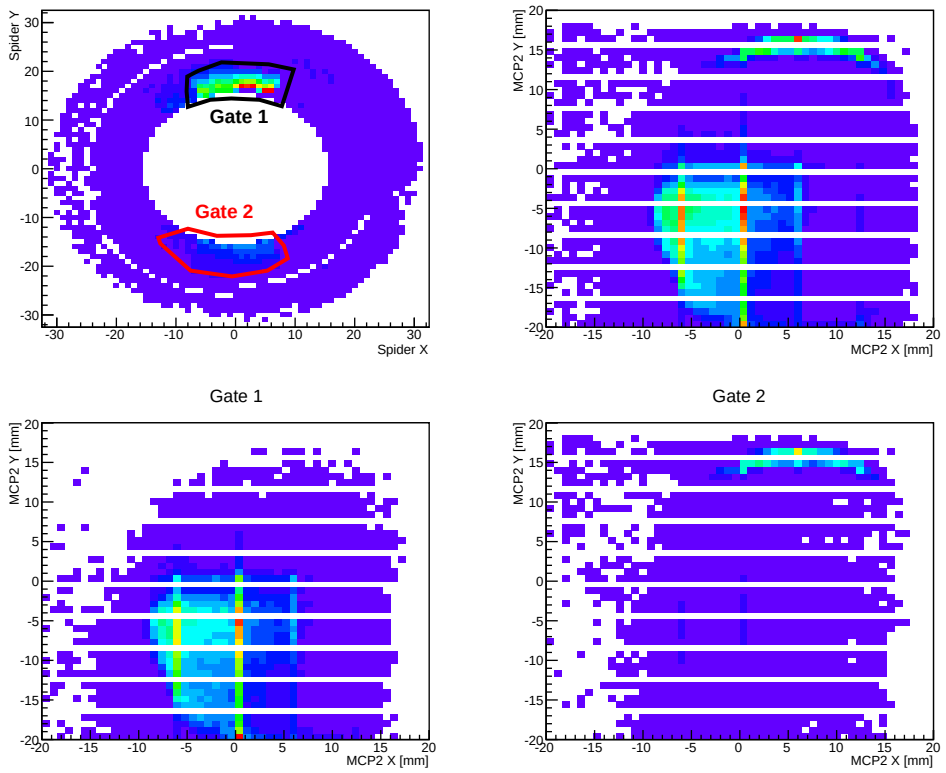

Figure 3: Hit pattern in Spider Si detector and MCP detector 2 (before secondary target). The two lower figures show the hit pattern of MCP2 with gate 1 (left) and gate 2 (right).

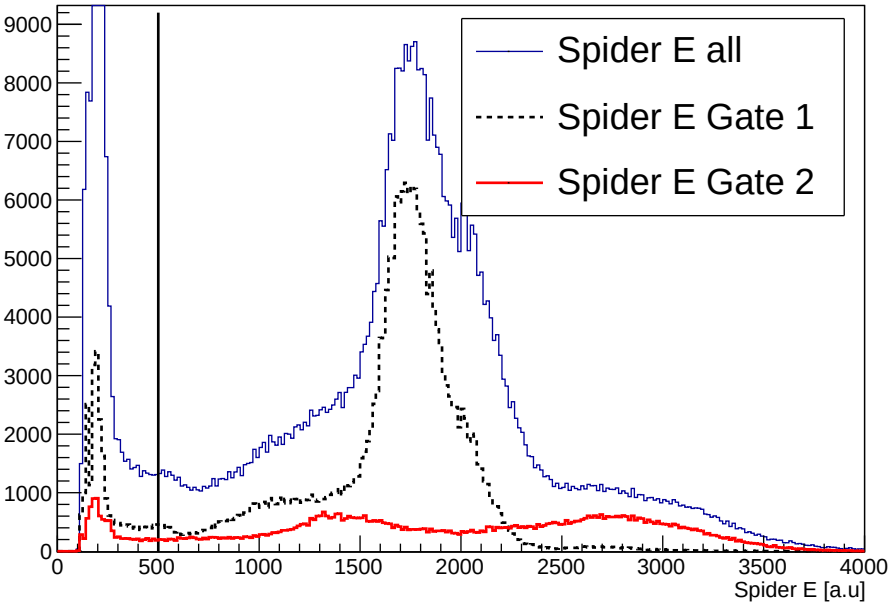

Figure 4: Particle energy as measured by the Spider Si detector. The vertical line indicates the gate used when looking at events in the Spider and MCP 2 detectors. For the meaning of gate 1 and gate 2, see text and figure 3.

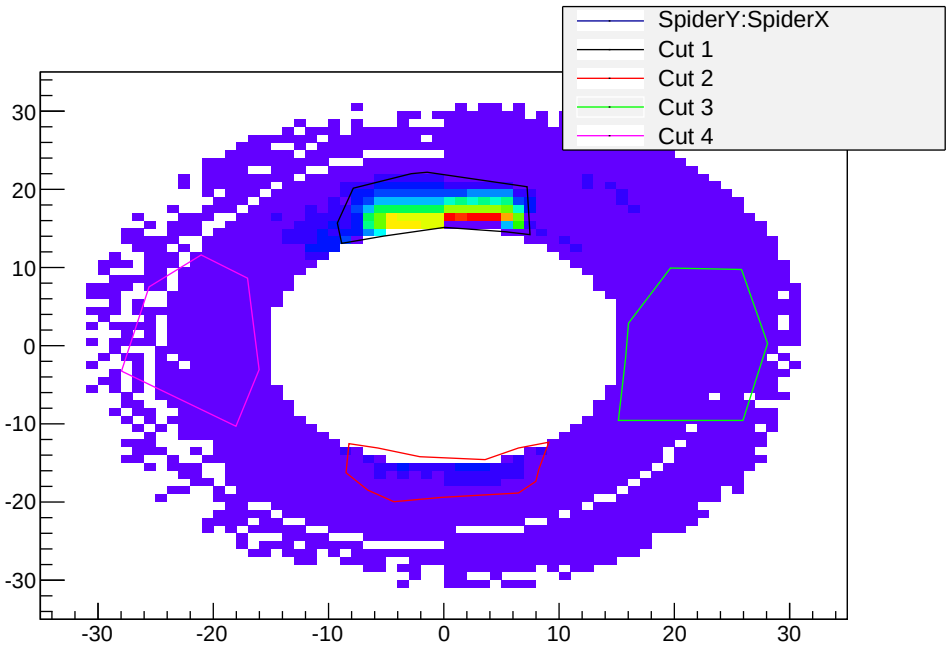

(a) Hit pattern Spider Si without secondary target

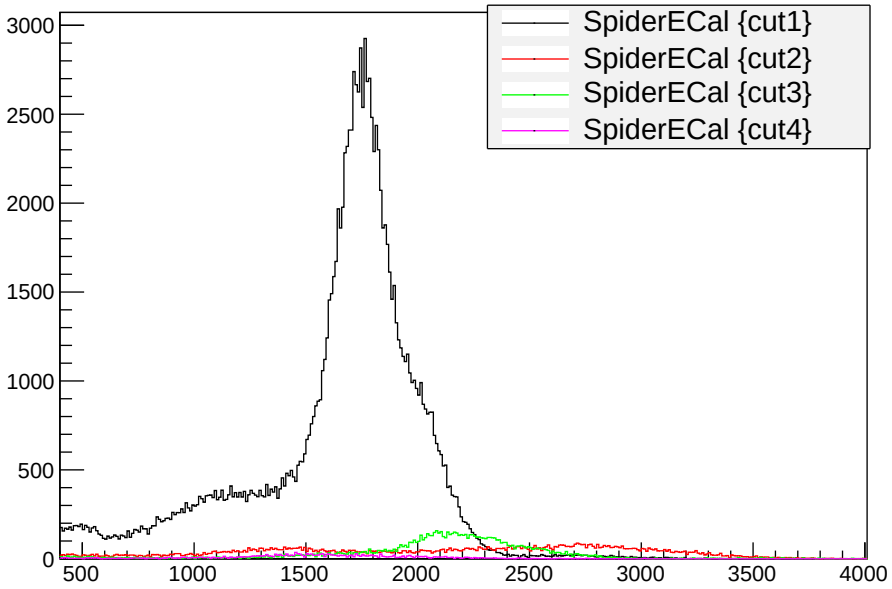

(b) Energy in Spider Si for different regions, see figure 5(a).

3.3. Confirmation of the production of ^{136}Sm

To make sure that we produced ^{136}Sm during the experiment, ^{136}Sm data was taken with and without primary beam in cycles of 10 minutes, corresponding to more than 10 halflives for ^{136}Sm. During the off-beam periods γ rays form the decays were detected using six $LaBr_3$ detectors. In figure 5 the decay chain of ^{136}Sm is shown. Apart form being an ER, ^{136}Pm is also populated from the decay of ^{136}Sm, and it is the 114 keV line from this decay that is used to identify the ^{136}Sm ions.

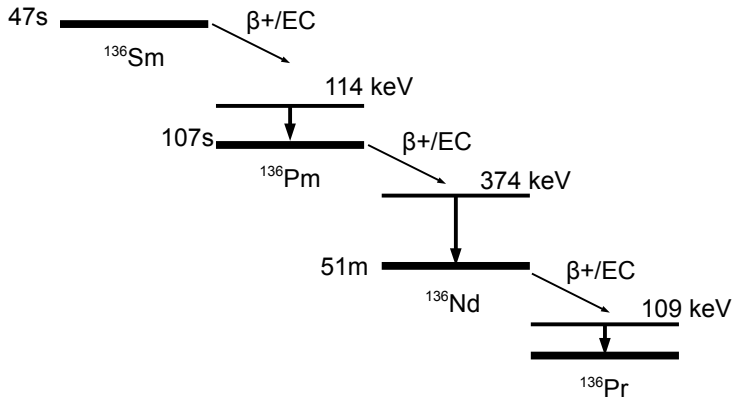

Figure 5: Decay scheme for the A=136 Isobars produced directly and via β decay.

In figure 6(a) the energy spectrum from $Labr_3$ detectors is shown, clearly showing a strong peak at about 110 keV, and at 374 keV. The peak at 110 keV is a convolution of the 109 keV line from the decay of ^{136}Pm and the 114 keV line from the decay of ^{136}Sm.

In order to identify and quantify the nuclei decaying the detected γ rays were binned in time bins of 20 s and put into histograms and the 109, 114, and 374 keV γ-ray lines were fitted, as shown in figures 6(b) and 6(c).

In figure 6 the number of counts per 20 s as function of time is shown for the 109, 114, and 375 keV γ-ray lines. The result is corrected for the difference in efficiency. Also shown are the solutions of the so-called Bateman equation with lifetimes taken from literature, but with the number of ions at $t = 0$

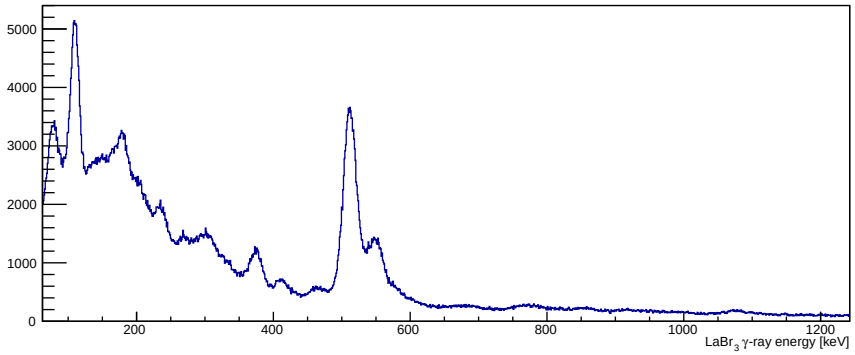

(a) γ-ray energy spectrum for the $LaBr_3$ detectors.

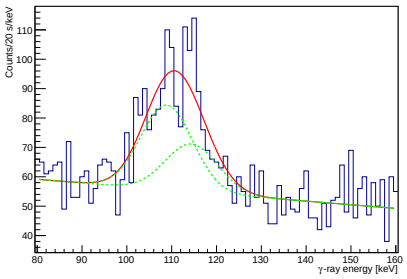

(b) Fit of the 109 and 114 keV γ-ray lines from the β decay of ^{136}Nd and ^{136}Sm, respectively

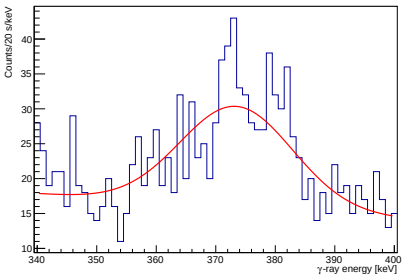

(c) Fit of the 374 keV γ-ray lines from the β decay of ^{136}Pm.

fitted. It is clear that production of ^{136}Sm and ^{136}Pm are comparable, in line with the result form PACE4 calculations.

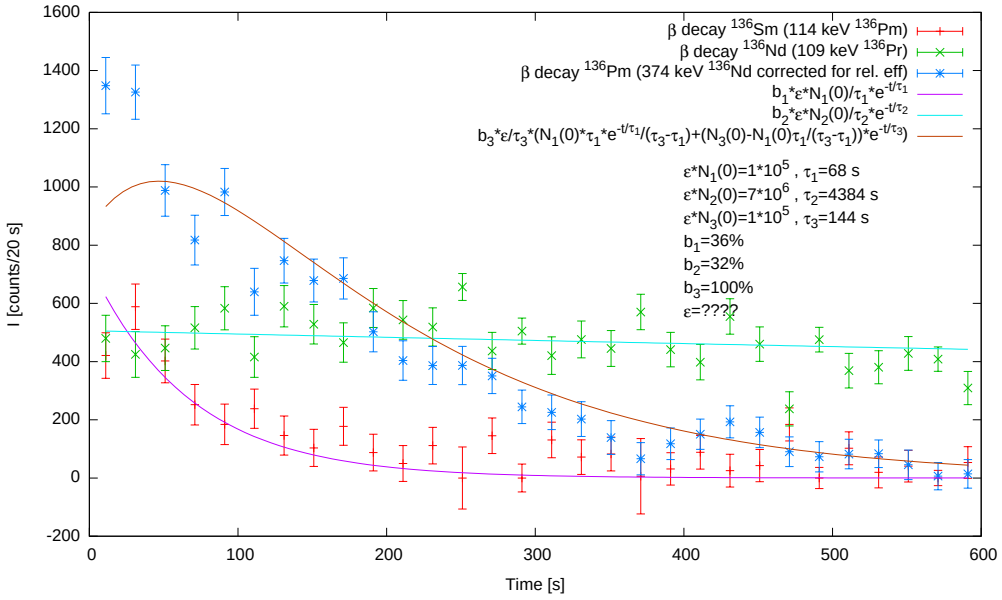

Figure 6: Decay curves for ^{136}Sm, ^{136}Nd, and ^{136}Pm taken after a cycle of beam off/beam on, each part for a period of 10 min.

4. Conclusions

The test performed in July 2012 at GANIL was performed, allowing to answer some of the initial questions relative to the feasibility of the experiment. With regard to the initial questions prompting the test experiment the following conclusions have been drawn:

4.1. Primary beam rejection.

non-conclusive.

4.2. Transmission of evaporation residues.

non-conclusive.

4.3. Relative production of ^{136}Sm.

The relative production of ^{136}Sm with respect to other ERs are in line with the estimates used in the proposal.

4.4. Identification of ^{136}Sm.

The gamma 114-keV line to identify ^{136}Sm has been seen and could be separated from the 109 keV line coming from ^{109}Nd as a function of time. For the physics experiment, high-resolution Ge detectors should be used for clean separation. **The physics experiment requests EXOGAM for both prompt and decay gamma spectroscopy**.

4.5. Comparison with ISOLDE

We would like to raise that the present physics case, given as a test case to prove the feasibility and power of the technique, is feasible at ISOLDE from recent beam developments of light Sm. The yield of ^{136}Sm has not been measured but Thierry Stora from CERN estimates from recent developments for another coulex experiment on light Sm nuclei (spokesperson: A. Görgen) that the yield of ^{136}Sm should be around 200 pps. Upgrades may be possible from 2017-2018. **The expected yields with the fusion technique proposed in our measurement exceeds CERN's estimates by a factor of 100 and is therefore competitive for the ^{136}Sm case.**

4.6. Nutshell conclusions

The E614 experiment should be feasible with the allowed beam time if the beam rejection and residue transmission is achieved. We think proper working conditions could be reached with the re-alignment of the optical elements of LISE performed since September 2012. A new test should be performed.

9.2.2 The E614 experiment

During the spring of 2013 the experimental setup was prepared at GANIL. At the same time extensive calculations for LISE in terms of production and transmission to the secondary target points were made by members in the E614 collaboration. In figure 9.1 a drawing of the used setup is shown. The LISE Wien filter (not shown) is to the right of the figure. This is from from where the evaporation residues arrive. They pass by the first MCP detector, impinge on the secondary target from where they either scatter or continue through the second MCP and are caught in the catcher foil in order to be counted using the 114 keV γ ray from β decay. Just after the target the double sided Silicon detector (referred to as Spider DSSD) was mounted to detect scattered ions. The idea was to detect γ rays from Coulomb excitation with a triple coincidence between the first MCP, the DSSD, and one of the EXOGAM detectors mounted close to the secondary target. By stopping and detecting the β decay downstream target an absolute number of ions on target was to be determined and with it the Coulex cross section and hence the electromagnetic matrix elements. In figure 9.2 and figure 9.3 photos of the setup are shown. Finally is the experimental setup as modeled in geant4 for simulations shown in figure 9.4.

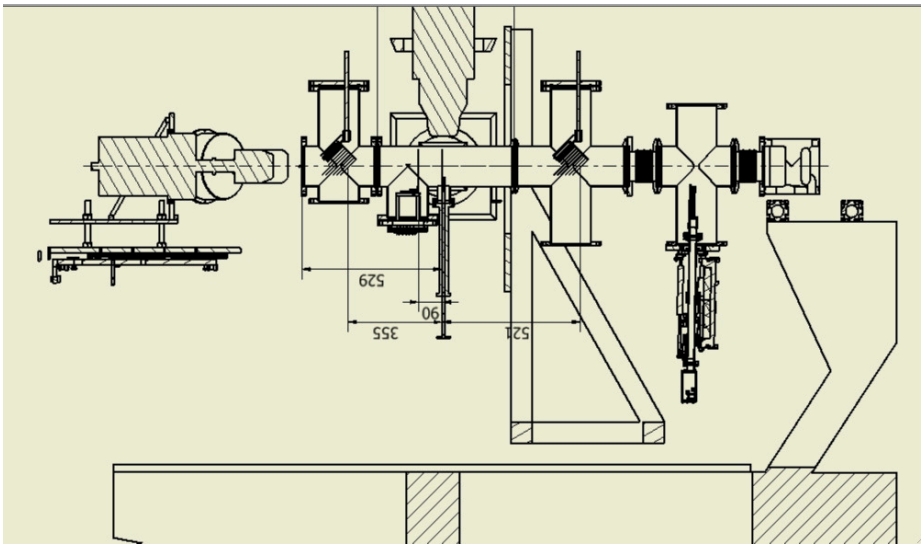

Figure 9.1: Drawing of the E614 experimental setup

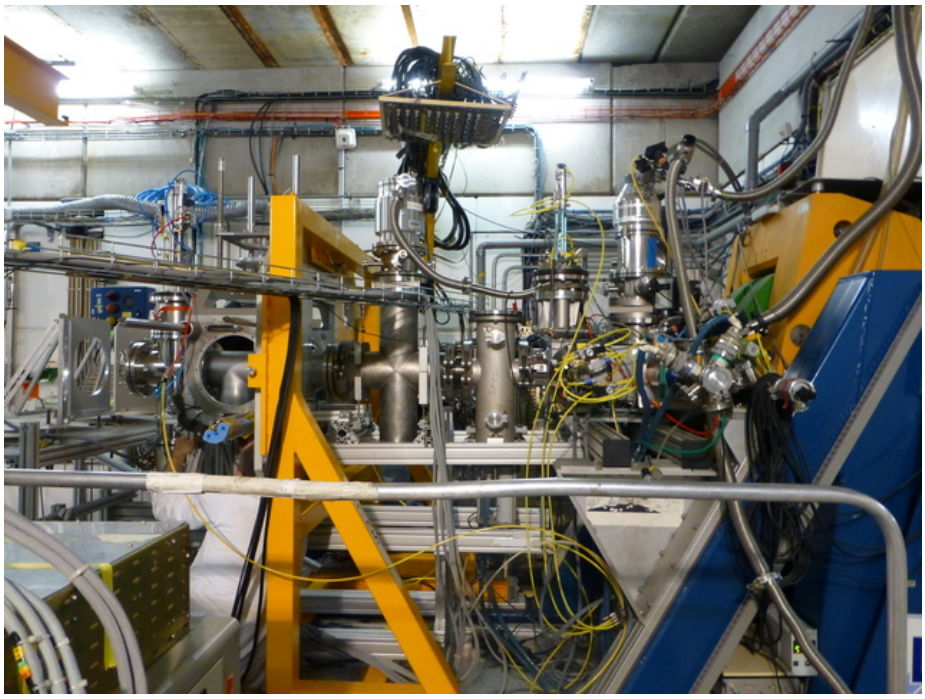

Figure 9.2: Photos of the experimental setup for E614 without the HPGe detectors.

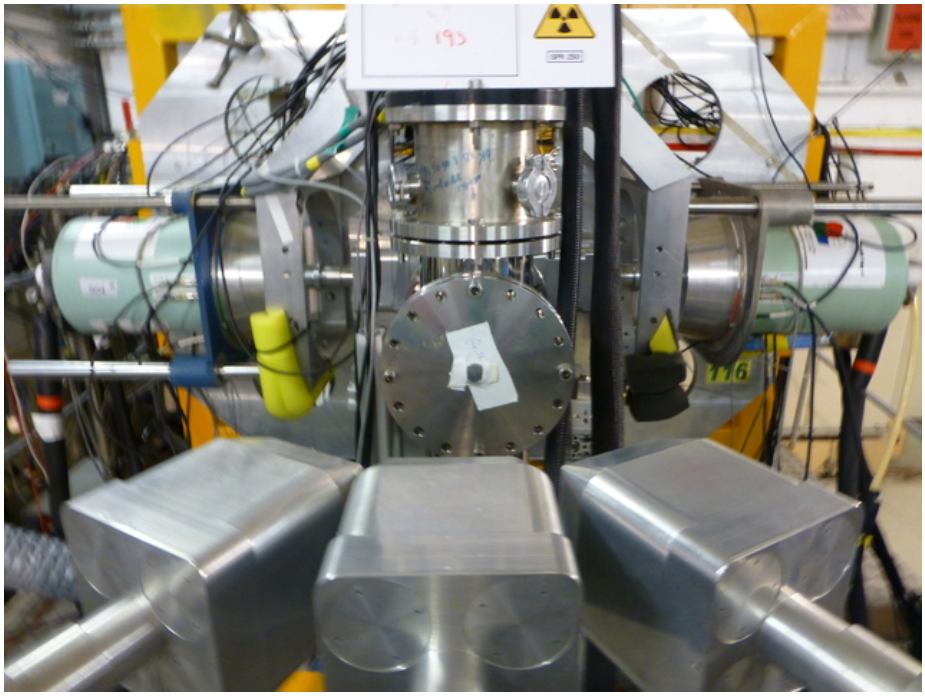

Figure 9.3: Photos of EXOGAM HPGe detectors used in the E614 experiment

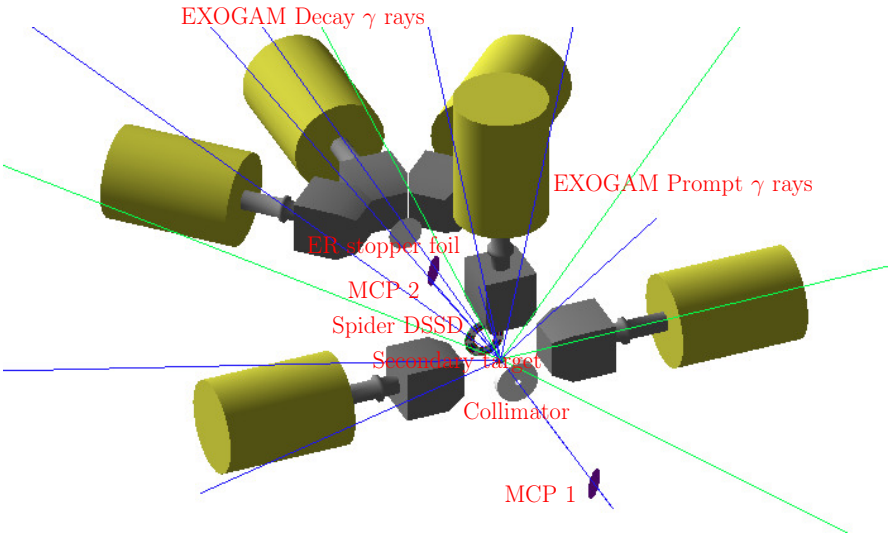

Figure 9.4: The experimental setup as modelled in geant4 simulations.

The experiment proved to be very complicated. Achieving good transmission of the fusion-evaporation residues combined with good rejection of the primary beam was very difficult. There were however ^{136}Sm seen in the β-decay spectra. It was believed during the experiment that one of the problems we had was the bad quality of "secondary beam" as it impinged on the secondary target, adding not only to the ambient background from β decay but also making the kinematical selection in the DSSD complicated. To improve the situation a collimator was added upstream the secondary target (shown in figure 9.4).

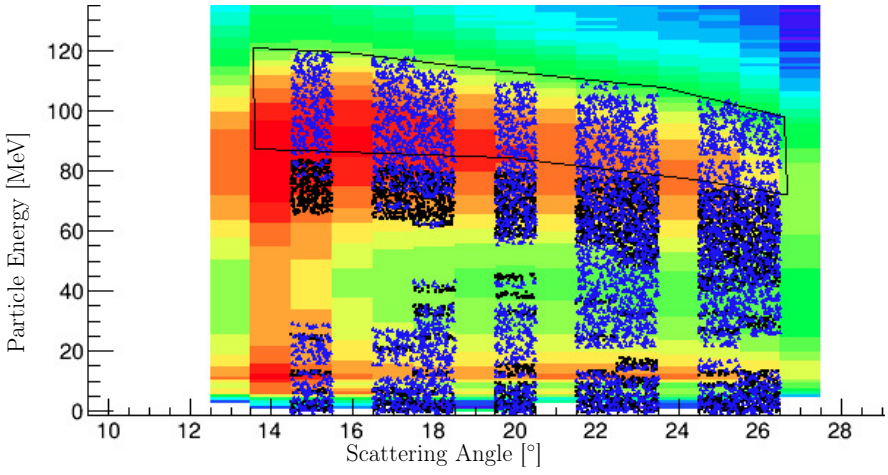

Figure 9.5: Experimental scattered partcile energy vs angle with simulations of scattered ^{136}Sm (blue triangles) and ^{72}Kr (black triangles). The cut made to try to select ^{136}Sm events is also shown.

In figure 9.5 the ion-energy vs scattering angle, as detected in the Spider DSSD,

is shown. It is overlaid with simulated distributions of scattered fusion-evaporation reaction products (blue triangles) and non-rejected primary beam of the same velocity (black triangles). Also shown is the gate used to select scattered secondary beam.

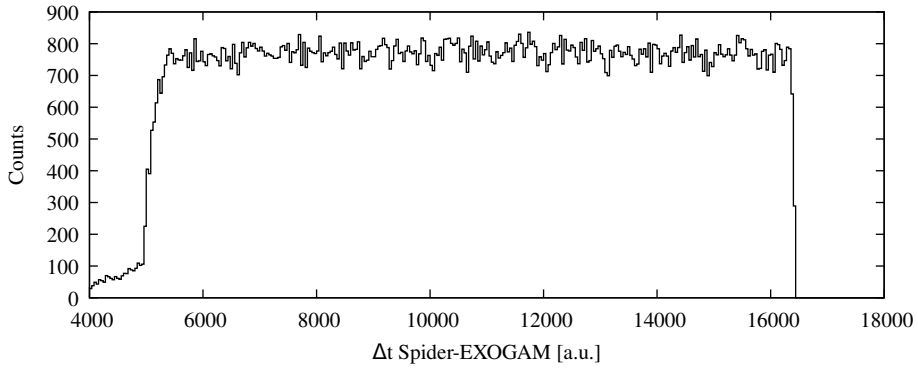

Figure 9.6: TAC spectrum between Spider Particle detector and HPGe EXOGAM for prompt γ rays. The prompt peak (very weak) is between channel 10240 and channel 10630. The spectrum is in coincidence with the gate shown in figure 9.5. The full range is 2 μs.

Using this gate the time-difference between ions detected in the Spider detector and γ rays detected in the EXOGAM detectors close to the secondary target can be made. This time difference is shown as a spectrum in figure 9.6. The absence of a clear prompt peak is flagrant. However, using the peak of the $2_1^+ \rightarrow 0_1^+$ transition in the non-rejected primary beam one can deduce that there is a prompt peak. Using this peak the γ-ray spectra shown in figure 9.7 are produced. Overlaid on the background subtracted prompt spectrum is a simulation (described further down in this text) of the spectra from the $2_1^+ \rightarrow 0_1^+$ in ^{136}Sm if produced by Coulomb excitation on the secondary target. The rather obvious conclusion is that we saw no Coulomb excited ^{136}Sm in the experiment.

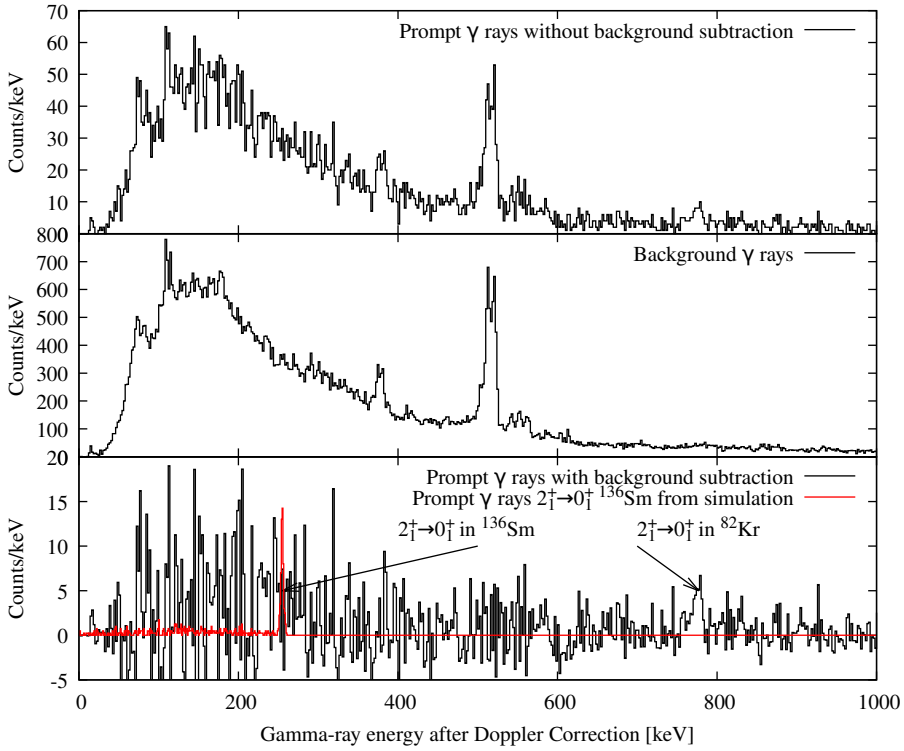

Figure 9.7: E614 γ rays. After background subtraction (in time domain) the only visible γ ray is the deexcitation of the 2_1^+ state in the primary beam ^{82}Kr. A Geant4 simulation of Coulomb excitation of the 2_1^+ state in ^{136}Sm is also shown as a reference. For the simulations see text for details.

In figure 9.8 are shown spectra taken by the EXOGAM detectors placed at the catcher foil. After the primary beam was stopped, data was collected for one minute in order to see the γ rays from the decay products and to measure the γ-ray peak intensities as a function of time to assure that the correct ion species were produced. The peak at 114 keV shows that ^{136}Sm was indeed produced and transported from the primary target to the secondary target (the direct production of more neutron deficient isobars form the ^{140}Gd compound nuclei is much smaller). However, as no prompt Coulomb excitation peak from ^{136}Sm could be seen no efforts were made to quantify the production of ^{136}Sm.

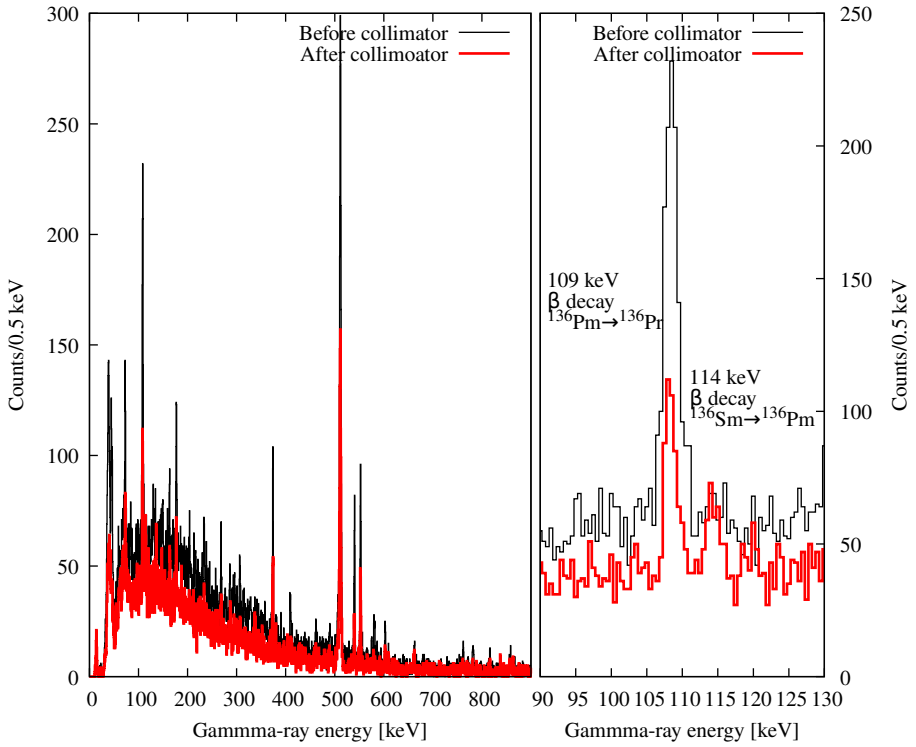

Figure 9.8: Gamma-ray spectra from the decay station. Data taken during 60 s directly after that the primary beam was stopped. Spectra shown before and after a collimation of the secondary beam was introduced upstream the secondary target.

A sophisticated simulation package based on the geant4 code of AGATA [233] was created in order to simulate the experiment. The geometry of the experiment and an event generator was written as add-on libraries that can be used at execution time of the AGATA code (i.e. can be used without modifying the AGATA code). The event generator includes a simple ^{136}Sm beam to simulate the most idealized case of a pure secondary beam with good beam optics. This mode was used to produce the simulated spectrum in figure 9.7. It also includes a mode simulating the cocktail beam of fusion evaporation products with beam optics as given by the calculations used to estimate transmission and rejection of the LISE Wien filter. In order to estimate the background from β decaying nuclei the simulations are keeping track of the "wall clock" time. The time structure of the beam is also simulated. This is done by creating a large number of files (~50000), each file corresponding to a time slice of 15 s. Each interaction in an event is then written to the corresponding file on disk. All events in each time slice can then be time sorted and events can be created by reading the files in time order. These simulations are time consuming, on a single Intel(R) Xeon(R) CPU E5-2609 0 @ 2.40GHz CPU core about 500 events per second could be simulated, to be compared to the about 75000 pps assumed in "the experiment" - one second of experiment takes 2 minutes to simulate. The build up of activity in the simulations can clearly be seen in the counts per seconds in the EXOGAM detectors as function of time shown in figure 9.9.

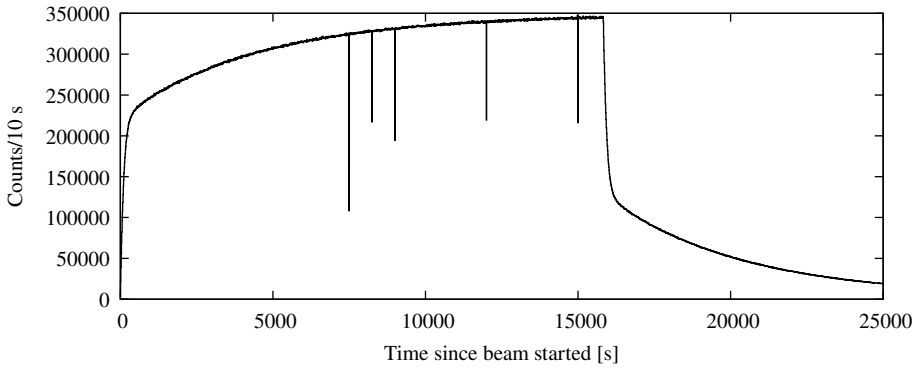

Figure 9.9: Number of counts per 10 seconds in the EXOGAM detectors as a function of beam time. The build up of activity is clearly shown as well as the decay after the stop of the beam in the simulations (after around 15000 s). The spikes are from some minor issues chaining root files.

Using simulated data corresponding to about one hour of experiment the time difference between scattered ions and γ rays in the EXOGAM detectors close to the secondary targets was made. The spectrum is shown in the upper panel of figure 9.10. It has a large resemblance with the experimental spectrum shown in figure 9.6. Also shown, from simulations including the Coulomb excitation of ^{136}Sm, the expected number of counts in the prompt peak. The γ-ray spectra for the two simulations are compared in the lower panel. The simulations shows that if the assumptions that went into the simulations, i.e. our best estimates before the experiment, would have been correct we could have seen the $2_1^+ \rightarrow 0_1^+$ γ ray in ^{136}Sm. However, the time resolution in the simulations (coming form the time binning used to create the histograms) were 8 ns, better than is expected from the experimental setup for γ rays at 255 keV. This is a possible explanation to the non observation in the experiment.

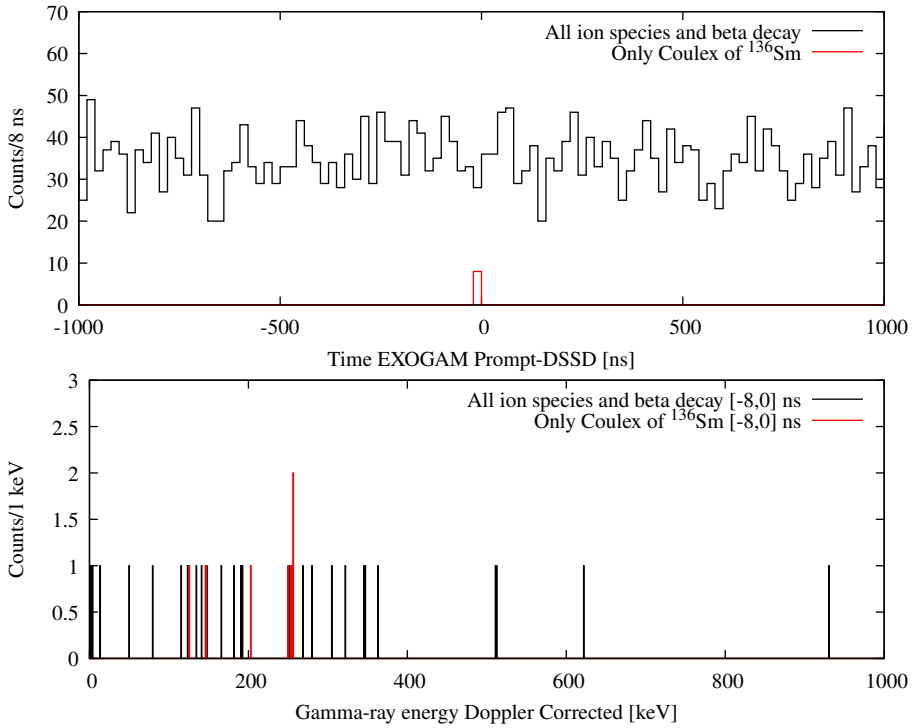

Figure 9.10: Upper panel: Simulated TAC between prompt γ rays and ions in the DSSD detector for simulations of all ion species and including β decay events (black) and only simulating the Coulex excitation events (red). Lower panel: Corresponding Dopper corrected γ-ray spectra when putting a condition on promp coincidences corresponding to the interval [-8,0] ns.

The simulated decay spectra are shown in figure 9.10, with shapes that are not very close to the experimental ones shown in figure 9.8. On the right panel in figure 9.10 the scaled experimental decay spectrum is also included. Apart from a missing peak, suggesting that the simulated cocktail is not correct, the intensity of the 114 keV line coming from the decay of ^{136}Sm is much smaller in the experimental data. This is the major part of the explanation of why we were not able to see any Coulomb exaction of ^{136}Sm in the experiment - the signal to noise ratio was just too low.

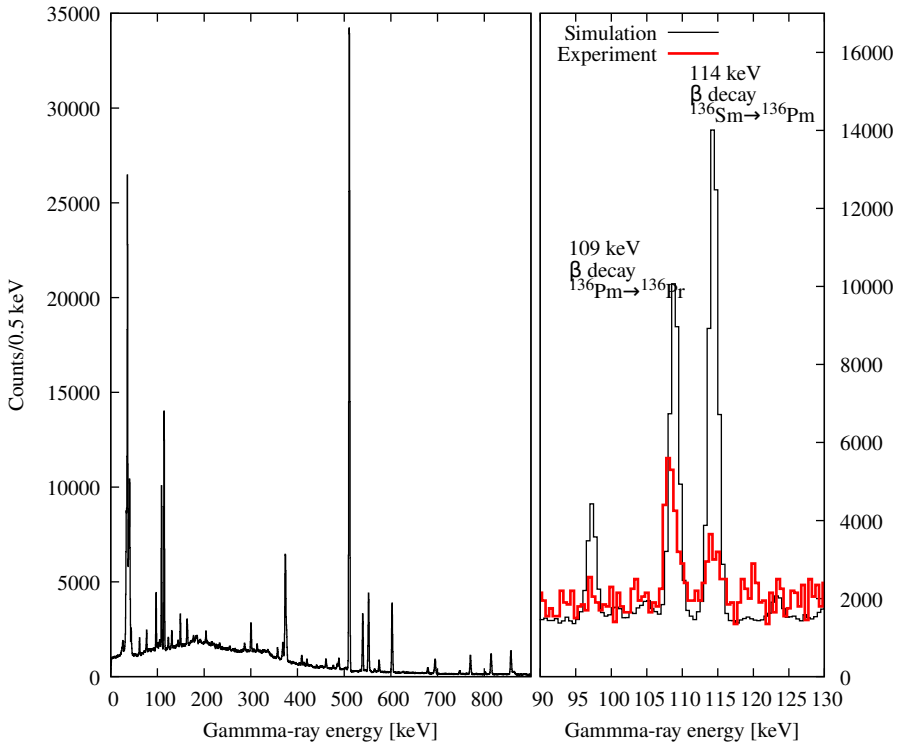

Figure 9.11: Simulated decay spectra. In the zoom on the decay of ^{136}Sm and ^{136}Pm the scaled experimental spectrum is also shown (in red). It is clear that in the experimental data the ratio of ^{136}Sm to everything else is much lower.

Chapter 10

Lifetime measurements using the RDDS method after incomplete fusion

10.1 Proposal (as sent to the ALTO PAC)

TANDEM-ALTO
PROPOSAL FOR EXPERIMENT

PAC session :	EXP # (Do not fill in):
February 2013	

Title**: Lifetime measurements using the RDDS method after incomplete fusion**

Is it a follow up experiment? [Yes/No]: No If yes, experiment number:

Spokespersons (if several, please use capital letters to indicate the name of the contact person):
A. GOASDUFF, J. Ljungvall

Address of the contact person:CSNSM, bat. 108, 91405 Orsay – Campus, France

Phone:+33 169154564	Fax:	E-mail:alain.goasduff@csnsm.in2p3.fr

Address of a backup contact person:

Phone:+33169155528	Fax:	E-mail:joa.ljungvall@csnsm.in2p3.fr

Other Participants or Organisations:
G. Georgiev, Th. Konstaninopoulus, C. Sotty, CSNSM
S. Franchoo, I. Matea, M. Niikura, I. Stefan, D. Verney, IPN Orsay
A. Kusoglu – University of Istanbul, Turkeu
A. Blazhev, IKP Cologne
A. Gengelbacb, J. Nyberg, Uppsala University
M.-D. Salsac, IRFU CEA Saclay
E. Clément, GANIL

Short abstract:

We propose to measure the lifetimes of exicted states in 71,72Zn using the RDDS method. The nuclei of interest will be populated using the reaction 7Li(70Zn,alphaxpyn), which we believe that the channels we will study will be produced mainly by incomplete fusion followed by particle evaporation. Particle transfer will also contribute to the cross sections. The experiment should allow us develop the use of incomplete fusion reaction together with the RDDS technique as a part of the preparation for future high-intensity radioactive beams. We should also be able to extract information on the interplay between collective and single particle degrees of freedom close to 68Ni.

Go to Page 2 →

Beam line (010, 110/PARRNe, 210, 320, 410, 420, 510.)**:**	420

Devices needed:	PARRNe		Bacchus		OSCAR		DIESE X		AGAT					
(mark with an **X**)	Split Pole		ORGAM	X	DIESE		ESKIMO							
Other devices (specify):														

Fill in completely:	**Ion(s)**	**Energy (MeV)**	**Intensity (nAe or pps)**	**UT/beam**	**Pulsed beam (yes/no If yes specify time structure)**
Tandem beam(s)	1.70Zn 2. 3.	**190**	10^{10}pps	15	no
ALTO beam(s)	1. 2. 3.				
ALTO source	1. 2.				

Fill in completely:	**Element / compound**	**Target manufacturer**	
		IPN[1]	other[2]
Targets	**7Li – in what form to be decided**		

TOTAL number of beam UTs Requested: (1 UT=8 hours):	Time (UTs) required for setting up the apparatus: Time (UTs) needed for off-beam calibration and dismounting:

Acquisition system: (mark with an **X**)	Tandem		COMET		other	X								
If other please specify:														

SAFETY:	list any hazardous equipment or substances to be used, such as. radioactive target, liquid nitrogen, explosive gas, etc.,:

New devices:	List any NEW devices needed for this experiment which still have to be bought or manufactured:
Liquid Nitrogen for HPGe filling	
At what date do you expect these to be available?	

Go to Page 3 →

[1] Please contact as soon as possible IPN target lab : petitbon@ipno.in2p3.fr
[2] Please specify if empty target frames at Tandem standard are requested

Special devices:	List any special devices needed for this experiment which would require to be mounted prior to the experiment (special target chambers, detector arrays, etc.):
Oups plunger	
How long will it take to mount the particular device(s) once the area is available to you?2 days	

Status of previous Tandem/ALTO experiments:	Give the status of previous experiment(s) made by this group in the last 3 years at Tandem/ALTO: e.g. results from or status of analysis of previous experiments at Tandem/ALTO, list publications, conference presentations, PhDs awarded etc :
ISI13 – "Test experiment for the CSNSM/IPNO/GANIL Plunger", published NIM A N-SI-48, being analyzed N-SI-50 - "Probing the boundary of shape coexistence south of Z=82: Lifetime measurements of excited states in ^{170}Os using the RDDS method", being analyzed	

Additional comments:	

Lifetime measurements using the RDDS method after incomplete fusion.

Abstract

We propose to measure the lifetimes of exicted states in ^{71,72}Zn using the RDDS method. The nuclei of interest will be populated using the reaction ^{7}Li(^{70}Zn,αxpyn), which we believe that the channels we will study will be produced mainly by incomplete fusion followed by particle evaporation. Particle transfer will also contribute to the cross sections. The experiment should allow us develop the use of incomplete fusion reaction together with the RDDS technique as a part of the preparation for future high-intensity radioactive beams. We should also be able to extract information on the interplay between collective and single particle degrees of freedom close to ^{68}Ni.

1 Introduction

Large resources are presently invested into radioactive beam facilities around the world, with several such facilities already running and even more coming online in the decade to come. These radioactive beams will allow us to investigate excited states in nuclei that we hitherto have not been able to reach using combinations of stable targets and beams. Typical examples would be reactions with neutron-rich nickel or tin isotopes.

Model independent determination of electromagnetic transition probabilities has proved to be a very stringent test of nuclear structure models. As such it is important that the spectroscopy of poorly or completely unknown nuclei is not limited to that of the energy of excited states but that methods developed with stable targets and beams are transposed into the environment of radioactive beams. One of the most precise and reliable technique to measure lifetimes in the picosecond range is the Recoil Distance Doppler Shift method (RDDS), also known as the plunger method. For this reason its use has been extended from the classical fusion-evaporation reactions to be used with several other production mechanisms such as multi-nucleon transfer[1], Coulomb excitation[2, 3] and induced fission reactions, often in inverse kinematics to be able to work with the expected target-beam combinations that are foreseen at the radioactive beam facilities. To the best of our knowledge, incomplete fusion reactions to reach neutron-rich nuclei using inverse kinematics have not yet been used togther with the RDDS technique and ^{7}Li target. Therefore there is an intereset to develop this technique to widen the palette

of possible reaction mechanisms avaible at future radioactive beam facilities. Incomplete fusion reactions using ^{7}Li have attracted a lot of attention in recent years for populating high-spin states in moderatly neutron-rich nuclei[4, 5, 6, 7, 8, 9].

Using the combined target-beam planned for this proposal we expect to populate reaction channels such as αxn and αpxn with cross sections in the order of 1-2 mb, leading to slightly neutron-rich nuclei such as ^{71,72}Zn. Lifetime measurements from this experiment can complement a fast-timing experiment performed in Bucharest 2010[10].

The neutron-rich even zinc isotopes are also of interest in the light of the increasing collectivity that has been noted as protons are removed from ^{68}Ni, i.e. in moderately neutron-rich iron nuclei[11, 12], indicating a softness of the Z= 28 proton shell closure, but more importantly showing the importance of the νd$_{5/2}$ orbital for the development of collectivity in the region. It is of interest to see if the role of the νd$_{5/2}$ neutrons remains important on the other side of the proton shell-gap, i.e., for the zinc isotopes. Although several recent experiments have addressed this region conflicting results[13, 14] suggesting different structural interpretations motivates further measurements using different reaction mechanisms to populate the states of interests.

2 Goals of the experiment

The goal of the experiment is two fold:

- Development of the use of incomplete fusion reaction in inverse kinematics for RDDS measurements.
- To measure the lifetimes of exicted states in ^{71}Zn, and possible remeasure the $2_1^+, 4_1^+$ in ^{72}Zn using an alternative reaction mechanism to populate the states.
- Determine, with obvious experimental uncertainties, the different production cross sections.

3 Proposed experiment

3.1 Experimental details

We are proposing the reaction ^{7}Li(^{70}Zn,αxpyn) with a beam energy of 190 MeV (10% higher than the Coulomb barrier) to populate excited states in Ga and Zn isotopes via incomplete fusion (higher Z nuclei will also be populated via xn channels from complete fusion and will be the dominating channels). We will use the Orgam array consisting of 30 Compton suppressed HPGe detectors with a total efficiency of 3%. The Oups[15] will be used for the RDDS measurements. Particle detection is foreseen although an efficient way to detect alpha particles emitted during incomplete fusion is difficult due to their angular distribution which is shaded by the Plunger device[16]. We believe it is possible to detect α particles within the angular range $35^\circ \leq \theta_{lab} \leq 56^\circ$ using a segmented plastic detector available at CSNSM. Using a relatively low beam energy this detector

should be able to detect several tens of percent of the emitted α particles. We will use the plunger device together with a degrader foil rather than a stopper foil, this to allow a simple extrapolation to radioactive beams.

We will try to use both particle-γ, $\gamma\gamma$-, and particle-$\gamma\gamma$ coincidences to clean the spectra from the dominating background from fusion-evaporation reactions, where dominating channels are of xn type. Emitted α particles should also have lower energies.

In figure 1 γ-ray spectra for two different target-degrader distances are shown where ^{72}Zn has been populated either via a fusion-evaporation reaction or via $2n$ transfer. Although the kinematics of these two reaction are not exactly that of an incomplete fusion reaction, together they should give an idea of the separtion of γ-ray peaks that we can expect. A degrader of Mg has been used, this to allow the beam to exit the target area, an important feature for future use together with radioactive beams.

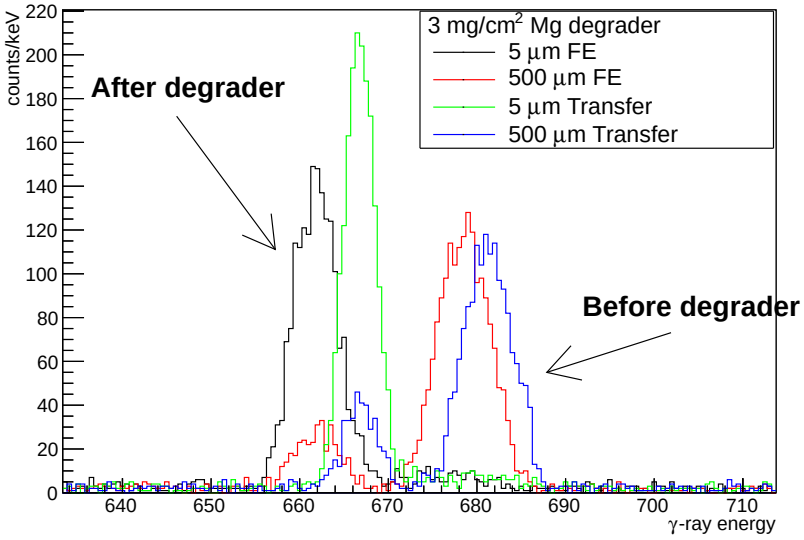

Figure 1: Gamma-ray spectra giving an idea of peak separation at $\theta = 46°$ for two limiting reaction mechnisms in the reaction ^{7}Li(^{70}Se,αp)^{72}Zn

3.2 Count-rate estimates

The count-rate estimate is done for 1 mb, the expected cross section for the population of ^{72}Zn. Assuming 1mg/cm^2 of ^{7}Li in the target and a beam intensity of 10^{10} particle per second gives a production rate of 100 ^{72}Zn/s. Given the efficiency of about 3% and the need for using $\gamma\gamma$ coincidences we can expect about 0.1 good events per second.

For particle-γ coincidences we should get a factor of about 5 more corresponding to a detection efficiency of about 15 for the particle detection that replaces the 3% of Orgam, giving about 1 good event per second.

For particle-$\gamma\gamma$ coincidences we can expect about 1 good event per minute for the ^{72}Zn reaction channel.

3.3 Technical difficulties to overcome

There is a set of technical issues that makes this experiment difficult to perform and requires additional investigations.

1. The target preparation: ^{7}Li is usually prepared as LiF target, but such a target can not be used in a RDDS measurement. A suitable target therefore has to be developed.
2. The large background from pure fusion-evaporation reactions might, despite using $\gamma\gamma$ gating, drown the small signals we are looking for. Hence the use of a charged particle detector is envisaged and it should be incorporated in the experimental setup. We plan to use a segmented plastic detector already existing at CSNSM. However, in order to cover as large angles as possible for the α particle detection some modifications of the Plunger-plastic detector setup is foreseen.

4 Beam-time request

The beam-time request is made on the basis of extracting a result for the lifetimes in ^{72}Zn. A statistical error of 5% would require at least 400 counts in each peak, or an optimistic 1000 good events. This suggest that we should envisage to measure each Plunger distance for at least 1000 minutes, giving about 24 hours per distance. In order to be able to judge the quality of a RDDS measurement there is a need for measuring points at distances covering both short, long, and distances covering the sensitive region. This can be done if at least 5 distances are measured. We therefore ask for a total of five days of beam time. **To summarize: We ask for a total of 15 UTs, i.e. five days of a ^{70}Zn beam at** 190 **MeV.**

References

[1] J. J. Valiente-Dobón *et al*, 2009 Phys. Rev. Lett. 102 242502

[2] A. Dewald *et al.*, Phys. Rev. C 78, 051302(R) (2008)

[3] W. Rother *et al.* Nucl. Instrum. Methods A 654, 196 (2011).

[4] G.D. Dracoulis *et al.* J. Phys. G:Nucl. Part. Phys. 23, 1191 (1997)

[5] S.M. Mullins *et al.*, Phys. Rev. C 61, 044315 (2000)

[6] A. Jungclaus *et al.*, Phys. Rev. C 67, 034302 (2003)

[7] R.M. Clark *et al.*, Phys. Rev. C 72, 054605 (2005)

[8] D.S. Judson *et al.*, Phys. Rev. C 76, 054306 (2007)

[9] H. Watanabe *et al.*, Phys. Rev. C 79, 024306 (2009)
[10] G. Georgiev, private communcation
[11] J. Ljungvall *et al.* Phys. Rev. C 81, 061301(R) (2010)
[12] W. Rother *et al.*, PRL 106, 022502 (2011)
[13] A. Obertelli, Private Communication.
[14] I. Celikovic, Zakopane 2012
[15] J. Ljungvall *et al.* Nucl. Instrum. Methods A 679, 61 (2012)
[16] B. Fornal, S. Leoni, *et al.* ISOLDE proposal

10.2 Experiment and outcome

The experimental setup was 17 HPGe detectors positioned in three rings at the angles 46.5°, 133.5°, and 157.7°. A segmented angular plastic detector downstream the target was used to detect the charged particles. This to have the γ-particle coincidence needed to select incomplete fusion in the background of fusion evaporation reaction channels.

10.2.1 Target issues

When the experiment was approved there was no clear decision taken on the target that was to be used. Based on experimentation at the target laboratory of IPN Orsay, the target used was finally a Li_2SO_4 target evaporated on a 0.8 mg/cm² Ni foil, with an uncertain thickness of the Li_2SO_4. Other failed attempts were

- Evaporation of LiF on 25 µm de Al : LiF attaches but Al too think for our measurement.
- Using Au (~ 2mg/cm2), the foils were destroyed or the LiF did not attach to the foil.
- Evaporation on Nd with a thickness 2 mg/cm2. The foils survived the evaporation but the LiF did not stick to the foils.

As a degrader a 5 mg/cm² Au foil was used.

10.2.2 Problems encountered during the experiment

There were some problems delivering the ^{70}Zn beam, making the effective time with beam on the target one day. Combined with problems with the Plunger feed back originating in the isolating qualities of the used Li_2SO_4 only data with long distances or with deliberate contact between the foils were taken.

10.2.3 Results and Conclusions

The experiment aimed at measuring lifetimes in ^{72}Zn populated via incomplete fusion. This in inverse kinematics to prepare for use with radioactive beams at, e.g., HEISOLDE, SPES or SPIRAL1/2 at GANIL. Without any particle-γ coincidence the γ-ray spectra are dominated by the Coulomb exaction of gold, nickel, and the ^{70}Zn beam. However, by demanding the prompt coincidence between the plastic detector and a HPGe detector (see figure 10.1), performing a background subtraction in time domain, and setting a gate on the energy detected in the plastic detector (see figure 10.2) γ-ray spectra containing reaction products are produced. As can be seen in figure 10.3 the spectra are dominated by fusion-evaporation products, in this case ^{72}Ga (106 keV, 165 keV, 393 keV...). Also shown in figure 10.3 are estimates of where γ rays from the first two excited states in ^{72}Zn should be seen. For the Ring 1, in the forward direction, the region of interest for the $2_1^+ \rightarrow 0_1^+$ transition (653 keV) is heavily contaminated with n,n' lines. However looking at ring 2 and ring 3, including the 847 keV from the $(4_1^+) \rightarrow 2_1^+$ transition a bit of imagination and there is some ^{72}Zn. It is however clear that in order to exploit the data a much better selection of events would have been needed.

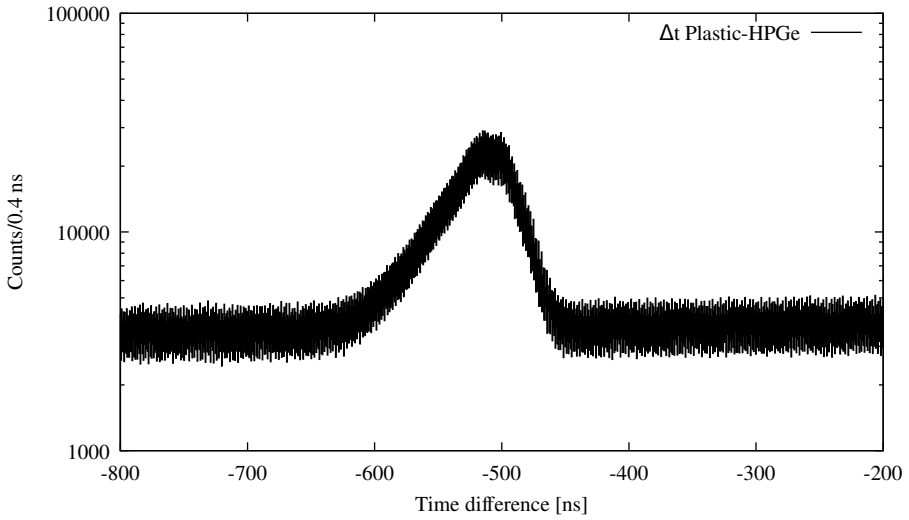

Figure 10.1: Time difference between anular plastic detector and HPGe detectors

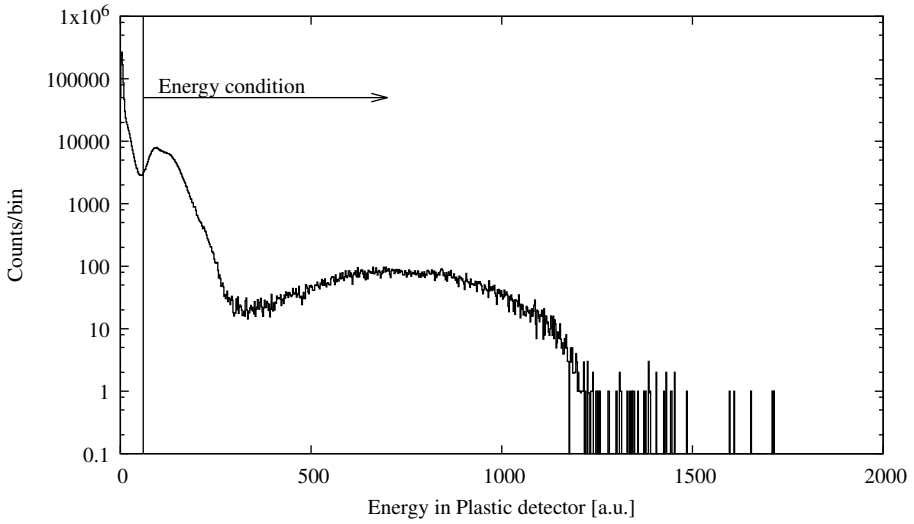

Figure 10.2: Energy spectrum for Plastic detector in coincidence with prompt γ rays.

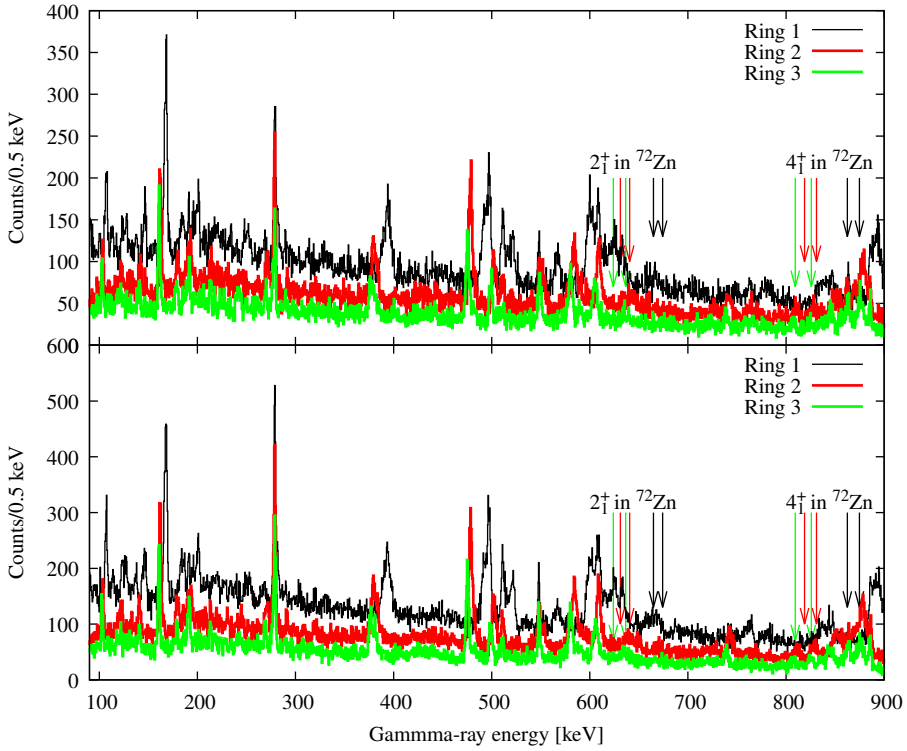

Figure 10.3: Gamma-ray spectra for two distances seprated by 750 μm. The arrows show the supposed location of the 2_1^+ and 4_1^+ in ^{72}Zn before and after the Au degrader, respectively. Although it is not excluded that the lines are present they are too week for lifetime analysis.

As to how to improve the selection, this would go in the path of measuring the full kinematics of the outgoing particles and having discrimination between protons and α in the particle detector. As for the reaction products that were populated at a level to make lifetime measurements possible, the limited number of distances taken with the beam time given made limited these possibilities.